25 Copies

NASA CONTRACTOR REPORT

NASA CR-66678-4

NASA CR-66678-4

MARS HARD LANDER CAPSULE STUDY

Volume III
Capsule Parametric Study

Prepared by
GENERAL ELECTRIC
RE-ENTRY SYSTEMS
for Langley Research Center

31 JULY 1968

NATIONAL AERONAUTICS AND SPACE ADMINISTRATION–WASHINGTON, D. C.

NASA CR-66678- 4

MARS HARD LANDER CAPSULE STUDY

Volume III
(Book #2)

CAPSULE PARAMETRIC STUDY

Issued by Originator as General Electric Document No. 68SD952-4 (Vol. III, Book 2)

PREPARED UNDER CONTRACT NO. NAS 1-8098 BY

GENERAL ELECTRIC
RE-ENTRY SYSTEMS
3198 Chestnut Street, Philadelphia, Pa. 19101

FOR
LANGLEY RESEARCH CENTER

NATIONAL AERONAUTICS & SPACE ADMINISTRATION

FOREWORD

The Mars "Hard Lander" Study Final Report is divided into four volumes and bound in eight books. The titles of the volumes and a brief description of the contents of each book are presented below.

VOLUME I - SUMMARY (CR-66678-1)

Volume I contains a summary of the study activity, the conclusions reached, and a description of a possible design implementation suggested by the study results.

This study indicates that meaningful scientific payloads of approximately 1500 pounds can be placed on the Mars surface, survive for several months, and transmit more than a hundred million bits of data to Earth.

In addition, the study provided data which shows that a smaller Capsule of 700 to 900 pounds has the ability to transmit approximately 10 million bits of imagery and additional scientific surface data.

VOLUME II - MISSION AND SCIENCE DEFINITION (CR-66678-2)

Volume II contains a description of the 'reference' mission plans, both direct entry and out-of-entry, the mission analyses conducted to define the reference plans, the assumed Mars models considered, and the science definition tasks accomplished to select entry and surface science packages/measurement sequences specifically designed to satisfy LRC's scientific goals.

VOLUME III - CAPSULE PARAMETRIC STUDY (CR-66678-3, -4)

A discussion of the analysis and results derived in determining the Capsule subsystems' design characteristics parametrically is provided for the range of assumed Mars Models and the reference mission plans. The synthesis of these subsystems into complete Capsule systems is presented in terms of Capsule performance, total imagery data obtainable, and surface lifetime.

CR-66678-3 presents the Capsule System Parametric Synthesis and Entry and Retardation Subsystem Studies. CR-66678-4 presents both studies of the Lander and Re-entry Subsystems and Appendices associated with the Parametric Study.

VOLUME IV- CAPSULE POINT DESIGNS AND SUPPORTING ANALYSES
(CR-66678-5, -6, -7, -8)

Volume IV contains a presentation of the detailed Capsule 'Point Designs', and their supporting analyses, derived to identify specific hardware approaches, weights, and system configurations; and confirm the correctness of the parametric results. In addition to the Capsule's engineering and design details, the results include development status, probability of success, and constraints imposed on the Orbiter by the Capsule mission.

CR-66678-5 contains a definition of the Capsule Point Design Requirements and descriptions of Point Designs 1 and 2. CR-66678-6 contains descriptions of Point Designs 3 and 4 and CR-66678-7 of Point Designs 5 and 6. CR-66678-8 provides additional information on Impact Attenuation, Surface Environment Definition, Effects on Point Designs due to Variations in Assumed Design Parameters as well as the Effects of a Lander on the Mariner Orbiter.

TABLE OF CONTENTS

TABLE OF CONTENTS (Continued)

BOOK 2

TABLE OF CONTENTS (Continued)

BOOK 2

LIST OF ILLUSTRATIONS

LIST OF TABLES

BOOK 2

LIST OF TABLES (Continued)

BOOK 2

4. LANDER SUBSYSTEMS

4. LANDER SUBSYSTEMS

4.1 SURFACE SCIENCE

4.1.1 SCIENCE PARAMETRIC DATA

This section is concerned with the parametric data resulting from the scientific requirements defined in Volume II. The number and types of possible parametric studies are limited by the state of development of some of the candidate payload science instrumentation. They are also limited by the discrete rather than continuous nature of the characteristics used to describe instrumentation, i.e., sensitivity, accuracy, and bandwidth. The type of studies that can be readily performed typically involve the interplay between measurement implementation and Capsule subsystem design. Two examples are: 1) the achievable atmospheric measurement accuracy during entry as a function of ballistic coefficient, sensor errors, and sampling rates; and 2) photoimaging deployment conditions as a function of boom lengths, weight, and vibration characteristics.

Aside from such studies, the science payload can be considered as a black box with a set of known interfaces with the remaining Capsule System. The effect on the Capsule System from perturbations in values which characterize these interfaces forms the basis for extensive system parametric studies. Table 4.1.1-1 presents a summary description of the minimum and expanded science subsystems which form these black boxes. It is recognized that variations to this complement are feasible and such variations would be dealt with parametrically in the same fashion as described here.

Consistent with the concept of characterizing the science subsystems as black boxes, it is possible to identify generic problem areas that may be parametrically evaluated. In summary, the more significant problems are:

1. Instrumentation Hardening - the requirement to harden to as high as several thousand g's poses potentially serious problems in Capsule volume requirements (for adequate three dimensional stroke displacement) and weight requirements (from instrument redesign). The present situation on the requirement definition is unresolved since further design work must be done by the instrument developers.

2. Photo Imaging Data Loads - the photo imaging experiment produces the majority of data for transmission. As such, the increase in total number of images, the use of stereo, and the use of color can readily triple the data load requirements. The impact on the total Capsule System design requires full evaluation but preliminary results indicate several design solutions are possible to handle the data load perturbation.

TABLE 4.1.1-1. MINIMUM AND EXPANDED PARAMETRIC SCIENCE PAYLOAD

Experiment	Minimum Science (One Day Life)						Expanded Payload (90 Day Lifetime)					
	Weight (lb)	Volume (in. ^{3})	Power (watts)	Max. Energy (joules)	Sample Rate	Date Load (Max) (bits)	Weight (lb)	Volume (in. ^{3})	Power (watts)	Max. Energy (joules)	Sample Rate	Date Load (Max) (bits)
1. Temperature												
1.1 Entry	1.5	4.5	3	$3.75X10^3$	3 per sec	$3.0X10^4$	1.5	4.5	3	$3.75X10^3$	3 per sec	$3.0X10^4$
1.2 Landed	2.0	6.0	4	$1.73X10^5$	6 per hr	$1.15X10^3$	2.0	6.0	4	$1.56X10^7$	6 per hr	$1.03X10^5$
2. Pressure												
2.1 Entry	3.0	36	6	$3.75X10^3$	2 per sec	$2.5X10^4$	3.0	36	6	$3.75X10^3$	2 per sec	$2.5X10^4$
2.2 Landed	1.4	13	2	$7.8X10^2$	6 per hr	$1.15X10^3$	1.4	13	2	$1.62X10^4$	6 per hr	$1.03X10^5$
3. Density	2.0	6.5	4	$5.0X10^3$	10 per sec	10^5	2.0	6.5	4	$5.0X10^3$	10 per sec	$1X10^5$
4. Atmospheric Composition	8.0	196	7	$8.75X10^3$	1 per 10 sec	$5.0X10^4$	8.0	196	7	$8.75X10^3$	1 per 10 sec	$5X10^4$
5. Photo Imaging	4.8	144	10	$6.5X10^2$	-	$1.02X10^7$	4.8	144	10	$1.95X10^3$	-	$3.06X10^7$
6. Soil Composition	9.5	186	5	$4.3X10^5$	1 per 3 hrs	$2.8X10^4$	9.5	186	5	$4.3X10^5$	1 per 3 hrs	$2.8X10^4$
7. Winds	5.0	25	6	$6.5X10^2$	3 per hr	$4.75X10^3$	5.0	25	6	$5.85X10^4$	3 per hr	$4.27X10^5$
8. Water Vapor												
8.1 Entry*	1.0	-	-	-	-	-	1.0	-	-	-	-	-
8.2 Landed	10.0	60	5	$1.08X10^3$	3 per hr	$1.8X10^3$	10.0	60	5	$9.7X10^4$	3 per hr	$1.62X10^5$
9. Clinometer	2.6	10	6	$1.44X10^2$	1 per 3 hrs	$1.12X10^2$	2.6	10	6	$1.3X10^4$	1 per 3 hrs	$1.0X10^4$
	50.8	687	58	$8X10^5$ ($2.22X10^2$ watt hrs)		$1.03X10^7$	50.8	687	58	$1.6X10^7$ ($4.45X10^3$ watt hrs)		$3.2X10^7$
10. Soil Moisture							9.0	18	80	$2.4X10^4$	Once Only	$3.2X10^1$
11. Airborne Particle Detection							4.0	125	0.5	$8.1X10^2$	1 per 4 hrs	$4.32X10^3$
12. UV Isolation							10.0	120	5.0	$8.1X10^3$	1 per hr (Daylight Only)	$5.4X10^4$
13. Large Molecule Detection							17.0	600	56	$7.7X10^4$	Once Only	$3.31X10^3$
							90.8	1550	199.5	$1.6X10^7$ ($4.45X10^2$ watt hrs)		$3.2X10^7$

* Ducting

3. Complexity of Deployment Schemes - the use of sophisticated deployment schemes to accurately place sensors, to move them to new sites, and to permit fine adjustments involves weight, power, and volume penalties that propagate through the Capsule system design. Studies on the simpler deployment schemes (cameras, wind detectors, temperature probes, etc.) do not impose excessive penalties, while the more sophisticated schemes require more development before their effects can be assessed.

4. Sampling Processes - Several experiments (mass spectrometer, gas chromatograph and water detection) require unique sampling methods that involve rigorous deployment requirements and detailed monitoring techniques. Their implementation can involve significant perturbations to the Capsule systems. Adequate studies to delineate the sampling requirements are still required, so that the effects on the interface subsystems are undefined.

5. Reliability - the results of reliability studies on sensor performance can lead to the use of redundant instruments which will have an obvious influence on the Capsule design. For example, the reliability in the facsimile camera head completing several rotations appears exceedingly low. The use of several devices therefore appears warranted.

6. Sterilization - the requirement to use sterilizable instruments can force either elimination of given experiments or the redesign of specific items. In either case, there will exist attendant changes in the Capsule system. At present, most of the items in the black boxes appear capable of sterilization and will most likely have a small overall perturbing effect.

The present parametric study on photo imaging addresses two of these problem areas. An evaluation is made of the viewing conditions as a function of boom placement and height and Lander design and orientation. The studies aid: 1) the understanding of the variability in the amount or planetary surface seen as a function of Lander attitude and 2) the definition of boom weights to minimize vibrations and maximize information content.

4.1.2 PHOTO IMAGING

The prime task of the landed science subsystem is to acquire photographic recordings of the planetary surface within a given bit constraint. The magnitude of the bit limit (1.02×10^7 bits) for the minimum imaging mission has resulted in the choice of a photographic mission in which four high resolution and four low resolution pictures are taken in four mutually orthogonal directions--the so-called

'Maltese Cross' configuration. The position of the camera (or cameras) must be such that the four picture formats contain the maximum amount of planetary surface. The random nature of some of the properties governing the constitution of the format mentioned above, such as the tilt of the landed spacecraft and the final form of the crush-up material, precludes a specific figure for the percentage of the surface in the total format being given. The objective of this section therefore will be to describe the study that has been pursued in order to place limits on the effects of these uncertainties and where possible to show how engineering design can improve surface coverage. Fig. 4.1.2-1 shows the 'Maltese Cross' configuration. Fig. 4.1.2-2(A) shows the shape of each format as suggested by NASA/LRC, a 70° x 25° format and nested within it the 5° x 5° high resolution format. Fig. 4.1.2-2(B) shows a format suggested by GE/RS of 60° x 29° which also has the 5° x 5° high resolution frame nested within it. The position of the high resolution frame relative to the rest of the format for fig. 4.1.2-2 (A) and (B) is not necessarily the final position that will be adopted.

4.1.2.1 Lander Geometry

The Lander instrumentation is contained in a disc-shaped container to the periphery of which is attached the crush-up material. Detailed drawings of the configuration are given in Volume IV, but it is sufficient for the purposes of this section to use a simpler diagram. This is shown in fig. 4.1.2-3, which is one half of a symmetrical radial section through the Lander. The dimensions identified are necessary to provide the required imaging data and may not appear on the engineering drawings of a similar section; their significance will be briefly described. A camera (A) is mounted on a support (xA) a distance (x) from the axis of symmetry of the landed vehicle. The uppermost edge of each photographic format is normal to (A) and for the singular case of a perfectly horizontal vehicle, this ray will be just above the horizon for a perfectly spherical planet. At some angle $(90 - \alpha)$ of declination a ray of light will just glance the edge of the uppermost section of crush-up (assumed uncrushed) and will intersect the surface at a point 0. APO represents the distance (called the glancing ray length) multiplied by the IFOV that gives the ground resolution; the length of APO is a function of the vehicle attitude relative to the horizontal. The distance of P from the axis of symmetry is R; the height of the camera above P is HCAM and from P to the surface is HCAP. HCAP will be a function of the length of the crush-up stroke and for calculation of the minimum APO the maximum crush-up stroke of 9-1/2 inches is used, giving rise to an HCAP minimum of 27 inches as shown. In a typical photo-imaging sequence the camera will be initially offset from the direction XP by an angle φ, φ being measured in the plane normal to the plane of the figure. The imaging sequence of events is started by a movement of a mirror such that a vertical scan occurs at the edge of the field (φ from XP) by the IFOV in a vertical direction $\alpha = 90^\circ$ to $\alpha = 20^\circ$ say) this sequence is repeated 2φ /IFOV times in synchronism with an azimuthal movement of the camera that enables it to cover an angle $\pm \varphi$ about the direction XP. The camera is then rotated $(90 - 2\varphi)$ degrees and the whole sequence is repeated, thus the second of the four fields of view is imaged: the process is repeated two more times to complete the 'Maltese Cross' pattern. As the camera

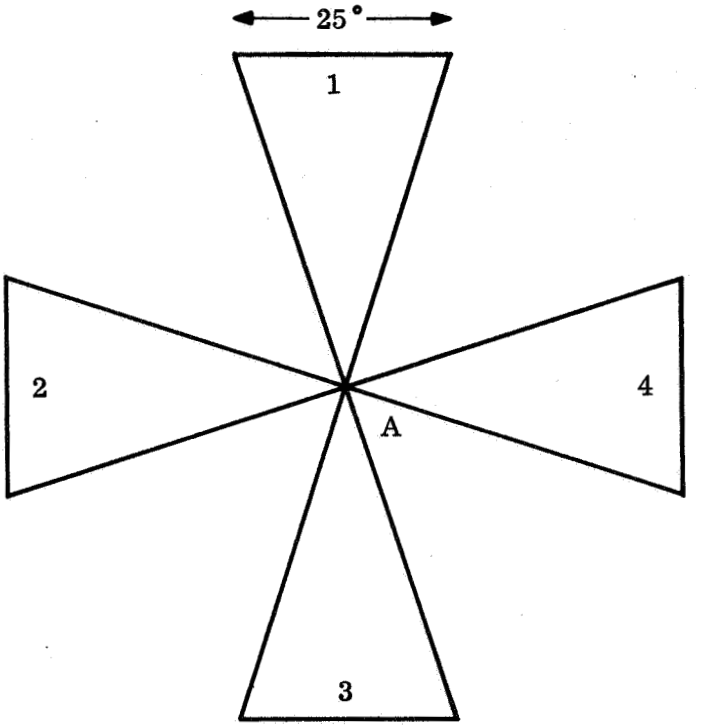

Figure 4.1.2-1. View of Low Resolution Photo Imaging Format - Elevation

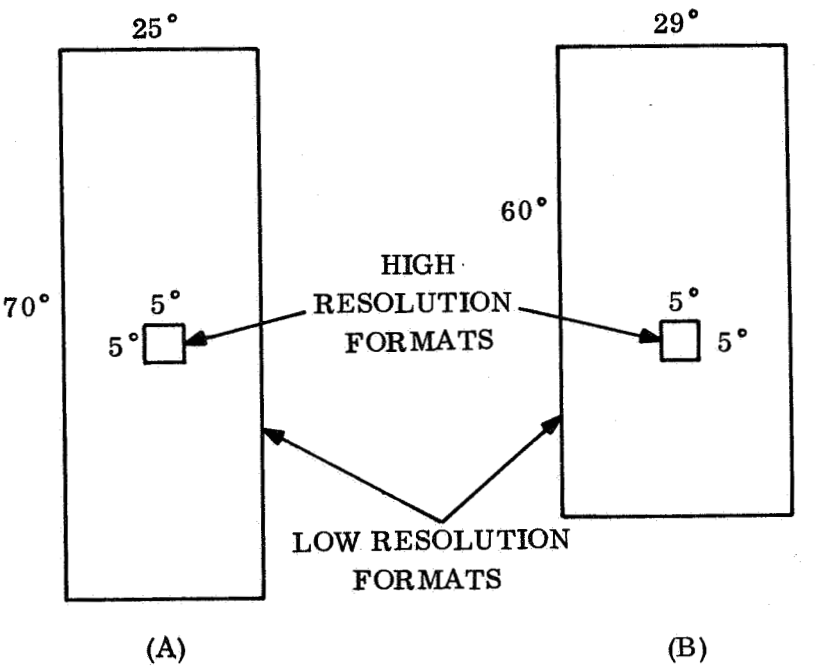

Figure 4.1.2-2. View of Photo Imaging Formats - Plan

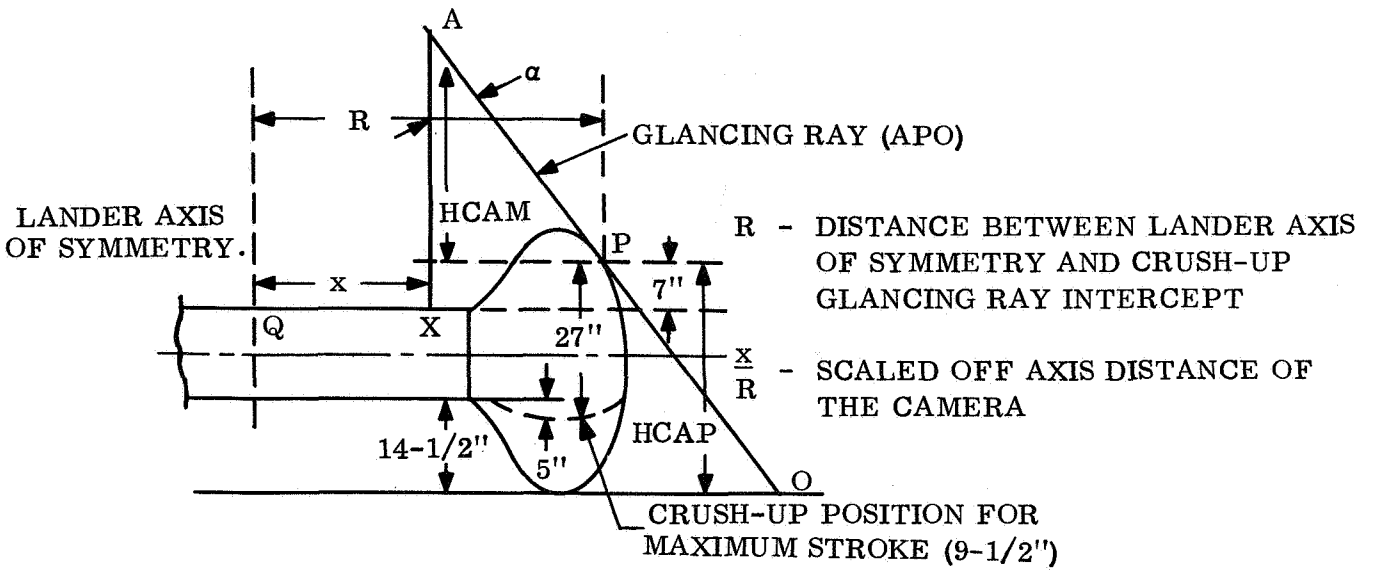

Figure 4.1.2-3. Radial Section of Lander

rotates about the axis of symmetry the inclination of the Lander causes the scene content to vary: this variation can best be described with reference to fig. 4.1.2-4. As φ increases L increases and since AX remains constant α is proportional to $\tan^{-1} L$. The tilt of the vehicle due to local protuberances and crush-up asymmetry is ϵ; δ (the camera axis displacement angle) is the angle between the camera reference axis ($\varphi = 0$) and the intersection of the vertical plane through the highest and lowest points of the vehicle and a horizontal plane through the landed space craft. The attitude of the landed vehicle relative to the local surface cannot be determined, since random phenomena are involved. A maximum value of ϵ has been chosen by calculating the inclination of the craft for one end fully crushed and the other resting on a 5-inch rock; the minimum value of ϵ is zero.

It is clear from the diagram that when α is less than the angle to APO, the edge of the crush-up enters into the field of view. In addition for $\epsilon \neq 0$ there are camera positions where the line normal to AX lies above the horizon. In both cited cases some of the format consists of sky and lander so that the space available within the format for surface imagery is diminished. In order to minimize the amount of format consisting of unwanted subjects, HCAM and x(QX) can be varied so that the intrusion of the crush-up into the format is minimized. In order to effectively cover a wide range of possibilities a computer program was written.

4.1.2.2 Parametric Computer Program

A main program called 'BOOM' and a subroutine called 'MINDIST' have been written for the GE deskside computer. The main program calculates the percentage of surface coverage in each format for all variations of ϵ, α and δ that are inserted

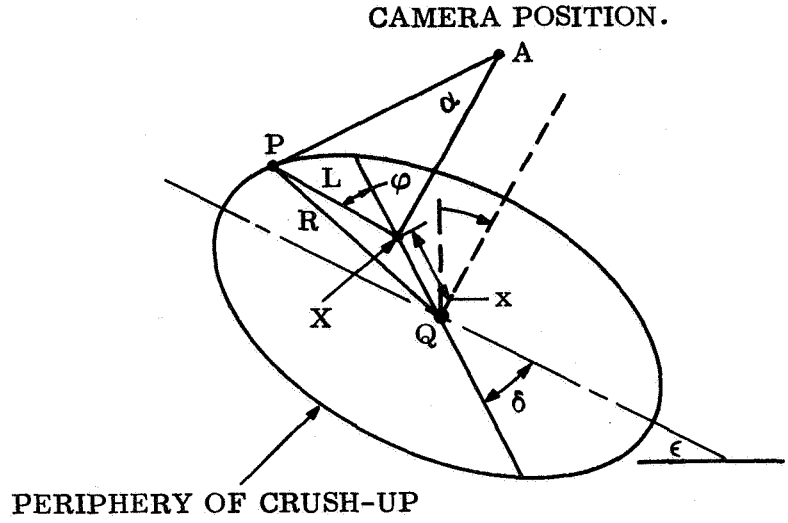

δ - CAMERA AXIS DISPLACEMENT ANGLE
ϵ - LANDER TILT ANGLE

Figure 4.1.2-4. Lander Geometry From Above

as inputs. The sum of the four separate formats is obtained and the average percentage of surface imaged is given as one of the outputs. The subroutine is used to calculate the minimum value of APO resulting for each configuration, since this distance is required for the camera design and also used in the determination of maximum ground resolution attainable. The values of the variables have been chosen to bracket the range covered by the six point designs; this data is shown parametrically. For specific values of the variables it is a simple matter to run the program for these values only. In the following section a sample of the outputs and graphs drawn up from the program are shown.

4.1.2.3 One Camera System

Figs. 4.1.2-5 and 4.1.2-6 show the percentage coverage achieved by a single camera that rotates to the four picture taking positions sequentially. At x = 0 the camera support is on the axis of symmetry of the Lander; the initial values for the camera off axis are for a distance(n)which is expressed as a ratio of the Lander parameter R (see fig, 4.1.2-3). In fig. 4.1.2-5, $\delta = 0$ and the variations in percentage cover arise out of differing values for ϵ and x/R. In fig. 4.1.2-6, the same values of

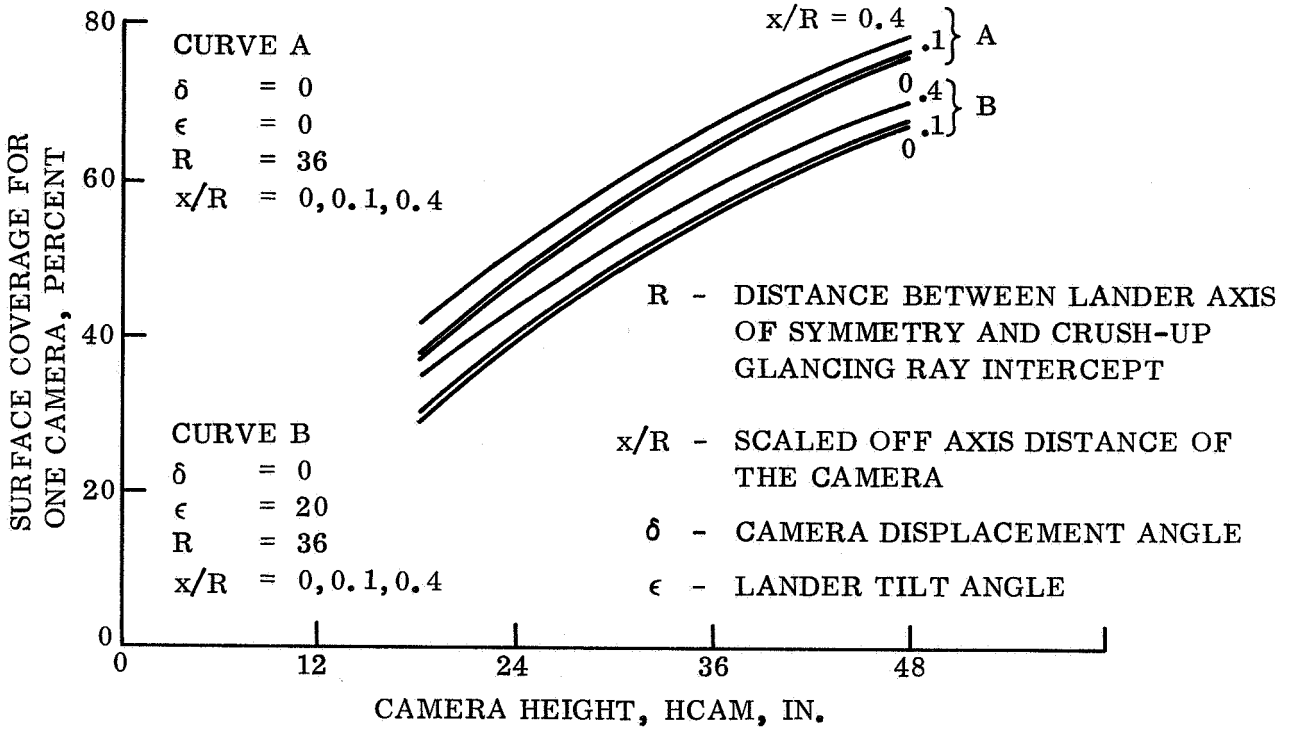

Figure 4.1.2-5. Surface Coverage for One Camera, δ =0

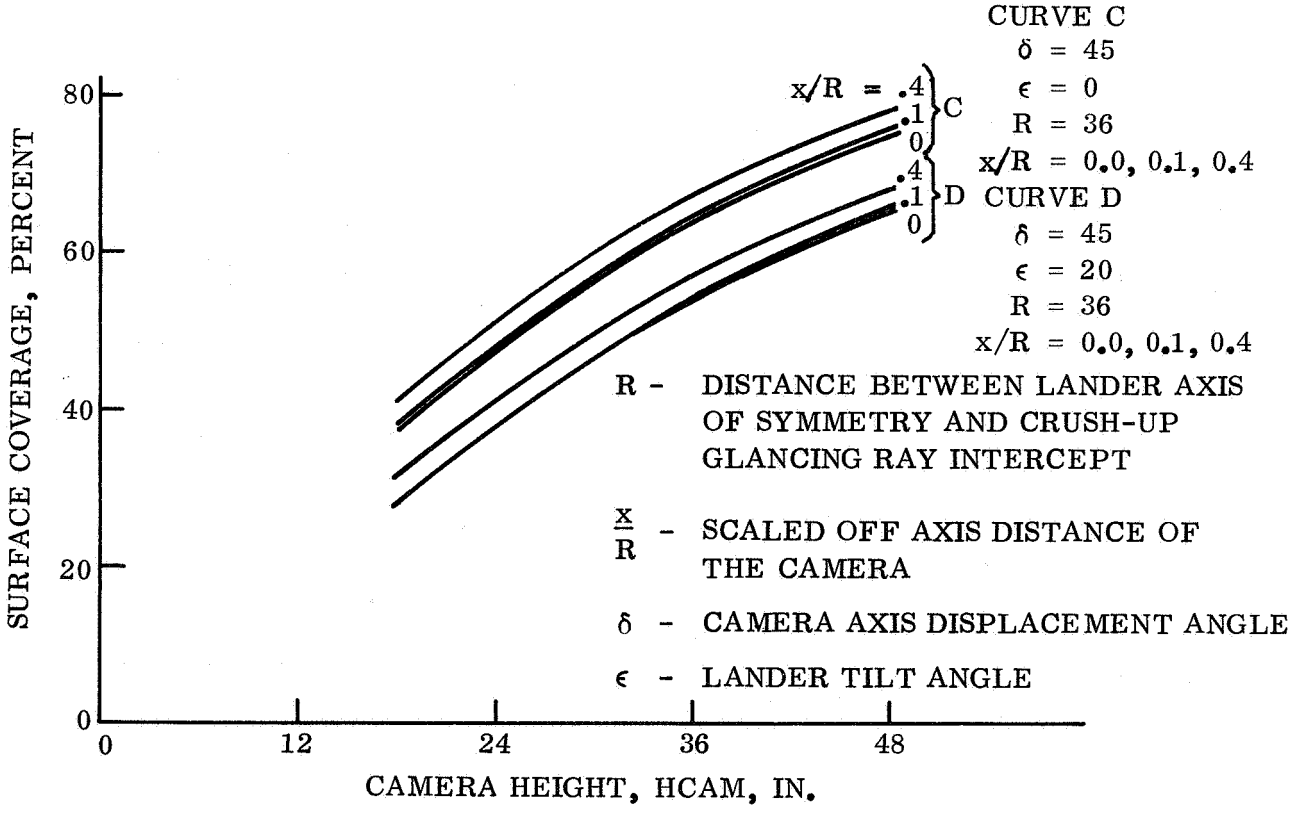

Figure 4.1.2-6. Surface Coverage for One Camera, δ =45

x/R and ϵ are plotted for $\delta = 45^\circ$. It is noticeable that for positions of the axis of symmetry, (x/R) has very little effect on the coverage at a given HCAM. The same is less true for ϵ but the change is only 8 percent for a 20° difference in ϵ. If the direction of the camera axis relative to the line of maximum slope of the landed vehicle is changed (δ) once again the effect on coverage is small, increasing with the Lander inclination, being about 4 percent for $\delta = 45$ and $\epsilon = 20^\circ$. However, in order to achieve a desirable surface coverage in the region of 75 to 80 percent the camera must be at a height of at least 42 inches above the top surface of the landed spacecraft, the camera height being the most significant parameter. The weight penalty for raising the camera to this height is severe (see para 4.1.1.3) and an alternative method for acquiring this coverage is necessary. A further disadvantage of a near the axis camera is the length of APO (OAMIN) shown in figs. 4.1.2-7 and 4.1.2-8: it must be remembered that OAMIN is the length of APO in the particular case when $\delta = 0$. In general, for $\delta \neq 0$, OAMIN will be larger.

4.1.2.4 Two Camera System

To overcome some of the disadvantages of a one camera system, the use of two cameras was investigated (see fig. 4.1.2-9). The two cameras are placed at positions 1 and 2. Each camera has the capability to take both the required high resolution and low resolution pictures, and takes pictures along two directions only, e.g., along either 1A and 1B or 1A' and 1B'. The latter alternative has the capability, in the particular case when the direction 1A' coincides with the greatest slope, of having the highest ground resolution attainable. In the general case, however, the average coverage for this case will be somewhat greater than the symmetrical arrangement of 1A - 1B (see figs 4.1.2-10 and 4.1.2-11). Taking a typical point design case for HCAM = 15 inches at x/R = 0.8, the coverage for 1A - 1B = 85.7 percent and 1A' - 1B' = 73.6 percent. The corresponding OAMIN's taken from figs 4.1.2-12 and 4.1.2-13 are for 1A - 1B = 48.2 inches and for 1A' - 1B' = 45.7 inches. The ground resolutions corresponding to these optical arm distances are given in figs. 4.1.2-14 and 4.1.2-15. For 0.1° IFOV the ground resolution for 1A - 1B = 2.12 mms and for 1A' - 1B' = 2.03 mms: for the 0.01° IFOV, looking along the same directions with the same OAMIN, the ground resolutions are one tenth of those given above. These examples are for one camera only looking out in two orthogonal directions; to get the percentage coverage and variation with ϵ and δ the calculations have to take into account the contributions of the camera situated at position 2. The results of some of these calculations are given in figs. 4.1.2-16 through 4.1.2-19. In addition to the data pertinent to the 70° x 25° format the similar data for the 60° x 29° is presented. The 60° x 29° format contains the same number of picture elements as the 70° x 25°, so that the total bits remain the same. The advantage of this format shape is that the amount of crush-up for a given camera position and height is less. The disadvantage is that OAMIN has a corresponding increase and thus presents a trade-off between ground resolution and surface coverage. In order to avoid confusion, only the curves for the extreme cases of δ and ϵ are presented. In fig. 4.1.2-16 an immediate comparison of the influence of ϵ and the selected viewing positions of the camera on the various parameters can be measured. For HCAM = 15 inches it is seen that a variation of ϵ from 0° to 24° causes a percentage cover change of about 12 percent for both viewing directions. Not shown is the effect of changing δ because this is about 3 percent, the same as that for the centrally mounted camera. The advantage of using the ABXY

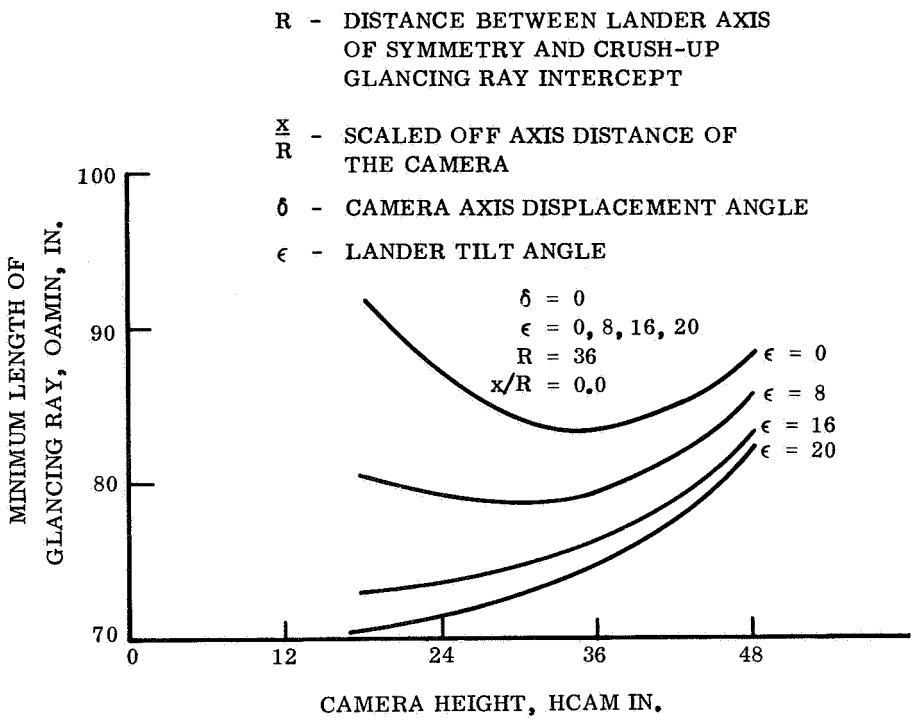

Figure 4.1.2-7. Length of Glancing Ray for One Camera Axially Mounted

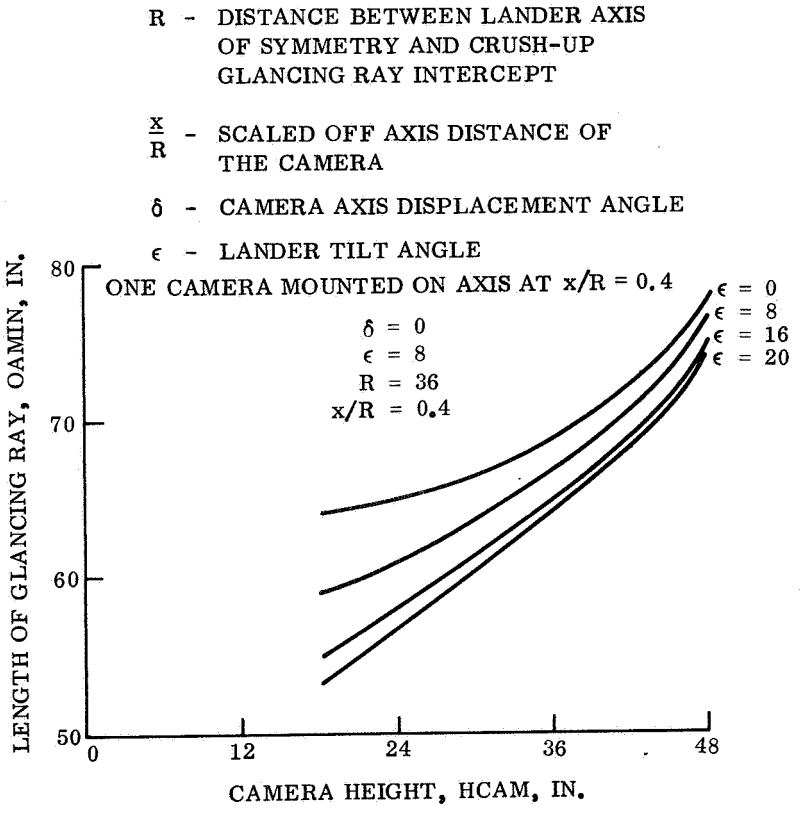

Figure 4.1.2-8. Length of Glancing Ray

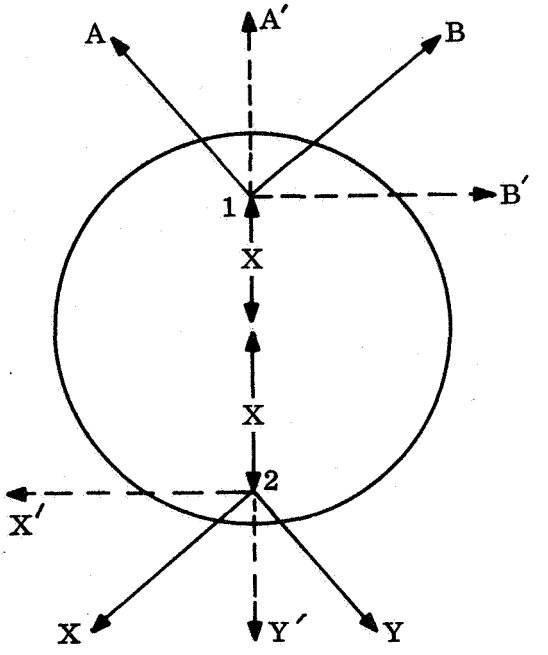

Figure 4.1.2-9. Geometry for Cameras Mounted Off Axis

directions of viewing are clearly demonstrated as an improvement of 1 to 13 percent throughout the whole range of HCAM. Fig. 4.1.2-17 repeats the data shown on fig. 4.1.2-16 for the picture format of 60° x 29° and again the improvement in coverage at a given HCAM is clearly evident. At HCAM = 15 inches for example, $\delta = 45^\circ$, $\epsilon = 0^\circ$; in direction ABXY there is an increase of 12 percent. The ABXY curves flatten off because the value of ϵ is such that the horizon intercept is the only feature intruding into the field of view. The capsule crush-up is cleared at HCAM = 18 inches and since the horizon intercept angle does not alter with HCAM the curves become flat. Conversely the A'B'X'Y' curves show that capsule intrusion into the format is still occurring at HCAM = 30°. Figs. 4.1.2-18 and 4.1.2-19 show how the maximum ground resolution changes with HCAM and the direction of viewing. Although the changes in resolution as a percentage are significant, the absolute values do not alter the capability of the system to resolve geological features by a significant amount.

4.1.2.5 Boom Vibration and Wind Loading

Owing to the process by which the facsimile camera forms a photographic image, careful consideration must be given to the stability of the camera. This is a general requirement of all picture taking techniques but is particularly significant in the facsimile technique, owing to the non-temporal correlation for different parts of the picture format. In general, two aspects of the problem have to be considered; the amplitude of the camera motion and the frequency. However, it is preferable to reduce camera motion to an insignificant level, in which case the frequency of the motion

becomes irrelevant; this is the approach that has been adopted. A criterion was established for the amount of motion that can be tolerated - this was chosen to be one tenth of the instantaneous field of view (IFOV). Therefore, in low resolution pictures an angular movement of 0.01° can be tolerated and for high resolution pictures 0.001° is acceptable.

The winds that give rise to the existing forces on the camera and its support vary with the VM models; however, the loading they produce on the camera system varies over a much smaller range than the wind velocities, owing to the compensating effect of the atmospheric density. Therefore, a maximum wind loading was determined that covers all the VM models, and the weight of the camera supports were calculated for different materials and support dimensions. The appropriate curves are shown in figs. 4.1.2-20 to 4.1.2-23.

4.1.2.6 Summary

The parametric study has clearly identified, as anticipated, the need to place the camera as close to the edge of the crush-up as engineering techniques will allow. This is the only practical way of preventing the crush-up from occupying an undesirable percentage of the format. Two other alternatives exist; the first is to use tall camera support masts, but inspection of the curves in para 4.1.2.5 shows that this increases the weight drastically, for each support has to be stable enough for the 0.01° IFOV. The other alternative readily achievable is to have a format that is nearly square in shape as opposed to the rectangle currently under construction. The penalty here is that the smallest object on the ground that can be resolved increases in size.

The current value of HCAM in the point designs is 15 inches, a position off axis corresponding to $x/R = 0.66$ -- this arrangement will yield a percentage cover extending from about 80 to 70 percent. An increase of HCAM of 3 inches or x/R of 0.14 could realize percentage covers of 100 to 80 percent. The study has shown that the relative position of camera pointing axis with Lander tilt axis (δ) is insignificant causing only a 3 percent change in the worst case. The effect of the tilt of the Lander (ϵ) has a more pronounced effect, causing a 12 to 13 percent change in coverage for an ϵ change of 0° to 24°.

The main advantage of the computer program is that parametric or point designs can be analyzed for surface coverage very quickly by inserting the appropriate values into the program, while general conclusions can be drawn from the extreme cases in the manner demonstrated above.

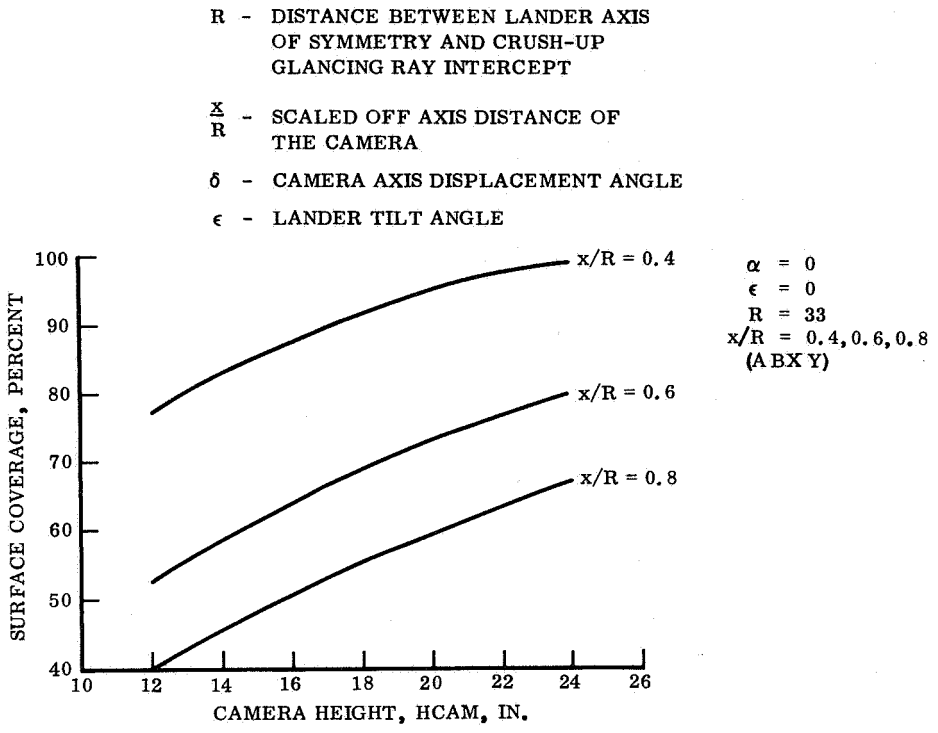

Figure 4.1.2-10. Percentage of Surface Covered for One Camera at Position 1 - Views A and B

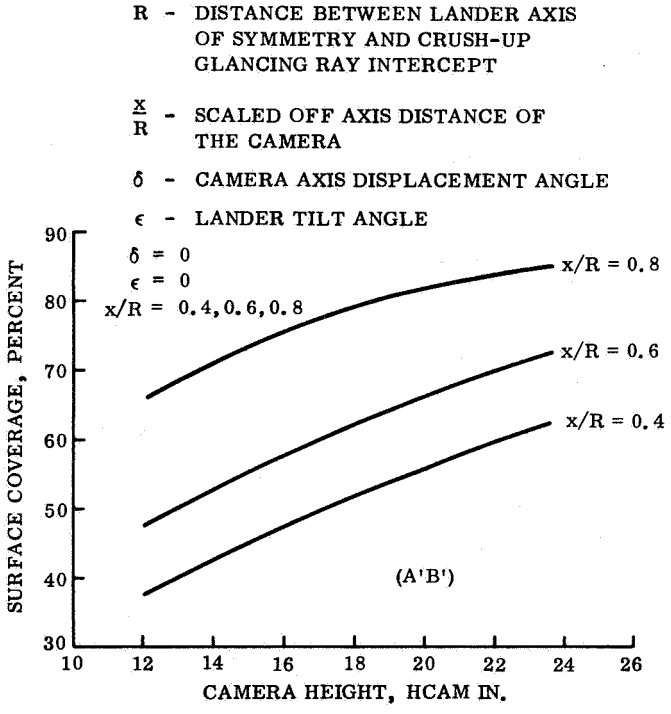

Figure 4.1.2-11. Percentage of Surface Covered for One Camera at Position 1 - Views A' and B'

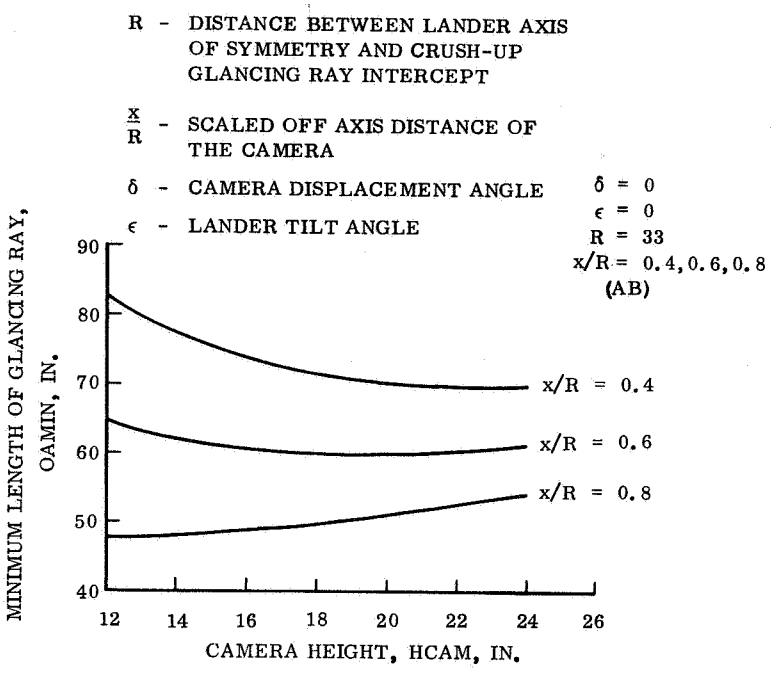

Figure 4.1.2-12. Length of Glancing Ray for One Camera at Position 1 - Views A and B

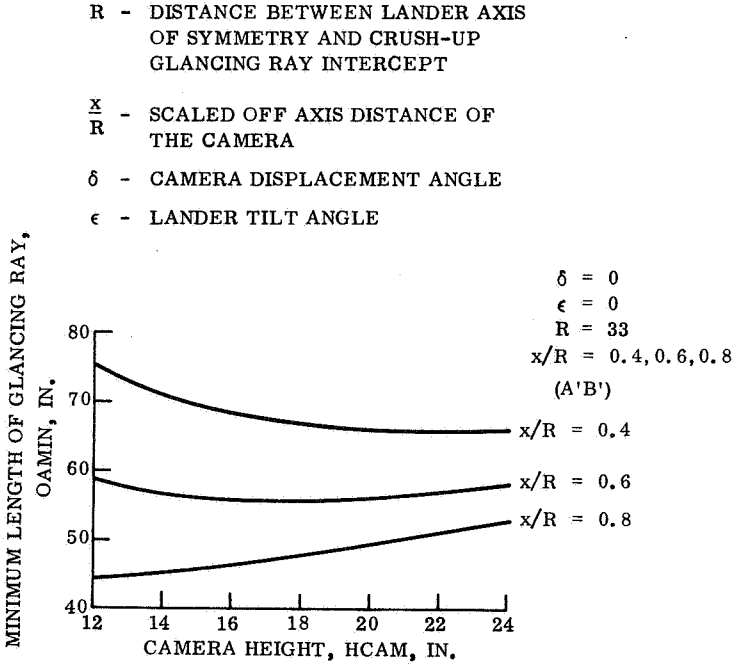

Figure 4.1.2-13. Length of Glancing Ray for One Camera at Position 1 - Views A' and B'

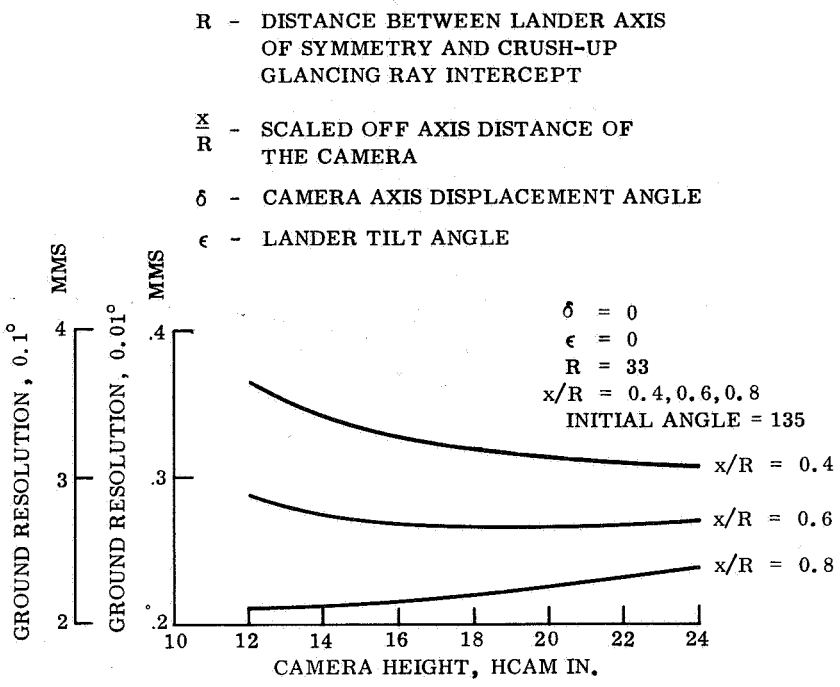

Figure 4.1.2-14. Ground Resolution for One Camera at Position 1 - Views A and B

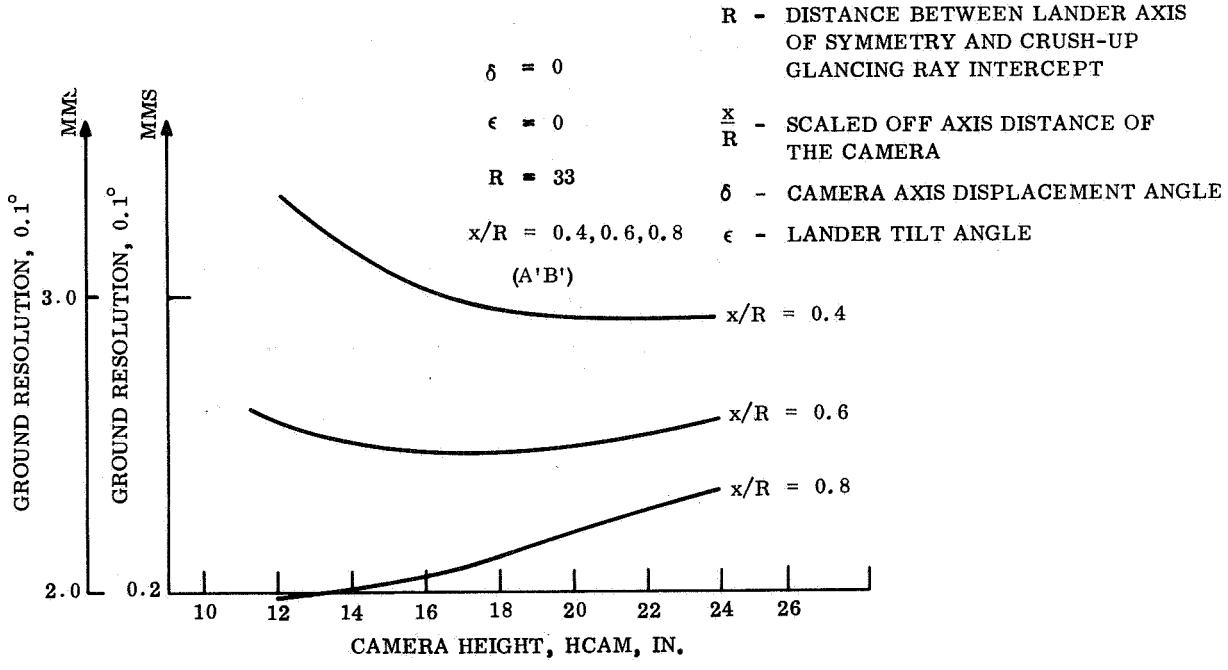

Figure 4.1.2-15. Ground Resolution for One Camera at Position 1 - Views A' and B'

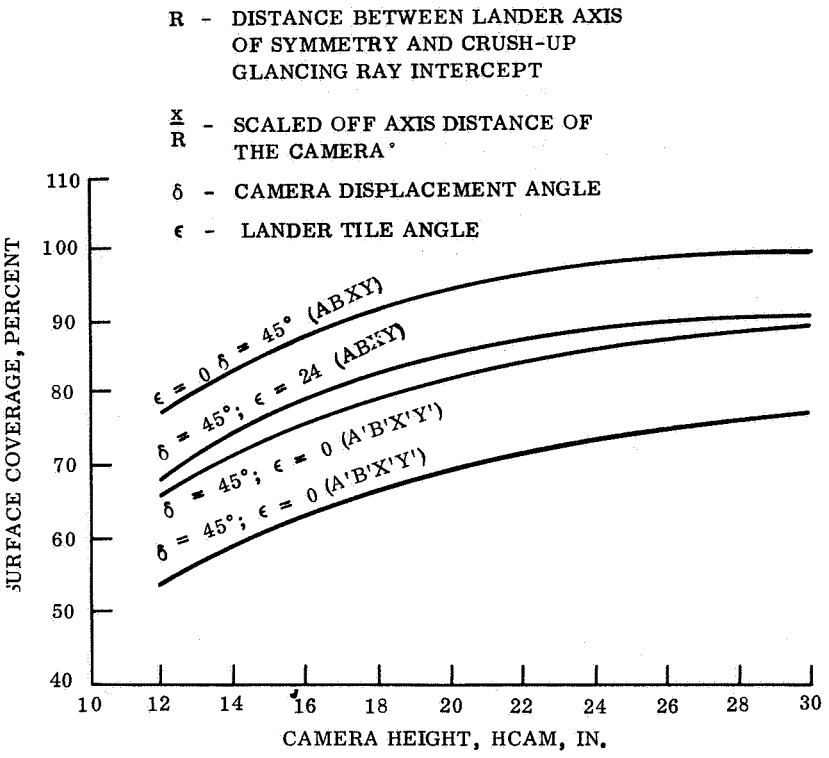

Figure 4.1.2-16. Surface Coverage for Two Cameras, 70° x 25°

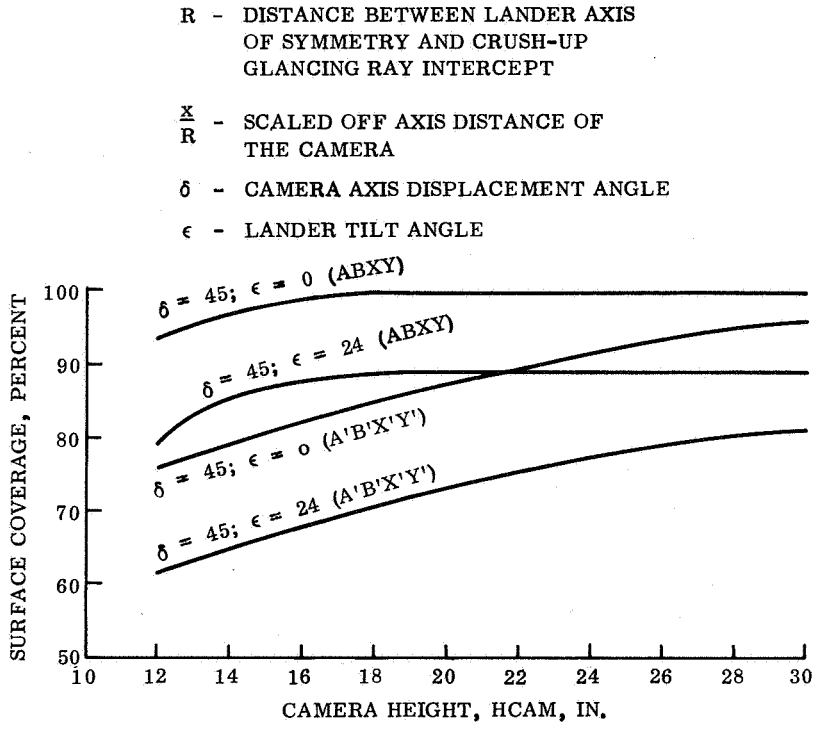

Figure 4.1.2-17. Surface Coverage for Two Cameras, 60° x 29°

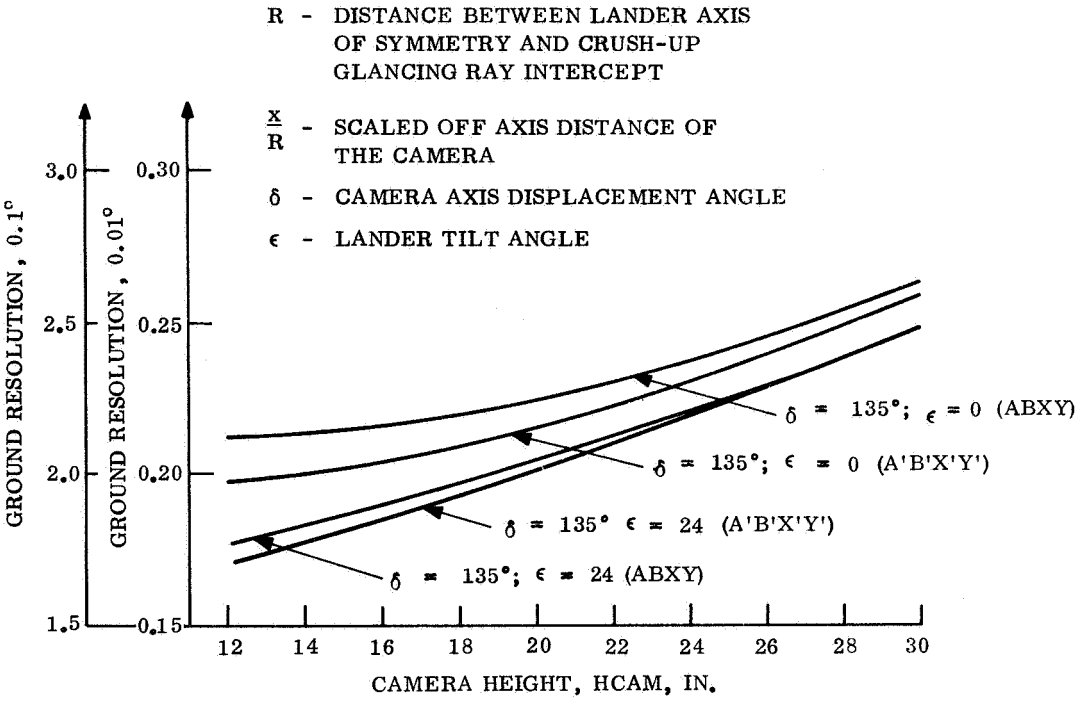

Figure 4.1.2-18. Ground Resolution for Two Cameras, 70° x 25°

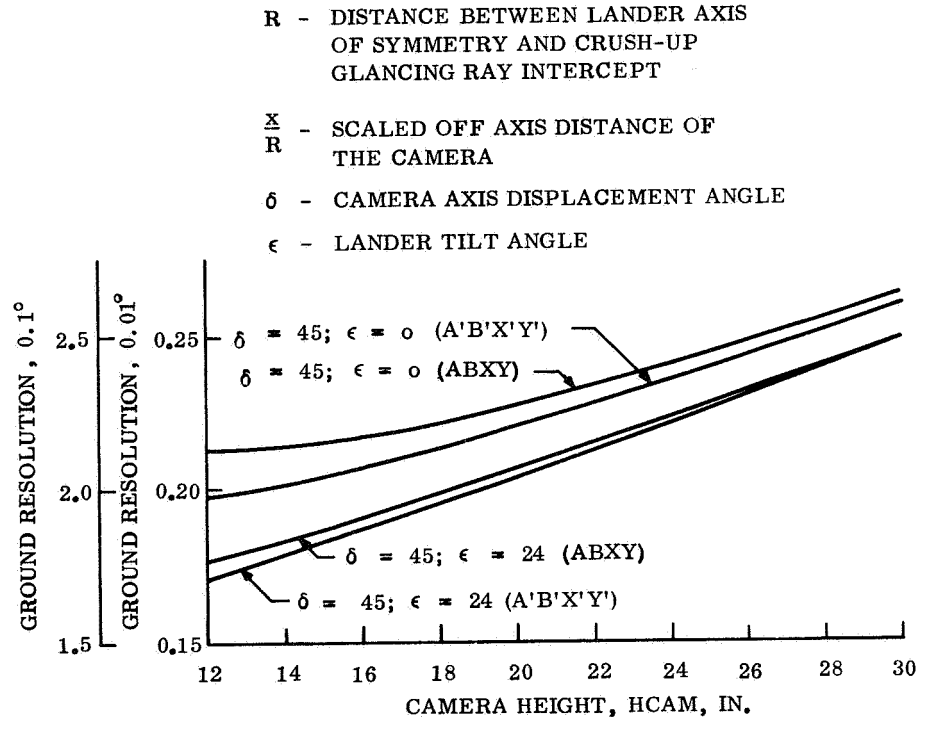

Figure 4.1.2-19. Ground Resolution for Two Cameras, 60° x 29°

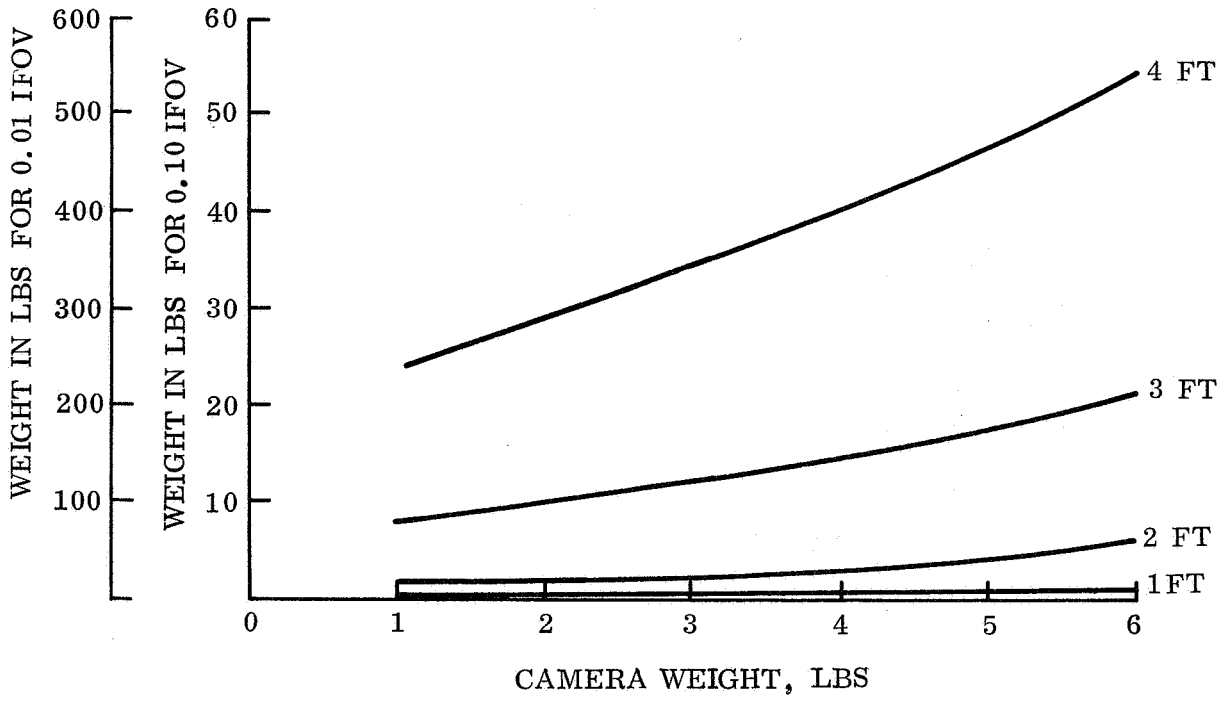

Figure 4.1.2-20. Two Inch Diameter Tube (Steel)

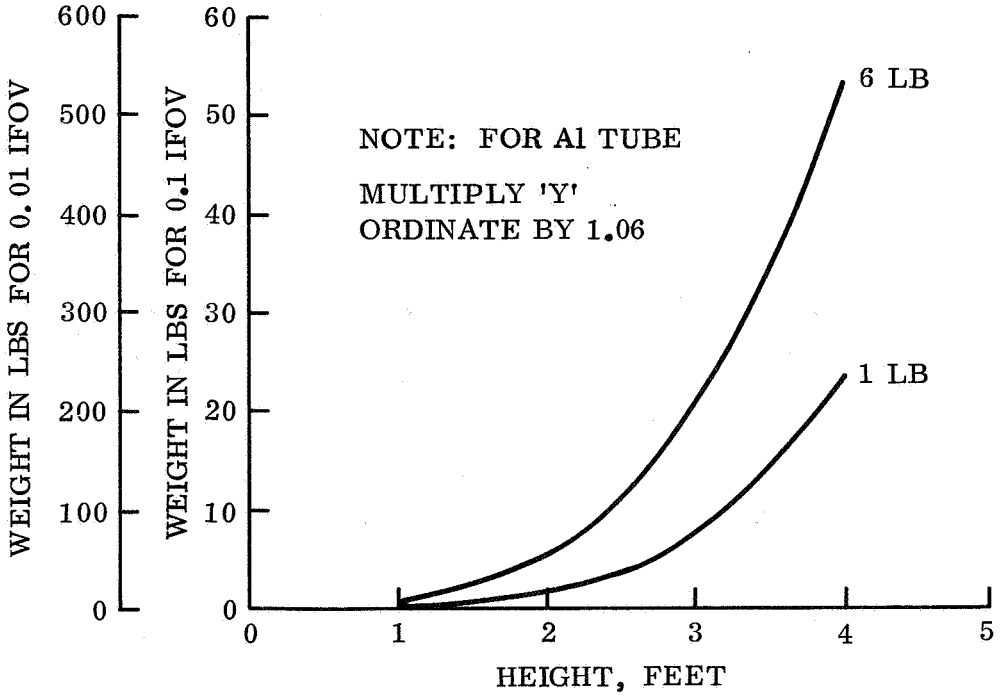

Figure 4.1.2-21. Two Inch Diameter Tube (Steel)

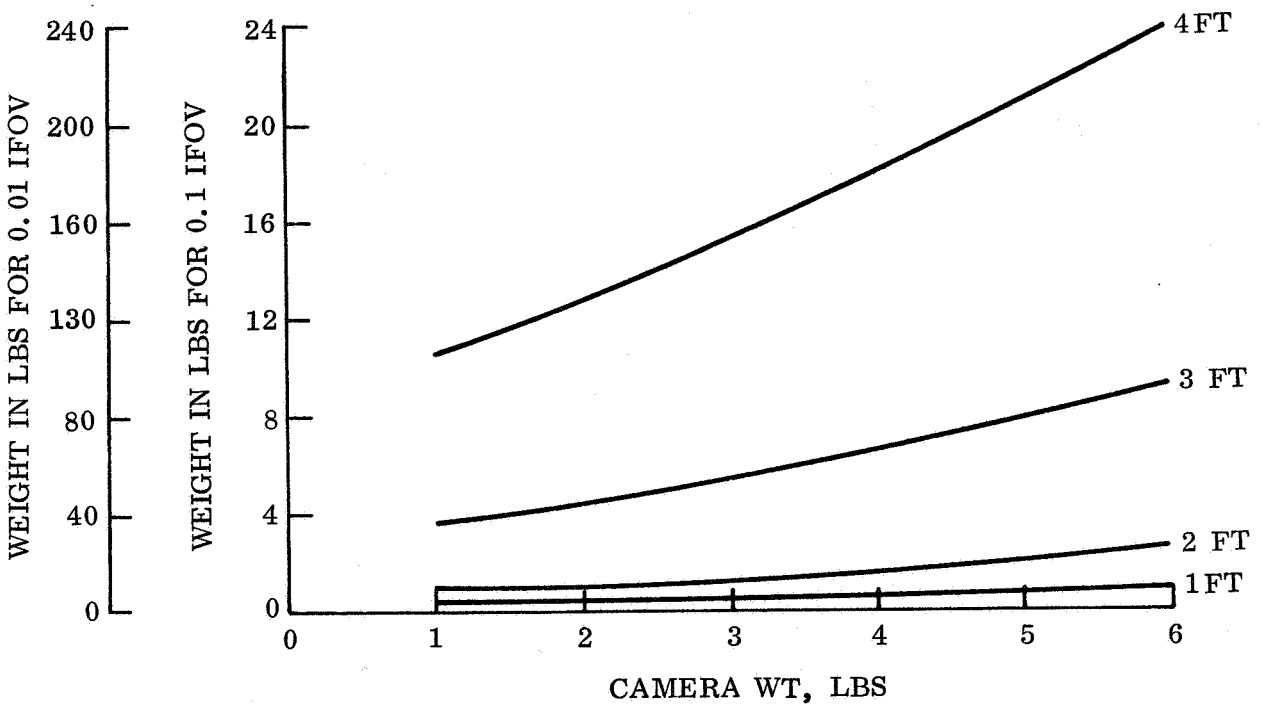

Figure 4.1.2-22. Three Inch Diameter Tube (Steel)

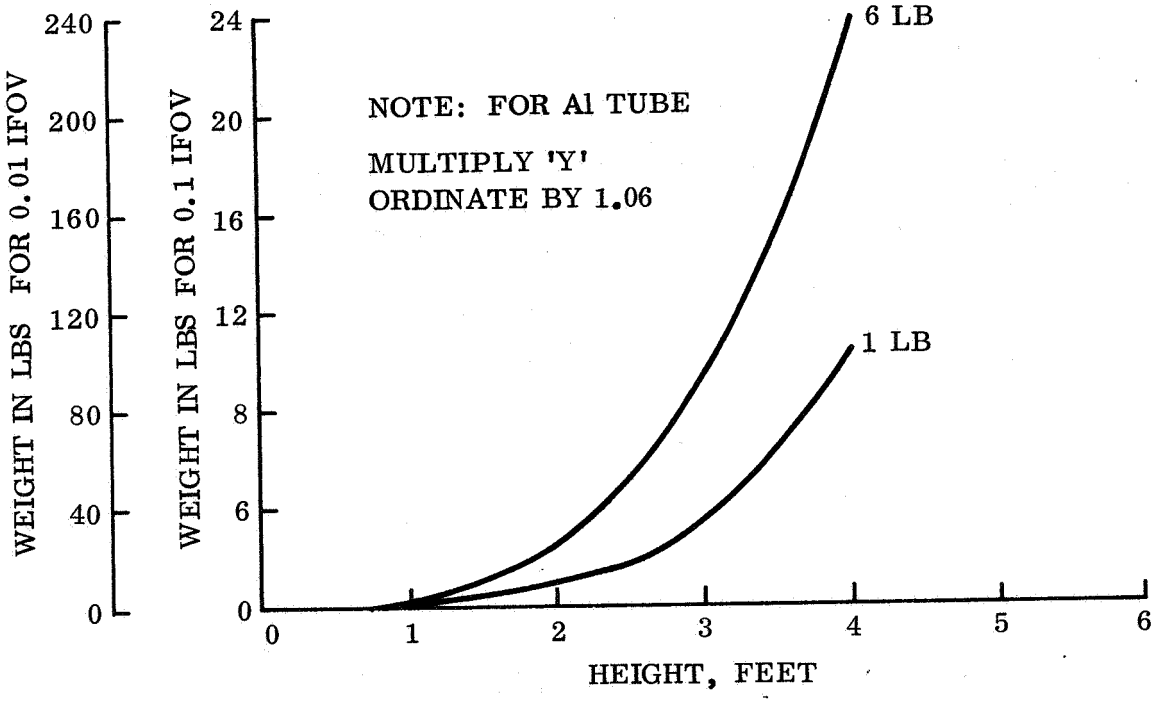

Figure 4.1.2-23. Three Inch Diameter Tube (Steel)

4.2 TELECOMMUNICATIONS

4.2.1 INTRODUCTION

The objective of the Communication System parametric study is to provide sufficient information to allow the synthesis of a communication subsystem design which satisfies the requirements of a stated reference mission. Two reference missions have been defined for the study, one each for direct entry and out-of-orbit entry. A broad range of significant telecommunications parameters have been considered which are based on the Mars '74 communication problem and are directly applicable to the reference missions defined.

Lander communication is initiated upon separation from the Orbiter and two communication modes are considered: a relay link from the Lander to the Orbiter and a direct link to Earth. The requirements of the Communication System, and approaches deemed most appropriate for the entry and landed phases are presented. For the systems used in deriving the parametric curves, the basis for the calculations are presented. The parametric curves enable the major performance characteristics of candidate communication systems to be readily identified. A brief description of the use of the curves and the communication capabilities are presented.

4.2.1.1 Requirements and Constraints

The basic requirement of the Capsule/Lander Communication System is to provide the data return capability consistent with the mission objectives for each phase of the mission. After separation and prior to entry, the information transmission requirement is low, consisting solely of diagnostic information. During entry, the transmission of science information is added. In the landed configuration, the information transmission requirement varies. Initially, the requirement is significantly increased by the addition of high data rate instrumentation, such as imagery. However, during the extended mission, the information transmission requirement is again low when the Lander is performing a meterological station function. An additional requirement of a reduced imagery mission during the extended lifetime again significantly increases the information transmission requirement.

The Communication System design is constrained by the trajectories and orbits, the characteristics and limitations of the Lander, the Orbiter, and the Deep Space Network (DSN) as well as the limitations imposed by operating near and on the surface of Mars. Some of the major constraints imposed by these various sources are indicated in table 4.2.1-1.

In addition to satisfying its basic requirements during the entry and landed phases of the mission, the Communication System must also provide for status monitoring both during Capsule cruise, via an r-f link, and during Spacecraft cruise, via the Spacecraft r-f link. In general, these functions do not place a burden upon the system since its design is dictated by the more stringent requirements of the prime mission support functions. Hence, the parametric data provided is most useful for the entry and landed phases.

TABLE 4.2.1-1. CAPSULE COMMUNICATION SYSTEM CONSTRAINTS

Interface	Constraint
Trajectories and Orbits	Communication range Range rate View angle View duration
Lander	Size, weight and power Antenna pointing
Orbiter	Size, weight and power for orbiter mounted capsule support equipment Antenna pointing capability Probability of successful operation
Planetary Environment	Breakdown in the atmosphere Reflections of r-f signals from the surface Surface slope characteristics
Deep Space Network	S-band frequencies: nominally 2295 MHz down-link 2115 MHz up-link 85-foot antennas, 1 to 3 210-foot antennas

4.2.1.2 Communication Considerations

The major function of the Capsule Communication System is to transmit data to the DSN stations via a relay station of the Orbiter, or via a link directly to Earth. The system supports Capsule operations through all mission phases from prelaunch check-out to the end-of-mission. The system performs the following operations:

1. Conditions, multiplexes, encodes and provides storage for the Capsule engineering and science data signals. These engineering signals include Lander environmental data and subsystem performance monitors for operational and diagnostic functions. The science signals include atmospheric data during Capsule descent into the planet atmosphere as well as on the surface and imagery data from the surface.

2. Modulates an r-f carrier with the data information for transmission, either directly to Earth or to the Orbiter for relay to the stations of the DSN.

Amplifies the r-f signal and provides the antennas required. Supports tracking if required. Receives command transmissions from the DSN.

3. Detects and decodes commands for the Capsule subsystems. The entry and landed phases of the mission constrain the design of the Communication system. Required operations during the other mission phases are also taken into account, but are not generally controlling factors.

Both the direct link from the Lander to the DSN stations, and the relay link via the Orbiter are considered to satisfy the Lander data transmission requirements. Both types of links can be designed to satisfy the communication requirements for all phases of the mission with the exception of the direct link for real time transmission during descent. The need for rapid reacquisition of the signal by the receiver following signal loss due to blackout or multipath-fading makes implementation of a direct link during entry more difficult to achieve. Studies of coning motion for the vehicle from separation down to where density damping occurs, near Mach 5 in the trajectory, reinforces the great difficulties attendant with implementing a direct link.

For equal transmitted power, the performance capability of the relay link is much greater than for a direct link in any mission phase, unless an Earth pointing antenna is used. In such a case, this Earth pointing antenna must provide a gain exceeding the combined gain for the relay antennas by about 30dB. For small vehicles where size and packaging complexity of the large antennas is difficult, the outstanding advantage of the direct link is the operational independence of the Lander from the Orbiter.

The capability of relay links to the Orbiter for both entry and landed phases and of direct links to the Deep Space Network (DSN) for the landed phase, are presented in parametric curves which follow for a wide range of transmitter powers and antenna gains. The relay link is discussed first, followed by the direct link. A summary comparison is made of the relative energy efficiency of the various systems. The rationale for the choice of candidate systems, a description of the systems, and the parametric curves from which the performance of the systems can be determined, are given for both links.

4.2.1.2.1 Relay Communication Mode

The entry and landed phases of the mission are of particular importance in the design of a relay communication system. During the entry phase, both real time transmission (interlaced with time delayed data) of the data collected during entry, as well as storage of the data for transmission after impact, or a mixture of the two, are approaches for retrieval of the entry data. The real time transmission approach provides the capability to obtain data on the characteristics of the atmosphere and on the vehicle performance prior to the hazards of landing.

A. Modulation and Detection

It is assumed that all of the data to be transmitted is in binary form. The most efficient means for r-f transmission and detection of binary data is phase shift keying (bi-phase modulation) with coherent detection. The implementation of a coherent r-f

detection system in the Orbiter for use during the entry phase is faced with many of the same problems described for the direct link during entry. It is more complex to implement than a non-coherent link. The latter can be implemented to meet the entry phase communication requirements without unduly taxing the Capsule power system for the relatively short (about one-half hour) operating time required. Such a non-coherent system is achievable with a low gain, broad beamwidth antenna on the Lander, so that no additional penalty need be incurred for attitude control. Therefore, a non-coherent FSK system is selected for the purpose of the entry mode study. Further, bi-phase modulation of the binary data on a square wave subcarrier of a frequency equal to the bit rate (split phase or Manchester coding) is recommended to reduce the problem of maintaining detector balance in the receiver, and to provide symbol synchronization. The parametric data provided for the non-coherent FSK is applicable for both the entry and landed phases.

Communications after landing may take place either when the Orbiter is near periapsis or when it is near apoapsis. Near periapsis the period of mutual visibility is about 15 minutes for ranges less than 3000 km. The doppler shift and rate of change of doppler shift are relatively high during this period. Near the horizon, variations in the lander antenna pattern may cause fading of the received signal at the Orbiter. Even though an FSK system is about 5 dB less efficient than a PSK system for high data rate implementations, the lesser complexity of the FSK system may outweigh its poorer performance. For communication near apoapsis, the range is longer (on the order of 35,000 km for the 1000 x 33,000 km orbit) and the duration of mutual visibility may be several hours; therefore the higher efficiency of the coherent link may warrant ist selection.

B. Antennas

In the parametric data given in para 4.2.2.2 the total gain of both the Lander and the Orbiter antennas is taken as a variable parameter. Antennas which are fixed to the vehicle are desirable for both the Lander and the Orbiter from a reliability standpoint. The gain achievable with a fixed antenna is low because of the wide angular coverage requirement (typically 90° minimum). The selection of a relatively low frequency (i.e., 400 MHz) allows a large aperature to be used and still obtain the broad beamwidth required.

The broad beamwidth requirement is obtained by requiring the antenna pattern to be symmetrical about the roll axis. If, during the entry phase, the Capsule roll attitude were fixed, the Lander antenna pointing could be biased toward the Orbiter. The "Capsule look angle" is actually the angle between the Capsule velocity vector and the line-of-sight (LOS) to the Orbiter. During the entry phase, the Capsule center line is not always aligned with the velocity vector; however, the deviation for a particular method of operation can be taken into account by creating an envelope around this nominal angle.

Once the Lander has impacted on the surface, the Orbiter passes overhead and the look angle moves to the other side of the Lander. During subsequent communication periods, the Orbiter LOS moves from one side of the Lander - to overhead - to the other side, and thus establishes the broad beamwidth requirements for the Lander.

C. Transmission Frequency

Previous studies (refs. 4-1 through 4-3) of relay links for Mars entry vehicles have concluded that the optimum frequency is in the 100 to 400 MHz range. The recent Orbiter and Lander design studies have been centered around 400 MHz.

As discussed above, the gains of both transmitting and receiving antennas are limited because of the broad beamwidths needed for fixed antennas. As a result, the effective aperture of the receiving antenna must be reduced as the transmission frequency is raised, indicating that a low transmission frequency will be more efficient. Low frequencies are also desirable because the efficiency of converting prime lander power to r-f power is higher. In addition, for a non-coherent detection system the use of low frequencies reduces the pre-detection bandwidth required to account for frequency drift and doppler shift, resulting in improved system performance. On the other hand, at the lower frequencies, high external noise power exceeds the advantage of the increased aperture of the receiving antenna. Furthermore, the size of the efficient antennas becomes ungainly and imposes severe constraints on the Lander and Orbiter configurations. An optimization study will be performed before the selection of a final design but for the purposes of this study, the frequency selection is not critical. 400 MHz has been chosen as the nominal frequency to aid the comparison of the current results with those of previous studies.

D. Transmitter Power

The allowable Capsule transmitter power is constrained by the availability of Lander prime power, but it is also desirable to limit it to a maximum of about 50 watts to avoid r-f electrical breakdown as the Capsule descends into the atmosphere. If the antenna breaks down, its performance is degraded, thus reducing the transmitted power level because of absorption and VSWR changes; the radiation pattern is also affected. The breakdown power level is a function of the atmospheric pressure and composition as well as the antenna configuration and transmission frequency. Numerous investigators (refs. 4-4 and 4-5) have established that for conventional antenna types such as monopoles and slots, the critical pressure for breakdown varies inversely with transmission frequency. At 400 MHz, the critical pressure is about 4 mm Hg or about 0.5 millibars, which corresponds to altitudes from 15 to 60 km for the range of Mars atmospheric models. Thus, breakdown is of greatest concern during descent, although once initiated it will persist to higher pressures than that which would initiate breakdown.

A basic goal of the antenna design approach is to avoid breakdown by reducing the maximum electric field strength. Avoidance of sharp edges, increasing the diameter of rod elements, end loading, and foaming or potting at regions of greatest stress are effective means of providing higher power handling capability. Based on experimental work carried out by General Electric and others, 50 watts appears to be a conservative upper value of transmitter power from the standpoint of breakdown and has been chosen as an upper limit for the current study.

E. Bit Error Probability

The relay link bit error probability has been assumed to be 5×10^{-3} for the total link returned to the DSN stations on earth. This is based upon previous studies, in particular the "Voyager Design Study" by the General Electric Company. The bit error rate is further broken down to allow 4×10^{-3} for the Lander to Orbiter link.

F. Entry Blackout

During the entry of the Capsule into the atmosphere, a highly ionized plasma layer is formed at the front of the Capsule by the shock wave. The gas passes through an expansion region into the wake. The Capsule line-of-sight to the Orbiter generally passes through the wake region, where the high density of charged particles interact with the r-f signal to attenuate the wave below a useful level for communications. For our studies, it has been determined that blackout may occur for both entry modes, and that the design of the Communication System must take blackout periods into account. The approach assumed is to store data during blackout and read the data out after blackout in such a manner that all stored data is transmitted before touchdown. Further, it has been assumed that the maximum blackout duration is short enough to allow sufficient transmission time before blackout to permit a single time delay.

4.2.1.2.2 Direct Link

Although a direct link to earth is not recommended for the transmission of entry data in real time, it is a reasonable approach for returning stored entry data after landing as well as data collected on the surface. Although the communication range of 150×10^6 km to 400×10^6 km is on the order 10^5 times as long as the range for a periapsis relay link, useful direct links with data rates ranging from a few bits per second to several thousand bits per second can be achieved with reasonable communication system designs. A principal advantage of the direct link, is the independence of its operation from the Orbiter mission.

A major constraint on the design approach for the direct link is the requirement for compatibility with the Deep Space Network (DSN). For the purposes of this study, the performance characteristics of the DSN stations have been taken from EPD-283, Planned Capabilities of the DSN for Voyager 1973, (ref. 4-6), and from the Sapce Programs Summaries (ref. 4-7). The latter source provides data on the sensitivity expected of the non-standard listen-only feed system for the 210-foot antenna planned for use on the Mariner 1969 program. This system is also recommended for the 1973 program. For compatibility with the DSN, the following major communication parameters are thus specified:

1. Transmission frequency: 2290 - 2300 MHz

2. Receiving antenna: 85 and 210 foot diameter

3. Receiving system temperature: 28°K - 55°K depending on feed configuration

4. Carrier phase lock loop bandwidths: 12 Hz and 4 Hz

   (Receivers with 4 Hz band widths are not currently available but are considered achievable for the 1973 mission.)

The maximum Lander transmitter power is selected to be 50 watts, which is considered a safe upper limit from the standpoint of r-f breakdown.

A. Antennas

The principal system approaches for a direct link are characterized by the different types of antennas used on the Lander:

1. Body fixed antenna

2. Vertically oriented antenna

3. Earth-oriented fixed antenna

4. Steered antenna

The usefulness of a body fixed antenna is somewhat limited by the range of surface slopes that may be encountered. The 34° maximum slopes lead to minimum beamwidth of 68°. Design margins are further reduced by the difference between the landing site latitude and the latitude of the sub-Earth point (near equatorial landing sites) and the slope due to unsymmetrical crush-up following impact. Some relaxation of this constraint can be permitted if operation below the -3 dB gain point is allowed for this worst case condition. The minimum beamwidth requirement can be reduced to twice the Earth-Lander latitude difference by using a vertically oriented antenna. Even smaller beamwidths are achievable if a means of pointing the antenna toward the Earth is used. If the capability exists to nod the antenna toward the Earth so that Earth passes near the peak of the beam at some time during the day, a high gain antenna can be used. Even though the communication time would be short for this case, a high data rate can be achieved and a large amount of data returned. If the antenna is steered to follow the Earth, the time period available for communication is typically several hours each day. Table 4.2.1-2 gives a comparative illustration of the data return capability of the different approaches for one set of specific conditions. It should be noted that the transmitter energy requirements for the indicated total data return are not the same: the energy per bit returned, however, is inversely proportional to the data rate indicated. On this basis the vertically oriented antenna is at least six times more efficient than the fixed antenna, and the Earth-oriented antennas, 600 times more efficient. For the parametric data, the maximum antenna gain considered is 24 dB, corresponding to about a 3 foot diameter parabolic reflector antenna.

B. Modulation and Detection

The direct link performance is calculated assuming the same modulation and detection method used on the Mariner systems. The binary data phase shift keys a square wave subcarrier, which need not have a frequency which is a integral multiple of the data rate.

The modulated subcarrier phase modulates the S-band carrier in the 2290 - 2300 MHz band. The Multiple Mission Telemetry System, (ref. 4-8) may be used for subcarrier demodulation except for the very low bit rate systems (below 8 bps).

TABLE 4.2.1-2. COMPARISON OF DIRECT LINK ANTENNA ALTERNATES

Arrival 4/10/74
Landing latitude, 10°N -- Max. earth elevation ≈ 75°
Transmitter power, 20 ω

Antenna	Beamwidth Degrees	Gain Less Pointing Loss, db	Data Rate BPS	Data Return Bits
Fixed	83° (min)	3 dB	5 (4 Hz $2B_{LO}$)	0 to $9x10^4$
Vertically oriented	40° (opt)	9.5 dB	30 (12 Hz $2B_{LO}$)	2.3×10^5
Earth-oriented fixed	10° (size limited)	24.8 dB	3400 (12 Hz)	8.2×10^6
Steered	10° (size limited)	24.8 dB	3400 (12 Hz)	1.2×10^8

For systems which utilize data rates above about 50 bps, the use of error control coding is recommended because of the performance improvement it affords at a minimal increase in capsule complexity (ref. 4-7 and 4-9). A data detection improvement of about 3 dB is achieved using block codes such as the (32, 6) code being implemented for Mariner 1969.

As for the relay link, the bit error rate is taken to be 4×10^{-3} for the data returned to Earth. In this case, the bit error rate does not have to be divided between two links.

4.2.2 COMMUNICATION CAPABILITY

The performance of the relay and direct links is summarized in this section. Relay performance at apoapsis and periapsis is considered. Also, an optimization of the periapsis relay data return capability is persented. The direct link performance includes the Lander antenna type and the date of arrival as parameters. Finally, for the various approaches, data rate, data return and required transmitter energy are compared.

4.2.2.1 General Results

Fig. 4.2.2-1 shows the achievable data rate for a relay link operating at apoapsis. This curve, as well as those following, is based on parametric data. The range is taken to be 35,000 km and a coherent link is assumed. The abscissa includes both Lander and Orbiter antenna gains and pointing losses. Reasonable limits on the range of the various parameters is indicated on the figure by the heavy lines.

Fig. 4.2.2-2 is a similar set of curves showing the non-optimized relay performance at periapsis. A non-coherent system operating at a range of 3000 km is assumed. The upper limit on data rate is taken to be 100 kbps for the conditions assumed; however, as shown in para 4.2.2.2, the optimization indicates that the data rate is limited by the Lander antenna design to 200 kbps, and the tilt of the vehicle also affects the data return capability. The lower limit of 1660 bps is based on a minimum data return of 10^6 bits per day and a maximum transmission time of 10 minutes per day. If a coherent system is used, the performance would be about 5 dB better, but the receiver acquisition time would have to be taken into account.

Fig. 4.2.2-3 shows direct link performance using a steerable antenna. A 1 dB pointing loss is included in the results. Mars-Earth ranges corresponding to two different arrival dates are considered. The performance difference in the two cases is 4 dB; this is accounted for by the two scales used for antenna gain. The upper limit on antenna gain is assumed to be 24.8 dB, which is the gain of a 3 foot dish having a beamwidth of 10°. Other bounds are also indicated on the figure.

In fig. 4.2.2-4, direct link performance using a fixed antenna is illustrated. The pointing loss in this case is taken to be 3 dB. The lower limit on data rate over a portion of the graph is imposed by the data return requirement of 10^6 bits in the time the Earth is within the beamwidth. For instance, a 24.8 dB antenna has a 10° beamwidth, which allows 2460 sec. of transmission at a Mars rotation rate of 24.6 hours per day. To transmit 10^6 bits of data in 2460 sec. requires a data rate of 407 bps. As antenna gain is reduced, the beamwidth increases, transmission time increases, and the data rate can be reduced. The relationship between minimum allowable data rate and antenna gain in this region is:

$$R_b \text{ (min)} = 23.5 \sqrt{G}$$

For near equatorial landing sites, particularly the lower northern latitudes, the difference between the Lander latitude and the declination of the Earth is small in mid-1974. On April 20, the sub-Earth latitude is 0°, and on about September 10, the maximum Northerly latitude of 24° is reached. Therefore, over this time period, the Earth passes within 24° of the zenith every day for landing sites between 0° and 24° North latitude. The use of relatively narrow beam (and consequently high gain) antennas oriented to the local vertical provides fairly good performance with what appears to be a relatively simple antenna erecting mechanism. Therefore, the performance of such antennas was investigated. The antenna beamwidth required to maximize the total amount of data returnable was determined based on the following assumptions:

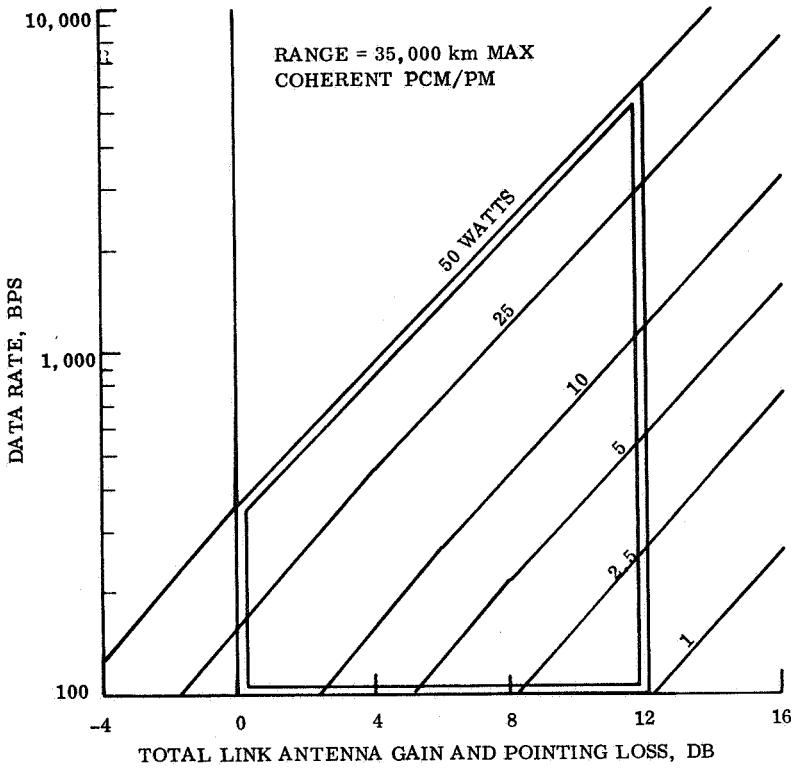

Figure 4.2.2-1. Relay Performance - Apoapsis

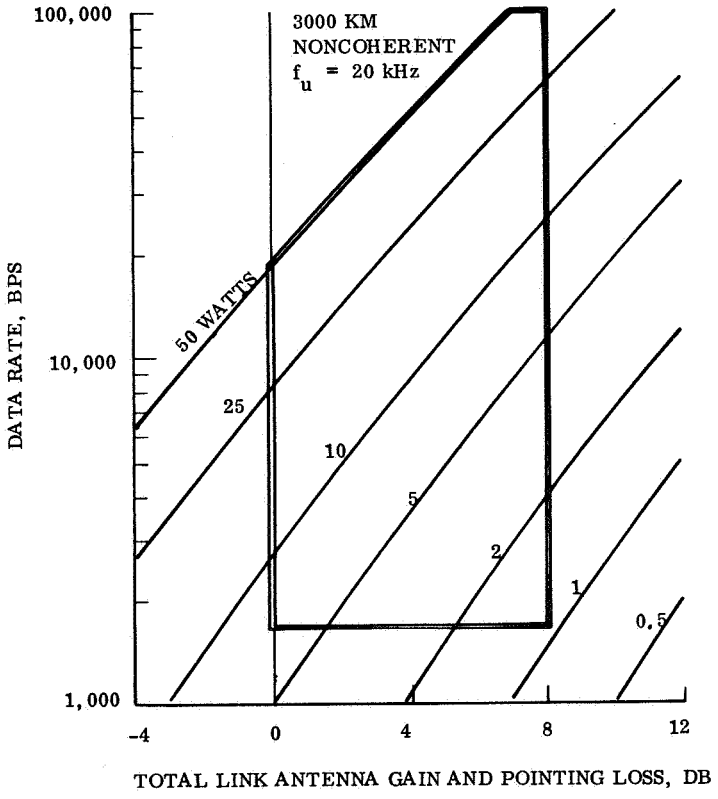

Figure 4.2.2-2. Relay Performance - Periapsis

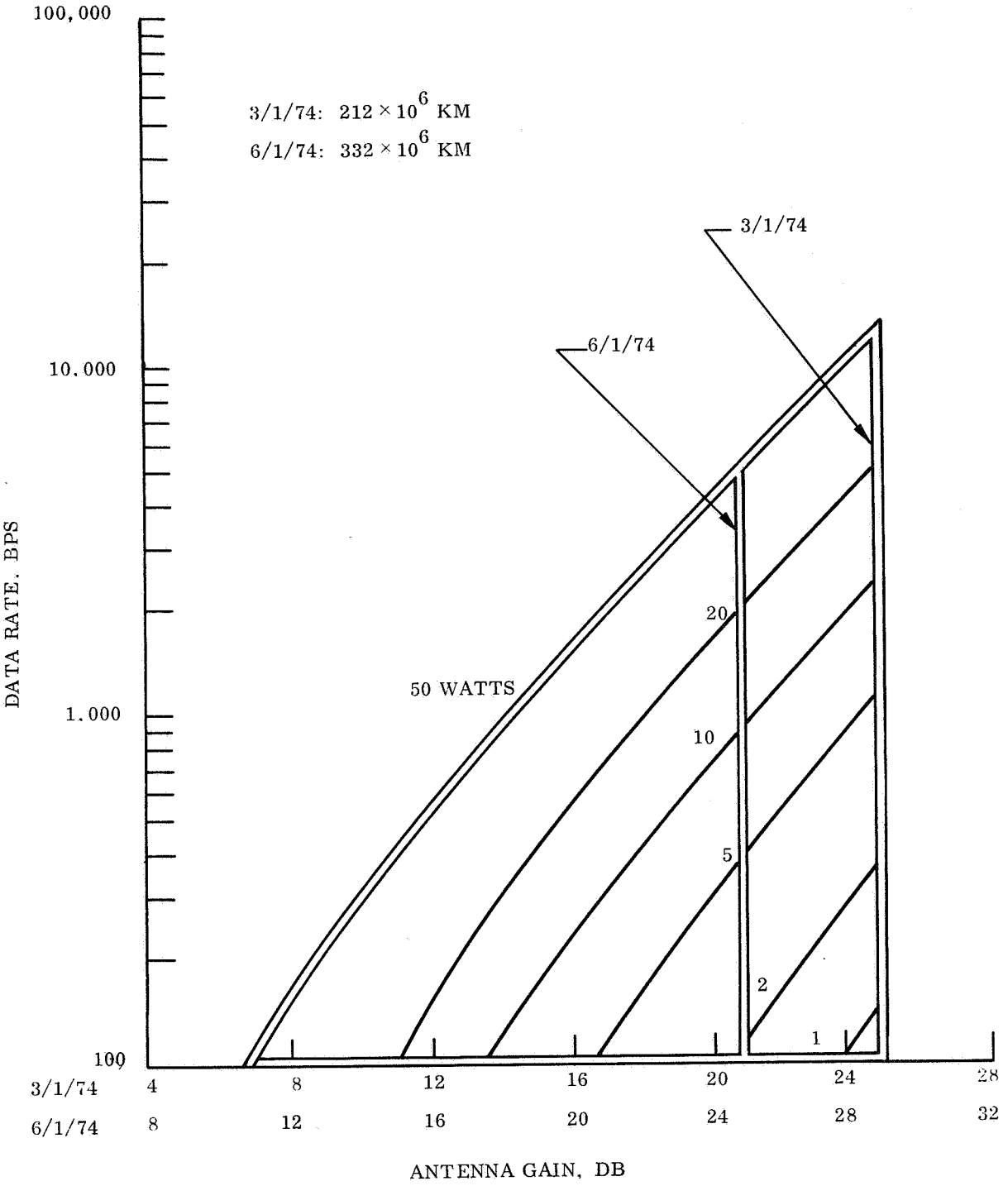

Figure 4. 2. 2-3. Direct Link Performance Steerable Antenna (1 dB Pointing Loss)

1. The landing site is near the equator.

2. The maximum difference between the landing latitude and the declination of the Earth was relatively small, about 30°.

3. A strong link was available, so that the data rate achievable varies nearly linearly with effective radiated power.

4. Communication will be guaranteed only when the Earth is within the 3 dB beamwidth of the antenna, and a constant data rate will be used, equal to the rate achievable under worst case conditions at the edge of the beam.

For these assumptions, the optimum antenna beamwidth is given by

$$\theta_a = 2\sqrt{2}\,|\lambda - \delta| = 2\sqrt{2}\,(\alpha) \text{ degrees}$$

where

λ = the landing latitude

δ = the declination of the Earth

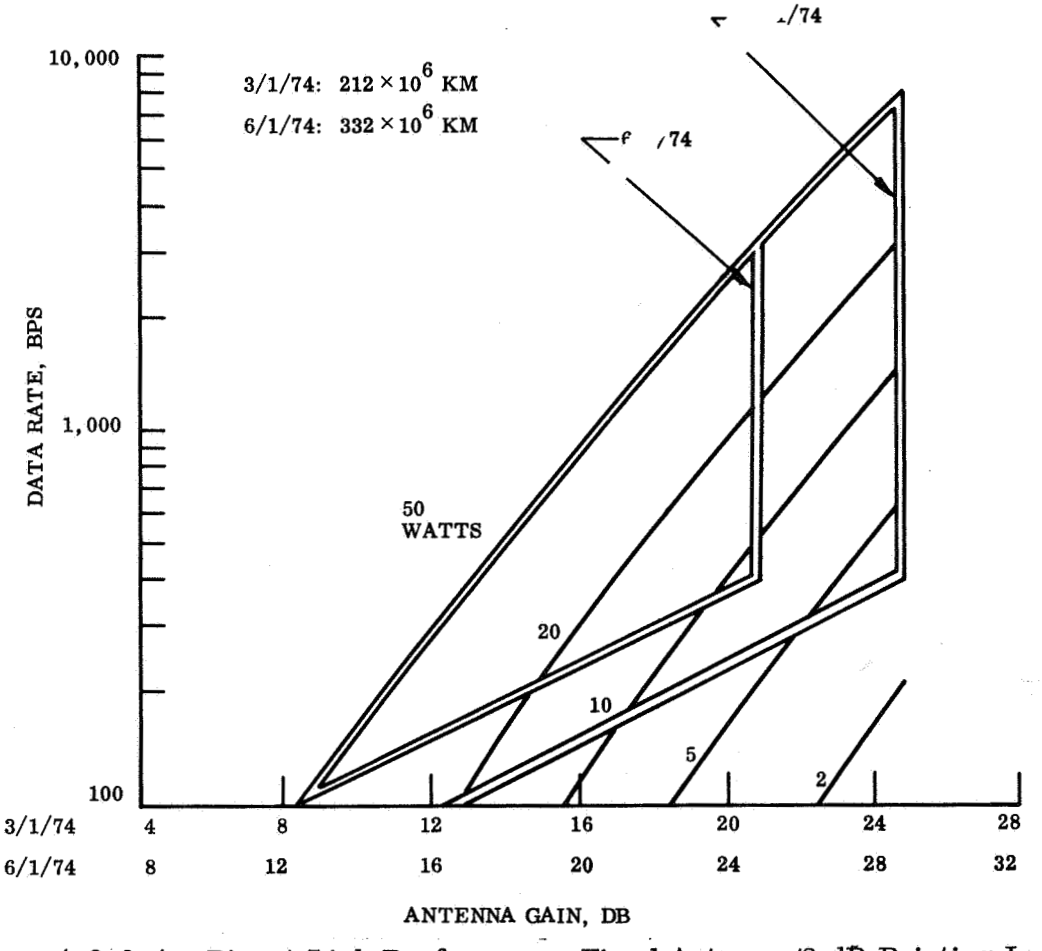

Figure 4.2.2-4. Direct Link Performance Fixed Antenna (3 dB Pointing Loss)

The duration of communications is given by:

$$T = 246\,\theta_a \sqrt{1 - 4\left(\frac{\alpha}{\theta_a}\right)^2} \quad \text{seconds}$$

where θ_a = antenna beamwidth

Fig. 4.2.2-5 shows the optimum antenna beamwidth for several landing latitudes. Fig. 4.2.2-6 shows the total data return achievable on a daily basis, assuming a 20 watt transmitter and that a DSN station is always available to receive when the viewing conditions are favorable. At the dates when the Earth passes directly over the landing site, the data return is limited to that obtainable with a peak antenna gain of about 24.8 dB, corresponding to a parabolic reflector antenna of three feet in diameter. Because the antenna beamwidth is optimized for each day, the performance indicated for a given antenna is restricted to only a few days.

In fig. 4.2.2-7 assumed limits were used to indicate the possible region of operation for each mode in terms of data rate, transmission time, and data return per day. The auxiliary graph on the right hand side of the figure indicates the potential data return per mission for a given data return per day.

Fig. 4.2.2-8 helps place the data return capability in perspective for energy-limited vehicles. The energy required to transmit 10^7 bits of data is plotted for each mode as a function of effective antenna gain. Only prime energy associated with the transmitter is considered, assuming a transmitter efficiency of 33 percent. For the relay links, the abscissa includes both Lander and Orbiter antenna gain and pointing loss; for direct links, only the Lander antenna gain and pointing loss is specified.

These plots illustrate several points:

1. Energy per bit is approximately inversely proportional to antenna gain.

2. Energy penalties are essentially the same for fixed and steerable direct link antennas.

3. Energy penalties for the apoapsis relay link and the direct links are approximately the same where an antenna gain is used that is appropriate to each type of link. Direct links require about 10 dB more antenna gain for the same required energy.

4. The periapsis relay mode is one to two orders of magnitude superior to the other modes in terms of energy penalty.

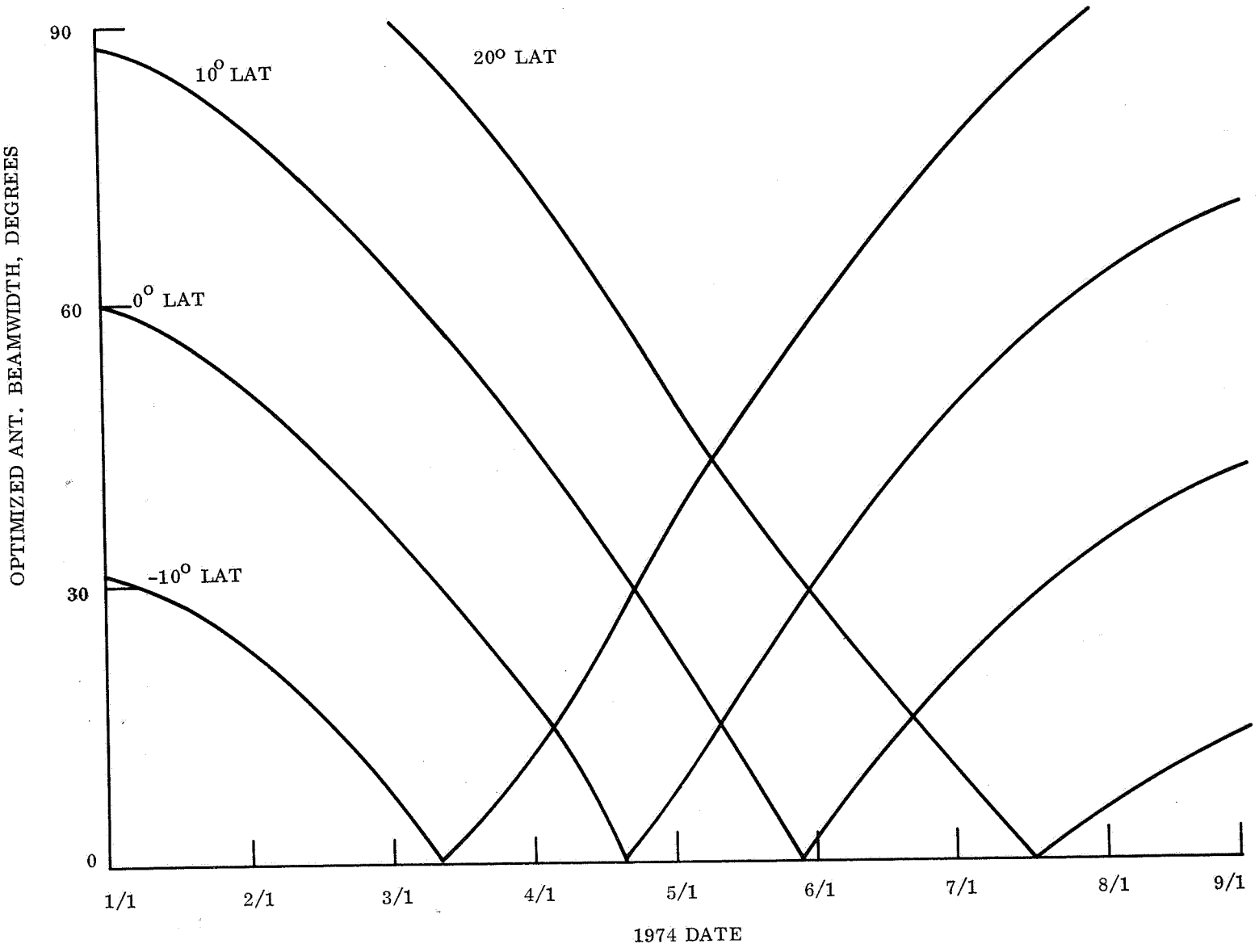

Figure 4.2.2-5. Direct Link - Vertically Oriented Antenna

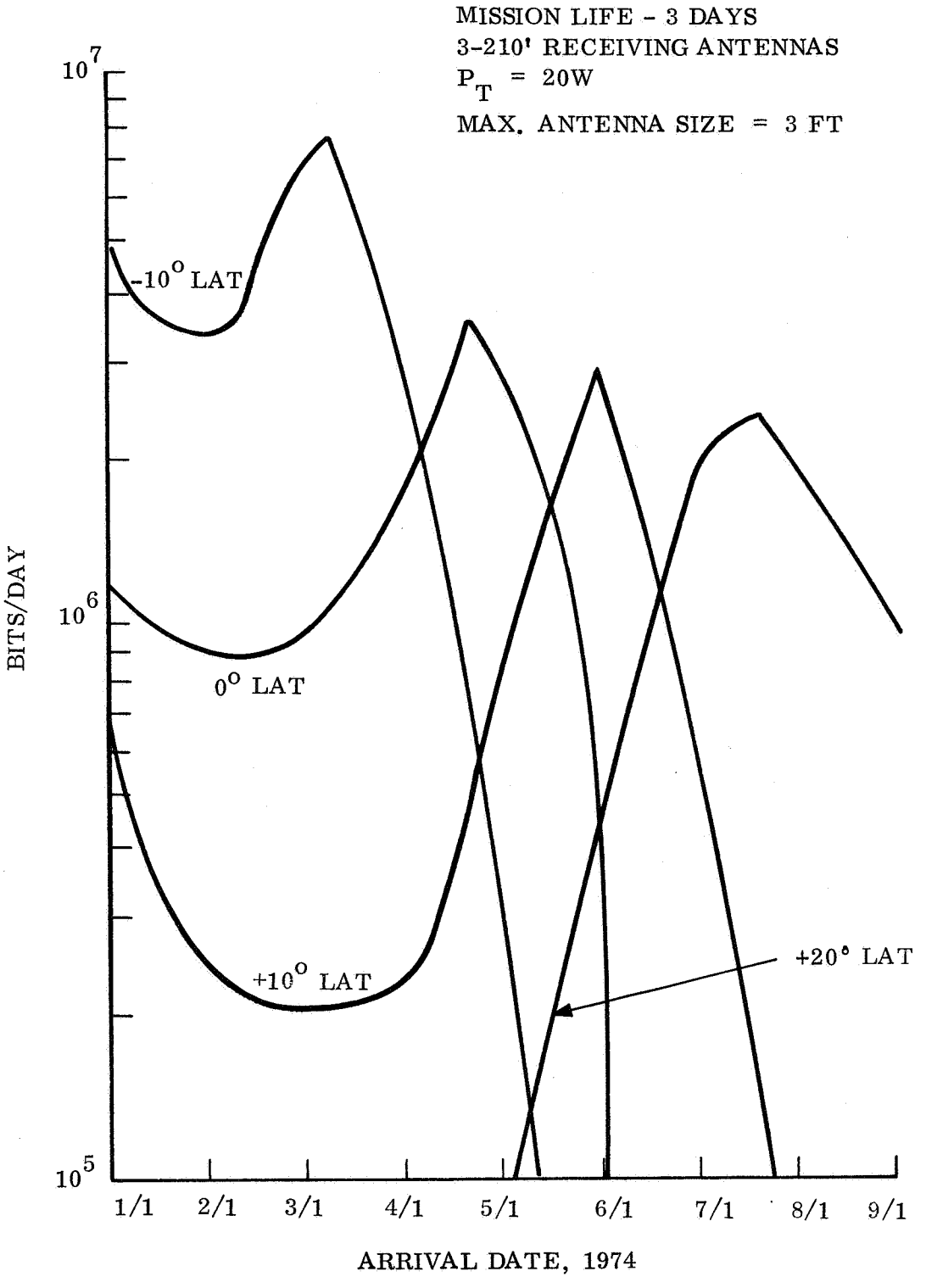

Figure 4.2.2-6. Direct Link Data Return Vertically Oriented Antenna Optimized Beamwidth

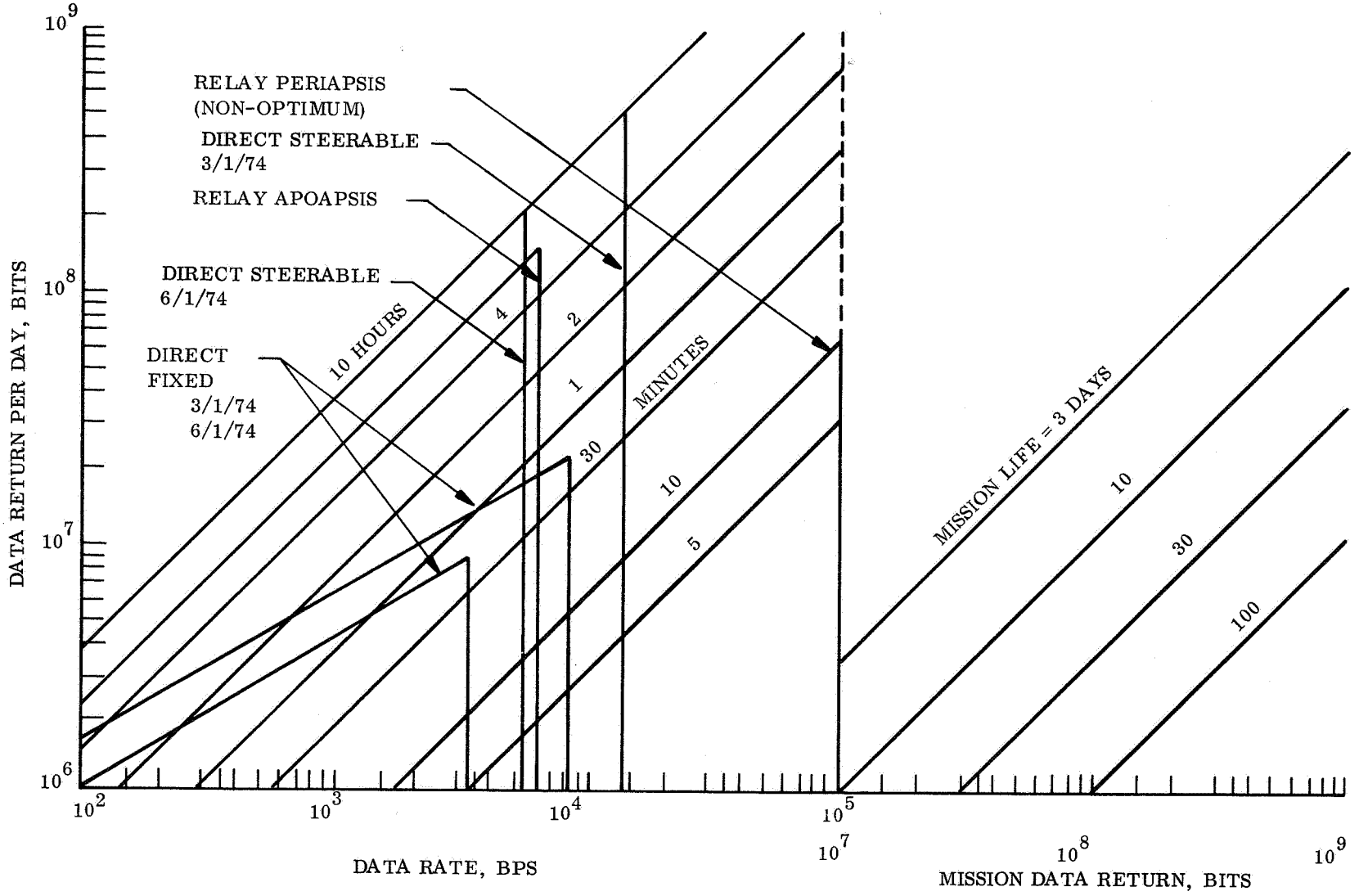

Figure 4.2.2-7. Data Return Potential

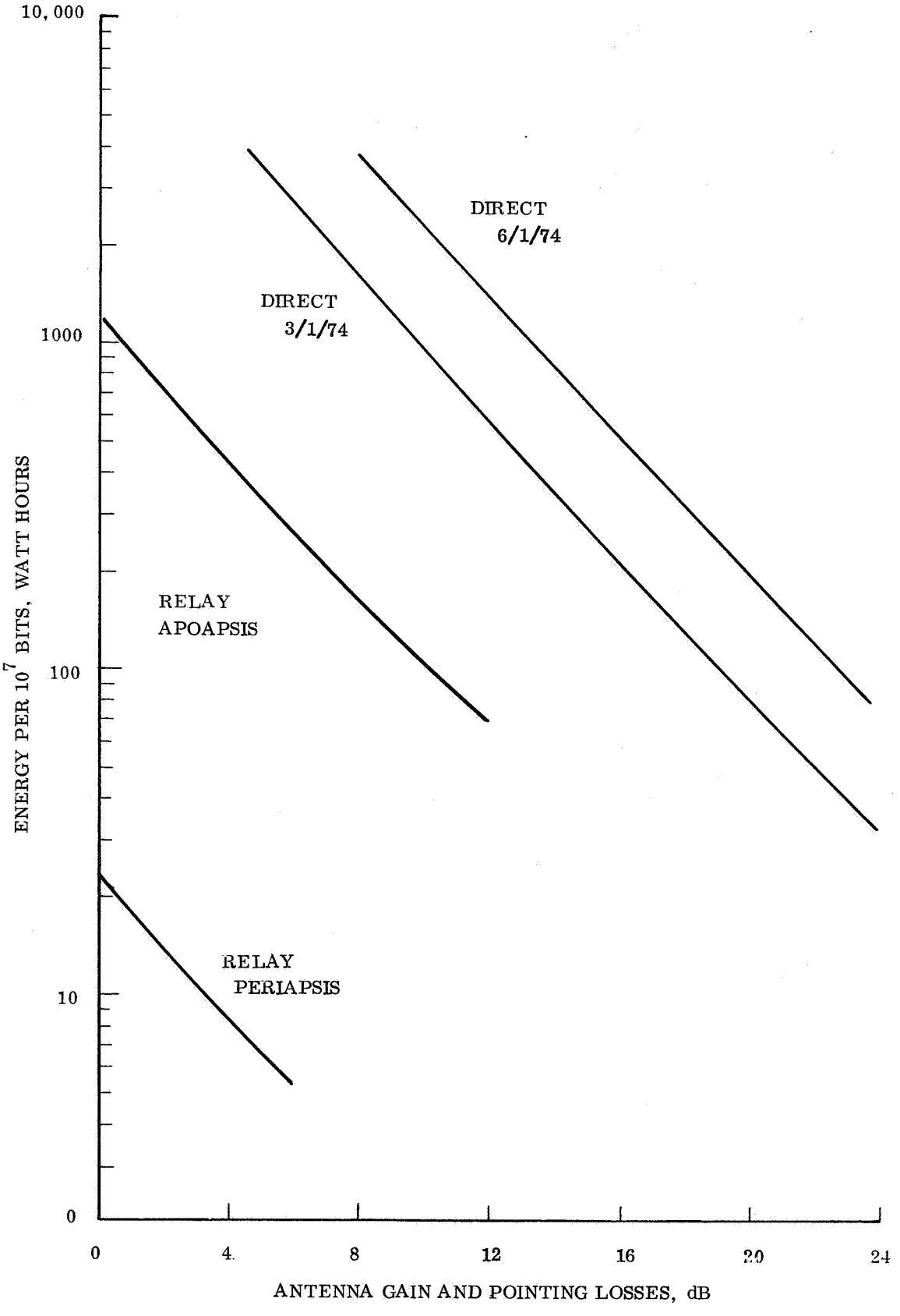

Figure 4.2.2-8. Energy per 10^7 Bits vs Effective Antenna Gain

4.2.2.2 Periapsis Relay Link Optimization

The relay link transmits data to the Orbiter during a periapsis pass and, hence, is subjected to highly dynamic communication link parameters, viz., line of sight range and angle. Additionally, the link is complicated by the requirement to have a small antenna and by uncertainty in Lander attitude, i.e., tilt.

The data rate that can be supported is primarily dependent on Lander to Orbiter range and the antenna gain along that line of sight. Since data rate cannot be dynamically varied as gain and range change, the optimization problem becomes one of determining the maximum product of bit rate times the corresponding transmission time available.

For the out-of-orbit entry case, the Lander to Orbiter range and angle periapsis pass parameters are very similar for the various proposed atmospheres such that representative data return optimization may be accomplished by considering only one model. Shown in fig. 4.2.2-9 are the range and angle from vertical for the VM-7 atmosphere model. Implicit is the assumption that the Lander site is the sub-periapsis point. The optimization technique, however, is applicable to any set of trajectory information.

Fig. 4.2.2-10 shows the antenna pattern for the small high-Q antenna employed for the 400 MHz relay link. This pattern is applicable to antenna operation over a large ground plane. Since the Lander diameter is on the order of a wave-length, the available ground plane is not large, indicating that the actual antenna pattern will vary from that shown. However, to obtain pattern details would require building and testing an antenna model.

Because the antenna pattern does vary significantly with angle-off-boresight, i.e., look angle, and the antenna is fixed relative to the Orbiter, tilt relative to the local vertical affects line-of-sight gain and, hence, available data rate.

Fig. 4.2.2-11 is a block diagram of the relay link system and table 4.2.2-1 is the design control table. The data link (Lander to Orbiter) employs non-coherent frequency shift keying (FSK) with Manchester coding and operates at 400 MHz. The transmitter normally has an output of 50 watts, the maximum allowable to avoid r-f breakdown problems at the Mars surface. For reference, a range of 1000 km and a unity (0.0 dB) antenna gain are used. A bit rate of 190 kbps can be sustained (4×10^{-3} bit error probability) with a margin of 6.3 dB which is equal to the worst case tolerance. Then the worst case (minimum) available bit rate is:

$$B = 1.9 \times 10^{11}\left(\frac{G}{R^2}\right) \text{ (bits/sec)}$$

where G is antenna gain and R is range in kilometers.

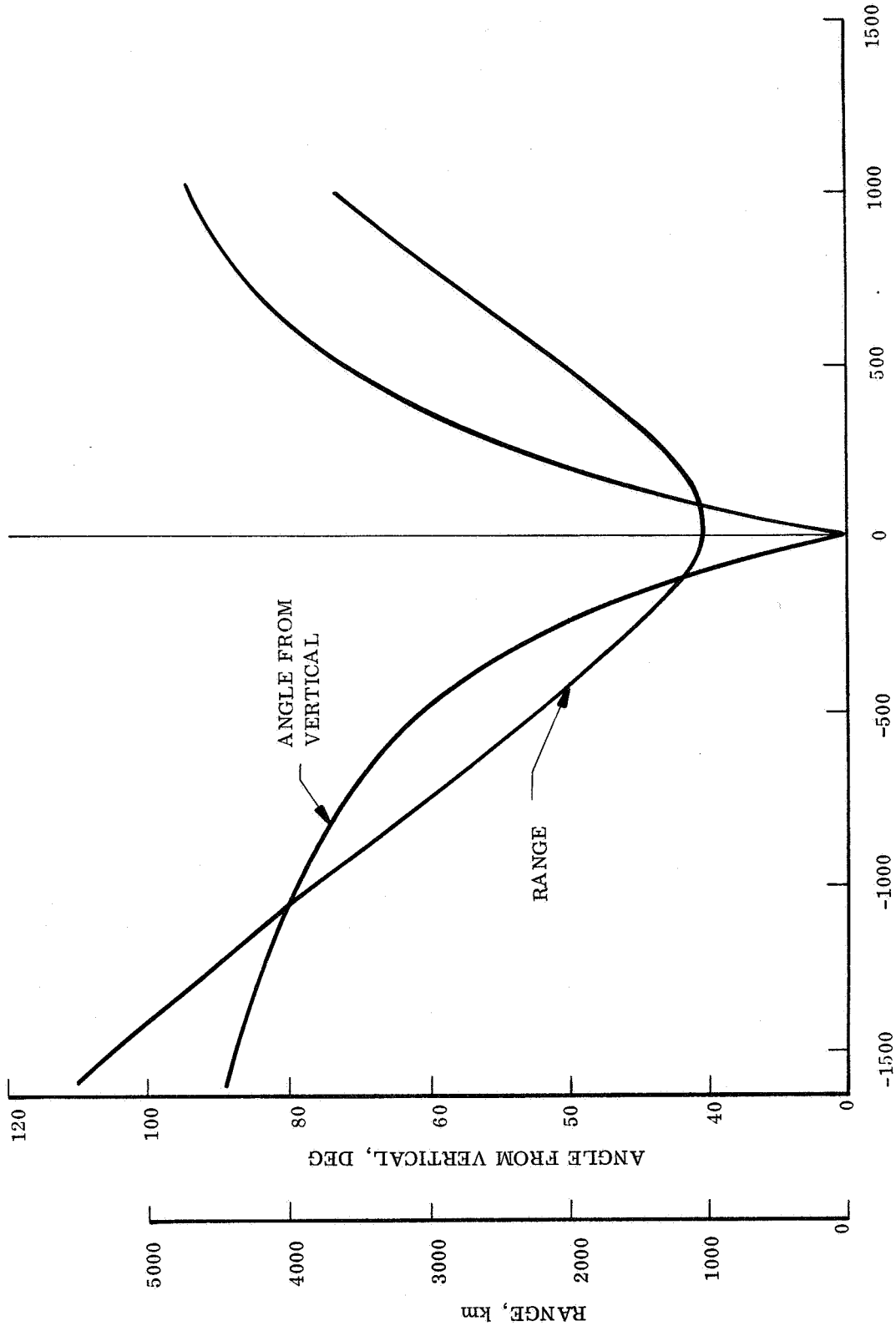

Figure 4.2.2-9. Reference Orbit Communication Parameters

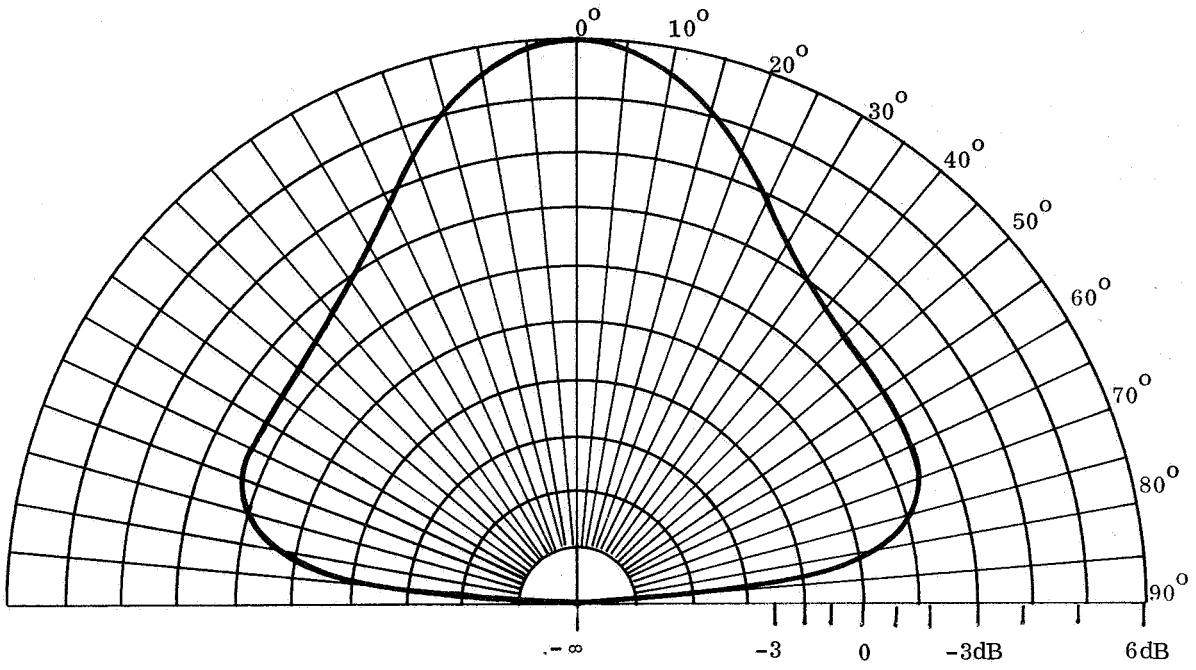

Figure 4.2.2-10. 400 MHz Antenna Pattern

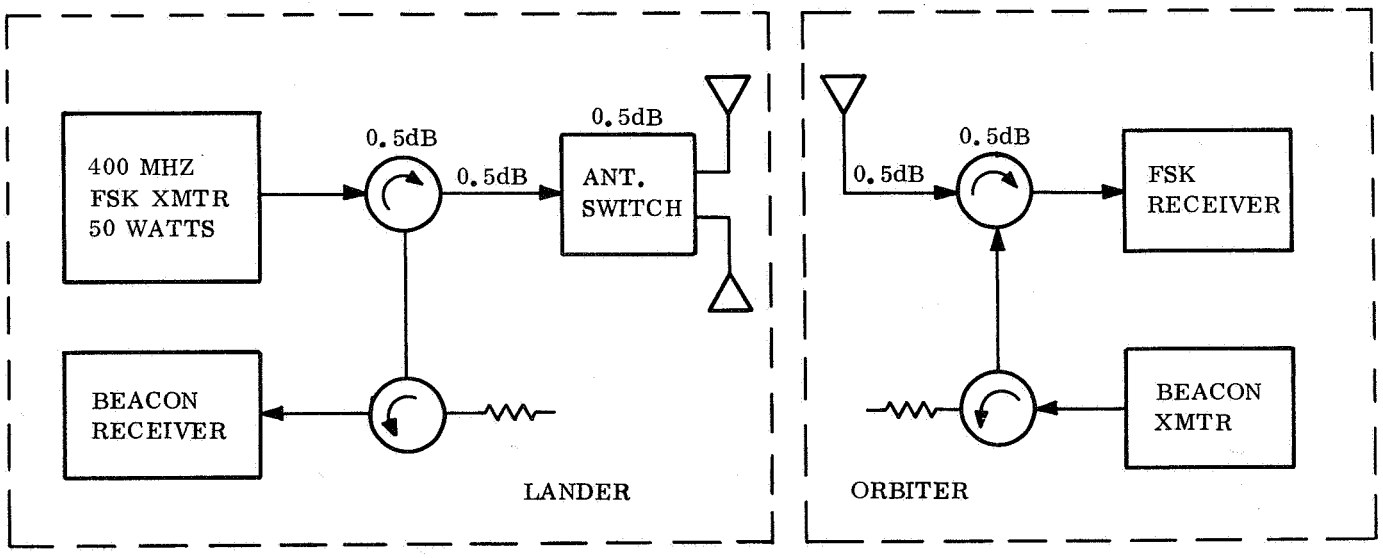

Figure 4.2.2-11. Block Diagram of Relay FSK System

TABLE 4.2.2-1. DESIGN CONTROL TABLES - RELAY (LANDED) AND BEACON

Parameter	Nominal Values and Worst Case Tolerances					
	Relay (Landed)			Beacon Link		
	Nom.	+ tol.	- tol.	Nom.	+ tol.	- tol.
Modulation Technique	FSK	--	--	CW	--	--
Frequency (MHz)	400	--	--	400	--	--
Transmitter Power (watts)	50	--	--	0.83w	--	--
(dBm)	47.0	0.0	1.0	29.3	0.0	1.0
Transmit Circuit Loss	-1.5	0.2	0.4	-1.5	0.2	0.4
Transmit Antenna Gain	0.0(1)	0.5	0.5	2.0	0.0	0.5
Transmit Ant. Pointing Loss	0.0	0.0	0.0	-1.0	1.0	0.0
Range (km)	1000(1)			1000(3)		
Space Loss	-144.5	--	--	-144.5	--	--
Polarization Loss	-1.0	1.0	0.5	-1.0	1.0	0.5
Receiving Antenna Gain	2.0	0.0	0.5	-0.8(3)	0.5	0.5
Receiving Antenna Pointing Loss	-1.0	1.0	0.0	0.0	0.0	0.0
Receiving Circuit Loss	-1.0	0.2	0.4	-2.0	0.2	0.4
Total Received Power (S), dBm	-100.0	2.9	3.3	-117.7	2.9	3.3
Effective Noise Temperature (°K)	650	--	--	724	--	--
Receiver Noise Power Spectral Density (N/B)	-170.5	0.0	1.0	-170.0	0	1.0
Bit Rate, 1/T (bps/dB)	190K/ 52.8	--	--	--	--	--
Frequency Uncertainty (kHz)	20.0(4)	--	--	16.0(5)	--	--
IF Bandwidth (kHz)	780.0	--	--	25.0	--	--
Required S/N/B	64.2(6)	0.0	2.0(6)	47.0	1.0	1.0
Required ST/N/B	11.4(6)	0.0	2.0(6)	3.0(2)	1.0	1.0
Threshold Data Power (dBm)	-106.3	0.0	3.0	-123.0	1.0	1.0
Margin	6.3	2.9	6.3	5.3	3.9	5.3

(1) Reference values.

(2) Signal-to-noise ratio in i-f bandwidth.

(3) Values chosen correspond to G/R^2 ratio required by relay link to support 160 kbps data rate.

(4) Transmitter stabilizer ±10 PPM; receiver stability ±5 PPM; doppler ±4 kHz.

(5) Same as (4) except only positive doppler need be considered.

(6) Nominal signal-to-noise ratio is theoretical value. 2dB adverse tolerance is allowed to account for detector performance degradation, e.g., non-ideal bit sync.

Using this relation and the Lander-Orbiter range and angle parameters, available bit rate versus time is computed for specific Lander tilt conditions. Typical results are shown in fig. 4.2.2-12. The reference condition of zero tilt shows a very sharp peak as the Orbiter passes overhead. This is the result of minimum communication range and maximum antenna gain. When the Lander is tilted in the Orbiter plane, the peak gain is pointed off of vertical and tends to counteract the bit rate loss resulting from increasing range. The net effect of in-plane tilt is a lower peak data rate and longer available transmission time at near peak data rates. On the other hand, pure out-of-plane tilt lowers the gain and, hence, available data rate at all times.

Optimization is accomplished by examining the communication time as a function of bit rate for positive and negative in-plane tilt and for out-of-plane tilt. The maximum total data that can be transmitted with confidence at a specific bit rate is the product of bit rate and minimum communication time for the three tilt conditions considered. The bit rate yielding the largest maximum total data transmitted is the optimum bit rate.

Fig. 4.2.2-13 shows the maximum data transferable and corresponding optimum data rate without regard to bandwidth limitations. The small high-Q antenna used has a bandwidth capacity on the order of 2 MHz which imposes a data rate limitation.

Using Manchester coding, a bandpass of four times the bit rate is required about each of the transmitted frequencies. Allowing a guardband equal to the bit rate* yields an r-f bandwidth requirement of ten times the bit rate. Thus, the antenna limits the maximum data rate to approximately 200 kbps. The resulting effect on data transferable is indicated in fig. 4.2.2-13.

Specific application of the results of this optimization study is deferred to the telecommunication sections of the point designs.

4.2.2.3 Effect of Mission on Communication System

The effects of the mission parameters, such as arrival date and landing latitude, upon the direct link are described in graphic form in figs. 4.2.2-14 through 4.2.2-19. In all cases described, a vertically oriented antenna and a 90 day mission design are assumed.

Fig. 4.2.2-14 shows the data rate capability as a function of arrival time, assuming the worst case data rate is used throughout the mission. The antenna beamwidth was optimized for the particular mission based upon the data of fig. 4.2.2-5. The initial dip in the curve indicates that the range is increasing more rapidly than the antenna gain is increasing. However, the condition is reversed and the peak data rate capability occurs around the latter part of April, 1974. The effect of latitude variations are discussed later.

*The guardband assumed here is estimated to be sufficient to reject the unwanted signal. Further investigation is required to evaluate cross-talk due to spectral spreading.

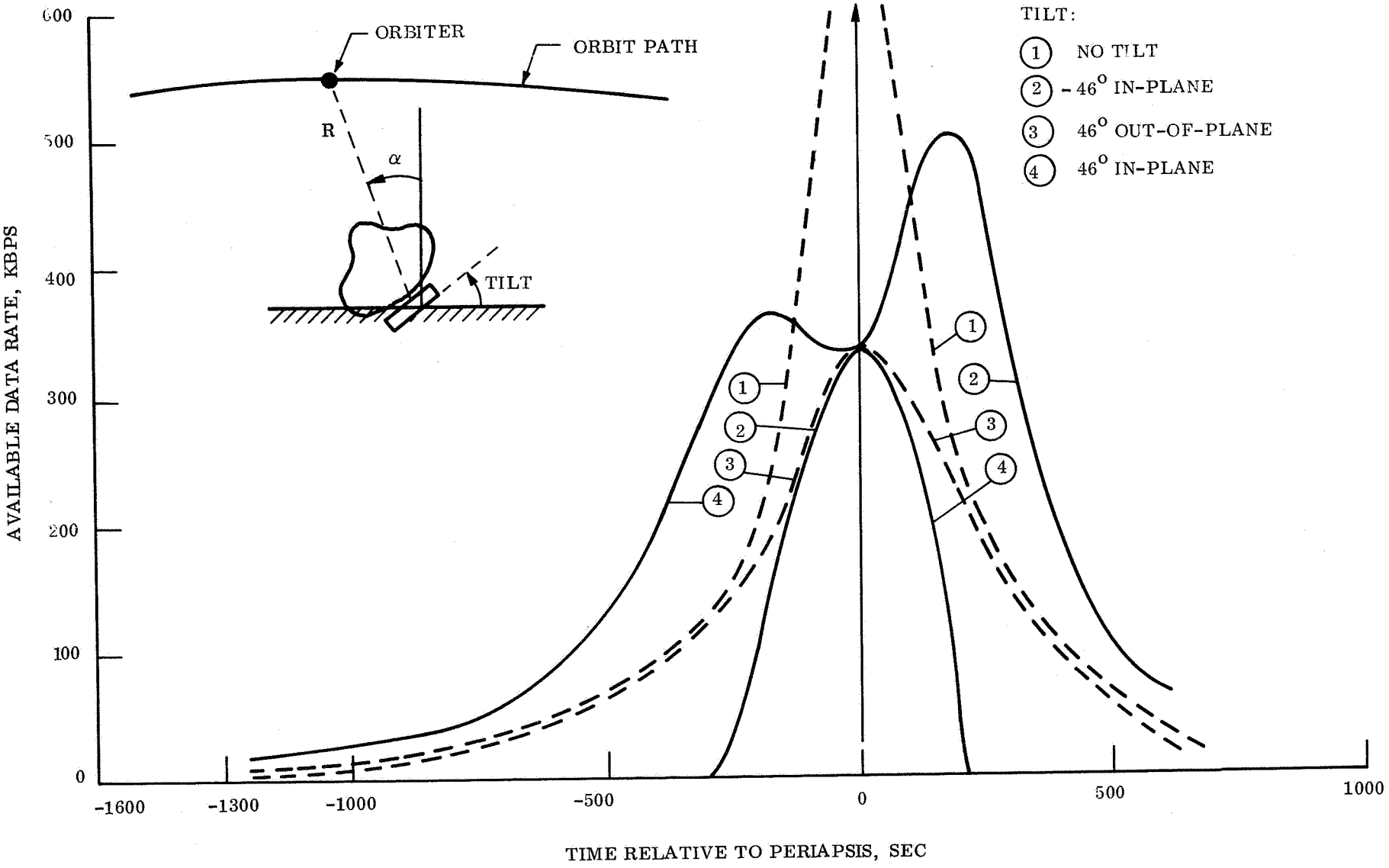

Figure 4.2.2-12. Available Data Rate vs Time with Adverse Tolerances

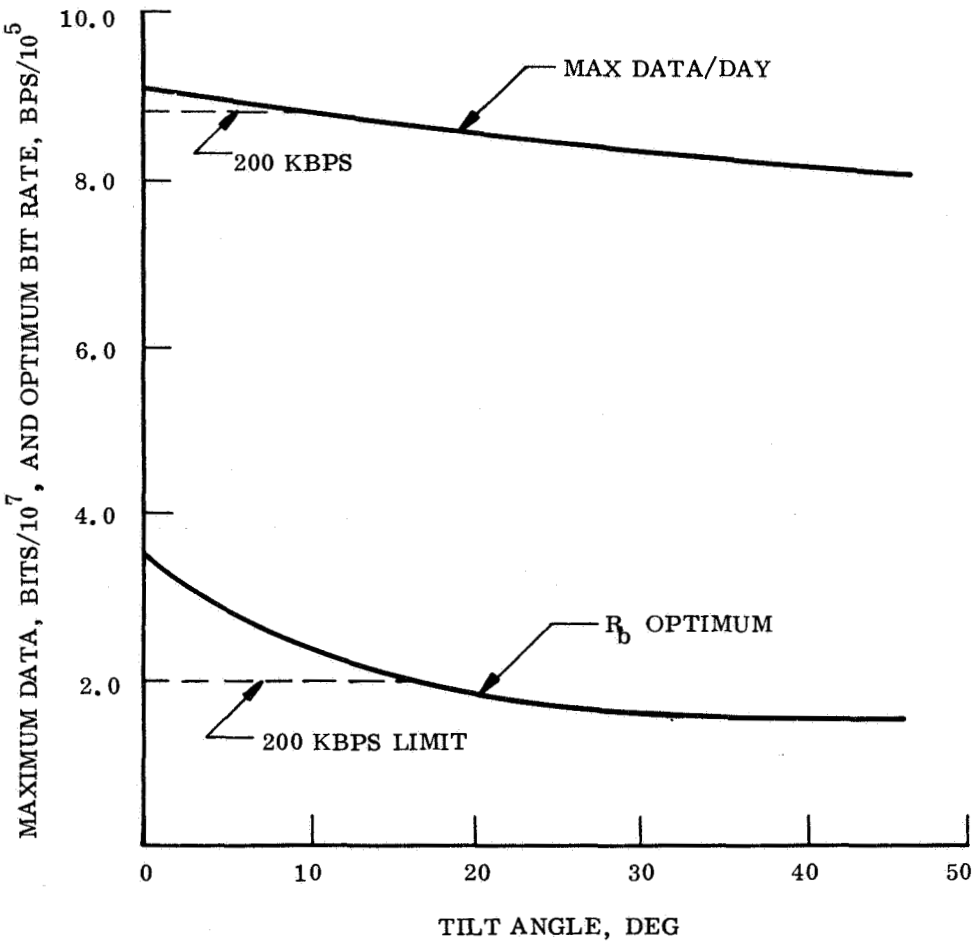

Figure 4.2.2-13. Maximum Data per Day and Optimum Bit Rate

The effectiveness of changing data rates during the mission is shown in fig. 4.2.2-15 for both the early encounter of 1/10 and the later arrival of 4/30. The data rate change shown is due to the increasing range during the mission. In the case of the 1/10 arrival, the received signal to noise density ratio decreases to a point where a further transition from coded to uncoded data transmission is required.

Figs. 4.2.2-16, -17, and -18 indicate the effect of landing latitude (or landing dispersion) on the Communication System performance. Fig. 4.2.2-16 indicates the allowable data rate during the mission lifetime for 10°N and 25°N latitudes. Fig. 4.2.2-17 shows the data return for various latitudes for a 4/30 arrival with a fixed transmission time based upon power limitations. The same data is shown in fig. 4.2.2-18 for a 1/10 arrival. At 50°N latitude the performance during the first half of the mission lifetime is marginal under the assumption of a constant data rate over the mission lifetime. Another mode of operation would have to be considered if this combination of latitude and arrival date is used.

The final graph (fig. 4.2.2-19) compares the data rate capability of a 50 watt and 20 watt transmitter during the mission life for a 4/30 arrival. In the case of

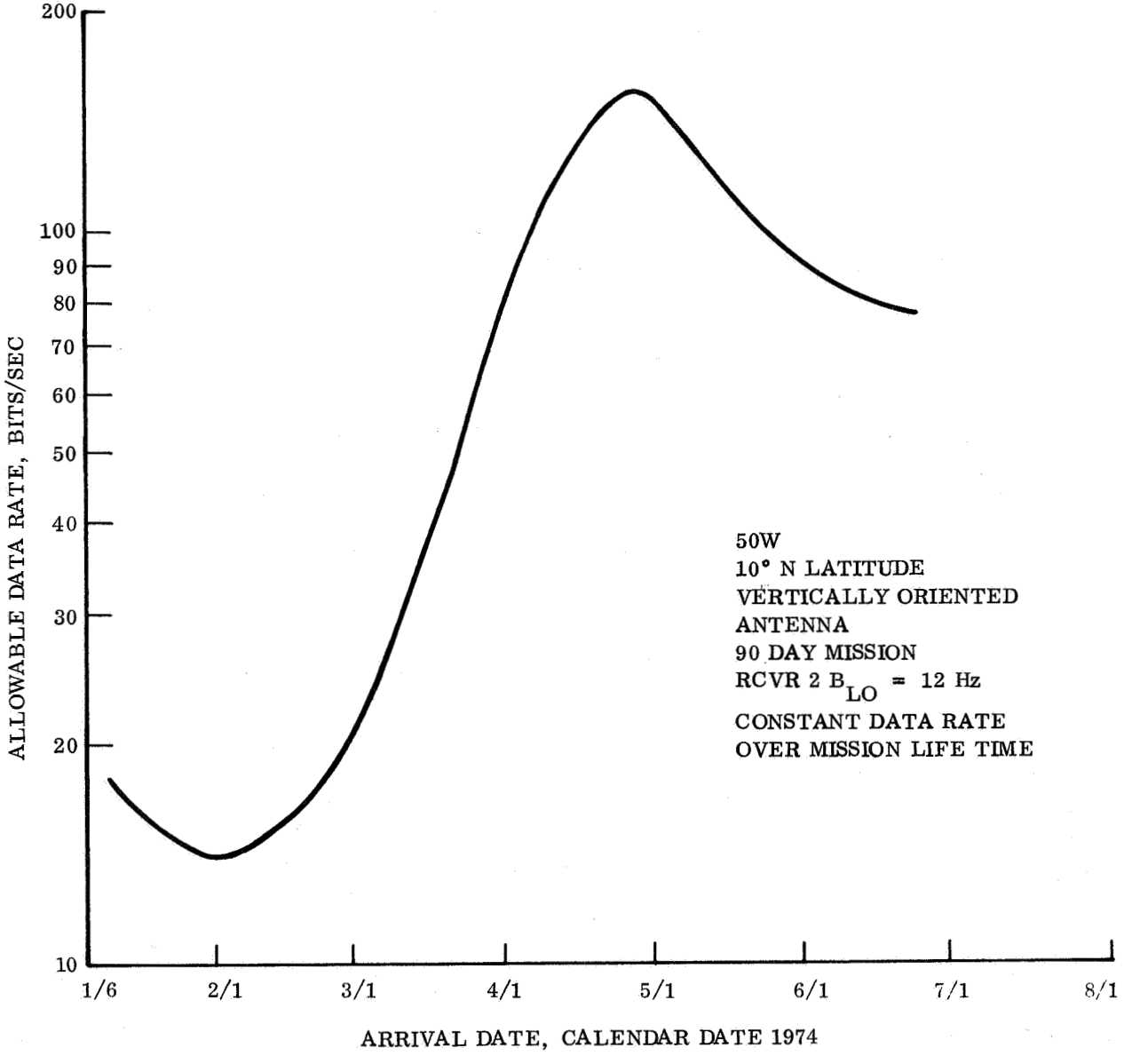

Figure 4. 2. 2-14. Direct Link Data Rate Capability as a Function of Arrival Time

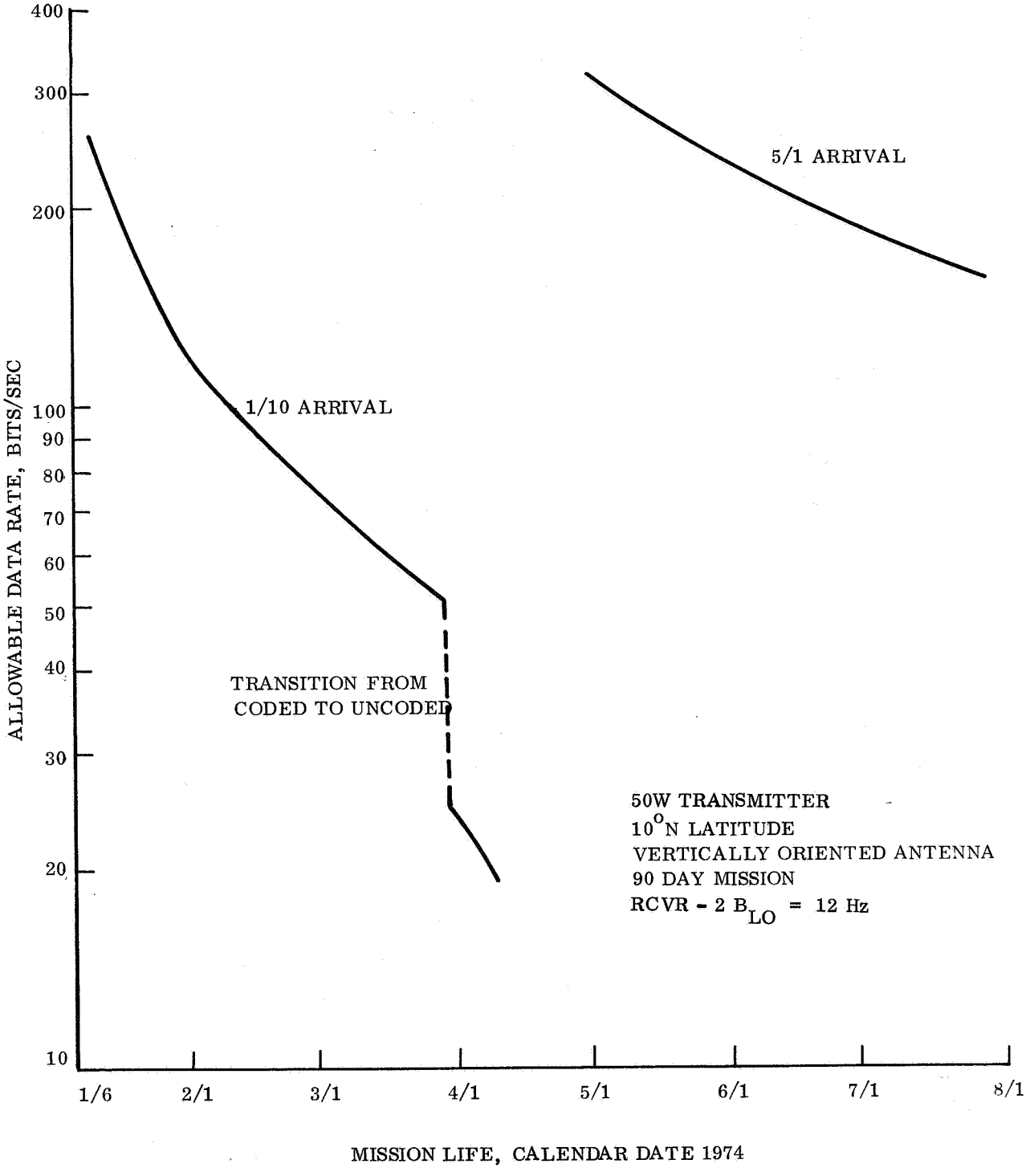

Figure 4.2.2-15. Direct Link Effectiveness of Changing Data Rates

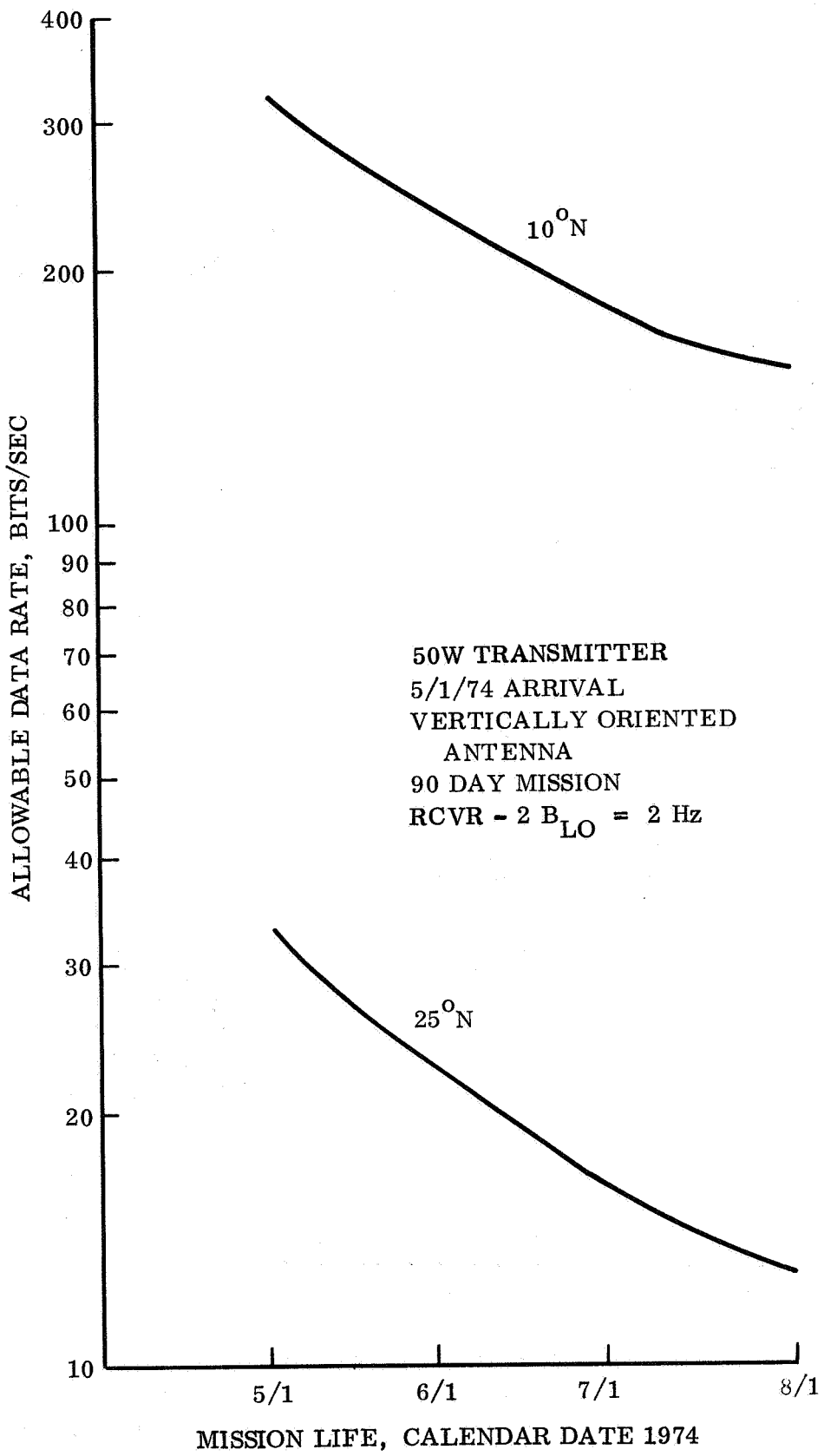

Figure 4.2.2-16. Direct Link Allowable Data Rate during the Mission Lifetime for 10^{o} N and 25^{o} N Latitudes

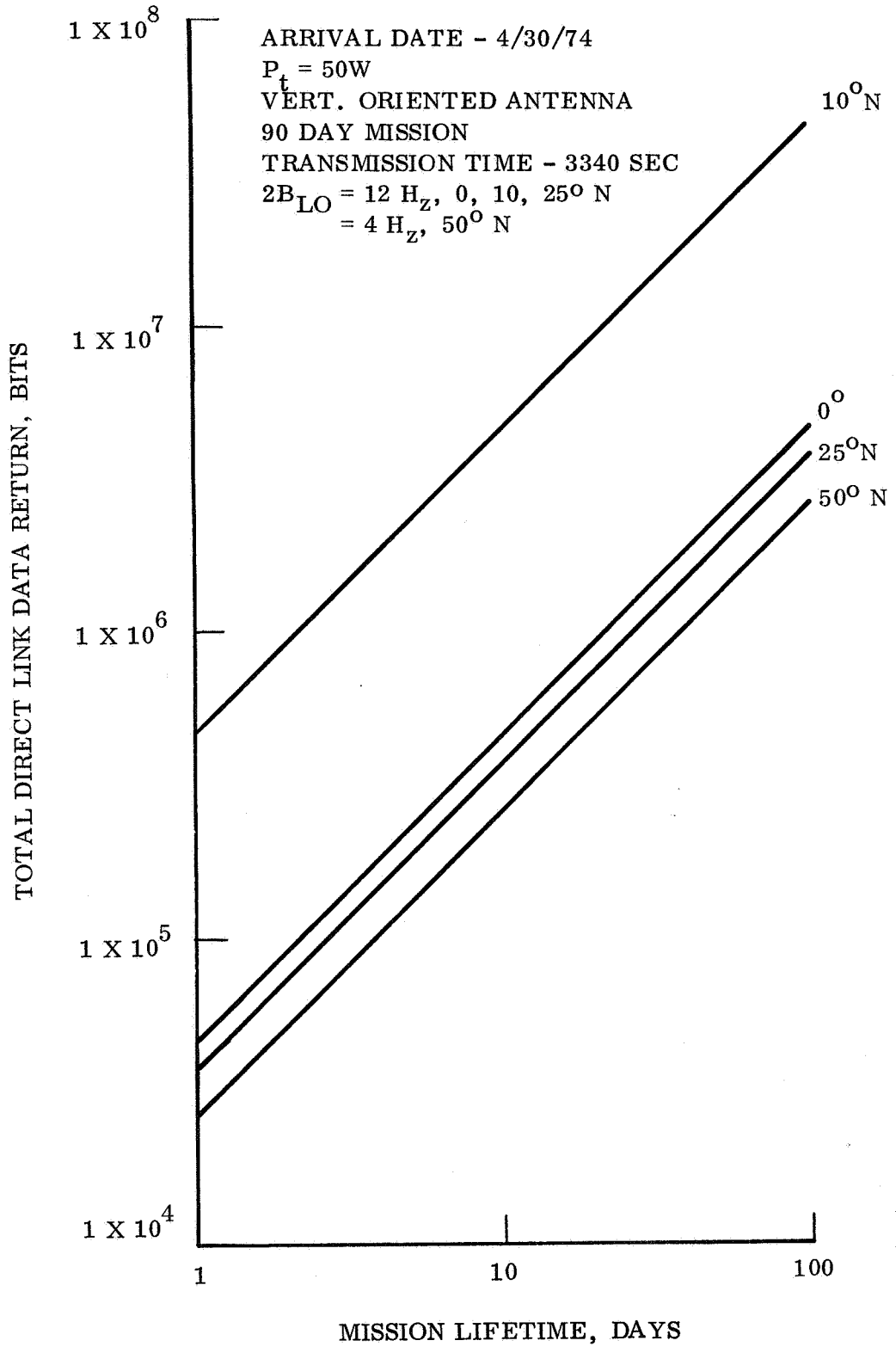

Figure 4.2.2-17. Data Return for a 4/30 Arrival with Fixed Transmission Time Based Upon Power Limitations

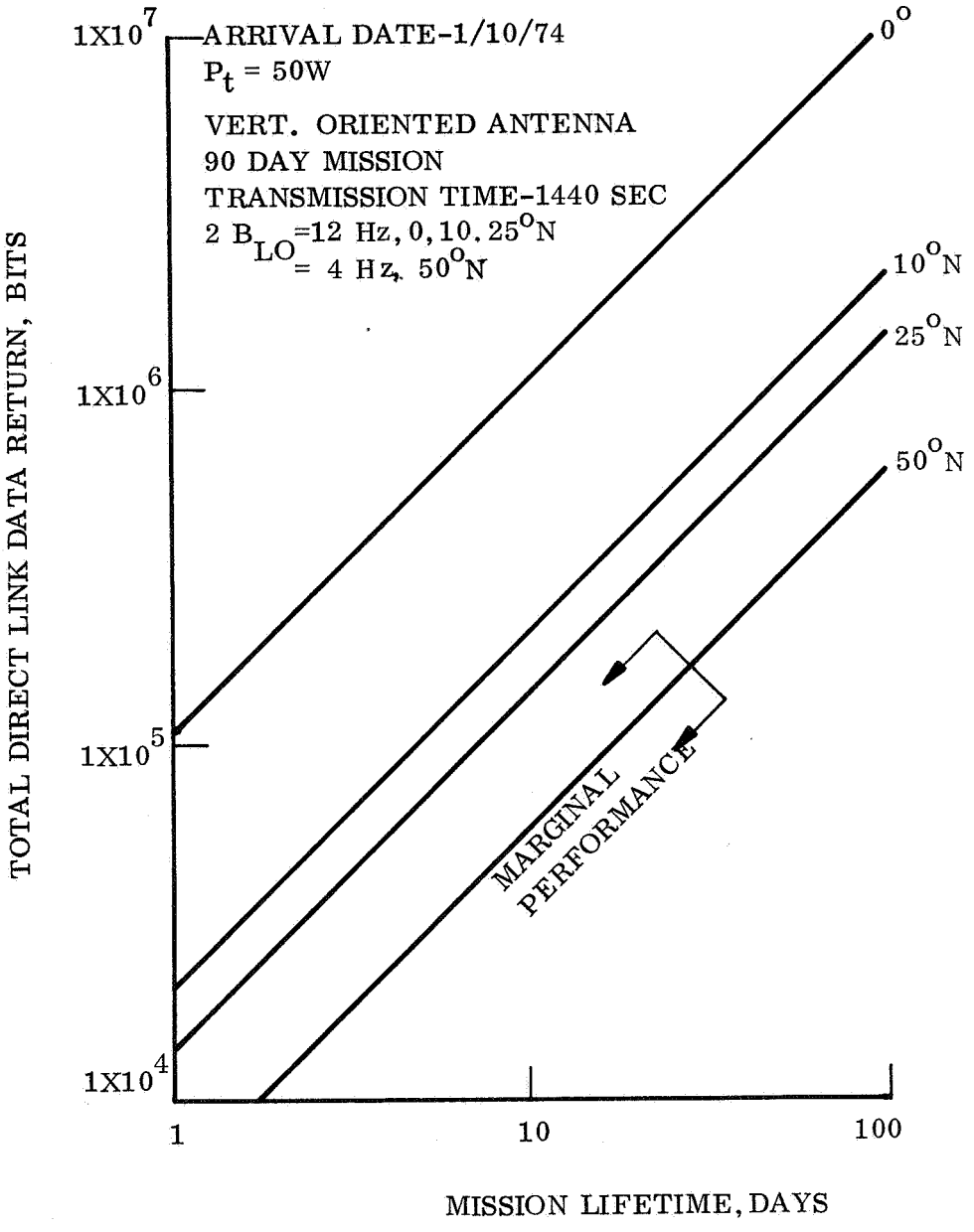

Figure 4.2.2-18. Data Return for a 1/10 Arrival with Fixed Transmission Time Based Upon Power Limitations

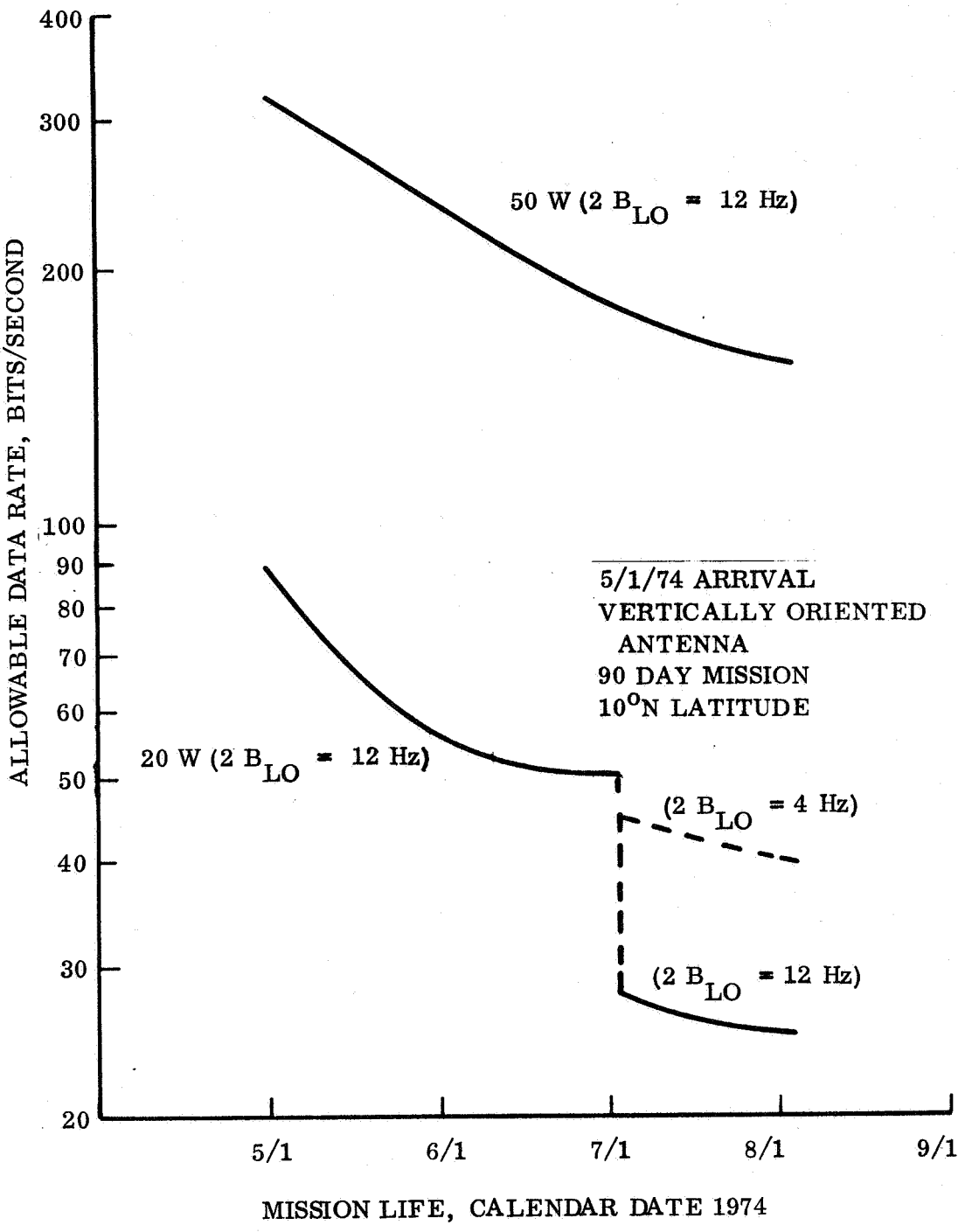

Figure 4.2.2-19. Direct Link Comparison of Data Rate Capability of 50 and 20 Watt Transmitters during Mission for 4/30 Arrival

the 20 watt transmitter (which has been developed for the Hard Lander application, para 4.2.3.5), the additional transition from coded to uncoded data return occurs. Since, at the low data rate, the bulk of the transmitted power is required for carrier lock at the ground receiver, it is of added interest to show the effect of switching to the proposed 4 Hz bandwidth. The data rate for this case is shown as a dotted line.

4.2.3 PARAMETRIC PERFORMANCE DATA

In this section, parametric data are presented from which communication system performance can be determined for a wide range of system variables for both relay and direct links. These data have been found useful and accurate in making approximate comparisons of alternate system designs. It has also been found, for specific applications, that some of the assumptions required modification to be compatible with variable ranges. For example, the r-f losses between the transmitter and the antenna depend on the length of cable runs and the number of connectors and rotary joints in the run, which are a function of the particular vehicle configuration being considered. For some Landers, electrically small transmitting antennas are considered which require matching, which reduces the efficiency of the antenna system, and hence yields a differenct relation between antenna gain and beamwidth than is presented in the following curves. Other parameters also vary with the specific implementation. For this reason, the expected performance of any particular design should be based on a detailed link calculation for that design, considering in detail all factors that affect performance.

4.2.3.1 Relay System Description

The parametric performance calculations for the relay link are based on the use of two types of systems: wideband non-coherent FSK and coherent PSK/PM. The characteristics of these systems that influence the parametric performance data are described in this section. A block diagram of the FSK system is shown in fig. 4.2.3-1, and the waveforms for this system are illustrated in fig. 4.2.3-2. The PCM data has an NRZ binary format with bit rate R_b at the input. This signal biphase modulates a square wave subcarrier having a frequency R_b to produce a split phase coded signal. The power spectrum of this signal has a $\sin^4 x/x^2$ envelope when the data is random, as illustrated in fig. 4.2.3-3. The split-phase signal frequency modulates a 400 MHz carrier for transmission to the Orbiter. The spectrum of the r-f signal is also shown in fig. 4.2.3-3. Where a single VCO is frequency modulated as shown in fig. 4.2.3-1, the shape of this spectrum depends on the modulation index (the ratio of the frequency deviation ΔF to the data rate R_b) (ref. 4-10). When the modulation index is high, as assumed in the present case, the spectrum contains both discrete and continuous components; half the power is in the discrete spectrum, and half in the continuous spectrum. The continuous spectrum has the same $\sin^4 x/x^2$ form as the baseband split-phase signal when the modulation index is high. In an alternate implementation, two independent oscillators are switched by the split-phase signal, and the spectrum is the same as that shown in fig. 4.2.3-3, irrespective of the modulation index (ref. 4-11). The selection of the approach to be used for a particular application depends on implementation considerations such as stability and reliability. The performance achievable with both approaches is the same.

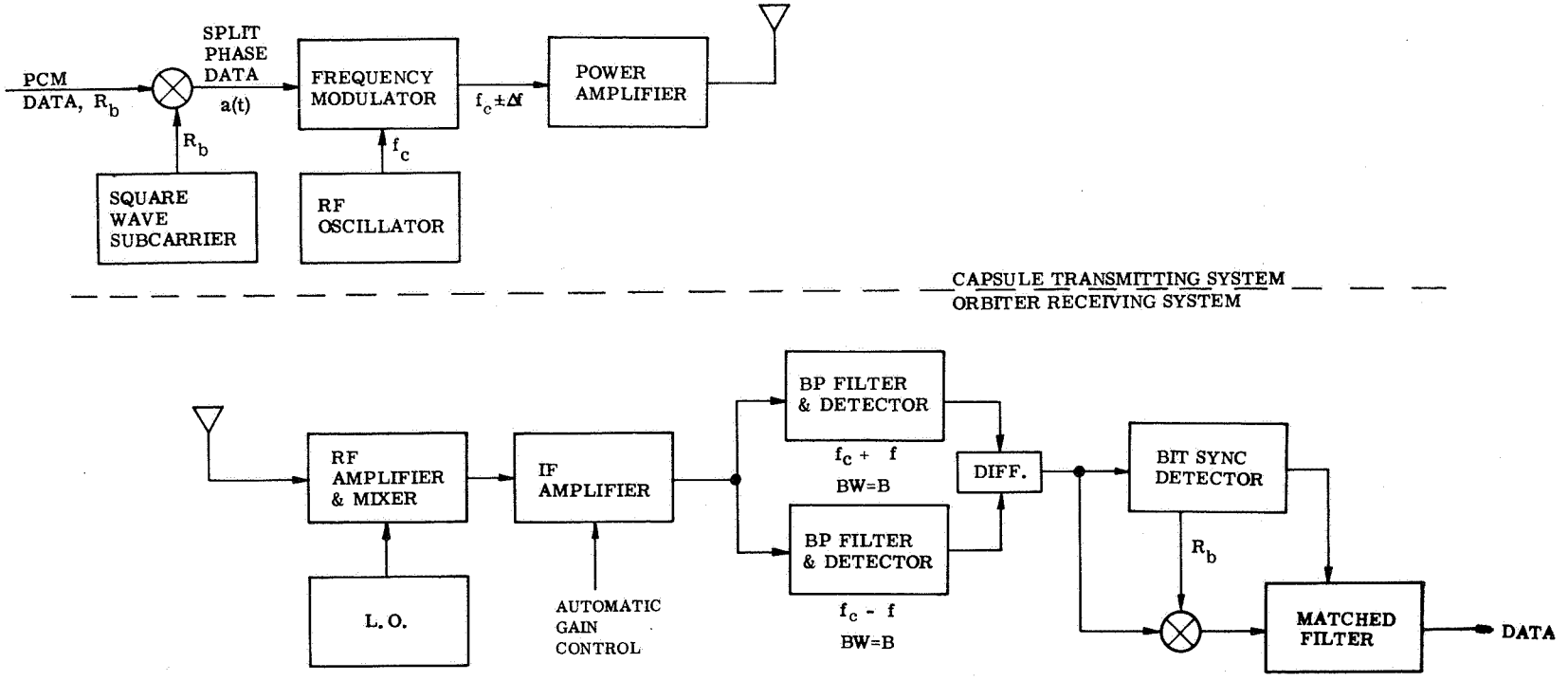

Figure 4.2.3-1. Wideband FSK System

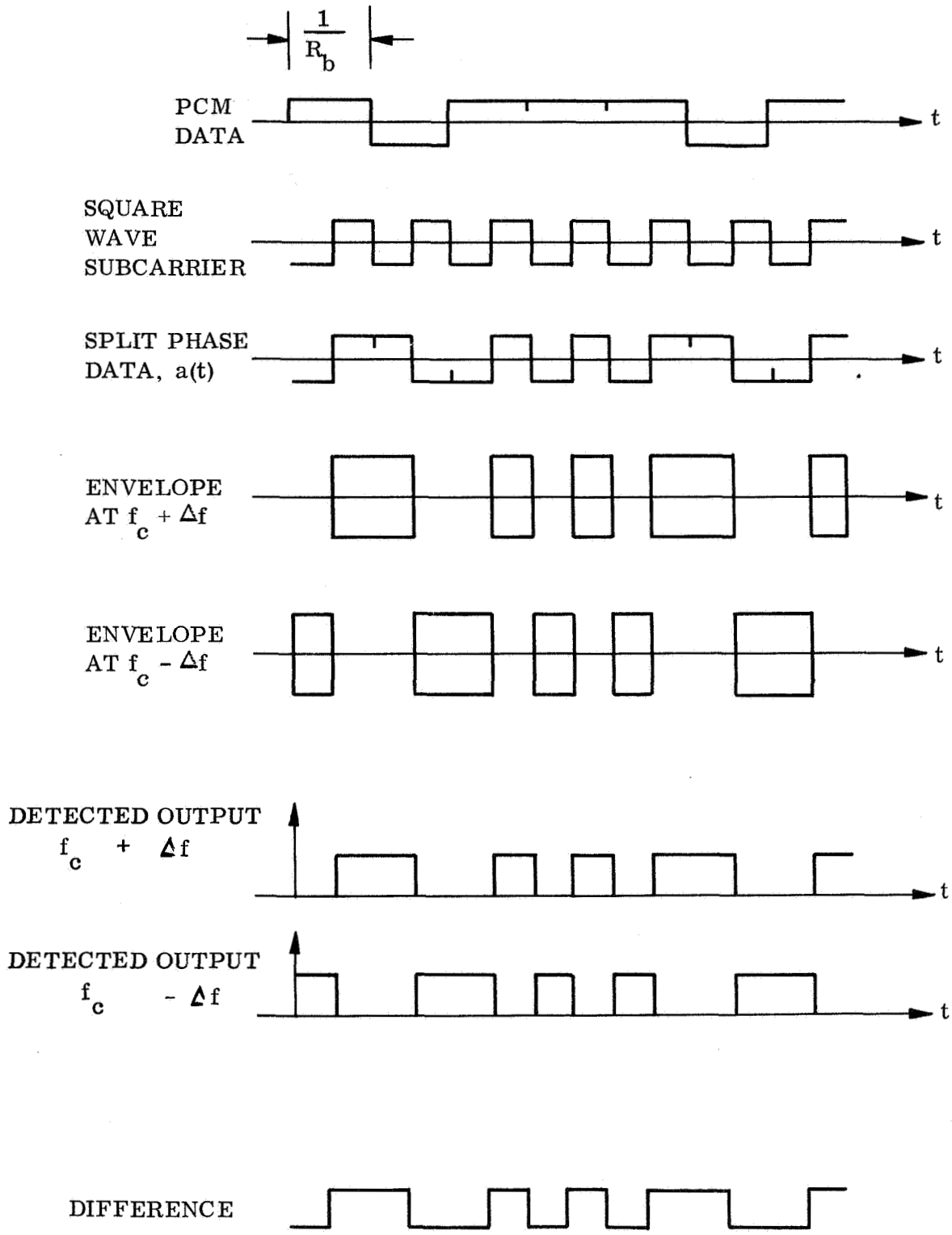

Figure 4.2.3-2. Waveforms for Non-coherent FSK System

In the Orbiter receiver, the 400 MHz signal is translated in frequency to i-f and then amplified. The i-f amplifier is gain-controlled to provide a constant output level. The two signaling frequencies are bandpass-filtered and detected in their respective channels. Because of the split phase format, the detector output can be ac-coupled. This eliminates the unbalance due to noise that can occur in the output signal when the detector is direct-coupled. Such an unbalance can result from unequal gains or unequal predetection bandwidths in the two receiving channels. This unbalance can seriously affect the performance of the receiver, especially when the predetection SNR is low (ref. 4-12). The two detected outputs are differenced and fed to the bit sync detector (one means available for the unambiguous recovery of bit sync from a split-phase signal is indicated in fig. 4.2.3-4). The bit sync detector generates a square wave subcarrier at frequency R_b to convert the split-phase difference signal back to the NRZ format. This signal is integrated in a matched filter and sampled to provide the data at the receiver output.

The performance of the wideband FSK receiver is a function of bit period T and predetection bandwidth B. The predetection bandwidth is somewhat wider than the bandwidth of the signal spectrum to allow for frequency uncertainties due to oscillator instability and doppler shift. Fig. 4.2.3-5 gives the required bit energy-to-noise power density ratio (E/No) as a function of the BT product, for a bit error probability, Pe, of 4×10^{-3}. The curve is based on an analysis due to Boyd (ref. 4-13) for BT values of 4 or less. For values of BT equal to 10 or more, an alternative approximation is used (ref. 4-12). In fig. 4.2.2-5 a smooth curve has been drawn between the two sets of data to provide values of E/No at intermediate values of BT.

A block diagram of the PSK/PM system is given in fig. 4.2.3-6. Again, split-phase coding of the data signal is used. The split-phase signal biphase modulates a square wave subcarrier at f_s. The modulated subcarrier phase-shifts the r-f carrier with a peak deviation θ_d which is less than $\pi/2$ radians. The resulting spectrum is illustrated in fig. 4.2.3-7. A subcarrier is used rather than phase-shifting with the data directly in order to leave a clear band around the carrier to eliminate the possibility that the receiver might lock onto a sideband should a long sequence of zeroes or ones occur in the data.

In the receiver, the VCO in the carrier phase-lock loop is continuously swept until acquisition is sensed, as indicated by the average value out of the quadrature phase detector. The subcarrier at frequency f_s is detected by squaring and locking to the second harmonic, $2f_s$. This component is then divided by two and used to demodulate the subcarrier. The split-phase data is detected using the same technique as for the FSK system. The worst case modulation loss used for the calculations is given in fig. 4.2.3-8 as a function of the data rate and the bandwidth of the carrier phase lock loop. The modulation loss shown was determined from the following considerations.

For the ideal detection of PSK/PM, the total input power required is determined by the receiver noise power spectral density (No), the signal to noise ratio (SNR) required in the carrier phase lock loop, bandwidth ($2B_{LO}$), and the ratio of data channel energy per data bit to noise density (E/No). For a given total received power, P, the following expressions hold:

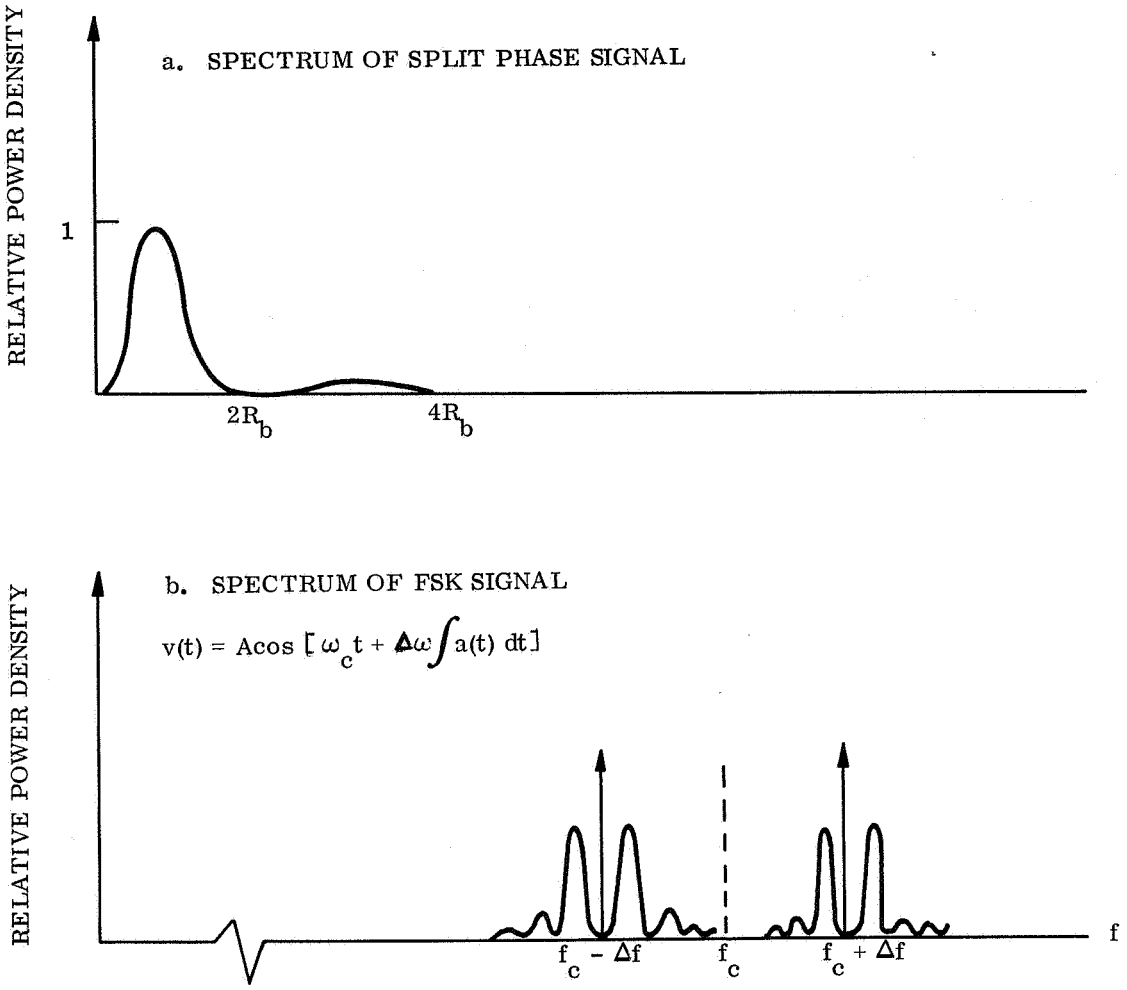

Figure 4.2.3-3. Spectra of Signals in FSK System

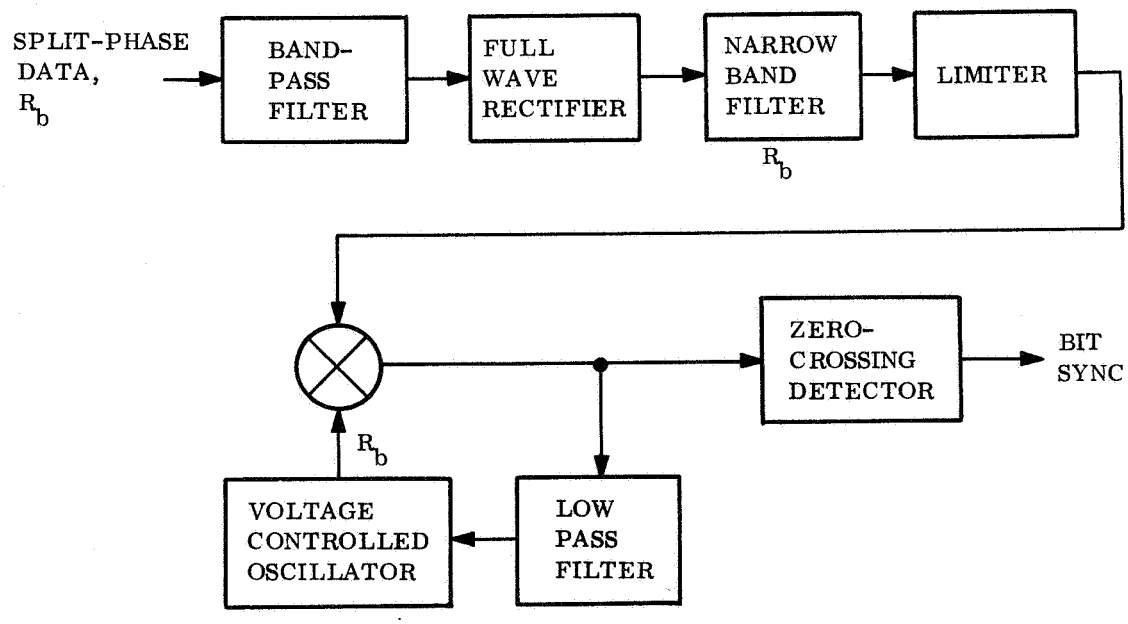

Figure 4.2.3-4. Bit Sync Scheme for Split-Phase Signals

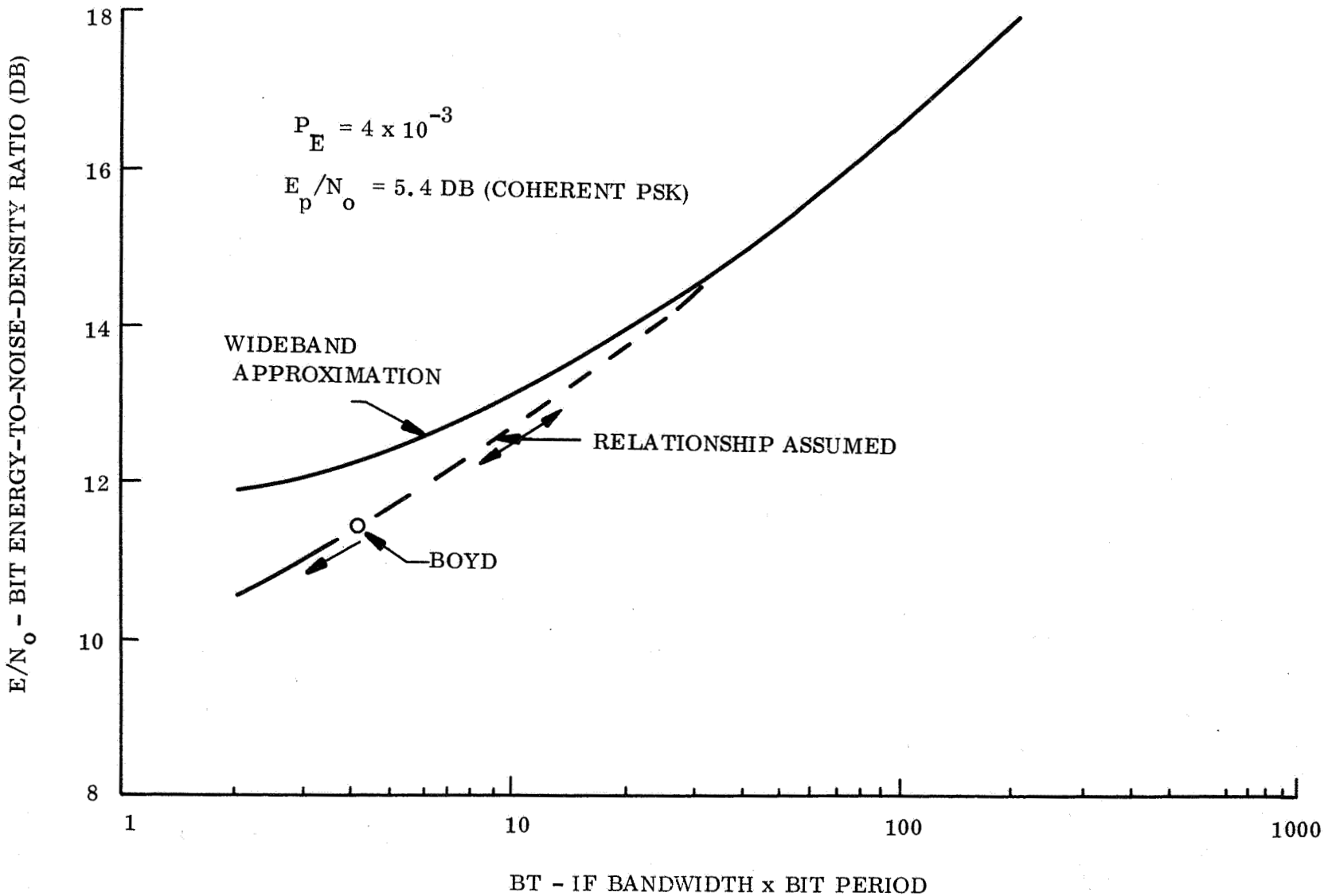

Figure 4.2.3-5. Bit Energy-to-Noise Power Density Ratio

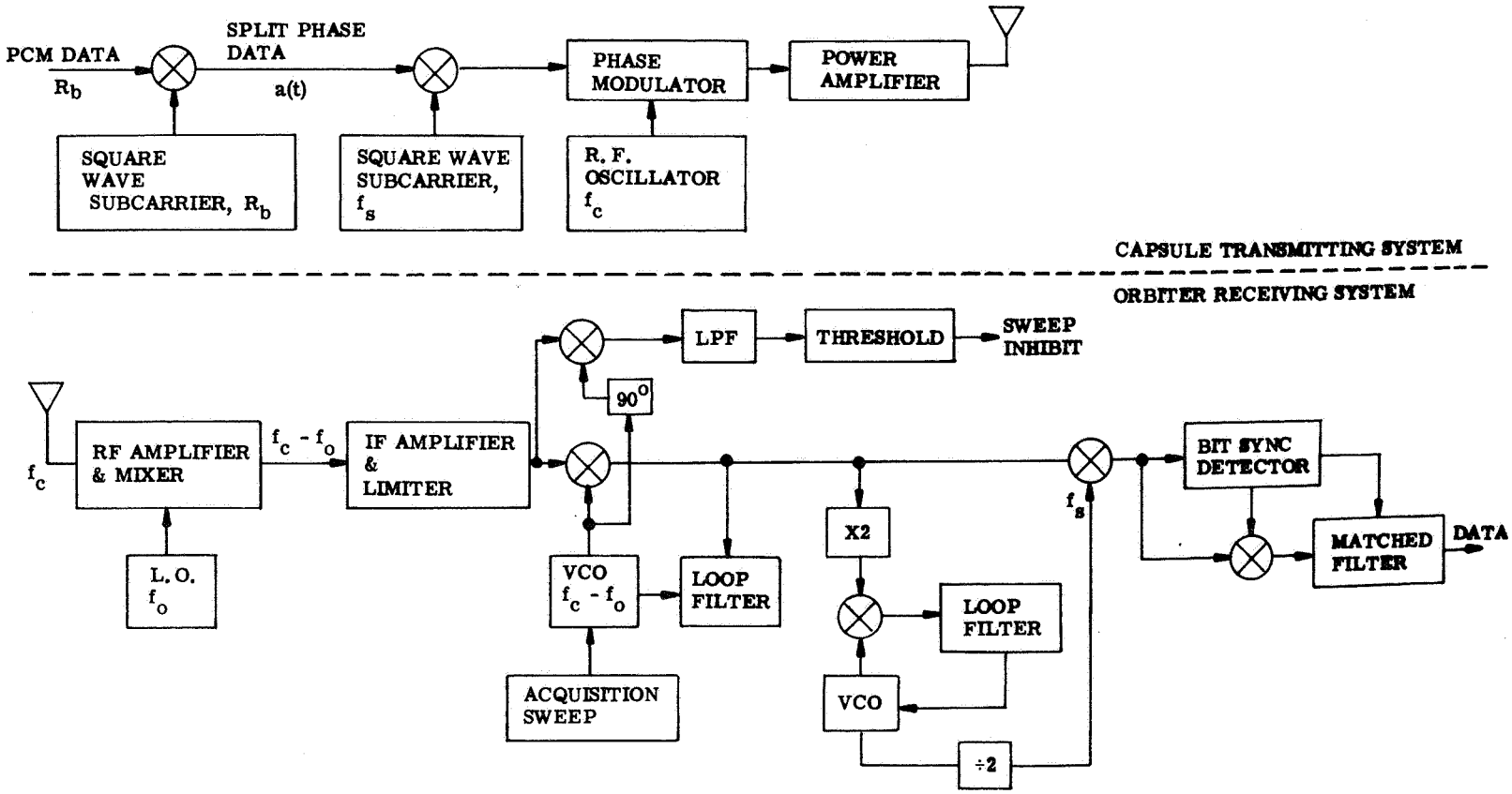

Figure 4.2.3-6. Coherent PSK/PM System

$$\text{SNR} \Big|_{2B_{LO}} = \frac{P_c}{N_o \times 2B_{LO}}$$

$$\frac{E}{N_o} = \frac{P_d T}{N_o}$$

where P_c and P_d are the portions of the total power in the carrier and data channels respectively, and T is the bit period ($1/R_b$). For a square wave subcarrier:

$$P_c = P \cos^2 \theta_d$$

and

$$P_d = P \sin^2 \theta_d$$

where θ_d is the modulation index (phase deviation). The "modulation loss" is given as:

$$L_c = \frac{P}{P_c} = \frac{1}{\cos^2 \theta_d}$$

$$L_d = \frac{P}{P_d} = \frac{1}{\sin^2 \theta_d}$$

The modulation loss that occurs in a given system depends on the accuracy with which the modulation index can be achieved and maintained. Design analyses have indicated that an error of less than 8 percent can be achieved.

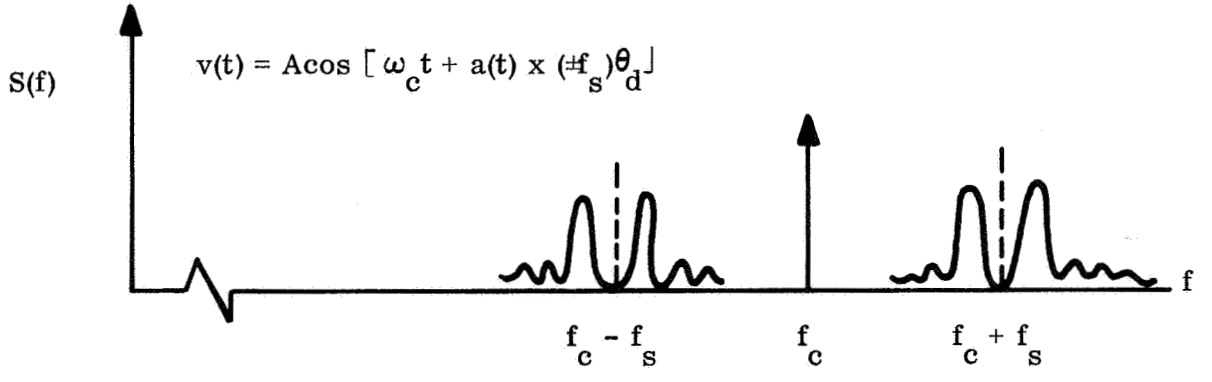

Figure 4.2.3-7. Spectrum of PSK/PM Signal

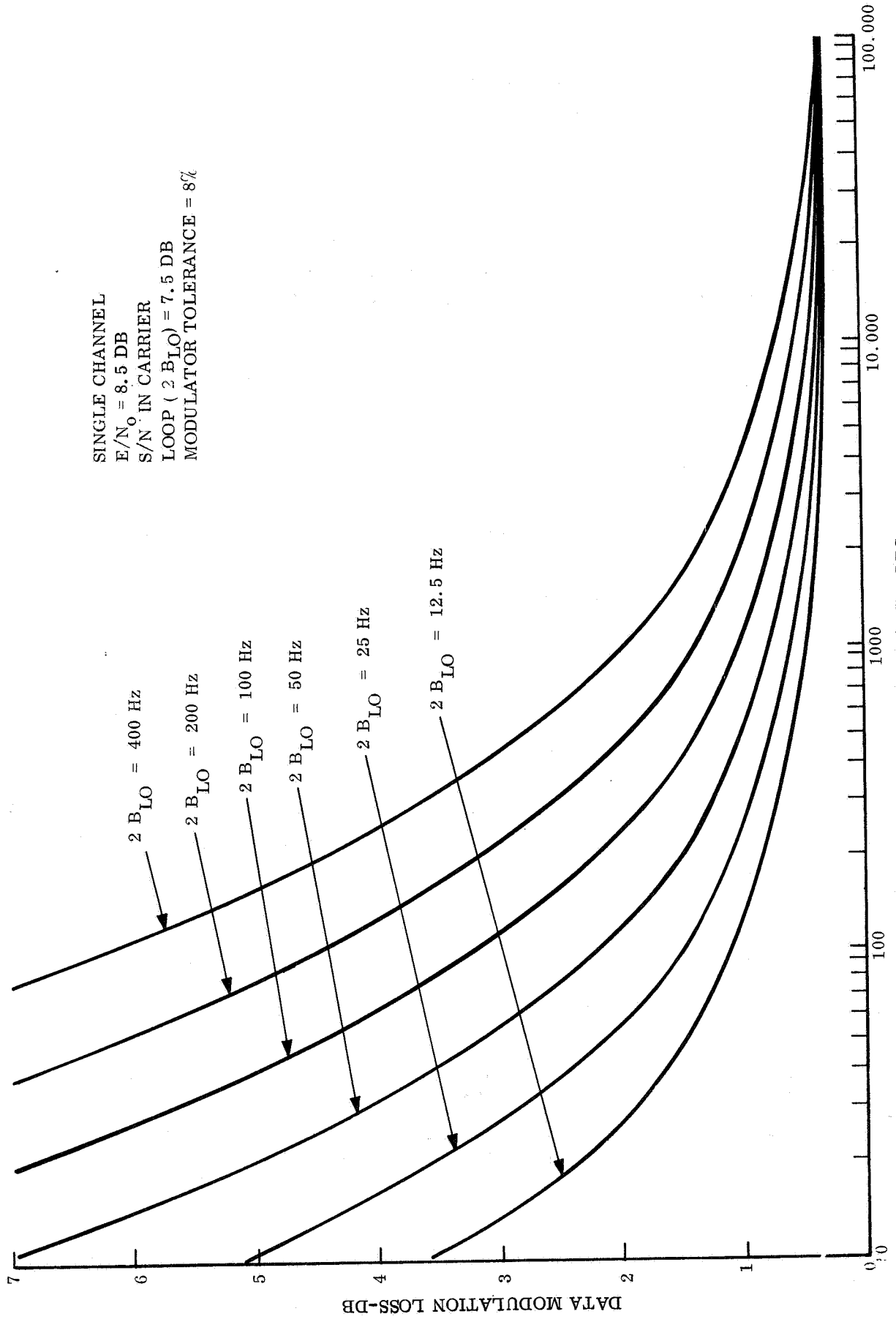

Figure 4.2.3-8. Data Modulation Loss

In order to meet the carrier and data channel signal power requirements, the following conditions then must hold:

$$\frac{P_c}{N_o\ 2B_{LO}} \geq \frac{P\ \cos^2\ (1.08\ \theta_d)}{N_o\ \ 2B_{LO}}$$

and

$$\frac{E}{N_o} \geq \frac{TP\ \sin^2\ (0.92\ \theta_d)}{N_o}$$

For the curve of fig. 4.2.3-8, the value of θ_d for which both the above conditions could be met was calculated, and the worst case data modulation loss was determined as

$$L_d = \frac{1}{\sin^2\ 0.92\ \theta_d}$$

In the parametric performance curves given in the next section, the total input power required is obtained from this curve using the relation:

$$P = \frac{P_d}{L_d}$$

4.2.3.2 Parametric Curves - Relay Link

The sequence in which the parametric curves are used depends on the information that is known and that which is to be defined. Here it is assumed that the known information is that associated with the mission:

1. B_d - required data return per day
2. T - allowable transmission time per day
3. θ_r and θ_t - allowable antenna beamwidths (receive and transmit)
4. R - maximum transmission range
5. $\dot{R}$ - maximum range rate uncertainty
6. $\ddot{R}$ - maximum range acceleration

The major parameters to be defined are:

1. G_t, L_{pt}, G_r, L_{pr} - antenna gains and pointing losses
2. P_t - transmitted power
3. E_d - required energy per day
4. B - predetection bandwidth for noncoherent detection
5. $2B_{LO}$ - carrier loop bandwidth for coherent detection
6. T_{acq} - carrier acquisition time for coherent detection

The process for utilizing the curves is summarized in the Relay Link Parametric Flow Diagram shown in fig. 4.2.3-9. Numbers near the block correspond to the figure number in this section. The "switch" at the center of fig. 4.2.3-9 allows the option of a coherent or a noncoherent system.

The following figures comprise the parametric design curves:

1. Fig. 4.2.3-10. DATA RATE VS DATA RETURNED PER DAY: The required bit rate for a given data return requirement and transmission duration.

2. Fig. 4.2.3-11. DOPPLER FREQUENCY UNCERTAINTY: The doppler frequency uncertainty in terms of the Lander/Orbiter range rate uncertainty. The relationship is:

$$\Delta f_{dp} \text{ (kHz)} = 1.33 \ \Delta R \text{ (km/sec)}$$

3. Fig. 4.2-3-12. REQUIRED S/N_o FOR NON-COHERENT FSK, SPLIT PHASE SIGNALS: The signal-to-noise-density ratio required for $P_e^b = 4 \times 10^{-3}$ using a noncoherent FSK system with split-phase signals. The data is taken from fig. 4.2.3-4, (para 4.2.3.1) letting $B = f_u + 4 R_b$ and $T = 1/R_b$ where f_u is the doppler plus oscillator frequency uncertainty and R_b is the bit rate. S/N_o is related to the E/N_o values given in fig. 4.2.3-4, (para 4.2.3.1) by:

$$S/N_o \text{ (dB)} = E/N_o + R_b + 2.0 \text{ (in dB)}$$

where the 2.0 dB is added to account for losses in the detection process. The value of the predetection bandwidth, B, has been selected to include the power between the first nulls of the i-f split-phase data spectrum ($\pm 2R_b$) plus the frequency uncertainty, f_u, associated with expected doppler and oscillator frequency drift.

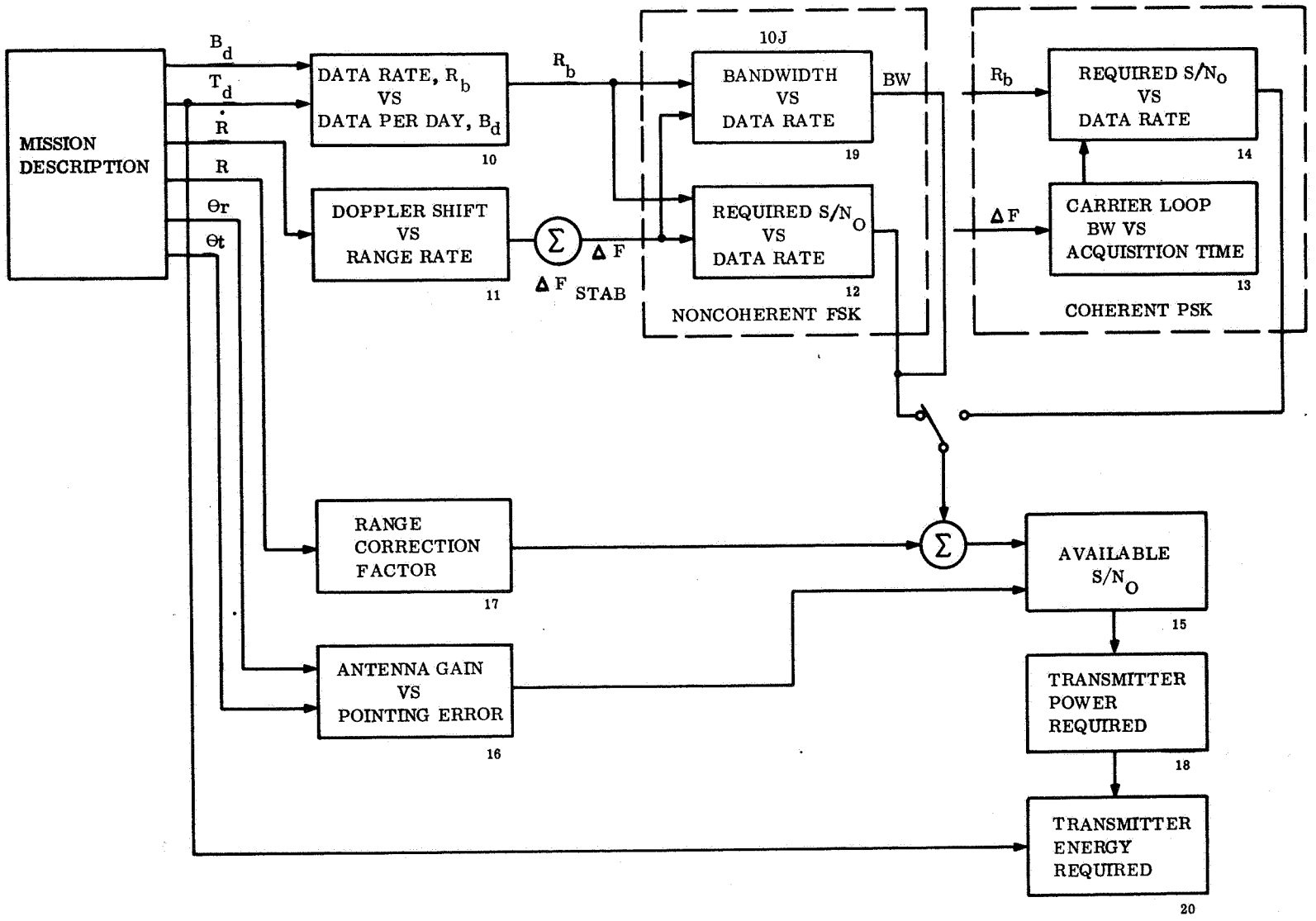

Figure 4.2.3-9. Relay Link Parameter Flow Diagram

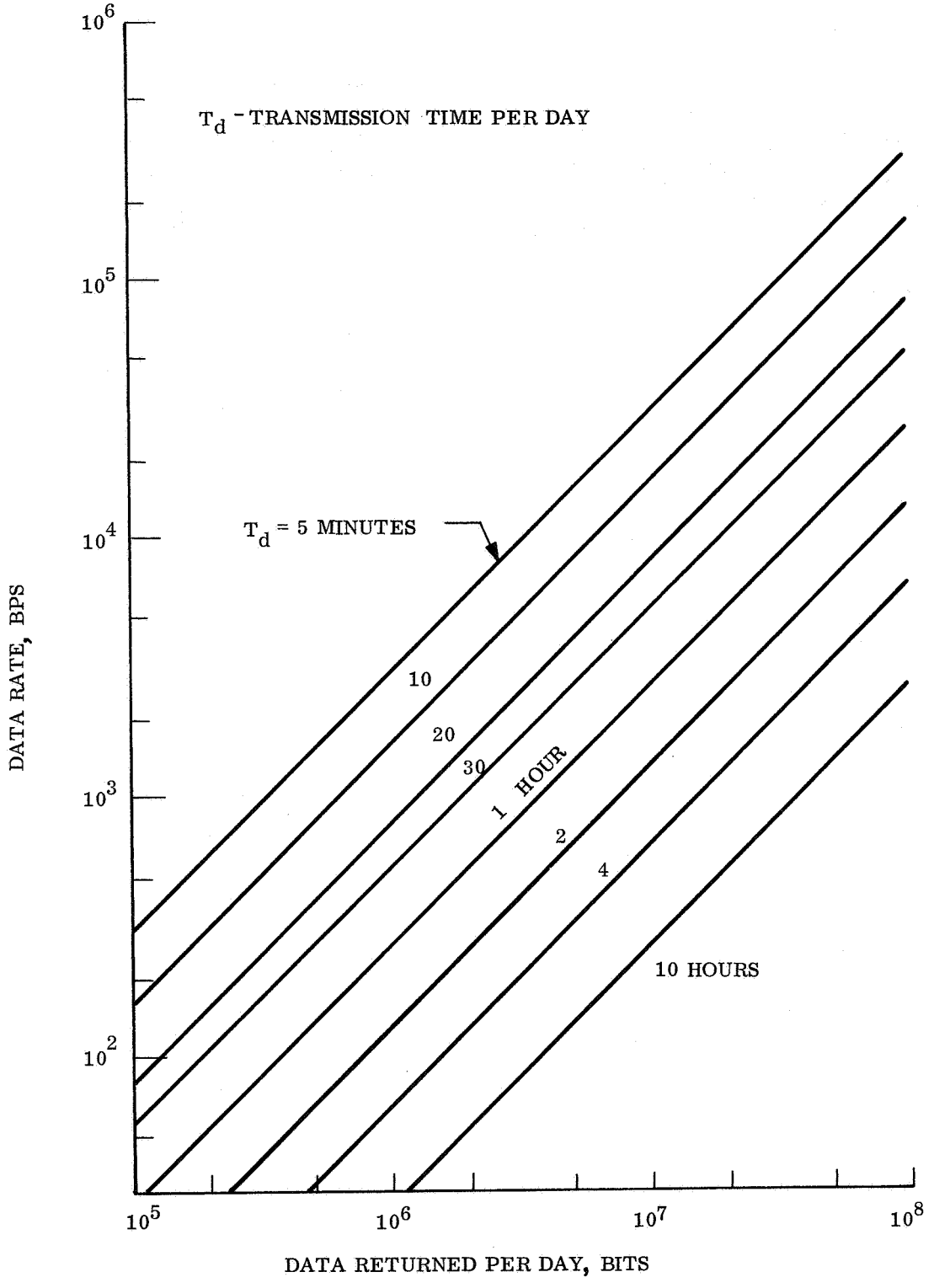

Figure 4.2.3-10. Data Rate vs Data Returned per Day

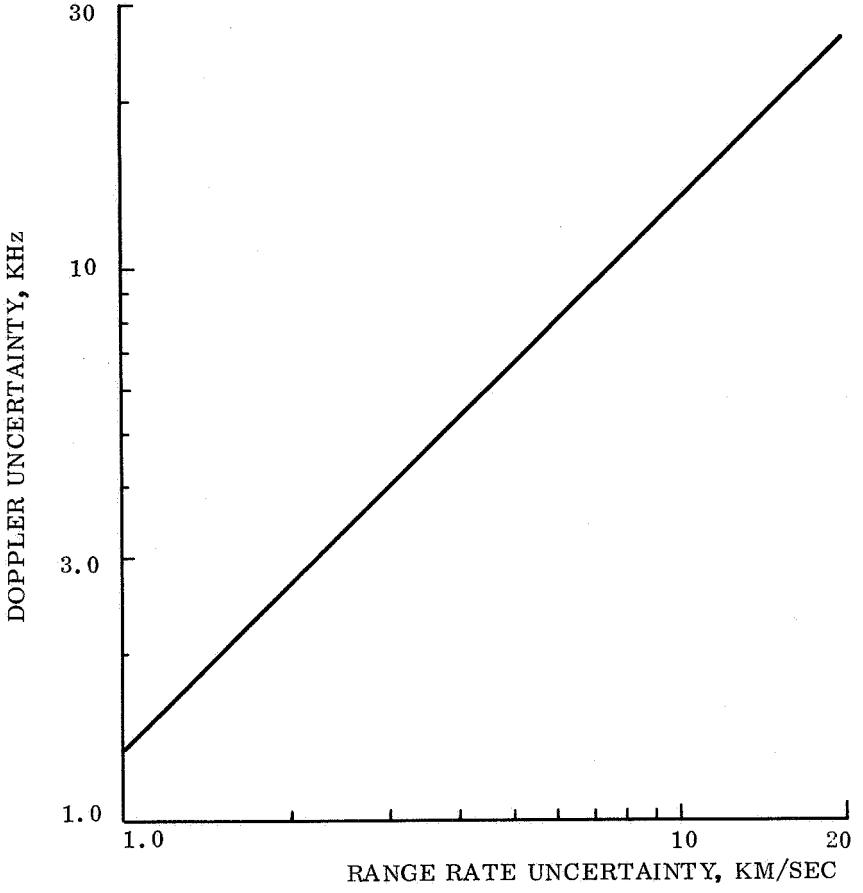

Figure 4.2.3-11. Doppler Frequency Uncertainty - 400 MHz

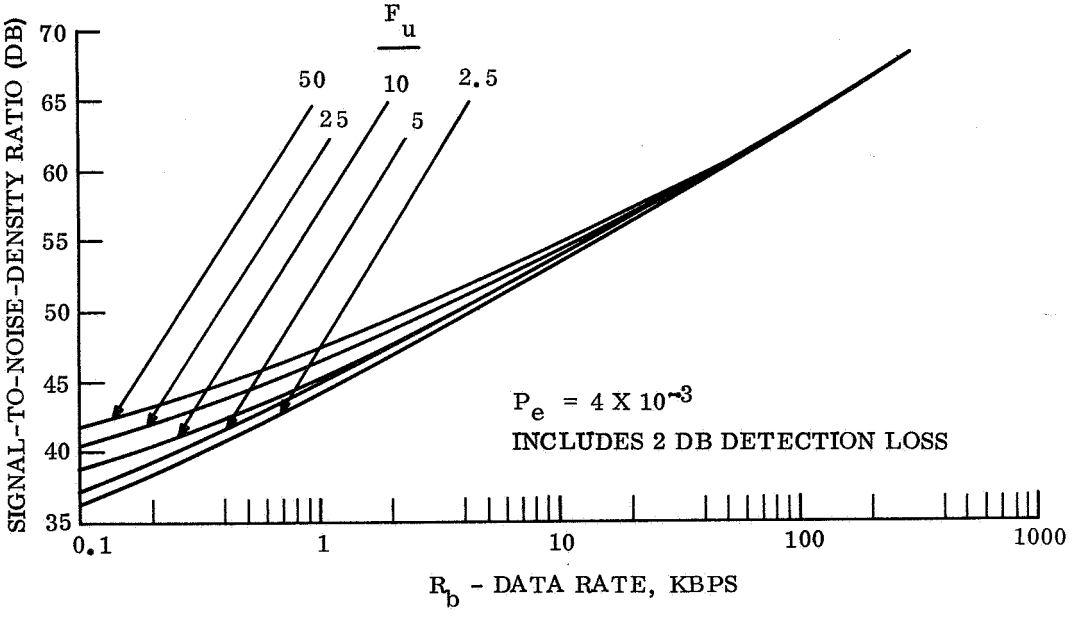

Figure 4.2.3-12. Required S/N_0 for Non-coherent FSK Split-Phase Signals

4. Fig. 4.2.3-13. LOOP BANDWIDTH VERSUS ACQUISITION TIME: The relationship between carrier acquisition time and loop bandwidth for a given frequency uncertainty (sweep bandwidth) for a 90 percent probability of acquisition in one sweep. The relationship used is the empirical equation derived by Frazier and Page (ref. 4-14), and modified by Gardner (ref. 4-15)

$$\Delta\dot{\omega}_{max} = \frac{\left[1 - \sqrt{\left(\frac{N}{S}\right)_{BL}}\right] \frac{\alpha}{\alpha_o} \omega_{No}^2}{1 + D}$$

where α is the signal suppression factor due to the limiter, α_o is the signal suppression factor measured at some arbitrary input SNR, ω_{No} is loop natural frequency measured at the same input SNR, and D is a factor depending on damping. Using a loop damping factor of 0.707 and letting $\alpha = \alpha_o$, then $D \approx O$, $B_L = B_{LO}$, and $\omega_{NO} = (0.945)\, 2B_{LO}$. Letting $(S/N)_{2B_{LO}} = 7.5$ dB or $(S/N)_{B_L} = 10.5$ dB, the relationship reduces to:

$$\Delta f_{max} = 0.1\,(2B_{LO})^2$$

The time for one complete sweep of the bandwidth, f_u, is then:

$$T_{acq} = \frac{f_u}{\Delta f_{max}} = \frac{10\, f_u}{(2B_{LO})^2}$$

5. Fig. 4.2.3-14. REQUIRED S/N_o FOR COHERENT PSK/PM: The signal-to-noise-density ratio required for coherent detection for several values of carrier loop noise bandwidths. The E/N_o requirement is assumed to be 8.5 dB (5.4 dB theoretical + 3.1 dB detection losses). The relationship is:

$$S/N_o = E/N_o + R_b - b_d \text{ (in dB)}$$

where R_b is bit rate and b_d is the data modulation loss obtained from fig. 4.2.3-8.

6. Fig. 4.2.3-15. AVAILABLE S/N_o AT RELAY RECEIVER: The S/N_o available at the Spacecraft receiver at a reference transmission range of 2000 km over a range of values of transmitted power and effective antenna gain. Effective antenna gain includes the peak gain of both the transmitting and receiving antennas and the pointing losses associated with each. A reference frequency of 400 MHz has been used. The noise figure of the receiver is taken to be 4 dB and the overall system temperature referenced to the receiver terminals is 650°K. This was derived from the relation:

$$T_s = (F - 1)\, T_o + L_{er}\, T_a + (1 - L_{er})\, T_L$$

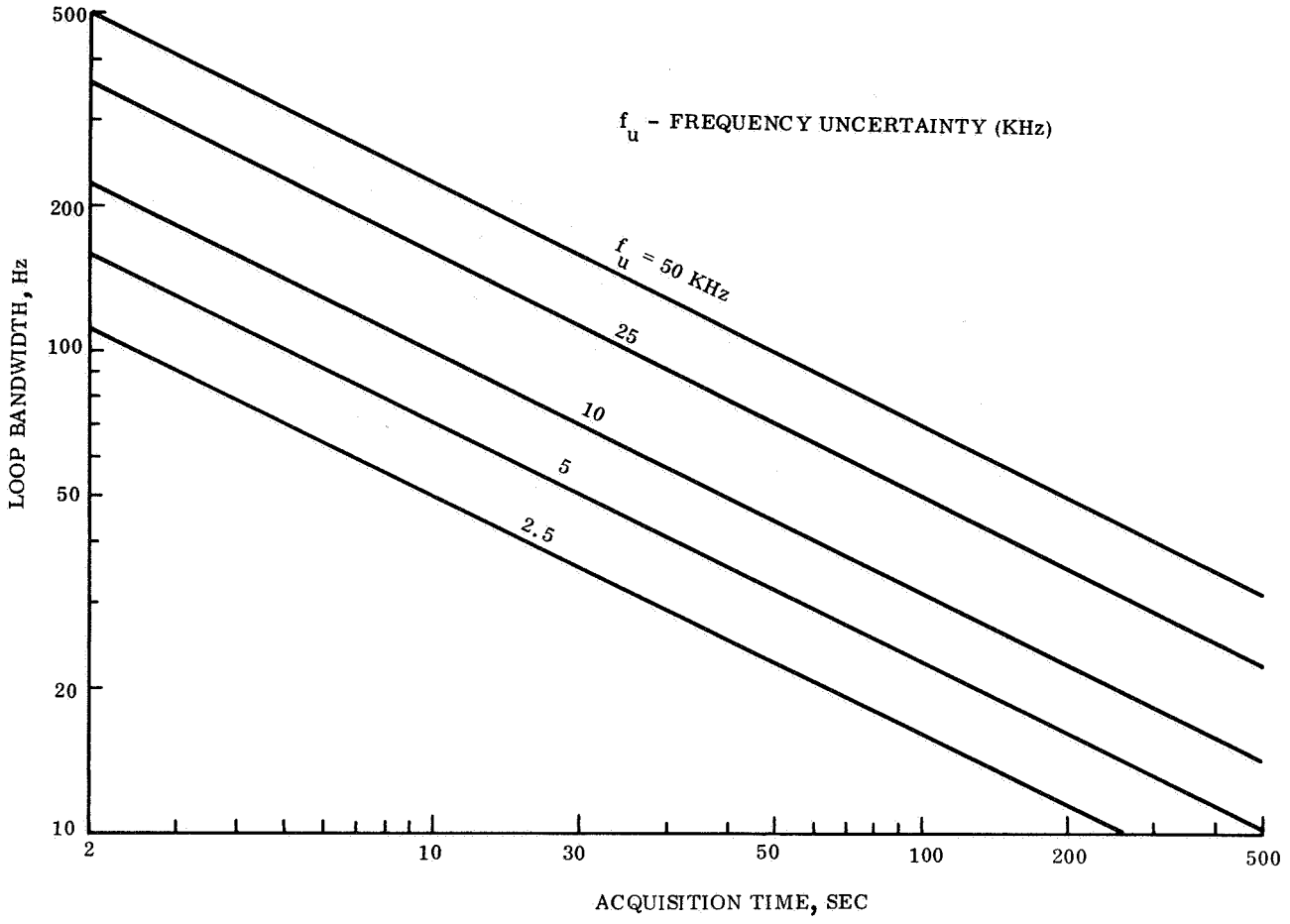

Figure 4.2.3-13. Loop Bandwidth vs Acquisition Time

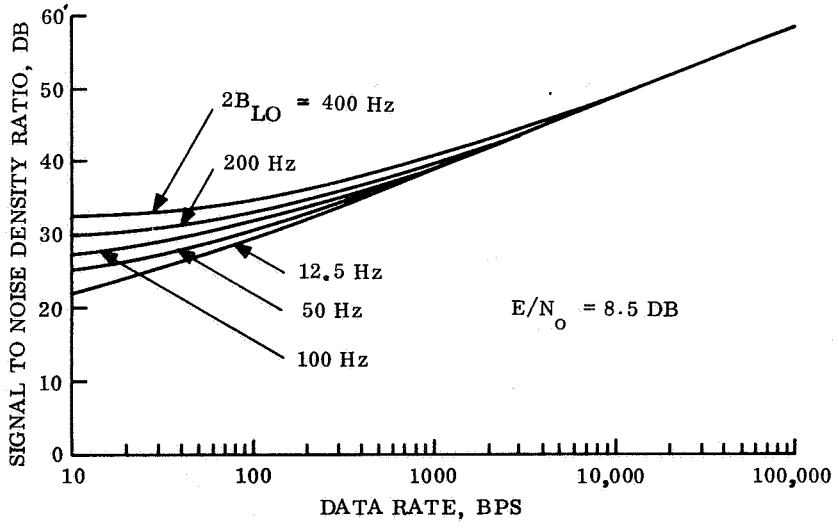

Figure 4.2.3-14. Required S/N_o for Coherent PSK/PM

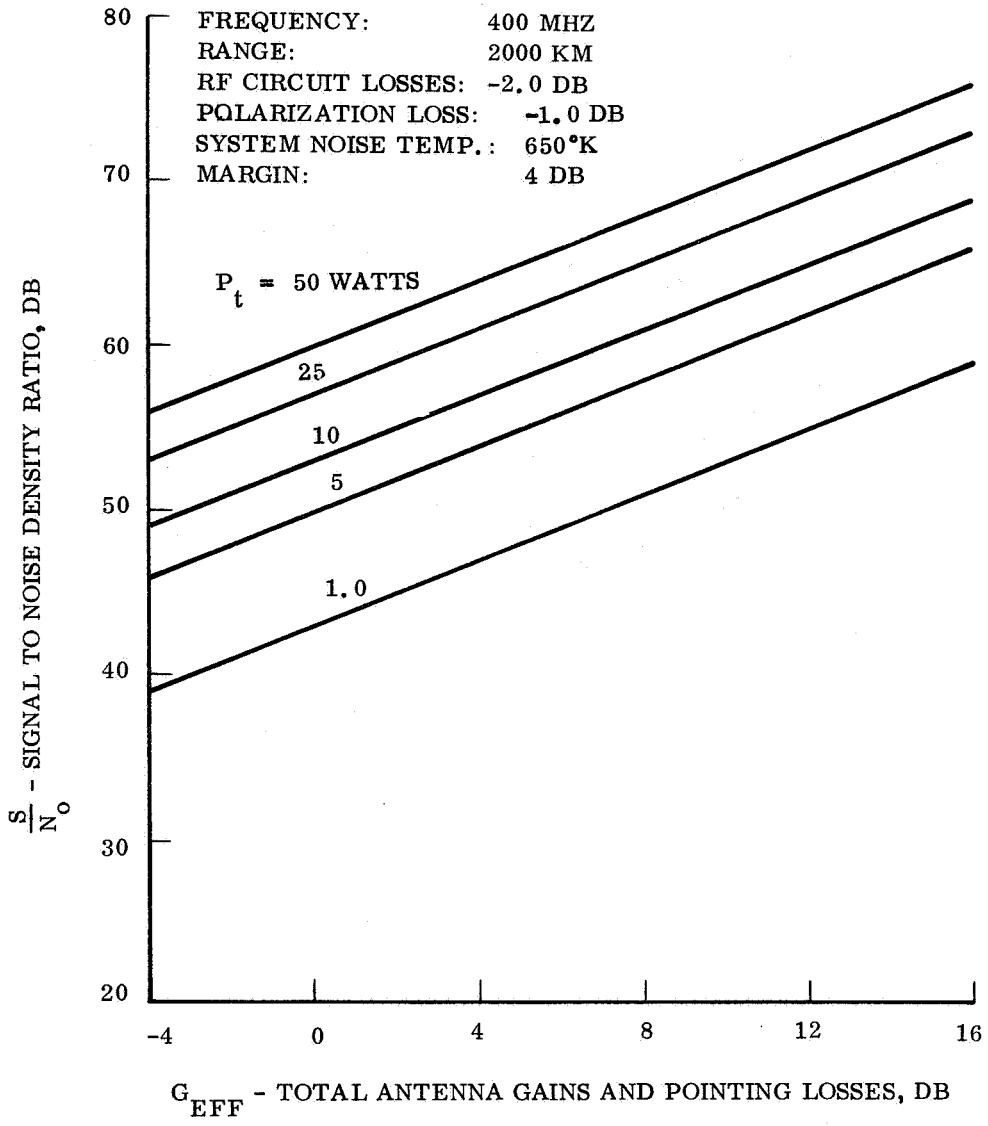

Figure 4.2.3-15. Available Signal-to-Noise Density Ratio at Relay Receiver

where

T_s = System temperature
T_a = Antenna temperature
T_o = reference temperature = 290°K
L_{er} = receiving r-f line loss = 1.0 dB
T_L = line temperature = 290°K

The antenna temperature, T_a, is taken to be 200°K, the approximate noise temperature of Mars. At 400 MHz this value is greater than that expected from galactic noise and is therefore taken as worst case. System temperature is then

$$T_s = (2.5 - 1)\ 290 + 0.79\ (200) + (1 - 0.79)\ 290$$
$$= 650^\circ K$$

Reference loss values used for the curves are 1.0 dB each for transmitting and receiving r-f circuit losses and 1.0 dB for polarization loss between the two antennas. In addition, a reference margin of 4.0 dB is provided for the system. Calculation of the available S/N_o is shown below for 0.0 dB overall antenna gain and 1.0 watt transmitted.

a.	Transmitted Power (P_t = 1.0 watts)	30.0 dBm
b.	r-f Circuit Losses	-2.0 dB
c.	Effective Antenna Gain (including pointing losses)	0.0 dB
d.	Space Loss (R = 2000 km, f = 400 MHz)	-150.5 dB
e.	Polarization Loss	-1.0 dB
f.	Total Received Power	-123.5 dBm
g.	Receiver Noise Density (T_S = 650°K)	-170.5 dBm/Hz
h.	Available S/N_o (without margin)	47.0 dB
i.	Available S/N_o (including 4.0 dB margin)	43.0 dB

7. Fig. 4.2.3-16. ANTENNA GAIN VS. POINTING ERROR: The estimated gain as a function of angle off axis for typical 400 MHz antennas. Approximate dimensions for the antennas are given in fig. 4.2.3-21 and in para 4.2.3.5.

8. Fig. 4.2.3-17. RANGE CORRECTION FACTOR: The change in S/N_o available at the Spacecraft receiver for values of Lander/Orbiter range other than the 2000 km reference range used in fig. 4.2.3-15.

9. Fig. 4.2.3-18. PRIME POWER REQUIRED FOR THE TRANSMITTER: The power required from the vehicle dc power bus for a given output r-f power.

10. Fig. 4.2.3-19. PREDETECTION BANDWIDTH FOR FSK SPLIT-PHASE SIGNALS: The predetection bandwidth (B) required for a given data rate and frequency uncertainty ($B = f_u + 4\ R_b$).

11. Fig. 4.2.3-20. TRANSMITTER ENERGY REQUIREMENTS: The relationship between transmitter prime power, transmission time, and the resultant energy required.

During the descent phase, signals transmitted from the Lander may be reflected from the planetary surface before arriving at the Orbiter receiver. These multipath signals may interfere with the desired signal which is received on the line-of-slight path

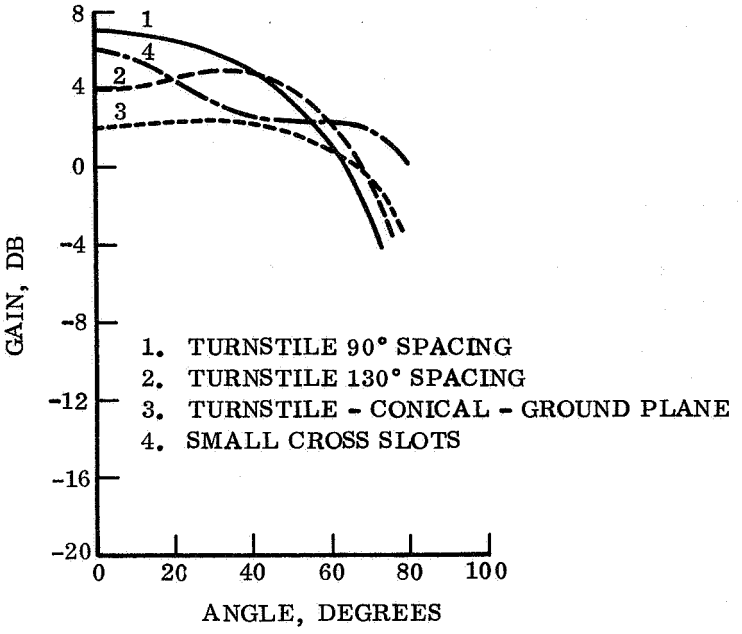

Figure 4.2.3-16. Gain vs Pointing Error for Typical Antennas

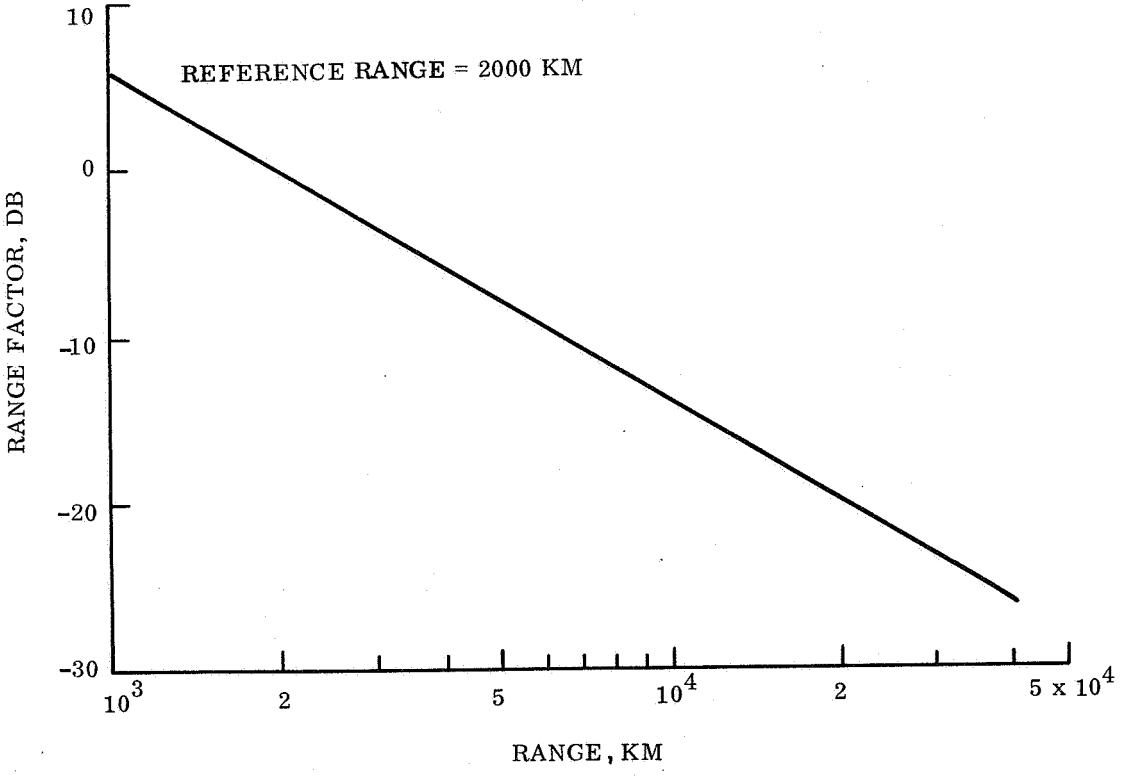

Figure 4.2.3-17. Range Correction Factor

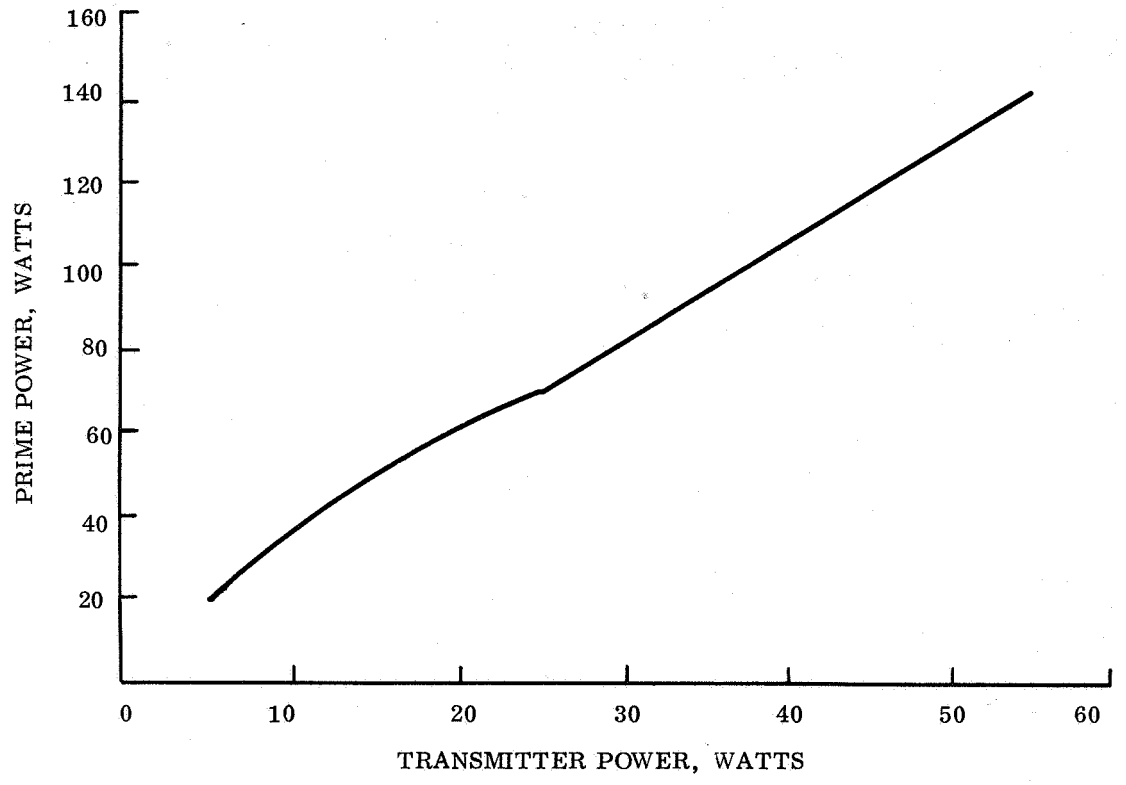

Figure 4.2.3-18. Prime Power Required for the Transmitter

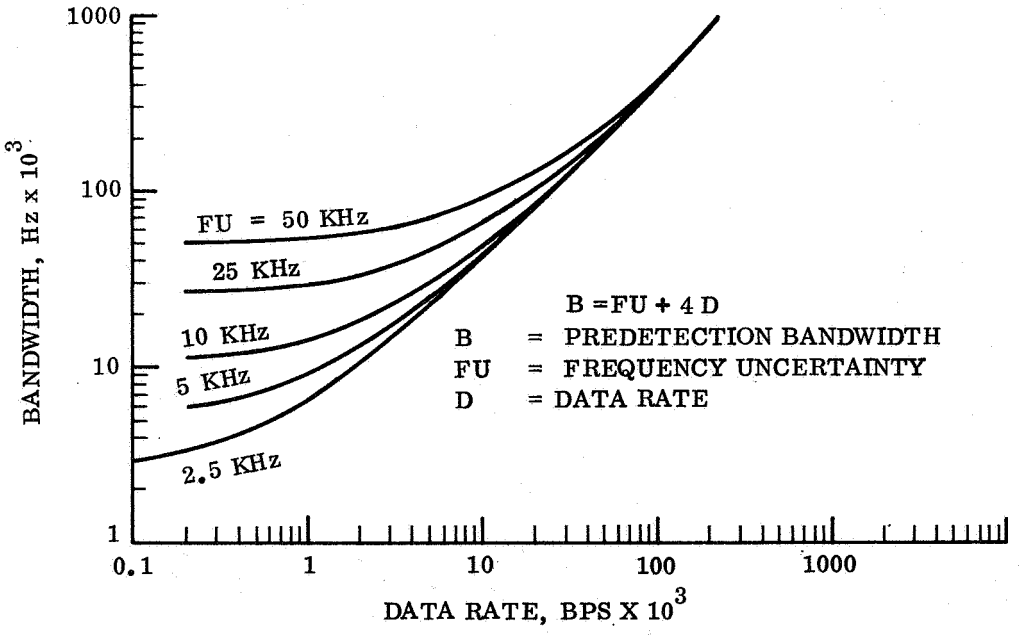

Figure 4.2.3-19. Prediction Bandwidth for FSK Split-Phase Signal

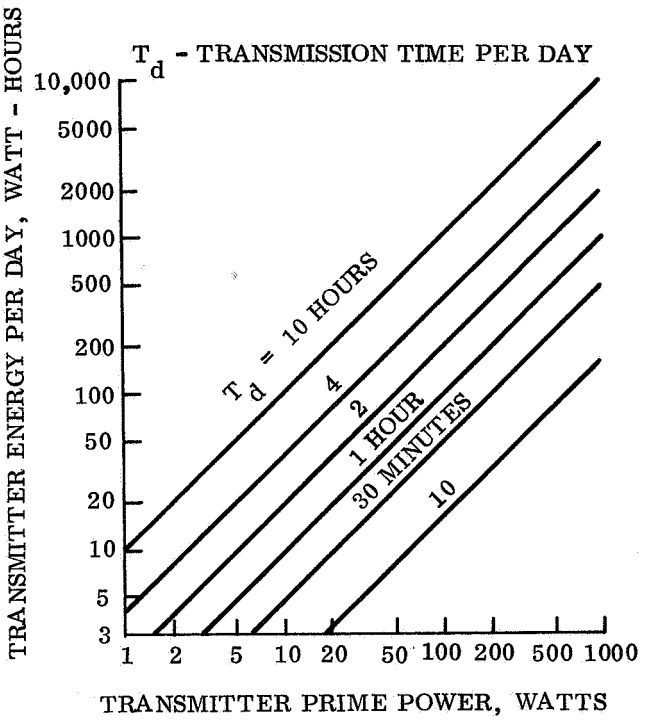

Figure 4.2.3-20. Transmitter Energy Requirements

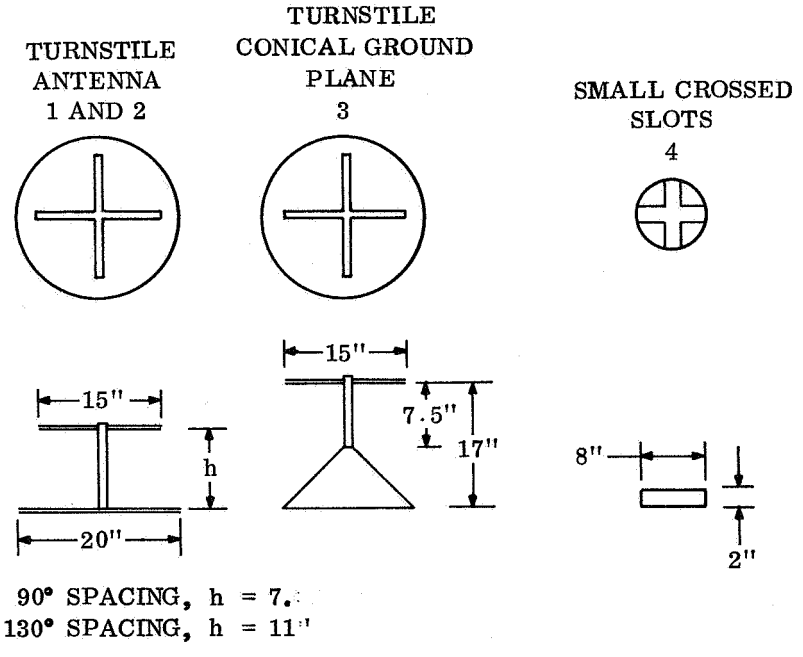

Figure 4.2.3-21. Typical 400 MHz Antennas

from the Lander. Whether this degradation or fading is fast or slow depends on the data rate and the doppler shift of the reflected signal relative to the line-of-slight (LOS) signal. If the relative doppler shift is large with respect to the data rate so that the composite received signal fluctuates rapidly within a bit interval, the fading is fast; if the amplitude of the composite signal can be considered constant during a bit interval, the fading is slow.

At entry, the relative doppler shift tends to be large because the Lander is drawing away from the Orbiter and is approaching the planet with a high velocity. The doppler shift between the LOS signal and the reflected signal is of the order of several kHz at entry (220 km altitude). At this altitude, the time delay between LOS and reflected signals can be one millisecond or more. When the Lander nears the surface, its velocity is nearly that of the planet, and the relative doppler shift is approximately 100 Hz. The relative time delay is about 10 microseconds when the Capsule is at an altitude of one mile, and drops to zero as the Capsule approaches the surface.

The effect of doppler shift and time delay of the reflected signal on communication performance depends on the type of communication system used. In the present instance, a wideband binary FSK receiver is employed on the relay link. If the relative delay is much smaller than the bit interval, the interference appears in the same channel of the FSK receiver as the desired signal; this is termed "same-channel interference". If the relative delay is comparable to, or longer than the bit interval, the interference and the desired signal can appear in opposite channels of the receiver. This is called "cross-channel interference".

Table 4.2.3-1 shows the fading conditions qualitatively for various data rates, based on the previous estimates of doppler shift and time delay.

TABLE 4.2.3-1. FADING CONDITIONS

Capsule Altitude	Data Rate (bps)			
	10^2	10^3	10^4	10^5
Entry	FF/SI	FF/CI	SF/CI	SF/CI
Near Impact	SF/SI	SF/SI	SF/SI	SF/SI
FF = Fast Fading		SI = Same-channel Interference		
SF = Slow Fading		CI = Cross-channel Interference		

All of the fading possibilities are represented in this example. "Same-channel interference" implies a relative time delay much smaller than the bit interval, while "cross-channel interference" implies a relative time delay comparable to or greater than the bit interval.

The effect of power reflected from the planetary surface can be specified in terms of the signal-to-interference ratio - as shown in fig. 4.2.3-22. When same-channel interference occurs in the fast-fading case, the performance is actually improved compared to the no-fading case. When the fading is fast and cross-channel interference occurs, some loss results, but the loss is relatively small. The worst case loss condition is slow-fading same-channel interference. This condition occurs near impact.

The interference level is a function of the surface reflectivity, the antenna pattern, and the vehicle-surface geometry.

A reasonable worst case interference level is -5dB when isotropic, polarization insensitive, transmitting and receiving antenna patterns are assumed. This level has been determined from various analyses of Martian multipath. A treatment of the problem by GE (ref. 4-16) is based upon a rough surface model of the planet which is due to Beckman (ref. 4-17). Preliminary computations yield an interference level of -8dB, based upon an average power reflectivity of 7 percent as determined by radio astronomy (ref. 4-18). The radar observations indicate that the reflectivity of Mars can be as large as 13 percent in certain regions. This is twice the average value, and results in a -5 dB interference level.

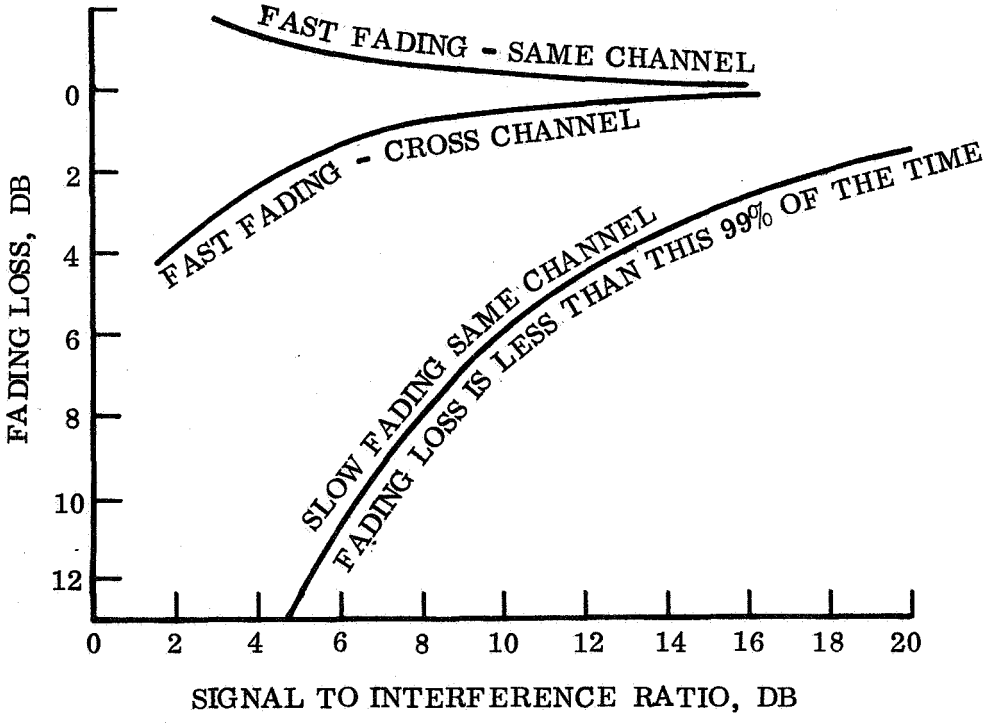

Figure 4.2.3-22. Performance of Wide-band FSK with Multipath Interference

Another analytical approach (ref. 4-19) gives maximum relative multipath levels of -4 dB for horizontal polarization and -8 dB for vertical polarization at 300 MHz. This surface is assumed to be dry and rough. The analysis applies for a Lander altitude of 4.5 km and for reflection angles of up to 80 degrees. The relative level is as low as -10 dB for horizontal polarization (at normal incidence and reflection) and -20 dB for vertical polarization (at the Brewster angle).

Others (ref. 4-20) have computed a maximum relative multipath of -6 dB based on planet characteristics derived from 430 MHz radar observations.

Polarization of the refelected signal, and antenna directivity should reduce the level below -5 dB. The reflected signal will be elliptically polarized due to the difference in horizontal and vertical reflection coefficients of the surface at 400 MHz. In addition, any surface reflections from the antenna main beam will result in a reversed circular polarization at the orbital receiver. These polarization effects should further suppress the interfering signals.

4.2.3.3 Direct Link Systems

The system configuration assumed for the Lander to Earth link is shown in fig. 4.2.3-23. For high data rate systems, the PCM data is coded in order to reduce the signal power required to produce the threshold bit error rate of 5×10^{-3}. For systems with data rates below about 50 bps, coding would not be used because performance is limited by sync recovery rather than data recovery. For such low rate systems, the data would be modulated on a high frequency subcarrier as on Mariner '69. In the coded system, a block code such as the 32, 6 code used on Mariner '69 or a convolutional code, such as the one being developed for Pioneer, is used. For both types of codes, the symbol rate is increased compared to no coding by the ratio of the number, η, of coded symbols transmitted for each k data bits. The symbols are split phase coded to enhance recovery of symbol synchronization, and phase modulated on the S-band carrier for transmission to the DSN station.

The configuration of the 210 foot antenna to be used for Mariner '69 is assumed. Using the listen-only feed and restricting operations to times when the elevation angle of the Lander exceeds 20°, the receiving system temperature is a maximum of 28°K, compared to a worst case temperature of 55°K as specified in EPD 283. It is expected that the DSN receivers will be modified to include a loop bandwidth of 4 Hz as well as the currently implemented 12 Hz bandwidth, thereby improving low data rate system performance. The Multiple Mission Telemetry System would be employed where possible, and the coding removed by the appropriate processor.

As in the case of the relay link, the modulation index is selected such that both the carrier channel and the data channel reach threshold at the same input power level. The carrier channel threshold is set by the carrier phase lock loop bandwidth ($2B_{LO}$) and the required signal to noise ratio (SNR) in that bandwidth. The data channel threshold is set by the product of the data rate (R_b) and the ratio of data energy per bit to noise spectral density (E/N_o). As the modulation index is adjusted so that the carrier channel power is decreased, the power in the data channel increases, allowing a higher data

rate to be achieved. However, as the SNR in the carrier loop is reduced, the VCO phase jitter is increased, thereby degrading the data channel performance. For a given set of values of carrier loop bandwidth and data rate, there is an optimum modulation index which will result in the best performance. This value has been calculated and is shown in fig. 4.2.3-24. The resulting E/N_0 required in the data channel is also given for the error control coding case and takes into account the degradation produced by carrier jitter. The bandwidth expansion of the DSN receiver, (ref. 4-21), with SNR is taken into account in calculating the jitter loss versus SNR in the loop, (ref. 4-22). At the lower data rates the SNR in the loop was fixed, and thus the jitter loss kept constant, to avoid out-of-lock problems at low SNR's. At the high data rates when almost all of the power is in the data channel, the SNR in the loop was also fixed, since little performance gain can be achieved by optimization. In determining the worst case modulation losses, the worst case E/N_0 plus carrier jitter loss was used, with an 8 percent modulation index tolerance. The worst case value of E/N_0 (excluding carrier jitter losses) assumed is 3.5 dB as shown in table 4.2.3-2.

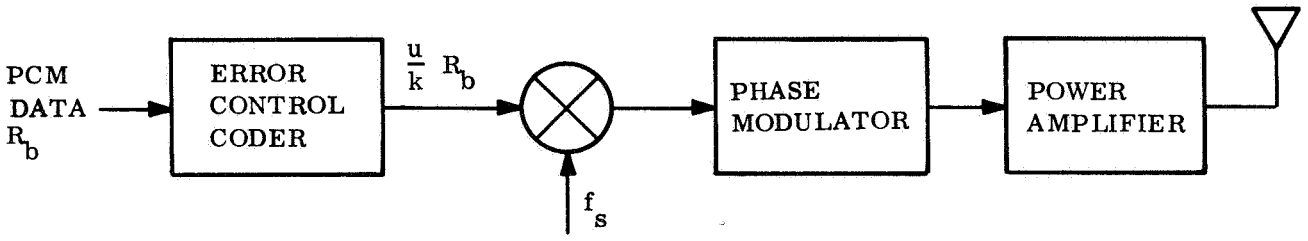

n = NO. OF CODED SYMBOLS PER DATA BLOCK

k = NO. OF DATA BITS PER DATA BLOCK

LANDER TRANSMISSION SYSTEM

DSN RECEIVING SYSTEM

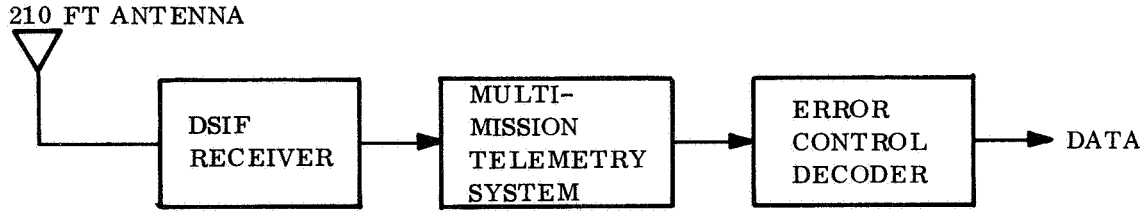

Figure 4.2.3-23. Direct Link System

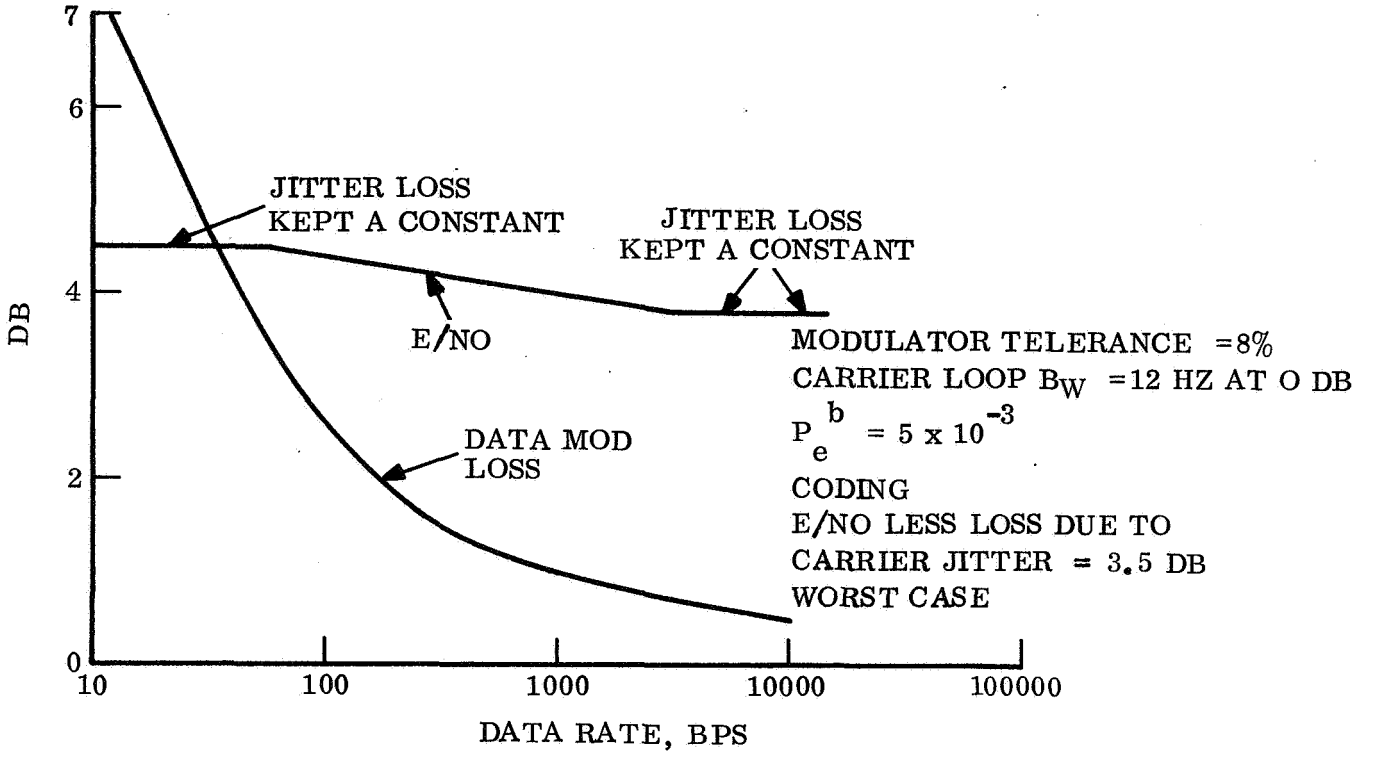

Figure 4.2.3-24. Modulation Loss and E/N_0 vs Data Rate for an Optimized Coherent Link - Single Channel

TABLE 4.2.3-2. CALCULATION OF WORST CASE E/N_0 EXCLUSIVE OF CARRIER JITTER FOR ENCODED DATA

2.1 dB	E/N_0 theoretical for 32,6 code, $P_e = 5 \times 10^{-3}$. See ref. 4-23 for data words of non-six bit length.
0.3 dB	Filter loss
0.2 dB	Subcarrier and bit sync jitter loss
0.9 dB	Margin or additional E/N_0 for data words of random length.
3.5 dB	

The modulation loss for low data rate systems, when coding would not be used, is shown in fig. 4.2.3-25. The required data channel E/N_0 was taken to be 7.4 dB based on the data in table 4.2.3-3.

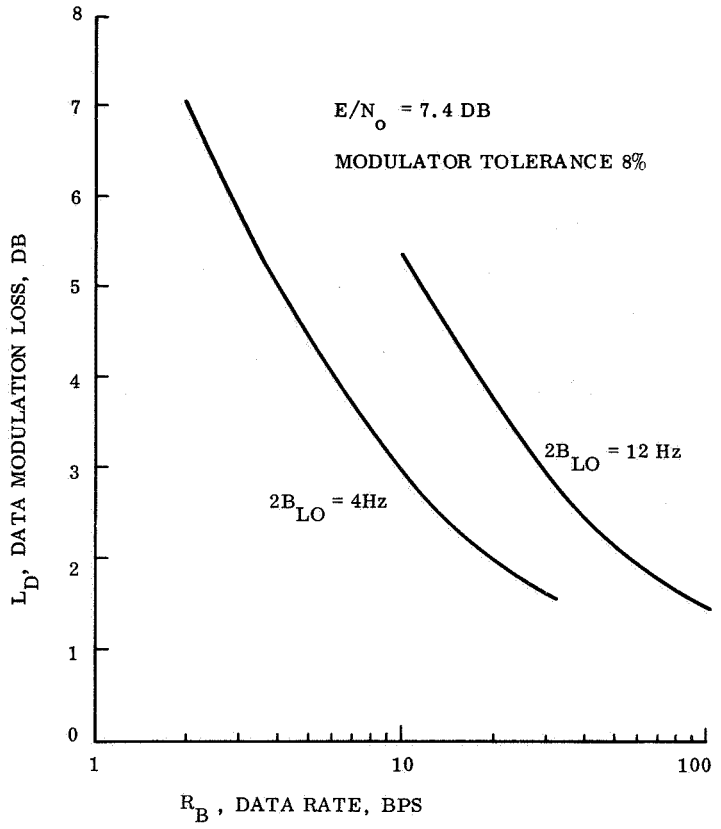

Figure 4.2.3-25. Data Modulation Loss for Systems without Coding

TABLE 4.2.3-3. REQUIRED E/N_o FOR LOW DATA RATE SYSTEM

Theoretical E/N_o for $P_e^b = 5 \times 10^{-3}$	5.2 dB
Filter loss	0.5 dB
Carrier jitter loss	0.8 dB
Subcarrier jitter loss	0.2 dB
Bit sync jitter loss	0.2 dB
Margin	0.5 dB
	E/N_o = 7.4 dB

4.2.3.4 Direct Link Parametric Curves

A possible sequence for using the parametric curves to obtain performance estimates for a direct link is indicated in fig. 4.2.3-26. Numbers near the blocks correspond to the figure numbers in the section. The following figures are presented:

1. Fig. 4.2.3-27. Data Rate vs Data Returned Per Day: the required bit rate for a given data return requirement and transmission duration.

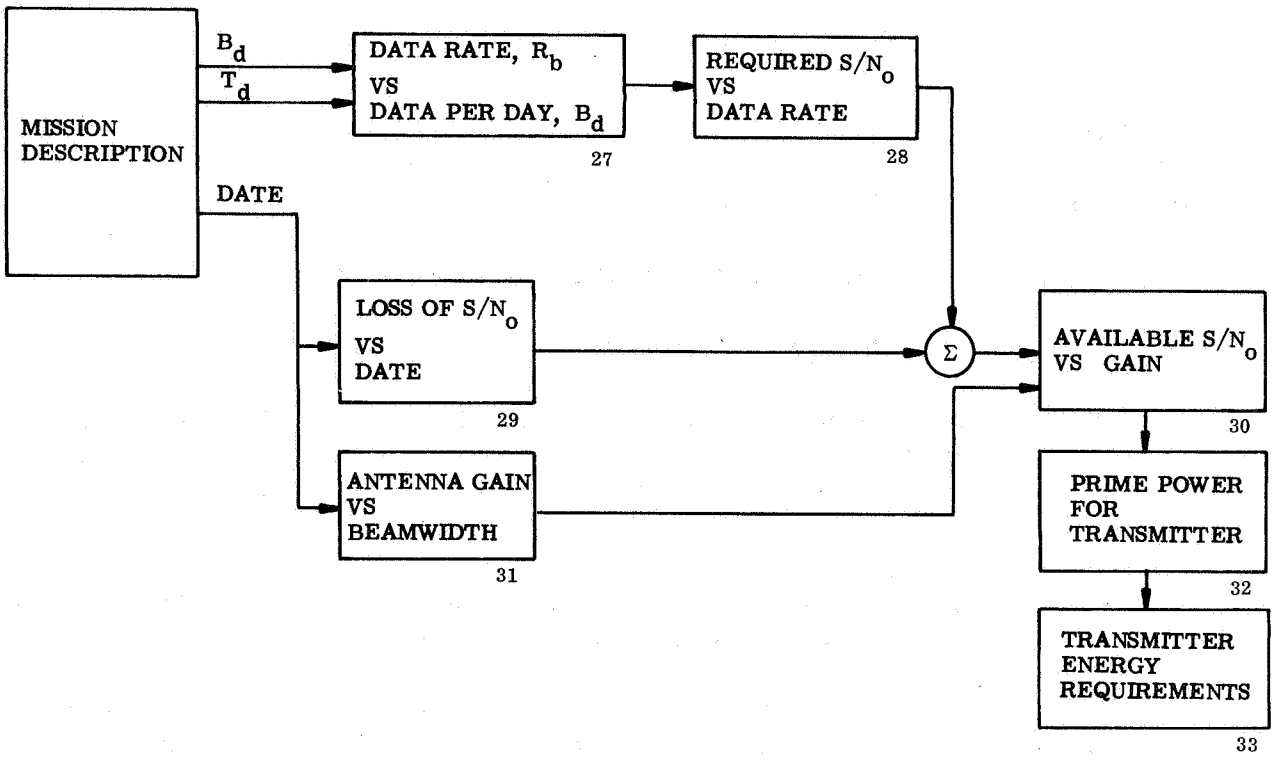

Figure 4.2.3-26. Direct Link Parametric Flow Diagram

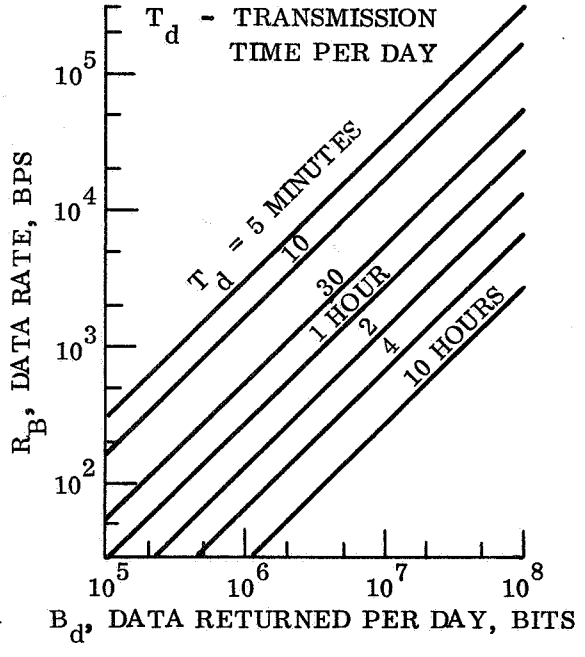

Figure 4.2.3-27. Data Rate vs Data Returned per Day

2. Fig. 4.2.3-28. Required S/N_0 for PSK/PM: the total signal power to noise spectral density required for PSK/PM, determined as follows:

$$S/N_o = R_b \cdot E/N_o \cdot L_D$$

where

R_b = bit rate, bps

E/N_o = signal energy per bit to noise power spectral density

L_D = data modulation loss

For the systems using error control coding, the E/N_0 and the modulation loss used are obtained from fig. 4.2.3-24. For low data rate systems which do not use error control coding, the modulation loss is obtained from fig. 4.2.3-25.

3. Fig. 4.2.3-29. Loss of S/N_0 Versus Date: loss of S/N_0 due to the range increase, with January 1, 1974, as the reference point.

4. Fig. 4.2.3-30. Available S/N_0: the S/N_0 available at the DSN receiver as a function of the product of antenna gain and pointing loss for radiated power levels of 20 w and 10 w. The S/N_0 is based on the communication range of 120×10^6 km existing on January 1, 1974. The link calculation is presented in table 4.2.3-4.

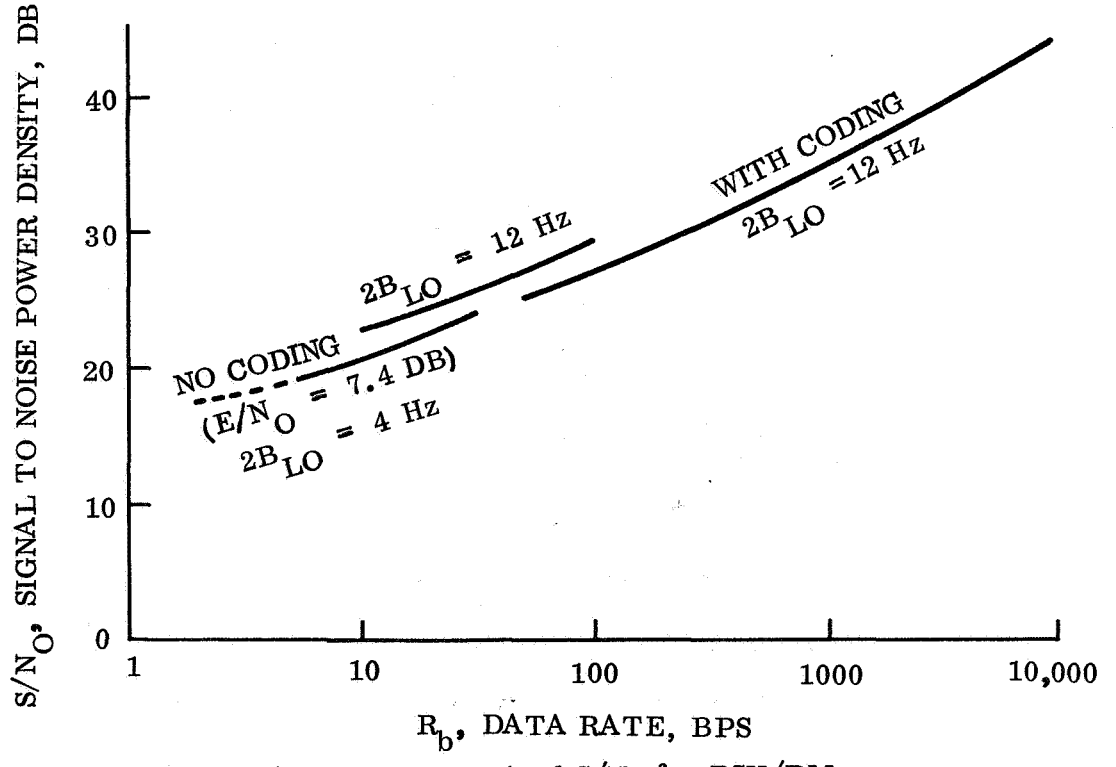

Figure 4.2.3-28. Required S/N_0 for PSK/PM

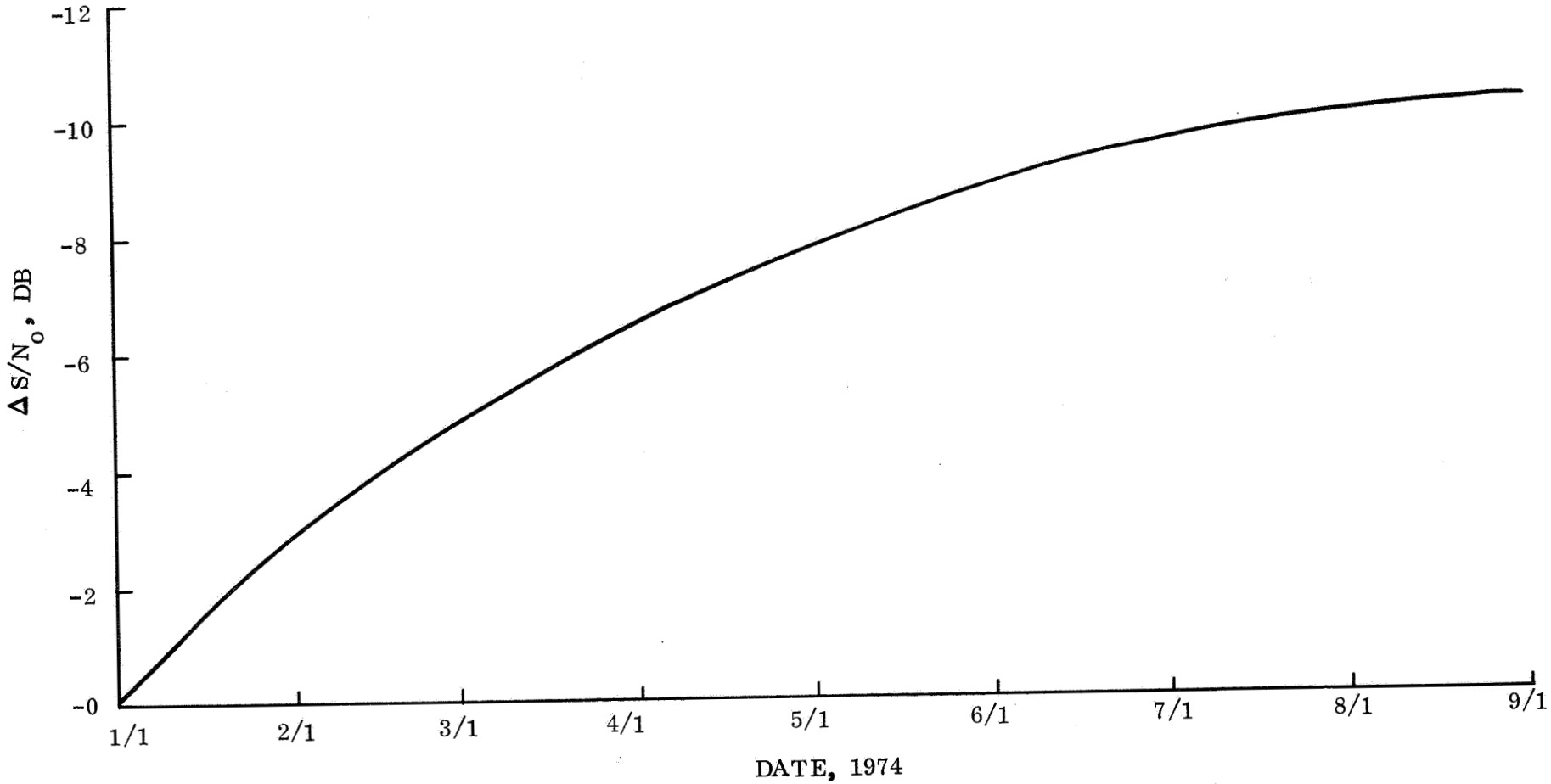

Figure 4.2.3-29. $\Delta S/N_o$ vs Date

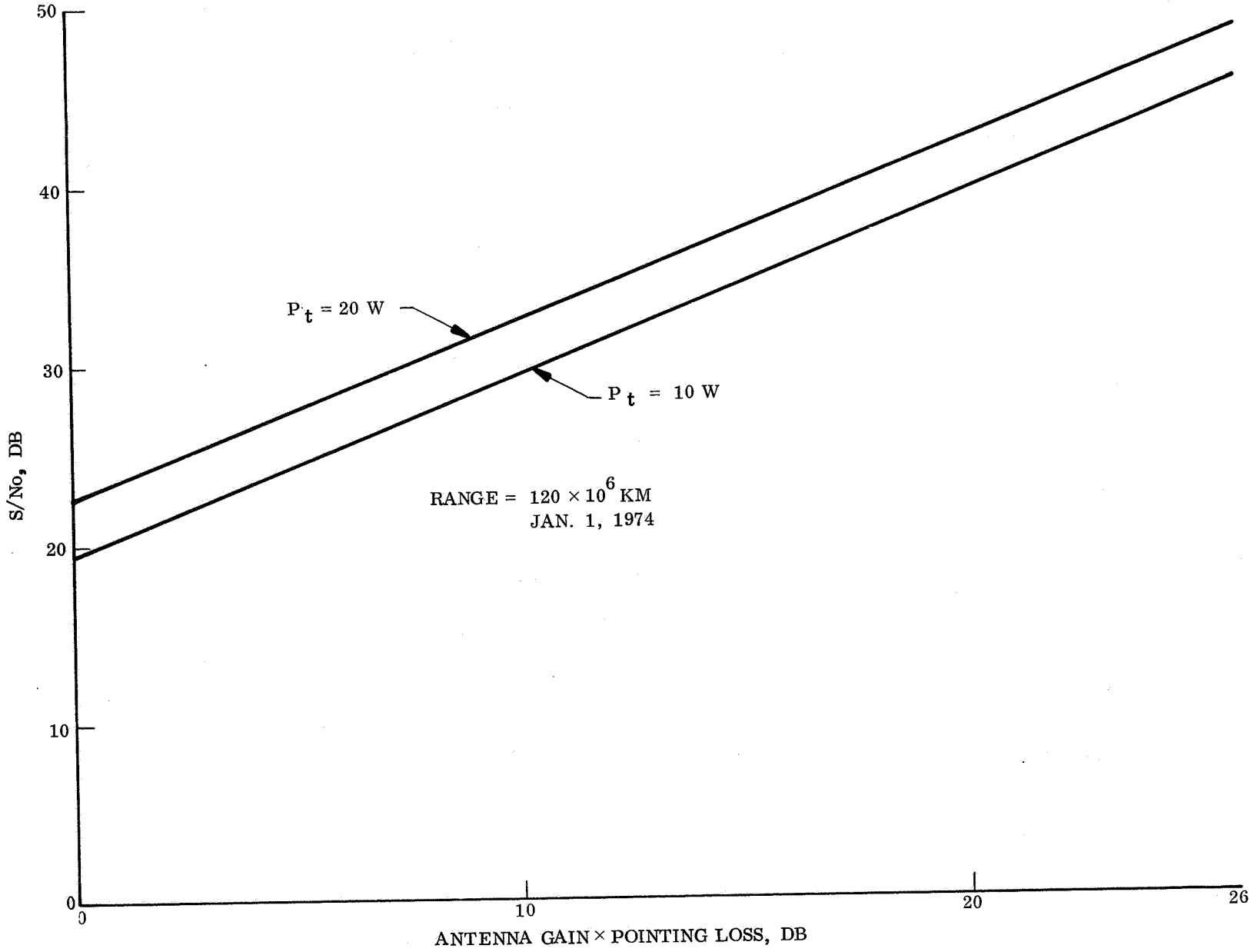

Figure 4.2.3-30. Available S/N_0 at DSN Receiver

TABLE 4.2.3.-4. DESIGN CONTROL TABLE

		Tolerance
Transmitted Power	P_t	-0.7
Transmitting Circuit Loss	-2.3	-0.4
Transmitting Antenna Gain	G	-0.4
Transmitting Antenna Pointing Loss	L_p	
Space Loss (R = 120 x 10^6 km, f = 2300 mc)	-261.3	
Polarization Loss	-0.1	
Receiving Antenna Gain (above 20° elevation angle)	61.0	
Receiving Antenna Pointing Loss	-0.3	
Receiving Circuit Loss	0.0	
Total Received Power (worst cases)	$P_t + G - L_p$ -204.5	
Receiver Noise Density (T_s = 28°K)	-184.1	
S/N_o	$-20.4 + P_t + G - L_p$	

5. Fig. 4.2.3-31. Antenna Gain vs Beamwidth: the antenna gain versus the 3 dB beamwidth, assuming a beam with a circular pattern cross-section and a 60 percent efficiency.

6. Fig. 4.2.3-32. Prime Transmitter Power: the prime dc power required by typical S-band TWT amplifier designs.

7. Fig. 4.2.3-33. Transmitter Energy Requirements: product of transmitter prime power and operation time is plotted.

8. Fig. 4.2.3-34. Mutual Visibility of Goldstone and Syrtis Major: mutual visibility between the 210 ft receiving antenna at Goldstone and Syrtis Major is shown for 0° and 20° elevation angles of Mars as seen from Goldstone. The Earth rise and set as seen from Syrtis Major is for 0° elevation angles.

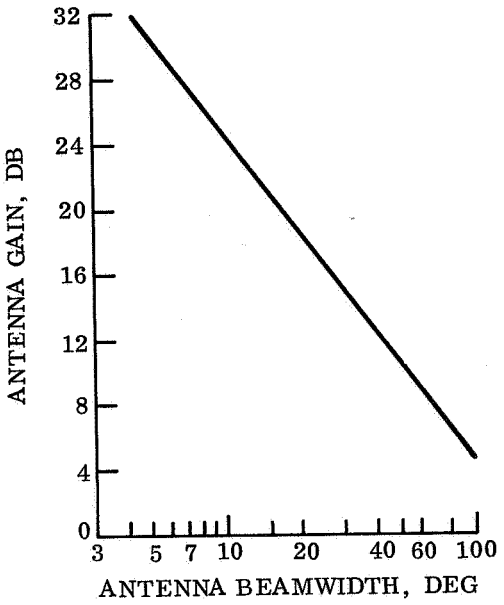

Figure 4.2.3-31. Antenna Gain vs Beamwidth

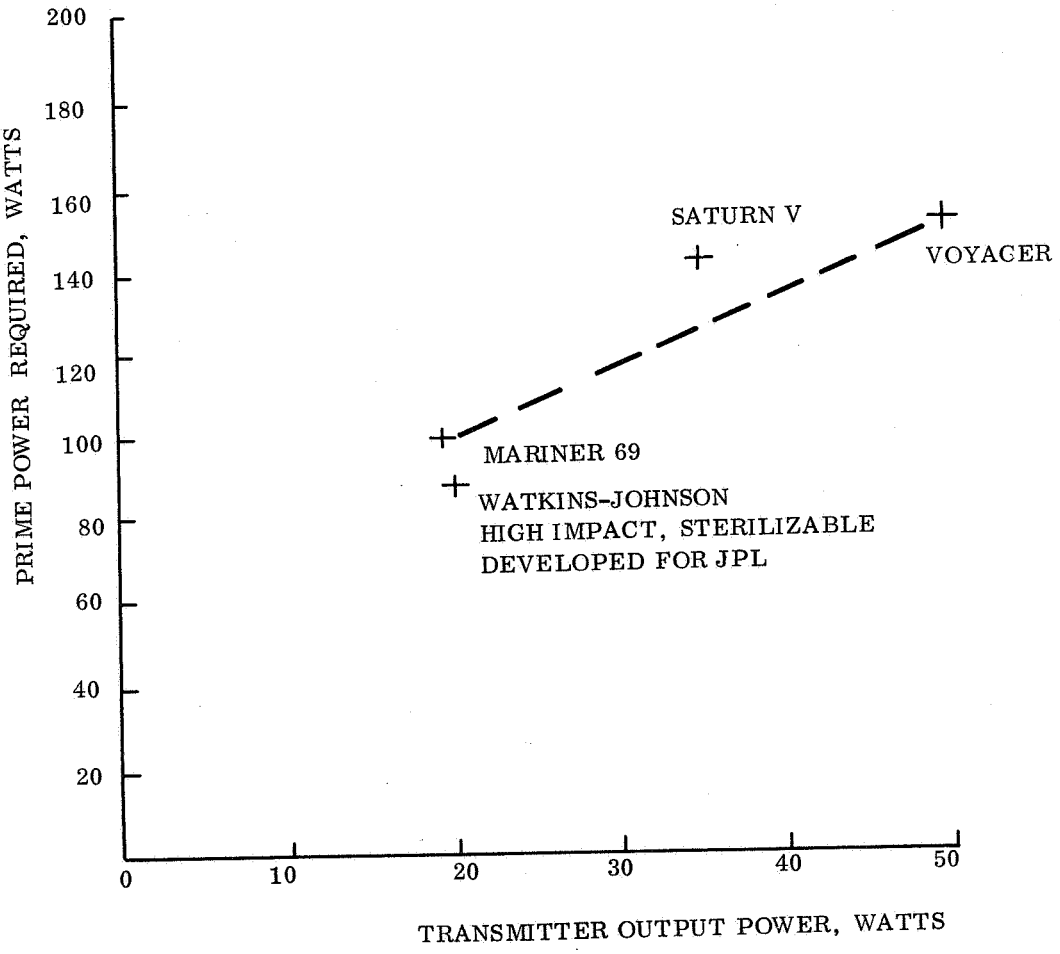

Figure 4.2.3-32. Prime Transmitter Power

9. Fig. 4.2.3-35. Earth and Sun Elevation Angles (10°N Latitude): The Earth and Sun elevation angles versus time (arbitrary starting point) are shown for a Lander at 10°N latitude. Included is the relative timing of the Earth and Sun elevation angles and the change with date.

10. Fig. 4.2.3-36. Earth and Sun Elevation Angles (20°N Latitude): The same as fig. 4.2.3-35 with the Lander at 20°N latitude.

11. Fig. 4.2.3-37. Earth and Sun Elevation Angles (Latitude Variable): the elevation angle history is presented with latitude as a variable for March 14, 1974.

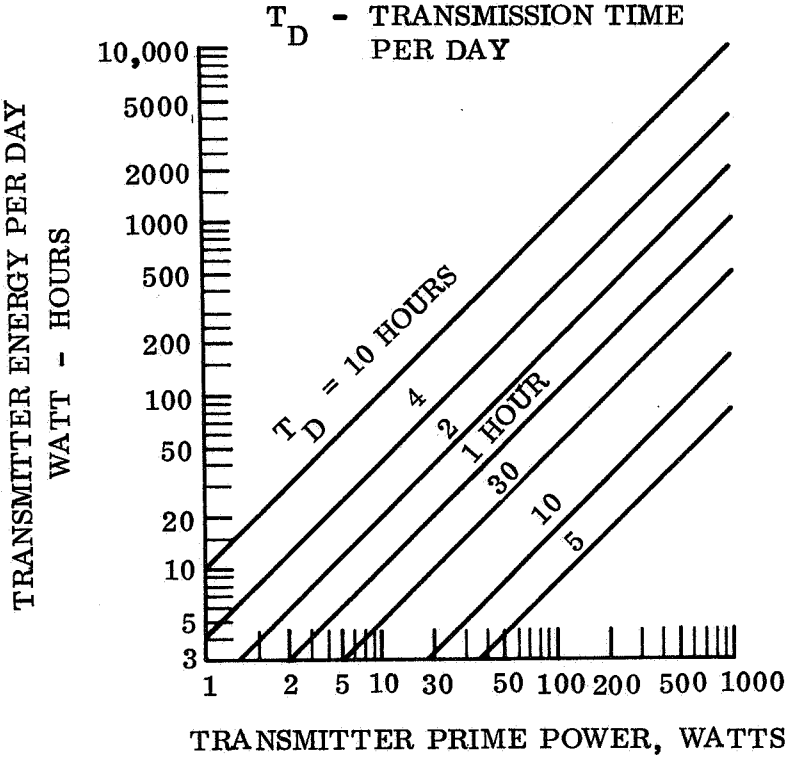

Figure 4.2.3-33. Transmitter Energy Requirements

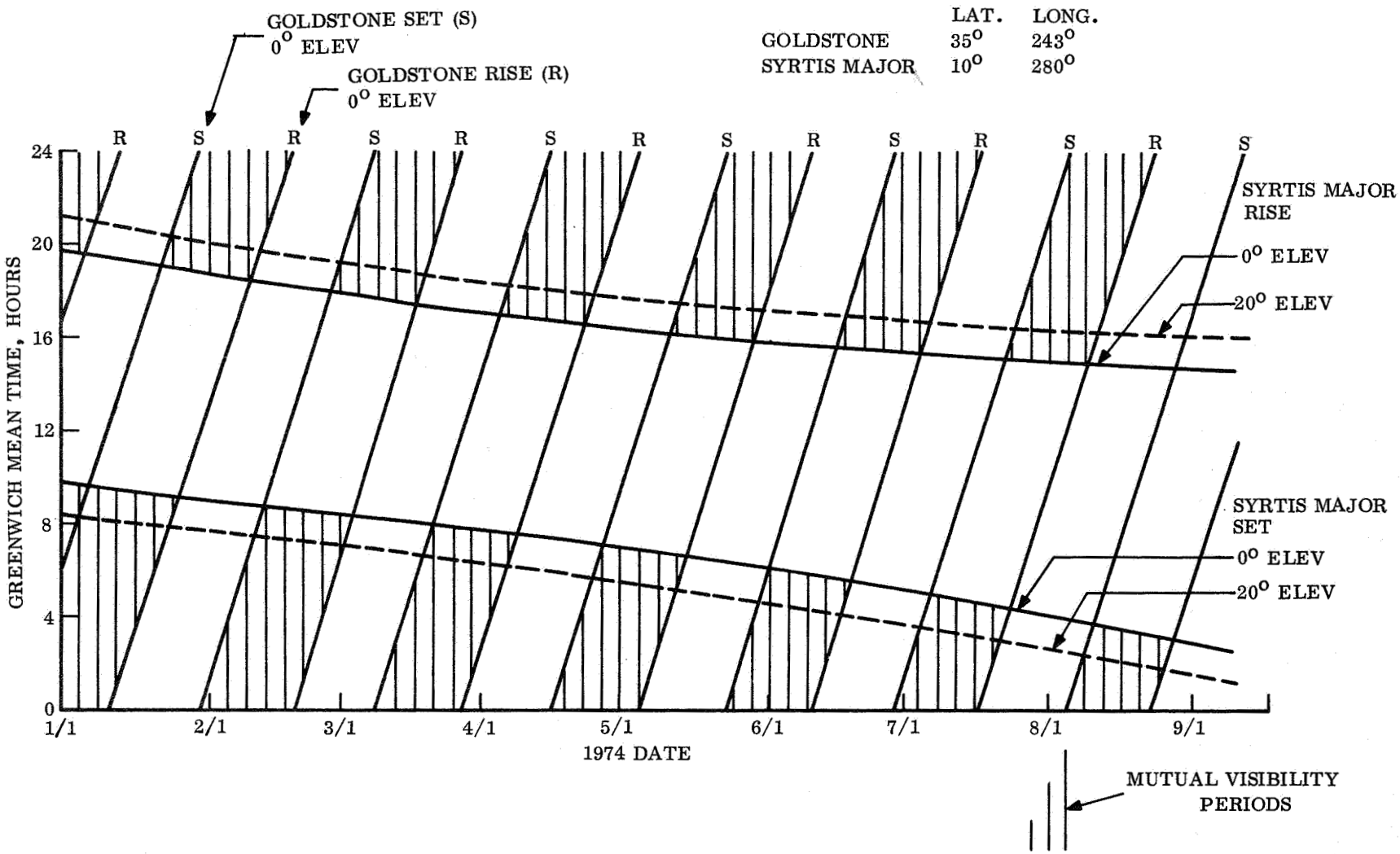

Figure 4.2.3-34. Mutual Visibility of Goldstone and Syrtis Major

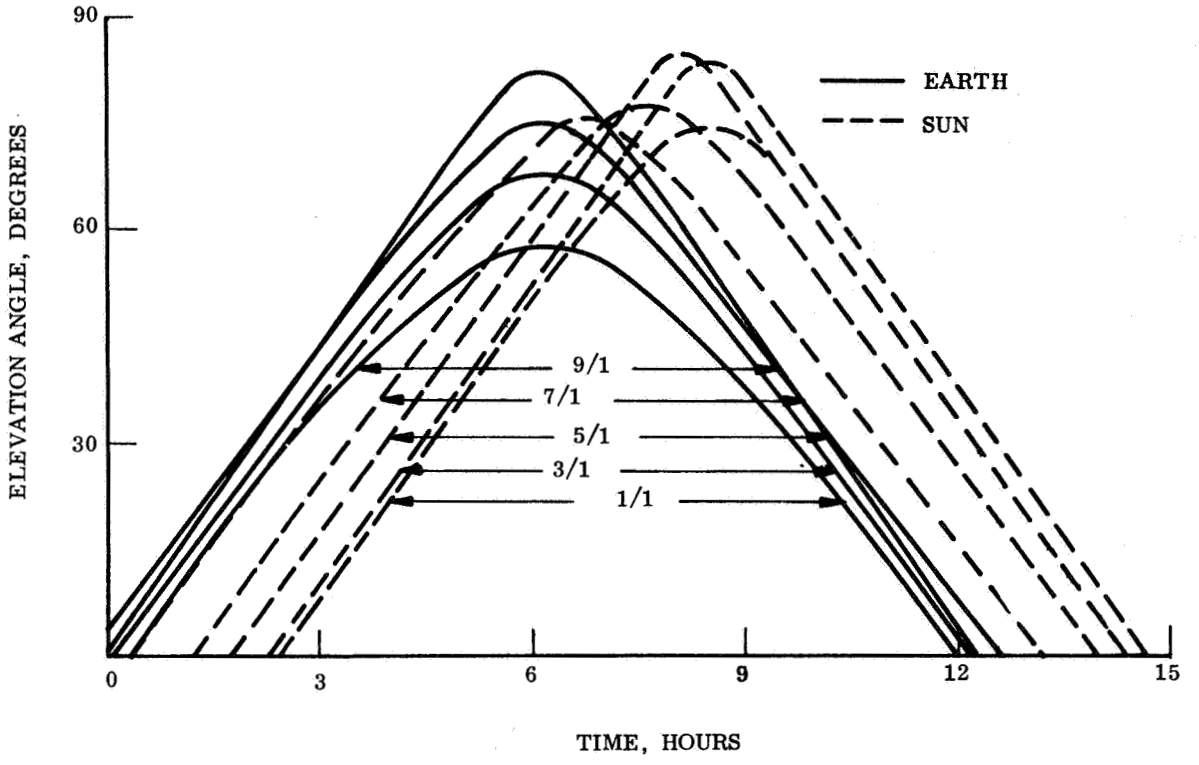

Figure 4.2.3-35. Earth and Sun Elevation Angles - Capsule at 10° N Latitude (1974)

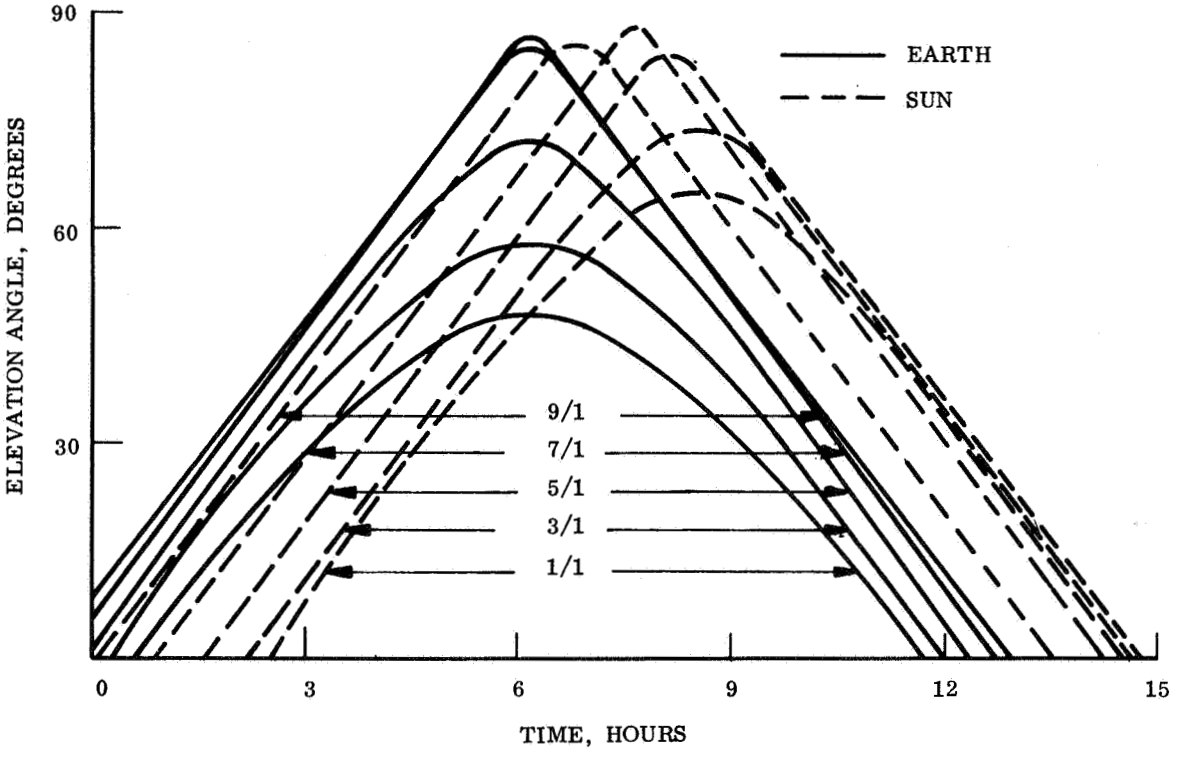

Figure 4.2.3-36. Earth and Sun Elevation Angles - Capsule at 20° N Latitude

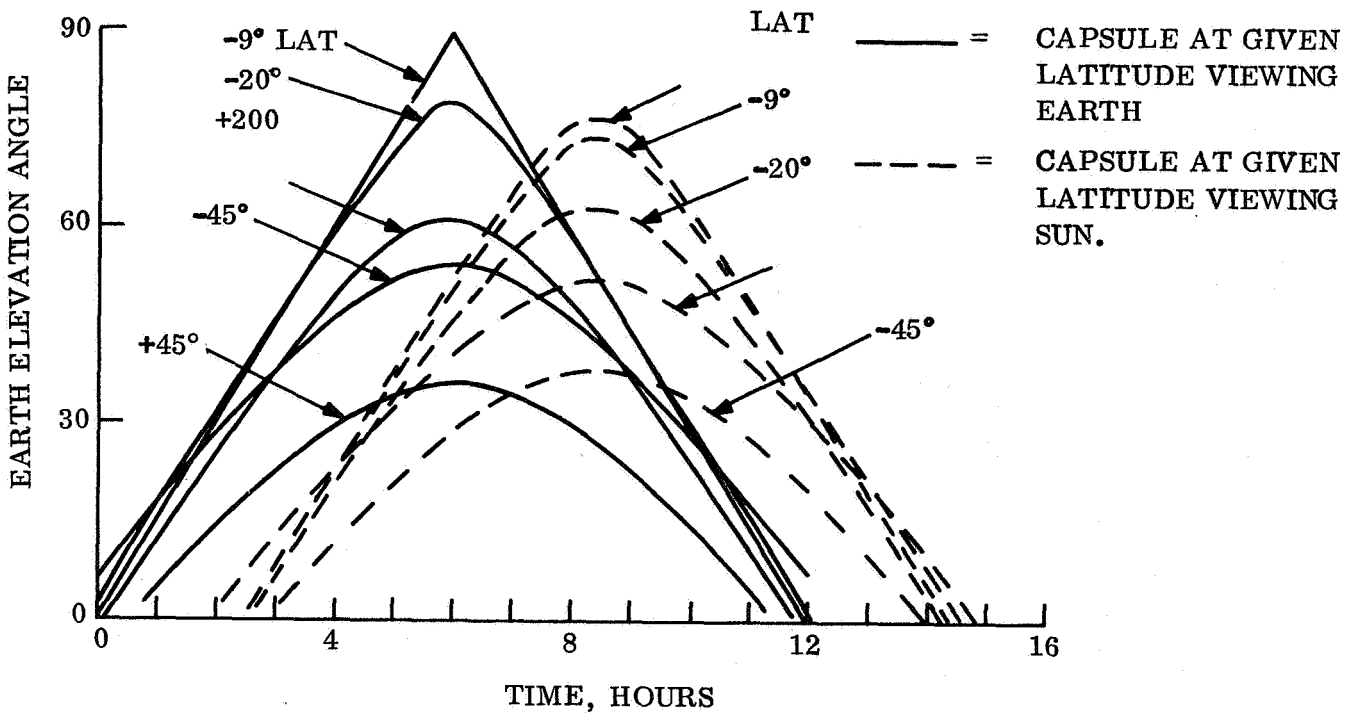

Figure 4.2.3-37. Earth and Sun Elevation Angle vs Time for Capsule Viewing Earth

4.2.3.5 Equipment Parametric Study

The purpose of the equipment parametric study is to provide the effect of mission requirements upon the component size, weight and power requirements. The investigation of radio frequency r-f equipments has been limited to the 400 MHz and 2.3 GHz frequencies based on trade-offs discussed in para 4.2.1.2 and operation with the DSN. Other equipments, such as the multicoders and memory units, have had the range of the significant performance parameter determined in part by the point designs; however, in these cases, the range is broad enough to make the results useful over a significant increase or decrease in requirements. In some instances, such as the beacon receiver, the transponder, and the data handling unit, the basic function and performance characteristics are not significantly changed over the ranges of missions considered, hence they are not presented parametrically. These components are discussed in detail in the point designs.

4.2.3.5.1 Antennas

The antenna investigation has been restricted to specific designs and associated predicted patterns at both 400 MHz and S-band with the exception of the theoretical gain versus beamwidth curve which assumes a pencil beamwidth and a 60 percent efficiency. The resultant antennas presented generally represent the range of acceptable antennas from a size consideration for the Hard Lander vehicle. In general, the antenna pattern has been required to be symmetrical about the vehicle/antenna axis because of the uncertainty in landing orientation.

The accuracy of the predicted patterns, particularly at 400 MHz, is questionable on the skirts of the main lobe; however, it should provide reasonable estimates for comparison purposes. To improve the accuracy of the patterns, measurements should be made on models of the intended vehicles; changes in the Lander configuration would, of course, alter the measured patterns to the same status as the ones presented here.

The antennas can meet any environment that the bulk nylon and foam (if desired) can meet. Hence, there are no anticipated problems in the antennas meeting the environmental requirements of the program. The mechanical deployment mechanisms present a more severe problem which is discussed in detail in Volume IV.

Four S-band antennas are shown in figs. 4.2.3-38, -39, and -40. The corresponding antenna patterns are illustrated in figs. 4.2.3-39 and -40. The wide beamwidth antenna (fig. 4.2.3-38A) is a one turn helix mounted in a conical cup. The nylon tube holding the helix does not extend about the conical cup. The 3 dB beamwidth of this antenna is approximately 120^{o} with a peak gain of 5 dB. The second antenna (fig. 4.2.3-38B) provides a peak gain of 7 dB with a 90^{o} 3 dB beamwidth. The predicted pattern is shown in fig. 4.2.3-39B. This antenna is similar to the previous one, except that the nylon tube extends an additional two inches above the conical cup and holds two helical turns.

The third antenna has a 33°, 3 dB beamwidth. This is shown in fig. 4.2.3-38C and its calculated pattern in fig. 4.2.3-40A.

A sketch of a 24 dB gain S-band array is shown in fig. 4.2.3-38D. It consists of seven helices, each in a conical cup similar to those in figs. 4.2.3-38A and B. Each helix is 14 inches long when released and is sewn into a nylon stocking of that length. The helices are compressed into cups until deployed. The cups are formed by metalizing the surfaces hollowed out of foam that sit upon the back of a stripline board that also incorporates the array feed. The calculated pattern is shown in fig. 4.2.3-40B.

The configuration of the wide beam 400 MHz antenna is that of a "pill-box" eight inches in diameter and two inches deep (fig. 4.2.3-41). The top surface of the box is flush with the vehicle outer surface and has two orthogonal slots two inches wide and eight inches long. The slots are tuned with capacitors to match the input and they provide circular polarization. The bandwidth of this antenna is about 2 MHz. The predicted pattern is shown in fig. 4.2.3-42.

Two other 400 MHz antenna designs are included. The first, shown in fig. 4.2.3-43, provides a broad beam width pattern. However, the bandwidth is increased significantly. The second antenna is a cross Yagi antenna (fig. 4.2.3-44). This antenna provides the highest practical gain at 400 MHz. It has a 9 dB gain with a beamwidth of 65° and has a bandwidth of 40 MHz.

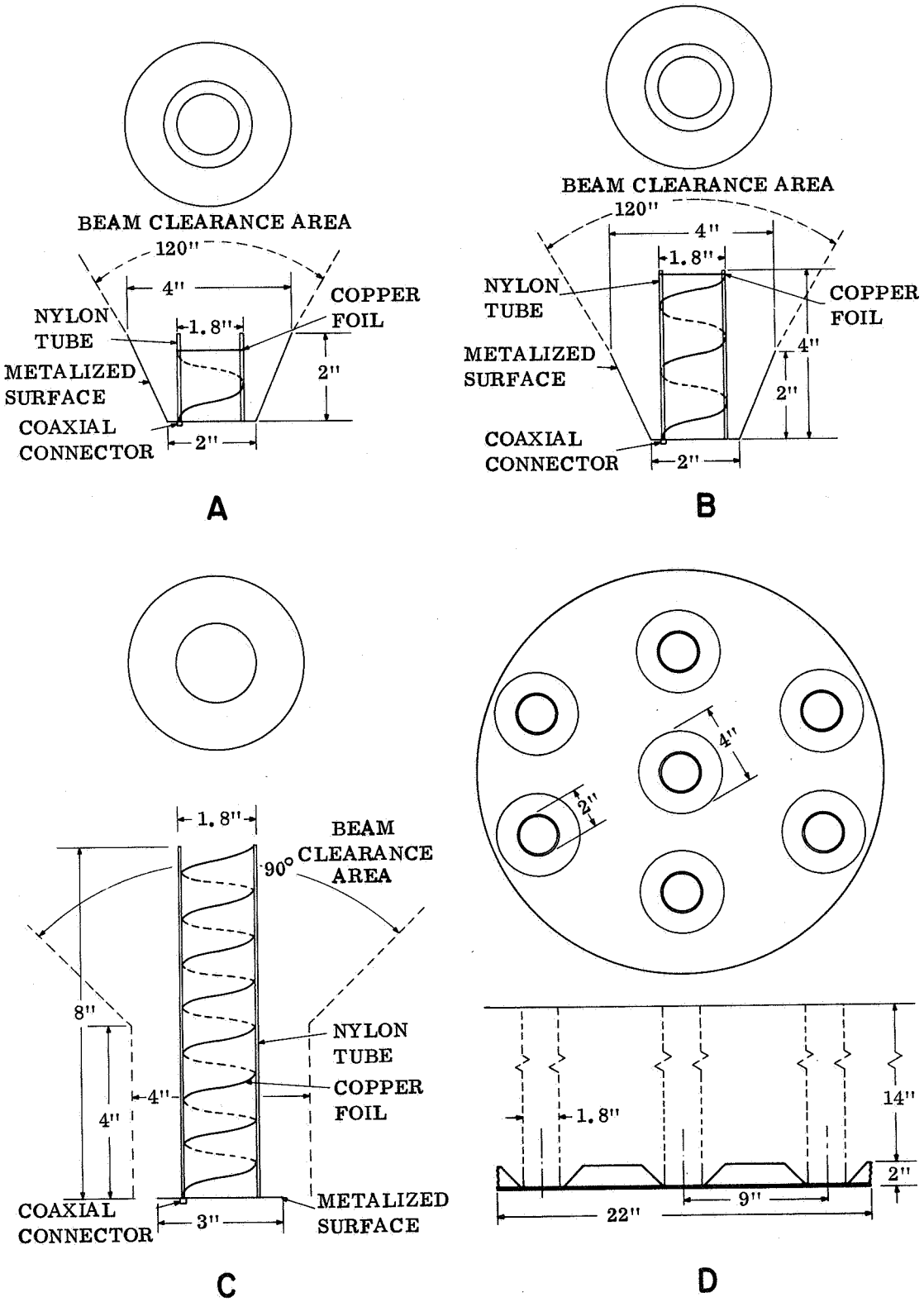

Figure 4.2.3-38. S-band Antenna Configurations

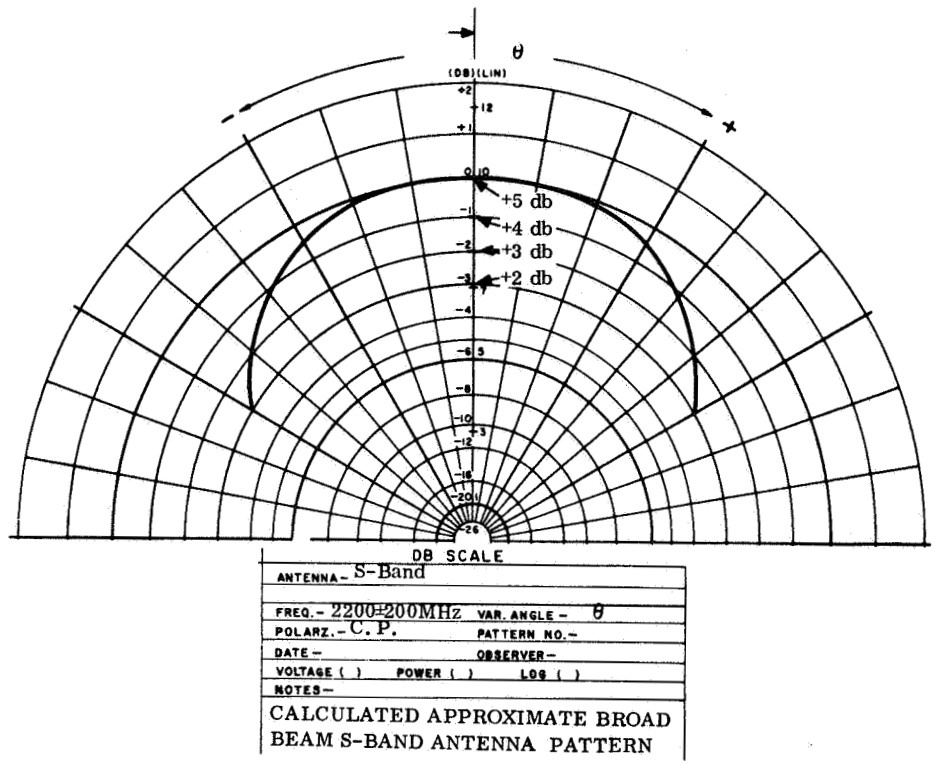

A-WIDE BEAMWIDTH

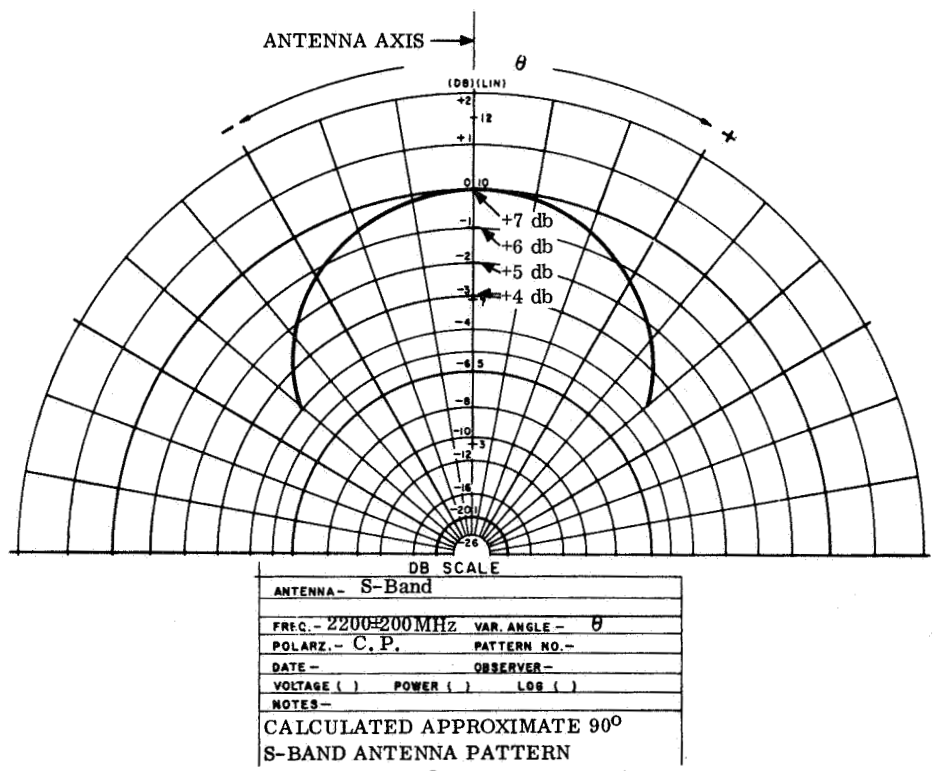

B. 90^{o} BEAMWIDTH

Figure 4.2.3-39. S-band Predicted Antenna Patterns

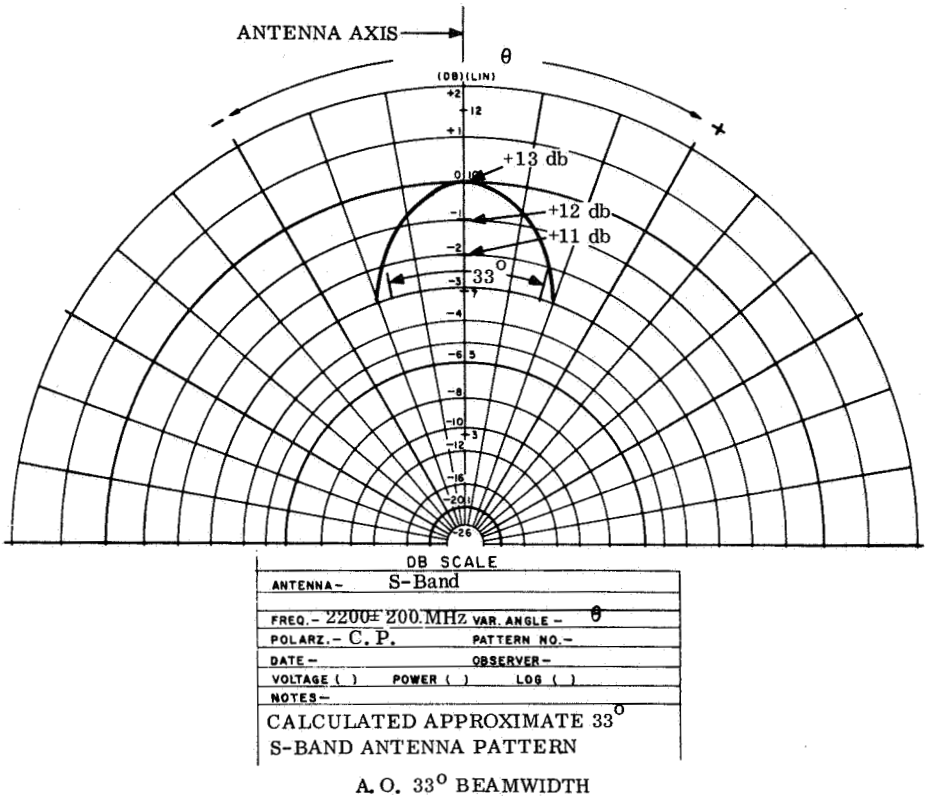

A. O. 33° BEAMWIDTH

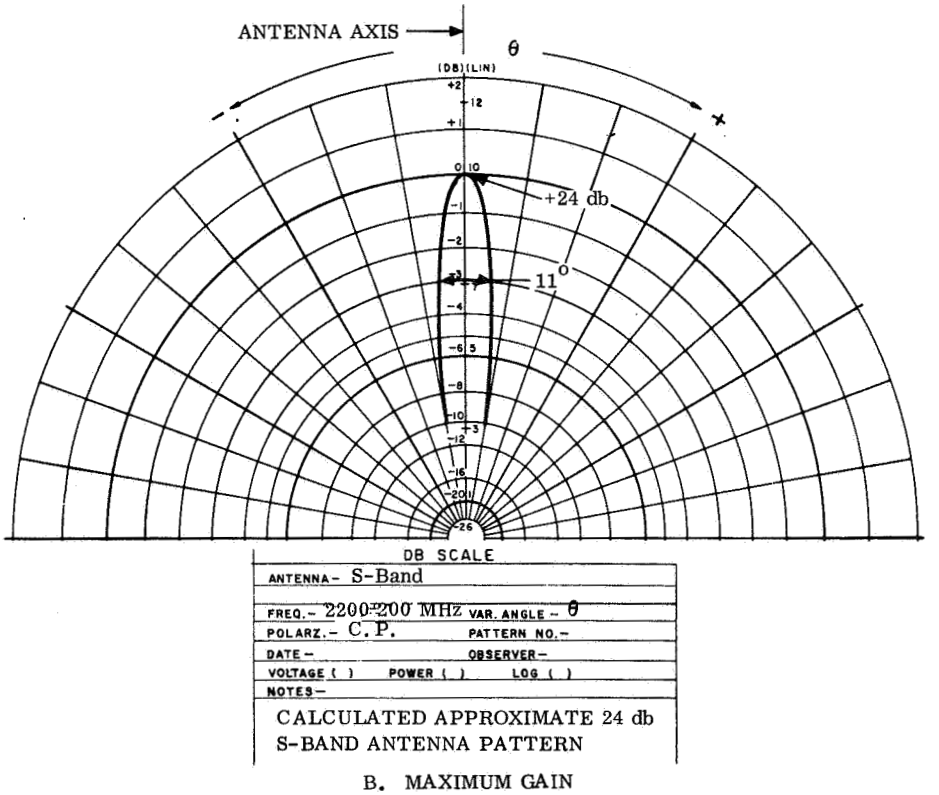

B. MAXIMUM GAIN

Figure 4.2.3-40. S-band Predicted Antenna Patterns

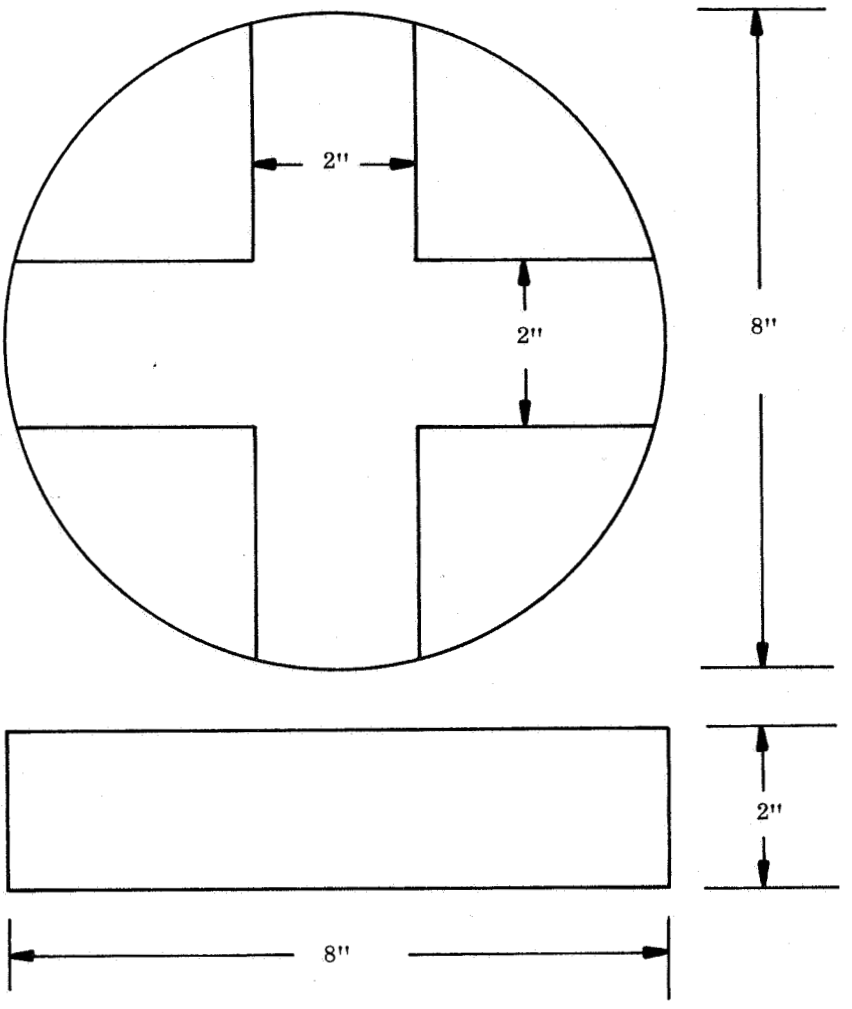

Figure 4.2.3-41. UHF Antenna

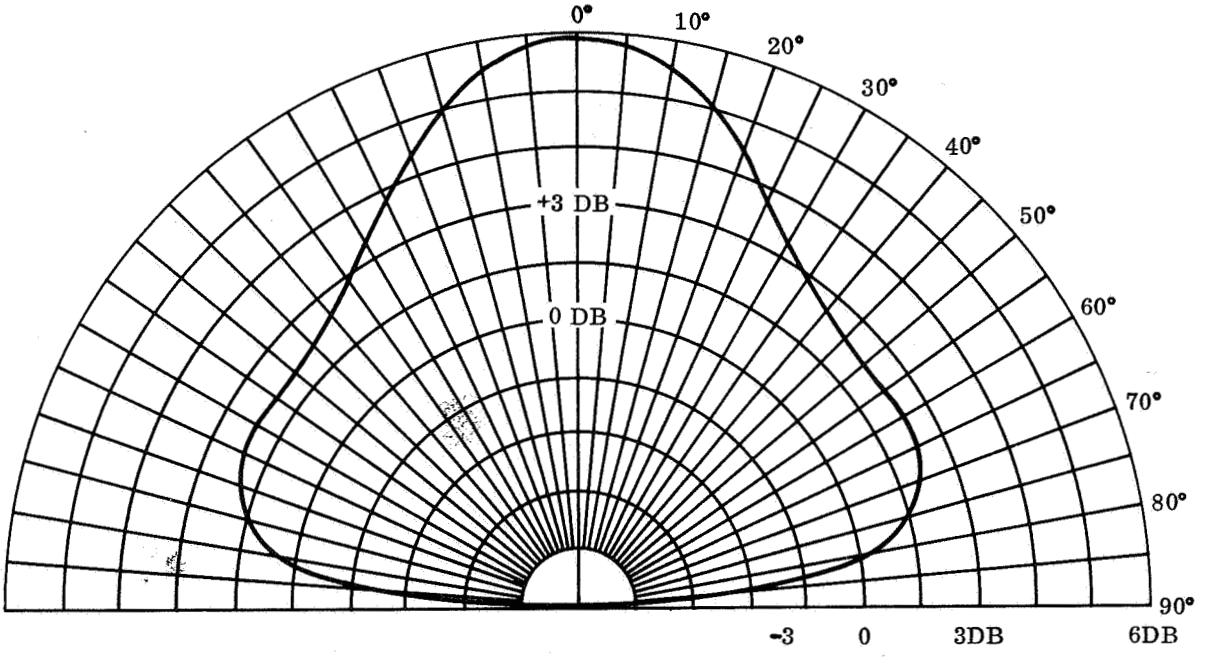

Figure 4.2.3-42. 400 MHz Antenna Pattern

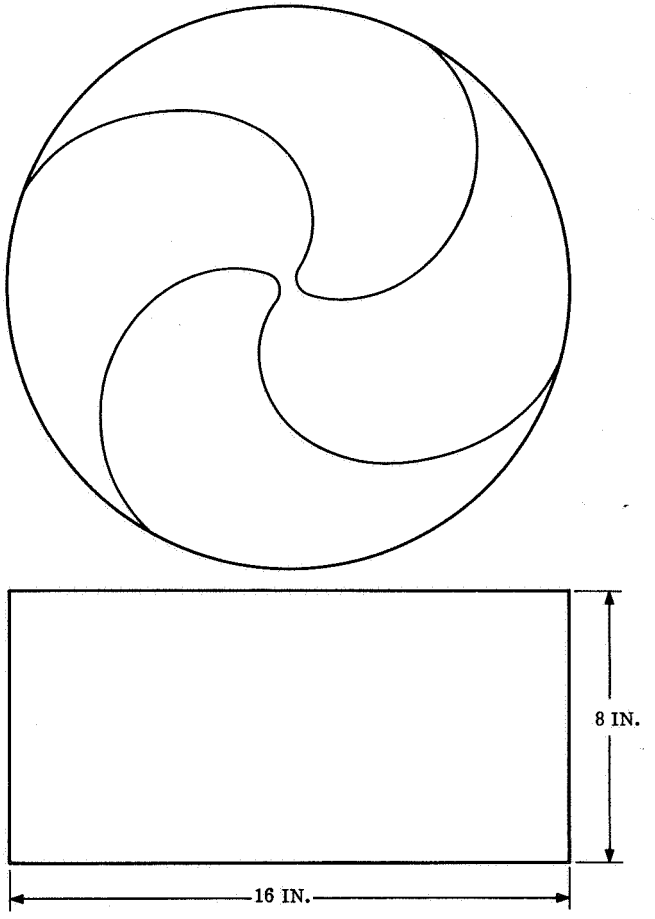

Figure 4.2.3-43. Broad Beam, Wide Bandwidth Antenna

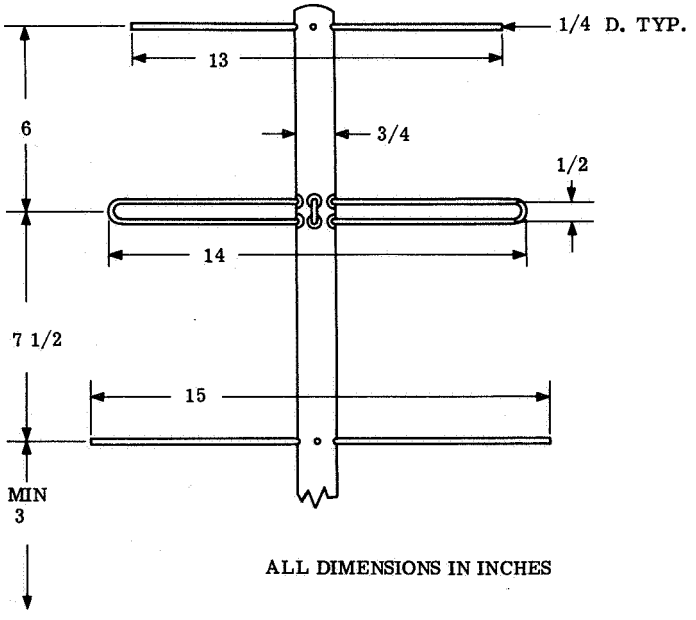

Figure 4.2.3-44. Maximum Practical Gain

4.2.3.5.2 Transmitter

The maximum transmitter power output considered is 50 watts at both 400 MHz and S-band to avoid antenna breakdown during entry. In the case of the S-band transmitter, primary consideration has been given to the 20 watt TWT amplifier developed by Watkins-Johnson for JPL to meet the high shock and sterilization requirements of a Hard Lander. It is this device which is used for the point designs; its design constraints were also used to determine the characteristics of a 50 watt device for parametric studies and Lander maps. The use of an all solid state transmitter was not considered since the current state-of-the-art of semiconductors limits their efficiency to 10 to 15 percent compared to the dc to r-f efficiency of the TWT of greater than 26 percent.

The 400 MHz transmitter will be solid state and characteristics are shown parametrically in figs. 4.2.3-45 and -46 for the range of power outputs of 5 to 50 watts. In order to meet the high shock environment, potting will be required throughout the transmitter. The transmitter oscillator stability will be 10 ppm over a temperature range of -40°C to +70°C with negligible warmup time at any temperature. Aging of the oscillator will be 1 ppm per year. While the state-of-the-art in temperature compensated crystal oscillators has reached the point where stabilities on the order of 1 ppm or better are achievable, the 10 ppm stability is considered conservative to allow for slight deformation of the crystal structure or holder due to the high shock levels.

4.2.3.5.3 Multicoder

The multicoder designs considered in the parametric study provide for several modes of operation with the selected mode or modes being controlled by the programmer. The parametric curves in fig. 4.2.3-47 show the effect of changing the composition of the 100 analog engineering channels from all high level (0-5V) channels to all low level (0-50 mV) channels. The base unit is based on 100 high level analog channels for diagnostic data, 22 high level science analog channels, and 17 digital input channels. In this case the unit dimensions are $3.5 \times 4.25 \times 6.0$ inches, the weight is 3.5 pounds and the unit would consume 11 watts. The effect of adding 8 bit parallel inputs is shown in fig. 4.2.3-48.

4.2.3.5.4 Effect of High Shock and Sterilization

The components of the telecommunication system are not generally susceptible to the high temperature associated with the sterilization process. Almost all of the electronic equipment will require complete potting of the components in order to meet a 1000 shock requirement, thereby complicating both their design and manufacture. Once this is accomplished it is anticipated that the increase to 3000 g's impact shock will not require further penalty. A 50 watt solid state VHF transmitter designed at GE was tested in a sterilization environment (145°C) and at 5000 g shock without degradation (ref. 4-24).

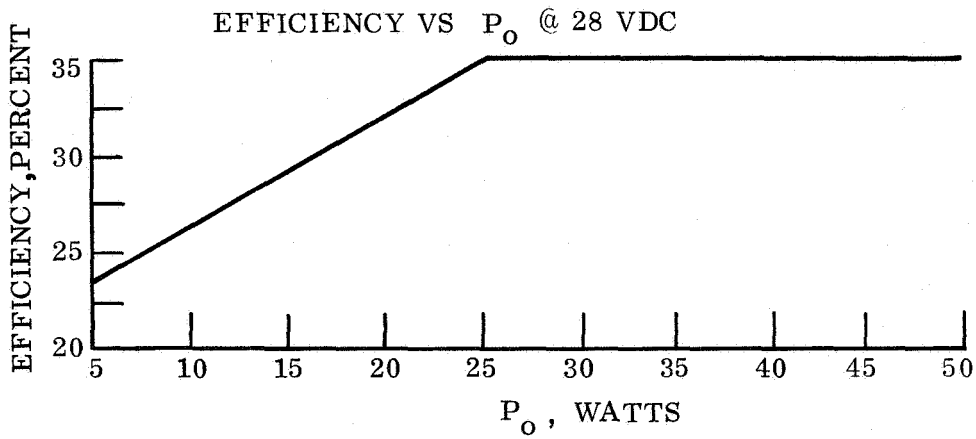

Figure 4.2.3-45. Efficiency of 400 MHz Transmitter vs Power Output

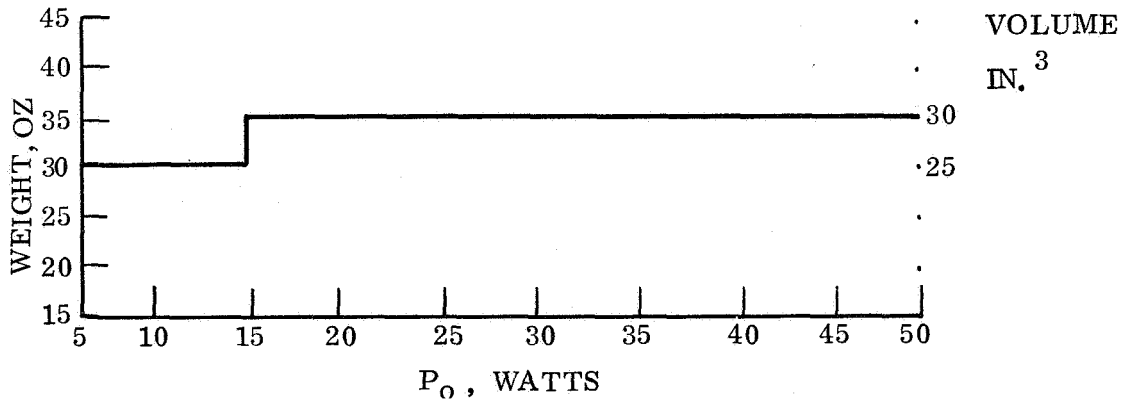

Figure 4.2.3-46. Size and Weight of 400 MHz Transmitter vs Power Output

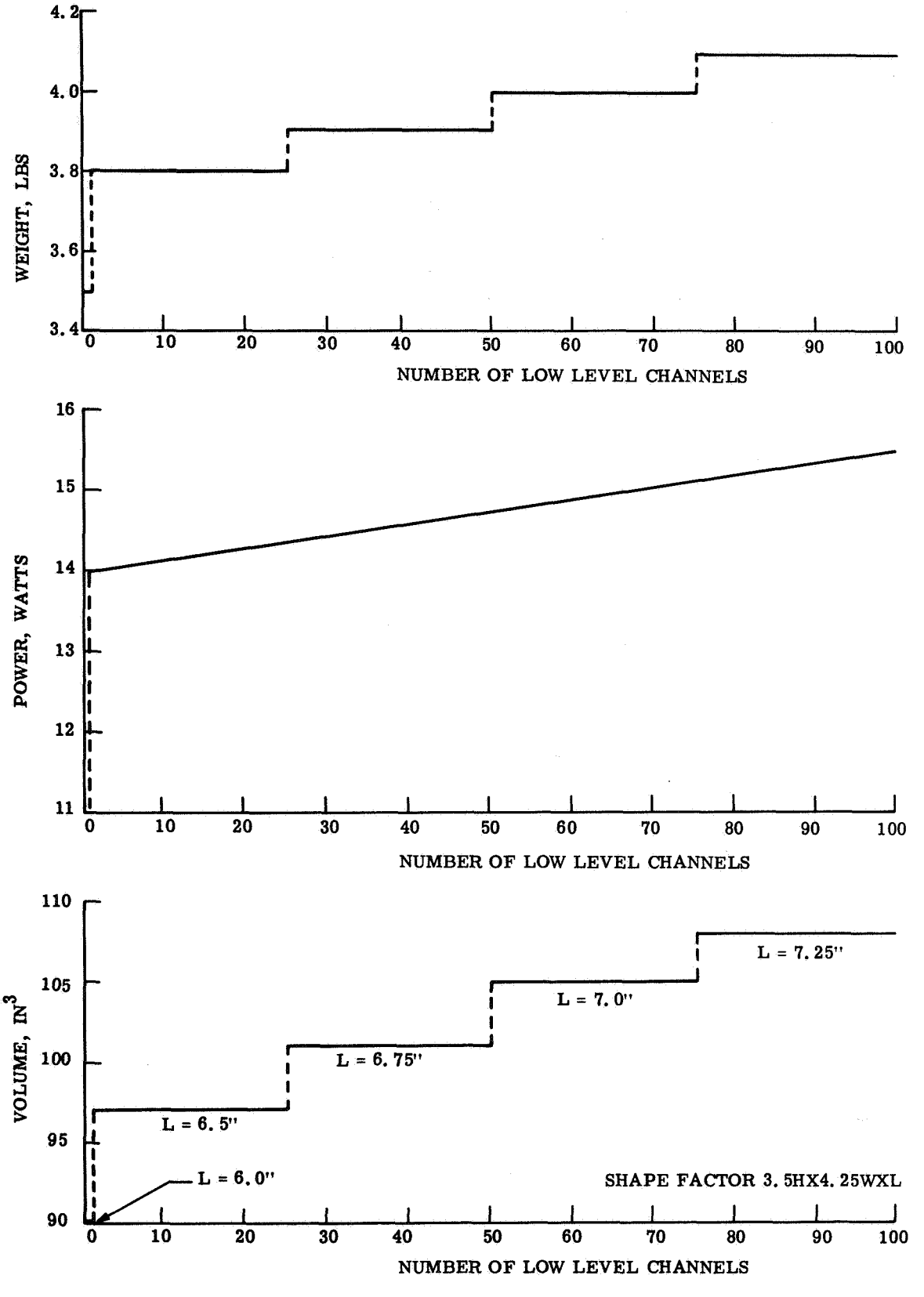

Figure 4.2.3-47. Increment of Size, Weight, and Power of Low Level Analog Channels

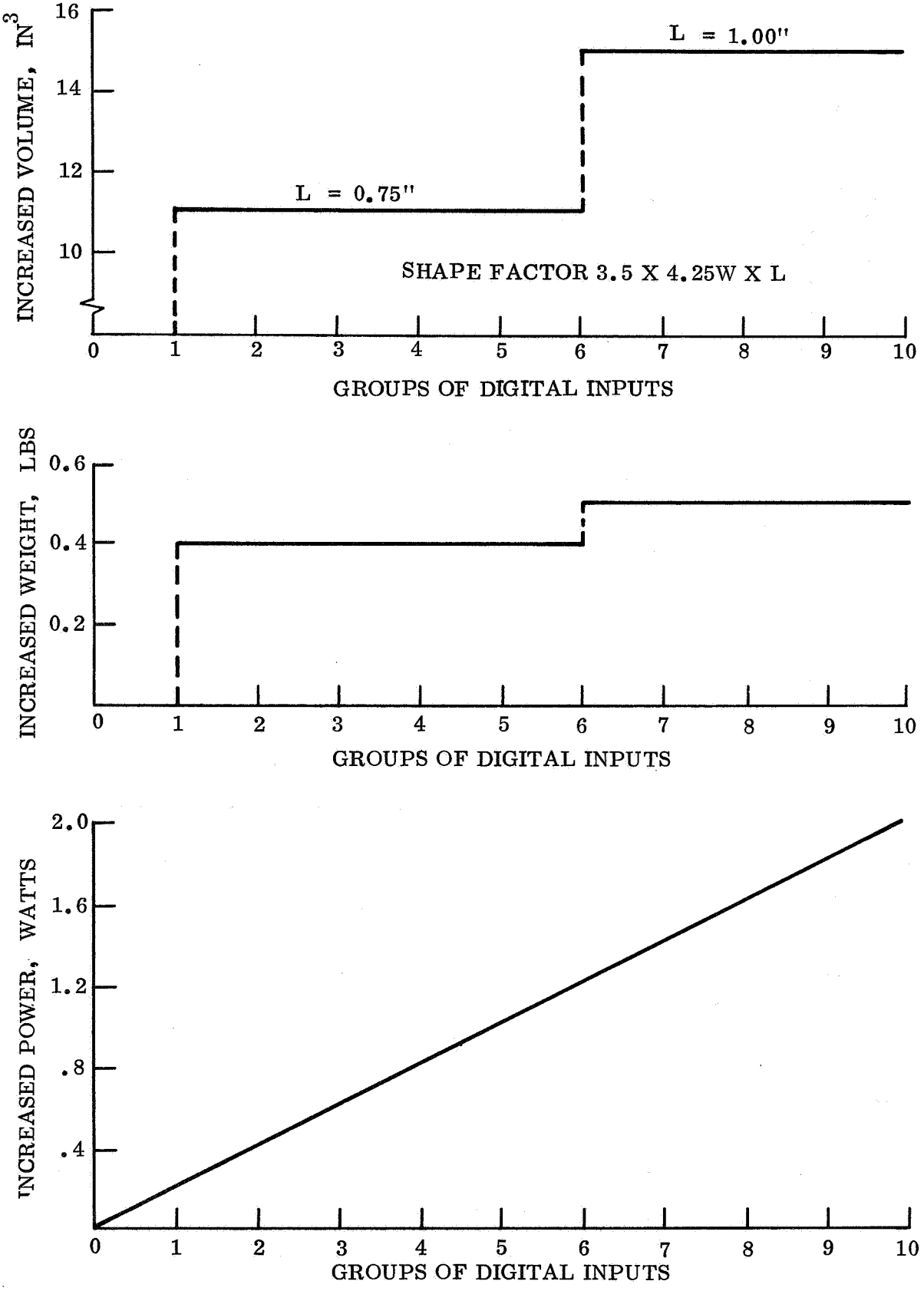

Figure 4.2.3-48. Increment of Size, Weight, and Power for Additional Digital Input Channels

4.2.4 SAMPLE COMPUTATION

4.2.4.1 Mission Definition

In this section, an example link solution is given for a specified mission, using the parametric data. The mission is defined as an out-of-orbit entry with a landing date of April 30, 1974. The landing site is at 10°N latitude; on Earth three 210 foot DSN stations are assumed to be available throughout the mission lifetime of 90 days. The initial data will be returned via a relay link while the extended mission will utilize a direct link. The data to be returned via the relay link consists of scientific and engineering measurements made after landing, up to 100,000 bits of stored entry data, and imagery data resulting in total bit return of 1.073×10^7 bits.

The data required to be transmitted daily on the direct link is 14,560 bits consisting of reduced science and engineering measurements.

From trajectory information, it was determined desirable to transmit the data during a five minute period during which the maximum range does not exceed 2000 km. This information is sufficient to evaluate the link performance from the parametric curves.

4.2.4.2 Periapsis - Relay Link

First consider a periapsis relay link. From the discussion in para 4.2.1.2, the preferred mode for a periapsis relay link is a non-coherent FSK system. From fig. 4.2.3-10, a data rate of 35.6 kbps is obtained as the data rate required to meet the mission objectives.

At this point, if the range rate were known, the doppler frequency could be determined from fig. 4.2.3-11. The oscillator frequency uncertainties of both the transmitter and the receiver local oscillator must be added to the doppler frequency uncertainty. This results in a minimum bandwidth constraint on the receiver. In the present case, a 20 kHz total frequency uncertainty is assumed.

With frequency uncertainty and data rate determined, the required signal-to-noise power density ratio (S/N_0) is obtained from fig. 4.2.3-12 as 59 dB, including 2 dB of detection loss.

The remaining parameter to be determined is the transmitter power required to satisfy the required S/N_0 obtained. Fig. 4.2.3-15 presents the available S/N_0 as a function of the total effective antenna gain and transmitter power at a range of 2000 km. Assuming a 0 dB gain antenna on the Lander and a 1 dB minimum antenna on the space Orbiter, the effective antenna gain is 1 dB. The required transmitter power is approximately 35 watts, including 4.0 dB margin and 2.0 dB detection loss.

4.2.4.3 Direct Link

The direct link Communication System can be determined in a similar manner. However a slightly different set of assumptions is utilized. The extended mission presents additional constraints, one of which is power conservation. The assumption is also made that it is desirable to return the maximum amount of data toward the end of the mission.

Assuming then that a vertically oriented antenna is desired, the beamwidth requirements can be obtained as shown in para 4.2.2.1. The optimum antenna beamwidth on 4/30 is 23°, while ninety days later it is 33°. The optimum beamwidth remains less than these values for the intervening time interval. Therefore, a 33° beamwidth vertically oriented antenna will provide a satisfactory view period of Earth during the entire mission life. The minimum period during which Earth is in view is 5750 sec (para 4.2.2.1). The corresponding peak antenna gain is approximately 14 dB from fig. 4.2.3-31.

Since the transmission time is to be minimized under the previous constraints, the next step is to determine the available signal-to-noise density ratio (S/N_0) in order to determine the maximum allowable data rate. A twenty watt TWT amplifier is known to be available for this application and its utilization is assumed. The difference in the space loss on 4/30 referenced to January 1, 1974, is about 7.8 dB more (from fig. 4.2.3-29) while at the end of the mission it is 10.0 dB. By selecting the worst case range (i.e., -10 dB increment in space loss) a worst case maximum data rate results.

Referring to fig. 4.2.3-30, the available S/N_0 on January 1, 1974, can be obtained directly for the case at hand. The vertically oriented antenna optimization assumes a 3 dB pointing error; therefore, the antenna gain times the pointing loss is 11 dB. Thus, the available S/N_0 for a 20 watt transmitter is 33.5 dB on January 1. Reducing this by the increased space loss of 10 dB gives 23.5 dB available S/N_0; this includes 1.5 dB margin for adverse tolerances, 2.3 dB transmit circuit loss and 0.1 dB polarization loss. The data rate is then obtained directly from fig. 4.2.3-28 as 15 bps uncoded for the 12 Hz receiver bandwidth.

The time required to transmit the 14,560 bits is about 970 sec, which is less than the available transmission time. The maximum data return capability on the last day of the ninety day mission is 84,000 bits allowing 150 sec acquisition time.

4.2.4.4 Apoapsis Relay Link

The requirement assumed in this case is to transmit the same data as in the periapsis relay case, that is, 1.073×10^7 bits. From the possible worst case slope of 34°, an additional slope of 12° due to unsymmetrical crush-up, and the desire to remain 10° above the antenna ground plane, it can be assumed that the transmission should be completed between elevation angles of 56°. From trajectory information, the available time for transmission is 16,200 sec. During this time, the maximum range is 33,180 km and the range rate excursion is about 182 km/sec resulting in a doppler frequency shift of 240 Hz.

An acquisition time of 100 sec is assumed as a reasonable time, resulting in a total time available for transmission of 16,100 sec and a required data rate of 672 bps.

As in the previous relay link, the frequency uncertainty due to the oscillators (both transmitter and receiver local oscillator) is 12 kHz. The total uncertainty is about 12.3 kHz (oscillator uncertainty plus doppler shift).

Using fig. 4.2.3-13 to obtain the receiver loop bandwidth for a 100 sec acquisition time and 12.3 kHz frequency uncertainty gives a 35 Hz bandwidth requirement. The required S/N_0 is as obtained from fig. 4.2.3-14, 38 dB. From fig. 4.2.3-17 the range correction factor of -24.5 dB is obtained. Combining the required S/N_0 and the increased range so as to be compatible with fig. 4.2.3-15 results in an "effective required" S/N_0 of 62.5 dB.

The antennas on both the Lander and Orbiter are assumed to be identical. In fig. 4.2.3-41 the gain over the required 80° angle from boresight is a minimum of 0 dB. The Orbiter has a worst case gain of 3 dB including pointing loss, resulting in a minimum combined antenna gain of 3 dB. From fig. 4.2.3-15 the transmitter power is read at 50 watts.

4.3 ELECTRICAL POWER AND DISTRIBUTION

A. Introduction:

The objective of this section is to provide parametric data on power sources, power conditioning equipment, power control, and distribution equipment which will permit the synthesis of Hard Lander designs. The approach is to start with the system power profile parameters which establish power source requirements. Four types of sources are considered: batteries, fuel cells, solar cells, and radioisotope thermoelectric generators. For each of these power sources, parametric data are developed which enable the sizing of the source and auxillaries for variations of the environmental and system conditions. Similar data are provided for the conditioning, control and distribution equipments.

Following this, the subsystem synthesis techniques are introduced. This involves data and relationships which permit the determination of storage battery, regulator, or conditioning requirements, and which result in a balanced combination for solar cells, fuel cells, and RTG's. In this manner, the size of solar panels, the charge regulator, and the associated storage battery are matched in capability to meet the power profile requirements. This section is developed through use of example calculations.

Finally, in the tradeoff section, various solar panel orientations are considered and the four power sources compared. As an aid to system comparisons and design selection, the regions or loci of least weight or volume have been developed parametrically. Summary curves are developed both with and without RTG's; with and without the use of a "three day" battery.

B. Study Organization and Presentation

The material that follows is organized to show the step-by-step development of parametrics. The requirements are first stated, followed by a description of the components on which the parametrics are based. The synthesis then follows. This includes assumptions, component parametric data, and usage of subsystem data. Lastly, the tradeoffs and optimum trends are developed.

Each of the subsections are identically organized with a discussion of the power sources: batteries first, followed by solar cells, fuel cells, and RTG's in that order. Next follow the inverter and regulators. Finally, the harness and connector data.

4.3.1 ELECTRICAL REQUIREMENTS AND DESCRIPTION

4.3.1.1 Functions

The electrical power and distribution subsystem provides the equipment which supplies, controls, and transmits electrical energy throughout the vehicle. The various electrical/electronic functions to be performed in the Lander are given in table 4.3.1-1.

TABLE 4.3.1-1. LANDER ELECTRICAL SYSTEM FUNCTIONS

Programming
Circuit protection
Voltage regulation
Electromagnetic compatibility
Power conditioning
Data encoding
Initiation
Sensing - pressure, temperature, acceleration, velocity, photoimagery, impact, motion, field intensity
Data transmission and propagation
Power transfer
Disconnection
Energy sources
Data distribution
Signal and command distribution
Power busbaring

4.3.1.2 Requirements

The requirements for the electrical energy as well as the control and distribution requirements are derived from electrical/electronic systems studies. Power profiles reflecting all the onboard electrical/electronic equipment are used to develop subsystem requirements. Generally these profiles contain three distinct operating periods; entry, initial landed operation, and the extended mission. In order to achieve practical designs in the extended mission, energy radioisotope techniques are introduced. This includes turning off all equipment except a timer, a UHF receiver, and associated voltage regulators as well as using radioistope elements for temperature control. Under these conditions a typical power profile may be summarized by table 4.3.1-2.

In the extended mission, considerable flexibility exists for performing various scientific measurements on Mars. Through the command system, the sequence of operations and the particular scientific instruments used may be changed. For the "minimum" science package, the resulting power profiles may be summarized parametrically (fig. 4.3.1-1). With imagery, the profile parameters are shown in fig. 4.3.1-2.

In addition to scientific instrument sequences, programming is required for pyrotechnic initiation, release operations, deployment functions, activation, transmission, sequencing and checkout. The associated requirements are summarized in table 4.3.1-3.

TABLE 4.3.1-2. POWER PROFILE SUMMARY

Mission Phase / Subsystem	Entry	First Day	Following Days*	Units
Electrical Equipment	71.6	251.5	0.75	Watt-Hours
Telecommunications	63.6	895.7	12.65	Watt-Hours
Scientific Payload	37.1	124.3	50.30	Watt-Hours
Total Energy	172.3	500. to 1650.	100 to 250	Watt-Hours
Average Power	86.2	5 to 60	4 to 10	Watts
Demand Factor	4.2	6 to 20	25 to 70	N.U.

* Does not include any imagery.

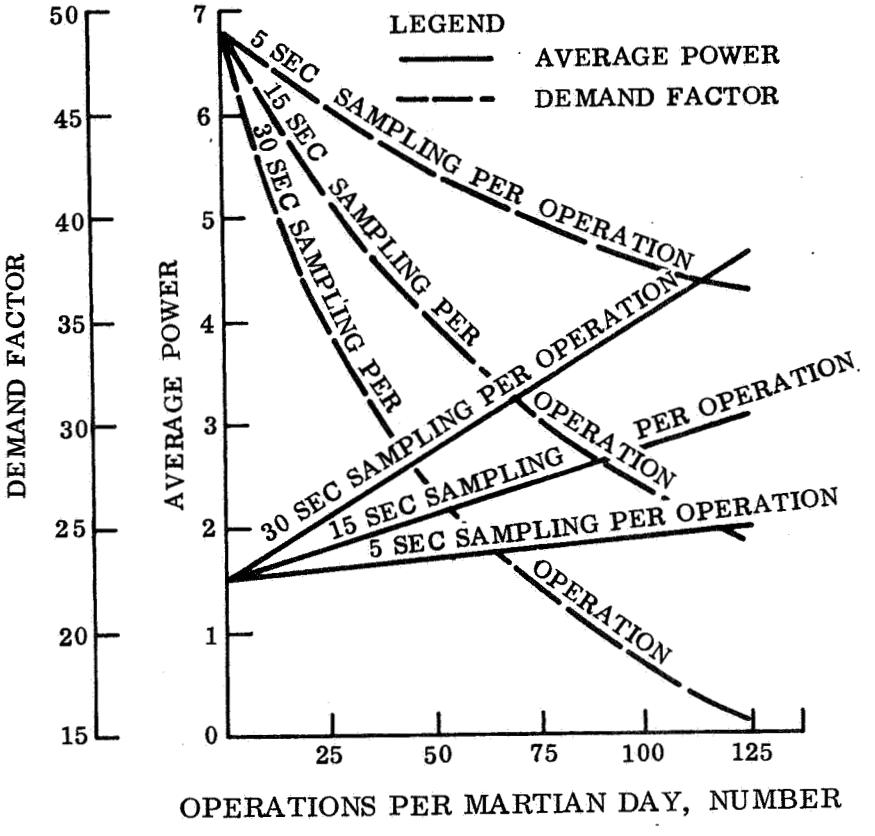

Figure 4.3.1-1. Extended Mission Power Profile Parameters

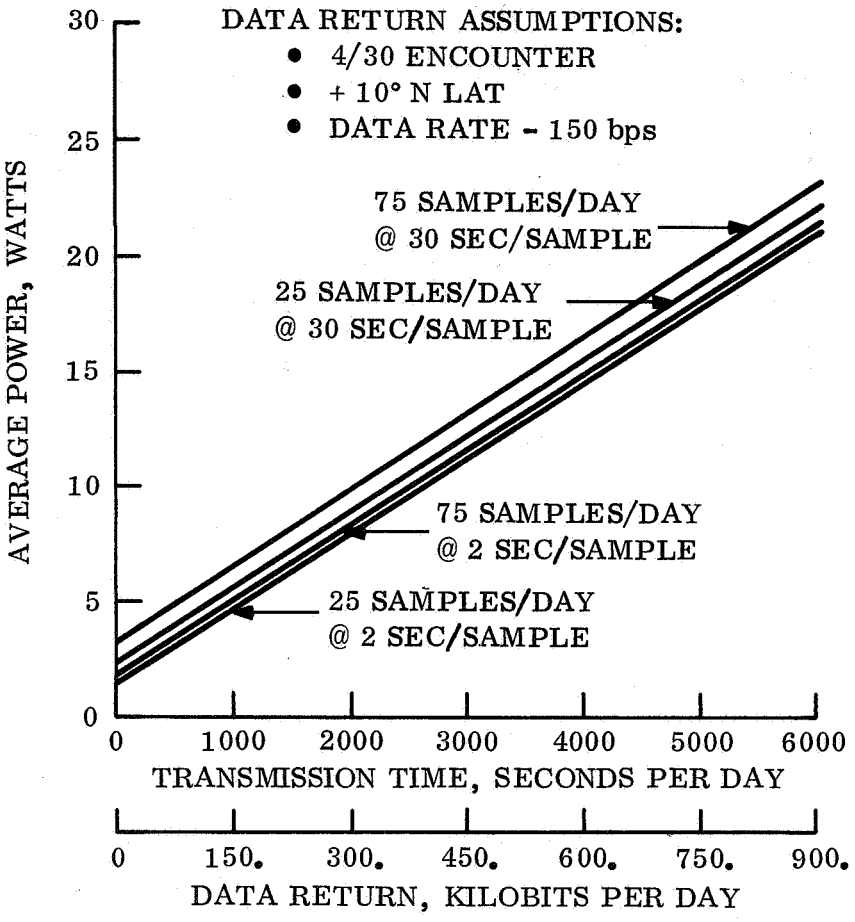

Figure 4.3.1-2. Extended Mission Power Profile Parameters (With Imagery)

TABLE 4.3.1-3. COMMAND, CONTROL AND SEQUENCE REQUIREMENTS

Mission Phase / Parameter	Launch and Cruise	Entry	Landed
Number of Channels *	4	3	4
Resolution	1.0 sec	1.0 sec	1.0 min
Accuracy	3.0 sec	1.0 sec	0.05%
Type	Fixed	Fixed with updated start	Flexible via command
* Channels as used here means programmed sequences.			

Electrical power may be regulated to achieve battery charge control or to provide voltage stability. These requirements are developed from the equipment needs in conjunction with the power profile. Typical values are noted in table 4.3.1-4.

TABLE 4.3.1-4. REGULATION REQUIREMENTS

Function / Requirement	Battery Charging	Electronics (data processing sequencing, etc.)	R-F Equipment	Scientific * Payload
Regulation Tol. (%)	± 0.4	± 5	± 10	± 0.5
Load Range (%)	0-100	± 20	± 20	25-100 **
Input Range (Volts)	0 to 42	24 to 42	24 to 42	24 to 42
Portion to be regulated (%)	100	80	95	100

* Certain instruments may require tighter voltage regulation at very low power levels.
** Applies only to the operating period; note that all payload instruments are off, in the dormant mode.

In the Mars Hard Lander harnessing will be required for approximately 35 components plus the scientific payload components. The minimum science package may involve nearly 30 additional components. Distances required for harnessing depend on the particular diameter of the landed subsystem container, the requirement varying from design to design over a range of 24 to 60 in.

4.3.1.3 Component Definition

4.3.1.3.1 Batteries

Four battery systems have been selected that are capable of sterilization, high shock resistance and cover the wide field of performance necessary for parametric investigations. Because of the controversial performance characteristics of sterilized silver-zinc batteries, this section has been expanded to provide data to justify the parametric curves in this report.

A. Silver Zinc Batteries

Eight battery manufacturers or users were solicited to determine the state-of-the-art. The Yardney Corporation, Whittaker Corporation and Gould National had not made any progress into sterilization techniques. General Motors had been contracted by JPL to develop a system and provided a sterilized cell capable of two months wet life and 11

watt hours per pound before the contract was terminated. Other work includes JPL/ESB, McDonnell/Douglas and GE/RS/Eagle Picher developments.

The McDonnell/Douglas work has been concentrated on a proprietory inorganic separator material. Sterilization has been successful and 11 watt hours/lb is possible, although the high impedence separator makes the cells, temperature and current density (demand factor) sensitive. Because of the brittle nature of the inorganic membrane it was considered doubtful whether the design would survive high shocks.

The JPL development contract with ESB and ESB-financed work has produced sterilized batteries with high shock resistance. Numerous types of separators are under consideration, most of which are irradiated cross linked polyethylenes with coboxalic grafts. RAI 116 and RAI 110 appear to be giving the best electrical performance. As in most vendor designs, the work is being performed on single cells. These cells have to be designed to withstand vapor pressures of the electrolyte during sterilization without distortion which considerably reduces the power-to-weight ratio. In spite of this disadvantage, power densities of 30 wh/lb are envisaged and 9 wh/lb achieved.

The ESB design includes support frames around each plate to increase rigidity on an otherwise floating plate. Shock applied in any direction causes the plate to move about the one fixed point which is the terminating sleeve. With low capacity cells and small light plates, high shock levels can be attained although some loss of active material must occur if any movement takes place. Obviously, with increased capacity cells, larger plate masses will cause deflection at lower g levels unless the support frames are prohibitively large. ESB report E-5-68 shows that their design is shock limited and in larger batteries, i. e. 80 AH's, 200 g shock would be the maximum possible.

General Electric and Eagle Picher design engineers embarked on a preliminary development phase, with the major objective being to provide a shock resistant sterile battery with similar characteristics to standard units. With Eagle Picher conventional design and manufacturing processes, Biosatellite batteries weighing 135 lb and giving 14,000 watt hours have been tested to 30 g's and 82 lb; 4,200 watt hour batteries for Centaur at 500 g's. These batteries were not tested to the limit and clearly indicate that with the Eagle Picher construction, higher shocks than those quoted in the ESB report can be achieved. To improve the shock resistance, it was further necessary to prevent the cell plates from moving and improve the binding strength of the negative plate. The manner in which this was done is described in General Electric Report TIS 67SD337 and summarized later in this section. With the completely rigid cell pack that this design provides, very high shocks are believed feasible on batteries weighing 200 lb, a size far beyond that envisioned for the Mars Hard Lander.

To provide high power densities and be capable of sterilization it was apparent that singel cell sterilization is not the best approach. A unique battery construction was devised which is also described in General Electric report TIS 67SD337 and summarized in this section.

A standard positive plate supported on a silver expanded grid was used in conjunction with a zinc oxide negative with approximate 2 percent polyethylene as a binder, 2 percent mercuric oxide for long stand capability and MnO_2 as an expander permitting improved redistribution during recharge.

The electrodes were separated by 0.002 in. polypropylene felt wrapped around each plate and six layers of modified Permion 307 Mn, "U" wrapped around the positive electrodes. The Permion separater was the type normally rejected by battery manufacturers screening tests because of excess porosity. Modification by soaking in permanganate and washing in oxalic acid increased the high temperature performance while reducing the pore size to a satisfactory level by filling the voids with MnO_2.

Polypropylene cases of normal thickness and fitted with relief valves were used* to house the cell packs which were stuck to the base of the cells. 45 percent KOH electrolyte was added.

Six such cells were connected in series and encapsulated in a stainless steel canister having an hermetically sealed lid. A water saturated pad was attached to the inside of the lid before sealing. See figs. 4.3.1-3 and 4.3.1-4.

*Cells had relief valves to permit gassing into an hermetic sealed outer can.

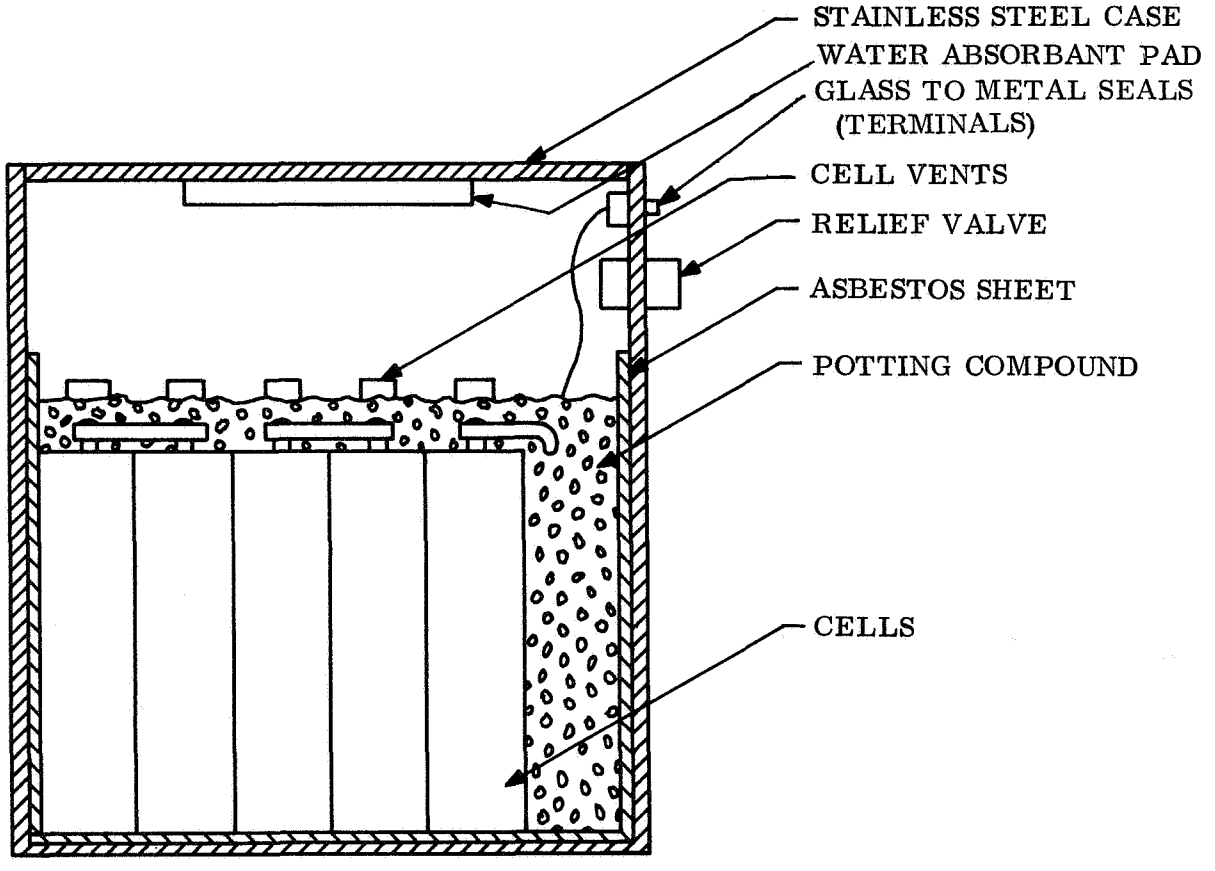

Figure 4.3.1-3. Battery Design

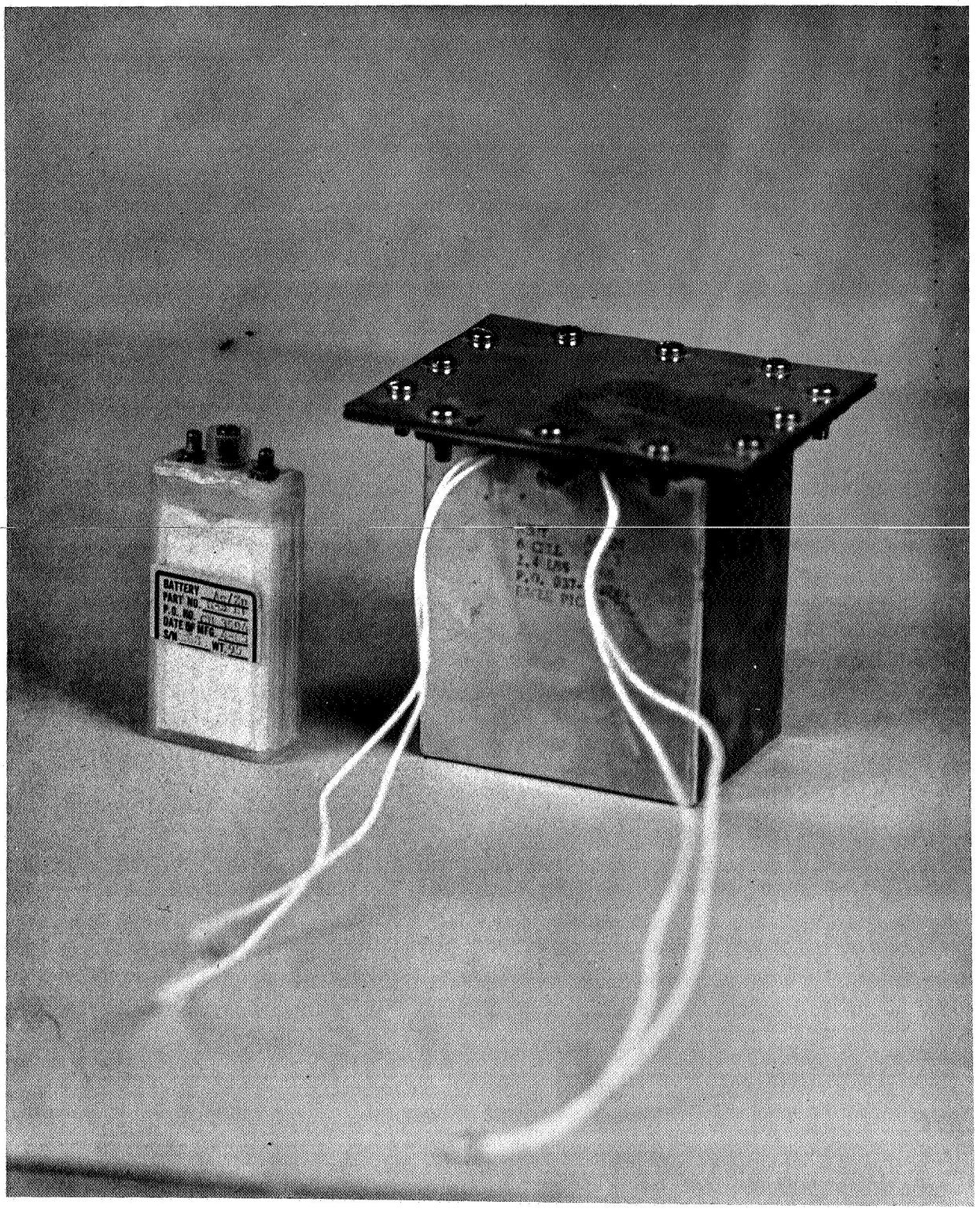

Figure 4.3.1-4. Battery, Model N3HT, and Individual Cell

Sterilized in this form, evaporation of electrolyte was prevented by the equalizing pressure of water vapor from the pad on the lid which kept the relief valves closed. The stainless steel can was designed to support the internal pressure, thus removing the need for heavy single cell design. Within the cell certain changes took place which provided a robustness for shock survival. Partial softening of the additives in the negative and the polypropylene felt provided some adherence of components across the whole cell pack. This is no way affected the performance of the semi-permeable membrane.

After sterilization in accordance with JPL Spec GMP-50436-O)SN-A and shocks of 2000-g six times in each axis, two batteries provided data that were used as the basis for the parametric study. One battery, stored in the charged state, exceeded 13 months life and another, which was stored in the discharged state for 10 months, still continues cycling after 34 months life. Table 4.3.1-5 gives performance data.

The battery that failed after 13 months was examined to determine the cause of failure and to investigate shock damage, if any. Failure was partially due to loss of hermetic seal in the battery case probably through a damaged glass-to-metal terminal. This loss caused some dehydration of the cells. Charged wet stand accelerated the normal electro-chemical degradation and migration of silver and zinc through the separators was extensive. The shock tests had no visible effect on the cells except for rippling of the folded edges of the separators. The resilience of the separator was sufficient to prevent fracture. GE TIS 67SD337 gives a complete analysis.

The test data presented in this report shows that the GE-RS/Eagle Picher design has superior wet stand capability, cycle life and shock resistance than any other design presently available. It is the only design that will meet the more severe requirements of hard landers. Continuing surveillance of all vendor developments will be necessary to enable GE to update curves when other vendor performance surpases that of the Eagle Picher battery.

This design concept appears to be more acceptable for Hard Lander vehicle designs than the alternatives because weight, volume and shock resistance are at a premium. In spite of 100 percent success on the cells and batteries, and high confidence in reproducibility, insufficient testing has been performed to offer reliability figures.

Limitations to performance are caused by the high impedence of the semi-permeable membrane. Changes in current density or temperature has a marked effect on voltage output as seen by the parametric curves.

B. Silver Cadmium Batteries

Silver cadmium batteries following the same design criteria as in A. above failed due to the cadmium plate reacting with the acrylic graft of the Permion 307 MN separator. Newer separators of the Permion series with modification as described in A. would probably resolve this problem.

TABLE 4.3.1-5. MEASURED DATA ON THE STERILIZED SILVER - ZINC SECONDARY EXPERIMENTAL BATTERIES

Wh/lb	Date	Stand (Days)	Charge (MA)	Gap (AH)	D/Charge (Amps)	Cap (AH)	Nom (V)	Cycle No.	Util Charge	Util Origin
40.2	10-1-65		500			11.5	8.4	1		- - -
34.2	10-1-65	2	500		2.5	9.66	8.5	2		83.5
39.4	12-14-65	7	500		2.5	10.75	8.8	3		93.5
41.4	1-9-67	25	500/100	12.0	2.5	11.25	8.82	4	93.8	98
38.1	4-4-67	83	500/100	8.4	2.5	10.54	8.7	5	126	92
37.3	4-12-67	7	500/100	10.55	2.5	10.2	8.77	6	96.8	89
38.2	4-20-67	3	500/100	10.54	2.5	10.4	8.8	7	98.6	90.5
34.8	4-26-67	5	500/100	9.7	2.5	9.5	8.8	8	98	82.7
36.4	5-4-67	7	500/100	9.7	2.5	10.0	8.75	9	103	87
34.6	5-15-67	10	500/100	10.07	2.5	9.5	8.73	10	88.7	82.7
34.2	5-23-67	7	500/100	8.78	2.5	9.4	8.74	11	99.5	81.8
30.2	5-31-67	2	500/100	9.57	2.5	8.4	8.6	12	88	73
30	6-8-67	1	500/100	8.8	2.5	8.3	8.7	13	94.4	72
29.4	6-14-67	1	500/100	8.8	2.5	8.14	8.67	14	92.5	71
27	6-21-67	1	500/100	8.0	2.5	7.75	8.68	15	97	67.4
26.8	7-19-67	21	500/100	8.2	Various	7.41	- -	16	90	64
26.5	7-28-67	2	500/100	9.3	Various	7.53	- -	17	81	66
26.1	9-12-67	41	500/100	7.31	Various	7.31	- -	18	100	63.5
25.3	10-20-67	31	500/100	7.82	2.5	7.32	8.65	19	94	63.8
21.5	12-7-67	5	500/100	5.44	2.5	6.0	8.6	20	111	52.2
23.5	1-2-68	30	500/100	6.31	2.5	6.55	8.6	21	102	57
25.2	3-11-68	18	500/100	7.5	2.5	7.06	8.6	22	94	61.5
24.8	5-6-68	2	500/100	7.88	0.5	6.94	8.6	23	88.1	60.2
14.4	5-13-68	1	1,.5,.1	2.82	0.5	4	8.6	24	142	35.0
21.5	5-14-68	1	1,.5,.1	5.73	0.5	6	8.6	25	113	52.1
19.85	5-15-68	1	1,.5,.1	5.97	0.5	5.55	8.6	26	93	48.3
19.65	5-16-68	1	1,.5,.1	6.0	0.5	5.5	8.6	27	91.5	48
19.65	5-17-68	1	1,.5,.1	5.28	0.5	5.5	8.6	28	104	48
18.4	5-20-68	1	1,.5,.1	5.09	0.5	5.15	8.6	29	101	45
17.9	5-21-68	1	1,.5,.1	5.02	0.5	5.0	8.6	30	96	43.5
17.55	5-22-68	1	1,.5,.1	4.88	0.5	4.9	8.6	31	100	42.7
17.3	5-23-68	1	1,.5,.1	4.77	0.5	4.85	8.6	32	102	42.2
22.6	5-24-68	1	1,.5,.1	7.58	0.5	6.3	8.6	33	83	50.9
18.3	5-28-68	1	1,.5,.1	5.19	0.5	5.1	8.6	34	98	44.3
17.6	5-29-68	1	1,.5,.1	4.96	0.5	4.9	8.6	35	99	42.7
17.2	5-31-68	1	1,.5,.1	4.67	0.5	4.8	8.6	36	101.5	41.7
16.85	6-5-68	1	1,.5,.1	4.81	0.5	4.7	8.6	37	97.5	40.9
17.2	6-3-68	1	1,.5,.1	4.81	0.5	4.82	8.6	38	100	41.9
15.9	6-6-68	1	1,.5,.1	4.61	0.5	4.45	8.6	39	92.5	38.8
19.8	6-7-68	1	500/100	6.03	0.5	5.55	8.6	40	92	48.2
22.2	6-14-68	1	500/100	9.43	0.5	6.2	8.6	41	65.6	54.0

Without this design approach, the silver cadmium battery would be little better than the nickel cadmium system. The parametrics are given in section 4.3.2, which follows, as figs. 4.3.2-2, -4, -7, -8, -10, -11, -12, -24, and -25. This approach is therefore based on a reasonable assumption that this problem can be resolved.

C. Nickel Cadmium Batteries

Many manufacturers have nickel cadmium batteries that have demonstrated sterilization immunity without significant loss in cycle life or electrical performance. Data is lacking on high shock resistance although the cell structure presents no insurmountable difficulties regarding strengthening.

Within the scope of the present study, the silver zinc or silver cadmium cell would meet the cycle requirements with considerable weight savings. For this reason only, consideration of the NiCd electro-chemical system has been deferred.

For extended missions, to meet cycle life requirements, silver-zinc battery weights would approach the lower level of the nickel-cadmium battery and would be replaced by this highly reliable system.

D. Thermal Batteries

Thermal batteries are ideal systems for high power demands and short mission durations. As such they will be used for certain re-entry functions which would otherwise deplete the prime battery energy and increase its weight and volume due to increased demand factor.

The device normally operates well above the sterilizing temperature range. Activation is achieved by an electrical impulse and an ignition train that melts the fuzed salt electrolyte, thus providing electrical output.

The parametric curves (fig. 4.3.1-5) indicate low power densities, but the weight penalty is not as severe as the weight increase required in the prime battery.

This contractor has built re-entry vehicles which have carried a total of approximately 850 thermal batteries on successful re-entry flights. Every available indication (T/M returns) show proper thermal battery operations without exceptions.

4.3.1.3.2 Solar Cell Panel (Photovoltaic conversion)

The parametric data developed here are based on 11 percent efficient (A. M. O., 28° C) Heliotek, 8 mil, 2 ohm-cm N/P cells with covers. The panel structure is an aluminum honeycomb sandwich with a minimum core density of 1.0 lb per cubic foot and a crushing stress of 30 psi.

A. Flat Pack

A flat pack concept has been developed to provide unique stowage features for the Hard Lander. This concept involves a hinged construction as illustrated in fig. 4.3.1-6.

Depending on the landing terrain, it is possible for a Hard Lander to bounce or roll in such a way that it comes to rest upside down. The folded solar package is rigidly mounted in the Lander and may be unfurled through either the top or bottom, whichever has landed facing up. A special feature of this concept is that regardless of which way the panel is unfolded, the deployment is such that the side of the panel containing solar cells will be facing the sky. In the folded condition, the panels are held firmly against the frames to provide shock hardening. This tension packaging is removed by operation of pin pullers which release the array for spring forced unfolding. In this way a single motion deployment is achieved.

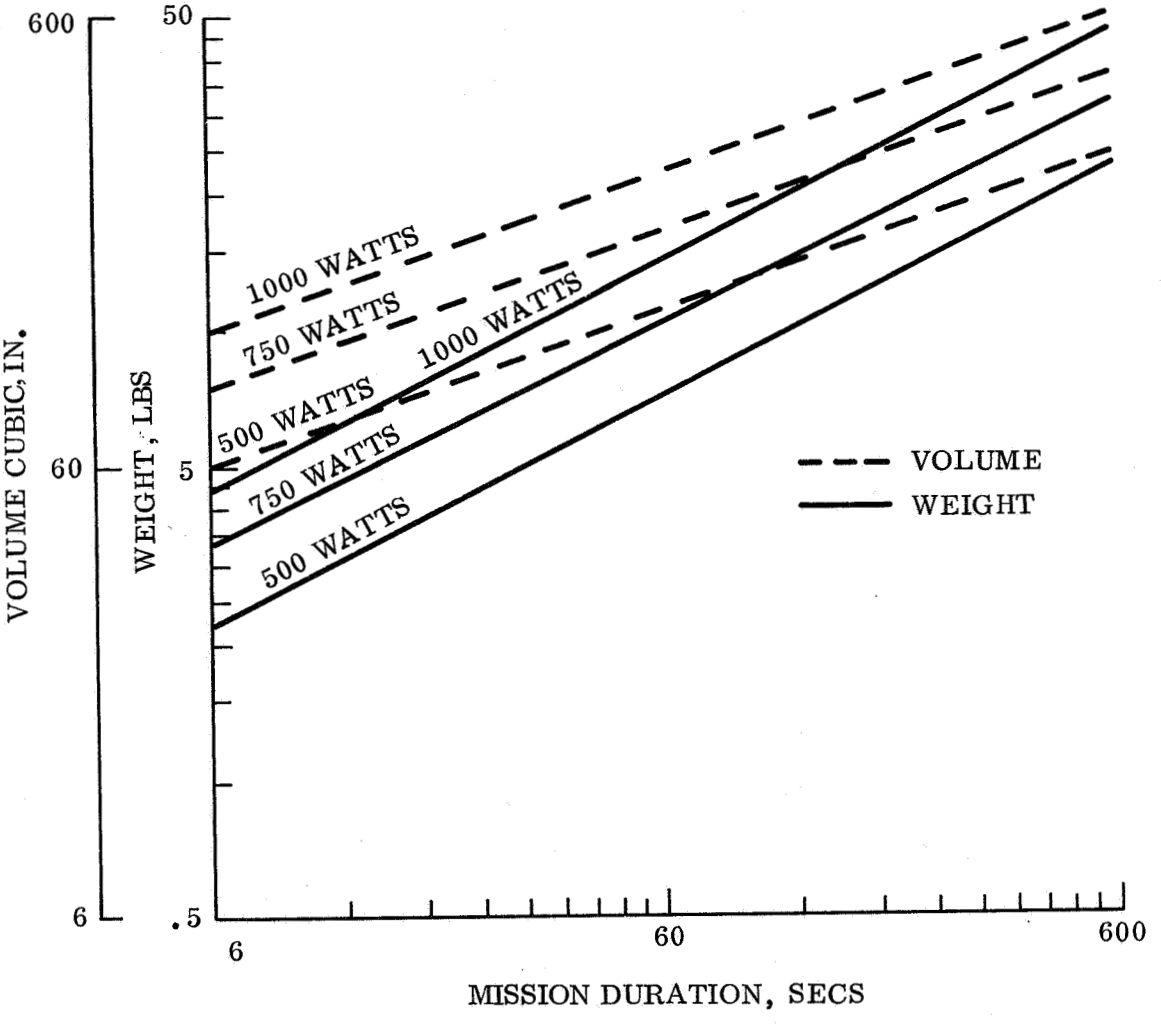

Figure 4.3.1-5. Performance Characteristics of Thermal Batteries With Chloride Electrolyte

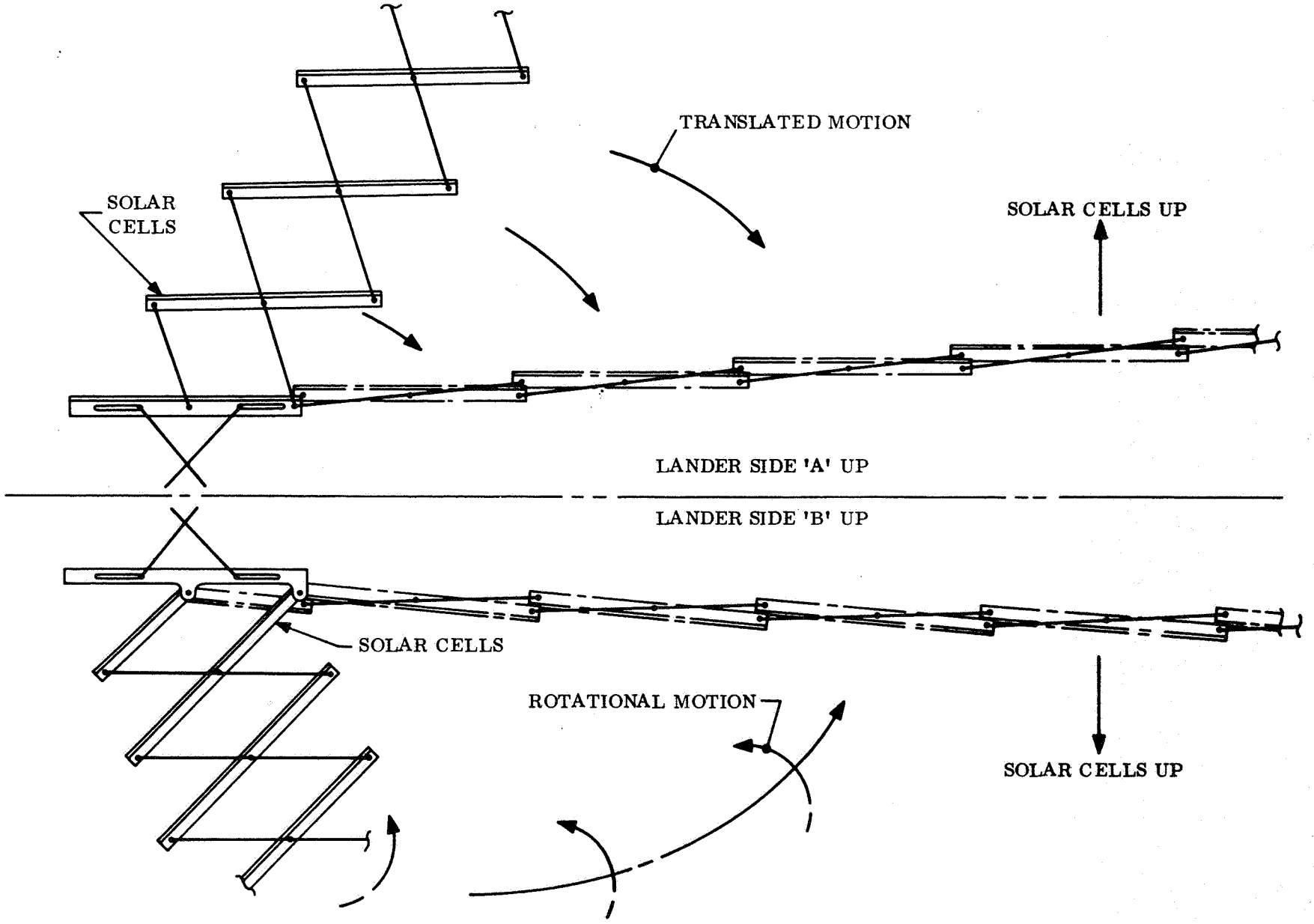

Figure 4.3.1-6. Unique Solar Array Unfolding and Deployment Mechanism.

B. Roll-Up Array

A flexible base solar array which is stowed in a rolled configuration is under development* for zero 'g' applications. By including a layer of damping material on the back of the flexible base, each solar cell will face damping in the rolled condition.

Through the use of high tension binding straps, a shock resistant package is obtained. In this approach the individual cells "float" during the shock environment, thereby avoiding the possibility of substrate flexure that may be encountered in large area sub-panels. In the deployment of this array, first an empty frame is unfolded and then the flexible solar array is unwound onto the frame using motor driven cables along the edges to provide operation and use in a gravity field.

4.3.1.3.3 Fuel Cells

For extended missions where solar cells may have unknown performance as a consequence of parameters such as cloud and dust attenuation, landing angles, etc., and when more exotic power sources are uneconomic, the fuel cell provides a suitable alternative.

The following three types have been considered: the high temperature H_2/O_2 system, the LiC1 system and the H_2/O_2 solid electrolyte ion exchange fuel cell.

The selection of a practical design is limited by the lengthy dormant period prior to landing. The high temperature hydrogen oxygen systems require heavy subsidiary control and monitoring equipment which make the weight factor a prohibitive feature in selection.

Fragility of graphite components in the lithium chloride systems, and difficulty in overcoming this problem, caused the rejection of this device for Hard Lander vehicles. At low shock levels it has many advantages.

The solid electrolyte ion exchange fuel cell in its present form can be remotely activated without heavy auxiliaries. No major technical difficulties are envisaged to design for shock resistance, although it is recognized that a substantial weight increase will be incurred.

The solid electrolyte material currently used in the ion exchange system for NASA's BIOSATELLITE** has demonstrated a capability of performing after being subjected to sterilization temperatures. Structural changes incorporating high temperature resistant materials will nominally increase weight. For these reasons, this system was chosen. Long term storage in the interplanetary phase necessitates the use of high pressure tankage as opposed to cryogenic storage. Sterilization and shock factors have been incorporated in the parametric studies.

* Contract JPL 951970

**Contract NAS-2-1900

The parametric data of figs. 4.3.2-38 through -43 include shock and sterilization factors together with those tabulated on the curves. Fuel cell stacks, reactant storage, product water storage, radiators, batteries, electrical and pneumatic regulators have been included.

4.3.1.3.4 RTG

For extreme mission durations, such as a year or more, where cumulative energy consumption excludes primary batteries and fuel cells, and where the ravages of the Martian environments cast doubt on solar cell longevity, the radioisotope thermoelectric generator is considered. The Hard Lander approach requires the use of ruggedized construction to withstand landing shock. For this reason the parameters are based on a concept under development by the Westinghouse Corporation.

These converters have been constructed in various lengths and diameters to obtain various voltages and power levels. Fuel capsules are yet to be fabricated for these particular devices. Electrical heaters have been used to simulate such isotope fuels as Pu^{238}, Sr^{90}, U^{232}, and Po^{210}. These designs have been investigated for electrical outputs of 20 to 100 watts raw unconditioned power.

4.3.1.3.6 Regulators and Inverters

Regulation may be obtained by semiconductor switching time-ratio control, by semiconductor analog control or by inverters with dc or ac regulation. Selection of the type depends on the need for isolation, for impedance match, for voltage boosting and for ac output. The semiconductor regulator without inversion provides lightest weight but none of the other four features. For purposes of this parametric study it is assumed that all battery charge regulators in the solar cell and fuel cell approaches are semiconductor TRC type and that all others are isolating inverter type.

4.3.1.3.7 Harnesses

The following harness insulation is recommended for interplanetary space vehicles.

Kapton, formally called H film, is an aromatic polymide resulting from the reaction of pyromellitic dianhydride and an aromatic diamine. It is used in conjunction with Teflon, FEP - fluorcarbon film. The main function of the FEP is to provide heat sealability since Kapton has no melting point and is, therefore, not heat sealable. The specific construction is referred to as HE-1/2T. This insulation consists of an outer wrap of 0.0005 in. polymide, 0.0005 in. FEP and an outer jacket wrap of 0.0005 in. TFE.

Heat sterilization, based on a temperature of 160°C, would have no detrimental affects on Kapton (H-film) insulation.

Harnesses which will be used for this type of mission have the following additional characteristics:

1. The wire is produced to MIL 81044.
2. The shielding is round braided tinned copper.
3. The connectors utilized will meet either of two specifications, MIL 38999 or NAS 1599.
4. The harnesses will be wrapped with RTV tape.

4.3.2 SUBSYSTEM SYNTHESIS

4.3.2.1 Assumptions and Constraints

The assumptions used in developing the electrical power and distribution parametric analysis are listed in the following paragraphs:

4.3.2.1.1 Battery Assumptions

1. To permit meeting shock and handling requirements the largest single battery to be constructed weighs 200 lb. Beyond this a multiple battery pack is assumed.

2. The environmental control system will use non-electrical means (radio-isotopes) to maintain the battery temperature between +50 and +80° F at all times (including cruise).

3. The wet stand loss follows an Ahrenis chemical rate law.

4. The terminal voltage may swing from 24 to 32.5 volts during discharging usage, and up to 42.5 volts during charging.

4.3.2.1.2 Solar Cell Assumptions

1. Flat pack solar array storage is used.

2. The maximum panel width is 18 in.

3. The maximum panel length is 35 ft.

4. The distant terrain produces a ±15 degree mask. (i.e., sunrise and sunset).

5. Unless otherwise noted on the curve, the solar array is deployed parallel to the local horizontal within 15°. (No angle penalty beyond the mask.)

6. Winds are considered to produce negligible loads.

7. The panel regulator provides a proper voltage match to the battery for full power utilization.

4.3.2.1.3 Fuel Cell Assumptions

1. Solid electrolyte ion exchange type fuel cell.

2. High pressure storage of oxygen and hydrogen.

3. Product water stored in expanding polyethylene type container.

4. Radiator is a geometrically designed pagoda shaped active type.

5. For radiator calculations, the planet surface temperature has been stated as 180°F, representing the worst case temperature. The landing angles are 15 and 0°.

4.3.2.1.4 RTG Assumptions

The RTG has a 360° view angle for radioactive cooling.

4.3.2.2 Component Parametric Data

The various working level or component parametric curves developed to permit Hard Lander synthesis are described below. For application and use of the curves see examples in para. 4.3.2.3.*

4.3.2.2.1 Battery Parametric Data

The battery parametrics were derived from empirically determined scaling or modeling laws supplemented by environmental and application functions.

It is recognized that the percentage of active material is greater in large batteries than in smaller ones. This means there will be more "watt-hours" per pound in the larger units. Empirical data indicates that sterilized silver-zinc battery weights vary as the 0.804 power of the watt-hour rating. Similarly, the percentage of the battery volume allocated to studs, wiring, connectors, and void spaces decreases in the larger sizes. Thus, the volume varies as the 0.78 power of the watt-hour rating. These parametric relationships apply to low discharge rate applications figs. 4.3.2-1 through -12. For high rates the battery becomes current rate limited and additional cell area must be provided. Even through the necessary total amount of active material remains the same, the increased cell area results in less efficient packing and material utilization. Defining the plate aspect factor as the ratio of plate length to thickness, it has been observed that the volume varies as the 0.21 power of the aspect factor in rate limited designs as indicated in figs. 4.3.2-13 and -14.

*Para. 4.3.3.2 shows that fuel cells offer advantages primarily in the higher power regions where active coolant approaches are used.

The battery must meet a specified output voltage range or regulation. This establishes the battery cut-off voltage and hence the cell cut-off voltage. Different cut-off points infer a different percentage utilization of the ampere-hour capacity. This phenomena is both demand, i.e., current, and temperature dependent. Higher currents produce more polarization drop requiring an earlier cut-off; lower temperatures aggravate this condition. The usable ampere-hours are found to vary linearly with maximum current with a two segment piece-wise linear curve used to represent the temperature sensitivity. Such calculations permit the determination of the factor or proportionate increase in capacity required so that the necessary watt-hours are obtained prior to cut-off. In this way the battery size and weight may be established as a function of minimum temperature and demand factor. The electrical parameter, demand factor, is defined as the ratio of peak power demand to average power consumption.

During the activated wet stand prior to use, and during the discharge period, the battery will suffer parasitic chemical action which results in the loss or unavailability of active material. This is a chemical rate phenomena, dependent on temperature, which was determined by using an Ahrenus type rate equation with rate doubling for each 10 centigrede degrees of temperature rise.

Mechanical designs to withstand shock and vibration result in container and potting weight increases. These effects are small enough that the particular functional relationship is not critical to battery design. An exponential relationship has been used in this study where, based on successful tests to 2000 g's for 10 milliseconds, the approach is to use normal aerospace shock resistant construction where the plate ends are potted to the cell case. These parametrics are useful to at least 2000 g's, where these precepts are valid and none of the materials reach the rupture stress level. Using potting techniques, this level requires a 7 percent weight increase.

It is recognized that vibrational failure occurs at the resonant frequency of a component in a particular design. Through studies of a large variety of battery types, sizes, and designs, GE/RS has developed stiffening techniques which shift the resonant frequency outside the required environment. This is achieved with about a 1 percent weight increase which is included though not always required. Vibration to the 30 'g' level thus involves a 1 percent weight increase.

Thus, the potting approach to shock hardening involves a 7 percent weight increase and the frequency shift approach to vibration hardening involves an additional 1 percent weight increase. Since these effects are so modest, curves have not been included.

Although the parametric approach has been described in terms of a primary battery, exactly the same considerations apply in the secondary application. However, when the battery must operate under a charge/discharge regime, an additional considerations, the depth of discharge is faced.

The depth of discharge parameter is defined by either of two constraints: the maximum recharge rate or the ravages of repeated cycling, i.e., fatigue or puncture. This is to say that the ability to get the charge back in time, or the total number of charge/discharge cycles the battery can stand, must be met.

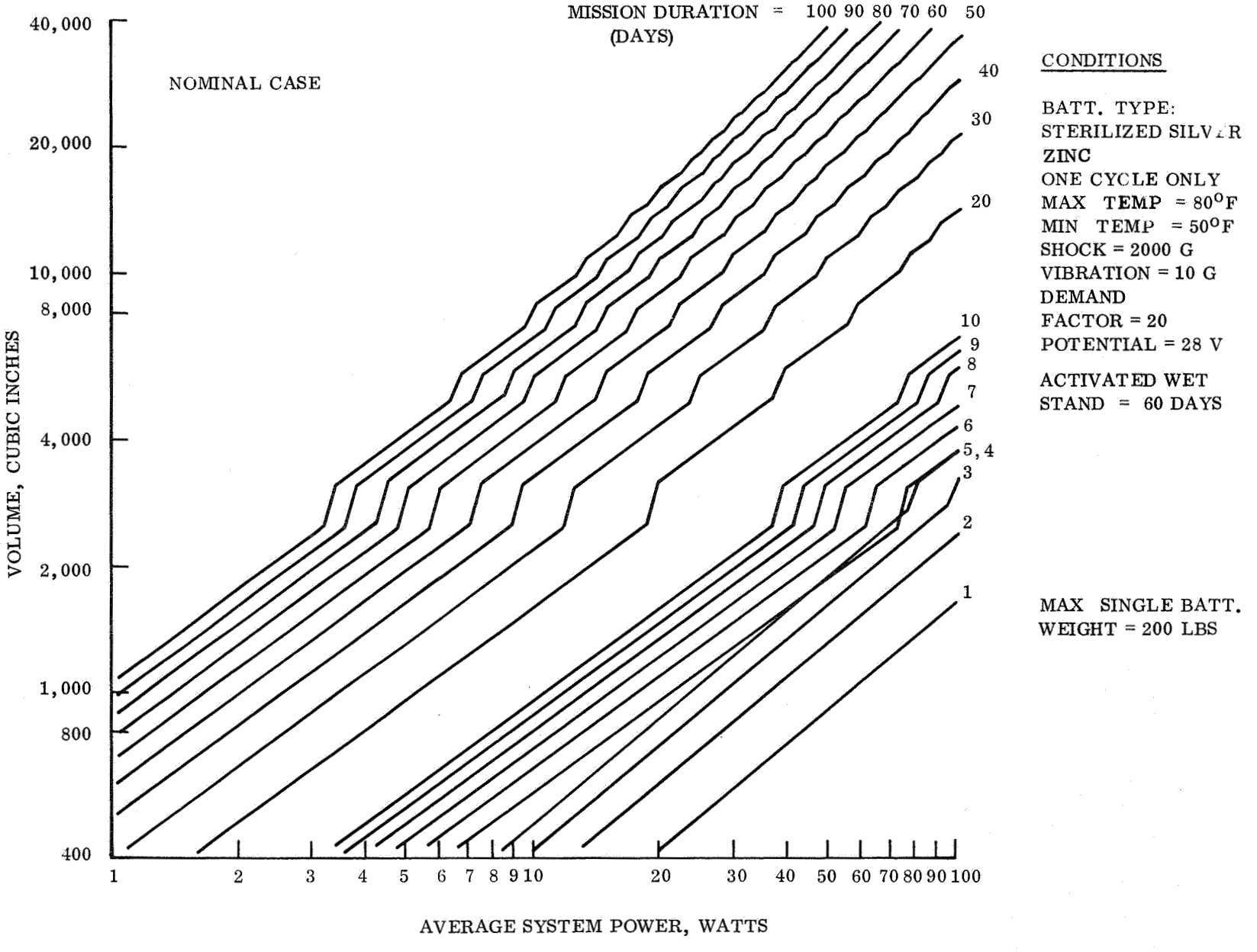

Figure 4.3.2-1. Sterilized Silver-Zinc Primary Battery Volume Parameters for Various Mission Durations (Nominal Case)

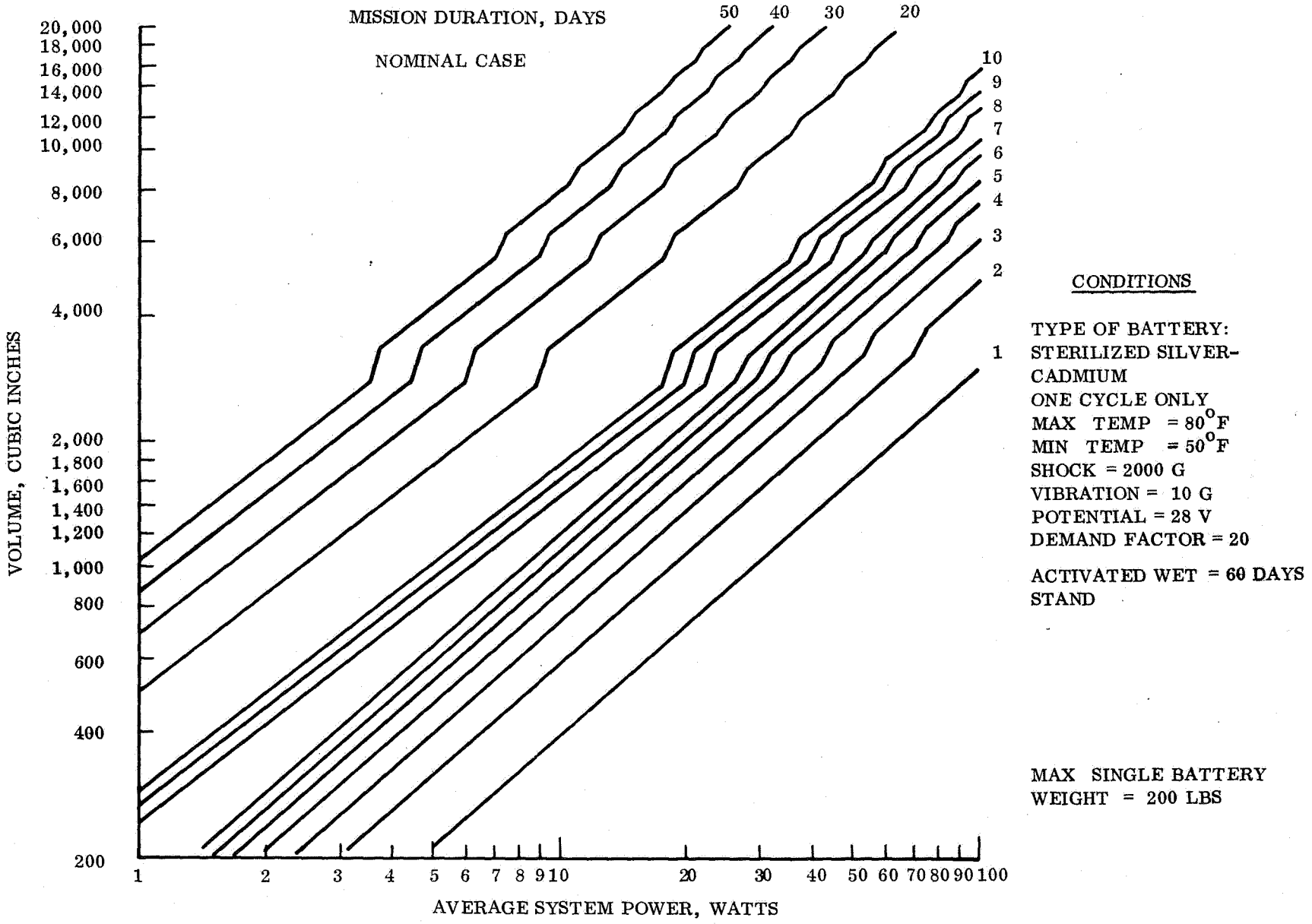

Figure 4.3.2-2. Sterilized Silver-Cadmium Primary Battery Weight Parameters for Various Mission Durations (Nominal Case)

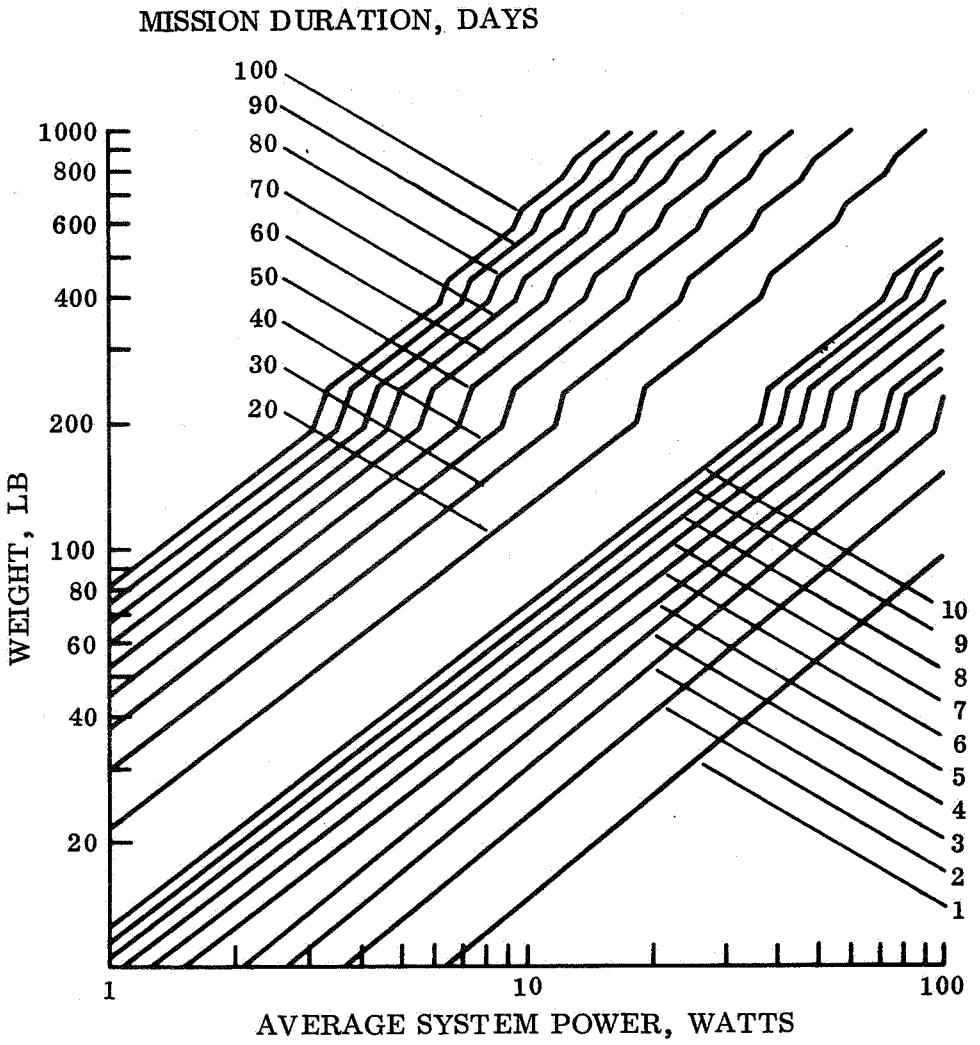

CONDITIONS

BATT. TYPE: STERLIZED SILVER-ZINC
ONE CYCLE ONLY
MAX TEMP = 80°F
MIN TEMP = 50°F
SHOCK = 2000g
VIBRATION = 10g
POTENTIAL = 28V
DEMAND FACTOR = 20
ACTIVATED WET STAND = 60 DAYS

MAX SINGLE BATT. WEIGHT = 200 LB

Figure 4.3.2-3. Sterilized Siver-Zinc Battery Weight Parameters for Various Mission Durations (Nominal Case)

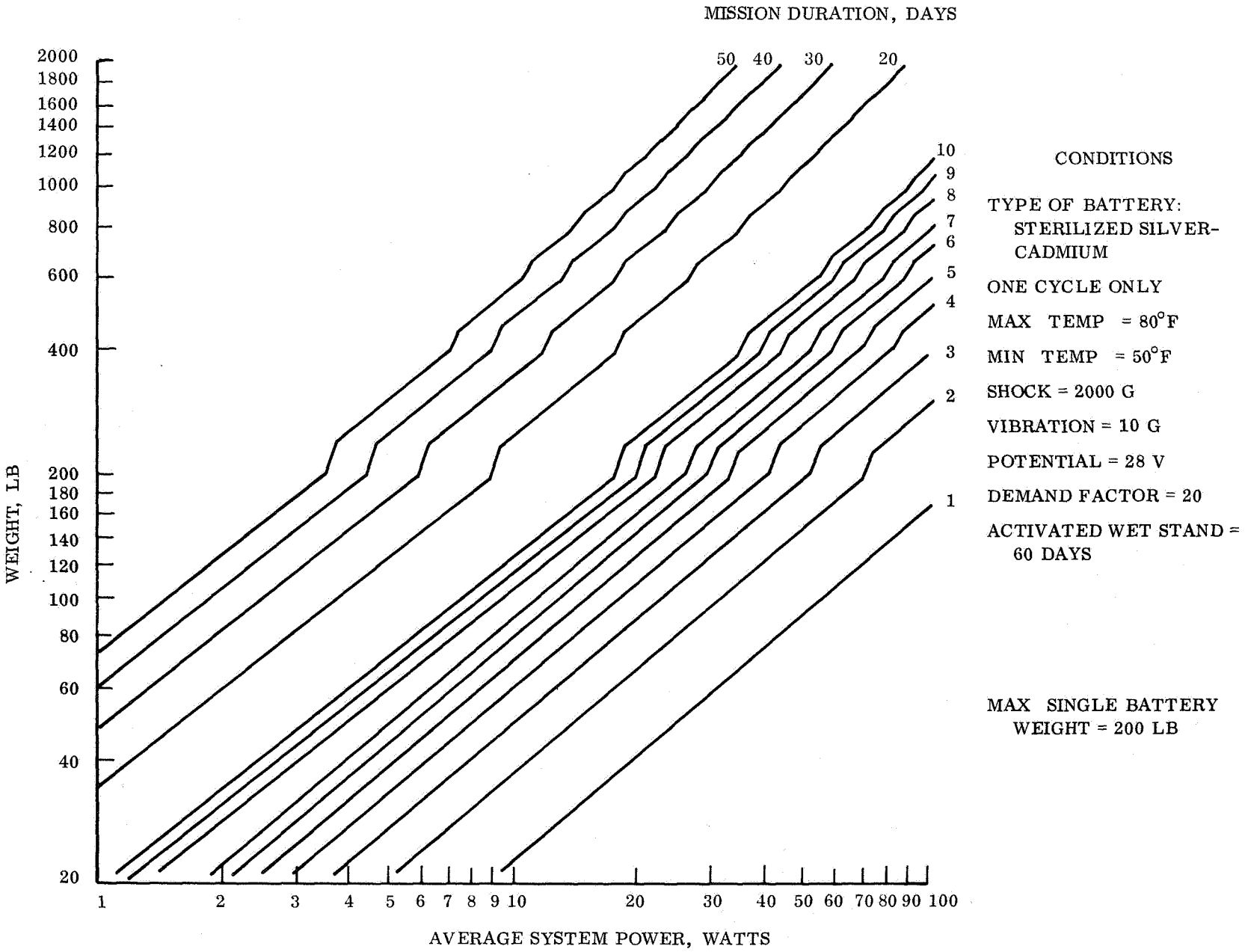

Figure 4.3.2-4. Sterilized Silver-Cadmium Battery Weight Parameters for Various Mission Durations (Nominal Case)

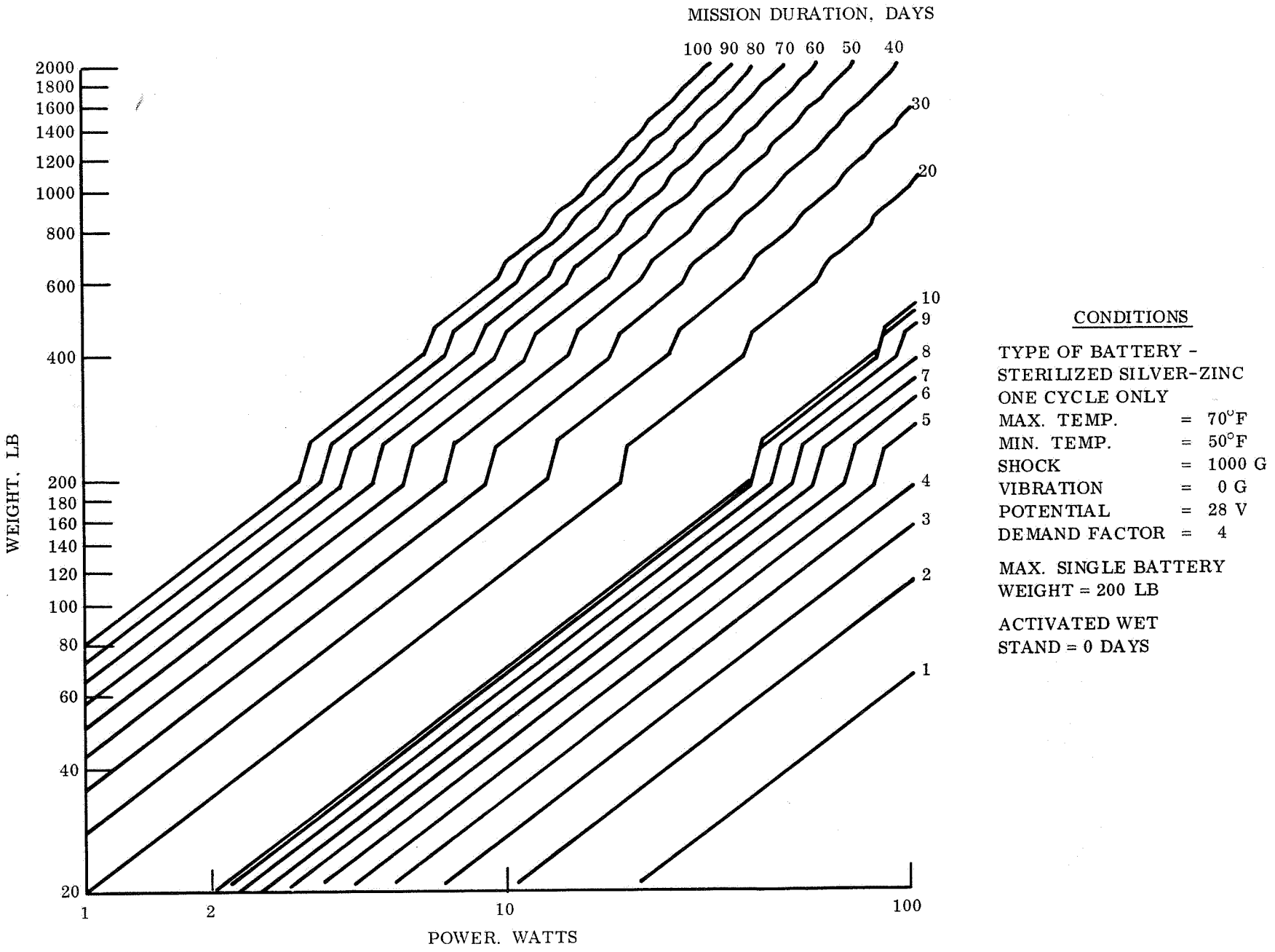

Figure 4.3.2-5. Sterilized Silver-Zinc Primary Battery Volume Parameters for Various Mission Durations (Optimal Case)

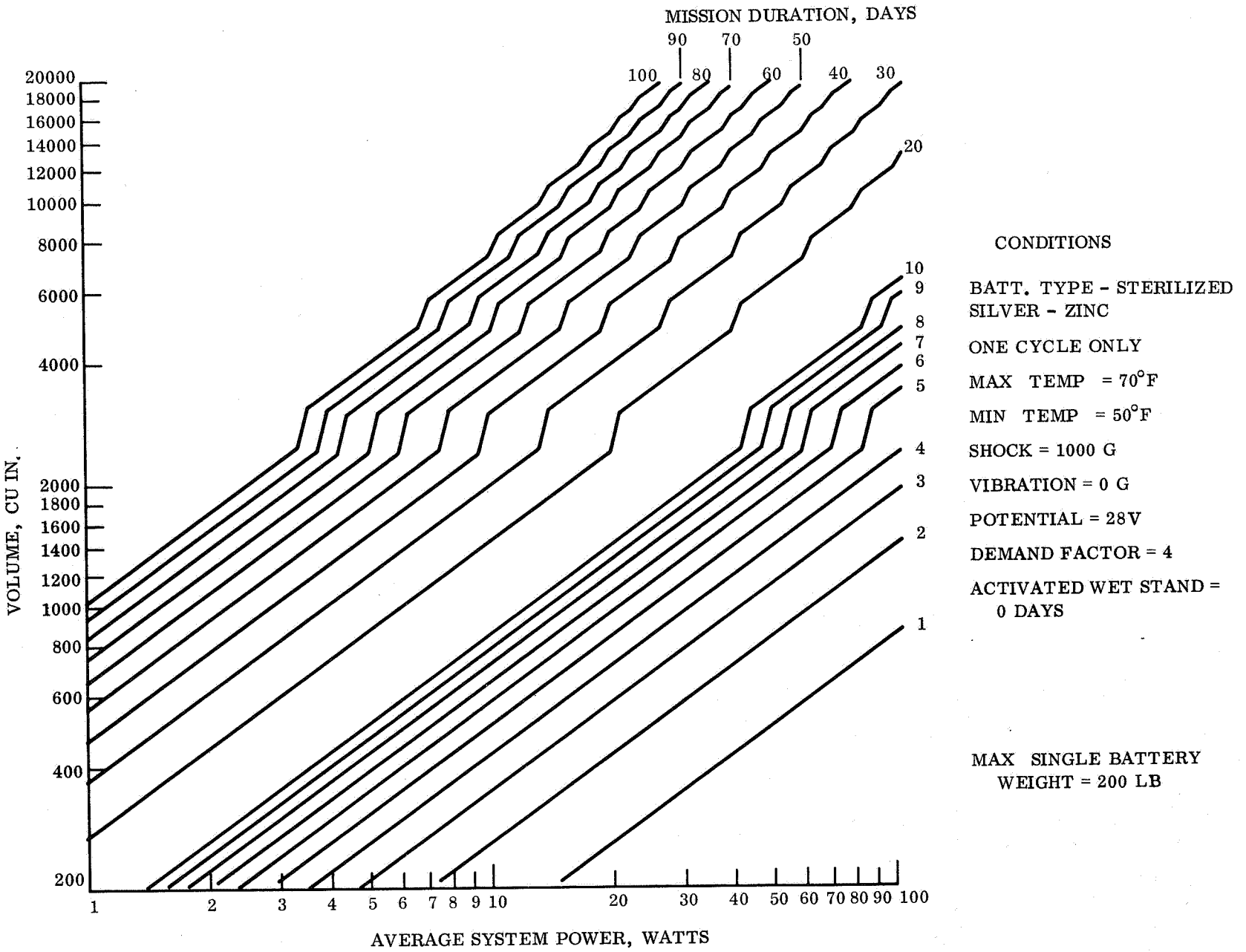

Figure 4.3.2-6. Sterilized Silver-Zinc Primary Battery Volume Parameters for Various Mission Durations (Optimal Case)

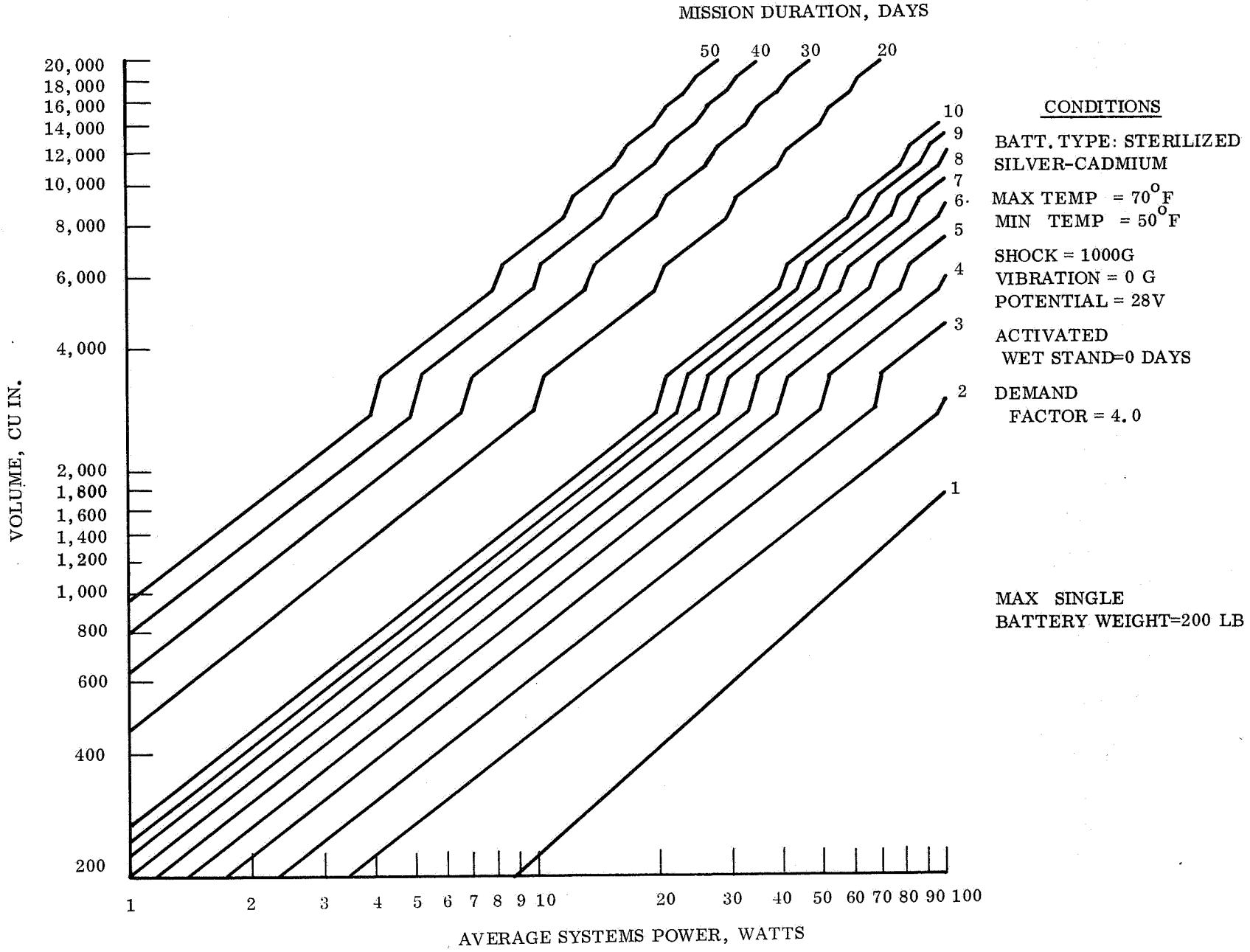

Figure 4.3.2-7. Sterilized Silver-Cadmium Primary Battery Volume Parameters for Various Mission Durations (Optimal Case)

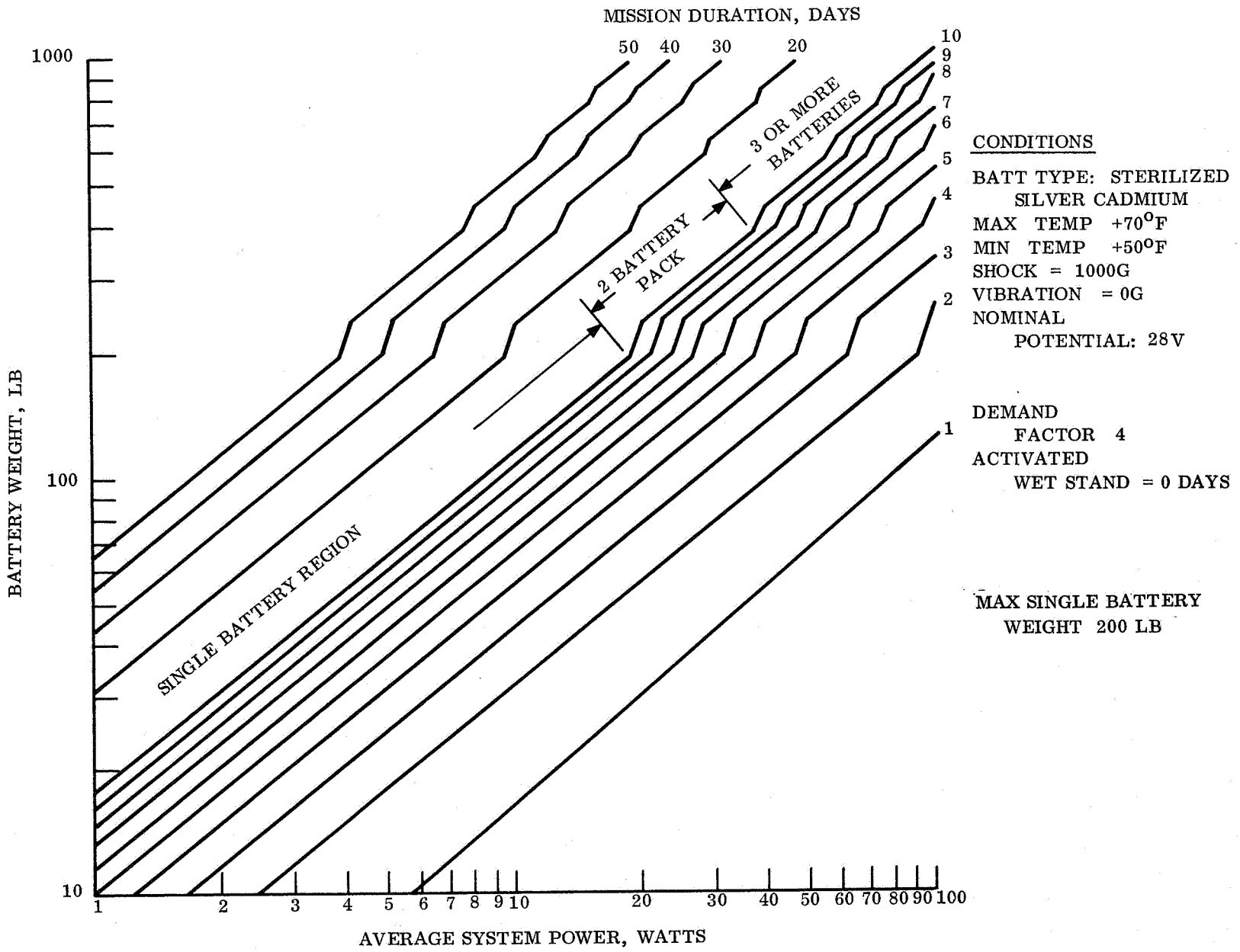

Figure 4.3.2-8. Sterilized Silver-Cadmium Primary Battery Weight Parameters for Various Mission Durations (Optimal Case)

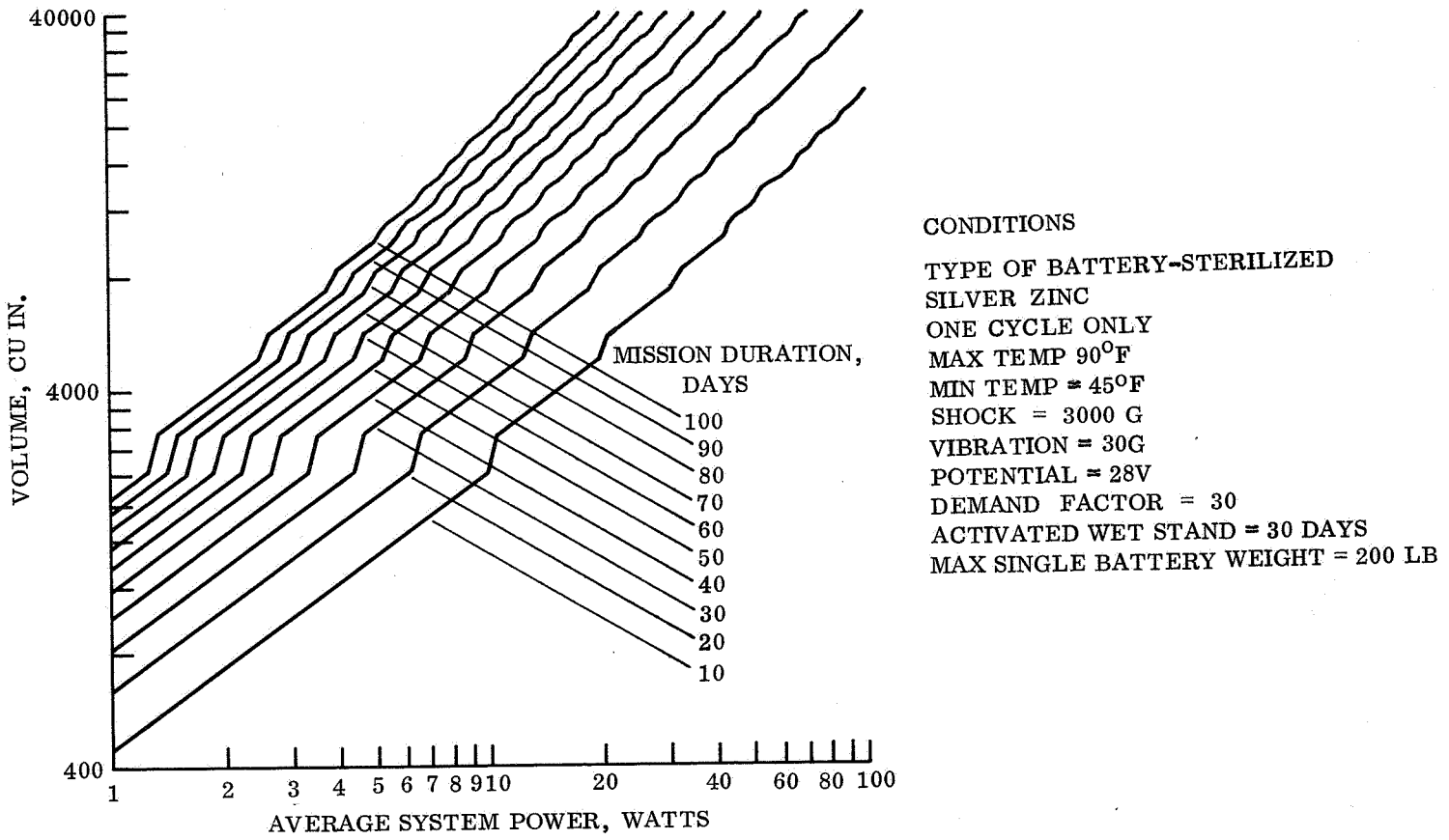

Figure 4.3.2-9. Sterilized Silver-Zinc Primary Battery Volume Parameters for Various Mission Durations (Worst Case)

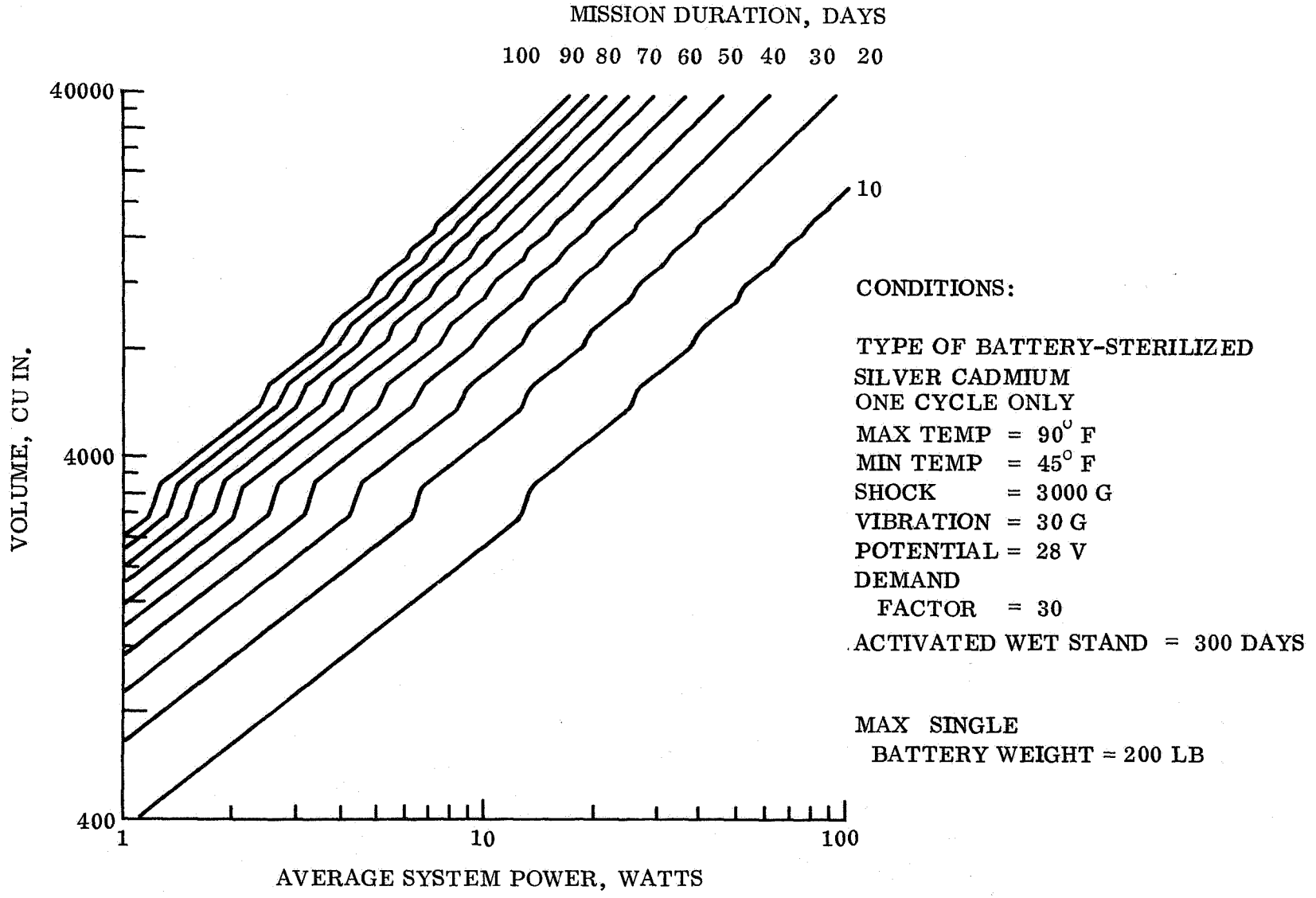

Figure 4.3.2-10. Sterilized Silver-Cadmium Primary Battery Volume Parameters for 10 to 100 Days Mission Duration (Worst Case)

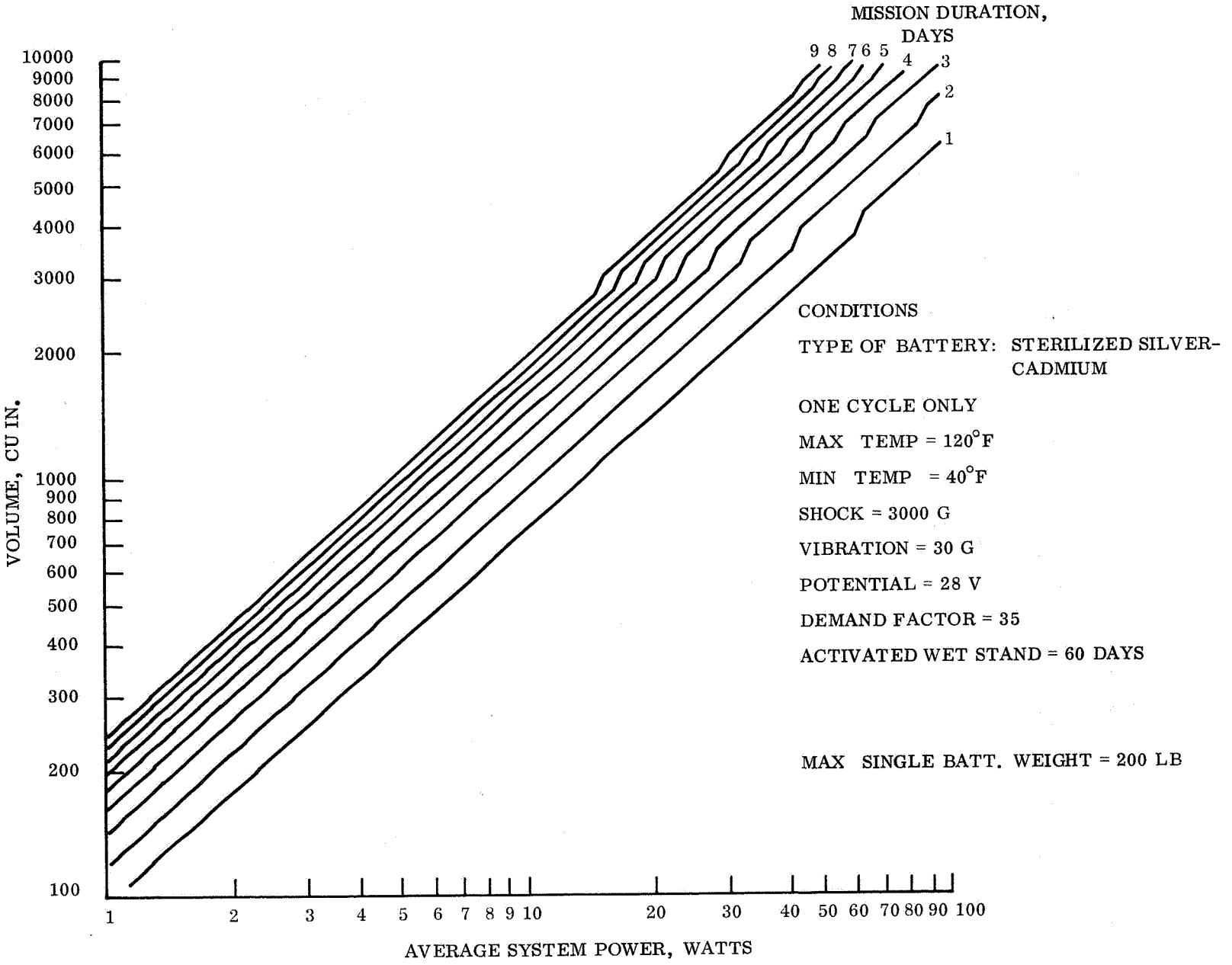

Figure 4.3.2-11. Sterilized Silver-Cadmium Primary Battery Volume Parameters for One to Nine Days Mission Duration (Worst Case)

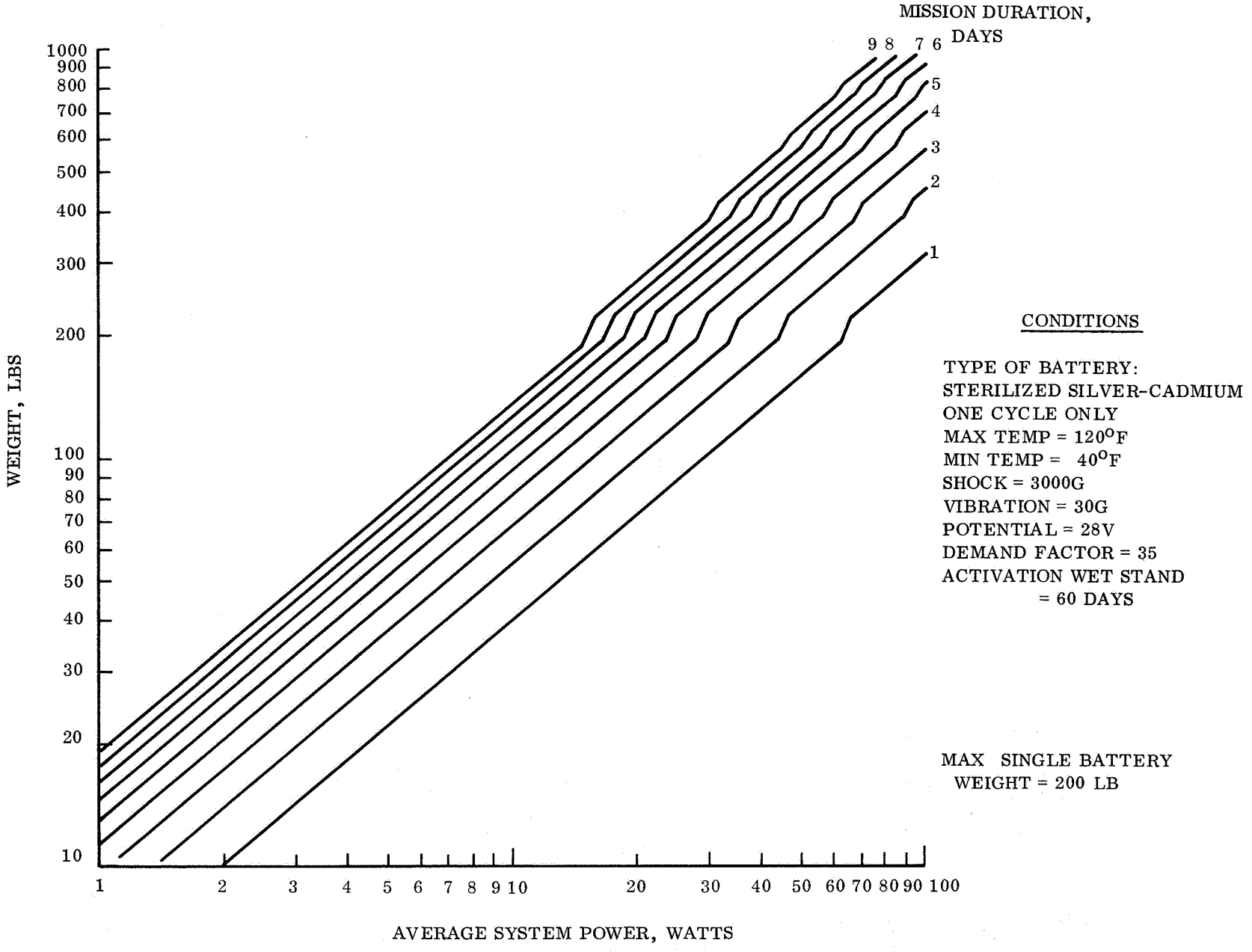

Figure 4.3.2-12. Sterilized Silver-Cadmium Primary Battery Weight Parameters for Various Mission Durations (Worst Case)

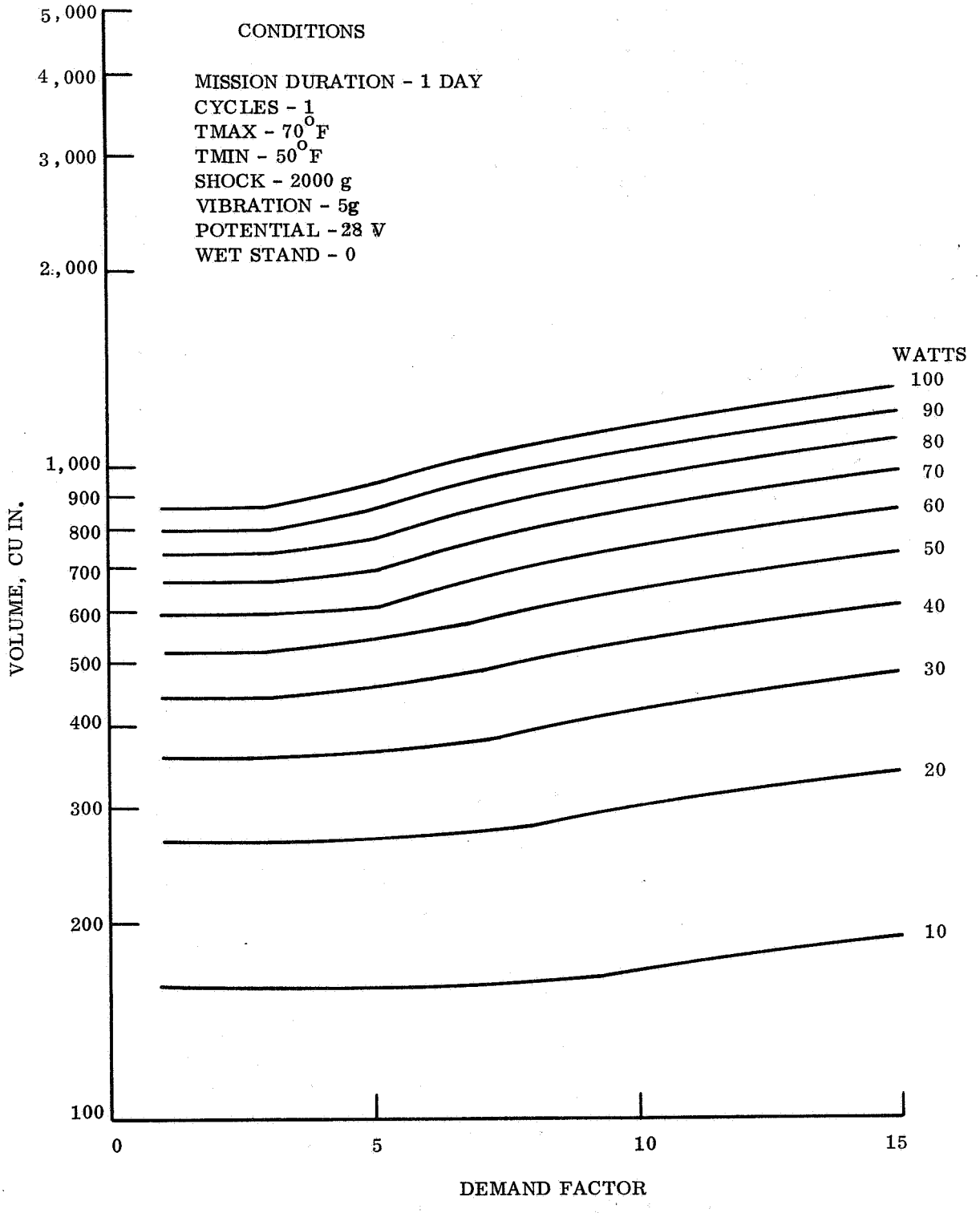

Figure 4.3.2-13. Influence of Demand Factor on Silver-Zinc Battery Volumes

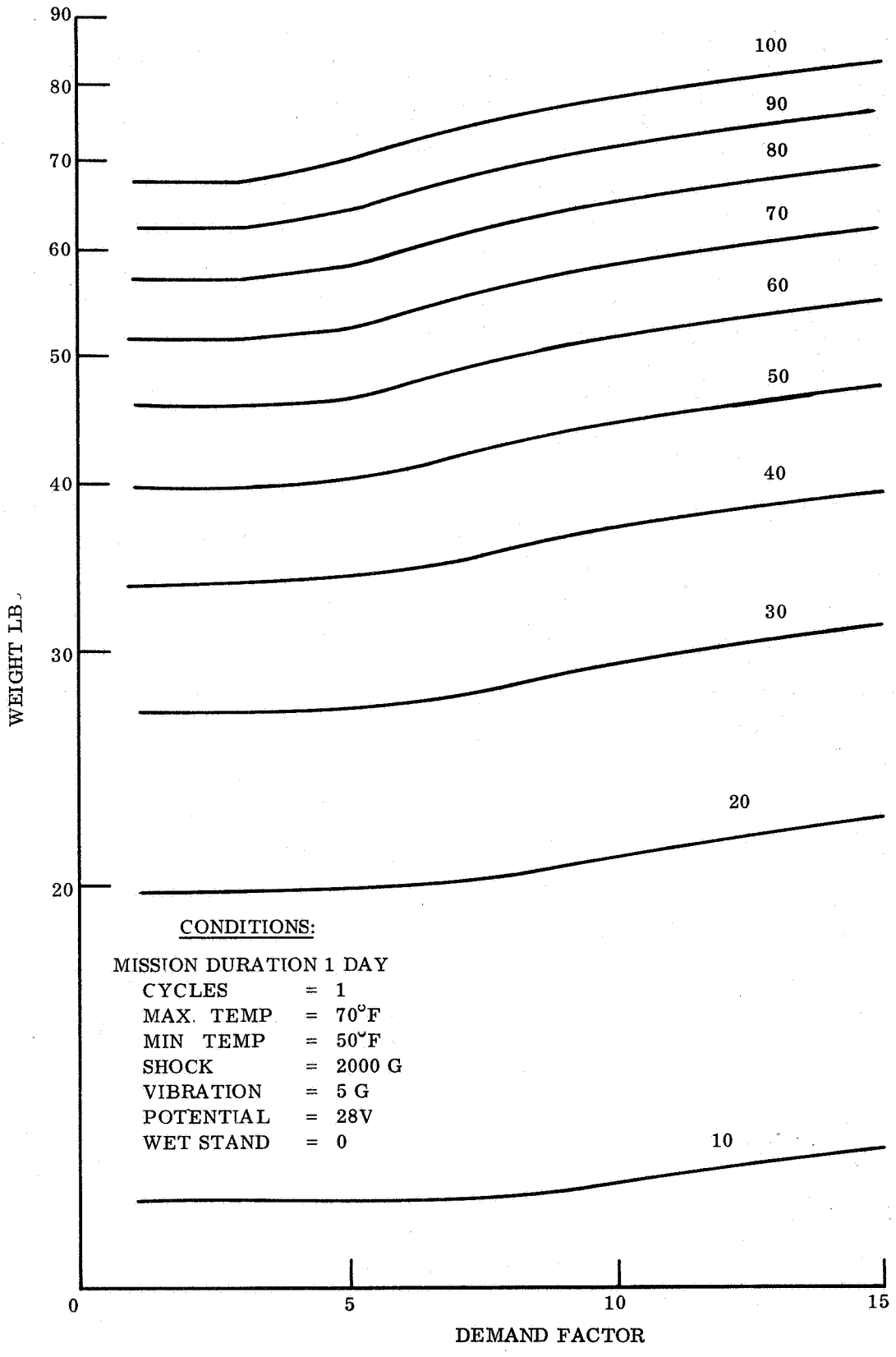

Figure 4.3.2-14. Influence of Demand Factor on Silver-Zinc Battery Volumes

For any battery type there is a maximum rate at which charge will be accepted, expressed as amperes per ampere hour of capacity. The reciprocal of this parameter is the minimum possible time required to fully charge a depleted battery, in hours. A larger battery must be used so that the charge will be accepted if the time available for recharge is less than this minimum time, a step which results in a depth of discharge less than 100 percent. This criteria is used unless the cycle life constraint is more restrictive.

Even if the charge is returned slowly, i.e., within the acceptable charge rate after an extended number of cycles, the separator may fail due to growth or separator puncture. The number of cycles which may be achieved prior to failure is found empirically to be related logarithmicaly to the depth of discharge. Thus, an increase in cycle life requires reduced depths of discharge. This requirement must be compared to the noted charge return rate limitation and is the most constraining of the two used in design. The cycle life data, given in fig. 4.3.2-15, are provided to give a more thorough understanding of these parametric relationships and to provide the reader with a full set of data for design synthesis. The GE 605/Datanet 30 digital computer has been used to carry out the above computations.

The previous parametric curves, fig. 4.3.2-1 through -12, have shown the weight and volume versus power level and mission duration for nominal and extreme environmental conditions to be encountered in Mars Hard Landers. Both silver-zinc and silver-cadmium couples are included. The influences of temperature and activated wet stand are illustrated in figs. 4.3.2-16 through -21. For similar information on secondary applications see figs. 4.3.2-22 through 4.3.2-27.

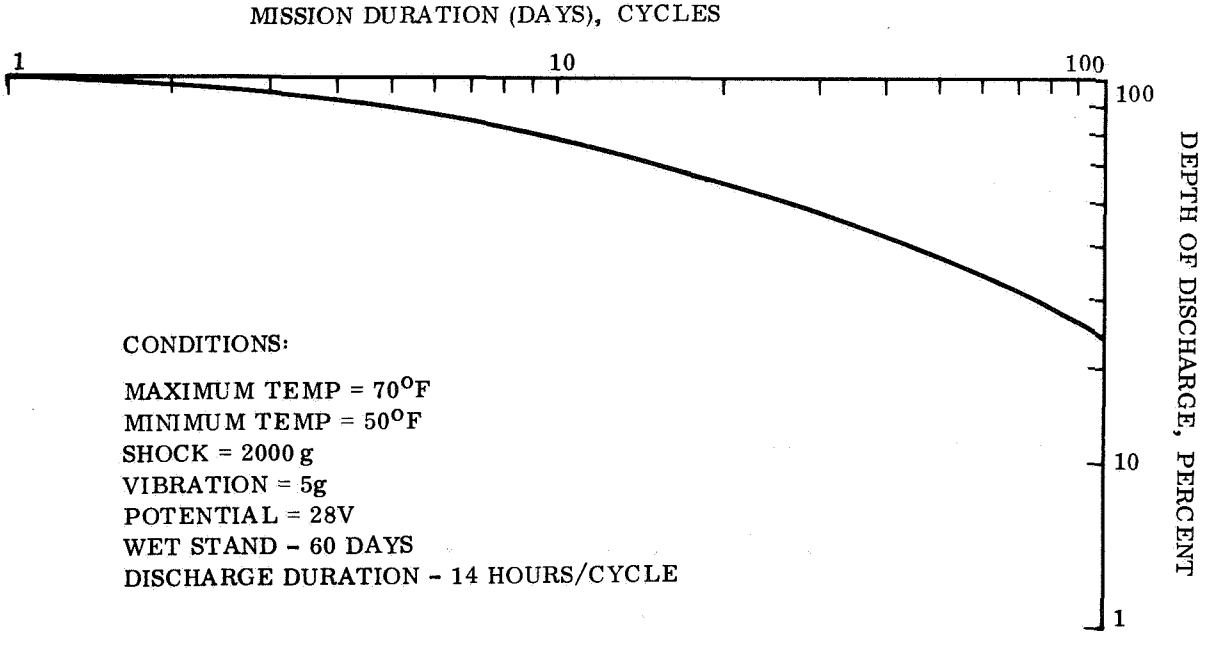

Figure 4.3.2-15. Depth of Discharge/Cycle Parametrics for Sterilized Silver-Zinc Battery

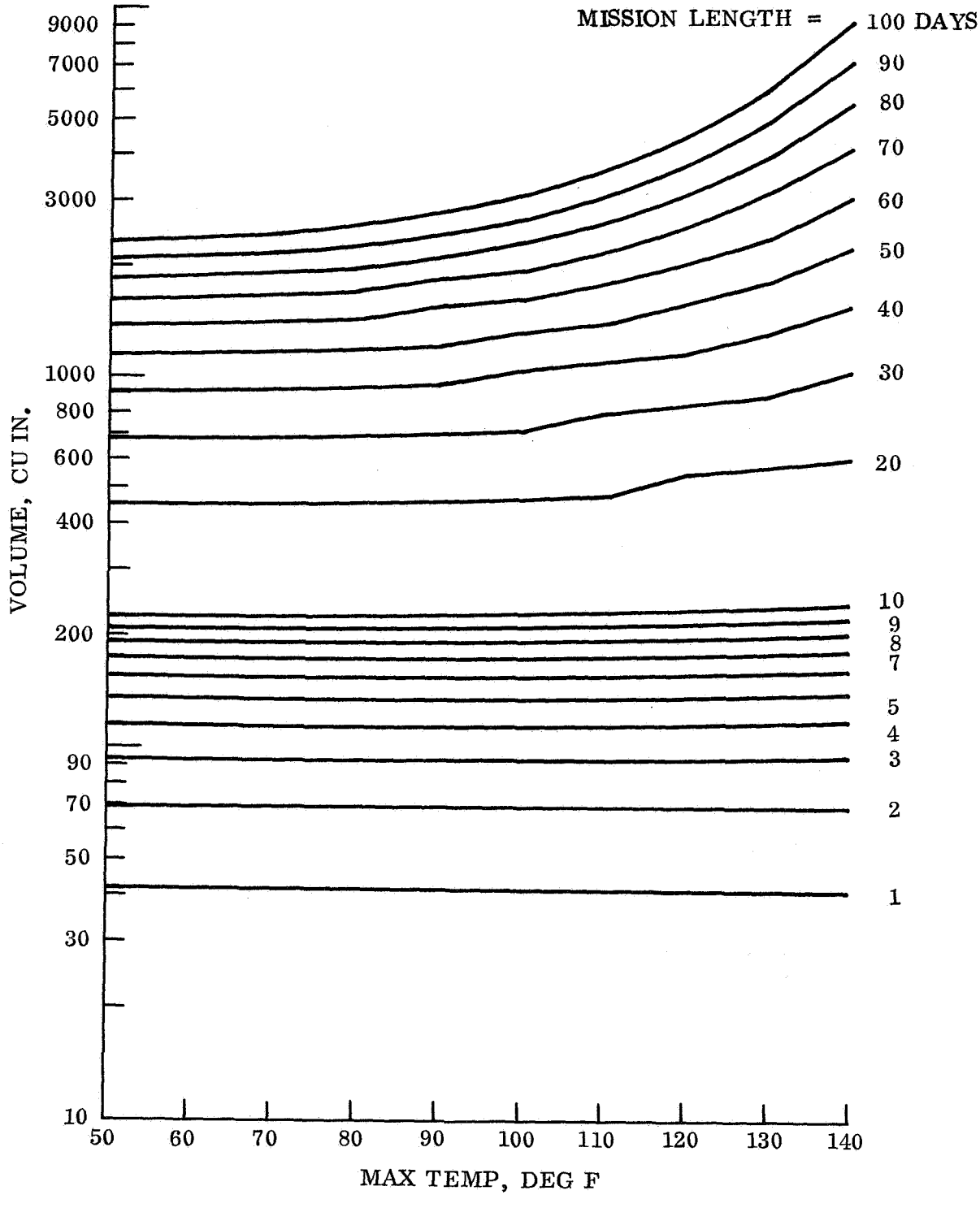

Figure 4.3.2-16. Influence of Maximum Temperature on Silver-Zinc Battery Weight

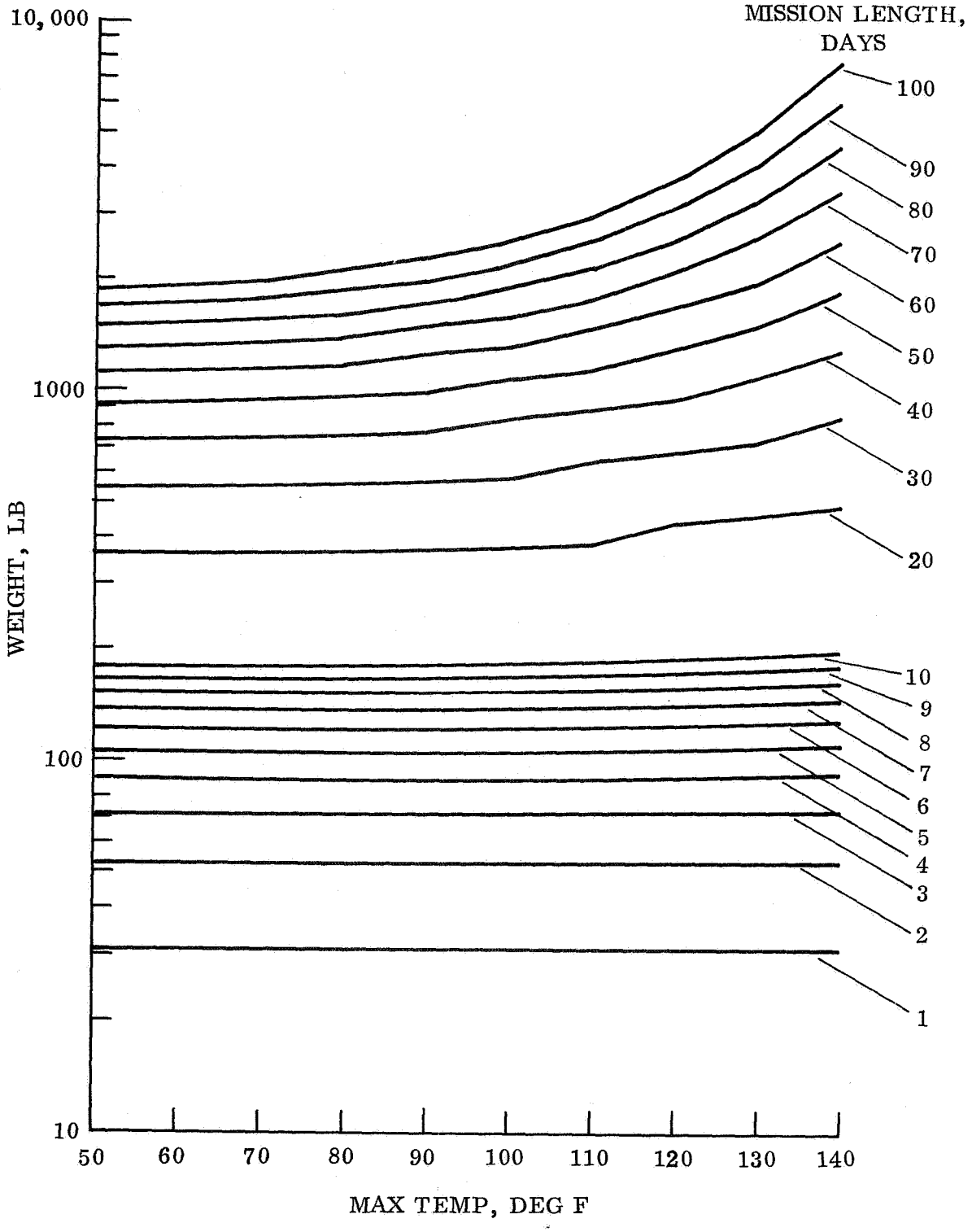

Figure 4.3.2-17. Influence of Maximum Temperature on Silver-Zinc Battery Weight

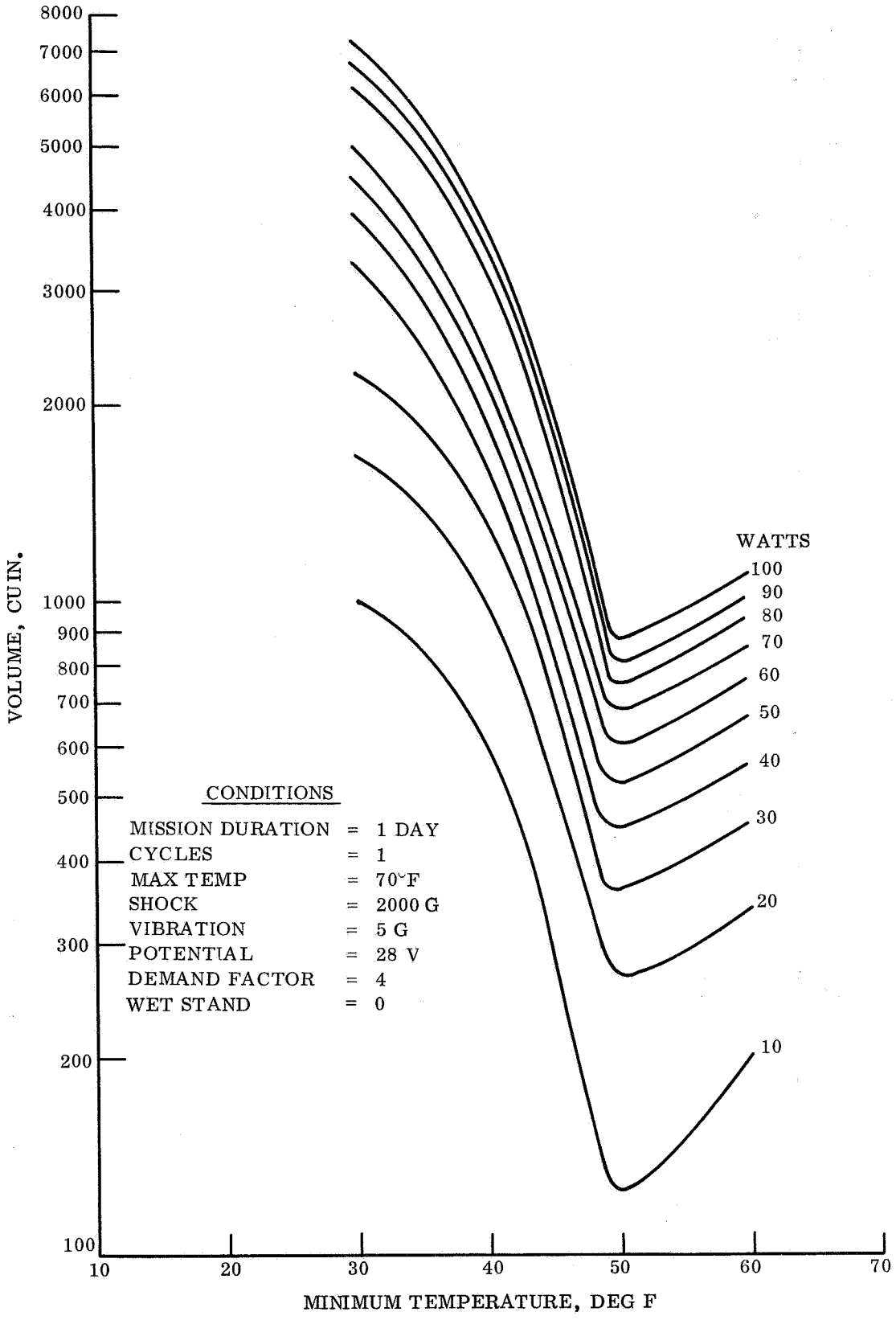

Figure 4.3.2-18. Volume Variation with Operating Temperature

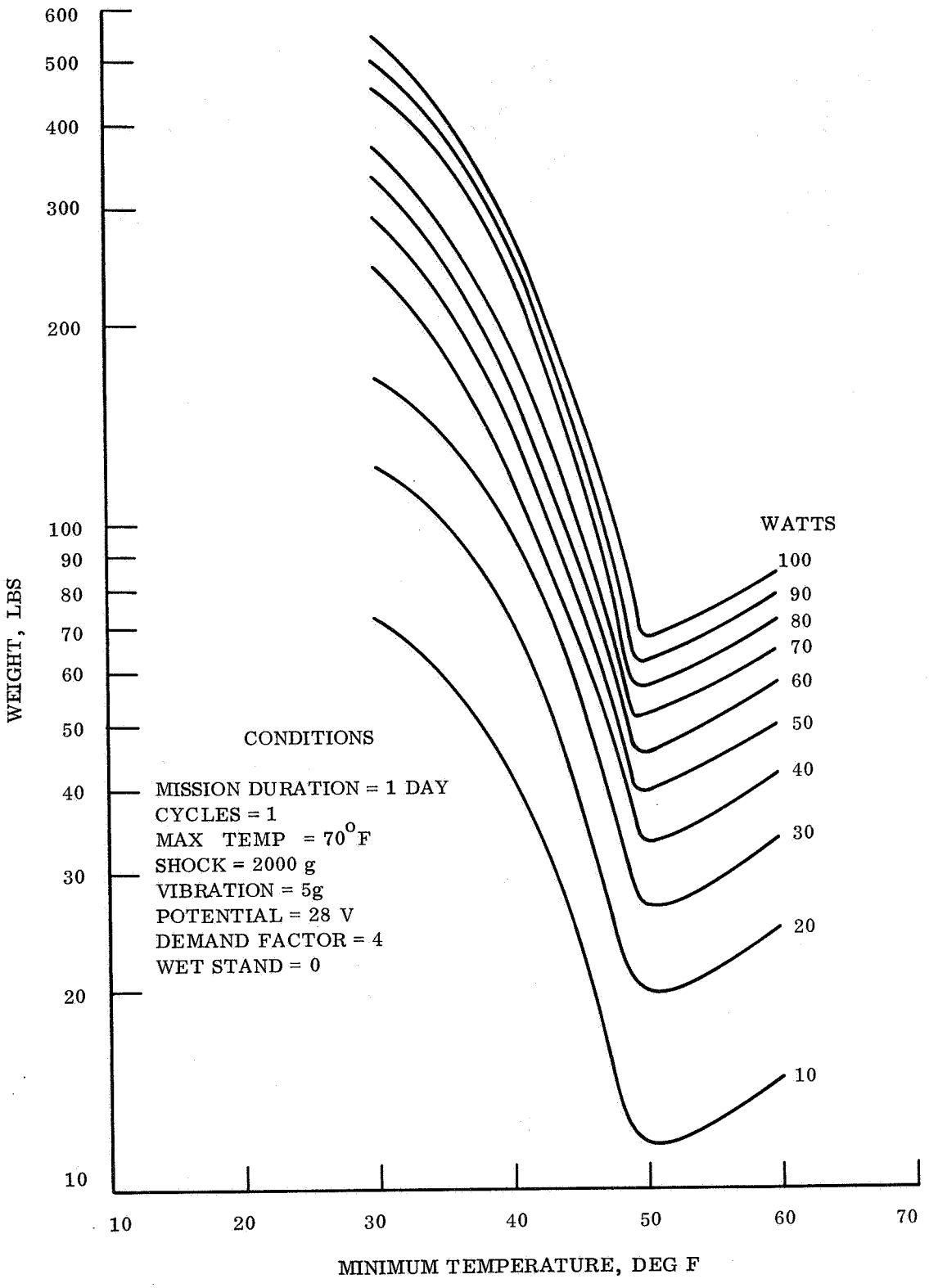

Figure 4.3.2-19. Weight Variation with Operating Temperature

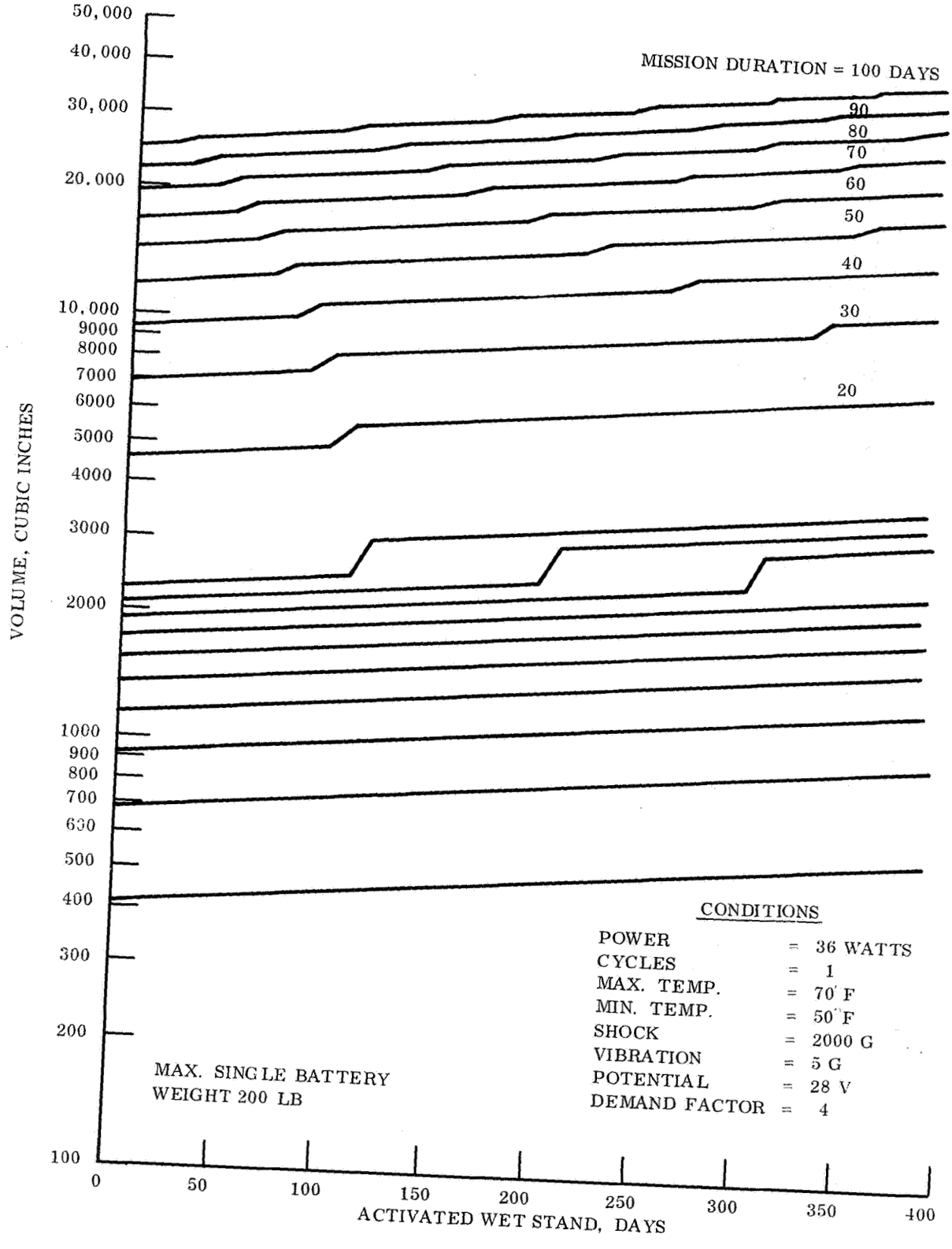

Figure 4.3.2-20. Volume Variation with Wet Stand Life

III

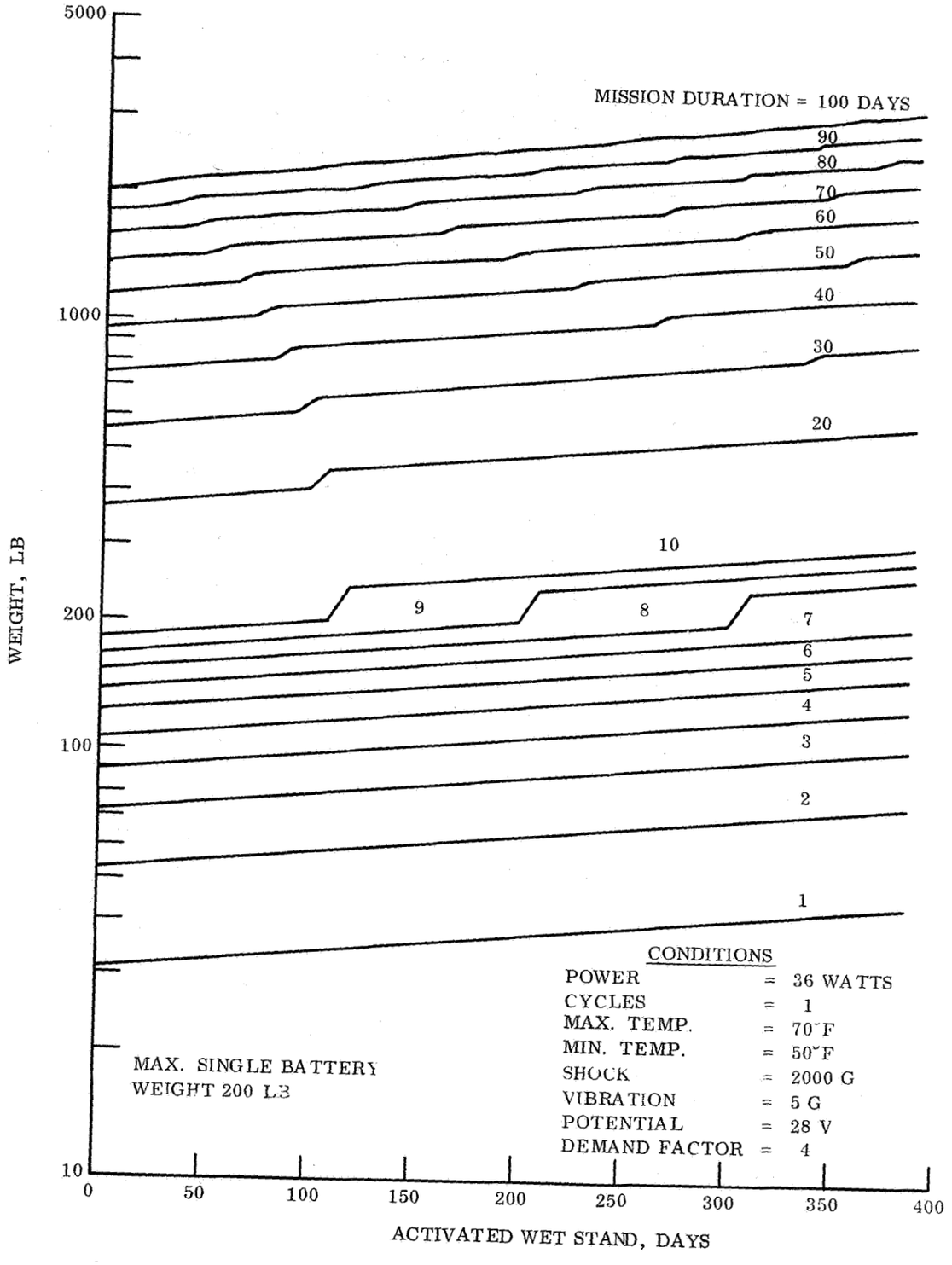

Figure 4.3.2-21. Weight Variation with Wet Stand Life

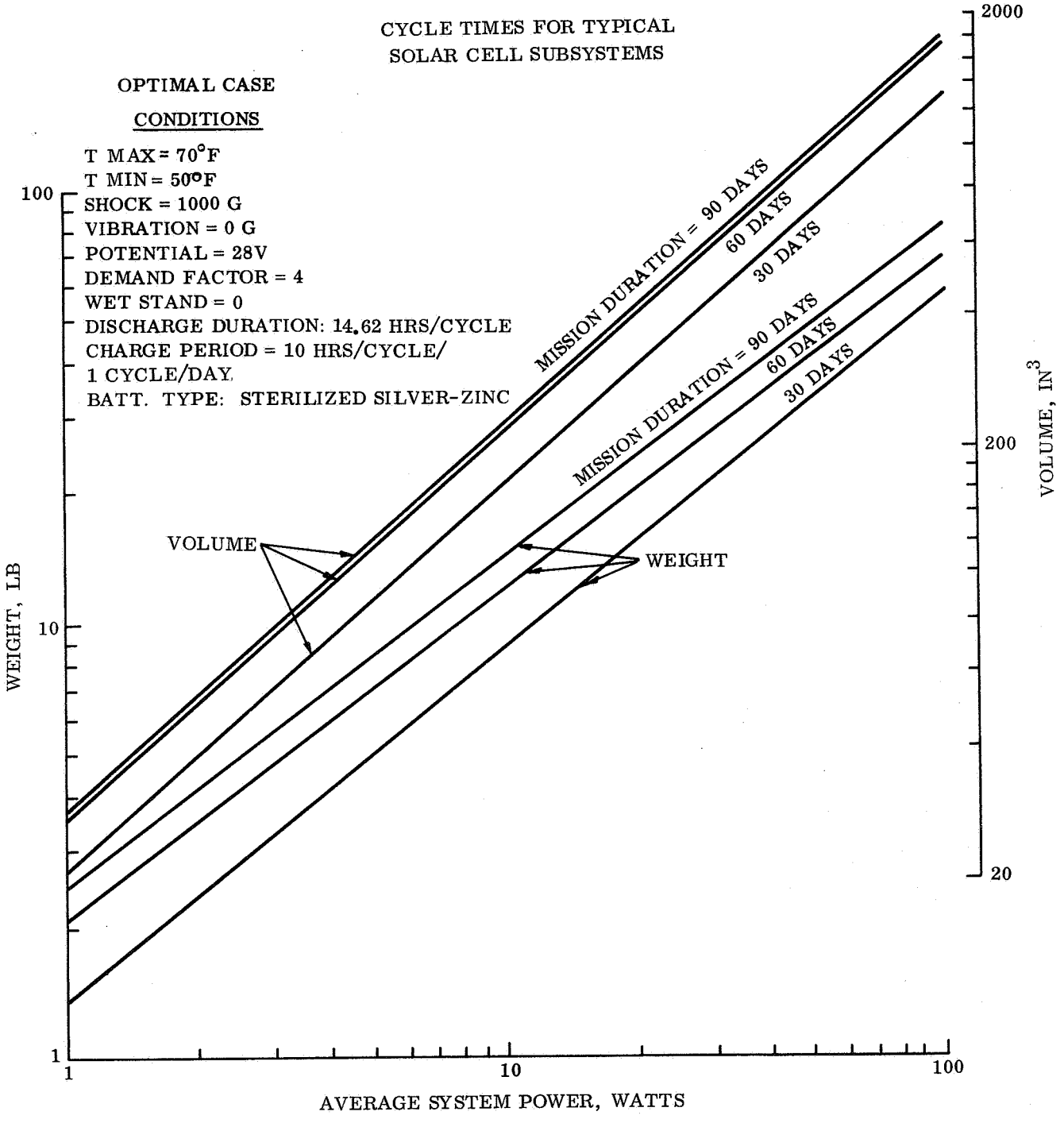

Figure 4.3.2-22. Silver-Zinc Battery Weight and Volume for Various Charge Cycles (Optimal Case)

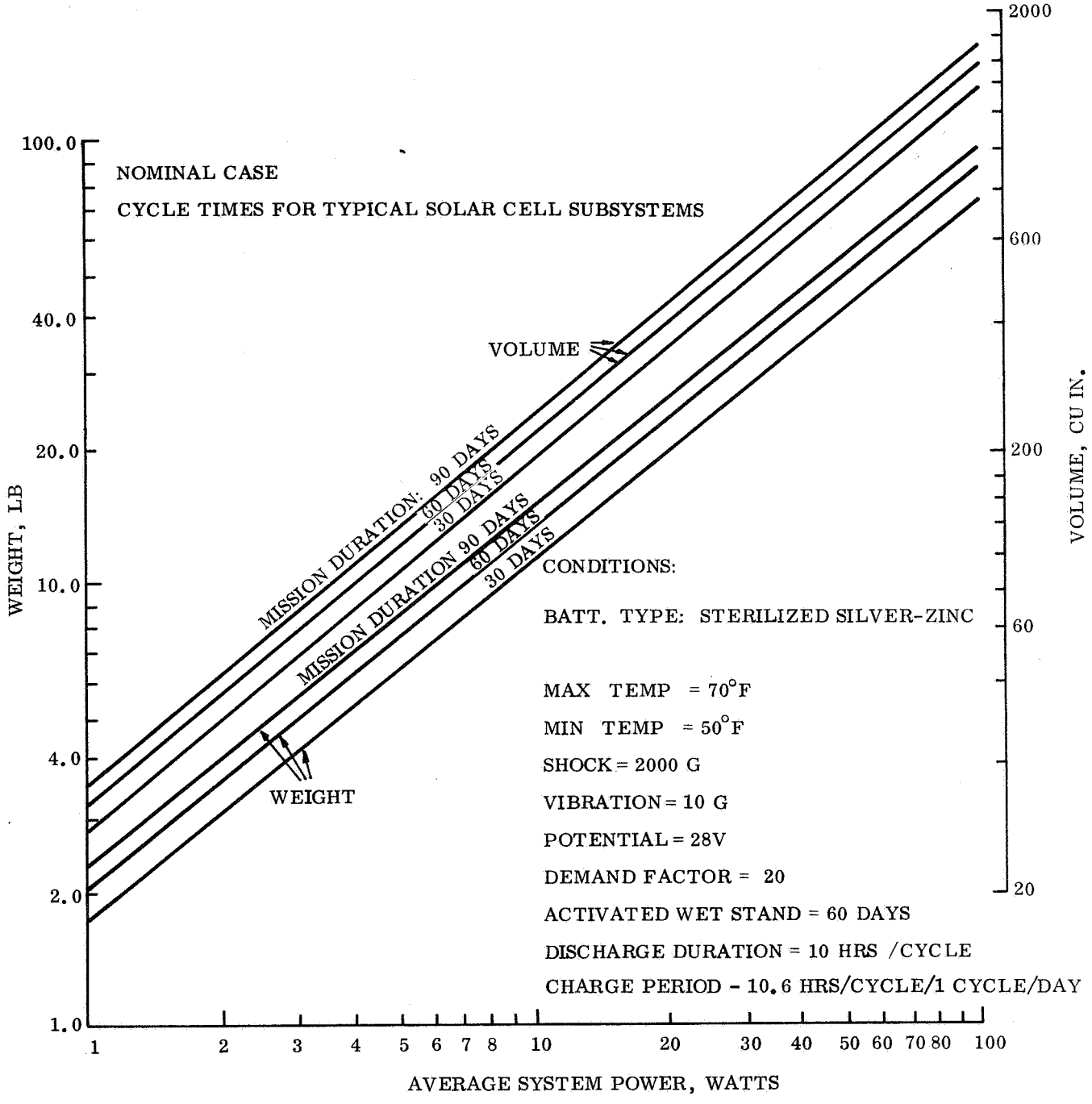

Figure 4.3.2-23. Silver-Zinc Battery Weight and Volume for Various Charge Cycles (Nominal Case)

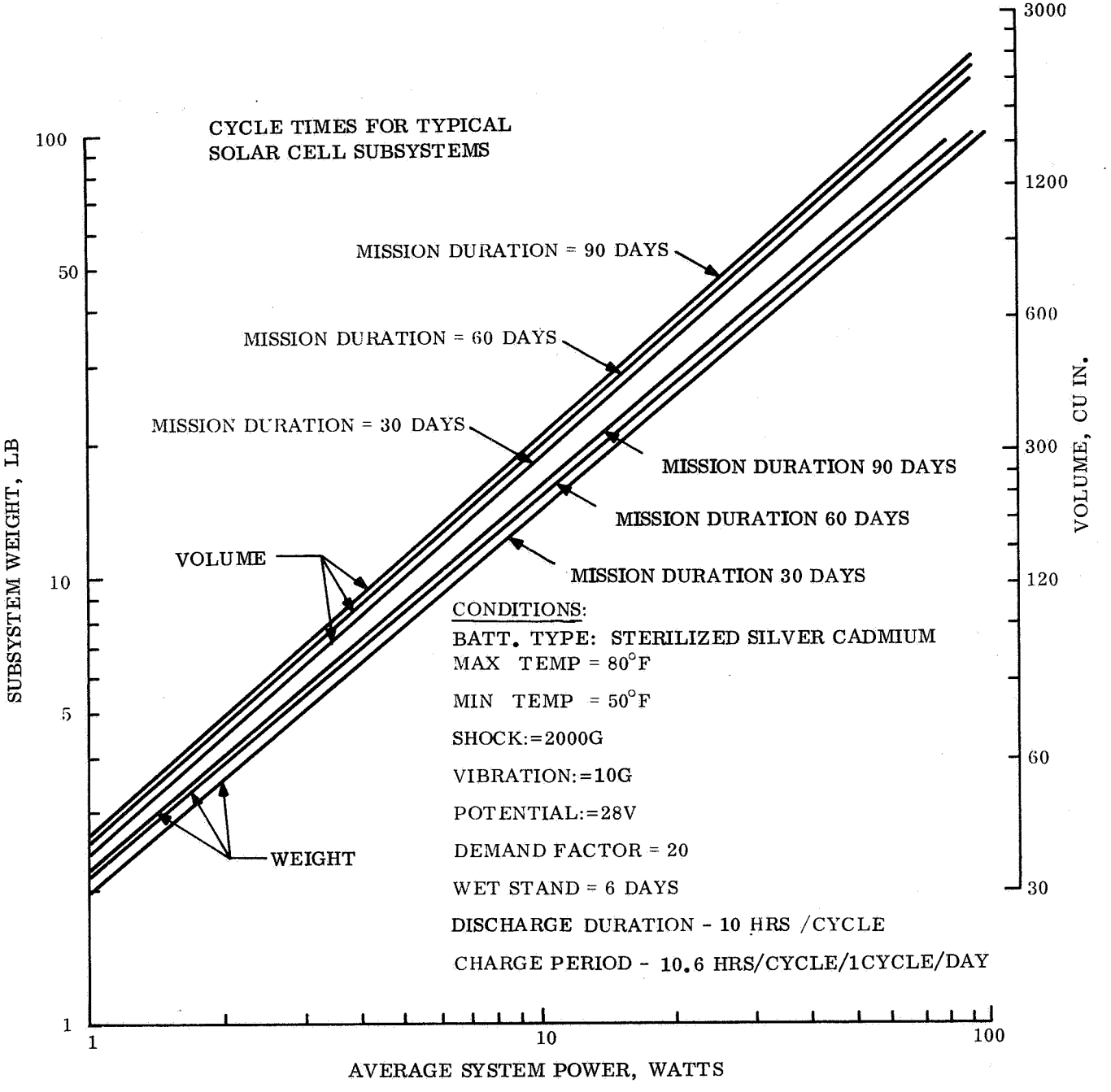

Figure 4.3.2-24. Silver-Cadmium Battery Weight and Volume for Various Charge Cycles (Nominal Case)

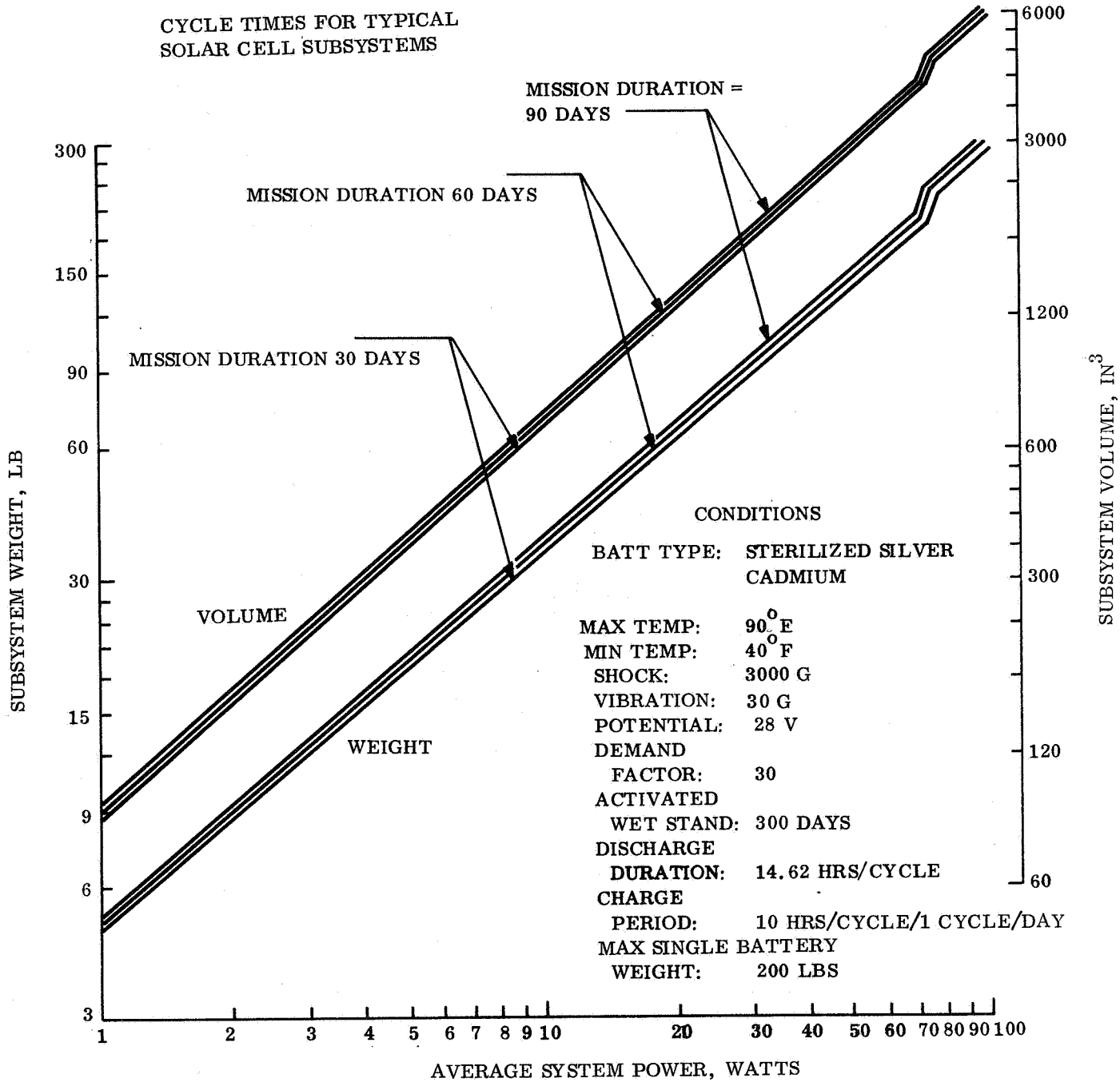

Figure 4.3.2-25. Silver-Cadmium Battery Weight and Volume for Various Charge Cycles (Worst Case)

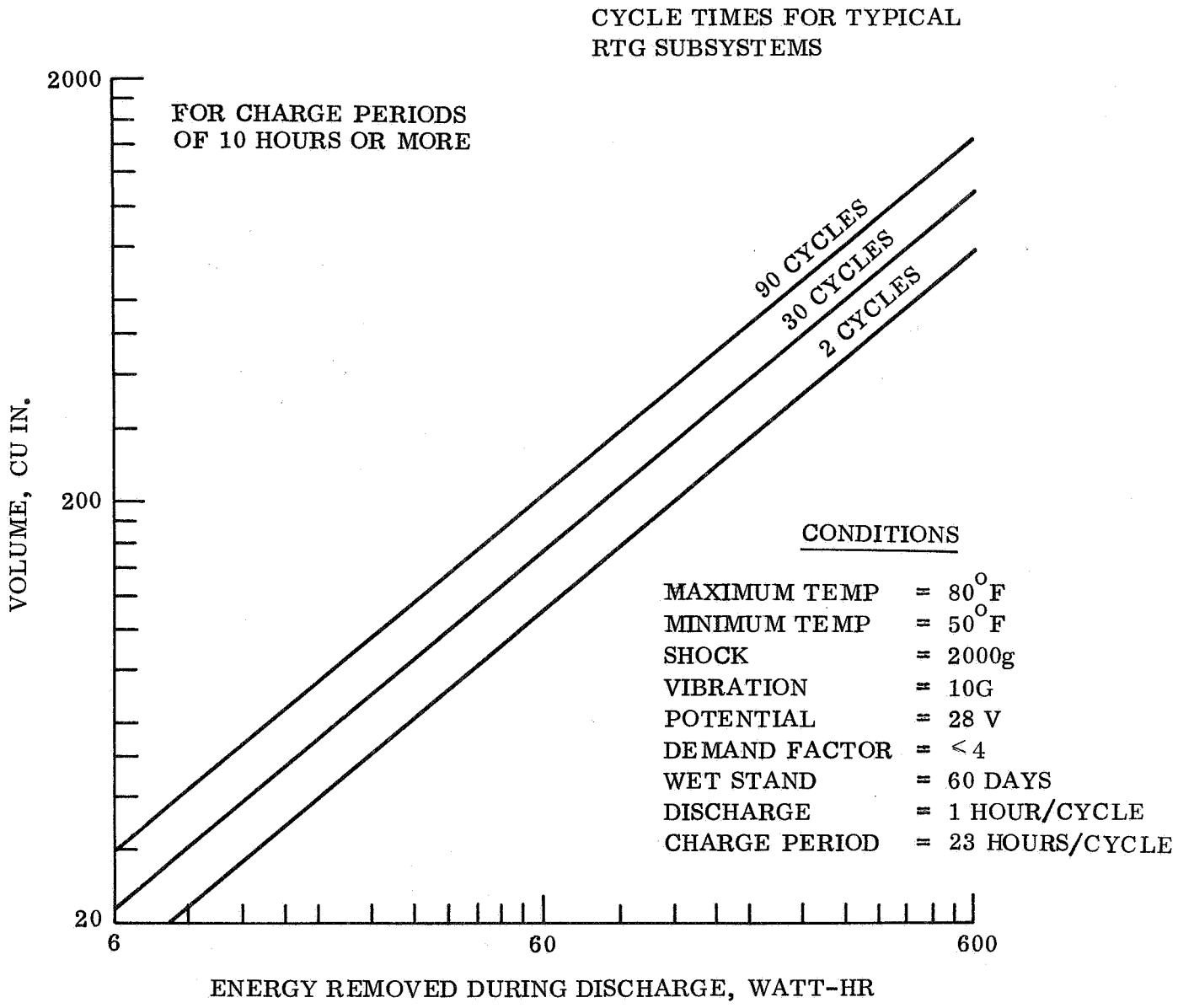

Figure 4.3.2-26. Silver-Zinc Battery Volume for Various Charge Cycles (Nominal Case)

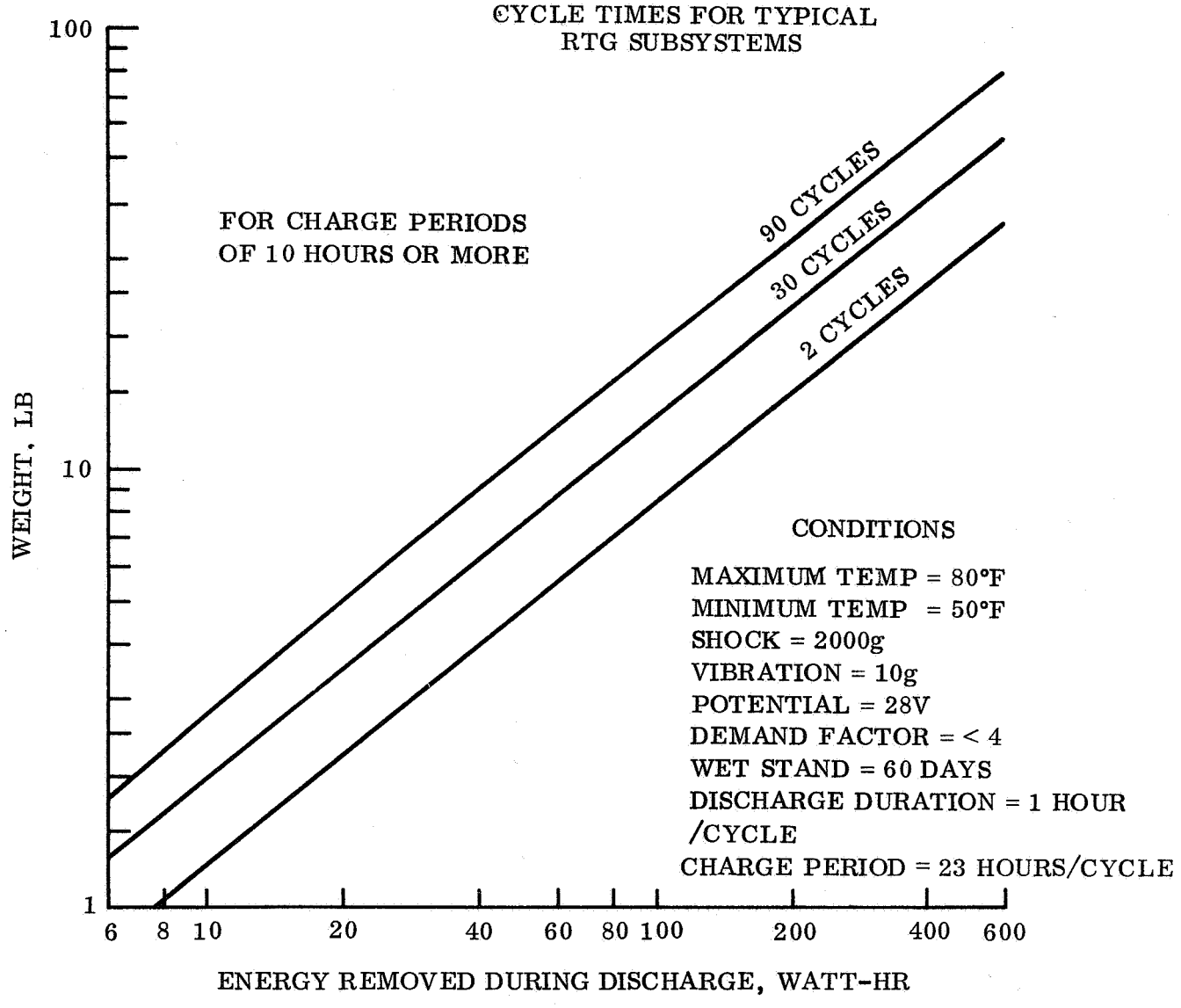

Figure 4.3.2-27. Silver-Zinc Battery Weight for Various Charge Cycles (Nominal Case)

4.3.2.2.2 Solar Cell Parametric Data

A. Solar Cell Output Data

The solar array may consist of one or more panels as deployed from the Lander. Where multiple panels are deployed from a random or uncontrolled landing orientation, the panels may be unfolded in a downward slant from the vehicle roll axis to enhance the possibility that a reasonable portion of the panels are out of the shade. In this approach, various numbers of panels and various slant angles are studied. With a single panel or a group of coplanar panels, considerations include landing level, landing on a slope, or possibility tilting the panel, once, following unfurling. This single tilting action may be used to level the panel or to face the noon sun. The solar array output under these various conditions is developed in the following curves. Of course, continuous sun orientation would provide the greatest power output per square foot of array. Considering the unknown effects of dust and other Martian environments on orienting mechanisms, the continuously oriented approach was eliminated from parametric study. A few reference points have been included to show continuous orientation where this is considered helpful to the user in judging the upper limit.

Figure 4.3.2-28 depicts the electrical output from a single panel or subpanel throughout a typical day. The particular conditions are noted on the curve. For maximum effectiveness it may be assumed that a buck-boost charge regulator is used to permit full utilization of this power or a small allowance made for solar array-battery voltage mismatch. The daily variation of power output for three 8-sided configurations is shown in fig. 4.3.2-29 for a level equatiorial landing at the equinox. The lack of symmetry in power output is caused by the lag in surface temperature through the day. Thus, the area under these curves represents the total energy in watt-hours/unit area received during each illuminated interval or day. To simplify the calculation of battery size and panel requirements, this may be expressed as an equivalent average power, in watts during the illuminated period. In this way the output may be represented by a single number, and the effects on output may be studied as a function of landed latitude, panel orientation and landing date.

To perform these calculations the following factors were considered:

1. The effects of landed latitude, landed pitch, and Sun elevation at the operating date.

2. Temperature analysis of the panel based on the daily variation of Mars surface temperatures.

3. The temperature dependency of the solar cell V-I curve.

4. Operation at the maximum power point.

For all configurations, the solar panel temperatures were calculated based on the NASA/LRC May '68 Specification for daily surface temperature variation and on the a ssumption that the panel was in a vacuum. This latter assumption was based on

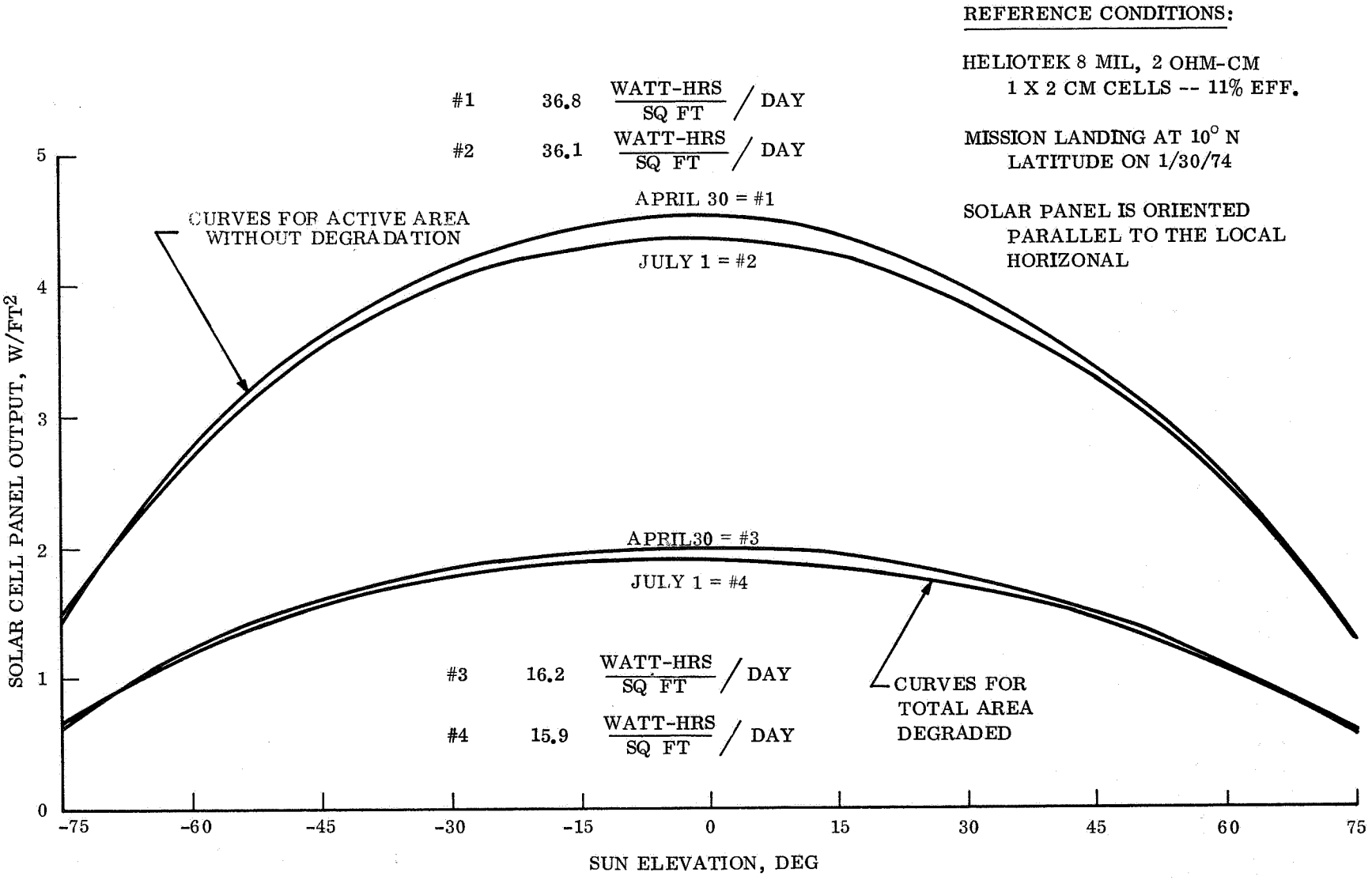

Figure 4. 3. 2-28. Solar Cell Array Output During Day

the fact that including convective cooling from Mars surface winds resulted in a temperature drop of only about 0.5°F.

The effect of angle of solar incidence on panel temperature was calculated at several angles, and it was found that the difference between panel temperature and ground temperature could be adequately represented by this relation:

$$\Delta T(\theta) = \Delta T(\text{Normal}) \times (\text{Cos } \theta)^{0.9}$$

The V-I characteristics of the array were based on 11 percent efficient (A. M. O. 28°C) Heliotek, 8-mil, 2 ohm-cm N/P cells, utilizing a previously developed computer program for V-I curve prediction.

The calculations were made by an incremental summation method using one step each Martian hour. This has been shown to be within 0.2 percent of a more precisely calculated value. All the above calculations were performed using Computer Programs on the GE 605/Datanet 30 system.

Results of these calculations are shown parametrically in fig. 4.3.2-30 through 4.3.2-36. The fixed position multipanel cases are shown first, followed by the single panel with and without tilt.

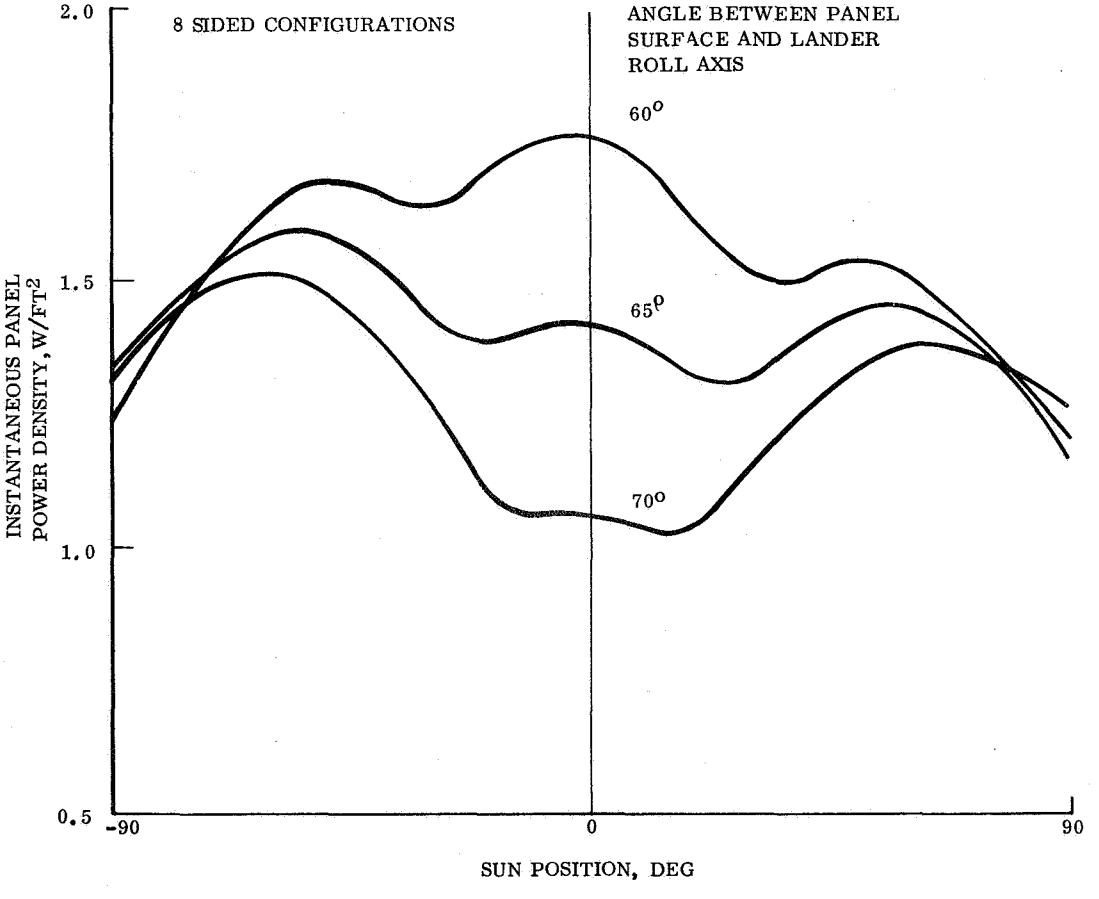

Figure 4.3.2-29. Typical Daily Power Variation

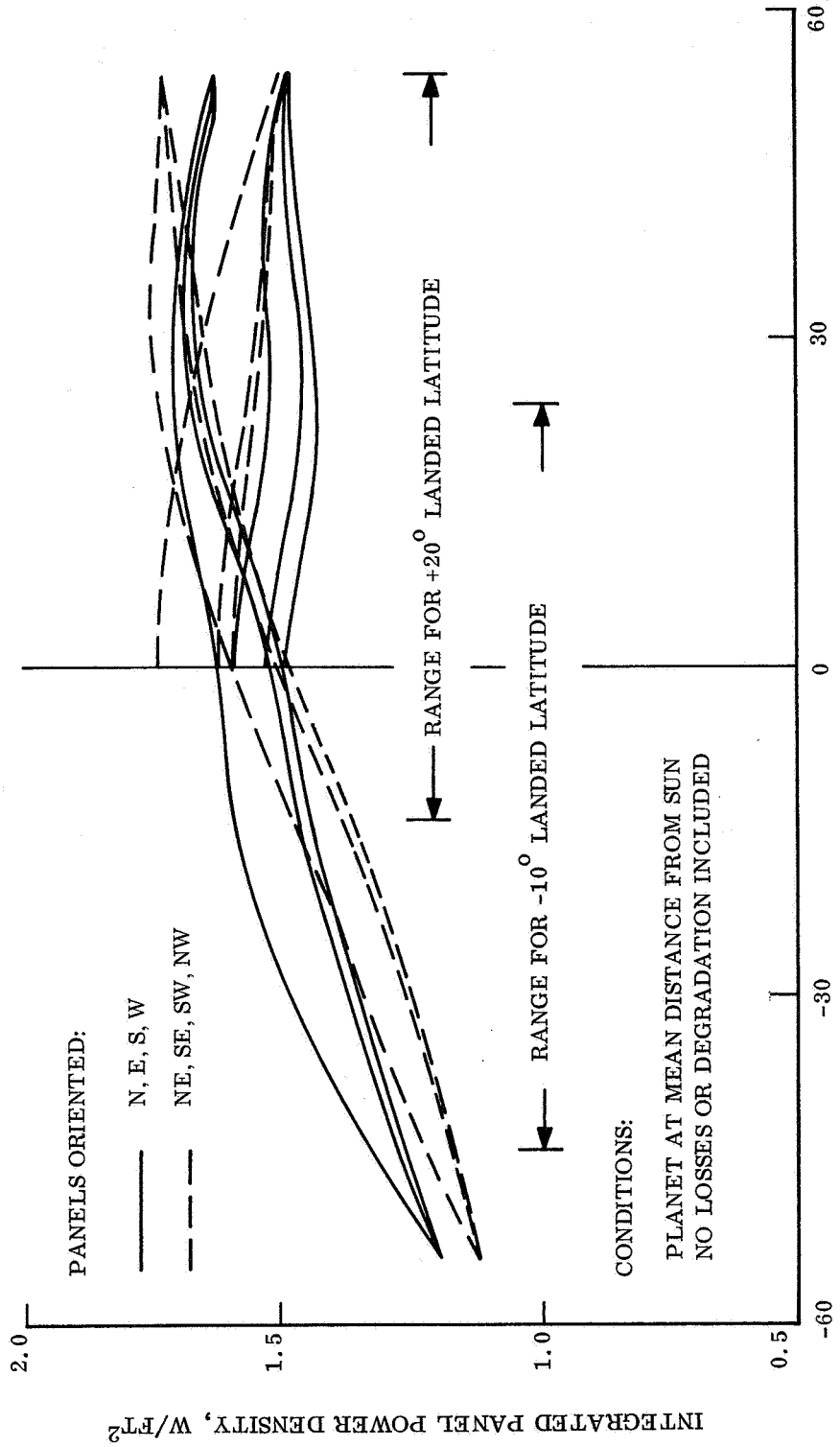

Figure 4.3.2-30. Integrated Panel Power Density from Fixed Tent Solar Array (60^{o} - 4 Sides)

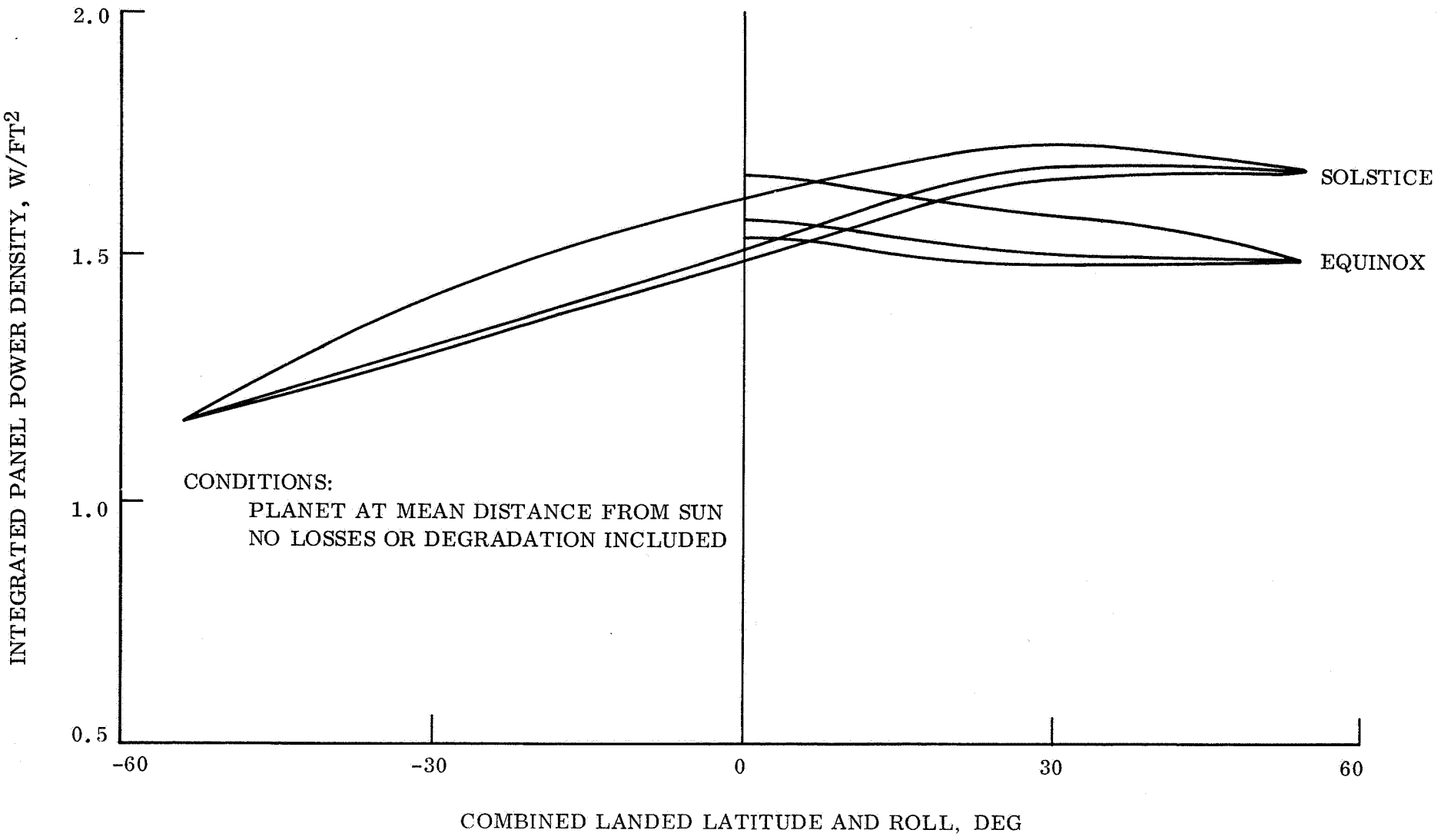

Figure 4.3.2-31. Integrated Panel Power Density from Fixed Tent Solar Array (60° - 8 sides)

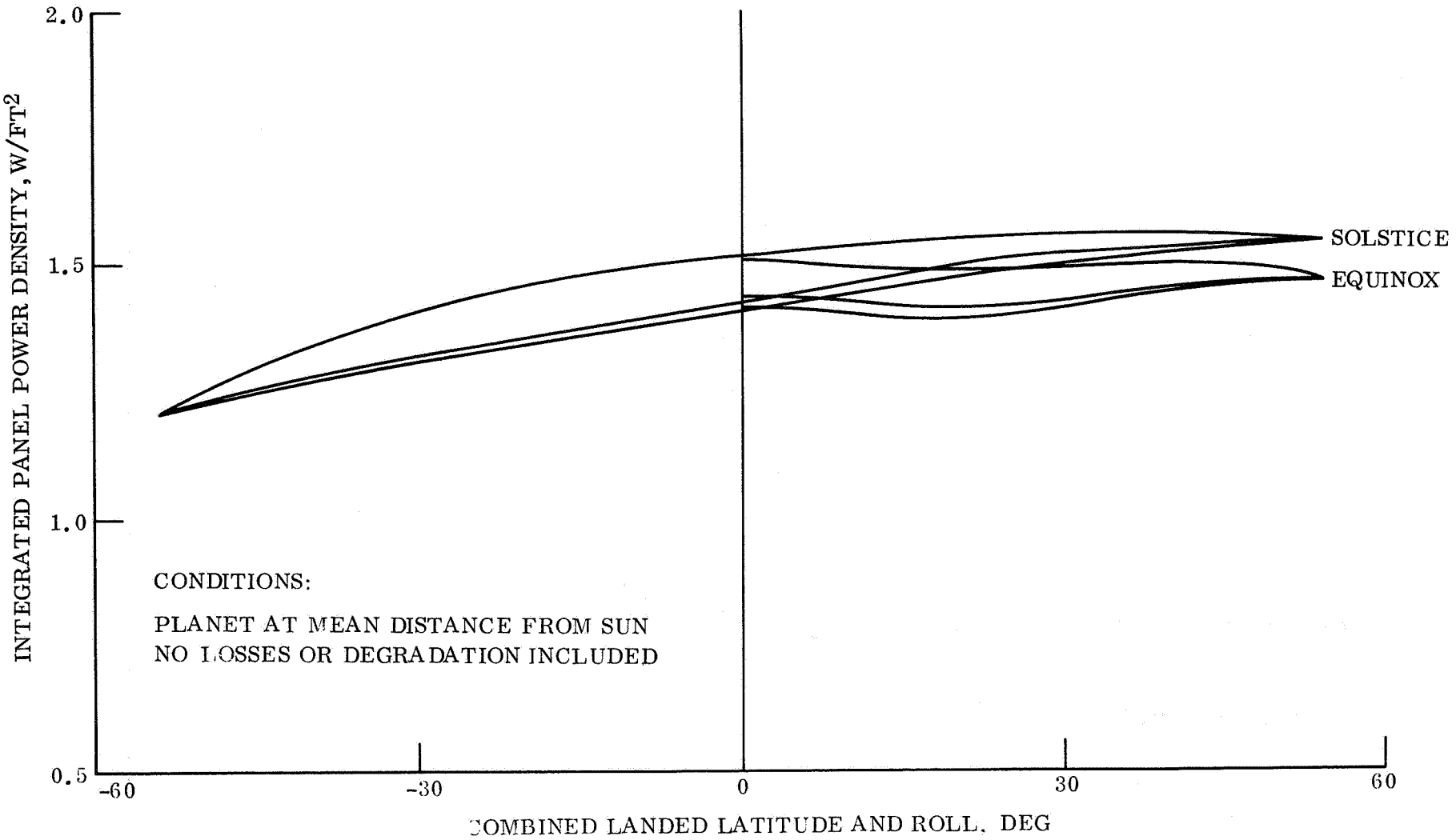

Figure 4.3.2-32. Integrated Panel Power Density from Fixed Tent Solar Array (65° - 8 sides)

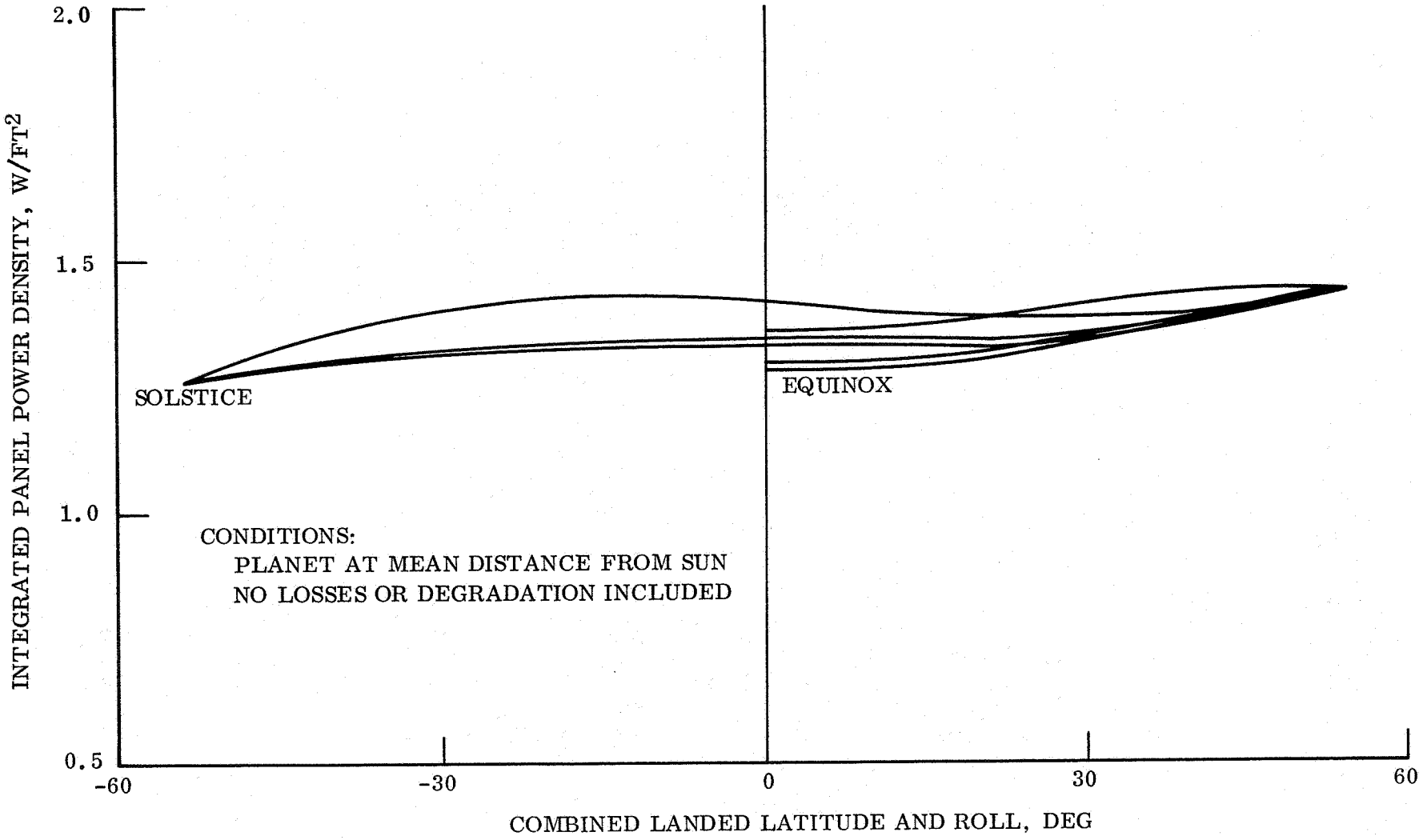

Figure 4.3.2-33. Integrated Panel Power Density from Fixed Tent Solar Array (70° - 8 sides)

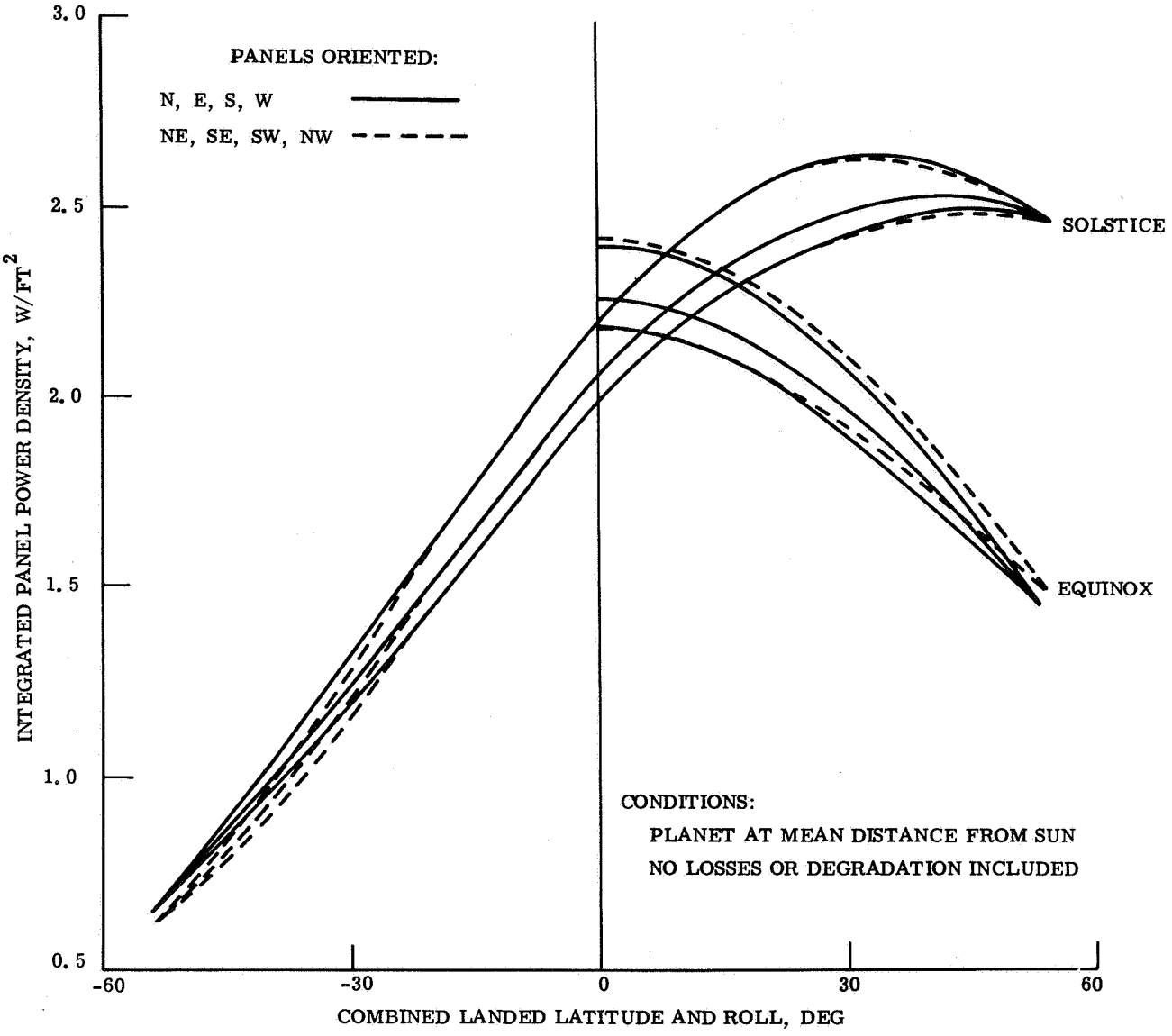

Figure 4.3.2-34. Integrated Panel Power Density from Fixed Tent Solar Array (30° - 4 sides)

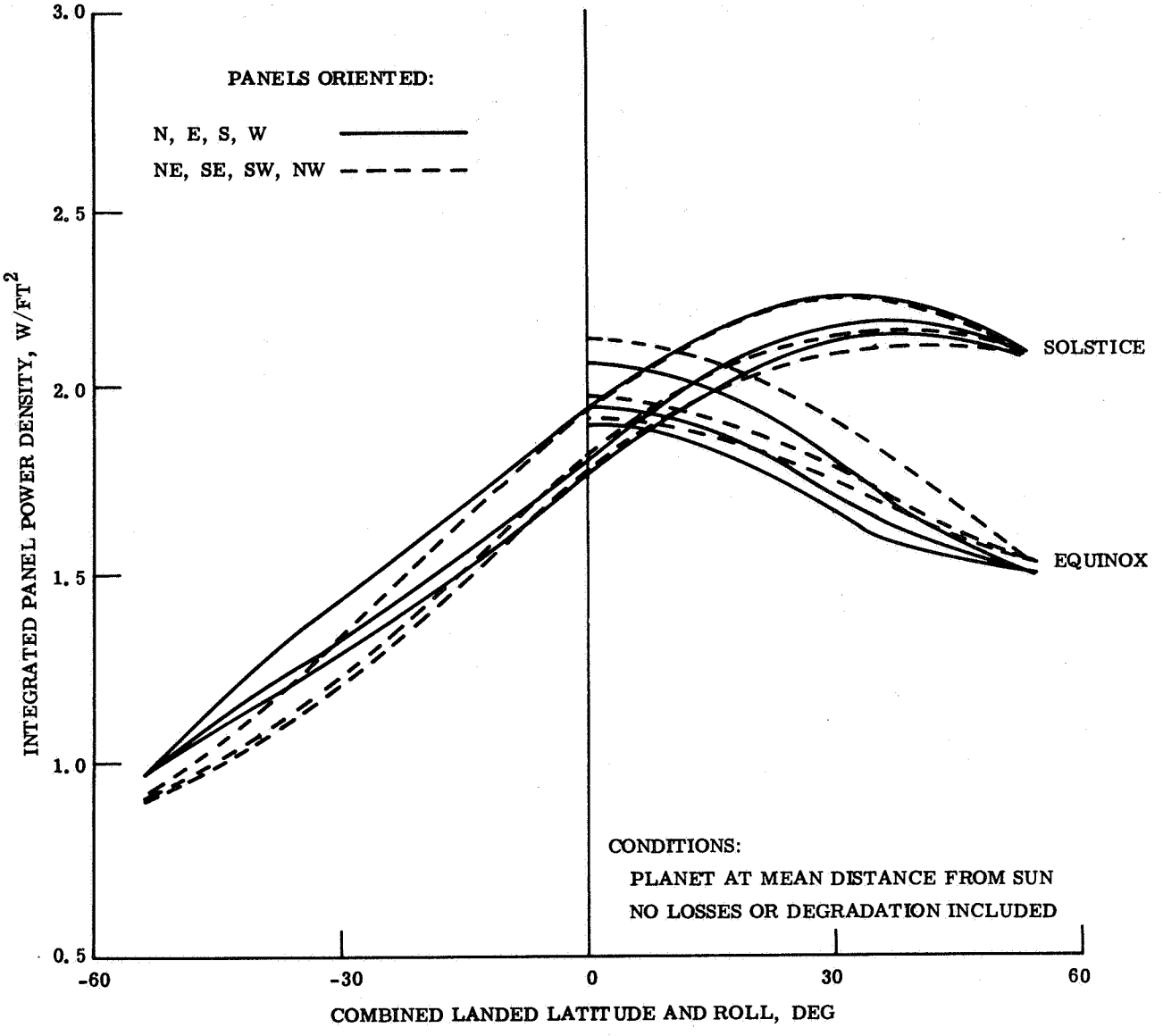

Figure 4.3.2-35. Integrated Panel Power Density from Fixed Tent Solar Array (45° - 4 sides)

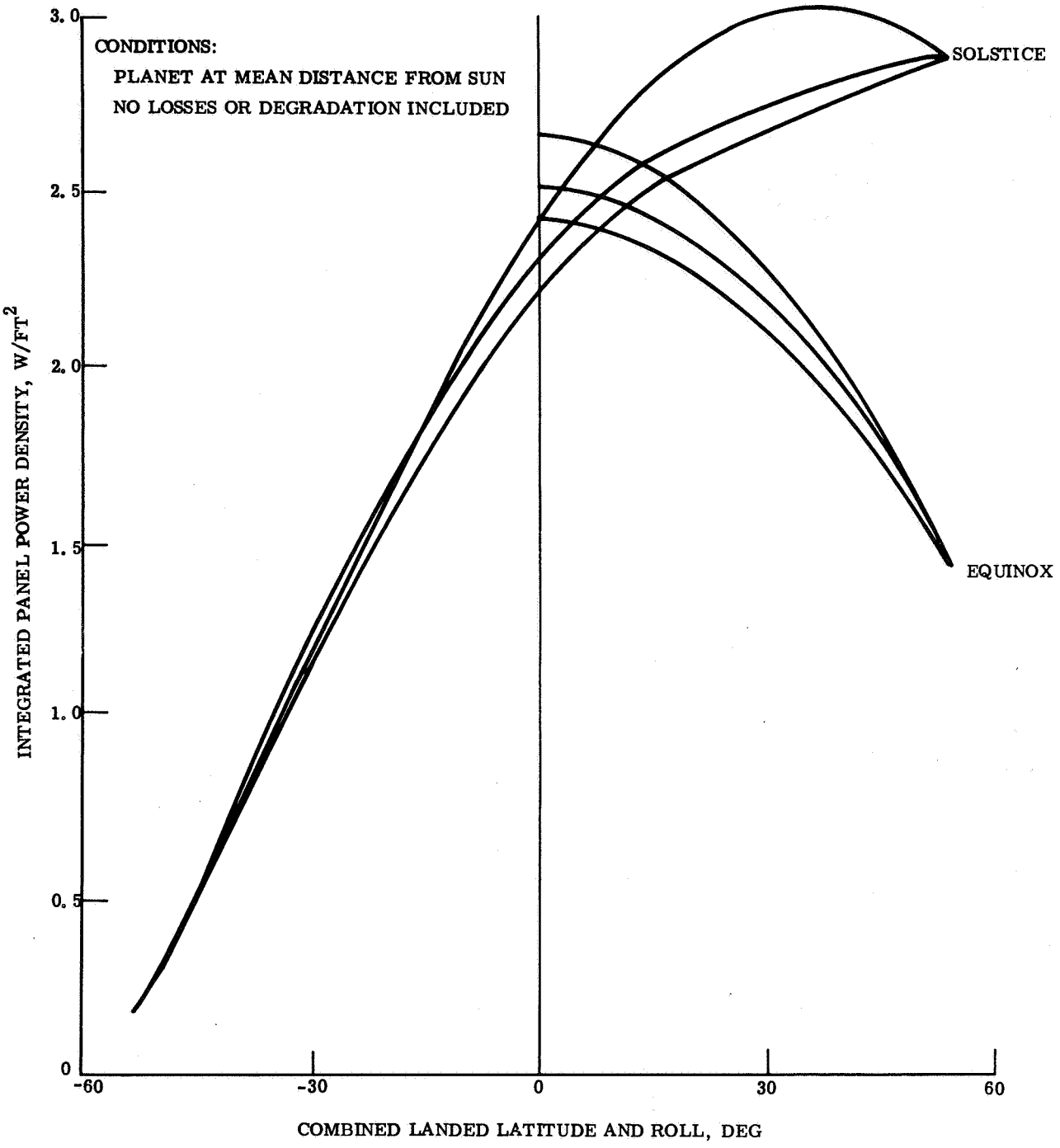

Figure 4.3.2-36. Integrated Panel Power Density from Horizontal Solar Array

B. Definition of Terms

Pitch - East (+) or West (-) component of the slope on which the Lander rests.

Roll - North (+) or South (-) component of slope.

Landed Latitude - Local Martian latitude.

The angles indicated in the figures are the angle at which the panels are inclined downward from the horizontal, as viewed from the center of the Lander, for a simulated tent-shaped array.

To assist in interpreting the curves, an example is given:

Landing latitude:	(+) 20°N
Maximum slope:	34 degrees

Therefore, the minimum and maximum values of combined landed latitude and roll are -14 degrees and +54 degrees, respectively. Therefore, for a 4-sided array with 60° angle panels, the apparent minimum daily average power is 1.20 w/ft^2, at -14°, not including the effects of shading by the hillside (see fig. 4.3.1-48).

In approximating the effect of shading, it is not necessarily accurate to reduce the "daytime" by the proportion of the hill slope angle. For the several cases examined in detail, the instantaneous power level during those periods lost by shading was less than the 12 hour average; hence, the loss will be less than proportionate.

In each set of curves, the lines will appear in groups of three. In every case the upper line will be for Pitch = 0 degrees. The lowest line will be for points following the negative pitch outline, with maximum negative pitch being -34 degrees, as shown. The power will be less for negative (westward) pitch than for positive (eastward) pitch because of the effects of array geometry and the lag in surface temperature.

For a point of comparison, an oriented array will produce an average 3.8 w/ft^2 during a 12 hour (Mars) day.

C. Panel Weights

The solar array weight consists of three parts; the panel structure with hinges, the cells with covers, and the tilting mechanism, if used.

The major parameter influencing panel weight is the shock level. Using the honeycomb sandwich approach, increased hardening to withstand shock is obtained by increasing the core density. Thus, the thickness or volume is unaffected. The anticipated structure weight as a function of shock level is illustrated in fig. 4.3.2-37. Although this shows the weight trend, it is recognized that actual development tests may show a base weight up to 2 times that shown.

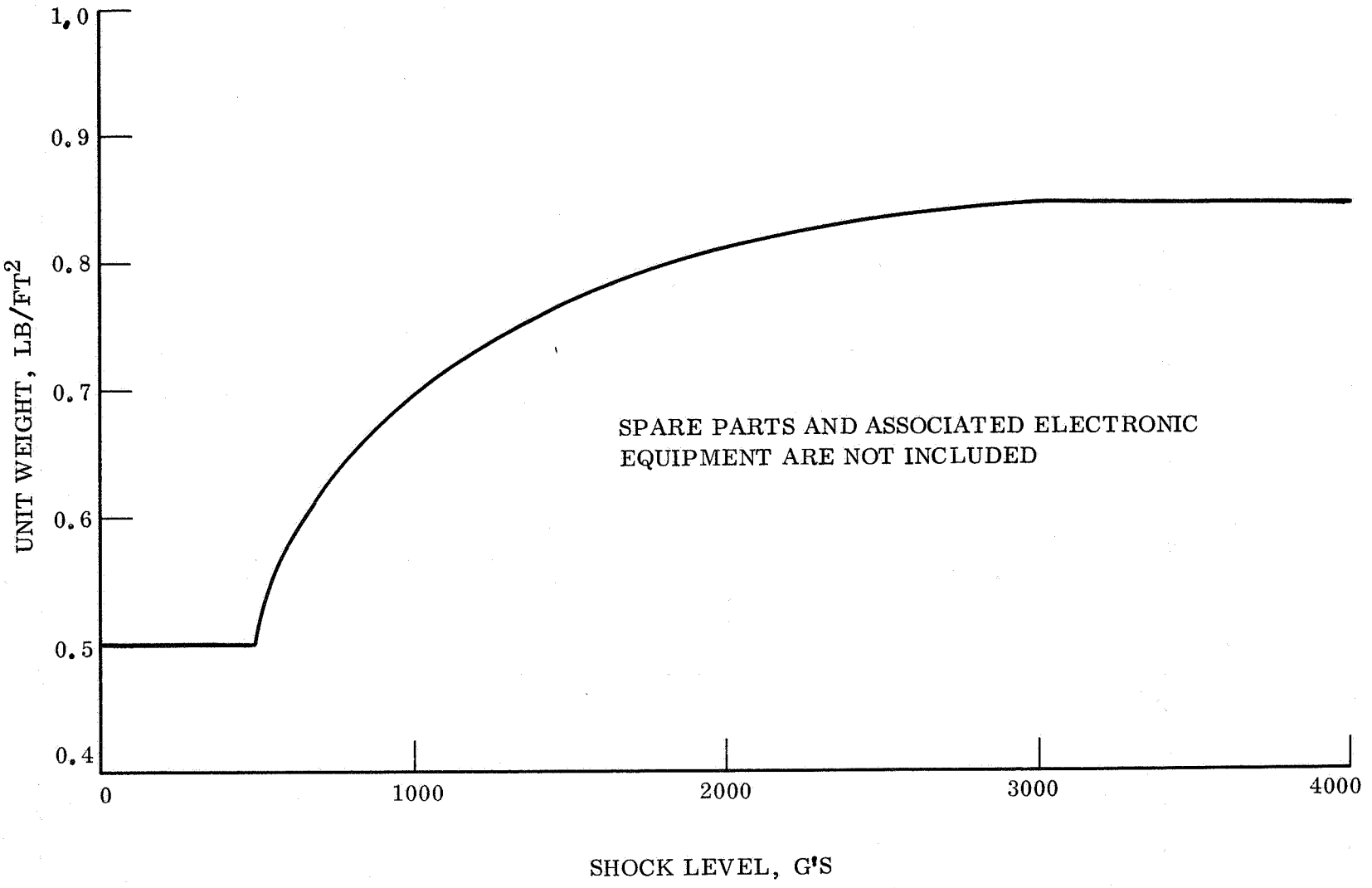

Figure 4.3.2-37. Unit Weight at Solar Array Structure

The weight of the solar cells, adhesive, and cover must be added to the structure weight. For this parametric study the values noted in table 4.3.2-1 were used.

TABLE 4.3.2-1. SOLAR CELL WEIGHT BREAKDOWN

5-mil Lexan cell cover sheet	0.029
Coversheet adhesive	0.025
Cells (8-mil)	0.132
Cell interconnection strips and solder	0.024
Cell-to-substrate adhesive, 10 mils	0.060
Terminals, diodes, wire, etc.	0.017
TOTAL	0.287 lb/ft^2

If the design includes a leveling, tilting, or orienting approach the weight of the drive mechanism is included. Representative weights used for this purpose are noted in table 4.3.2-2.

TABLE 4.3.2-2. ORIENTATION EQUIPMENT WEIGHTS

Sun Sensors	0.2 lbs each panel
Signal Amplifier	0.4 lbs, one only
Power Amplifier	0.5 lbs, one only
Drive mechanism	4.0 lbs, one per axis per panel

4.3.2.2.3 Degradation and Loss Factors

The power outputs, indicated in figs. 4.3.2-28 through -36, represent ideal outputs without any attenuation or degradation. To obtain the actual output the factors listed in table 4.3.2-3 are included.

TABLE 4.3.2-3. DEGRADATION AND LOSS FACTORS

Orientation factor	0.923
Filter transmission	0.939
Cloud attenuation (blue haze)	0.90
Atmospheric attenuation	0.993
Erosion factor	0.8
Accumulated dust attenuation	1.0
Instrumentation, measurement and alignment	0.956
Soldering degradation	0.98
Proton damage factor	0.939
Meteorite damage	1.0
Spectral factor	1.0

All these power output values must be further reduced by the packing factor. Approximate packing factors realizable are listed in table 4.3.2-4.

TABLE 4.3.2-4. PACKING FACTOR VALUES

Rectangular panel	0.85 - 0.90
Trapezoidal panel	0.75 - 0.85

The packing factor is defined as the ratio of the active solar cell area (based on 1.9 cm^2 for a 1 cm x 2 cm cell) to the gross panel area.

4.3.2.2.4 Fuel Cell Parametric Data

The parametric curves of figs 4.3.2-38 through -43 include shock and sterilization factors together with those tabulated on the curves. Fuel cell stacks, reactant storage, product water storage, radiators, batteries, electrical and pneumatic regulators have been included.

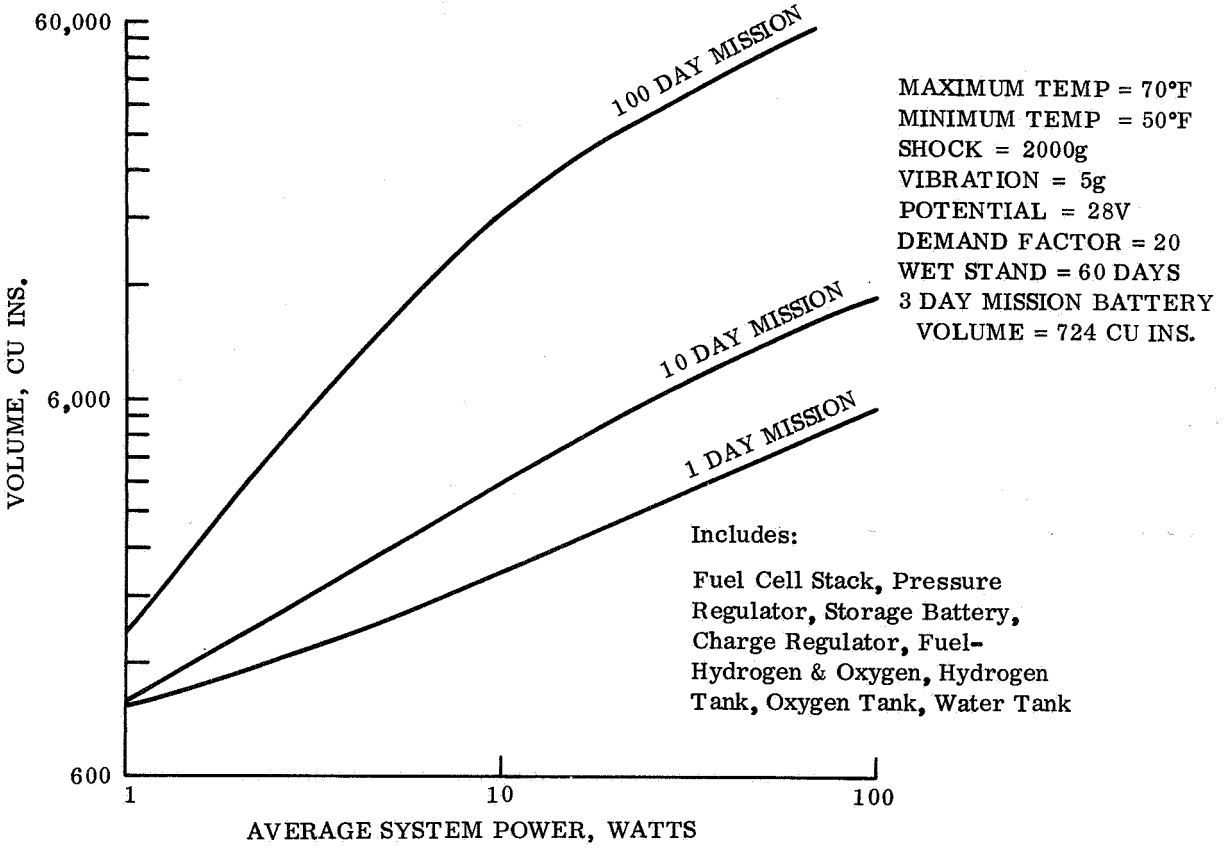

Figure 4.3.2-38. Sterilized Solid Electrolyte H_2/O_2 Fuel Cell Volume Parameters with Three Day Battery (Nominal Case)

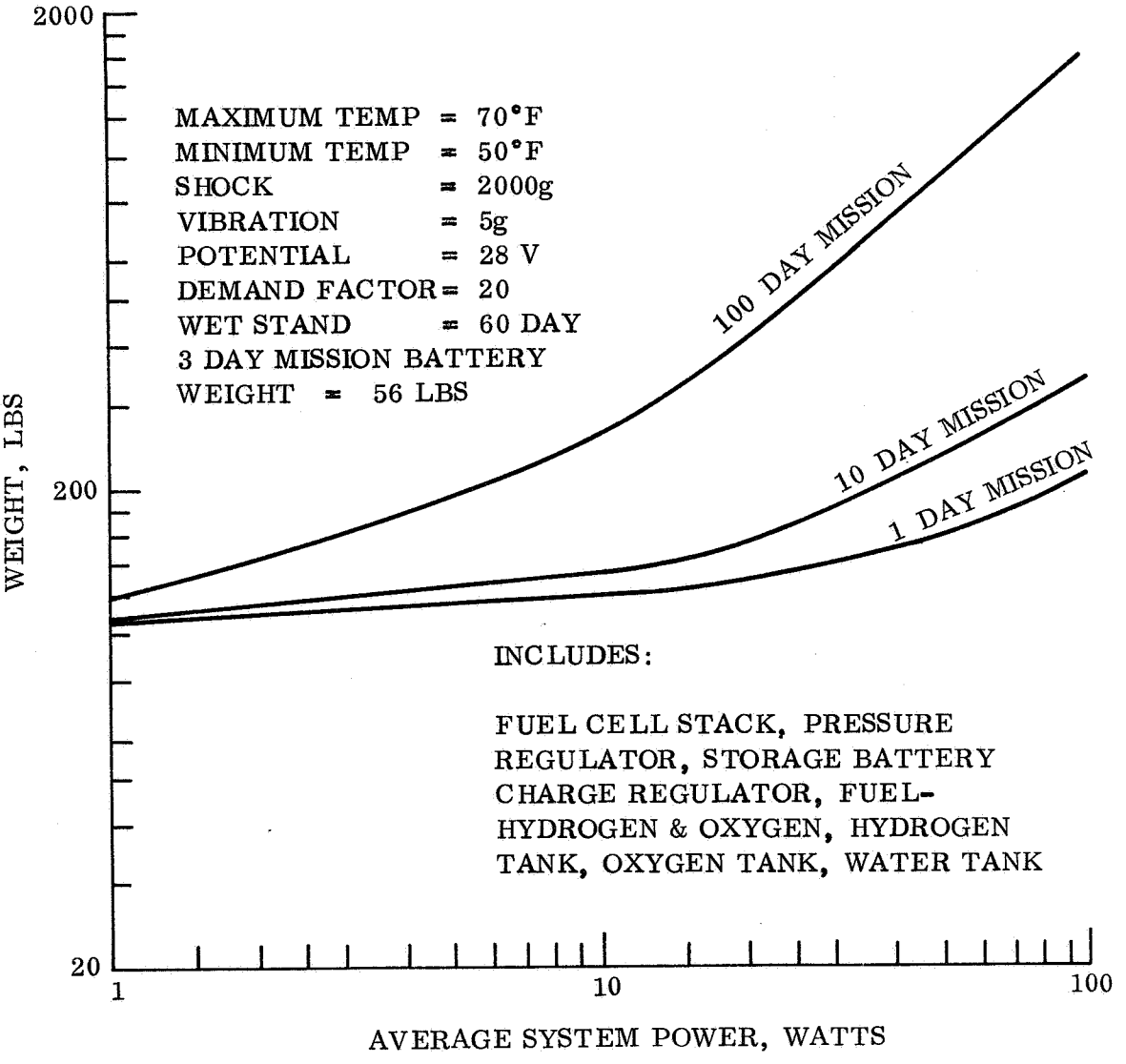

Figure 4.3.2-39. Sterilized Solid Electrolyte H_2/O_2 Fuel Cell Weight Parameters with Three Day Battery (Nominal Case)

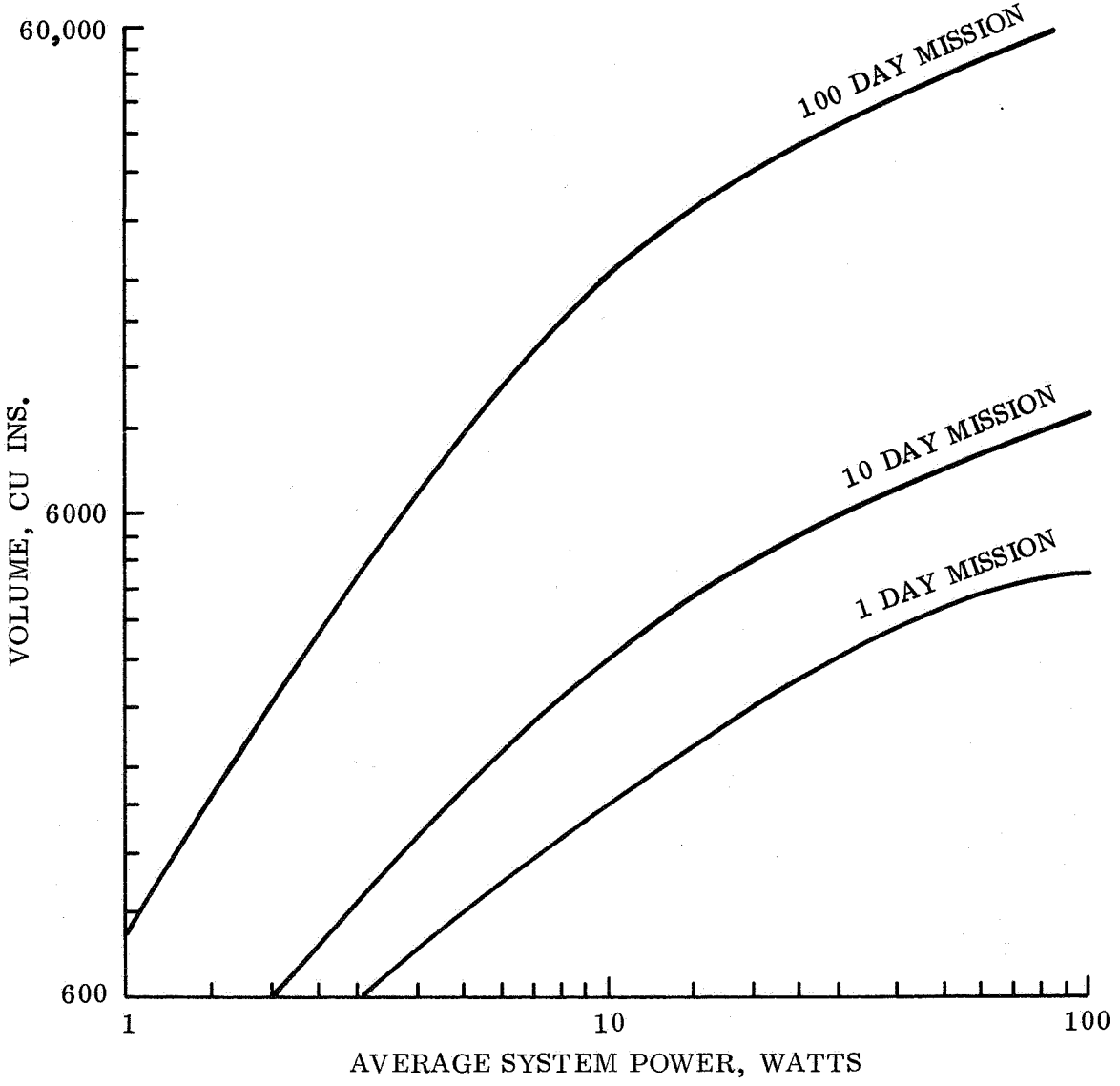

MAXIMUM TEMP = 80°F
MINIMUM TEMP = 50°F
SHOCK = 2000g
VIBRATION = 5g
POTENTIAL = 28V
DEMAND FACTOR = 20
WET STAND = 60 DAYS

INCLUDES:

Fuel Cell Stack, Pressure Regulator, Storage Battery, Charge Regulator, Fuel-Hydrogen & Oxygen, Hydrogen Tank, Oxygen Tank, Water Tank

Figure 4.3.2-40. Sterilized Solid Electrolyte H_2/O_2 Fuel Cell Volume Parameters without Three Day Battery (Nominal Case)

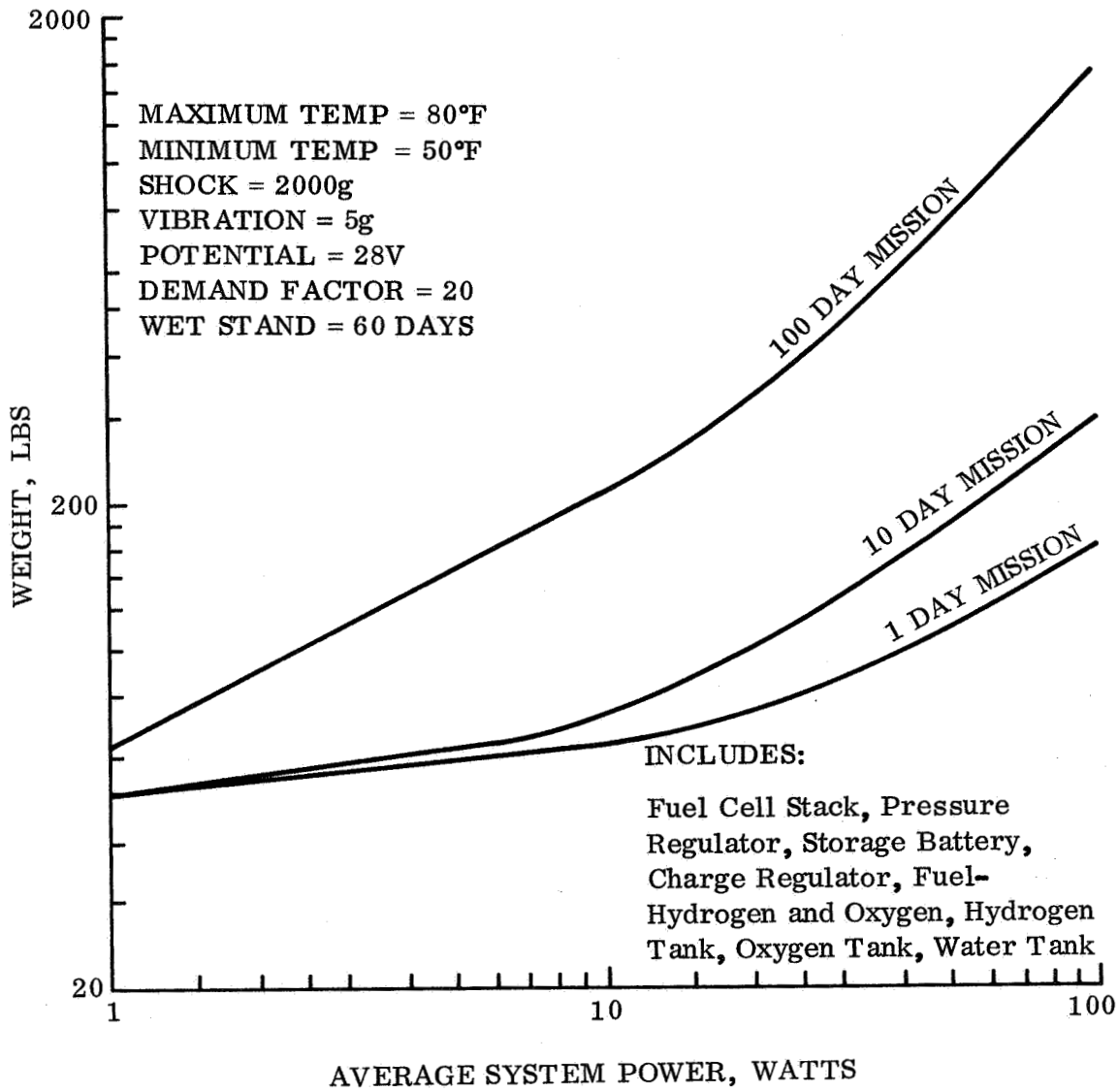

Figure 4.3.2-41. Sterilized Solid Electrolyte H_2/O_2 Fuel Cell Weight Parameters without Three Day Battery (Nominal Case)

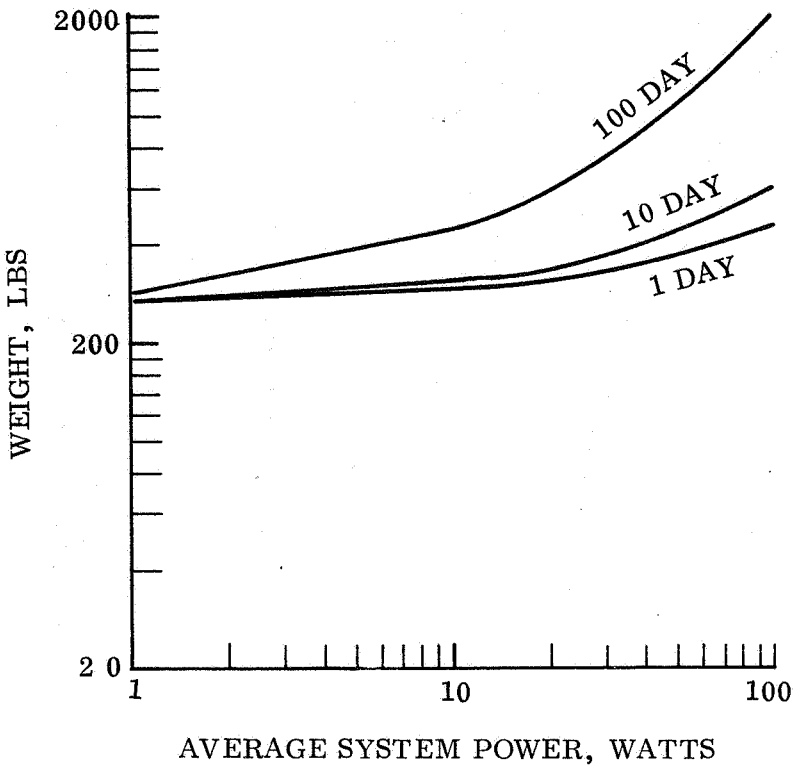

MAXIMUM TEMP = 90°F
MINIMUM TEMP = 45°F
SHOCK = 3000 g
VIBRATION = 30 g
DEMAND FACTOR = 30
POTENTIAL = 28 VOLTS
WET STAND = 300 DAYS
3 DAY MISSION BATTERY
WEIGHT = 178 LBS

INCLUDES:

FUEL CELL STACK, PRESSURE REGULATOR, STORAGE BATTERY, CHARGE REGULATOR, FUEL-HYDROGEN AND OXYGEN, HYDROGEN TANK, OXYGEN TANK, WATER TANK, RADIATOR

Figure 4.3.2-42. Sterilized Solid Electrolyte H_2/O_2 Fuel Cell Weight Parameters with Three Day Battery (Worst Case)

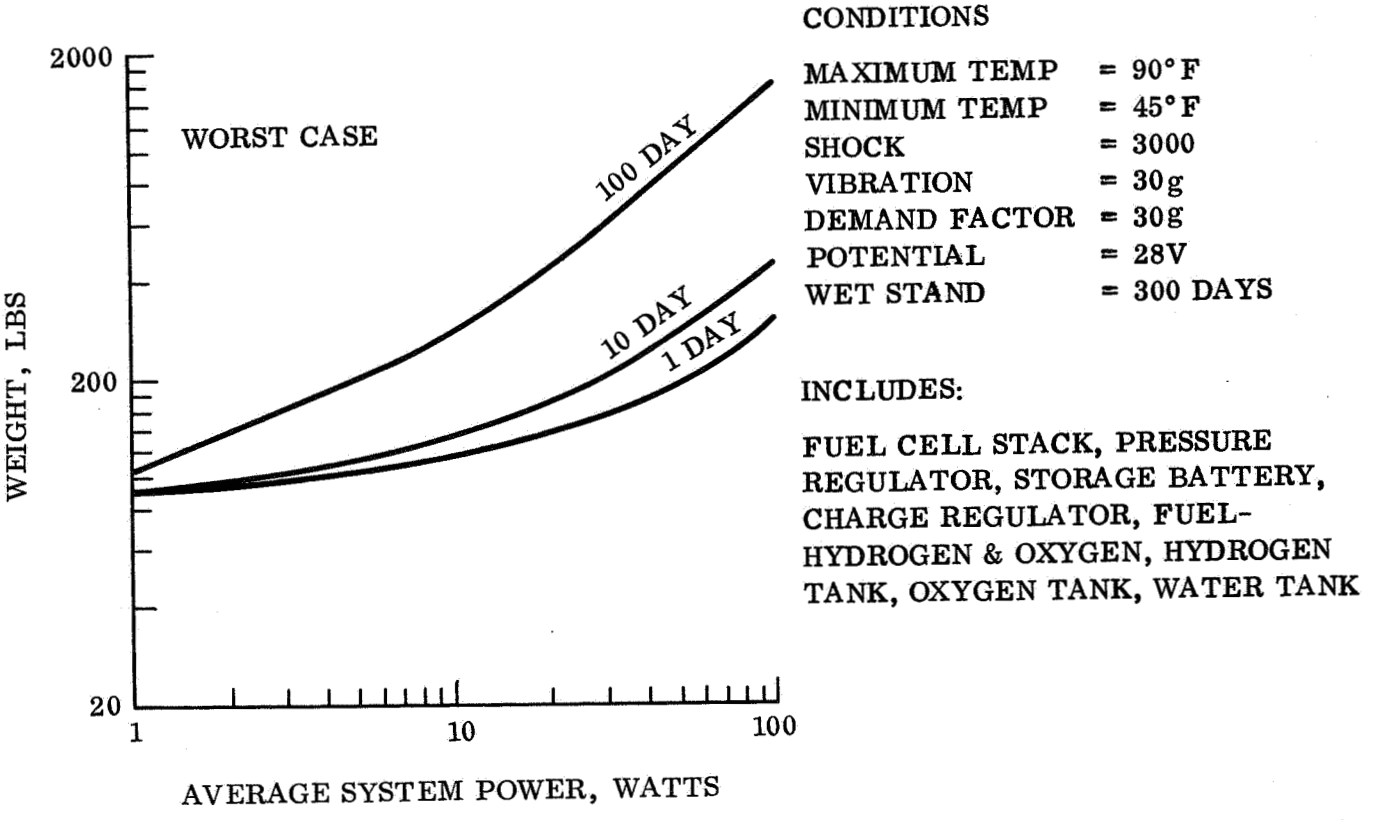

Figure 4.3.2-43. Sterilized Solid Electrolyte H_2/O_2 Fuel Cell Weight Parameters without Three Day Battery (Worst Case)

4.3.2.2.5 Regulators and Inverters Parametric Data

The regulator and inverter are impedance limited in small ratings and thermally limited in large sizes. High temperatures reduce the effectiveness of heat sinks requiring larger, heavier designs. At the very low temperatures increased semiconductor drive is required. To withstand the shock environment it is necessary to add potting materials in critical areas until, at the higher shock levels, the entire component is potted. This results in increasing weights to meet increased shock levels while the volume is constant.

These considerations form the basis for fig. 4.3.2-44 which shows isolating inverter weights and volumes. Fig. 4.3.2-45 provides similar data for non-isolating inverters.

4.3.2.2.6 Harness Parametric Data

Total vehicle harness weight was obtained by analyzing accumulated data from several previous harness configurations. The number of components, the number of connectors, the weight of the in-flight disconnect(s), and the length and base diameter were manipulated with an algebraic relationship and then summed to give the total harness weight. All of the analytical relationships were put into a computer program (ref. PIR 8253-8132). It is important to note that each parameter for the program is identifiable at the proposal stage.

A graph was plotted, see fig. 4.3.2-46, which shows the total harness weight for constant diameter vehicles as a function of the number of components contained within the volume.

For example, assume the following:

1. base diameter 34 inches

2. two connectors per component

3. total number of components

NOTE: The total vehicle harness weight is fifteen pounds. The height-to-width ratio is constant.

4.3.2.2.7 Inflight Disconnect Data

Electro-electro mechanical disconnect connectors have been incorporated. These connectors provide low impulse separation and have special roll off features to minimize entry errors caused by tip off or disconnect shock.

The design and parametric data of figs. 4.3.2-47 and -48 includes high temperature connector sealing techniques and the receptacles hardened for landing shocks.

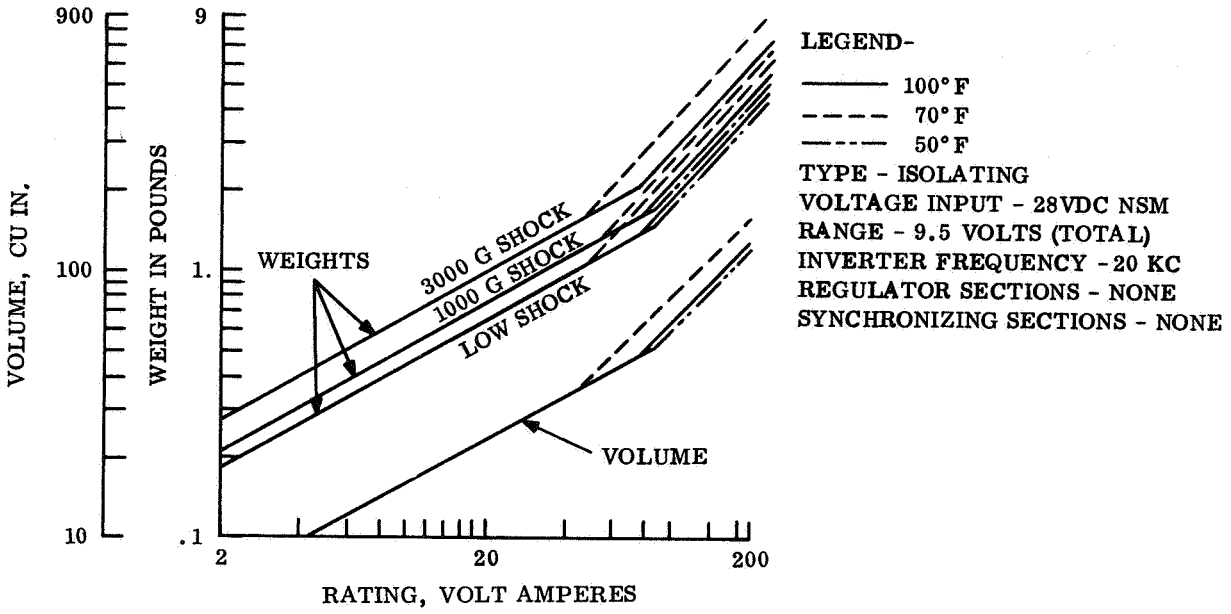

Figure 4.3.2-44. Electrical Power Inverter Parametric Curves

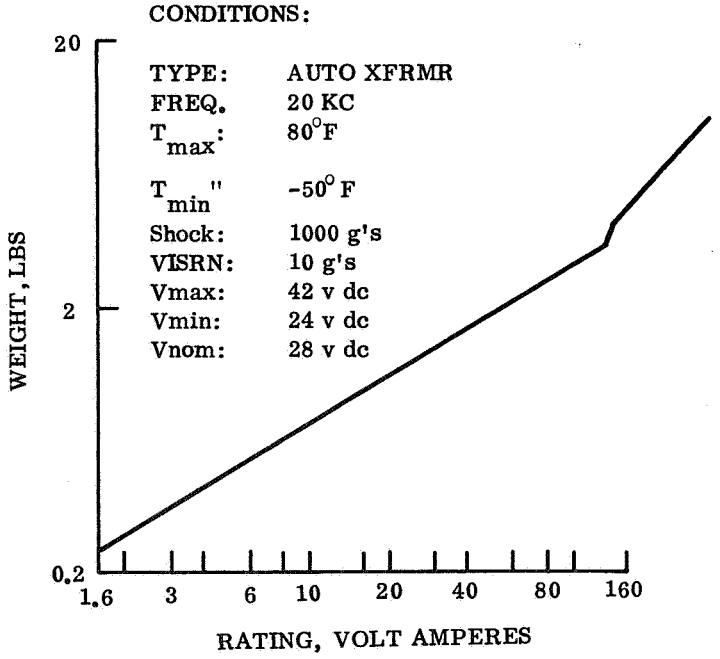

Figure 4.3.2-45. Inverter Weight Curve (Non-Isolating)

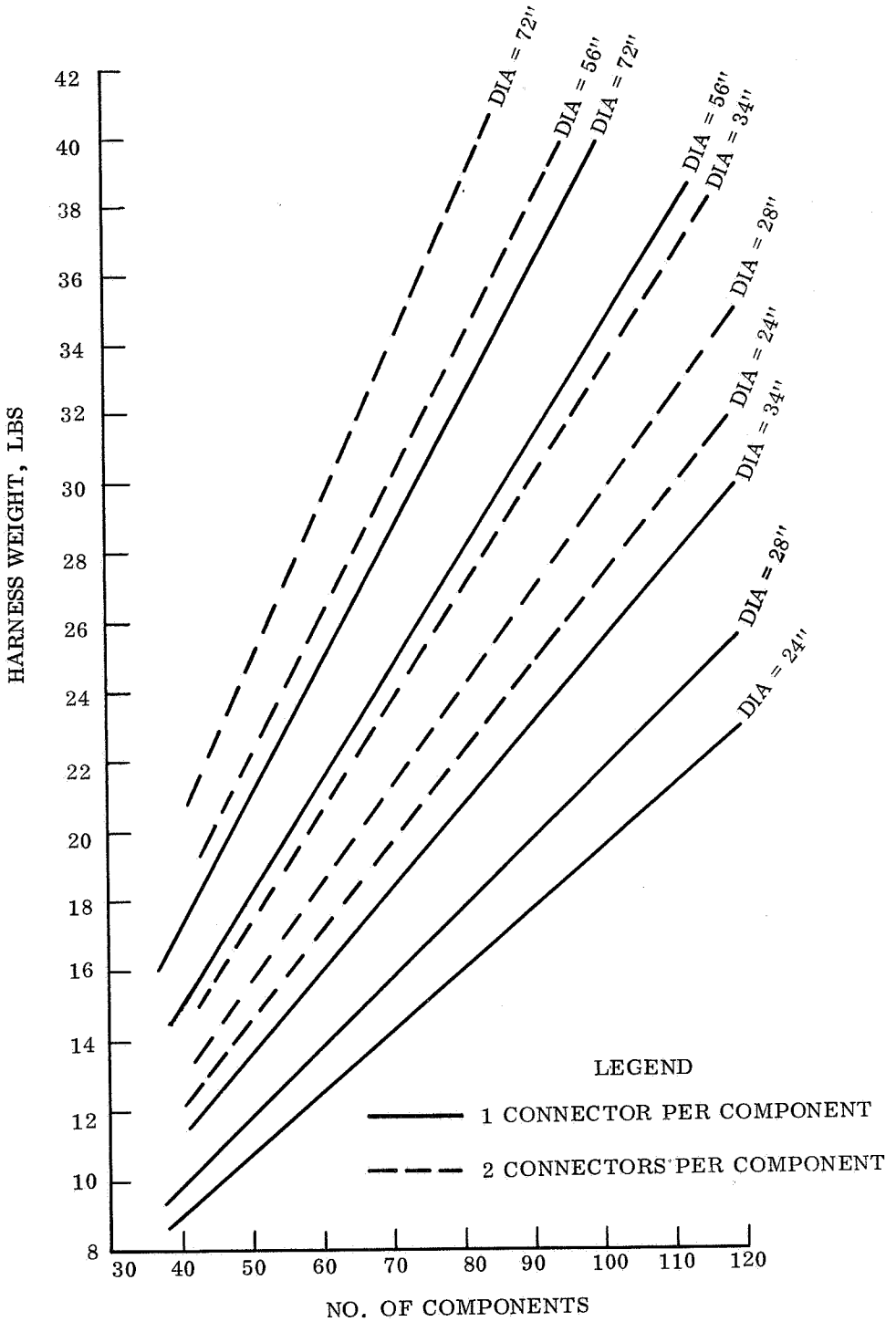

Figure 4. 3. 2-46. Harness Weight Parameters as a Function of Components

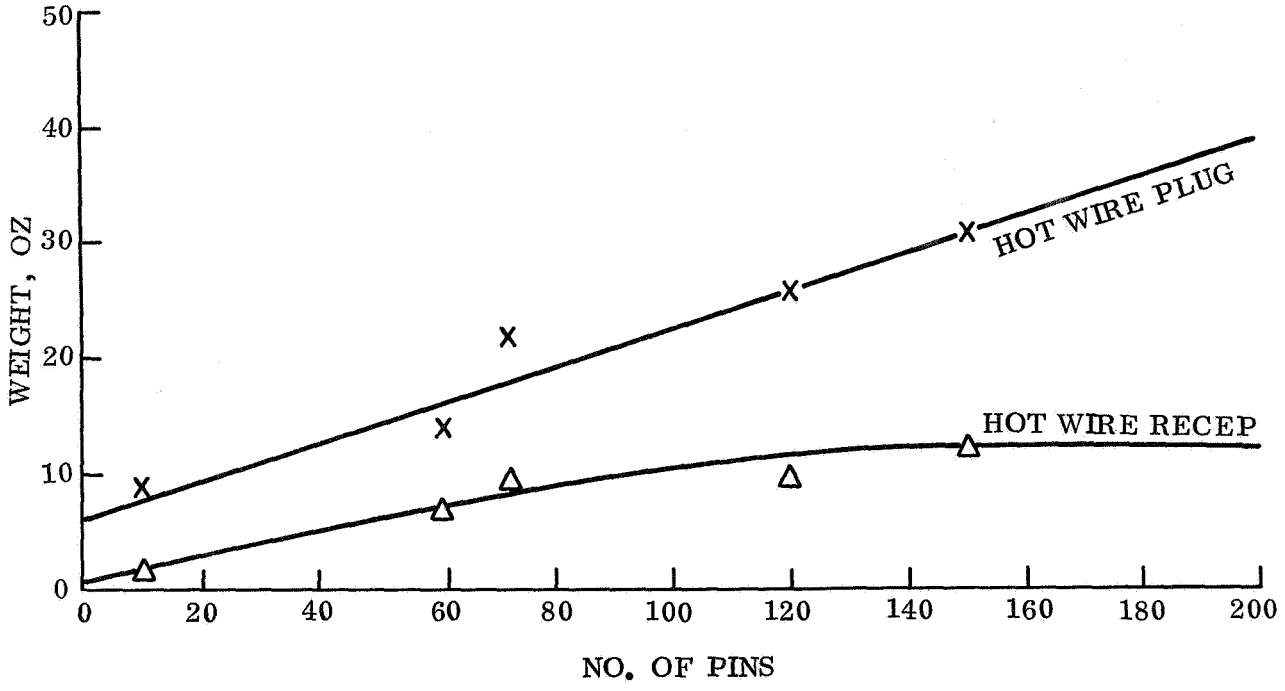

Figure 4.3.2-47. Inflight Disconnect Weight as a Function of Size 20 Contact Quantity

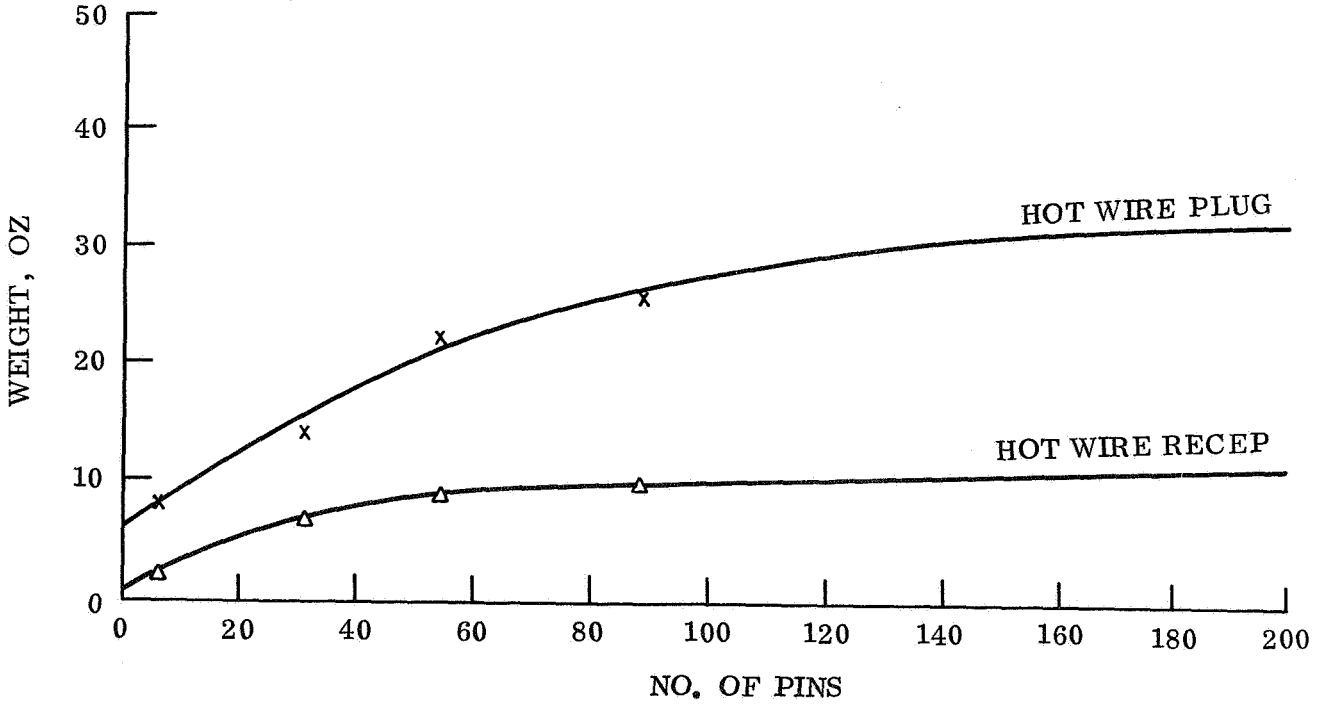

Figure 4.3.2-48. Inflight Disconnect Weight as a Function of Size 16 Contact Quantity

4.3.2.3 SYNTHESIS TECHNIQUES (Data Usage)

Examples will be used to introduce the interaction of the various components, mission requirements, the subsynthesis parametrics and the use of all the parametric curves.

4.3.2.3.1 Primary Battery Power Subsystem

In order to calculate battery weights and volumes outside the range of the parametric curves the following method may be adopted:

For batteries with no recharge facilities on the landed vehicle -

1. Select the nominal parametric curve, fig. 4.3.2-3
   Record the weight for the mission duration and power level, = W1

2. Select weight/TMAX curve, fig. 4.3.2-17
   W1 will change by (W (TMAX)/W (80))-1

3. Select weight/TMIN curve fig. 4.3.2-19
   W1 will change by (W (TMIN)/W (50))-1

4. Select weight/activated wet stand curve fig. 4.3.2-21
   W1 will change by (W (AWS)/W (60))-1

5. Select weight/Demand Factor curve fig. 4.3.2-14
   W1 will change by (W (DF)/W (20))-1

The new weight would be

W1 x (1 + Σ of the changes).

The new volume would be calculated in a similar manner.

For batteries having recharge facilities -

1. Select the nominal parametric curve, fig. 4.3.2-3.
   Record weight for average power at the one cycle discharge duration.

2. Perform sections 2 through 5 inclusive of previous para.

3. Calculate the depth of discharge considering both recharge rate and cycle life. If the charge period is less than $1/\alpha$, use fig. 4.3.2-49.

W1 = 555 lb

T Max Factor = (182/183)-1 = -0.004

T Min Factor = (87/87)-1 = -0

Demand Factor = (69/87)-1 = -0.207

Wet Stand Life = (185/195)-1 = -0.066

Weight = 555 (1-0.27) = 402 lbs

The new weight would be:

$$W_N = \frac{W2 \times (1 + \Sigma \text{ of changes}) \times 100}{\text{Depth of discharge}}$$

Example - Curve optimal case conditions used for check fig. 4.3.2-6

Power = 100 watts

Minimum duration = 10 days

T Max = 70° F

T Min = 50° F

Shock = 1000 g

Vibration = 0 g

Potential = 28 volts

Demand factor = 4

Wet Stand life = 0 days

4.3.2.3.2 Solar Cell Power Subsystem

The solar power subsystem contains a solar energy conversion panel, a storage battery for the night operation, a battery charge regulator and, if selected, tilting or orienting equipment.

As an example consider:

Landing Date ..... April 30, 1975
Landed Latitude ..... 10° North
Mission duration ..... 90 days

Establish the scientific measurement program and use figs. 4.3.1-1 and -2 to determine the system power demand in the extended mission.

For example:

Payload	Minimum science
Operation	Once per hour, 25 per day
Interrogation period	30 seconds each
Transmission time	2500 seconds per day

In this case from fig. 4.3.1-2 read:

P_{ave} = 10.3 watts and D.F. = 27.2

Determine the illumination parameters using figs. 3.6-1 and 3.6-4 from Section 3.6 of Volume II. For an April 30, 1968 landing note;

Illuminated period = 10.6 hours

Solar distance = 1.645 A.U.

Sun declination = 14.5°

In order to use these parameters it is necessary to examine the changes throughout the planned mission duration. In this case the Sun-Mars distance increases during the period April 30 to July 3, 1974 and then decreases for the balance of the 90 day mission. During the mission, the Sun declination increases from +14.5 degrees to +23.5 degrees with accompanying periods of illumination from 10 to 10.6 hours. If a non-tilted array is planned, the landed roll and pitch angles must be considered to conjunction with the Sun declination. Thus the worst case may occur on the first day, on the day when the tilt opposes the maximum Sun declination; on July 3, 1974, when the Mars-Sun distance is greatest, or on the last day of the mission when accumulated degradation is highest. For this example the worst case occurs on July 3, 1974; hence use

Illuminated period = 10.6 hours

Solar distance = 1.665 AU

Sun declination = 21.70

The next step is to compute the power required from the panel during illumination. This involves three factors: first, the panel must power the load and replace previously used battery charge during the illuminated period, second more ampere-hours must be returned to the battery than used due to charge inefficiency, and third, the charging must be done at a potential above the battery counter emf while in normal usage the available potential is below the battery emf due to the polarization. Figure 4.3.2-49 provides this information.

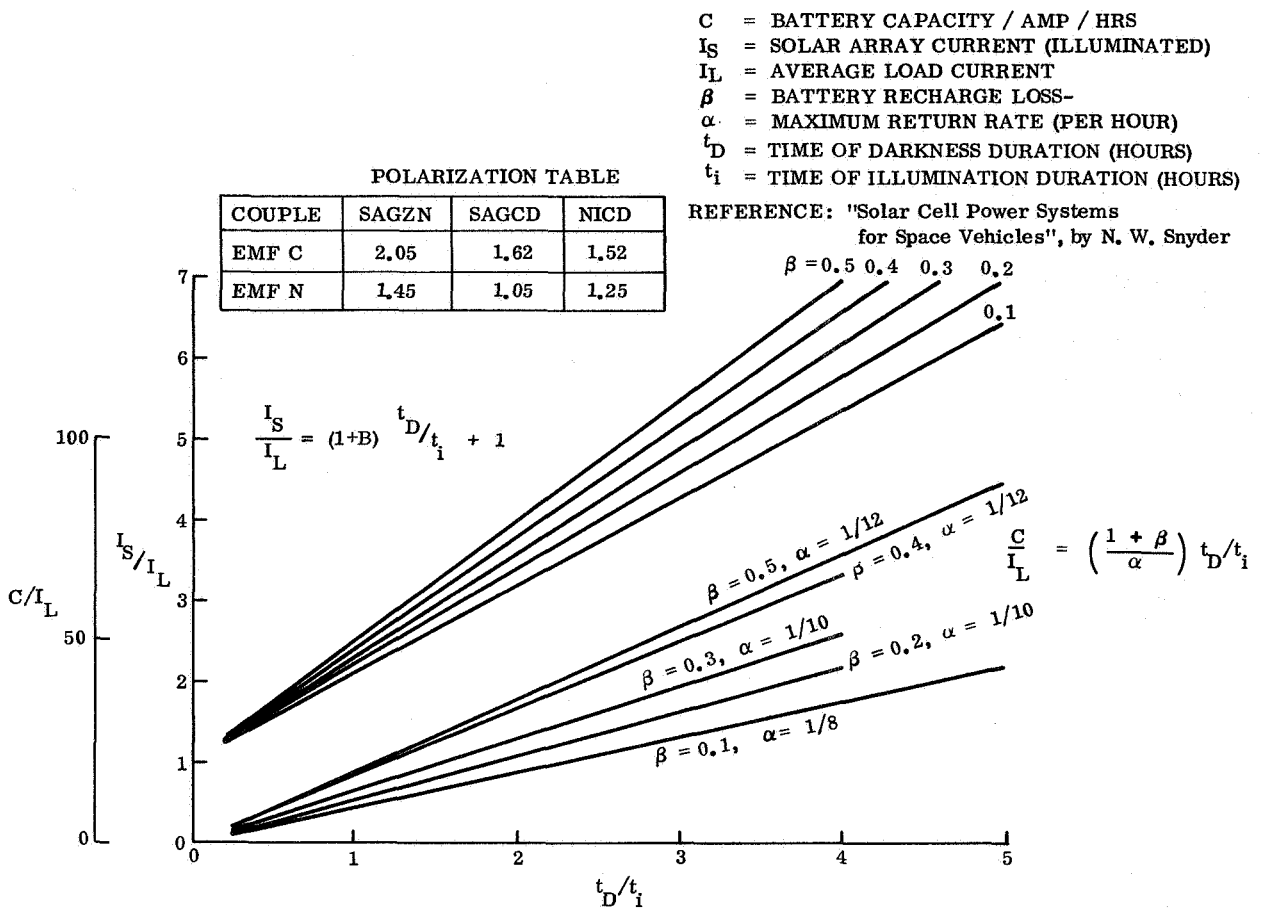

Figure 4.3.2-49. Solar Power Subsystem Rating Parametrics

To use this curve, compute the ratio of darkness to illumination as

$$\frac{t_D}{t_i} = \frac{24.62-10.6}{10.6} = \frac{14.02}{10.6} = 1.32$$

and find:

$$\frac{Is}{I_L} = 2.46.$$

For a 28 v system.

$$I_L = \frac{PAVE}{V_T} = \frac{10.3}{28} = 0.368 \text{ ampere}$$

Hence the solar panel average output current needed during illumination is:

$$Is = 2.46 \times 0.368 = 0.905 \text{ ampere}$$

This current must be delivered at a voltage given by:

$$V_p = \frac{EMFC}{EMFN} \times V_T + IR + ED$$

where ED represents the diode and regulator forward drops. Thus, using the polarization table given in fig. 4.3.2-49:

$$V_p = \frac{2.05}{1.45} \times 28 + 1.0 + 1.8 = 42.4 \text{ vdc}$$

From these values the panel output requirement is obtained as

$$P = VsIs = 42.4 \times 0.905 = 38.2 \text{ watts}$$

Next, the panel area may be determined. For the case at hand, using fig. 4.3.2-36, or if a single horizontal panel is considered, the power output will be 3.47 watts/ft sq (ideal).

The losses and degradations given in table 4.3.2-3 may be applied directly or as rms combined independent groups. By direct multiplication,

$$P_{end} = 3.47 \times 0.923 \times 0.939 \times 0.90 \times 0.993 \times 0.8 \times 0.956 \times 0.98 \times 0.939$$

$$= 1.89 \text{ watts/sq ft.}$$

NOTE

The loss factor may be adjusted for other application conditions as follows:

The orientation factor (OF) varies as the cosine of the orientation accuracy:

$$OF = \text{Cos } \theta$$

The filter transmission (TM) varies exponentially with thickness and UV exposure. The atmospheric attenuation depends on the pressure or density, e.g.,

$$TM = \frac{1}{10^{SL \times P}}$$

where $SL = 1.58 \times 10^{-4}$ per millibar and P is the pressure in millibars.

The loss of output caused by light diffusion which is produced by cover glass erosion will be of the form:

$$EF = 1.0 \text{ UEF } (1 - e^{\frac{-MD}{ETC}})$$

Where MD is the mission duration and ETC is the erosion time constant.

Where ultimate erosion factors, (UEF), between 0.05 and 0.20 have been observed and where the erosion period to 63 percent of ultimate, (ETC), depends on particle mass and velocity.

Since the biobarrier/canister protects Lander solar cells during interplanetary cruise and since the meteorites which penetrate the Martian atmosphere may be neglected in comparison to dust erosion, this factor is not used in the Lander analysis.

Spectral factors are obtained by the convolution of the frequency content of the filtered light at the point of operation with the particular solar cell response function. Considering the low density atmosphere of Mars, it is assumed that the spectral content of sunlight at Mars is identical to A. M. O. sunlight near Earth. Any selective filtering produced by the blue haze or clouds is included in the cloud attenuation factor.

Returning to the numerical example, the active panel area (APA) required is:

$$\text{APA} = \frac{P}{P_{\text{end}}} = \frac{38.2}{1.89} = 20.2 \text{ ft}^2$$

Of course, portions of the panel involve inactive material so that the total panel area (TPA) is obtained using the packing factor (PF). In this case,

$$\text{TPA} = \frac{\text{APA}}{\text{PF}} = \frac{20.2}{0.85} = 23.8 \text{ ft}^2$$

Now the panel dimensions for stowed condition may be computed. It is recognized that for unfolded flexural rigidity and adequate beam strength the unfolded panel length to width ratio should be less than six. Physical layout limitations will define the maximum panel width (MPW); thus, the number of panels (NP) required may be determined as:

$$\text{NP} = \frac{\text{TPA}}{6 \times \text{MPW}}$$

In a non-hammerheaded design where the maximum panel width, MPW, is approximately 18 inches, (1.5 ft).

$$\text{NP} = \frac{23.8}{6 \times 1.5} = 2.6 \approx 3 \text{ panels}$$

With each panel being 0.5 inch thick, and with 20 percent of the stack height assigned to elevating mechanisms, the number of sub panels (NSP) is determined as:

$$\text{NSP} = \frac{\text{FPH}}{0.5} \times 0.8 = 1.6 \text{ FPH}$$

where FPH is the vehicle "flat pack" height.

For a vehicle 16.5 inches high,

$$NSP = 1.6 \times 16.5 = 26 \text{ subpanels}$$

The area of each panel (AP) is

$$AP = \frac{TPA}{NP} = \frac{23.8}{3} = 7.93 \text{ ft}^2$$

and the area of each subpanel (SPA) is

$$SPA = \frac{AP}{NSP} = \frac{7.93}{26} = 0.305 \text{ ft}^2$$

Sine each panel and hence each subpanel is 18 inches across, the width of the subpanel (WSP) is:

$$WSP = \frac{SPA}{MPW} = \frac{0.305}{1.5} = 0.203 \text{ ft} = 2.45 \text{ inches}$$

Allowing 1/4-inch clearance on all sides, the stowed solar array will consists of three packages, each having the dimensions $16.5 \times 18.5 \times 3.45$ inches.

Next, the panel weight is determined. For an example at 1000 g's, fig. 4.3.2-37 and table 4.3.2-1 provide:

Structure	0.700 lb/ft^2
Cells and attach	0.287 lb/ft^2
TOTAL	0.987 lbs/ft^2

Thus the panel weight (WP) is

$$WP = TPA \times \rho$$
$$= 23.8 \times 0.87 = 23.5 \text{ lb}$$

Note: The actuating linkage and drive mechanism weights must be added to the panel weight to obtain the total solar array weight.

To establish the battery rating refer once again to fig. 4.3.2-23. The battery rating is determined by the charge removed during the darkness period and either of two depth of discharge criteria. One such criteria is the discharge limit set by the maximum rate at which the battery will accept charge; the other is cycle life limitations of the battery separators, this life limitation being logarithmically related to the depth of discharge.

From fig. 4.3.2-49 at a darkness-illumination ratio of 1.32, it is found that $C/I_L = 14.6$.

On the other hand, from fig. 4.3.2-15 it is seen that at 90 cycles plus, say, another 10 cycles for checkout and interplanetary cycling, a total of 100 cycles, the depth of discharge is 34 percent. Then,

$$0.34\,C = I_L \times 10.6 \text{ or } C/I_L = \frac{10.6}{0.34} = 31.2$$

Thus using the limiting case the battery rating is

$$C = 31.2\,I_L = 31.2 \times 0.368 = 11.5 \text{ ampere-hours}$$

and

$$E = VT \times C = 28 \times 11.5 = 323 \text{ watt-hour.}$$

From fig. 4.3.2-1, or more directly fig. 4.3.2-23 and -24, using a 14.1 hour discharge, it is seen that the battery has:

Weight = 19.5 lbs

Volume = 320 cu in.

Of course, in many cases an operational battery is defined by the power needs for entry and the first few days of operation with imagery. If such requirements provide a larger battery than is required for the extended mission as calculated above, the larger battery should be used for the extended mission as well because the resultant reduction in depth of discharge will permit operating in the high output efficiency monovalent region, will enhance battery charge efficiency and will increase the applied cycle life.

A further step is to define the charge regulator which controls the flow of power from the solar array to the battery and operating electrical/electronic system loads. The regulator must handle both the panel open circuit voltage - during trickle charging, and the panel short circuit current - when addressing a discharged battery.

Since a solar cell that initially delivers in the order of 10 mw/cm^2 has an open circuit voltage of 0.701 volt and a short circuit current of 0.066 ampere the regulator rating may be estimated by

$$VA = \frac{0.701 \times 0.066}{10 \times 10^{-3}} P = 4.6\,P$$

$$= 23.8 \times 4.6 = 110 \text{ volt amperes.}$$

From the curve for non-isolating inverters which could be used for buck-boost operation, fig. 4.3.2-45.

Weight = 1.43 lbs

Volume = 53 cu in.

Finally, the orientation equipment is considered. The above panel calculations are predicated on a horizontally deployed array. If it may be assumed that the vehicle landed within 15° of level, no further equipment is needed. Otherwise provision must be made for a single tilting action to bring the panel to a level position.

Using table 4.3.2-2 for three panels,

Level sensors	0.6
Amplifier (signal)	0.4
Power amplifier	0.5
Drive mechanisms	24.0
	25.5 pounds

The total subsystem weight is

Panel	23.5
Battery	19.5
Regulator	1.43
Orientation equipment	25.5
	69.9 pounds

4.3.2.3.3 Radioisotope Thermoelectric Generator (RTG) Power Subsystem Parametrics

The RTG power subsystem contains a thermoelectric heat energy to electrical energy converter unit, the RTG; a power inverter, a voltage regulator, and a storage battery.

As an example, consider the following extended mission:

Payload: minimum scientific payload

Operation: Once per hour, 25 per day

Interrogation Period: 30 seconds each

NOTE

A single panel configuration would produce a 53.5 lb total.

These calculations have been performed for different parameter values and the reader may obtain the results for many of the practical cases from the resulting subsystem curves given in figs. 4.3.2-50 through 54. These calculations were performed via programs on the GE 605/Datanet 30 digital computer.

In this case from fig. 4.3.1-1 read:

Pave - 20.3 watts and D.F. - 27.2

First determine the converter/radiator package size and weight. This depends on the fuel age (P_u^{238} has an 89 year half-life), the environmental temperature, the heat rejection fin view angle, and the nuclear radiation shielding, if any. Parametric data may be presented in terms of converter output or net output to the user. These differ by the amount of inverter loss, regulation loss, and battery charging losses.

Next, the inverter is sized. RTG units usually achieve about 5 percent efficiency in the heat to electric energy conversion. Hence, it is necessary to extract and make available as much electrical power as possible. This is achieved by impedance matching per the maximum power transfer theorem. For this reason an isolation inverter with an impedance matching transformer is used. The output voltage from the RTG depends on the limited number of thermoelectric elements for which there is installation space.

Thus the output voltage is proportional to the RTG rating. The impedance matching transformer also steps the voltage to the desired level, e.g., 28v.

Figure 4.3.2-44 is used to find the inverter weight and volume:

Weight - 1.01 lbs

Volume - 33.5 cu in.

The voltage regulation may be considered next. The impedance matching described in the previous step will produce a 2 to 1 voltage change as the electrical demand goes from no load to full load. To meet this requirement, regulation is introduced, usually in connection with the inverter - either on the ac side or as a post rectification section. Although this is usually packaged with the inverter, a reasonable estimate of the parametric variations may be obtained by using fig. 4.3.2-45.

In this example:

Weight - 0.6 lb

Volume - 20 cu in.

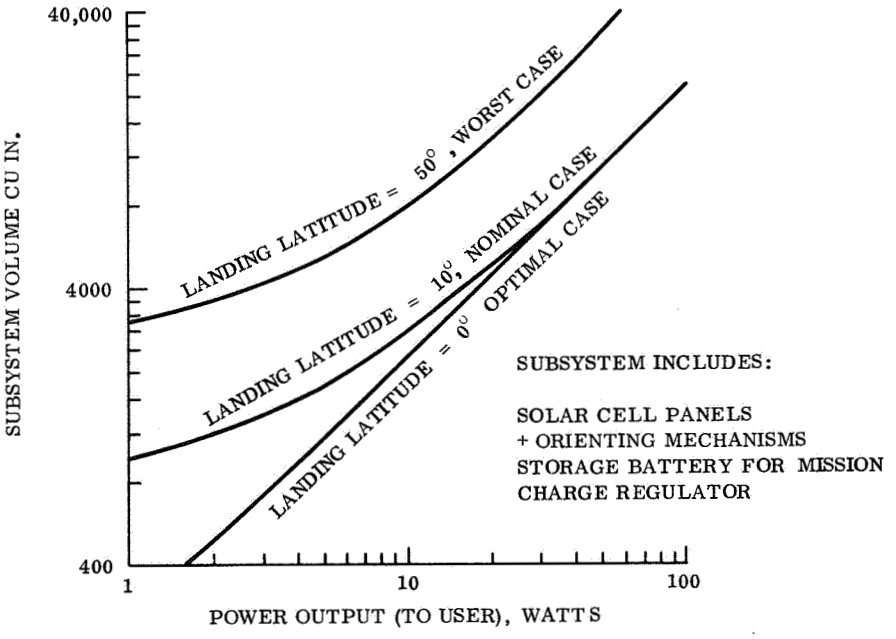

CONDITIONS

Battery Conditions

Batt Type = Sterilized Silver Zinc

	Optimal	Worst	Nominal
Max Temp	70° F	90° F	80° F
Min Temp	50° F	40° F	50° F
Shock	1000 G	3000 G	2000 G
Vibration	0 G	30 G	5 G
Activated Wet Stand	0 Days	300 Days	60 Days
Minimum Voltage	24 V	24 V	24 V
3 Day Battery Weight	0 lbs	55.7 lbs	178 lbs

Solar Power Reference Conditions

Heliotek 8-mil thick; 11% eff.; 1×2 cm cells in a flat pack array with an electric mechanism to provide horizontal orientation

Orientation half-angle accuracy = 15°

Surface angle to local horizontal = ±15° max

Planetary Day = 24.62 hours

Panel angle to local horizontal = 0°

	Optimal	Worst	Nominal
Solar latitude	-6°	-6°	-6°
Time of illumination of Solar Panel	10.3 hrs/day	7.9 hrs/day	10.1 hrs/day
Mars - Sun Distance	1.6310 A.U.	1.5530 A.U.	1.6310 A.U.

Figure 4.3.2-50. Solar Power Volume Parameters for Optimal, Worst, and Nominal Cases Based on Landing January 10, 1974

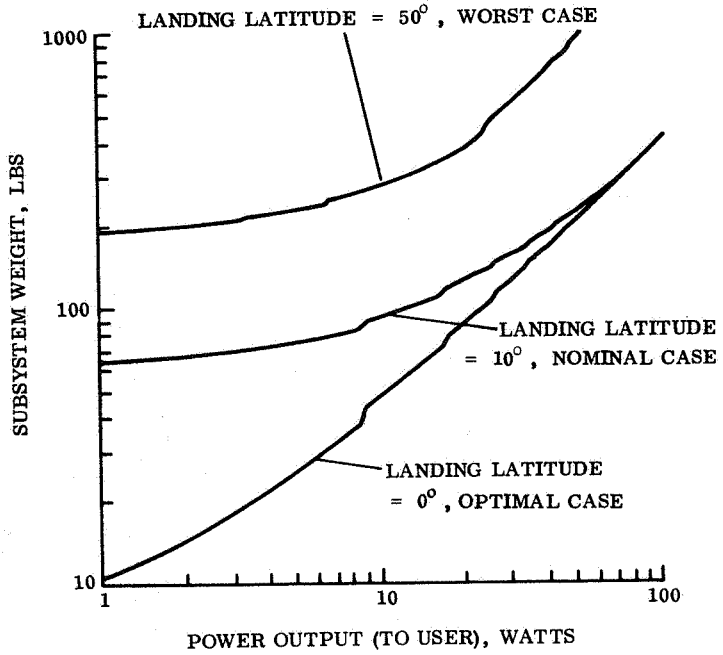

CONDITIONS

Battery Conditions

Batt Type = Sterilized Silver Zinc

	Optimal	Worst	Nominal
Max Temp	70°F	90°F	80°F
Min Temp	50°F	40°F	50°F
Shock	1000 G	3000 G	2000 G
Vibration	0 G	30 G	5 G
Activated Wet Stand	0 Days	300 Days	60 Days
Minimum Voltage	24 V	24 V	24 V
3 Day Battery Weight	0 lbs	55.7 lbs	178 lbs

Solar Power Reference Conditions

Heliotek 8-mil thick; 11% eff.; 1 × 2 cm cells in a flat pack array with an electric mechanism to provide horizontal orientation

Orientation half-angle accuracy = 15°

Surface angle to local horizontal = ±15° max

Planetary Day = 24.62 hours

Panel angle to local horizontal = 0°

	Optimal	Worst	Nominal
Solar latitude	-6°	-6°	-6°
Time of illumination of Solar Panel	10.3 hrs/day	7.9 hrs/day	10.1 hrs/day
Mars - Sun Distance	1.6310 A.U.	1.5530 A.U.	1.6310 A.U.

Figure 4.3.2-51. Solar Power Weight Parameters for Optimal, Worst, and Nominal Cases Based on Landing January 10, 1974

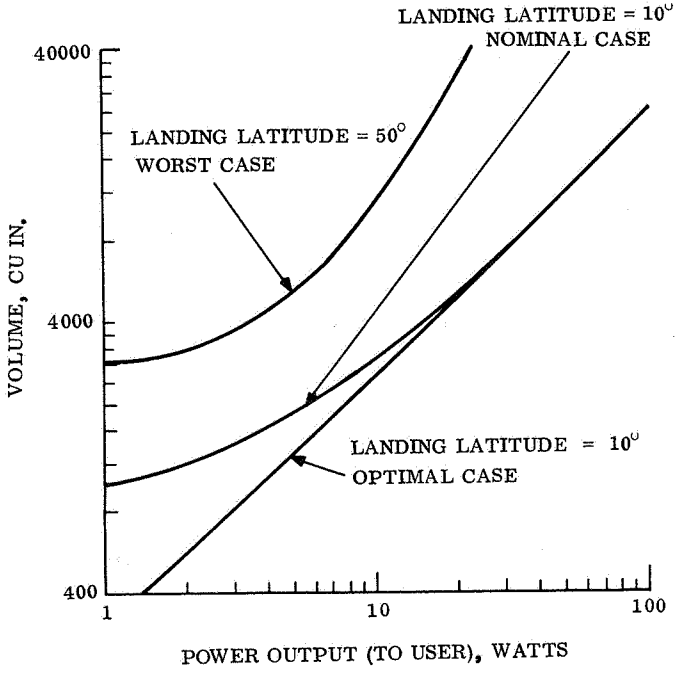

BATTERY CONDITIONS:

Type of Battery - Sterilized Silver-Zinc

CASE:	OPTIMAL	NOMINAL	WORST
Max Temp	70°F	80°F	90°F
Min Temp	50°F	50°F	45°F
Shock	1000 G	2000 G	3000 G
Vibration	0 G	5 G	30 G
Min Voltage	24 V	24 V	24 V
Activated Wet Stand	0 Days	60 Days	300 Days
Weight of 3-Day Battery	0 lbs	55.7 lbs	178.0 lbs

SOLAR POWER SUBSYSTEM REFERENCE CONDITIONS

ARRAY

Heliotek 8-mil thick; 11% eff.; 1 × 2 cm cells. Panel is oriented parallel to horizontal once by an electric mechanism.

ENVIRONMENT

Orientation Half-Angle Accuracy = 15°
Planetary day = 24.62 hrs.
Surface Angle to Landed Position = 15°
Panel Angle to Local Horizontal = 0°

CASE	OPTIMAL	NOMINAL	WORST
Solar Latitude	23.5 N	23.5°N	14.5°N
Time of Illumination of Panel	10.5 hrs/day	10.5 hrs/day	11.5 hrs/day
Mars to Sun Distance	1.648 A.U.	1.649 A.U.	1.645 A.U.

Figure 4.3.2-52. Solar Power Volume Parameters for Optimal, Worst, and Nominal Cases Based on Landing April 30, 1974

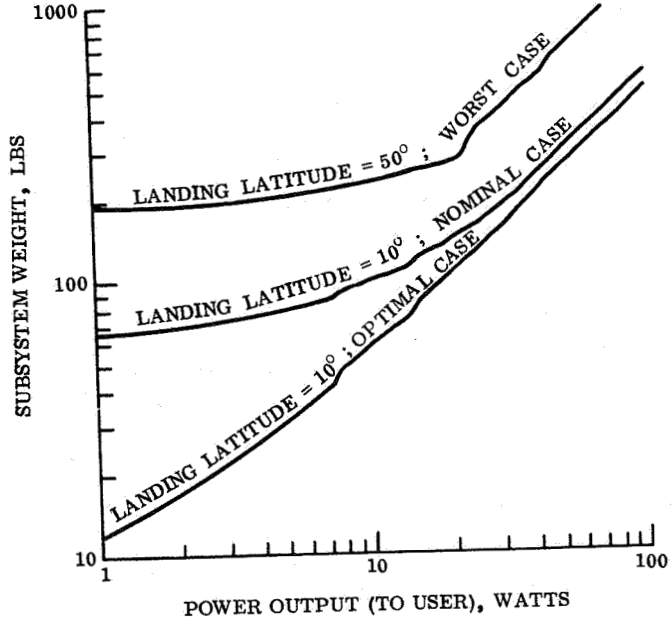

BATTERY CONDITIONS:

Type of Battery - Sterilized Silver-Zinc

CASE	OPTIMAL	NOMINAL	WORST
Max Temp	70°F	80°F	90°F
Min Temp	50°F	50°F	45°F
Shock	1000 G	2000 G	3000 G
Vibration	0 G	5 G	30 G
Min Voltage	24 V	24 V	24 V
Activated Wet Stand	0 Days	60 Days	300 Days
Weight of 3-Day Battery	0 lbs	55.7 lbs	178.0 lbs

SOLAR POWER SUBSYSTEM REFERENCE CONDITIONS:

ARRAY

Heliotek 8-mil thick; 11% eff.; 1 × 2 cm cells. Panel is oriented parallel to local horizontal once by an electric mechanism.

ENVIRONMENT

Orientation half-angle accuracy = 15°F
Planetary Day = 24.62 hrs
Surface Angle to Landed Position = 15°
Panel Angle to Local Horizontal = 0°

CASE	OPTIMAL	NOMINAL	WORST
Solar Latitude	23.5°N	23.5°N	14.5°N
Time of Illumination of Panel	10.5 hrs/day	10.5 hrs/day	11.5 hrs/day
Mars to Sun Distance	1.649 A.U.	1.649 A.U.	1.645 A.U.

Figure 4.3.2-53. Solar Power Weight Parameters for Optimal, Worst, and Nominal Cases Based on Landing April 30, 1974

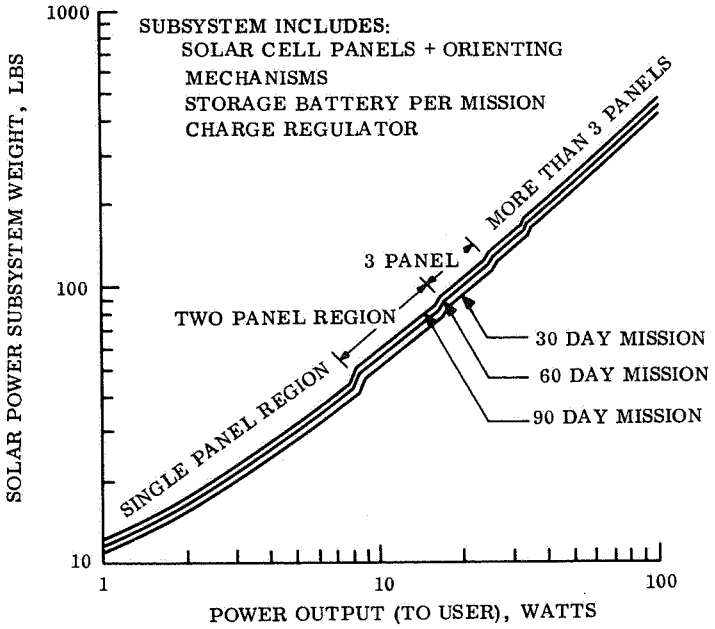

CONDITIONS:

BATT. TYPE: STERILIZED SILVER ZINC
MAX TEMP. = 80°F
MIN TEMP. = 50°F
SHOCK = 1000 G
VIBRATION = 10 G
ACTIVATED WET STAND = 60 DAYS
NOMINAL POTENTIAL = 28 V
MINIMUM VOLTAGE = 24 V
CYCLES = MISSION DURATION
MAX. SINGLE BATTERY WEIGHT = 200 LBS

SOLAR POWER REFERENCE CONDITIONS:

LANDING CONDITIONS DEVELOPED FROM APRIL 30, LANDING AT 10° NORTH MARS LATITUDE
HELIOTEK 8-MIL 11% EFF 1 x 2 CM CELLS
FLAT PACK ARRAY WITH HORIZONTAL ORIENTATION BY ELECTRIC MECHANISM
ORIENTATION HALF-ANGLE ACCURACY = 15°
MARS - SUN DISTANCE = 1.6495 A.U.
PLANETARY DAY = 24.62 HRS
SURFACE ANGLE TO LOCAL HORIZONTAL = ±15° MAX.
TIME OF ILLUMINATION OF SOLAR CELL PANEL = 10.6 HRS/DAY
PANEL ANGLE TO LOCAL HORIZONTAL = 0°
SOLAR LATITUDE = 14.5°N

Figure 4.3.2-54. Solar Power Volume Parameters for Various Mission Durations Based on Landing April 30, 1974

Finally, the storage battery rating is established. The RTG produces power from the conversion of isotope decay heat into electricity. Since the isotope heat is continually released, based on an 89 year half-life, the RTG is always capable of delivering maximum rated power and any power that is not used represents energy lost. Hence, to permit rating the RTG at the average power level rather than at the peak demand, a storage battery is used. This battery must provide the amount the instantaneous demand exceeds the average value.

Although the general approach to battery specification for an RTG power subsystem is identical to the solar cell case it should be noted that, unlike the solar cell case with the RTG, the battery performs its operation over rather short time intervals with the balance of the day available for recharge. In power profiles of the type summarized in figs. 4.3.1-1 and -2 about 67 percent of the energy is delivered when the power demand exceeds average. Thus the following applies:

Pave system = 10.3; DF (syst) = 27.2 and the associated battery parameters are given by,

$$\text{Pave (Bat)} = \text{FB Pave (syst)} \frac{(1 - TD/TC)}{TD/TC}$$

and

$$\text{D.F (Bat)} = \frac{(\text{D F (syst)} - 1)\ TD/TD}{\text{FB}\ (1 + TD/TC)}$$

where FB is the faction of energy delivered by the battery, TD is the battery discharging period and TC is the battery charing period.

For TD/TC = 0.0422; e.g., 0.8 hour transmission plus 0.2 hour data collection and therefore for a one hour discharge period and a 23.62 hour charge period, with FB = 0.67;

$$P_{ave}\ (\text{Bat}) = 0.67 \times 10.3\ (1.0422) = 171 \text{ watts}$$

$$DF = \frac{(27.2-1)\ (0.0422)}{0.67\ (1.0422)} = 1.58$$

Using figs. 4.3.2-26 and -27, for 90 cycles of operation the battery required has,

Weight = 26.0 lb

Volume = 410 cu in.

The results of similar calculations are illustrated in figs. 4.3.2-55 and -56.

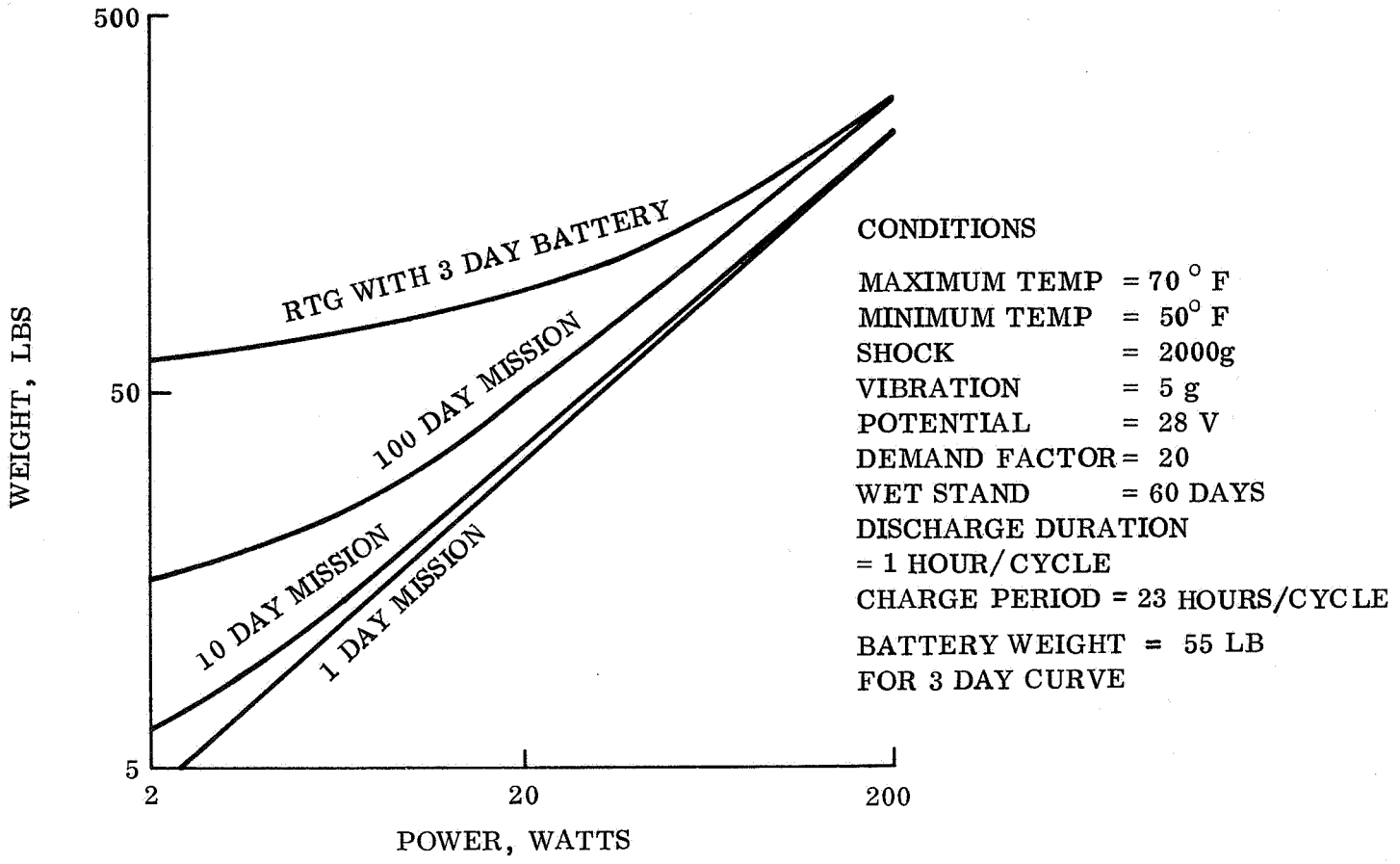

Figure 4.3.2-55. RTG Nominal Case Weight Parametrics

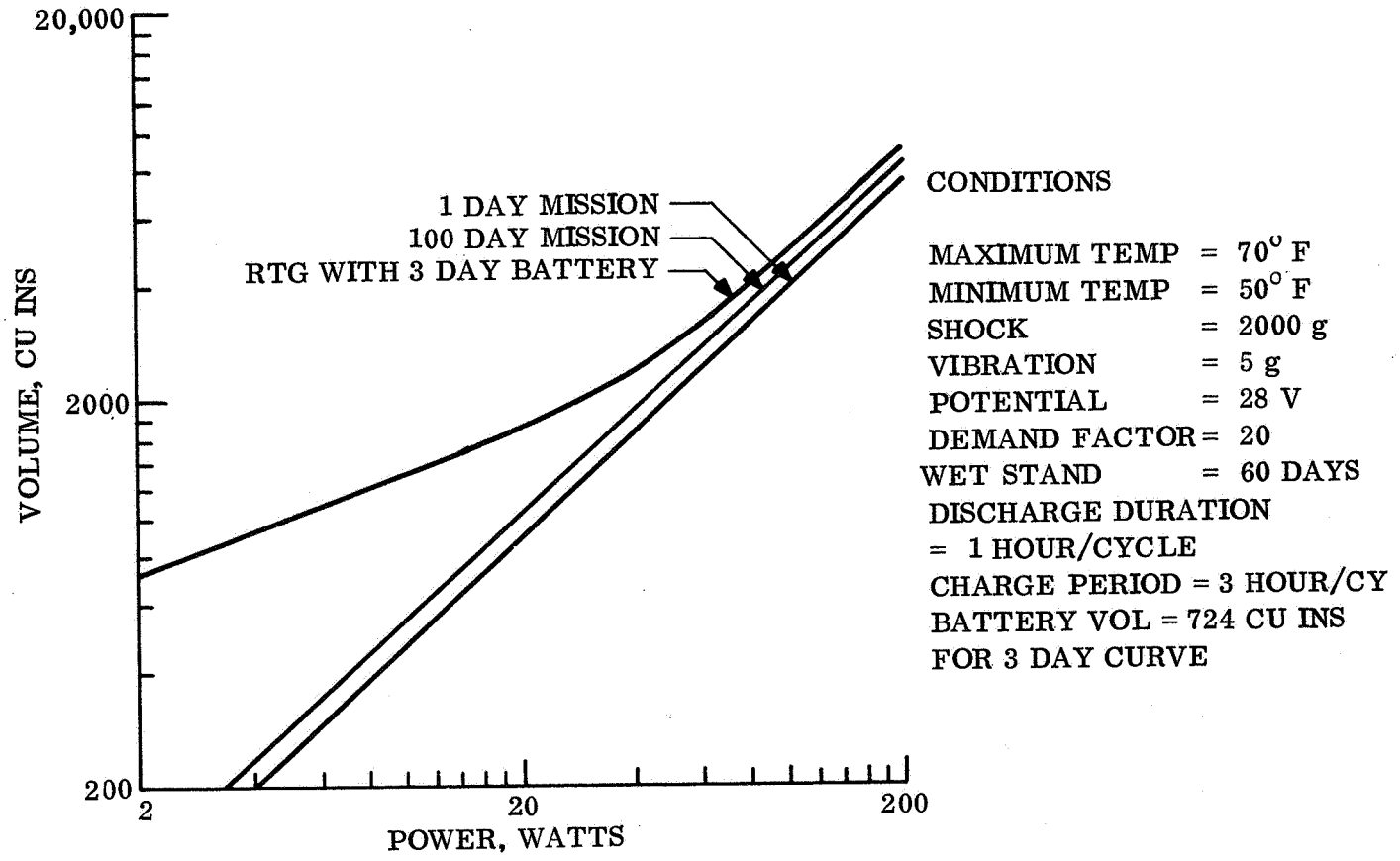

Figure 4.3.2-56. RTG Nominal Case Volume Parametrics

4.3.3 TRADE-OFF STUDIES

4.3.3.1 Solar Power Trade-offs

Figure 4.3.3-1, Solar Cell Power Subsystem Comparison Curve, provides trade-off data on the method of orientation for a solar array landed on January 10, 1974 at various landing latitudes. Factors which had major effects on the weight of the power system were 1) the time of illumination of the panel; 2) the angle of the Sun with respect to the panel, which was a function of latitude and orientation method; 3) variation of Mars-Sun distance; 4) the lack of orienting mechanism in the case of a non oriented array.

The curves of fig. 4.3.3-1 can be used to determine the optimum orientation method, from a weight standpoint, for any given latitude. For example, at 10° (or any latitude) the continuously Sun-oriented array produces the lightest system. However, the second-lightest system, the non-oriented array, would be the best overall choice if reliability were considered. At greater landing latitudes, the problem is more difficult, since the weight differences between the various tilted arrays become significant and the weight of the non-tilted is greatest. At high latitudes, the once Sun-tilted array will be the best overall choice, although the continuously Sun-oriented array is lightest. Thus, for 10°, the landing latitude of greatest interest, the non oriented array is the best design. The non-oriented array weight was developed on the assumption that chances of landing in a valley or on a steep slope were quite remote. In all cases, 15° of masking of the Sun morning and evening was assumed, and a landed slope of 15° away from the Sun was determined the worst tilt likely to be encountered.

In a similar manner, trade-offs may be performed evaluating the benefits of different landing dates. These parametric results are summarized in figs. 4.3.3-2 through -5 for landing sites at 25°N and 10°N latitude. These curves are based on solar panels having a leveled attitude within 15° of horizontal; a condition which may be achieved either by landing on relatively level terrain, figs. 4.3.3-2 and -3, or through the use of orienting mechanisms to level the array following unfolding, as shown by figs. 4.3.3-4 and -5. Other conditions selected for this trade-off study are noted in the figures.

The results show that in 1974 for the higher latitude, e.g., 25°N, the later landing dates, such as June through August will minimize solar power subsystem weight and size. On the other hand, for a 10°N latitude site in a 1974 encounter, the landing date has very little influence on weight, the earlier date having a slight advantage. In comparing 25°N latitude and 10°N latitude sites, it is seen that the 10°N site requires less solar power equipment weight for landing prior to March 15th while the 25°N latitude design is together thereafter when using non-oriented arrays which are nearly horizontal.

4.3.3.2 Parametrics for Power Source Selection

The power source loci curves of weight and volume provide a means for rapidly selecting a power source type giving the lightest weight or smallest volume for a given mission duration.

The curves separating the power source regions have been determined by superimposing the power source parametric curves from Section 4.3.2. The crossover point where two sources have the same weight or volume is found.

The constant weight or volume lines are also found from the superimposed parametric curves. It is clear that for a given weight in the battery range, the minimum duration will get shorter if average power is increased. When the boundary line is crossed into the fuel cell region, the slope changes and is a function of hydrogen and oxygen usage. If the boundary line into the solar array is crossed, the constant weight lines become almost horizontal with increasing minimum duration. A decrease in power with increasing mission duration is a function of solar cell decay and increasing battery size to provide more cycles. The RTG range is similar to the solar array range.

Figs 4.3.3-6 and -7 are weight and volume loci for batteries, solar arrays, fuel cells and RTG's with a three day mission duration battery instead of a topping battery. The high power density of the RTG completely obliterates the fuel cell and solar array. Since economic considerations may limit RTG usage to extremely long missions. Figs. 4.3.3-8 and -9 show the same curve without the RTG. In these it can be seen that a fuel cell is competitive on a weight basis only. The fuel storage volume is the major reason why the fuel cell does not show in the volume loci. Further, the fuel cell's competitive region is above 55 watts for mission durations near seven days.

Figs. 4.3.3-10 and -11 are the loci curves that include the three-day mission battery as a topping battery instead of a minimum battery sized for the extended mission. The RTG has not been considered for the same reason as explained earlier. Very little volume advantage is gained by the solar array, but both the fuel cell and battery operating areas expand when the three day battery weight must be carried with the solar cells.

Directing attention to the case where a three day battery is carried for early mission assurance and examining the battery/fuel cell/solar cell sources, fig. 4.3.3-10 shows that Mars Hard Lander weight savings will result from using batteries for missions having duration up to about 18 days and using solar cells for extended missions.

Similarly, fig. 4.3.3-11 indicates Mars Hard Lander volume savings result from using batteries for missions with planned durations up to about 30 days and solar cells for more extended durations.

It should be noted that higher shock levels would extend the battery region since the battery size and weight are least influenced by the high shock environment.

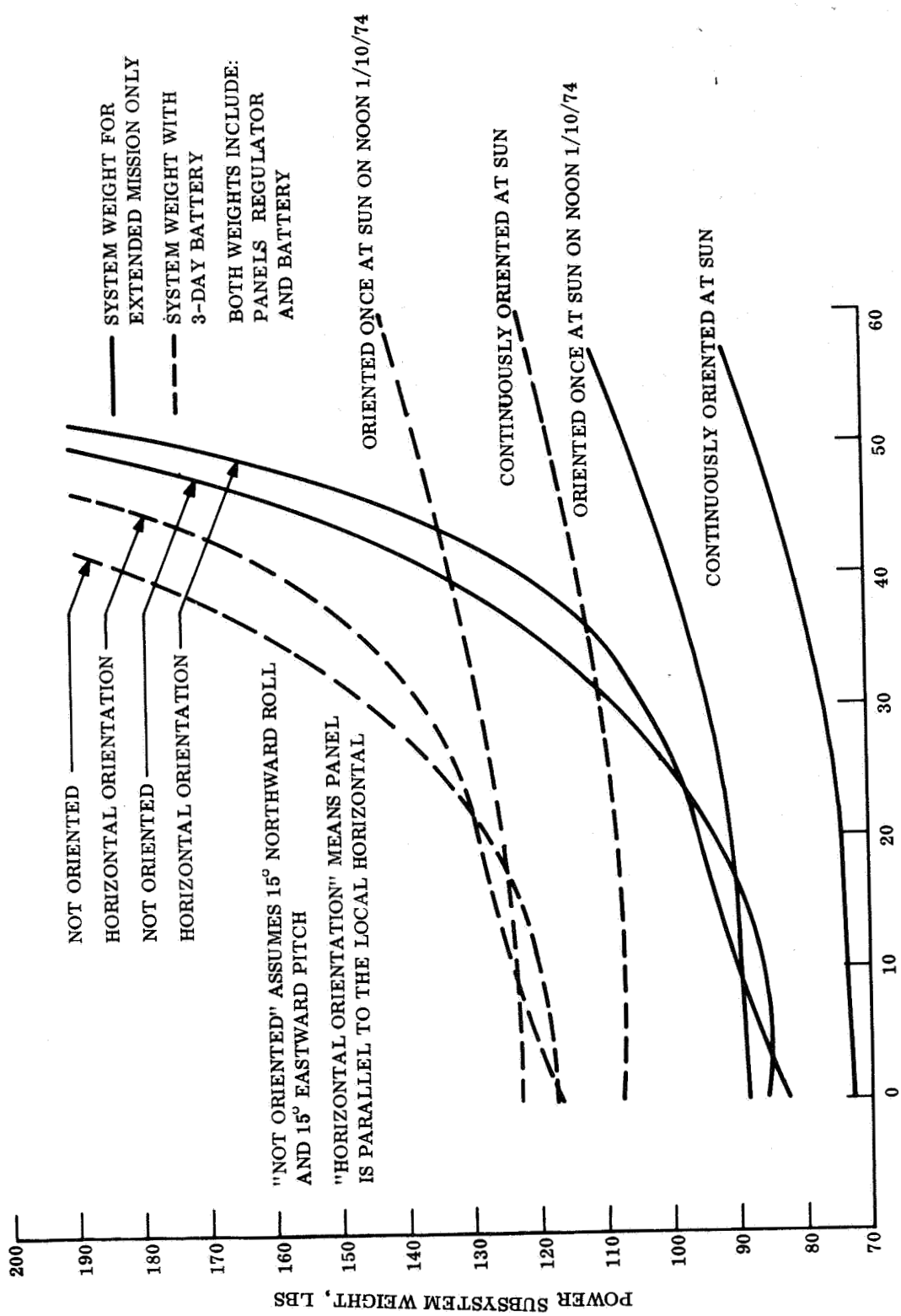

Figure 4.3.3-1. Solar Cell Power Subsystem Comparison Curve

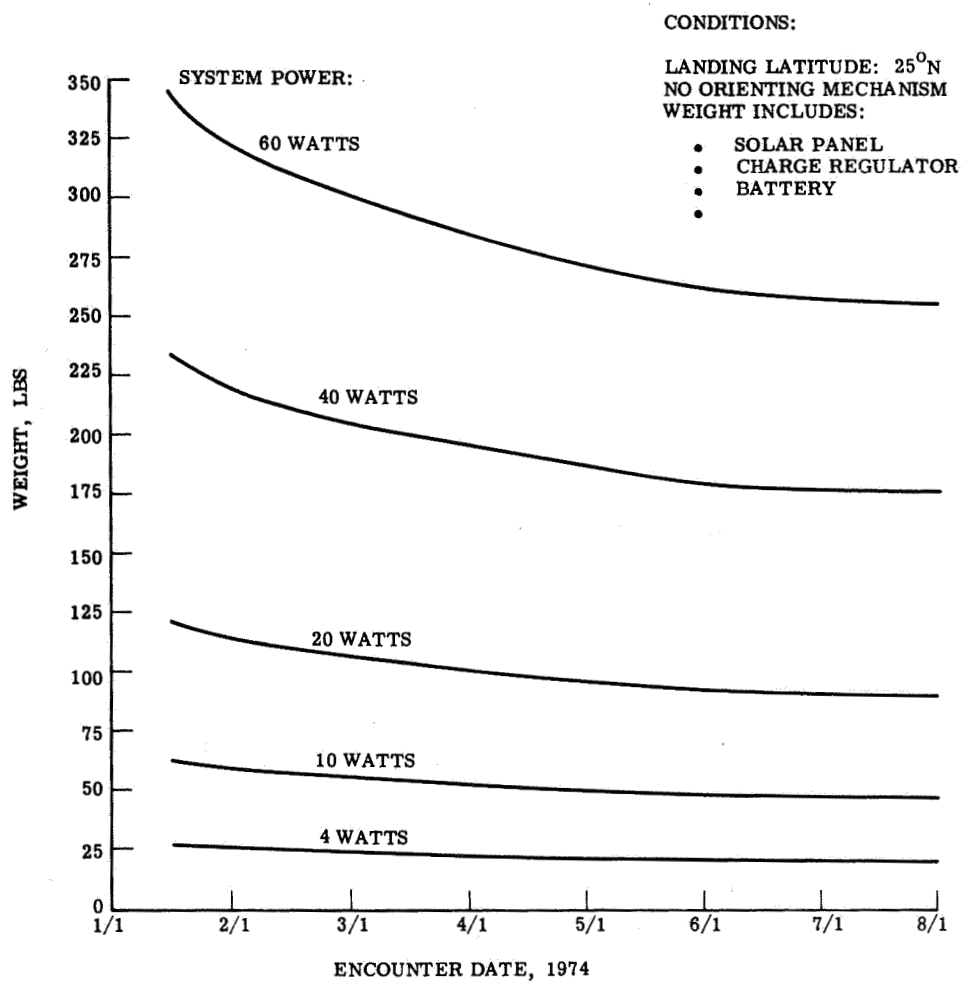

NOTES:

MISSION DURATION: 90 DAYS
TYPE OF BATTERY: SILVER-ZINC
MAX TEMP: 80°F
MIN TEMP: 50°F
SHOCK: 1000 G
VIBRATION: 10 G
MINIMUM VOLTAGE: 24V
NOMINAL POTENTIAL: 28V
ACTIVATED WET STAND: 60 DAYS
CYCLES: 90
MAX SINGLE BATTERY WEIGHT = 200 LBS

SOLAR POWER REFERENCE CONDITIONS:

HELIOTEK 8 MIL, 2 OHM-CM, 1x2 CM SOLAR CELLS.
ELECTRICALLY ORIENTED PANEL
FLAT PACK ARRAY
ORIENTATION HALF-ANGLE ACCURACY
PLANETARY DAY: 24.62 HRS

TIME OF ILLUMINATION/DAY, SOLAR LATITUDE, AND MARS-SUN DISTANCE AS IN PARA 4.3.2.3

TERRAIN LIMITS = ±15° MASK

Figure 4.3.3-2. Solar Array Power Subsystem Weight vs Landing Date for Terrain at 25°N Latitude (without Orienting Mechanism)

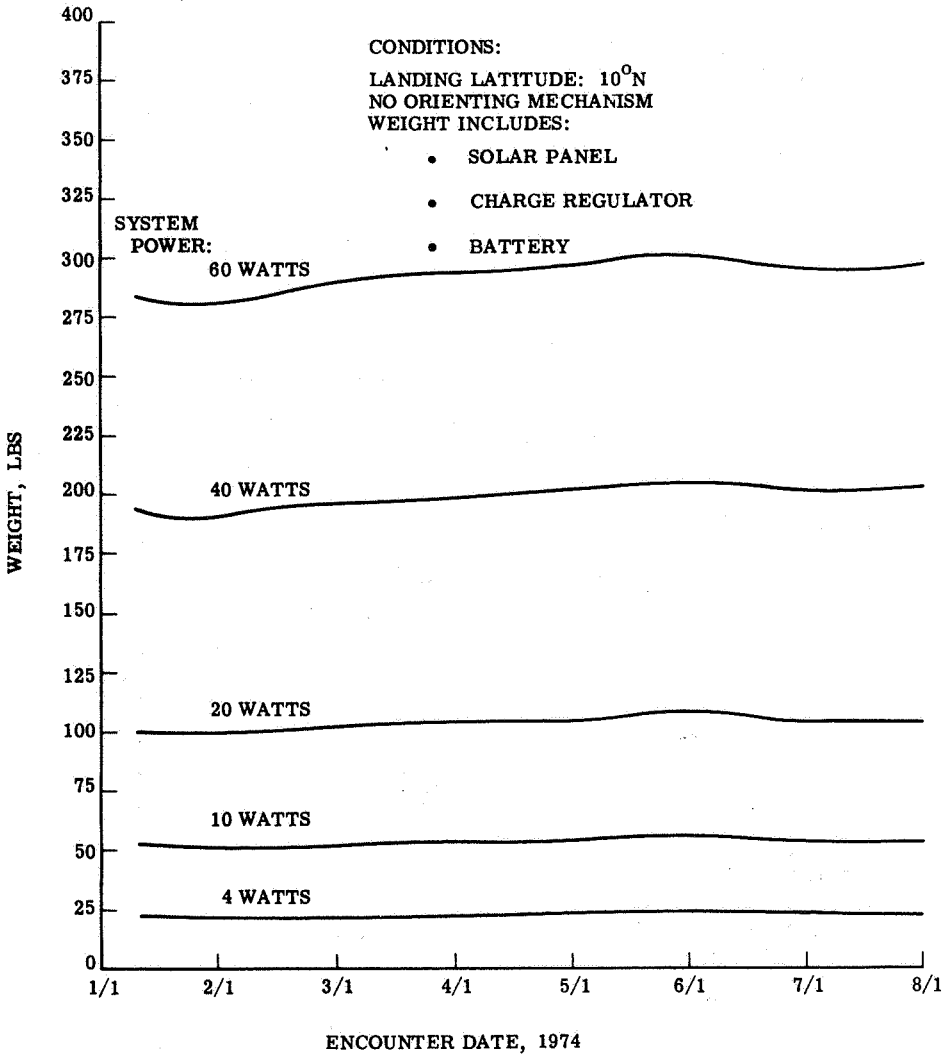

NOTES:

MISSION DURATION: 90 DAYS
TYPE OF BATTERY: SILVER-ZINC
MAX TEMP: 80°F
MIN TEMP: 50°F
SHOCK: 1000 G
VIBRATION: 10G
MINIMUM VOLTAGE: 24V
NOMINAL POTENTIAL: 28V
ACTIVATED WET STAND: 60 DAYS
CYCLES: 90
MAX SINGLE BATTERY WEIGHT = 200 LBS

SOLAR POWER REFERENCE CONDITIONS:

HELIOTEK 8 MIL, 2 OHM-CM, 1x2 CM SOLAR CELLS.
ELECTRICALLY ORIENTED PANEL
FLAT PACK ARRAY
ORIENTATION HALF-ANGLE ACCURACY
PLANETARY DAY: 24.62 HRS

TIME OF ILLUMINATION/DAY, SOLAR LATITUDE, AND MARS-SUN DISTANCE AS IN PARA 4.3.2.3

TERRAIN LIMITS = ±15° MASK

Figure 4.3.3-3. Solar Array Power Subsystem Weight vs Landing Date for Terrain at 10°N Latitude (without Orienting Mechanism)

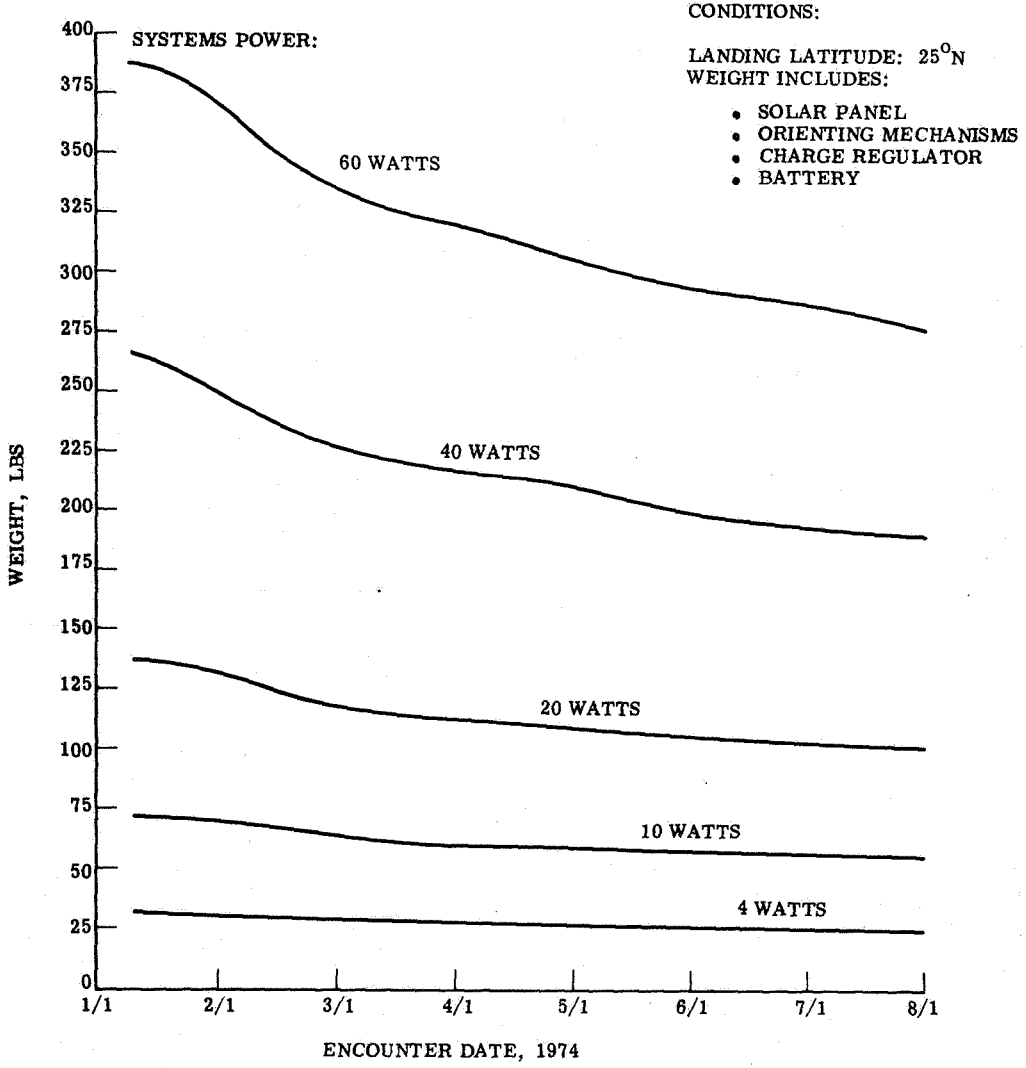

CONDITIONS:

LANDING LATITUDE: 25°N
WEIGHT INCLUDES:

- SOLAR PANEL
- ORIENTING MECHANISMS
- CHARGE REGULATOR
- BATTERY

NOTES:

MISSION DURATION: 90 DAYS
TYPE OF BATTER: SILVER-ZINC
MAX TEMP: 80°F
MIN TEMP: 50°F
SHOCK: 1000 G
VIBRATION: 10 G
MINIMUM VOLTAGE: 24V
NOMINAL POTENTIAL: 28V
ACTIVATED WET STAND: 60 DAYS
CYCLES: 90
MAX SINGLE BATTERY WEIGHT = 200 LBS

SOLAR POWER REFERENCE CONDITIONS:

HELIOTEK 8 MIL, 2 OHM-CM, 1x2 CM SOLAR CELLS.
ELECTRICALLY ORIENTED PANEL
FLAT PACK ARRAY
ORIENTATION HALF-ANGLE ACCURACY
PLANETARY DAY: 24.62 HRS

TIME OF ILLUMINATION/DAY, SOLAR LATITUDE, AND MARS-SUN DISTANCE AS IN PARA 4.3.2.3

TERRAIN LIMITS = ±15° MASK

Figure 4.3.3-4. Solar Array Power Subsystem Weight vs Landing Date for Terrain at 25°N Latitude (with Orienting Mechanism)

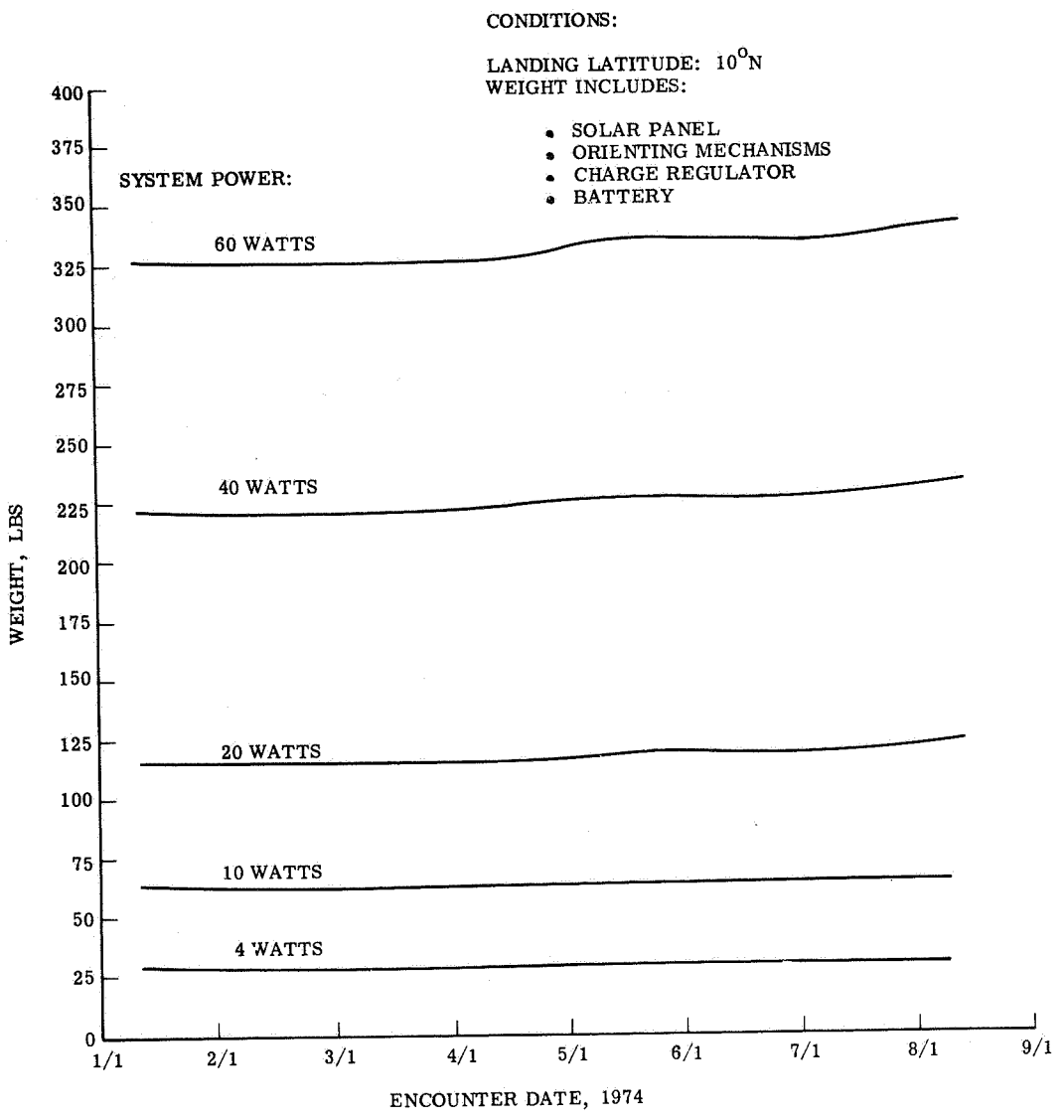

NOTES:

MISSION DURATION: 90 DAYS
TYPE OF BATTERY: SILVER-ZINC
MAX TEMP: 80°F
MIN TEMP: 50°F
SHOCK: 1000 G
VIBRATION: 10 G
MINIMUM VOLTAGE: 24V
NOMINAL POTENTIAL: 28V
ACTIVATED WET STAND: 60 DAYS
CYCLES: 90
MAX SINGLE BATTERY WEIGHT = 200 LBS

SOLAR POWER REFERENCE CONDITIONS:

HELIOTEK 8 MIL, 2 OHM-CM, 1x2 CM SOLAR CELLS.
ELECTRICALLY ORIENTED PANEL
FLAT PACK ARRAY
ORIENTATION HALF-ANGLE ACCURACY
PLANETARY DAY: 24.62 HRS

TIME OF ILLUMINATION/DAY, SOLAR LATITUDE, AND MARS-SUN DISTANCE AS IN PARA 4.3.2.3

TERRAIN LIMITS: ±1.5° MASK

Figure 4.3.3-5. Solar Array Power Subsystem Weight vs Landing Date for Terrain at 10°N Latitude (with Orienting Mechanism)

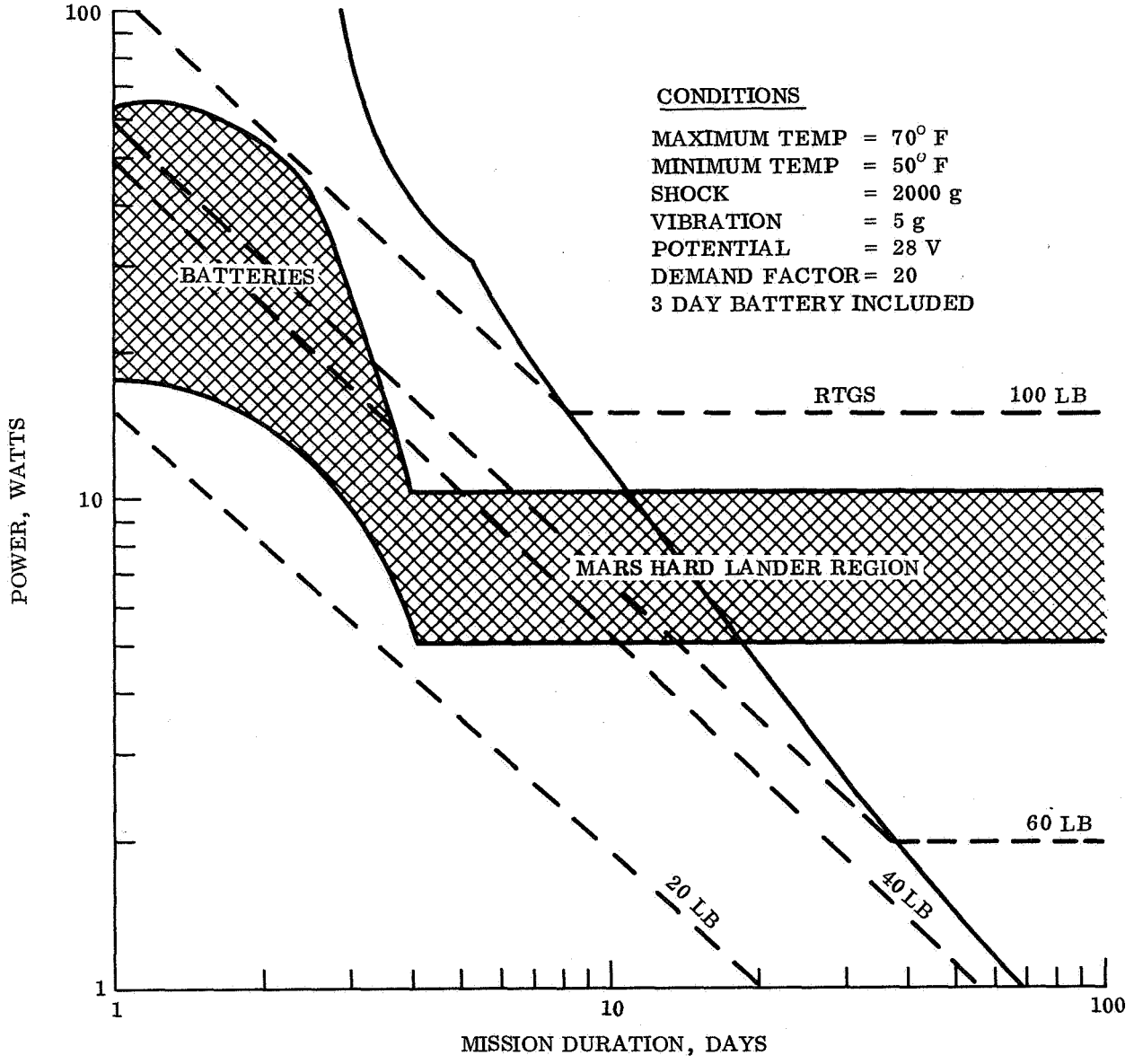

Figure 4. 3. 3-6. Weight loci Curve for Fuel Cells, Solar Arrays, RTG's, and Batteries with Three Day Batteries

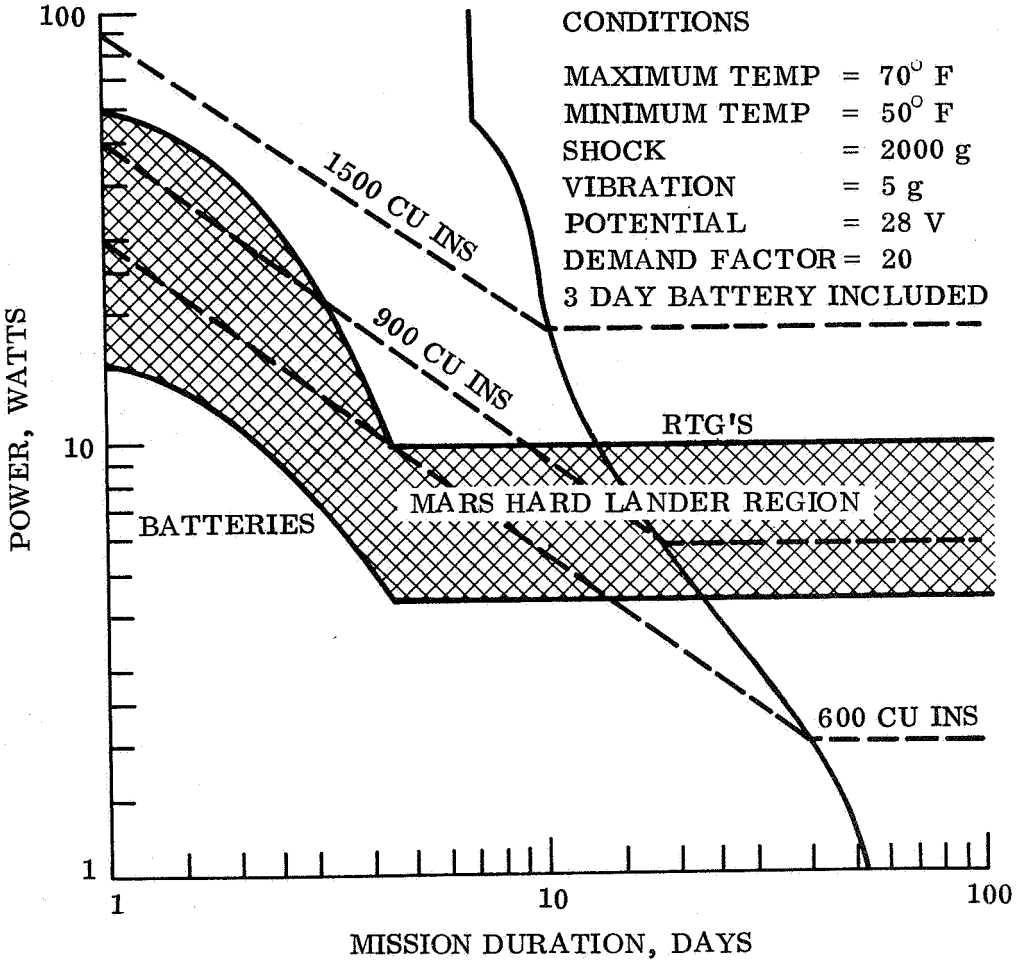

Figure 4.3.3-7. Volume loci Curve for Fuel Cells, Solar Arrays, RTG's and Batteries with Three Day Battery

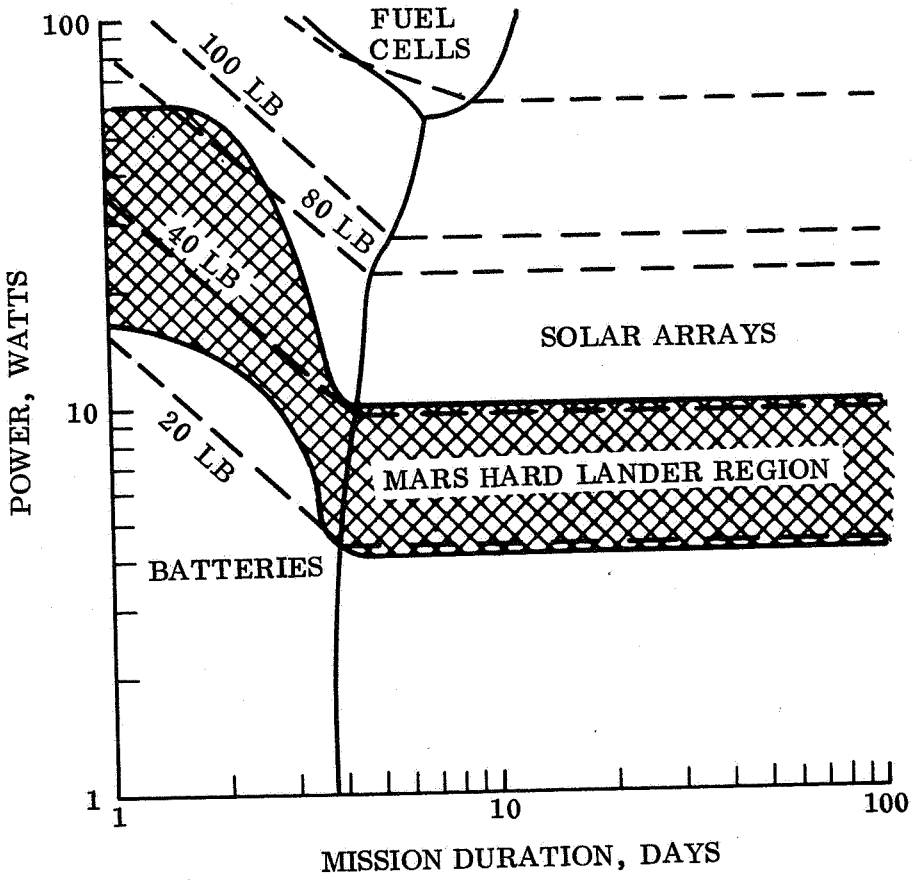

CONDITIONS

MAXIMUM TEMP	= 70° F
MINIMUM TEMP	= 50° F
SHOCK	= 2000g
VIBRATION	= 5 g
POTENTIAL	= 28 V
DEMAND FACTOR	= 20

Figure 4.3.3-8. Weight loci Curve for Fuel Cells, Solar Arrays and Batteries without Three Day Battery

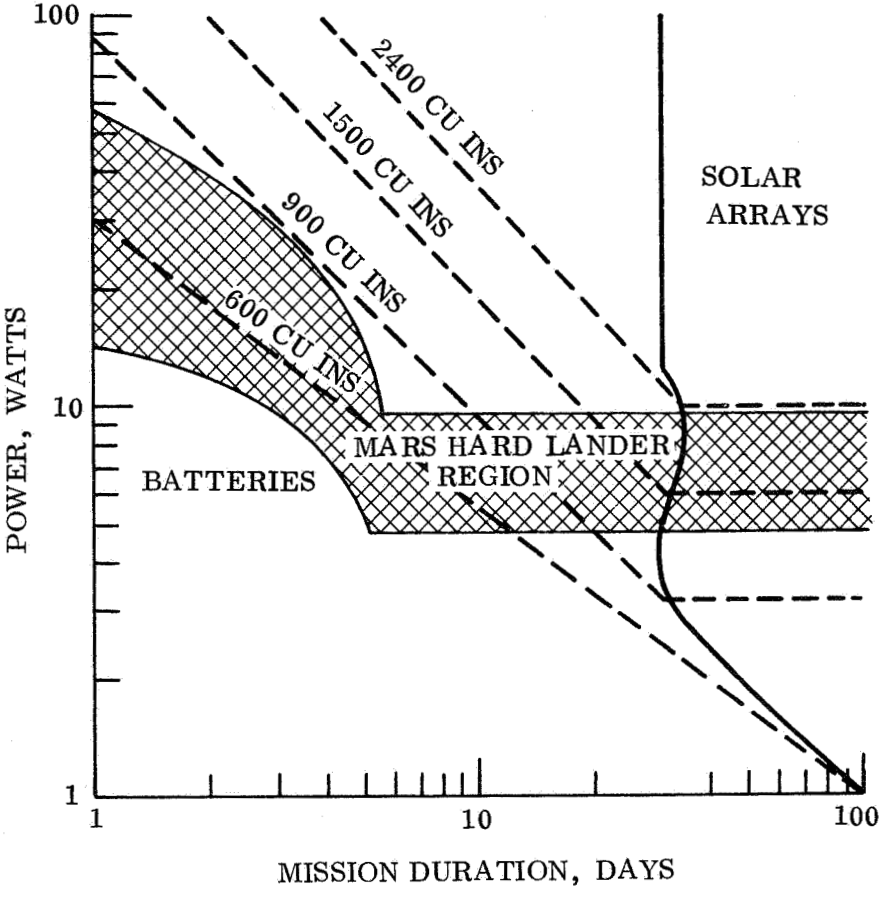

CONDITIONS

MAXIMUM TEMP	=	70 $^{\circ}$ F
MINIMUM TEMP	=	50° F
SHOCK	=	2000 g
VIBRATION	=	5 g
POTENTIAL	=	28 V
DEMAND FACTOR	=	20

Figure 4.3.3-9. Volume loci Curve for Fuel Cells, Solar Arrays, and Batteries without Three Day Battery

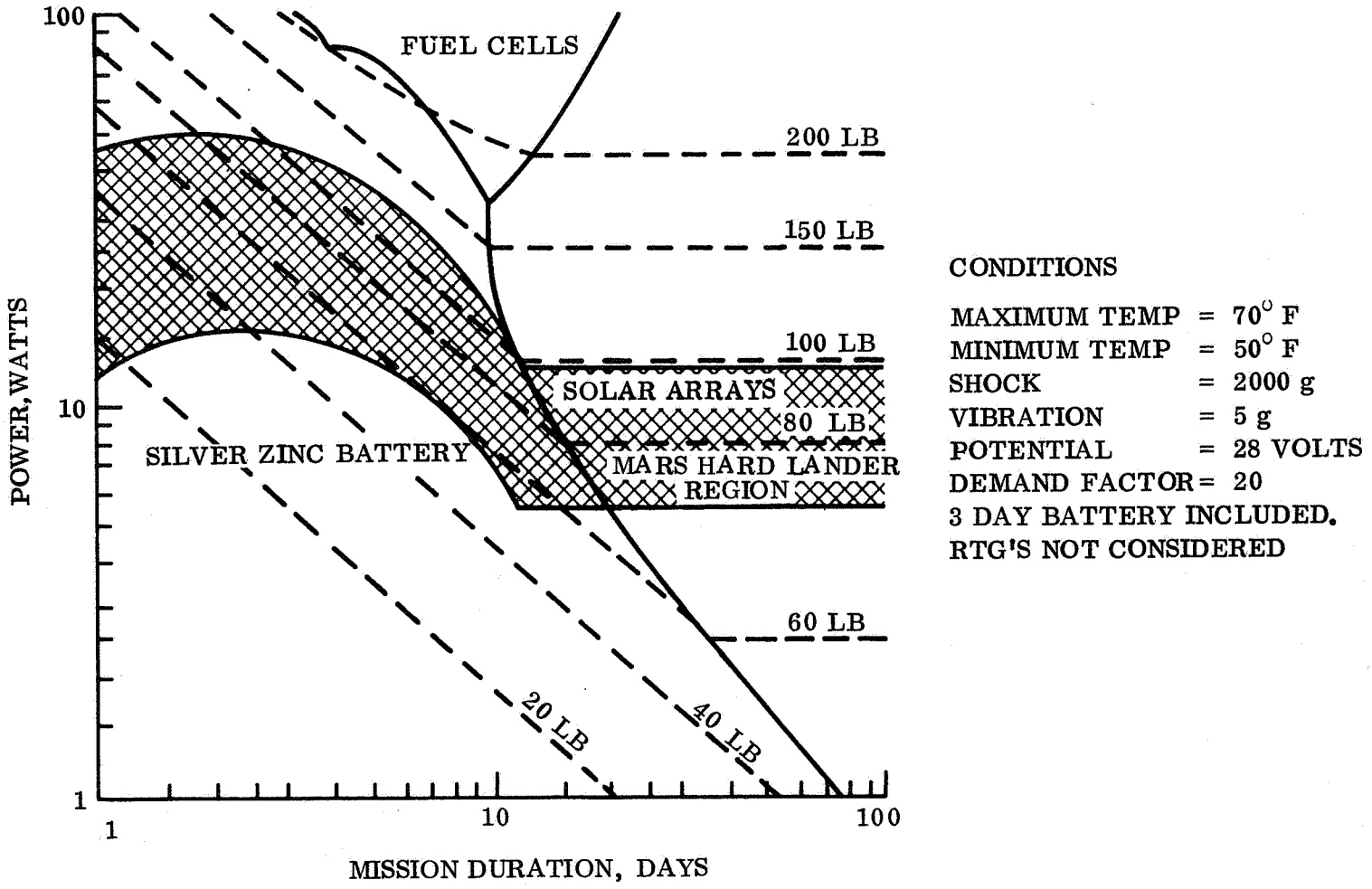

Figure 4.3.3-10. Weight loci Curve for Fuel Cells, Solar Arrays, and Batteries with Three Day Battery

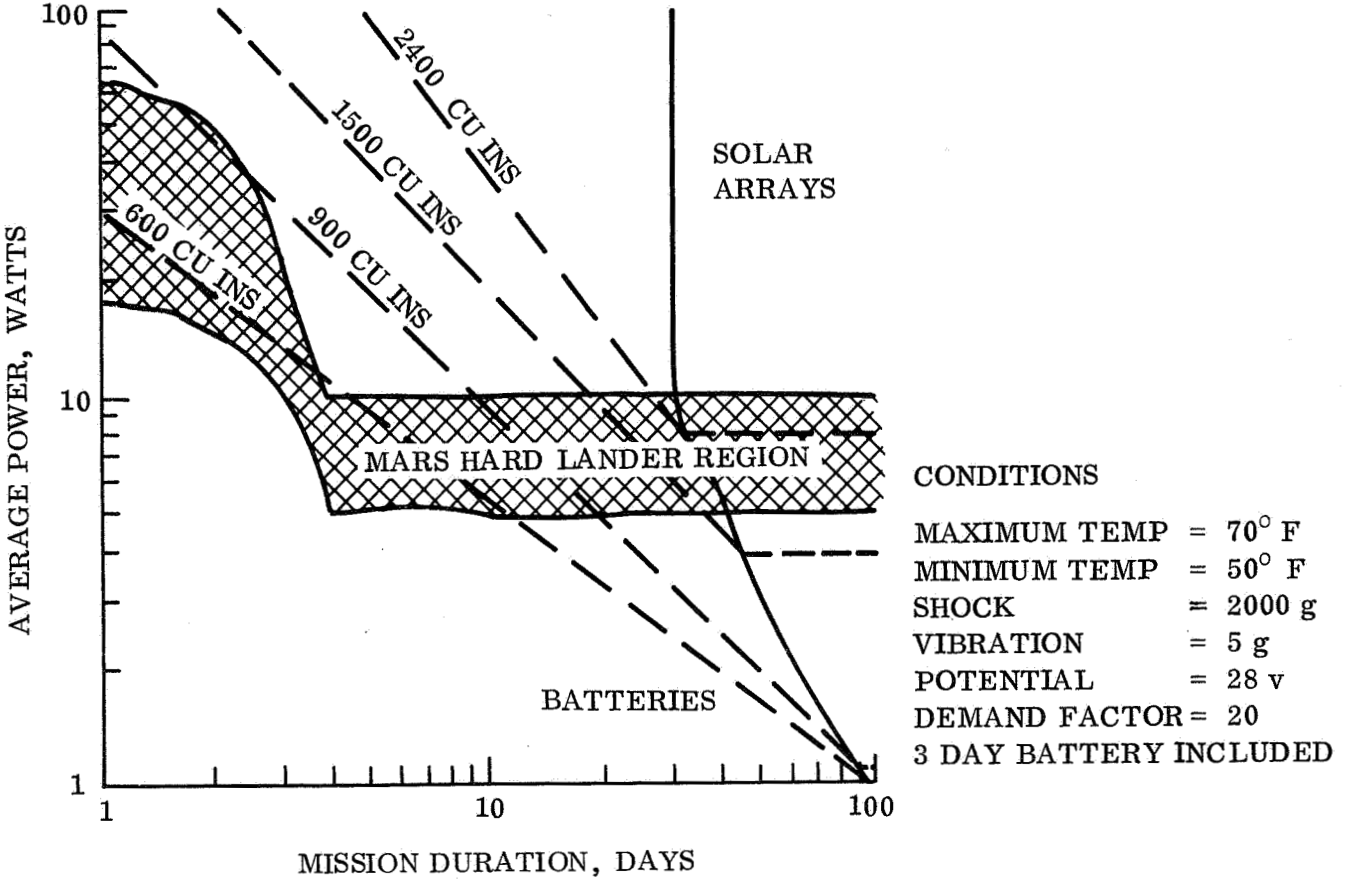

Figure 4.3.3-11. Volume loci Curve for Fuel Cells, Solar Arrays, and Batteries with ThreeDay Battery

4.4 ENVIRONMENTAL CONTROL

4.4.1 REQUIREMENTS

The selection and design of an internal thermal control system for the Mars Hard Lander is strongly influenced by the external environment in which the Lander must operate, length of operation time, payload temperature requirements, component heat dissipation, power source, and Lander shape. The major Lander operating time will be in an environment which is at a lower temperature than the desired component operational temperature. The maximum environmental heat flux for Mars is approximately 195 Btu/hr-ft^2 compared to 440 Btu/hr-ft^2 for Earth. This results in surface temperatures as low as 310°R. It is therefore evident that an internal control system is required which is capable of heating the payload components.

For short duration missions where a battery powered Lander will be used, thermal control is achieved with an insulated payload and local electrical heaters or radioisotope packets. For extended missions, the Lander design will employ either a solar cell or an RTG power supply. Thermal control methods associated with these types of power supply are similar to the battery powered Lander except for the weight penalties associated with cooling the RTG and providing a means of heating the payload with RTG waste thermal energy during cold periods.

4.4.2 LANDER APPLICATION

The amount of heat loss from the Lander is controlled by the thermal characteristics of the insulation material, thickness of insulation between the payload and the environment, and the external surface radiative properties of the Lander. The type of materials selected must also have the capability to withstand high impact shock, vibration and sterilization requirements without experiencing degradation. A foam type insulation (e.g., styrofoam or polyurethane) is the only insulation available that meets these specifications. It also has the characteristics of very low density and low thermal conductivity which are necessary in obtaining an optimum design. For minimum heat loss, a foam material with a density of 5 lb/ft^3, a thermal conductivity of 0.025 Btu/hr-ft^2 - °R and a surface emissivity of 0.1 was chosen as a baseline for the parametric trade offs.

An idealized thermal control system can only be achieved through a Lander configuration that has minimum heat leak characteristics. Since the primary mode of heat transfer from the payload is by radiation, it is necessary to select a skin material with the lowest emissivity property attainable. A literature survey was undertaken to select some candidate materials which satisfy the radiative requirements. Results indicate a surface emissivity value of E = 0.1 is compatible with the current availability and can be achieved through a metal plating process. Some materials taken from Reference 4-25 are listed as follows with their measured total normal emissivity.

	Material	Heat Treatment in Air	Temperature (°F)	Emissivity
1.	Silver plate on type 231 corrosion resistant steel (0.0003 inch thickness of plating)	303 hrs at 494°F	200	0.04
			400	0.04
			600	0.05
			800	0.06
		1000 hrs at 692°F	200	0.05
			400	0.05
			600	0.05
			800	0.07
2.	Gold plate (0.0001 inch) on 0.0005 inch nickel plate on type 321 corrosion resistant steel	None	200	0.07
			340	0.06
			480	0.06
			620	0.07
			750	0.09
3.	Nickel Electroplated on iron, then polished		Room temp	0.045 to 0.11

Silver, gold, and nickel are extremely stable in most atmospheres in that they resist the normal chemical reactions which cause emissivity changes. Dust contamination will not effect the rate of heat loss from the surface since radiation will still continue to be the mode of heat transfer in the reduced atmosphere. The primary mode of degradation for a metal surface such as the materials listed above is reduced to abrasion which might occur in sand storms. A GE Space Science Laboratory report (R68SD7) by C. H. Mok shows that erosion of metals is negligible at the wind speed requirements of 67 m/sec. Even though this requirement exists at an altitude of 100 n. mi. above the planet surface and wind speeds will be significantly less at ground level, a 67 m/sec wind will not produce any erosion.

4.4.3 TEMPERATURE CONTROL

Most of the payload components and all of the electronic support equipment can be categorized as requiring mounting surfaces having temperatures between -40 and +135°F. The most temperature sensitive component in the Lander is the battery with the criteria being that their mounting surfaces and effective environment temperatures are to be maintained between 50° and 100°F. The problem of thermal control is reduced to a study of satisfying the lower temperature limit since the maximum equilibrium temperature of Mars will not exceed the upper temperature specification of the payload. Parametric data was constructed for the range of allowable temperatures which included -40° to +50°F.

Thermal response of the payload was achieved by considering heat conduction through the payload and radiation heat transfer from the outside surface to space and the planet surface. Fig. 4.4.3-1 represents the diurnal Mars surface temperature profile used in the analysis which is in accordance with the NASA/LRC Mars engineering model parameters. A maximum solar heat flux input to the vehicle of 195 Btu/hr-ft^2 - $^\circ$R was assumed occurring at noontime and decreasing linearly until the payload is shadowed from the Sun. Due to the low atmospheric pressure on Mars and the low gas density, the heat transferred by natural convection is less than 5 percent of that transferred by radiation and was therefore neglected.

The basic Lander subsystem configuration will not be different for either a solar cell or a battery powered Lander. Therefore, the thermal control methods for a battery powered subsystem are applicable for the solar cell system. For an RTG power supply, additional weight for thermal control must be provided through the use of a passive, liquid loop, or an expendable coolant system. Trade-offs were performed for a series of RTG sizes assuming an RTG allowable temperature of 450°F.

4.4.4 SYSTEM SYNTHESIS

4.4.4.1 Battery and Solar Cell Thermal Control

The thermal control parametric data was established by constructing a model thermally connecting the payload with its outside environment. Heat leak was then calculated as a function of insulation thickness, component allowable temperature, and surface area. The sensitivity of these parameters to heat leak is summarized in figs. 4.4.4-1, -2, and -3. In fig. 4.4.4-4, an insulation weight can be determined for various Lander surface areas and insulation thicknesses.

The heat loss by conduction varies significantly as a function of the thermal resistance path between the components and the planet surface. The associated heat leak for different conductance values is shown in fig. 4.4.4-5 for the range of payload temperatures.

At this point two separate design approaches were evaluated: a completely isolated payload where all components are mounted on a common structure resulting in an isothermal temperature response for the entire payload (Type I); and an insulated payload with an isolated battery compartment which enables the battery temperature to be controlled through local electric heaters and lets the rest of the payload respond to the environment (Type II).

Results for Type I are summarized in figs. 4.4.4-6 through -15. Figs. 4.4.4-6 through -8 depict the approximate time when heater power is required to maintain the payload at a particular temperature for one diurnal cycle. These curves show the different requirements for 2, 4, and 6 inches of insulation between the payload and the environment. Based on these responses, fig. 4.4.4-9 was constructed showing the heater power requirements (watt-hr/day), as a function of allowable temperature for various insulation thicknesses.

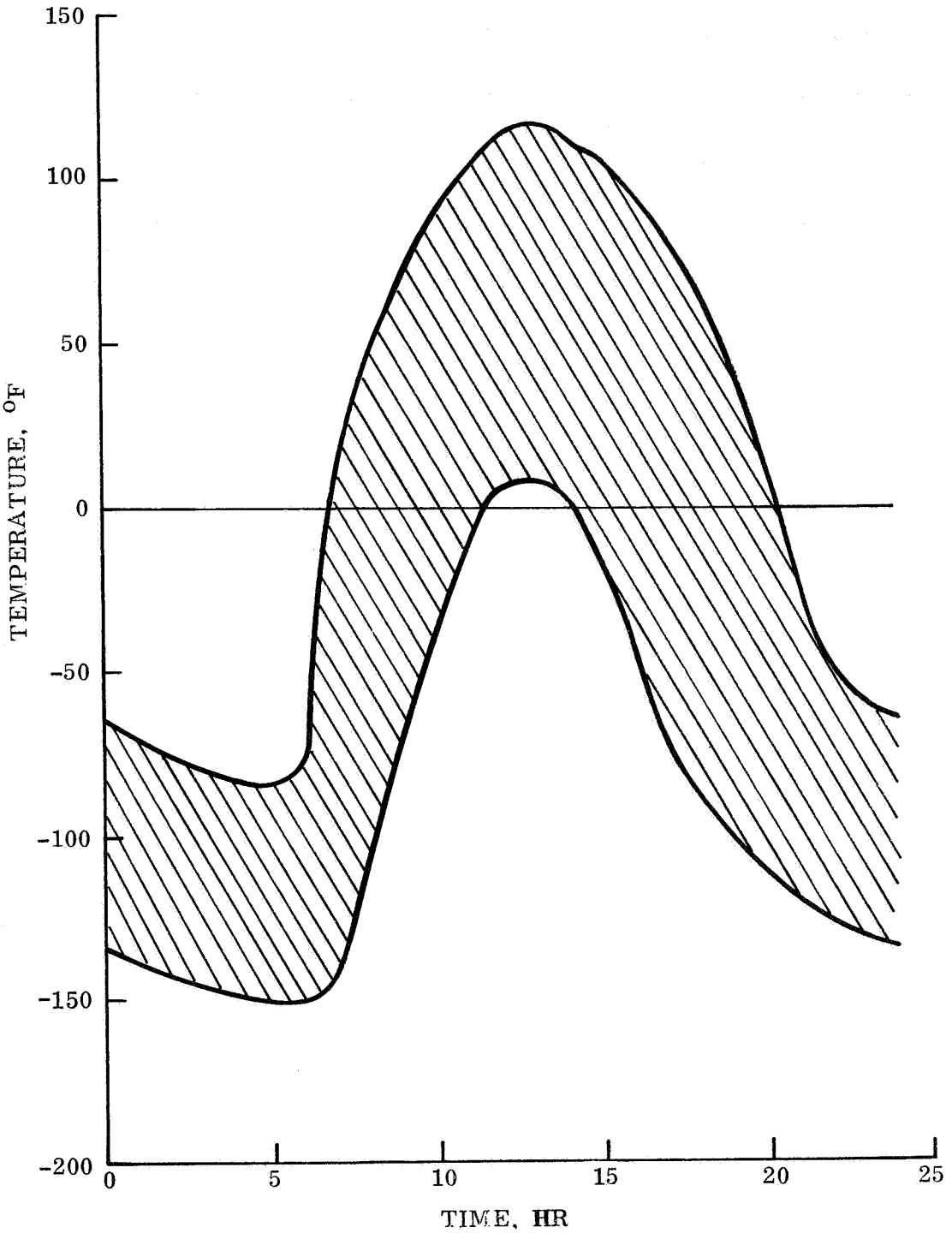

Figure 4.4.3-1. Daily Temperature Variation of Surface of Mars at the Equator

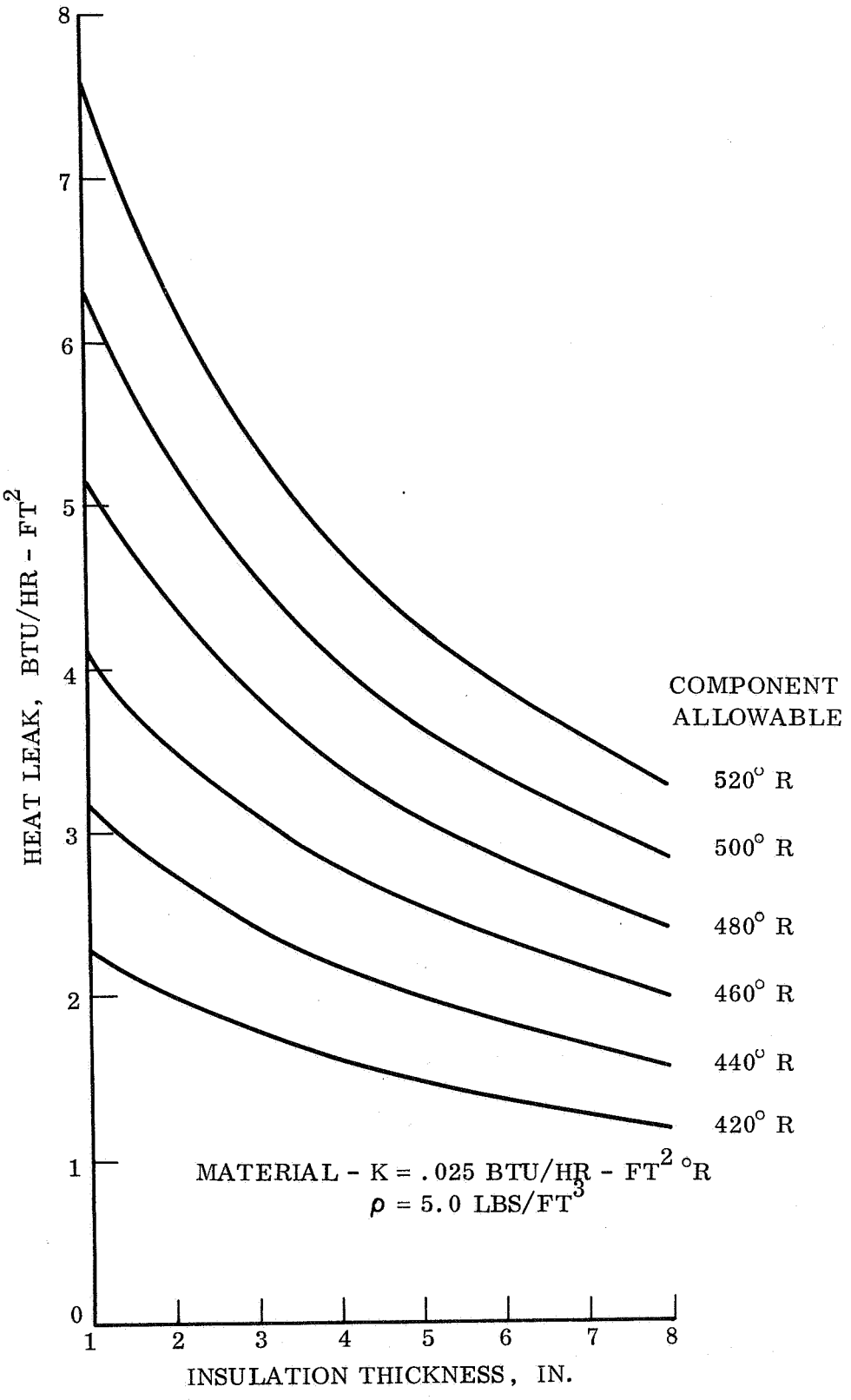

Figure 4.4.4-1. Lander Radiation Heat Leak vs Insulation Thickness

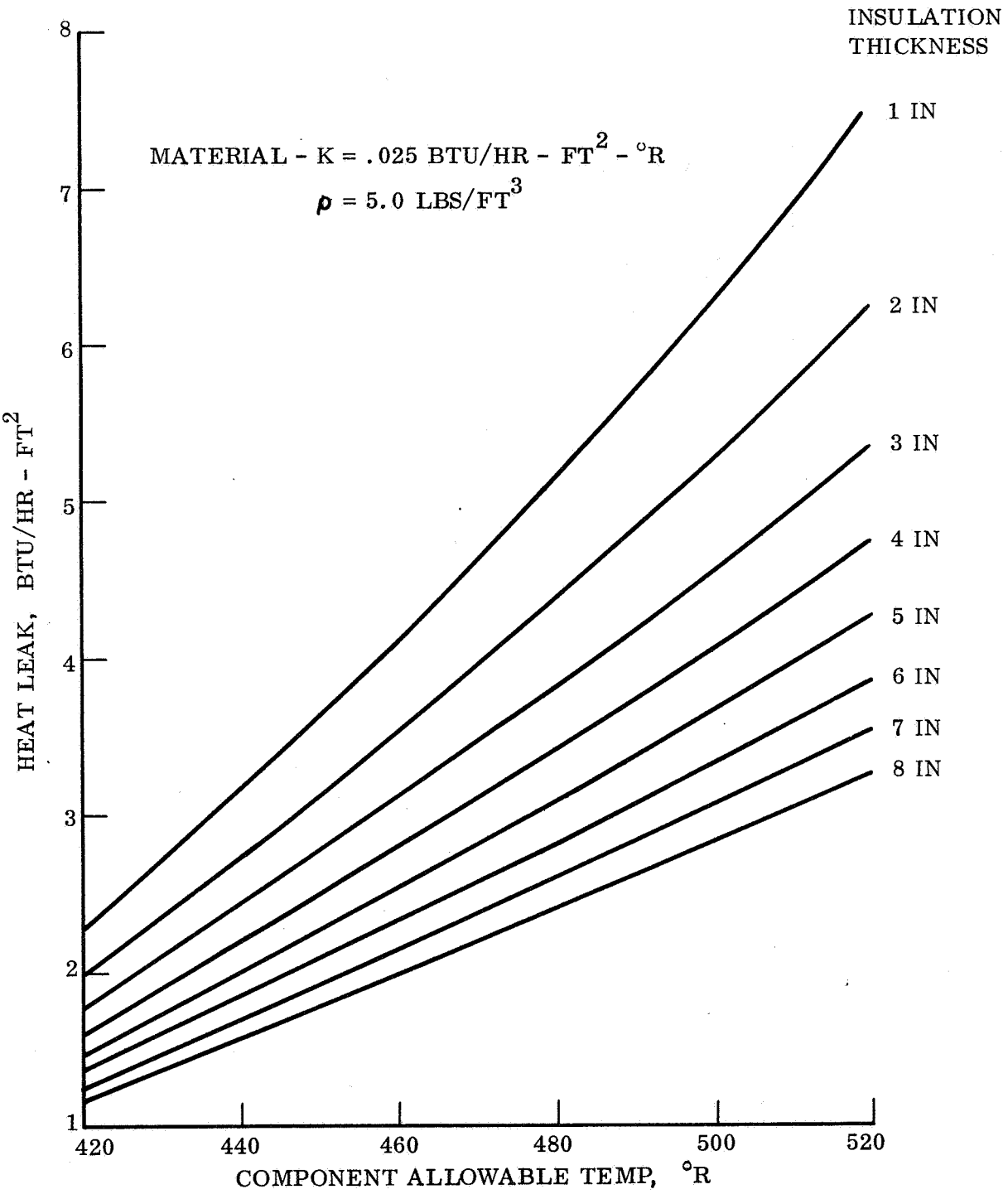

Figure 4.4.4-2. Lander Radiation Heat Leak vs Component Allowable Temperature

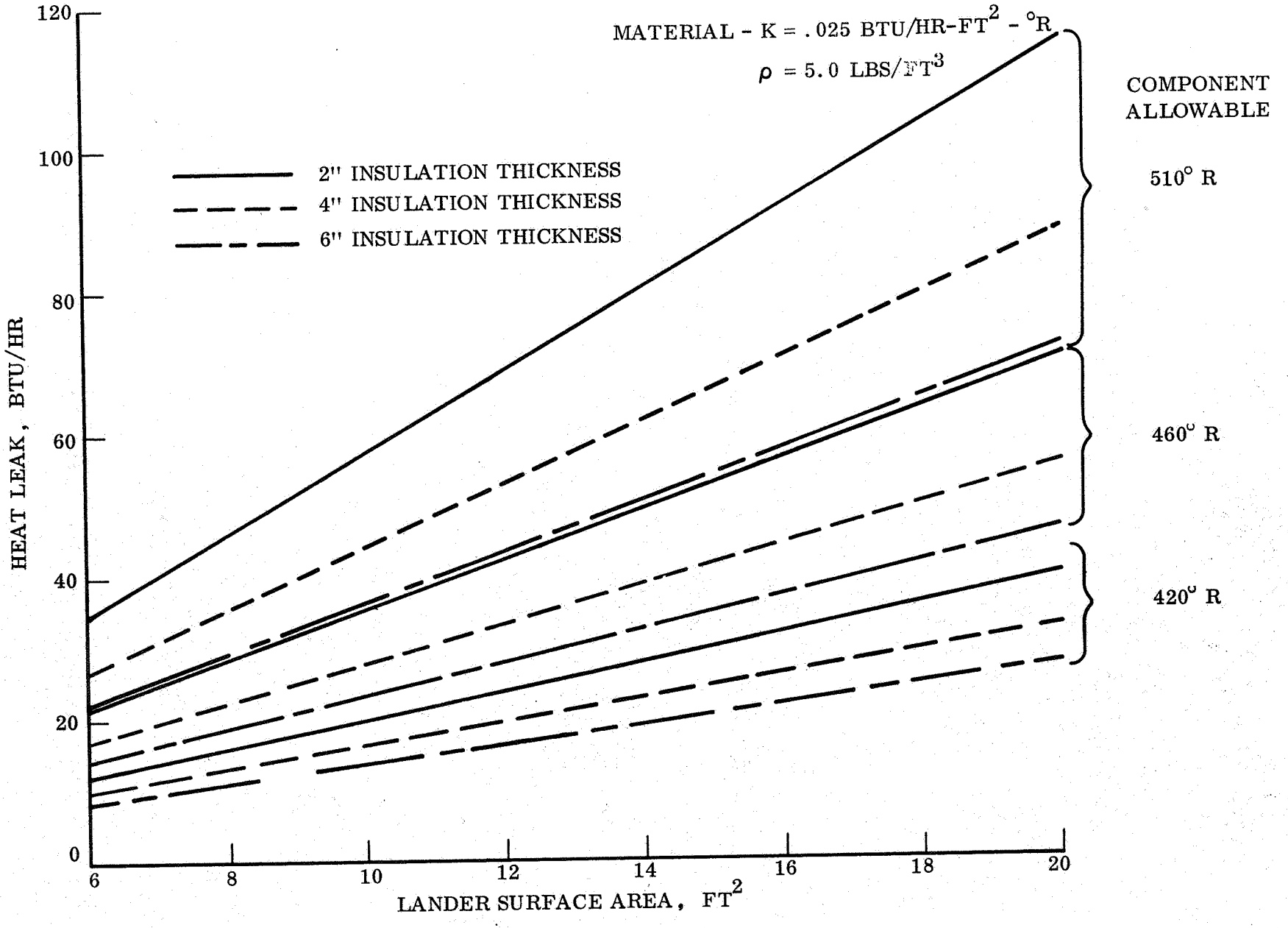

Figure 4.4.4-3. Radiation Heat Leak vs Lander Surface Area

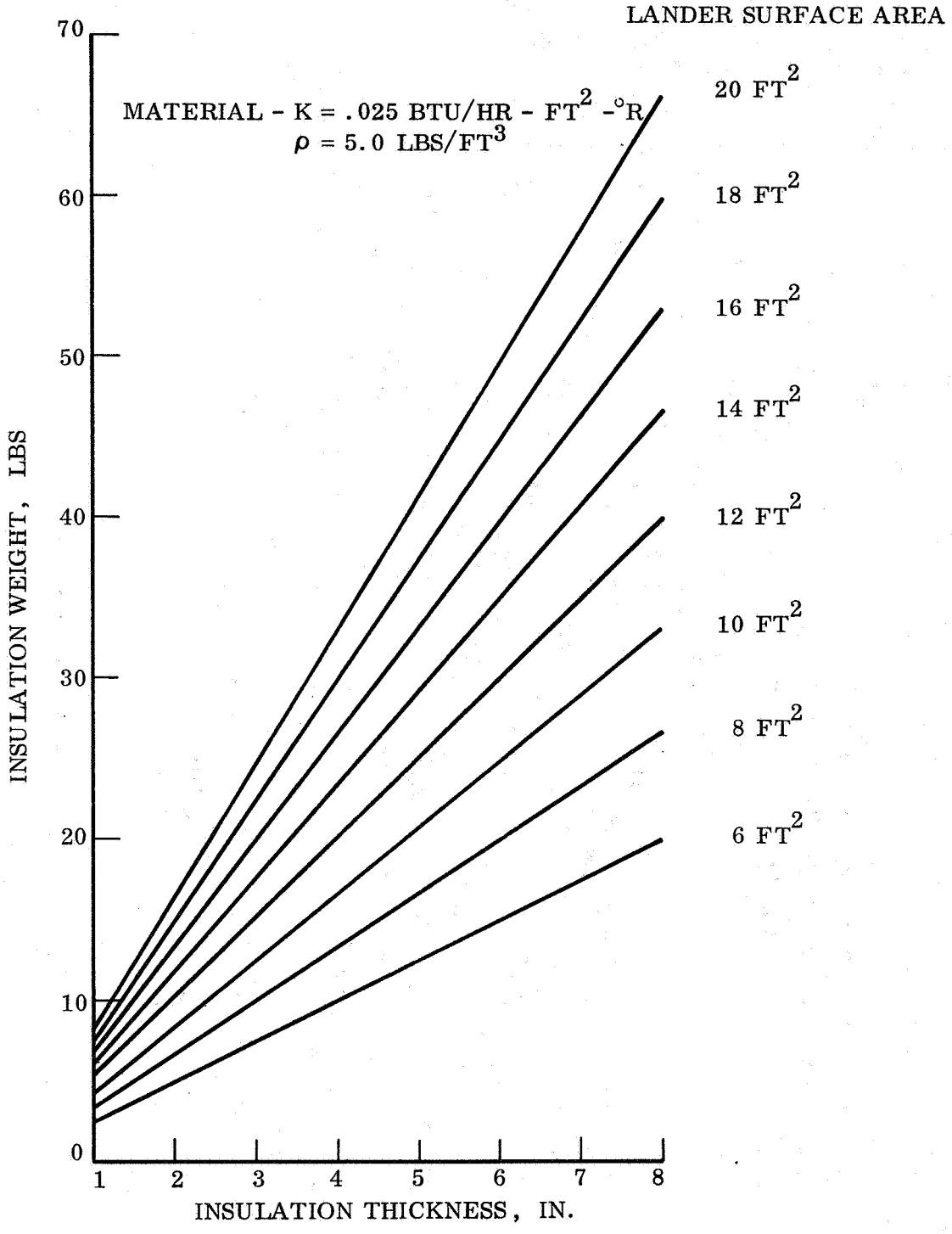

Figure 4.4.4-4. Insulation Weight vs Insulation Thickness

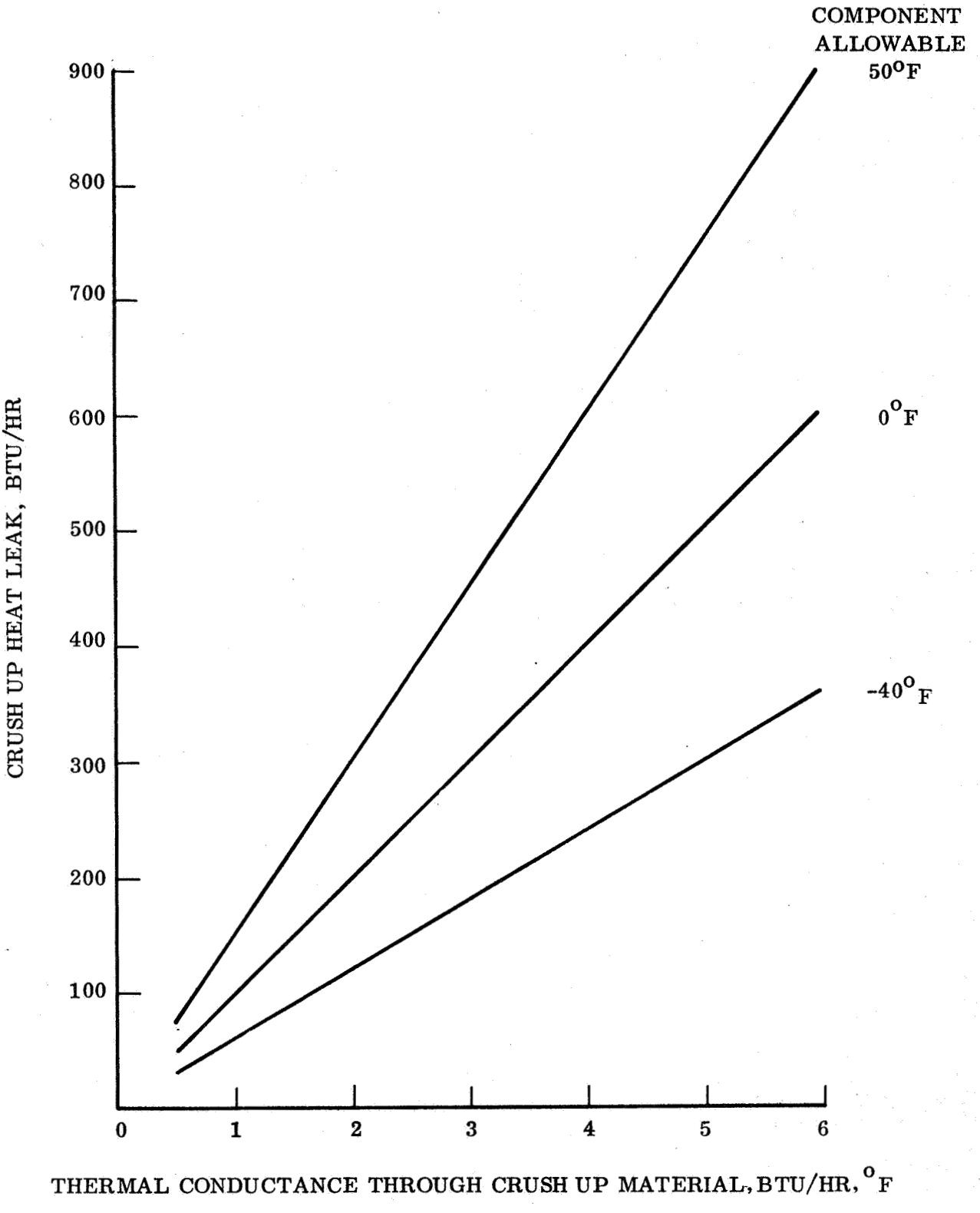

Figure 4.4.4-5. Structure to Surface Heat Leak vs Thermal Conductance

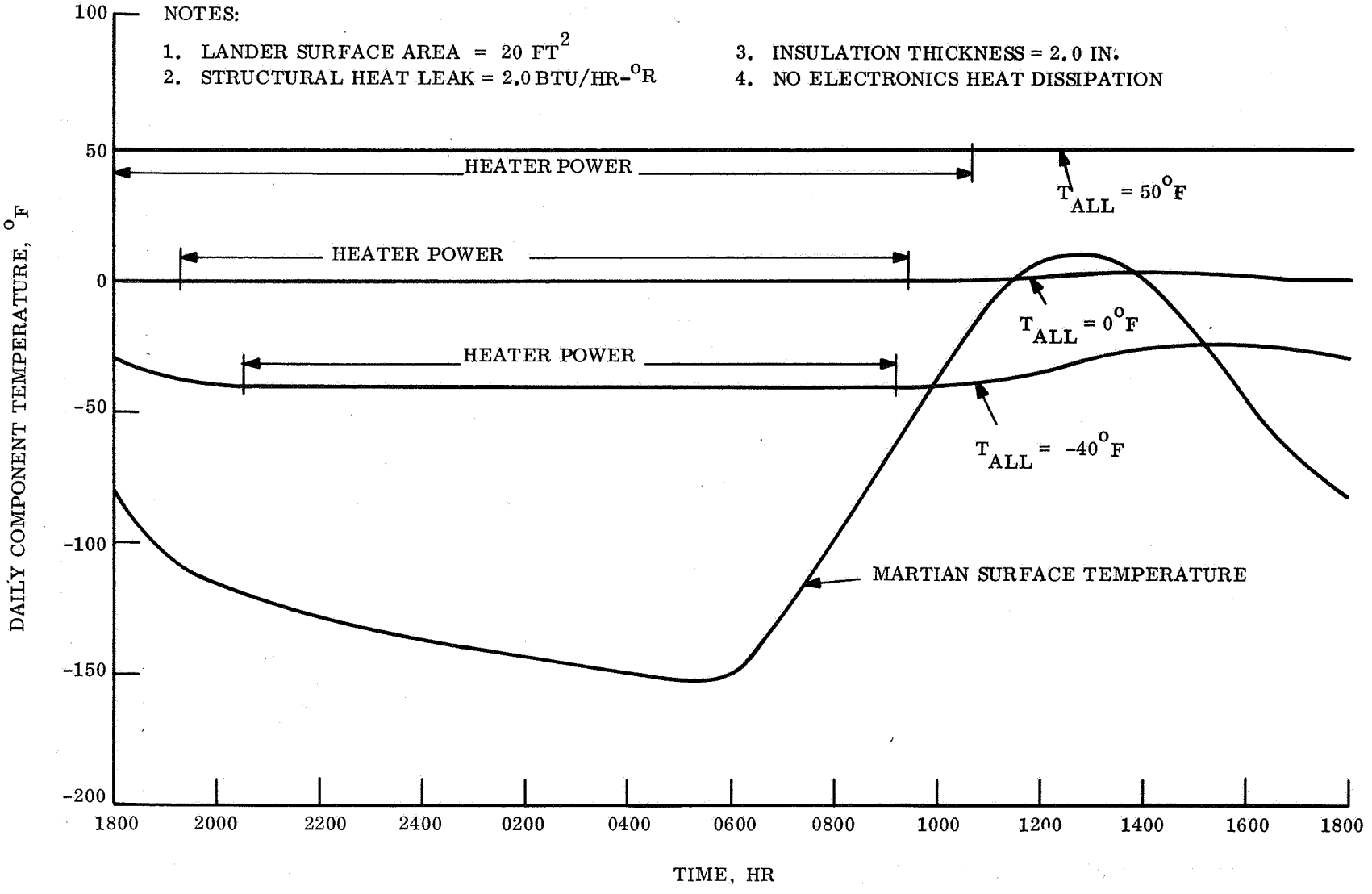

Figure 4. 4. 4-6. Steady State Daily Component Temperature vs Time

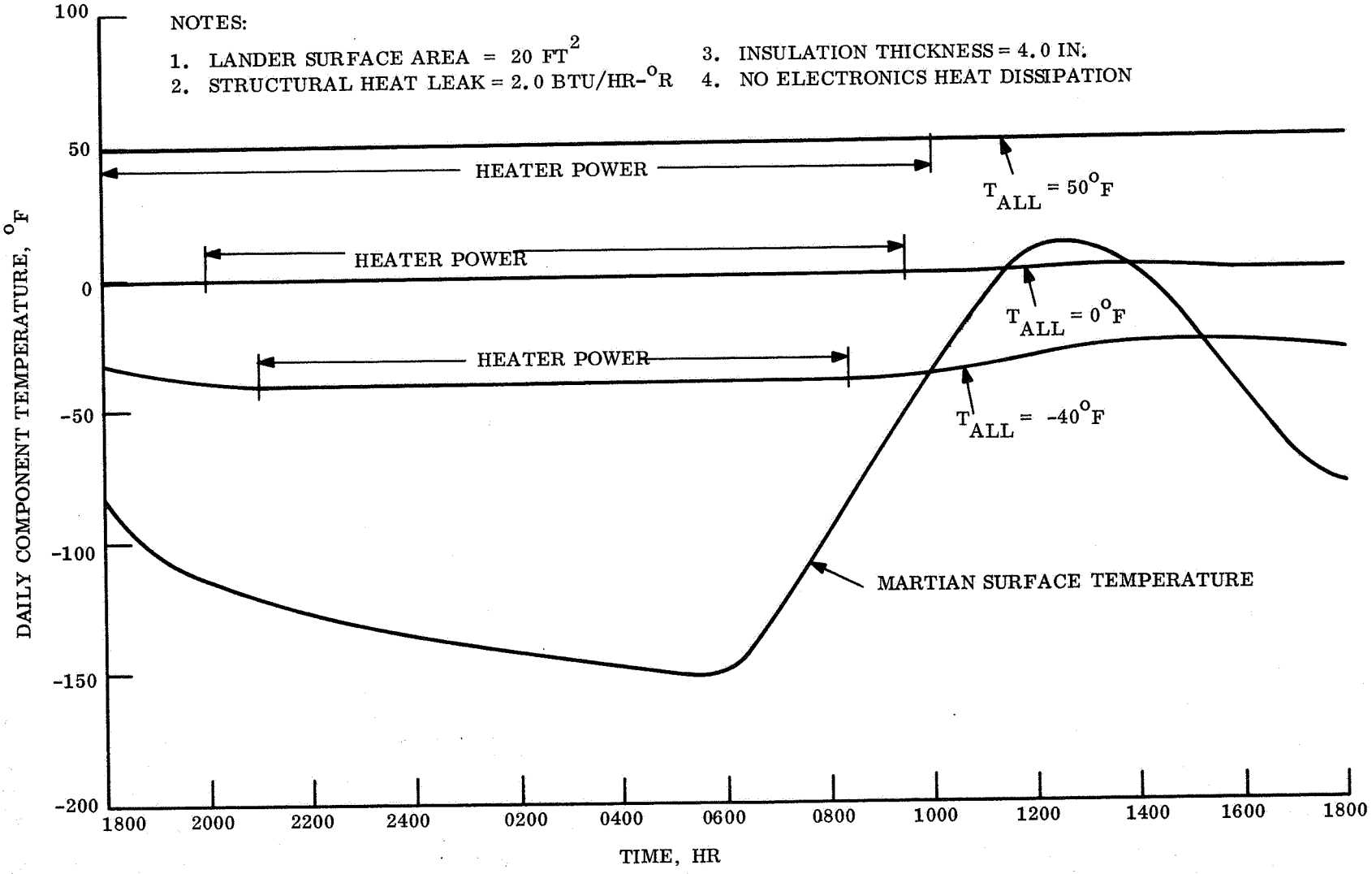

Figure 4. 4. 4-7. Steady State Daily Component Temperature vs Time

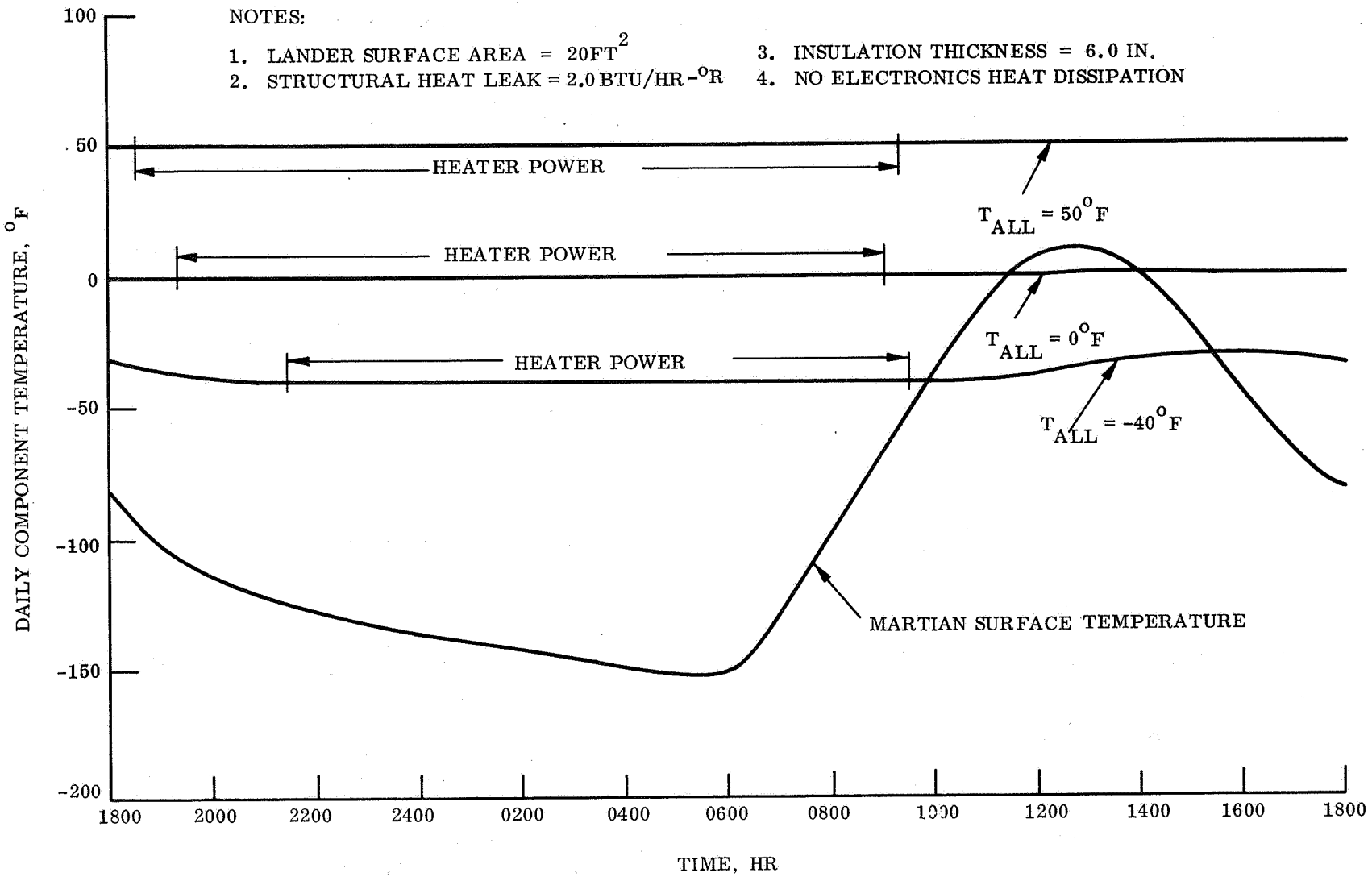

Figure 4.4.4-8. Steady State Component Temperature vs Time

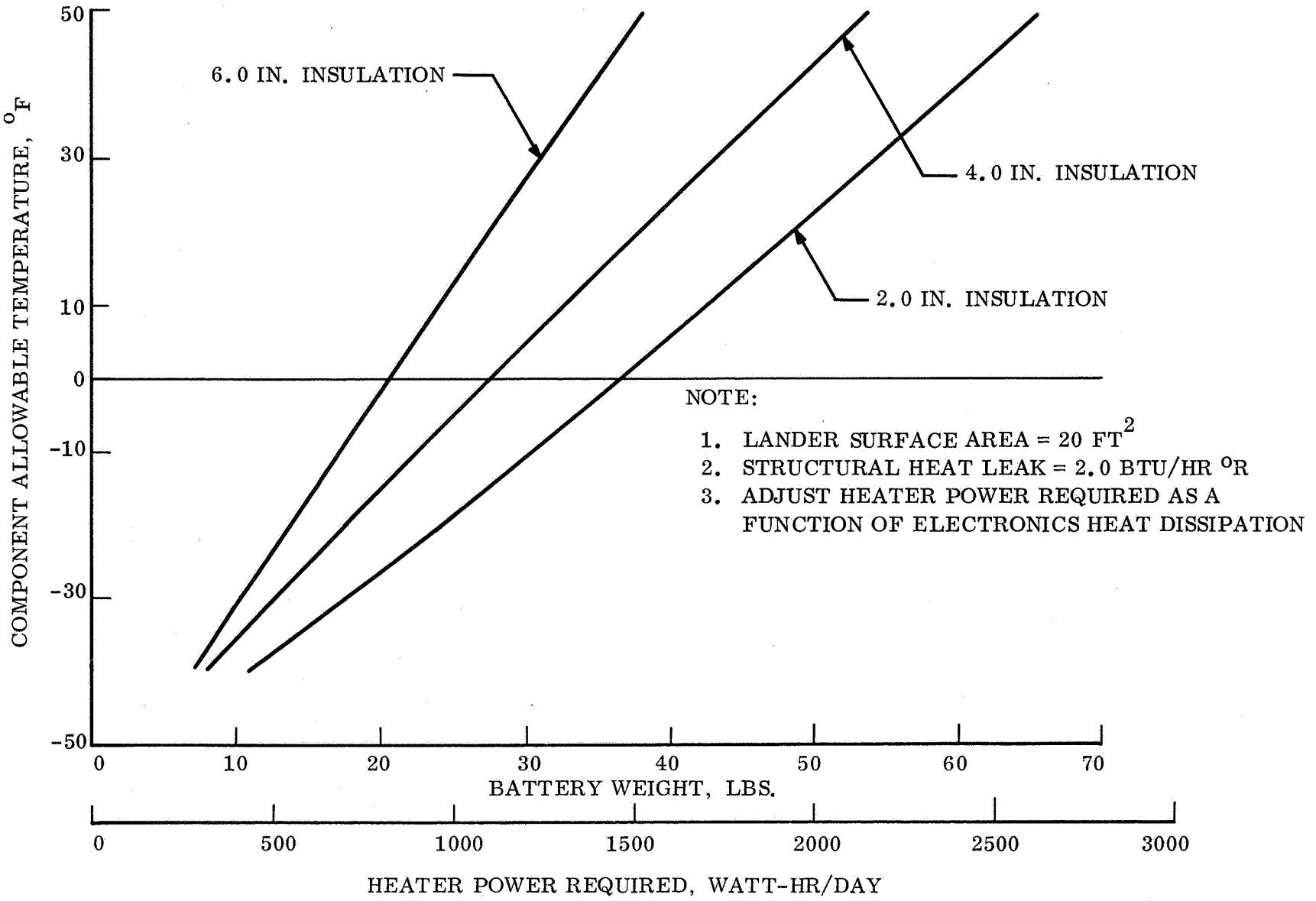

Figure 4.4.4-9. Component Allowable Temperature vs Heater Power Required

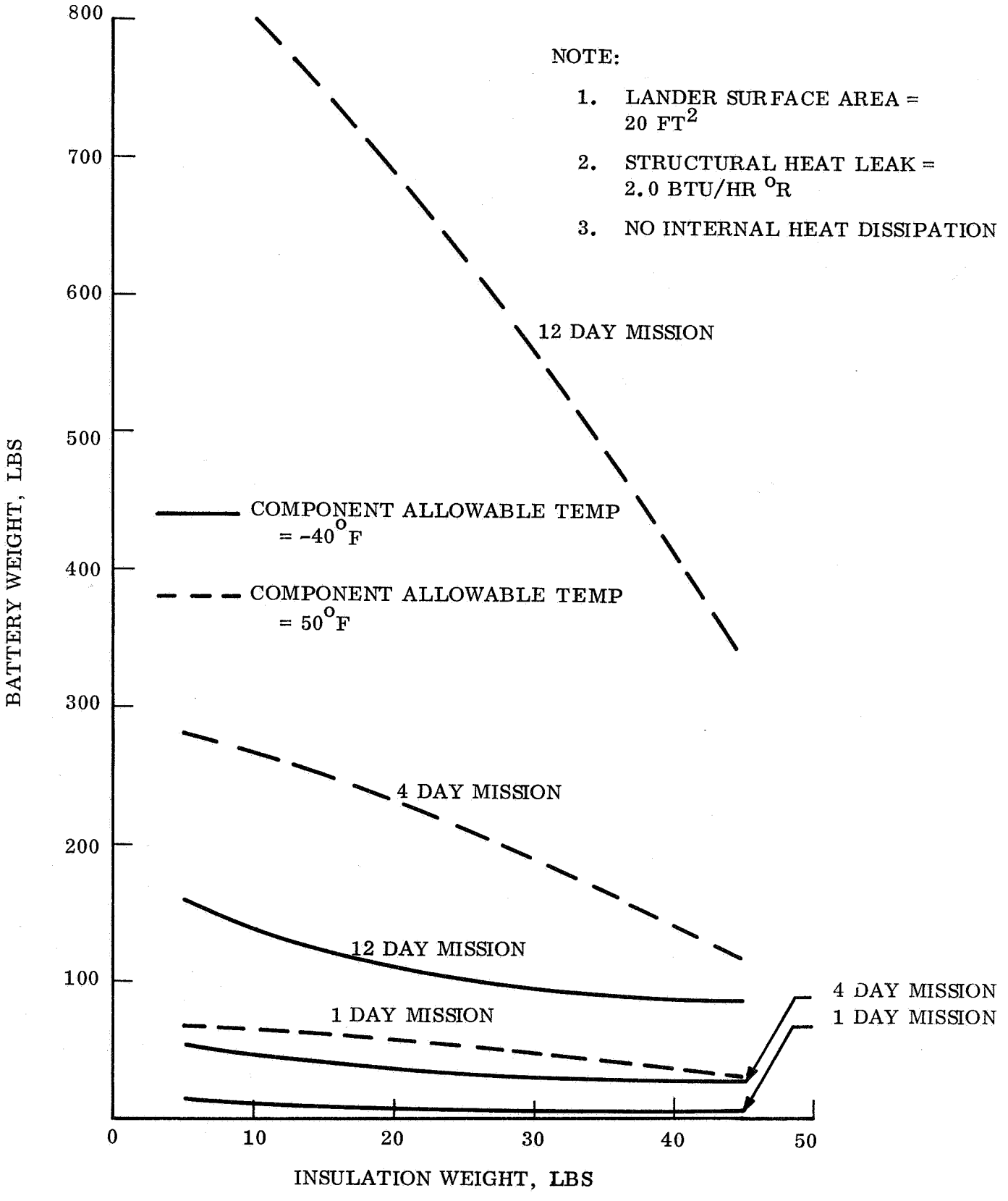

Figure 4.4.4-10. Battery Weight vs Insulation Weight

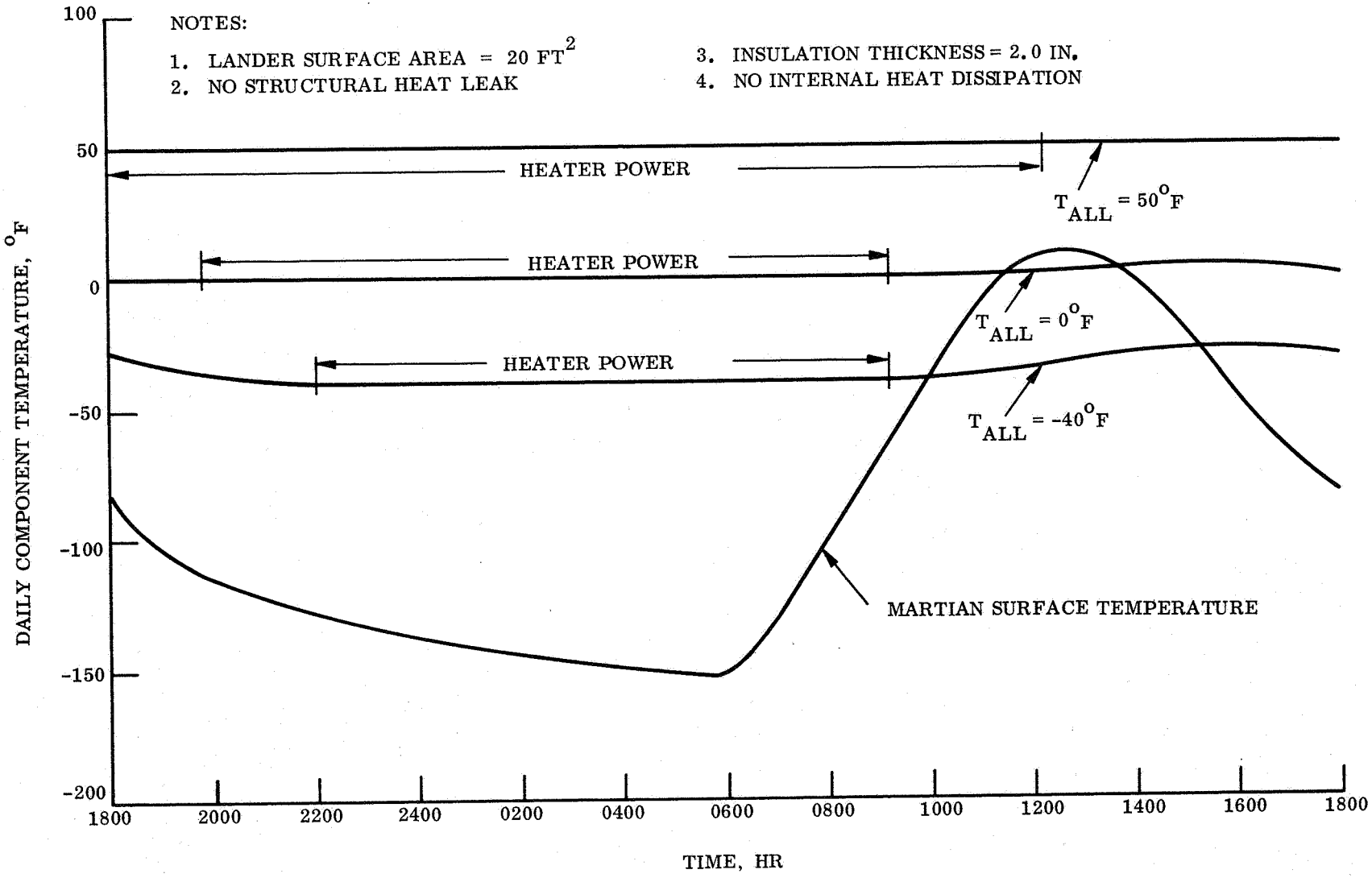

Figure 4.4.4-11. Steady State Daily Component Temperature vs Time

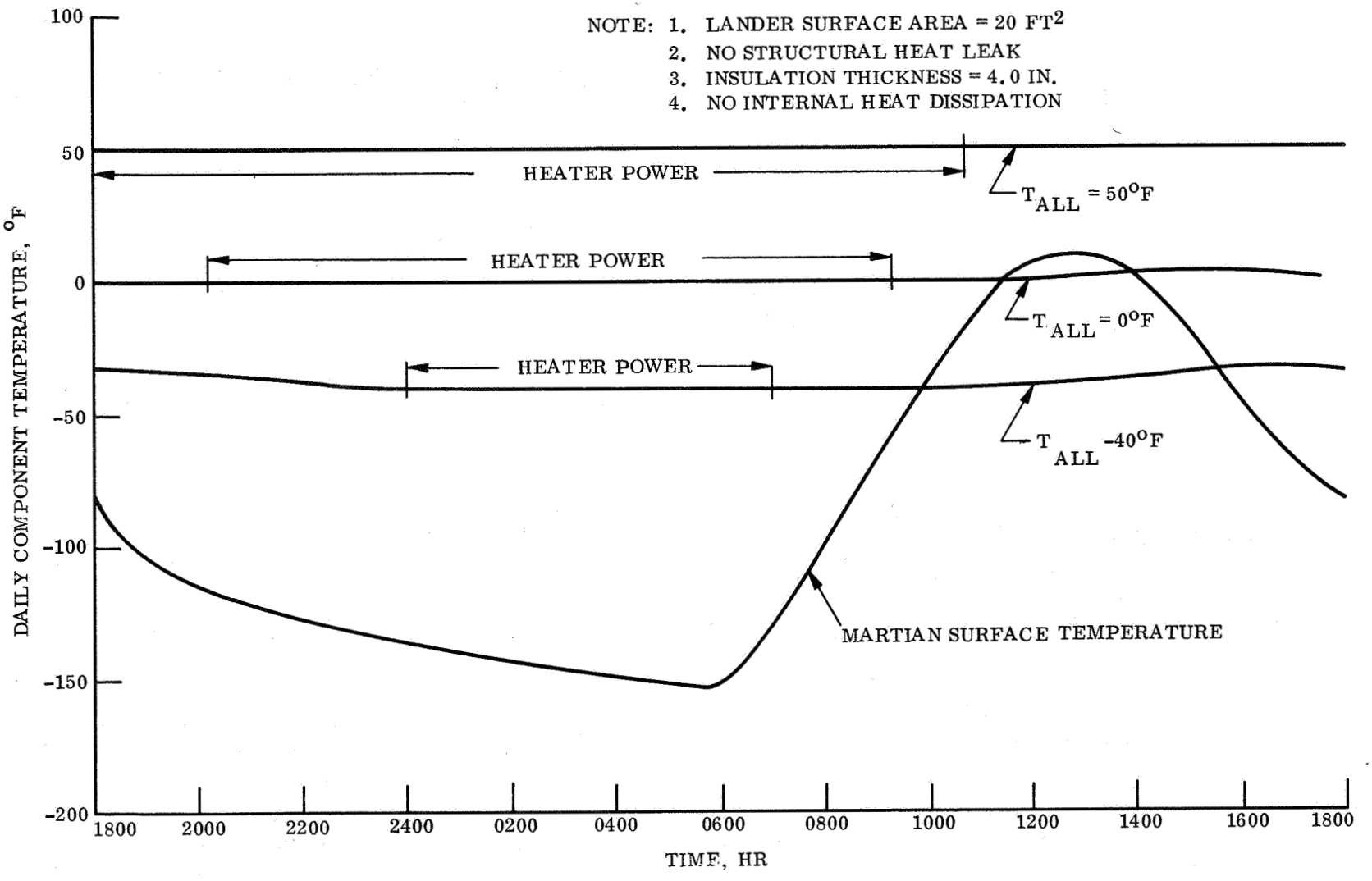

Figure 4. 4. 4-12. Steady State Daily Component Temperature vs Time

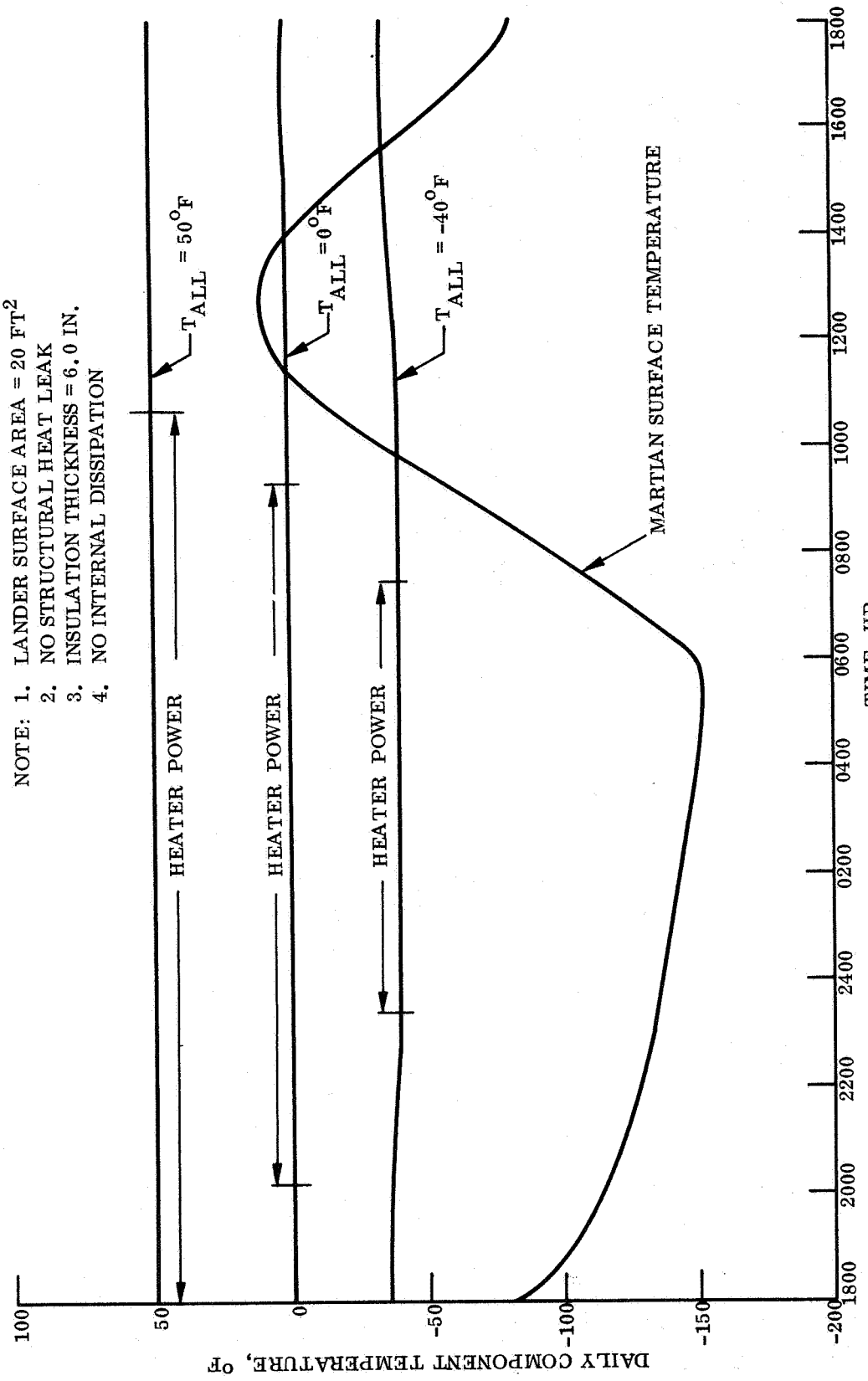

Figure 4. 4. 4-13. Steady State Daily Component Temperature vs Time

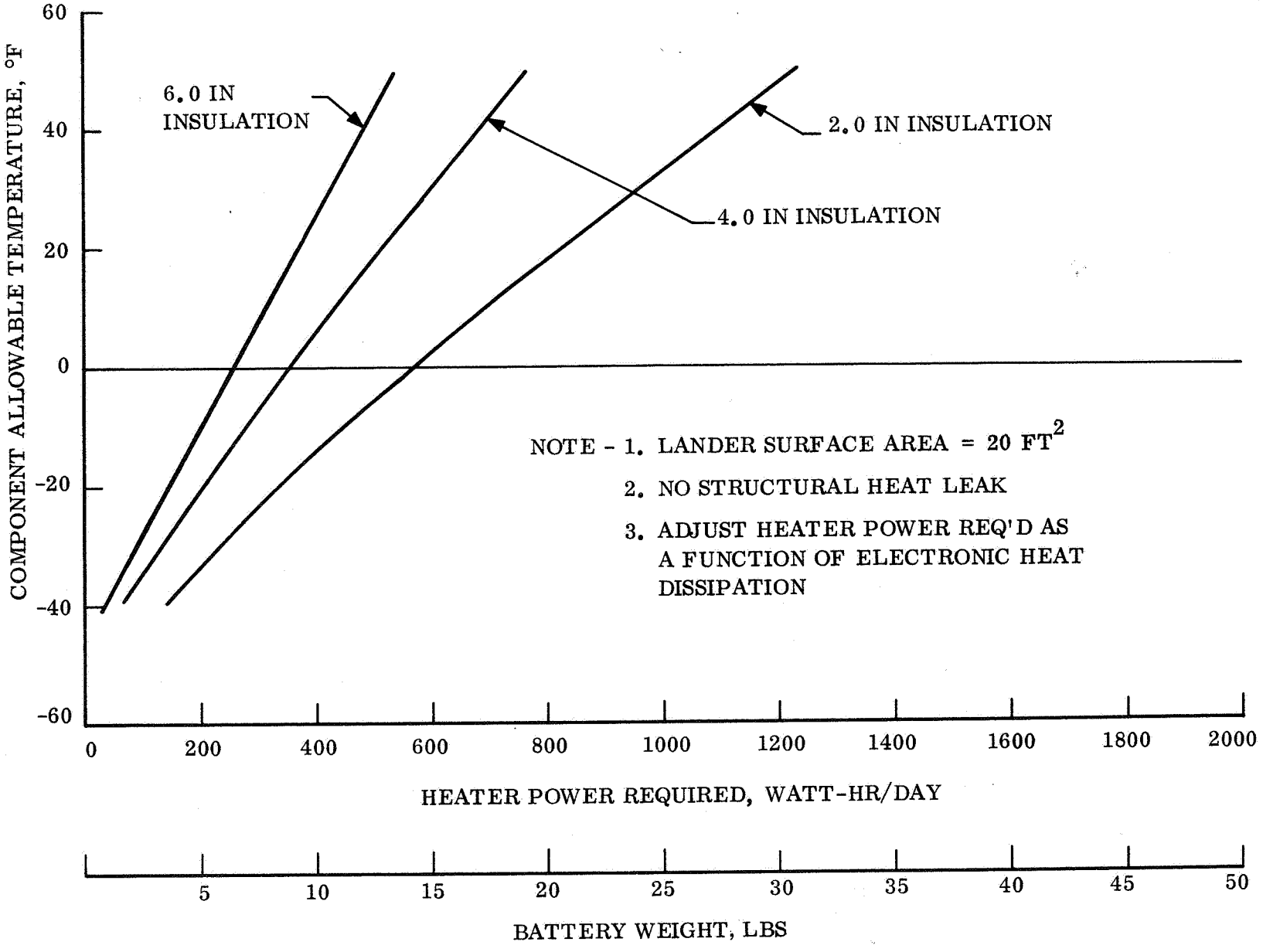

Figure 4.4.4-14. Component Allowable Temperature vs Heater Power Required

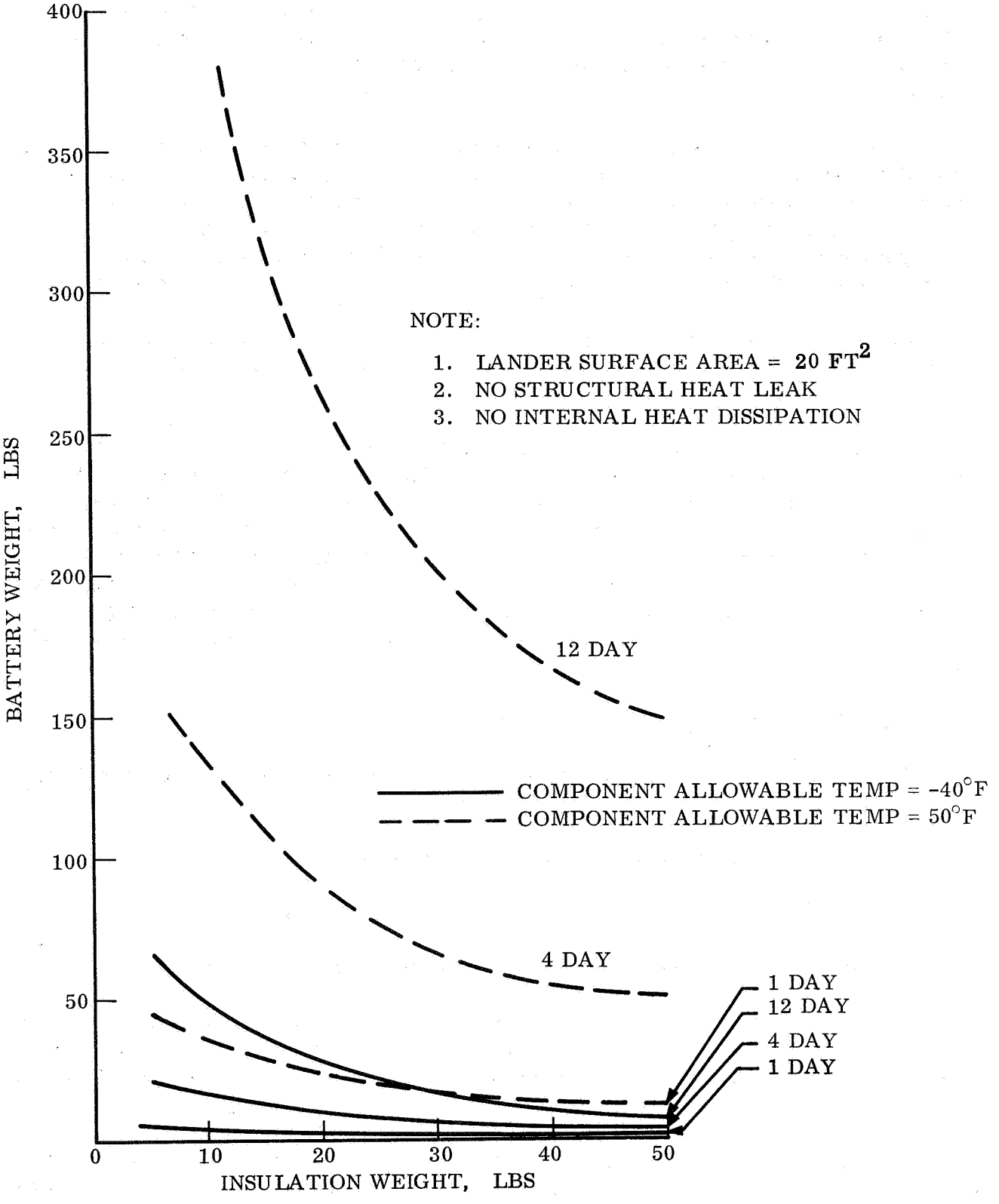

Figure 4.4.4-15. Battery Weight vs Insulation Weight

Figs. 4.4.4-6 through -10 were based on a payload to surface conduction heat leak (from fig. 4.4.4-5) of 2.0 Btu/hr - °R. Figs. 4.4.4-11 through -15 establish the power and insulation requirements for a Lander without conduction heat loss to the surface.

To protect the components against overheating during extensive operating periods, a heat fusion technique is proposed. There are materials available in the form of both waxes and salts which have proper melting points and sufficient state change energies for these applications. Typical weight requirements for transmitter power dissipations is presented in fig. 4.4.4-16. This curve is based on a wax heat of fusion value of 100 Btu/hr with a weight factor of two allowed for a case to contain the wax.

Optimum thermal control weights are plotted in figs. 4.4.4-17 through -20. These curves cover the extreme minimum payload temperature allowables, various length missions and different heat leak possibilities.

The parametric data for Type II, which assumes thermal control of the battery only, is shown in figs. 4.4.4-21 through -24. Figs. 4.4.4-21 through -23 depict the steady state heat loss which must be replaced to maintain a particular component temperature. These curves are shown as a function of battery surface area for various insulation thicknesses. Fig. 4.4.4-24 demonstrates the necessary heat addition required to increase the battery temperature to its operating level. This approach would be applicable if it is desirable to store the battery at a lower temperature than its operating value in order to conserve battery power allocated for thermal control during long non-operating periods.

4.4.4.2 RTG Power Source Thermal Control

Thermal control of an RTG power supply can be accomplished by several different methods:

1. Passive control using radiator fins on the RTG,

2. An active system using a liquid loop with a space radiator,

3. An expendable coolant system which rejects heat by vaporizing a fluid.

Each of these systems may find application in different phases of the mission. For example, an active system during interplanetary travel, an expendable coolant system during powered flight and entry into Mars and a passive system for post impact thermal control.

Weights associated with each of the three systems are shown parametrically in figs. 4.4.4-25, -26, and -27, and table 4.4.4-1. Fin weights for the passive temperature control system (figs. 4.4.4-25 and -26) are for near optimum configurations, whereas the weights for the active systems (fig. 4.4.4-27 and table 4.4.4-1) are only typical.

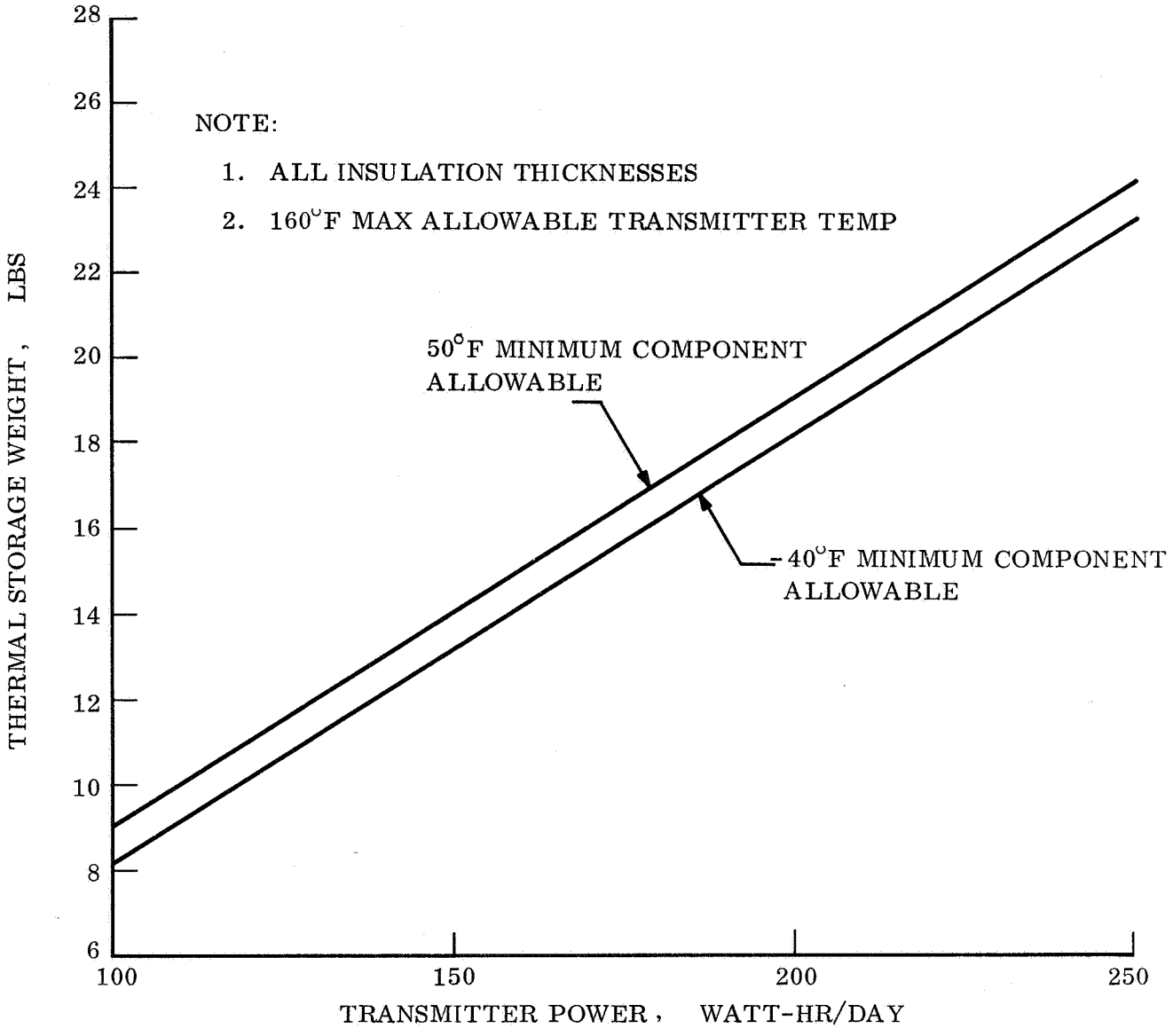

Figure 4.4.4-16. Transmitter Power vs Thermal Storage Weight

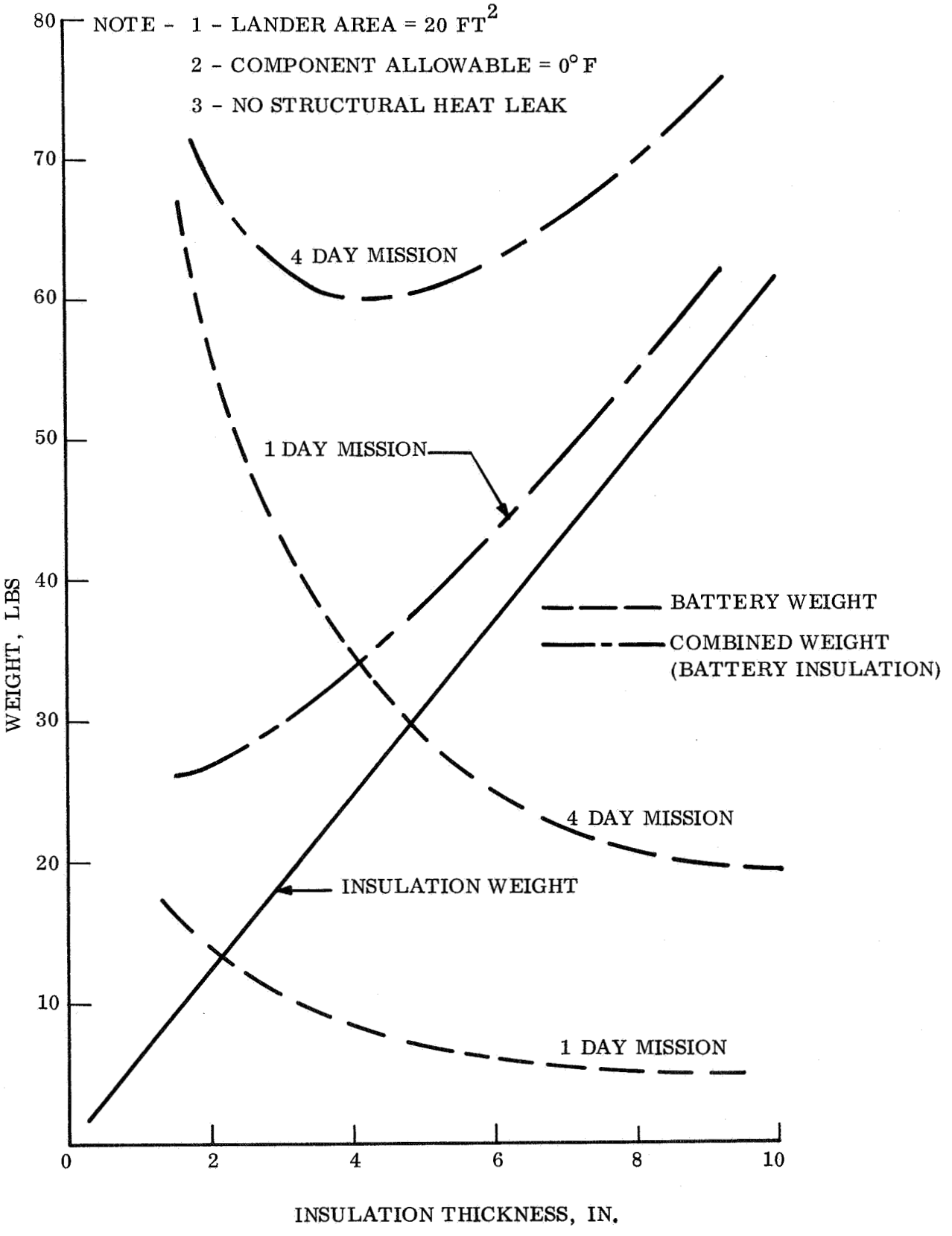

Figure 4.4.4-17. Thermal Control Weight vs Insulation Thickness

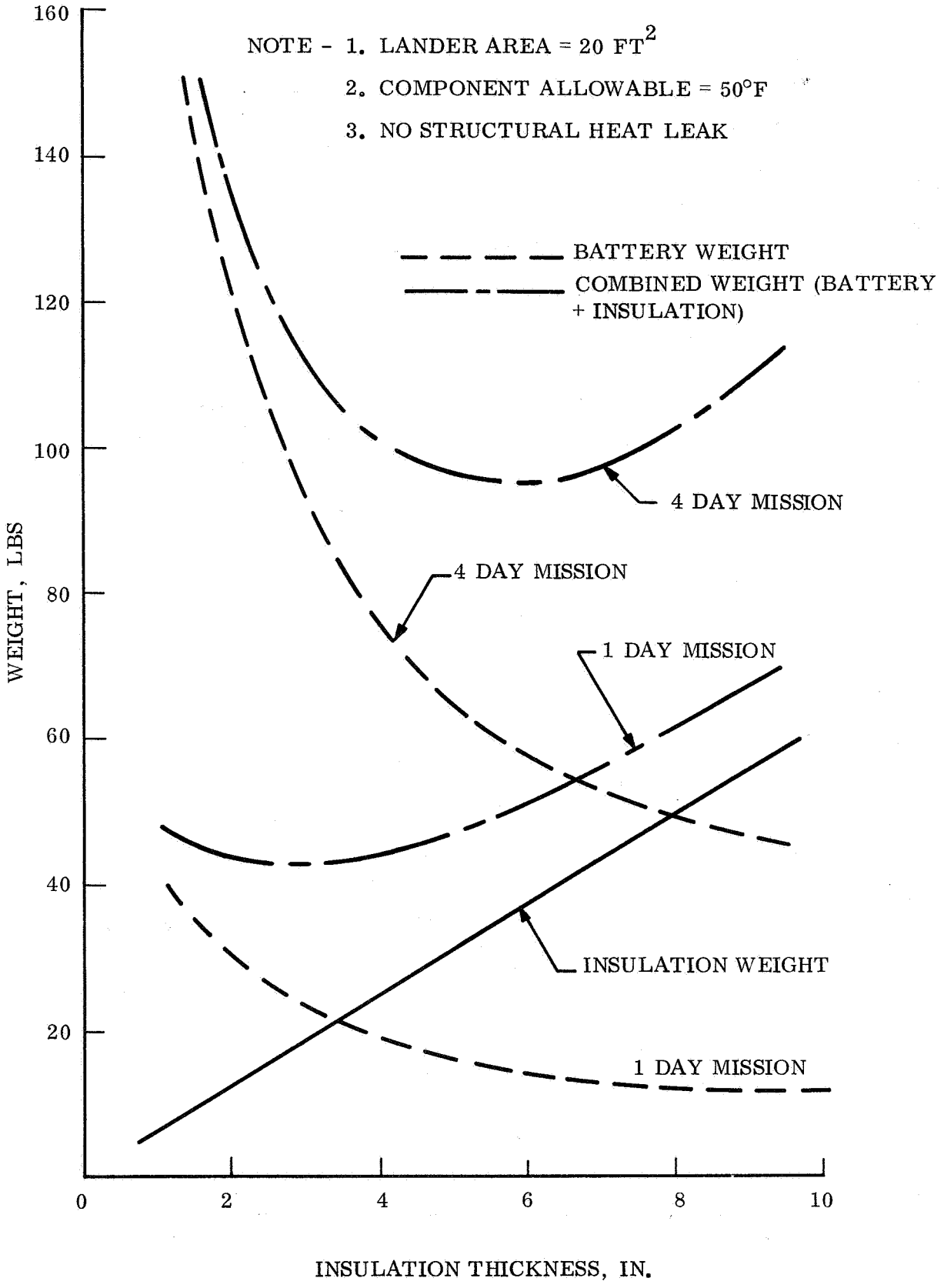

Figure 4.4.4-18. Thermal Control Weight vs Insulation Thickness

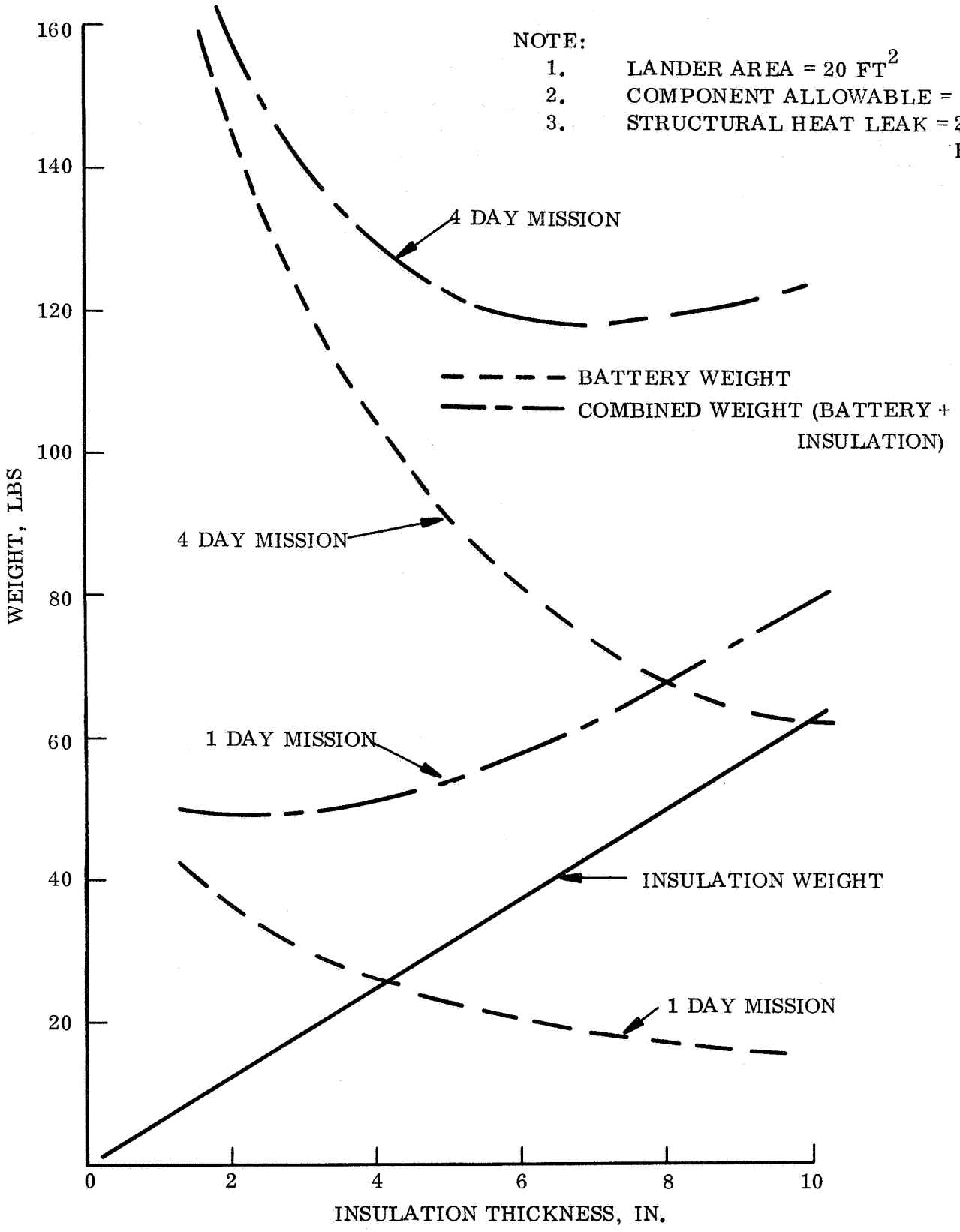

Figure 4.4.4-19. Thermal Control Weight vs Insulation Thickness

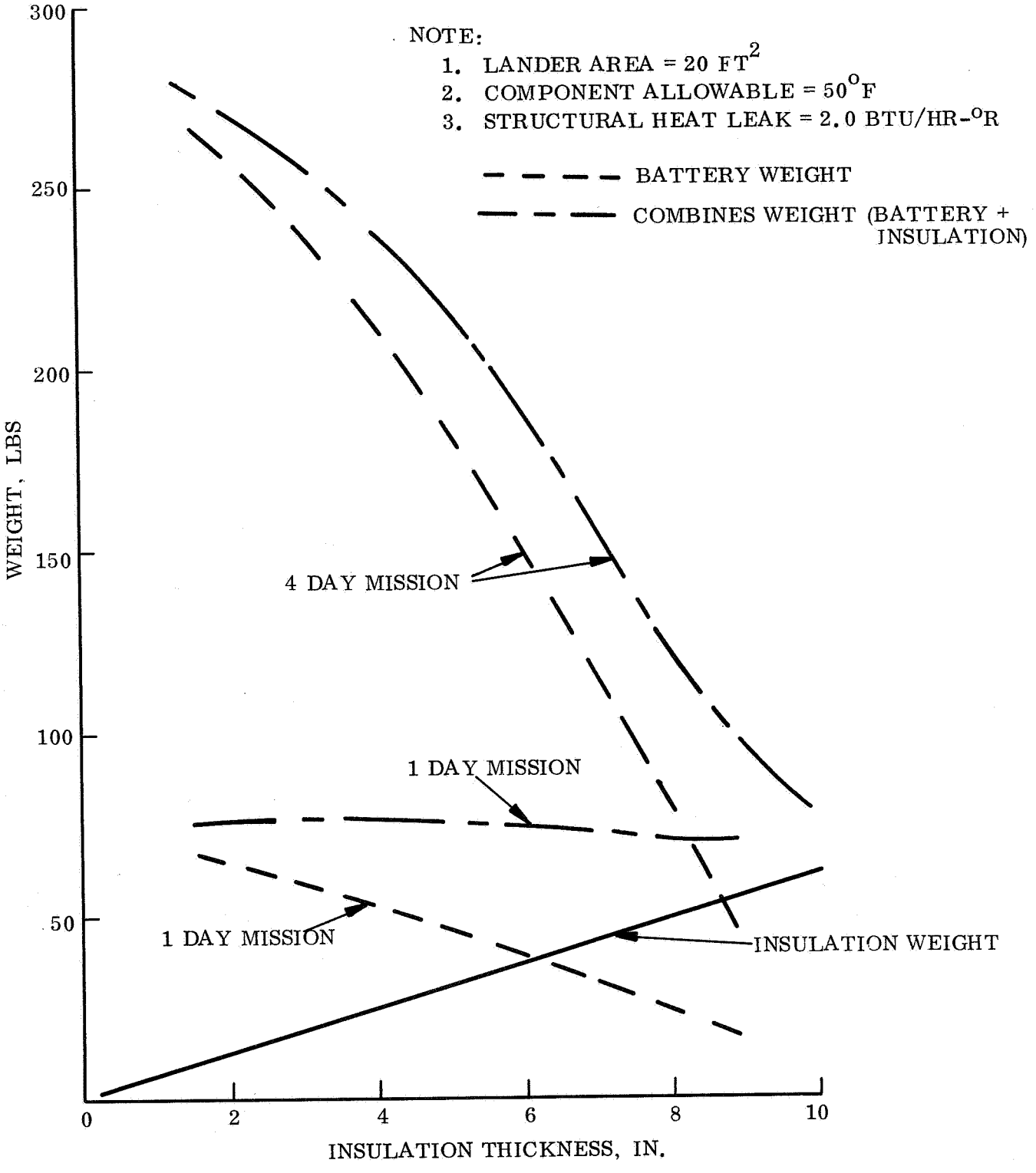

Figure 4.4.4-20. Thermal Control Weight vs Insulation Thickness

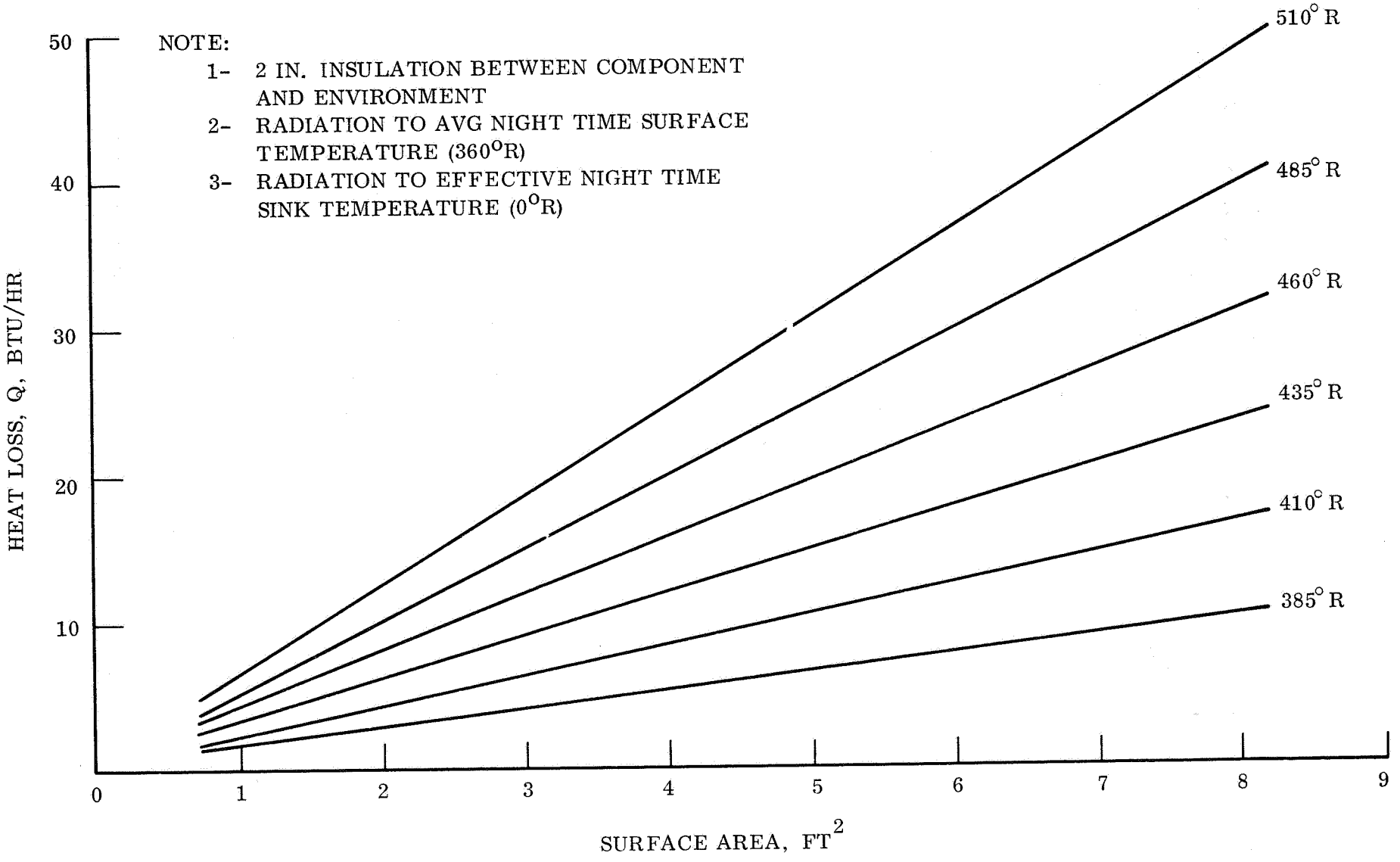

Figure 4.4.4-21. Steady State Heat Loss vs Component Surface Area for Various Component Allowable Temperatures

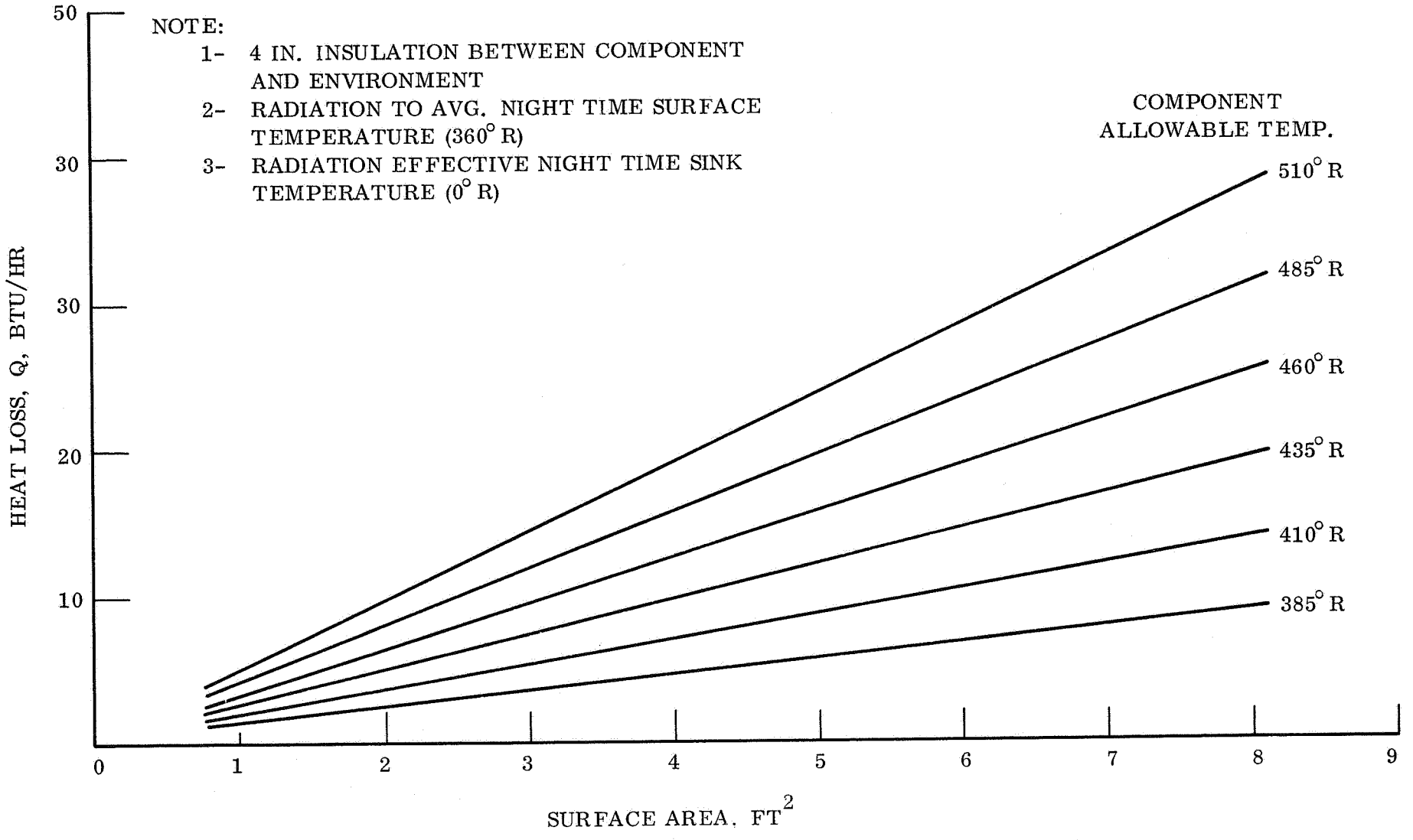

Figure 4.4.4-22. Steady State Heat Loss vs Component Surface Area for Various Component Allowable Temperatures

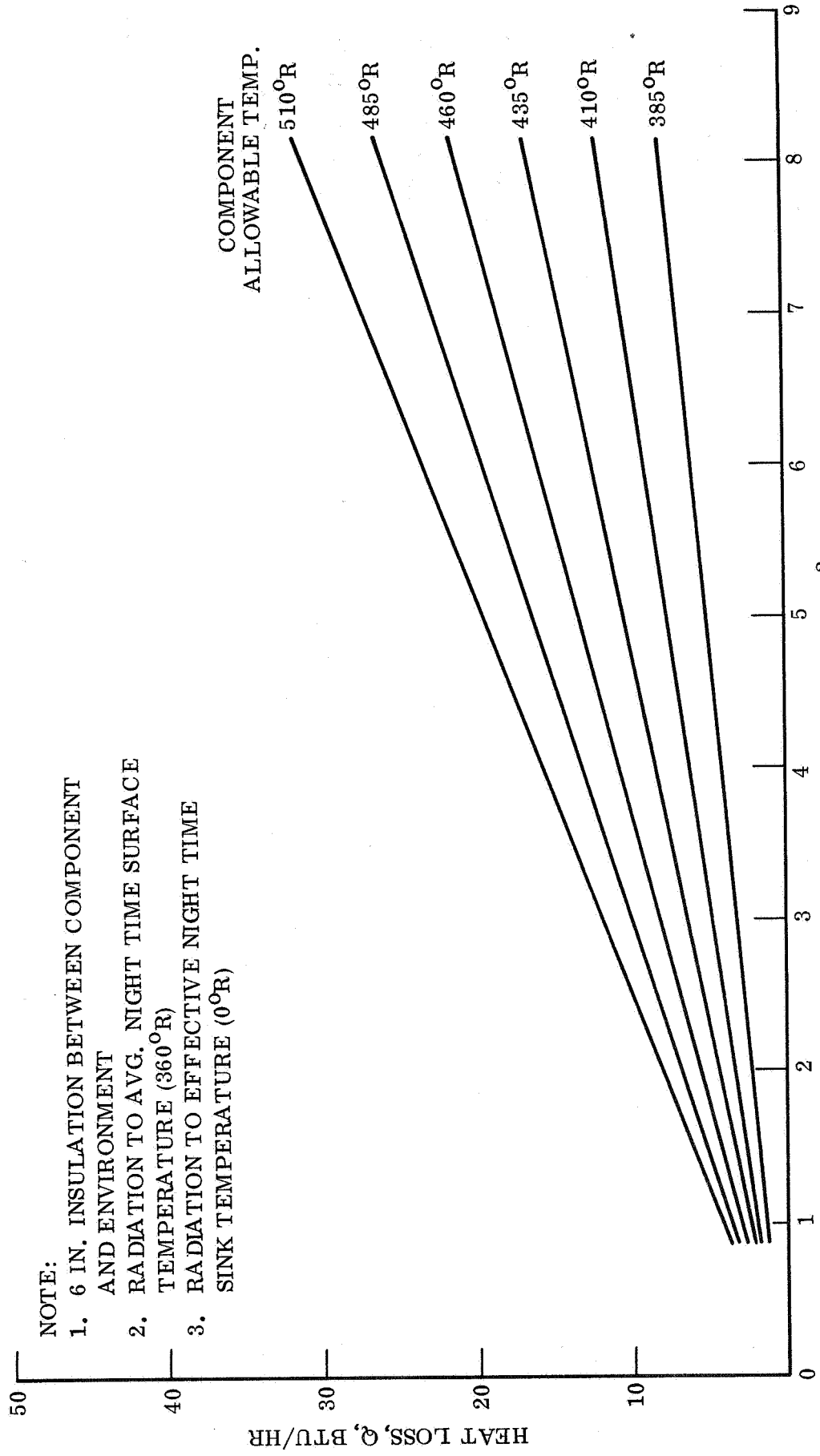

Figure 4.4.4-23. Steady State Heat Loss vs Component Surface Area for Various Component Allowable Temperatures

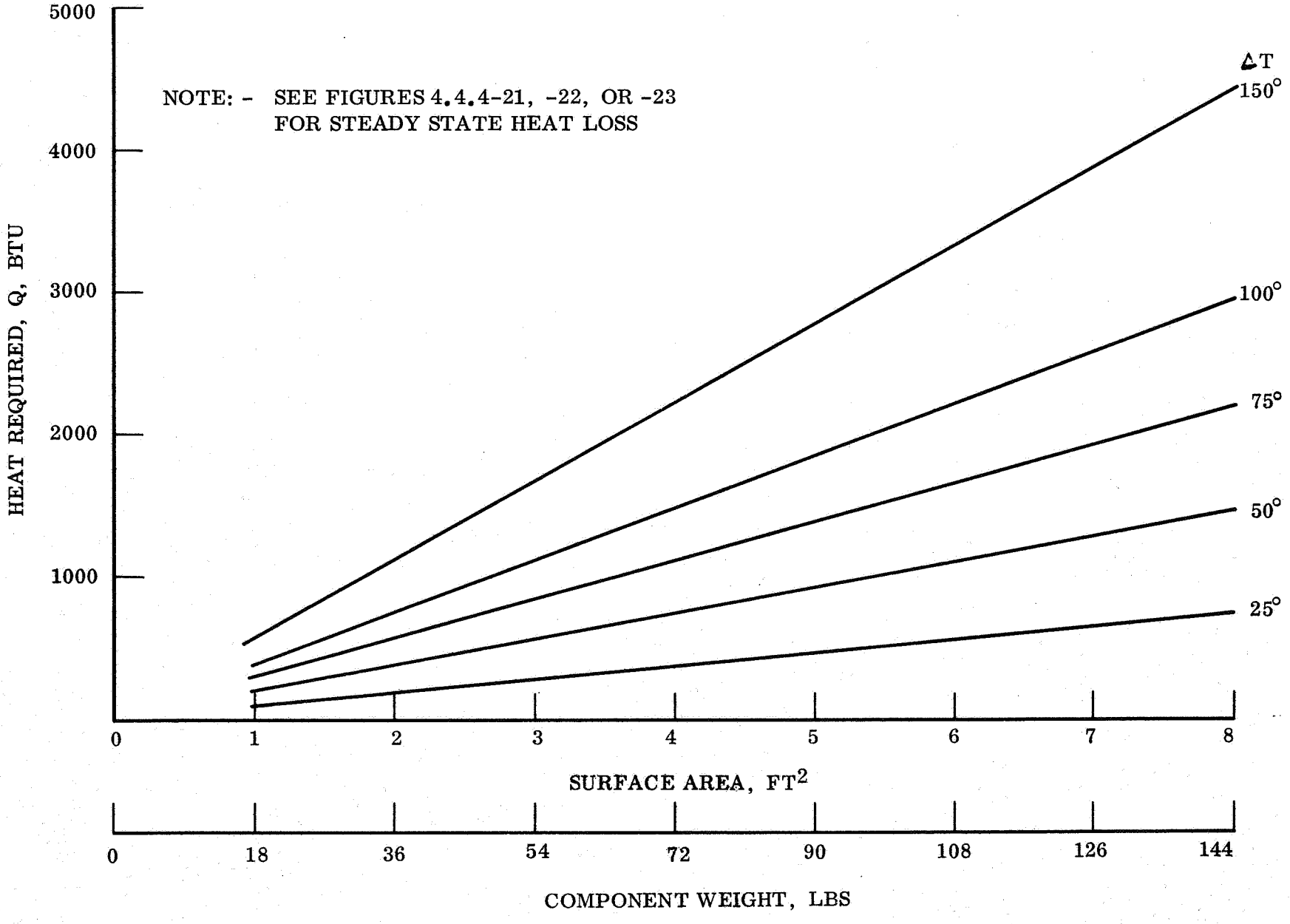

Figure 4.4.4-24. Additional Heat Required to Elevate Component to an Increased Operating Level

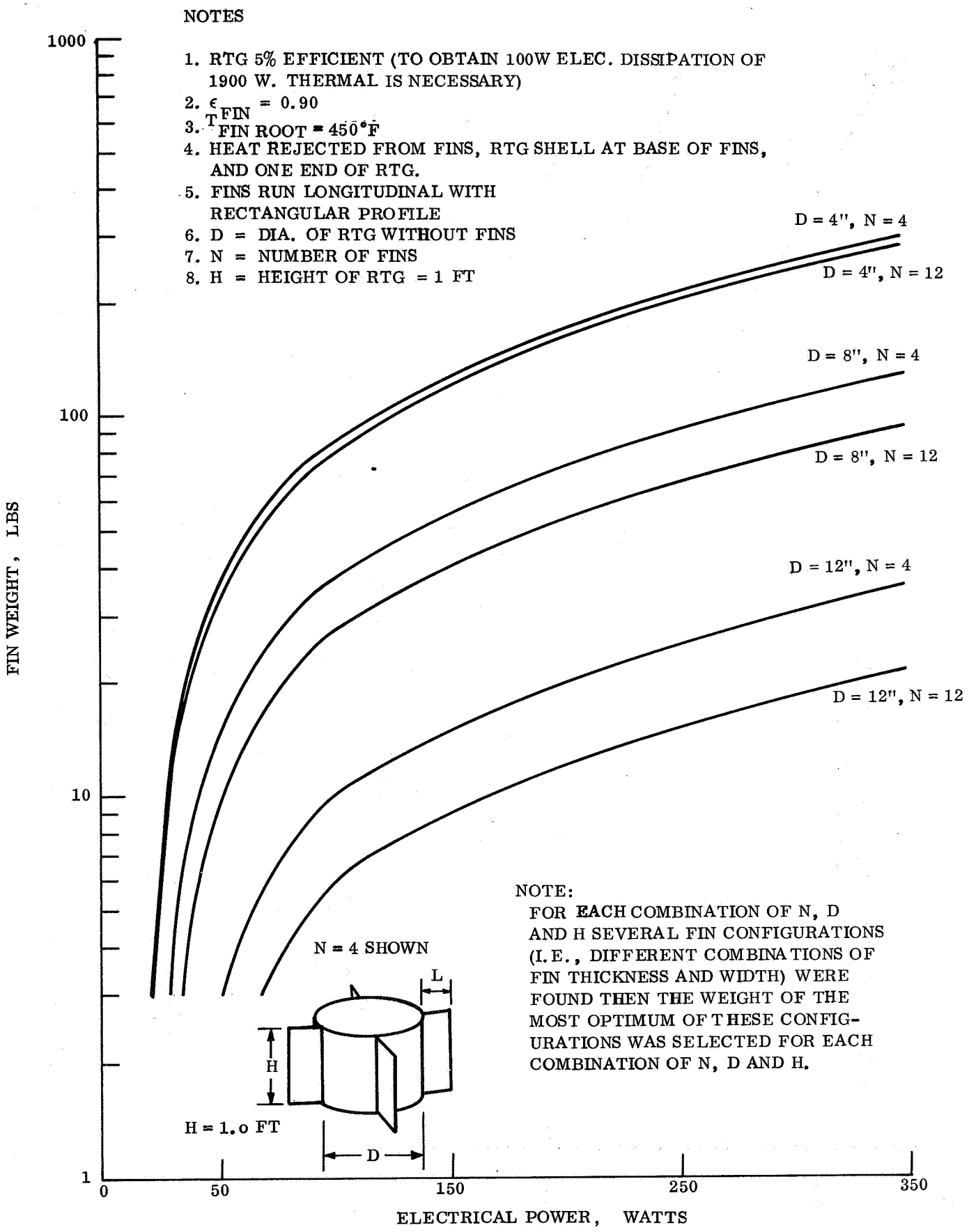

Figure 4.4.4-25. Near-Optimum Fin Weights for RTG Modules

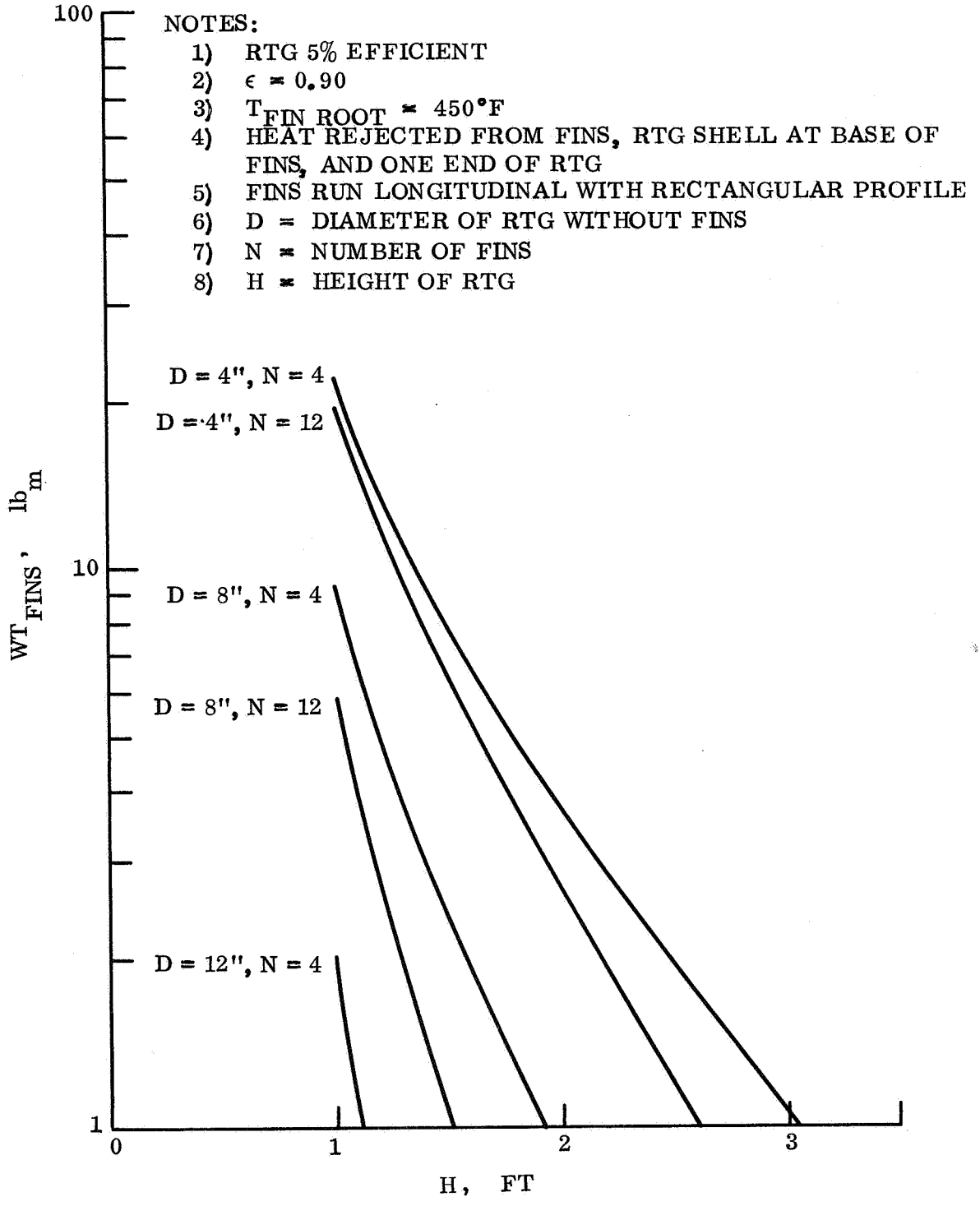

Figure 4.4.4-26. Near Optimum Fin Weights for 40 W RTG Module

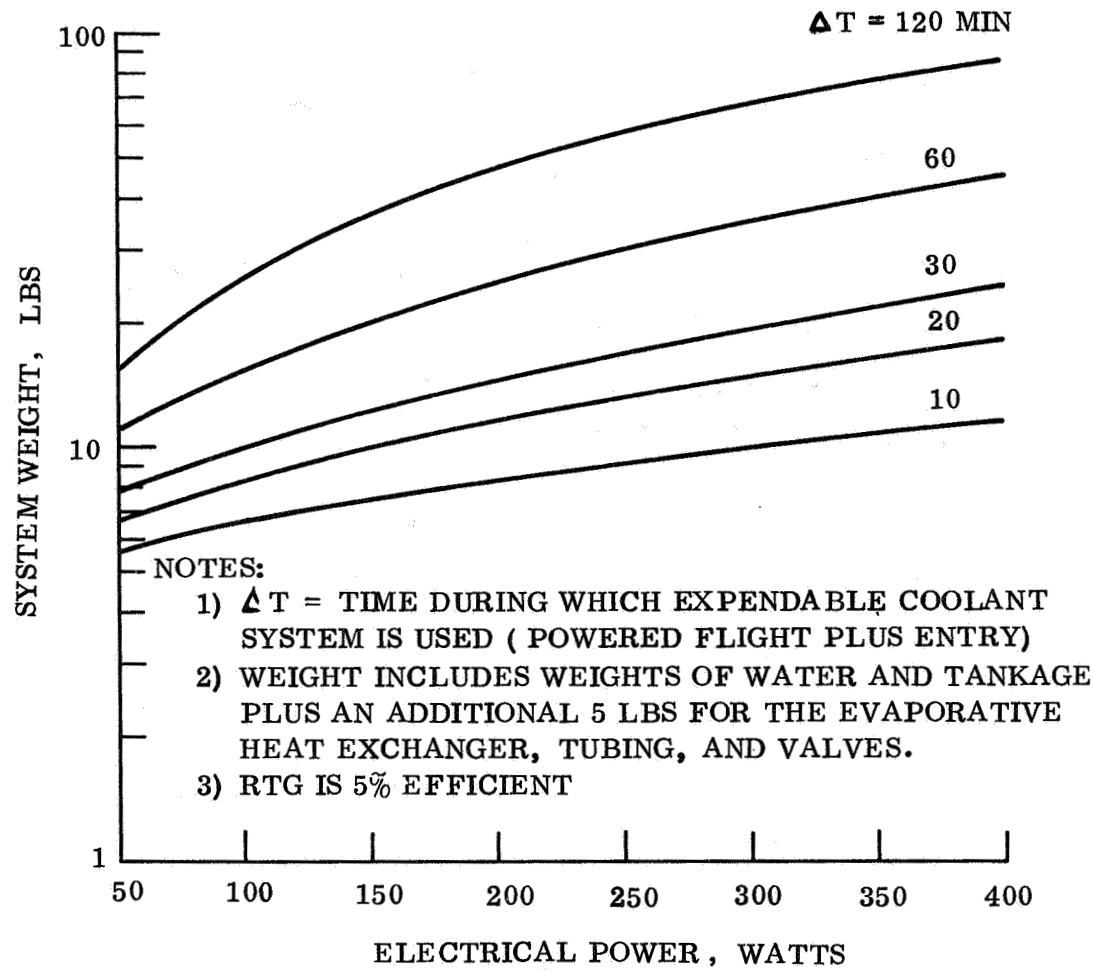

Figure 4.4.4-27. Weight of Expendable Coolant System for RTG

4.4.4.2.1 Passive System (Radiator Fins)

The passive thermal control approach for the RTG power supply would consist of radiator fins. The determination of the size and corresponding fin weights depend upon such variables as

1. Number of fins (N)
2. Diameter of RTG (D)
3. Height of RTG (H)
4. Power dissipation (QRAD)
5. Fin root temperature (TR)
6. Thickness (t) and length (L) of fins.

A sketch of the fin configuration is shown in fig. 4.4.4-25. It can be seen from the configuration that the number of fins (N) has an increasing effect, with RTG diameter, upon how much blockage there is between the RTG body and space. Blockage reduces the RTG's capability to radiate thermal energy.

The near-optimum fin weight is shown as a function of electrical power in fig. 4.4.4-25. Fin weights for a 40 watt (electrical) RTG module as a function of RTG height is shown in fig. 4.4.4-26. It was assumed that the RTG has an overall efficiency of 5 percent with an allowable fin root temperature of 450°F. To optimize fin weight several fin designs (i.e., different combinations of t and L) were selected for each combination of N, D and H. The weight of the most optimum design was then selected for each particular combination of N, D and H. The fin weights presented in figs. 4.4.4-25 and -26 are not strongly influenced by the range of sink temperatures which the RTG will experience on a Mars mission since it operates at a relatively high temperature compared to the sink temperature.

4.4.4.2.2 Active System (Liquid Loop With a Space Radiator)

The estimated weight breakdown for an active coolant system for various RTG power levels is shown in table 4.4.4-1. This system utilizes a liquid loop and space radiator as shown in the following diagram.

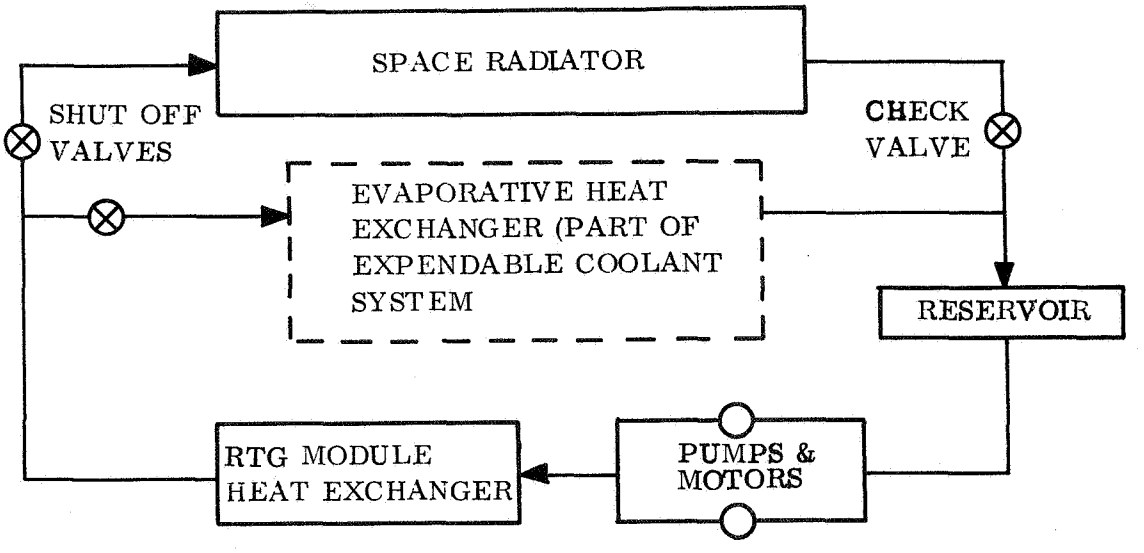

Although the power levels shown are much higher than the expected range of electrical requirements, the values shown in table 4.4.4-1 are representative since all items become constant except for possibly the radiator area.

4.4.4.2.3 Expendable Coolant System

During powered flight when the space radiator of the active coolant system is covered by the shroud and during entry into Mars after the radiator has been jettisoned with the biobarrier/cannister, an expendable coolant system would be utilized for

removing the dissipated heat from the RTG. Such a system is shown in the diagram below. Weights of this system are shown parametrically in fig. 4.4.4-27.

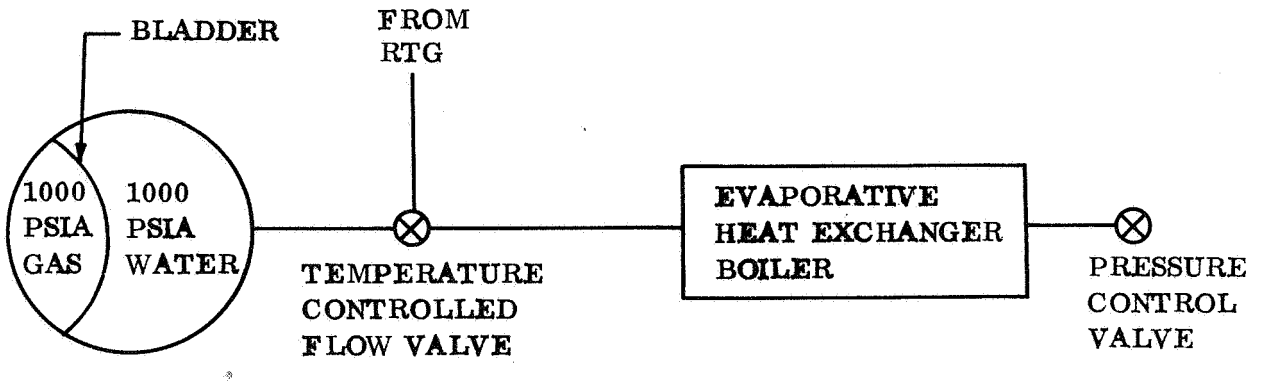

An alternate design approach using a heat pipe as a means of heat rejection looks particularly attractive from a weight standpoint. Light, low temperature ($\leq 100^{\circ}F$) heat pipes would draw the heat from the RTG cavity and pass it out to the sterilization canister surface. Such pipes would provide an excellent heat source for Lander thermal control during the flight. Heat pipes in this range weight on the order of 0.2 lb/ft length.

4.4.5 SUBSYSTEM CAPABILITY

The use of an insulated payload and local electrical heaters is a realistic design approach in satisfying the thermal control requirements for the battery operated Mars Hard Lander. The most practical design configuration would be to mount the temperature limited components on an isolated structure, thereby achieving an isothermal temperature response for the entire payload. The feasibility of using electrical heaters is impractical for missions longer than approximately four days since the batteries and/or increased power supply capabilities required to provide the electrical energy become prohibitive from a weight standpoint. But it may be possible to eliminate the battery as a means of heating the payload. Radioisotope packets distributed throughout the payload could be used to provide the necessary heat. However, some active or semi-active thermal control device (i.e., heat pipe) would have to be introduced in order to prevent isotope dissipation from aggravating the heat rejection when operating in extreme environments. This would require an extensive development program before introducing it into an actual Lander design.

TABLE 4.4.4-1. ESTIMATED WEIGHTS OF ACTIVE COOLING SYSTEM (LIQUID LOOP) FOR RTG

Qelect. (Watts)	Weight Flow Rate (lbm/hr)	Radiator Surface Area (ft^2.)	Power Required (Watts) (To Pump)	Radiator Weight (lbm)	Motor Pump Weight (lbm)	Tubing Weight (lbm)	Coolant Weight (lbm)	Reservoir Weight (lbm)	Valve Weights (lbm)	RTG Heat Exchanger Weights (lbm)	Total Weight (lbm)
100	116	12.4	14	13	6	4	2	1.5	3	4.5	34
500	580	62	60	58	8	6	4	2	4	15	97
1000	1160	124	120	115	8	8	9	4	5	30	180
3000	3470	372	214	345	12	32	35	10	6	90	530

NOTES:
1) Radiator and heat exchanger weights not optimized
2) $\epsilon = .8$
3) $\eta_{FIN} = .7$
4) $T_{RAD} = 400°F$
5) No blockage of radiator is assumed
6) $t_{FIN} = 1/16"$
7) $\Delta_{PSYS} = 15$ psia
8) Monisopropylbiphenyl (MIPB) coolant
9) Flow rate based on $\Delta T_{FLUID} = 100°F$

4.5 IMPACT ATTENUATION AND STRUCTURE

4.5.1 GROSS VEHICLE ATTENUATION REQUIREMENTS AND CRITERIA

The Attenuation Subsystem is required to dissipate the Lander kinetic energy while, at the same time, limiting decelerative forces to levels that the landed subsystems can tolerate. In essence, crush-up impact attenuation devices have three principal traits which are designer-specified: (1) the basic attenuator material, (2) material density, and (3) attenuator thickness. The attenuator material to be used is determined from mission constraints and the various environments. For the Hard Lander study, the active environmental constraints include sterilization of the Lander package, an extended in vacuuo interplanetary transit, and exposure to space irradiation. These considerations, as well as the mission requirement for an RF-transparent container envelope, indicate phenolic fiberglass honeycomb as a reasonable reference material for purposes of the parametric study. The density of the particular honeycomb material to be used is dictated by impact conditions: total landed weight, tolerable peak g-level, and Lander geometry/footprint characteristics. These factors establish the required honeycomb crushing stress which is directly related to the material density. The third attenuator design parameter, thickness, is specified by the kinetics of the impact situation. Thus, the impact velocity vector, the tolerable deceleration level, and the particular Lander footprint characteristics establish the necessary stopping distance or stroke required to decelerate the Lander without exceeding the allowable g-level. Surface protrusions or rocks will require increased thickness as a safeguard against penetration of the payload container. Additional material beyond that which is required for deceleration stroke distance is included to allow for incomplete material crush-up. Another factor influencing the design thickness is provision for a safety factor against off-design impact conditions and imperfect estimates of Lander g-tolerance.

An added criteria on gross crush-up attenuator thickness must also be applied. The requirement that the thickness be so limited that established, predictable failure mechanisms will produce the desired energy dissipation. For honeycomb material, this means that the thickness must be small enough so that gross buckling or shear failures do not occur before an orderly crush-up. The repeatable, predictable response of a proven material underlies the selection of phenolic fiberglass honeycomb of the density range and composition used in this study.

Prior to beginning the parametric analysis which is conservatively based on encounter with an infinitely rigid soil (outcroppings for example), it was necessary to assess the extent of penetration which could be expected on realistic soft-soil conditions.

Although it is possible to make calculations of dynamic penetration into soils by making assumptions on bearing strength, intergranular friction, and other sources of energy absorption as penetration proceeds, it is probably more accurate to make use of empirical data available on penetration of low-speed projectiles into soils. With the latter approach, the main source of uncertainty lies in the process of extrapolating results from known terrestrial soils to the less dense (assumed) Mars soil, rather than in the errors inherent in making assumptions on the entire dynamic penetration process.

Ref. 4-26 contains the results of many experimental measurements of the penetration of steel balls and other high density projectiles into sand, soft rock, and hard rock. Correlation is made via a ballistic density term γ as follows:

$$\gamma = \frac{W}{\frac{\pi}{6} \rho_S D^3}$$

where W is the weight of the impacting body and $\pi/6\ \rho_S D^3$ is the weight of a steel sphere of diameter D. An approximate formula for penetration, Y, into dry sand at 210 fps may be obtained from fig. 3.1 of ref. 4-26 as follows:

$$Y = 3.1 \gamma D$$

For a typical Mars Lander Vehicle with $D \cong 75$ in. and W = 930 lbs:

$$\gamma = \frac{930}{\frac{\pi}{6} (0.283)(75)^3} = 0.0149$$

$$Y = 3.1\,(0.0149)(75) = 3.46\,\text{in.}$$

It is difficult to assess the difference between penetration of a toroidal shape like the Mars Lander design and that of the spheres used in the above calculation, but perhaps the correlation could be based on the relative submerged areas. For the sphere, the bearing area would be $\pi (DY - Y^2) = 776$ sq in. while the toroid submerged 3.46 inches would have a bearing area over 2,000 sq in. On this basis, the toroid would penetrate even less than 3.46 in.

Ref. 4-27 presents the following empirical formula, based on more recent data on soil penetrations:

$$Y = 6.4\ SN \sqrt{W/A}\ \ln (1 + 2\ v^2 \times 10^{-5})$$

where S is a soil constant, N is a nose shape constant, and A is the frontal area of the projectile in sq in. Taking S = 5 for a loose dry sand, N = 0.6, and A ≅ 2,500 sq in.:

$$Y = 6.4\ (5)\ (0.6)\ \sqrt{930/2500}\ \ln 1.88 = 7.4 \text{ in.}$$

A possible cause of the factor-of-two difference between the estimates made above may lie in the fact that ref. 4-26 used data on small diameter steel balls (0.356 in. to 4.3 in.) while ref. 4-27 used projectiles in the 3 to 18 in. range. Applied to the large size Mars Lander, one would therefore tend to lean toward the 7.4 in. prediction. In either case, however, it is sufficient to note that these penetrations into the least resistant soil (of the dry variety - mud penetrations are quite deep) are quite small, and may be expected to be less for impact on harder media.

Note that the Mars soil is anticipated to have a density of 1 ±0.6 gm/cm^3, while the empirical results above were obtained with sand densities of about 1.6 gm/cm^3. The method of ref. 4-26 would scale penetration inversely with target density, which would increase the 3.46 in. prediction to 5.54 in. for the least dense Mars soil. Ref. 4-27 uses penetration inversely proportional to the square root of density, and the 7.4 in. prediction is increased to 9.4 in. for the least dense Mars soil. To summarize, it appears that the highest empirical estimate is 9.4 in., and the expected value would be somewhat lower.

In regard to the g-loadings experienced by components aboard the Lander, it must be noted that total stopping distance is the significant parameter. For a constant deceleration process:

$$\text{Average g} = \frac{(210)^2(12)}{64.4\,Y} = \frac{8,220}{Y} \text{ g's}$$

In this case Y is the penetration plus the crushup stroke of the honeycomb, or about 12 in. plus soil penetration. Therefore, on impact with an unyielding surface, the average deceleration would be 685 g's, while the highest penetration estimate made above produces an average deceleration of 384 g's. The greatest influence on g-loading is therefore found to be the crushup stroke rather than penetration, and the exact calculation of penetration is not of utmost practical importance.

On normal impact of the Mars Hard Lander, with yielding and energy absorption provided primarily by the crushup material of the Lander and by penetration into the Mars surface (and only to a minor extent by local flexibilities within the component package), it is assumed that all components will experience approximately the same deceleration-time history. In this discussion average decelerations will be used as a reference. In the point designs, however, actual pulse shapes are used.

The preceding paragraphs have presented estimates of penetration into the Mars surface by using empirical data provided in refs. 4-26 and -27, at an impact velocity of 210 fps. Since the impact velocity is expected to vary, further calculations are made for velocities from 100 fps to 300 fps. Average decelerations, $V^2/2Y$, are also included and plotted in fig. 4.5.1-1.

Note that the slopes of the curves in the figure are similar, despite the 2:1 difference in numerical values (discussed previously). If 2,000 g is selected as an order of magnitude approximation, constant in the 100 to 300 fps velocity range of a constant and selection deceleration independent of velocity implies a constant-force penetration process, then in this case the force would be (930) (2,000) = about 2,000,000 lbs as the Lander penetrates the Mars surface. Taking the crushup of the honeycomb material as a more-or-less constant force process for purposes of this discussion and assuming an 8 in. deflection at an impact velocity of 200 fps, the average deceleration on impact with a rigid surface would be $(200)^2/(2)(0.667)(32.2) = 933$ g's. This is about half the surface-penetration resistance, which implies that most of the deflection will be obtained from crushup rather than from surface penetration.

If the Mars surface resistance is constant and yields exactly at 2,000 g's and the honeycomb yields at 1,000 g's and does not increase in resistance as it crushes, the entire stopping process would resemble impact on a rigid surface, since the Mars surface would not be penetrated at all. However, one might expect the honeycomb resistance curve to have peaks above the Mars surface resistance curve, and the actual decelerations would be somewhat below 1,000 g's. For conservative estimating, however, 1,000 g's is appropriate for normal impact.

Since most components will not have the mounting space to permit δ variations of more than a few inches, and $Y \cong 8$ in. or more, it appears that the average rigid-body decelerations cannot be reduced much more than 20 percent.

The main function of shock mounting applied to the Mars Hard Lander components will be to prevent excessive dynamic responses of individual components to the acceleration-time inputs. If, for example, the higher frequency oscillations in the input pulse should tend to coincide with a lower mode of a component, the response could be amplified to a very high value, since this would be a case of forced vibrations. In this case the shock mount can be designed to perform two functions:

1. Move the component-plus-mount frequency away from a resonance with the forcing function.

2. Provide damping to further reduce responses to high frequency inputs.

The requirements for individual shock mounts will be developed in detail design by preparing a dynamic computer model of the Lander and its components, and subjecting the model to the deceleration-time inputs expected on impact. An analysis has

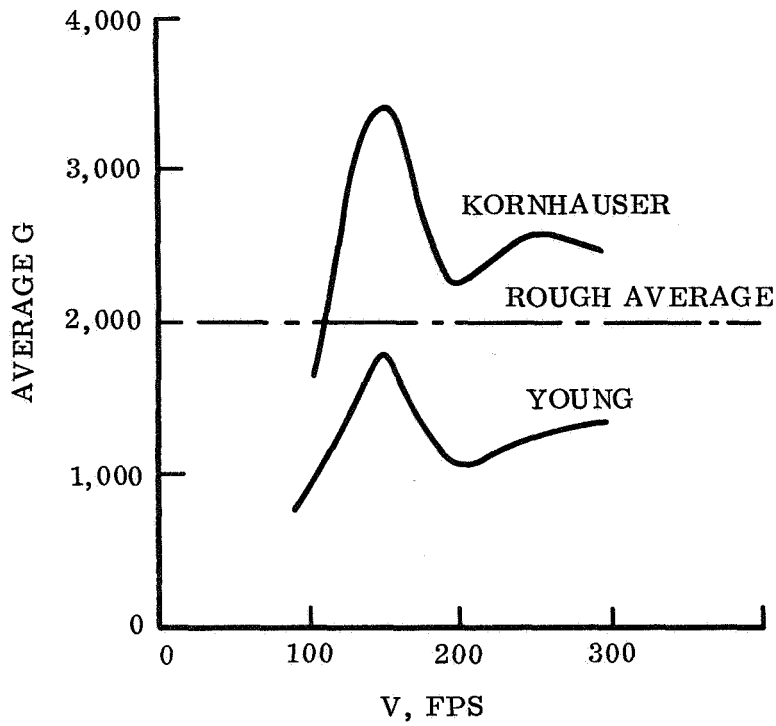

Figure 4.5.1-1. Penetration Effects for Average Deceleration

Penetrations Calculated from ref. 4-27 (Kornhauser)

V, fps	100	150	200	250	300
P, dia	1.1	2.0	3.0	4.0	6.0
Y, in.	1.23	2.24	3.36	4.43	6.72
Avg g	1,520	3,380	2,220	2,600	2,490

Penetrations Calculated by Young's Equation, ref. 4-28

V, fps	100	150	200	250	300
Y, in.	2.14	4.34	6.87	9.49	12.05
Avg g	875	1,740	1,080	1,230	1,390

been performed on a typical Hard Lander to quantitatively assess the previous conclusions. An important conclusion is that ground penetration will be on the order of inches for a realistic soft soil condition. Thus, early fears that very deep penetrations would take place and endanger experiment deployment are unwarranted.

4.5.1.1 Impact Attenuation of Components

When the Lander impacts on an edge, there exists the possibility that high angular accelerations may cause high loading on components located at the outer extremity of the container. Two things can occur, high angle impact or low angle impact, as shown in fig. 4.5.1-2.

4.5.1.1.1 Case A

The overall force, F_o, over the area of impact may be expected to be less than for normal impact, F_n, because less area of crushup material is being loaded. Roughly, the force will be proportional to the area of contact; thus F_a, F_n and the deceleration of the c.g. will be less than the value $G = F_n/M$ for normal impact.

In fig. 4.5.1-2(a), it is apparent that impact on one edge introduces a second major change in the form of an angular acceleration of the entire body. Components near the point of contact will experience the highest accelerations:

$$G = G_1 + r_1 \ddot{\alpha} \qquad (1)$$

$$G = F_a/M + r_1 \ddot{\alpha}$$

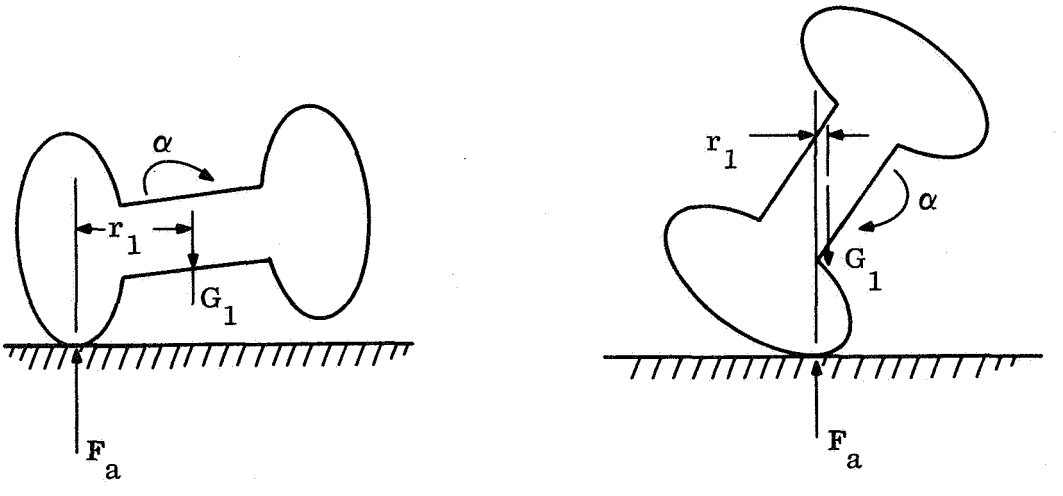

a. Low Angle b. High Angle

Figure 4.5.1-2. Angular Acceleration Conditions

Angular acceleration:

$$I\ddot{\alpha} = F_a r_1 \tag{2}$$

Combining eq. 1 and 2:

$$G = F_a/M + F_a r_1^2/I$$

$$= (F_a/F_n)G_o\ (1 + Mr_1^2/1) \tag{3}$$

$$G/G_o = (F_a/F_n)\ (1 + Mr_1^2/I)$$

Taking $r_1 = 2$ ft, $M = 930$ lbs, and $I = 2,020$ lb-ft^2

$$Mr_1^2/I = 1.84$$

$$G/G_o = 2.84\ F_a/F_n \tag{4}$$

One would expect the area of contact to be considerably less than half that for normal impact, probably in the 1/10 to 1/3 range. It thus appears, roughly, that impact at an angle will produce about the same decelerations as on normal impact, or probably lower.

4.5.1.1.2 Case B

For this situation of impact angle, the same equations apply. However, analysis has shown that the force is about the same as the normal, flat impact:

$$F_a \cong F_n$$

The moment arm r is much less than in Case A, leading to the same conclusion that high angular acceleration g's will not occur. The average decelerations experienced by the overall lander, $V^2/2Y$, may be decreased for any particular component on a shock mount with stroke δ to a new value, $V^2/2(Y + \delta)$:

$$G/G_o = Y/(Y + \delta) \tag{5}$$

Three major structural spring-damper elements exist between ground and a typical component in the Lander vehicle. These are the container structure, the prime

component mounting shelf, and the local mounting structure to a particular component. A vibration analysis that considers each of these prime structural elements could use the model below:

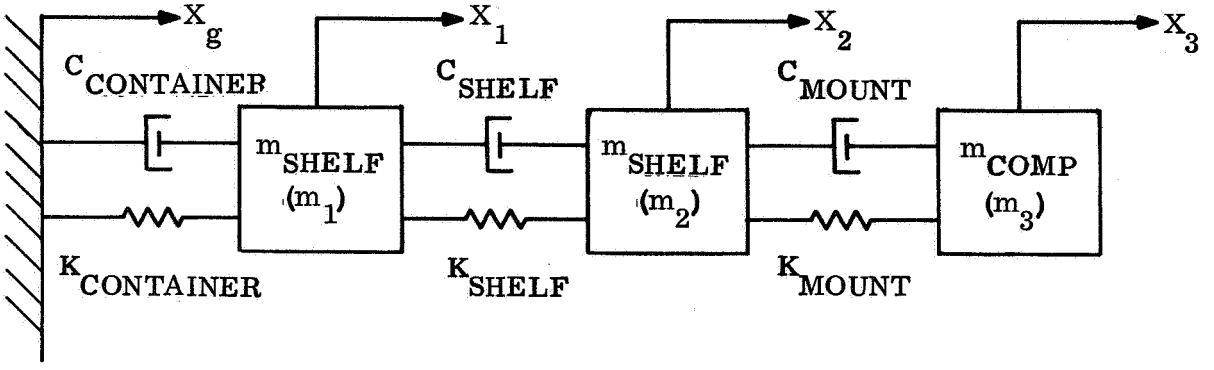

If a spring-damper structure exists that can attenuate the g-load from the ground to the component, this element will be attainable from a variety of combinations of primary shelf and local mount designs. Since, at present, the design of both of these structural elements is quite fluid, no useful purpose is served by considering them separately. Thus, the model that will be used in the present shock response analysis will be:

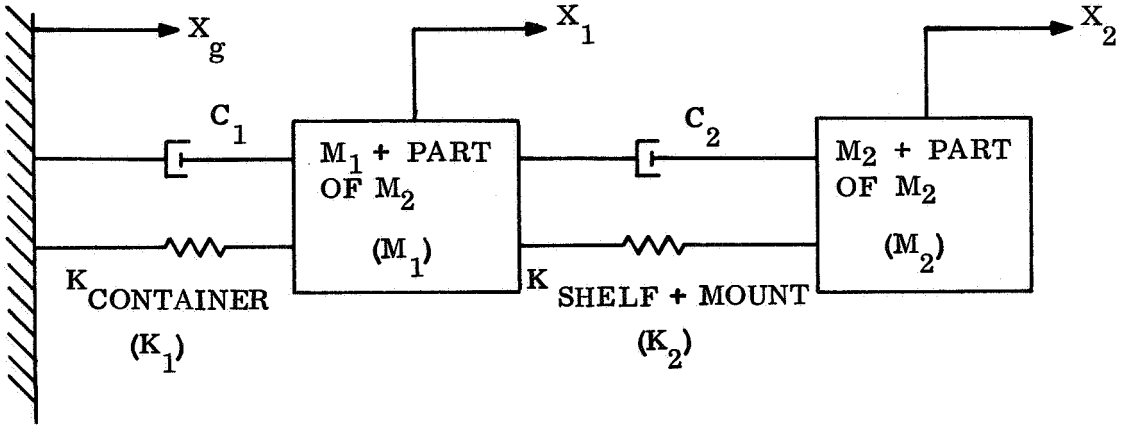

The solution of this two degree-of-freedom system can be used to determine the acceleration response of the component. If the equations of motion for this system are formulated:

$$M_1\ddot{X}_3 + C_1\dot{X}_3 + K_2X_3 - C_2\dot{X}_4 - K_2X_4 = -M_1\ddot{X}_g$$

$$M_2(\ddot{X}_4 + \ddot{X}_3) + C_2\dot{X}_4 + K_2X_4 = -M_2\ddot{X}_g$$

where

$$X_3 = X_1 - X_g$$

$$X_4 = X_2 - X_1$$

The most general approach to solution of the equations of motion is to find a general solution to the set of equations, then parametrically vary each of the constants of the motion to determine the combination that best reduces the acceleration response of the component. This is quite possible, but it would involve a great deal of labor. The number of parameters worthy of detailed study can be reduced by consideration of the nature of the solution and the allowable open design variations.

First, we may assume the masses to be fixed and the container stiffness, K_1, to be fixed since these will, in general, be determined by factors other than the component response. Similarly, the damping in the container structure probably will be determined by factors beyond control, so that G_1 may be established as a constant. Thus, the only parameters to be investigated are C_2 and K_2.

For an initial trial, it may be recognized that damping plays a relatively small role in containing the amplitude of component acceleration response, since the excitation is transient and not steady state. Therefore, the existing damping in both the shelf and in the container for this preliminary may be neglected. Thus, the constants of interest would be:

$$M_1^* = 220/386 = 0.5699 \ \frac{\text{lb-sec}^2}{\text{inch}}$$

$$M_2^* = 380/386 = 0.9845 \ \frac{\text{lb-sec}^2}{\text{inch}}$$

$$C_1 = 0$$

$$C_2 = 0$$

$$K_1^* = 0.2209 \times 10^6 \text{ lb/inch}$$

with K_2 as the parameter to be studied.

The only other information needed to complete the problem are the initial conditions and the forcing function. To determine the initial condition we assume that the Lander is dropping at constant velocity just prior to impact.

*These numerical values were chosen as representative of typical Hard Lander designs.

If the vehicle is considered to be moving at constant velocity toward a non-moving planet, we can just as easily picture a planet moving toward a stationary vehicle. For this condition the initial conditions of the dynamic model at impact are:

$$X_1 = \dot{X}_1 = X_2 = \dot{X}_2 = 0$$

The actual profile of impact and the simplification of that complex shape used in the present analysis are shown in fig. 4.5.1-3. From this point onward, the solution is strictly an exercise in basic dynamics, and discussion or illustration of the procedure is omitted. The result is two equations for the acceleration response of the mass M_2 as a function of time and of the spring K_2. One of these equations is valid during the period when the forcing function is applied, while the second describes the motion after the forcing function is removed. Two additional equations are developed that define those times when the response hits a peak (the response is periodic and so has periodic peaks). These last two equations also are functions of K_2. Using the equations for various values of K_2, has been calculated. The curves are shown in figs. 4.5.1-4 and -5.

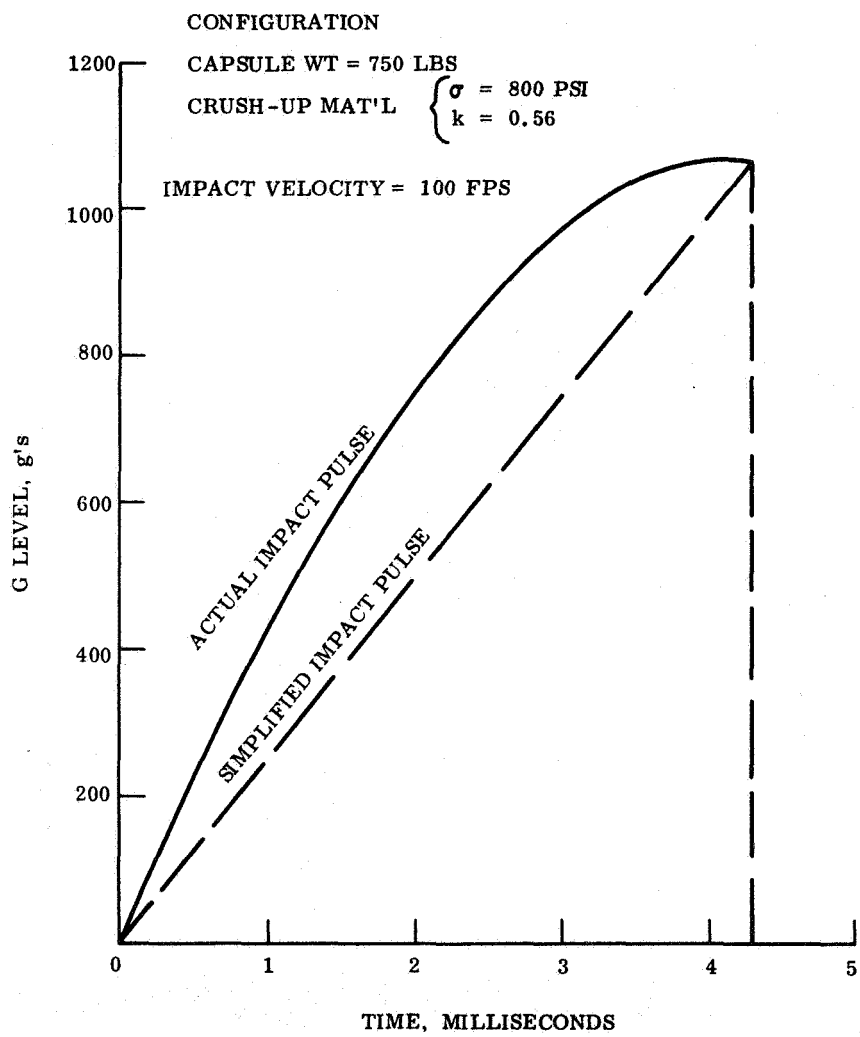

Figure 4.5.1-3. Shock Pulse for Lander Capsule

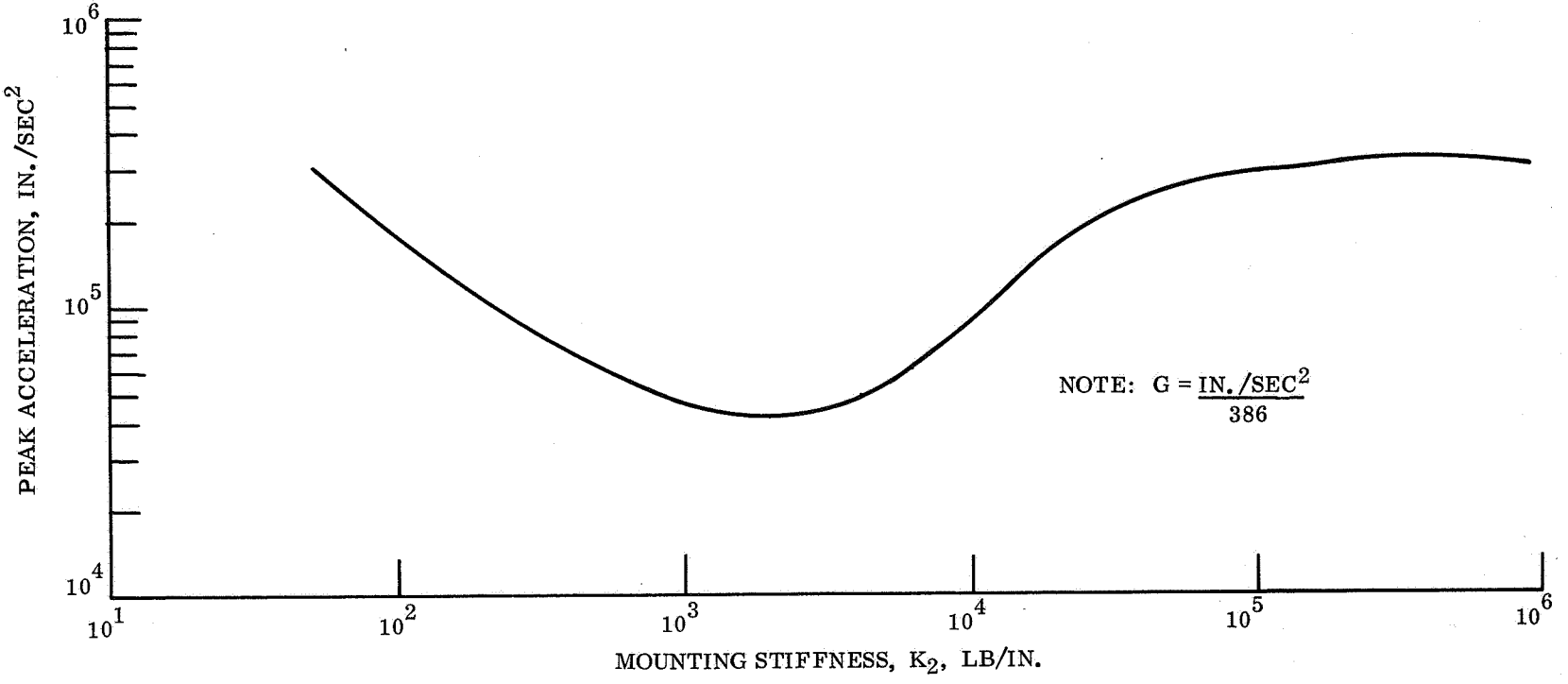

Figure 4.5.1-4. Peak Component Acceleration Response as a Function of Mount Stiffness

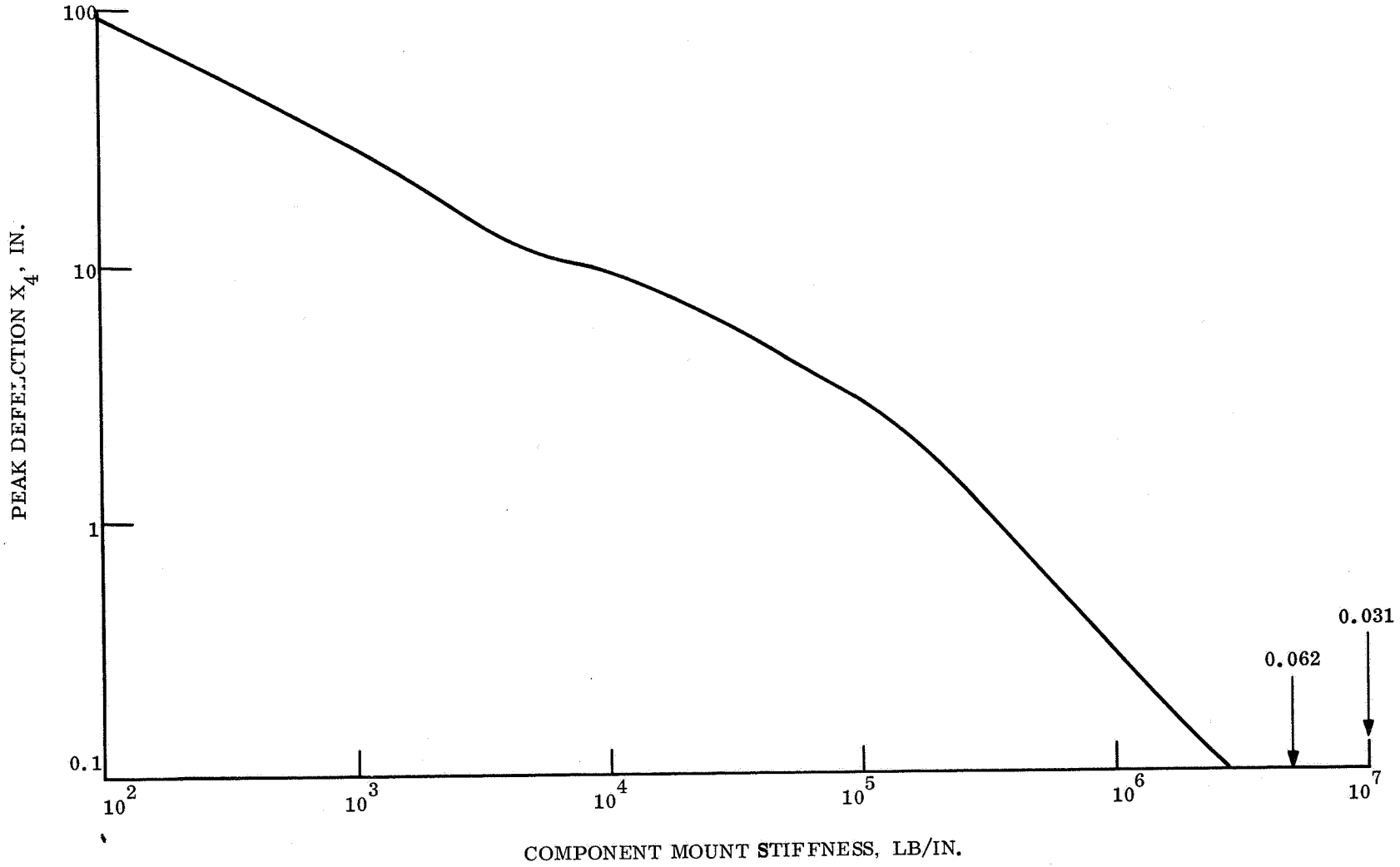

Figure 4.5.1-5. Component Mount Stiffness

4.5.1.2 Discussion of Results

An indicative peak response as a function of component mount support is shown in fig. 4.5.1-5. The results indicate that a definite spring rate exists for which the component acceleration response will be a minimum. For the present set of numbers, that stiffness is 2000 lb/in but it must be recognized that the figure will vary as the other system parameters (K_1, M_1, M_2, etc. are varied). Further, at 2000 lb/in., the acceleration attenuation is about 8:1. However, that ratio will be highly dependent upon the actual pulse shape and upon the linearity (or lack of linearity) of the spring K_2.

Unfortunately, significant reductions in 'g' response require large deflections, as shown in fig. 4.5.1-3. It does not appear feasible to obtain these reductions with shock mounts or by tailoring component mounting stiffness. As was stated before, these devices will be used primarily to minimize g-level amplification.

4.5.2 ENVIRONMENTAL DEFINITION

4.5.2.1 Surface Condition

Mars surface conditions, as well as impact velocity and kinematical requirements, interact to determine the impact attenuation design. The condition of a surface includes the following elements: surface bearing strength, effective surface friction, slopes, rocks and protrusions. Surface bearing strength is of special importance in the design of crush-up impact attenuation systems. In designing for an infinitely rigid surface, maximum use is made of the crush-up honeycomb and the full theoretical stroke is crushed. As elasticity and deformability are introduced into the surface model, less of the honeycomb will be crushed and the balance of the stopping distance required for proper deceleration is provided by penetration and crushing of the ground surface. For design purposes, it is conservative to size the impact attenuation system based on an infinitely rigid ground surface. This approach allows one to safely descend on extensive rock outcroppings as well as the less rigid and more likely situation of an elastic soil mass.

For impact upon elastic soil surfaces the approximate depth of penetration can be estimated as previously discussed in Section 4.5.1.

Rocks and surface protrusions are specified by use of a characteristic dimension. For the primary parametric studies the rocks are assumed of such properties that they have 5 in. of damage potential or penetrating capability. The effect of rocks of 5, 10, and 15 in. in effective depth is also included in some of the trade-offs. In sizing the attenuator, rock protection is provided by evaluating two expressions:

$$t = \text{stroke} + \text{rock height} \quad (1)$$

$$t = \text{stroke/eff} + \text{factor of safety} \quad (2)$$

The larger quantity is selected for the thickness in a particular direction around the Lander. The reasoning underlying eq. 1 is that, after the full stroke is used, an additional depth of honeycomb equal to the height of a rock still is available to protect the payload container against penetration. This same material is considered as providing a factor of safety on stroke and makes provision for material compaction. Refer to fig. 4.5.2-1. Eq. 2 is based on the following: the theoretical stopping distance (stroke) is computed and increased by an amount to allow for a factor of safety and a material efficiency factor; the extra material then is counted also as active in providing rock protection capability to the crush-up system. This "double counting" can be justified by the randomness of the factors contributing to the attenuator thickness, i.e., the probability of encountering rocks of full penetrating capability (in this case 5 in. or more), and the stroke efficiency being at its lowest value, and touchdown velocity conditions being more severe than those programmed in the mission are believed negligible and of such small consequence that the mission probability of success would not be significantly altered.

4.5.2.1.1 Slopes

The slopes upon which the Lander may impact are important in sizing the impact attenuation system for two reasons. First, the vector resultant of descent and horizontal wind velocities is dependent upon the slope impacted. The normal velocity component is used to compute the stroke. Second, the slopes encountered when considered

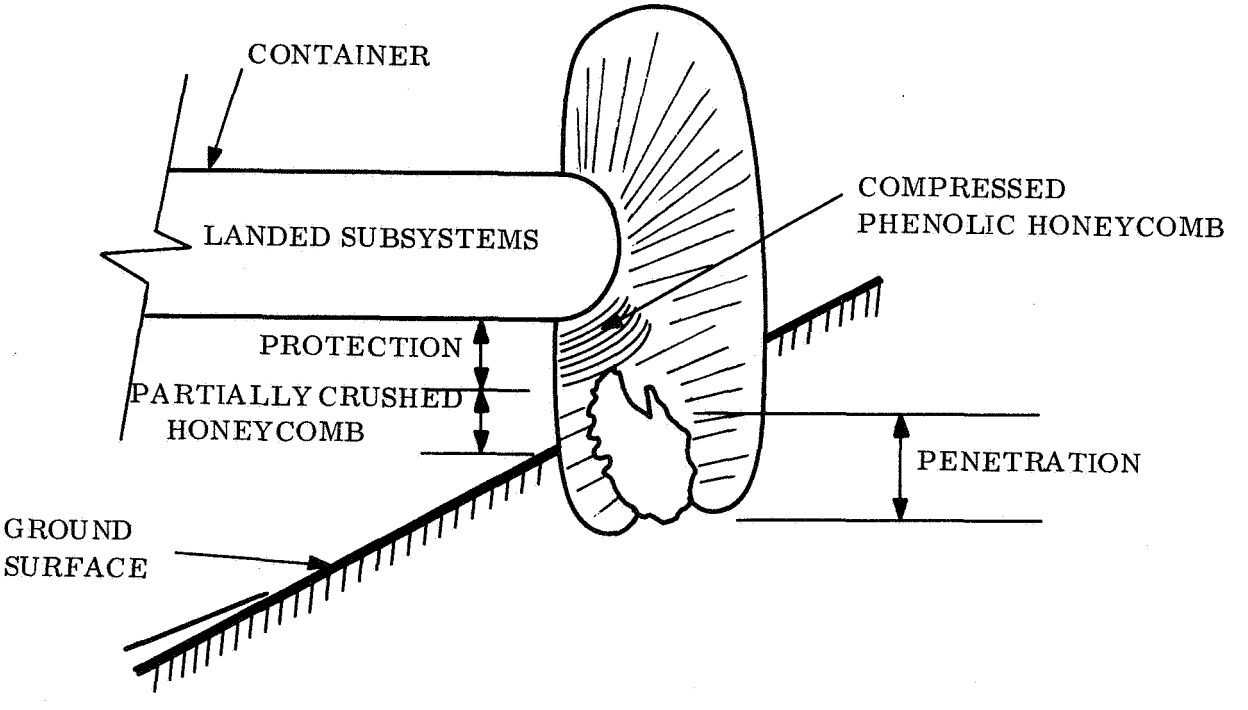

Figure 4.5.2-1. Rock Protection Size Requirements of Honeycomb Attenuator

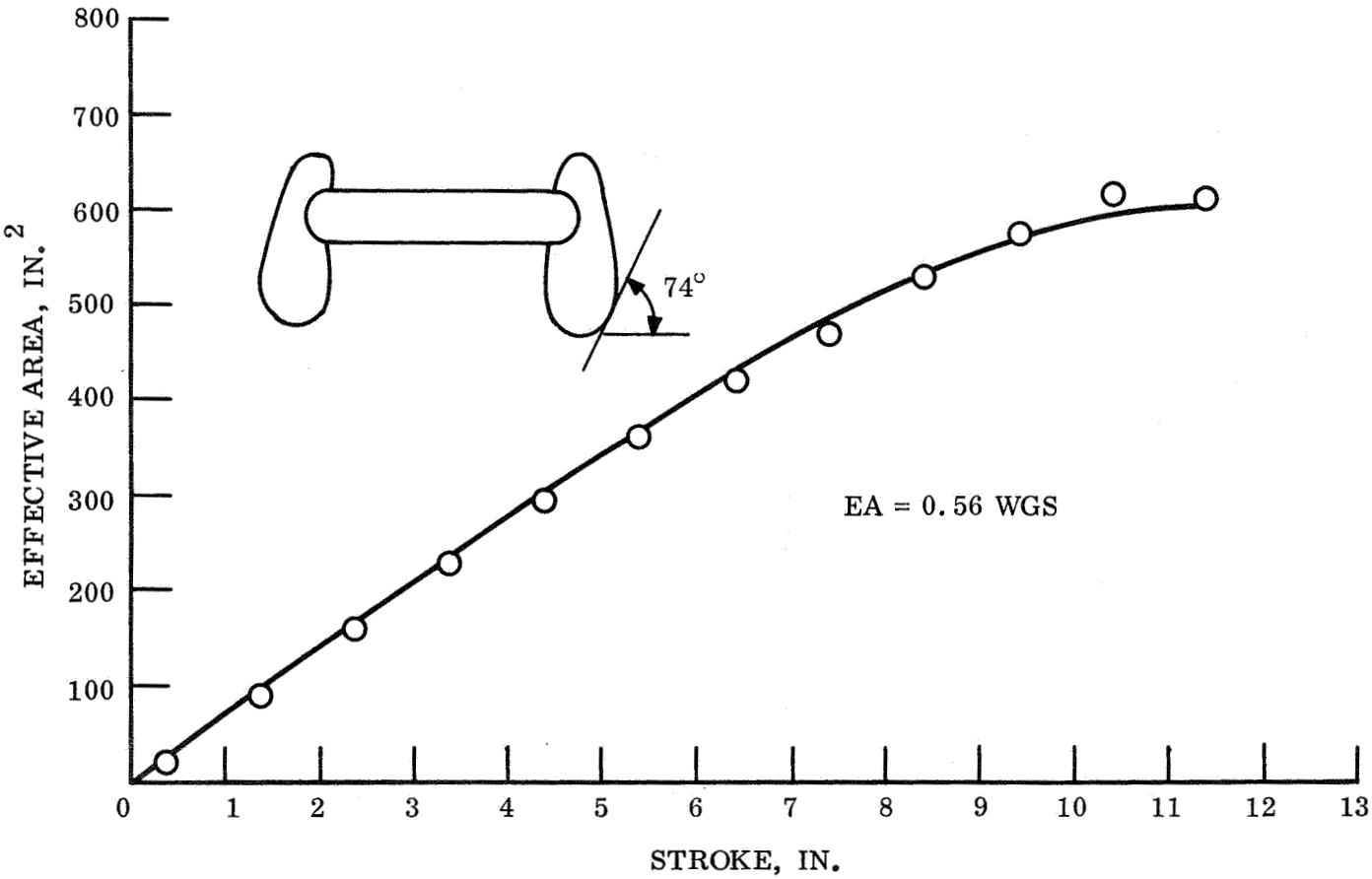

Figure 4.5.2-3. Effective Area vs Stroke for Multi-directional Shape $\theta = 0^\circ$

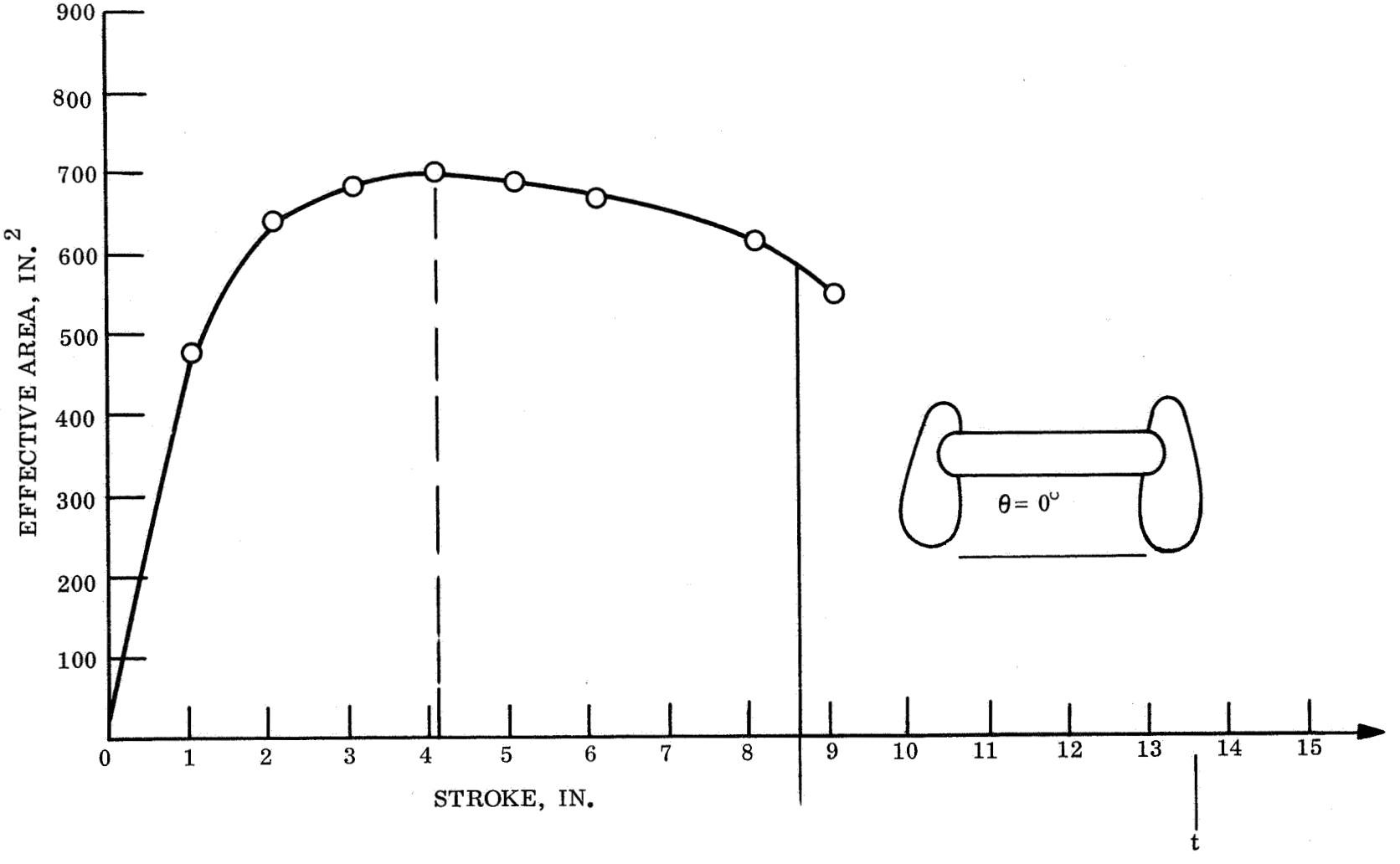

Figure 4.5.2-2. Effective Area vs Stroke for Multi-directional Shape $\theta = 74^{\circ}$

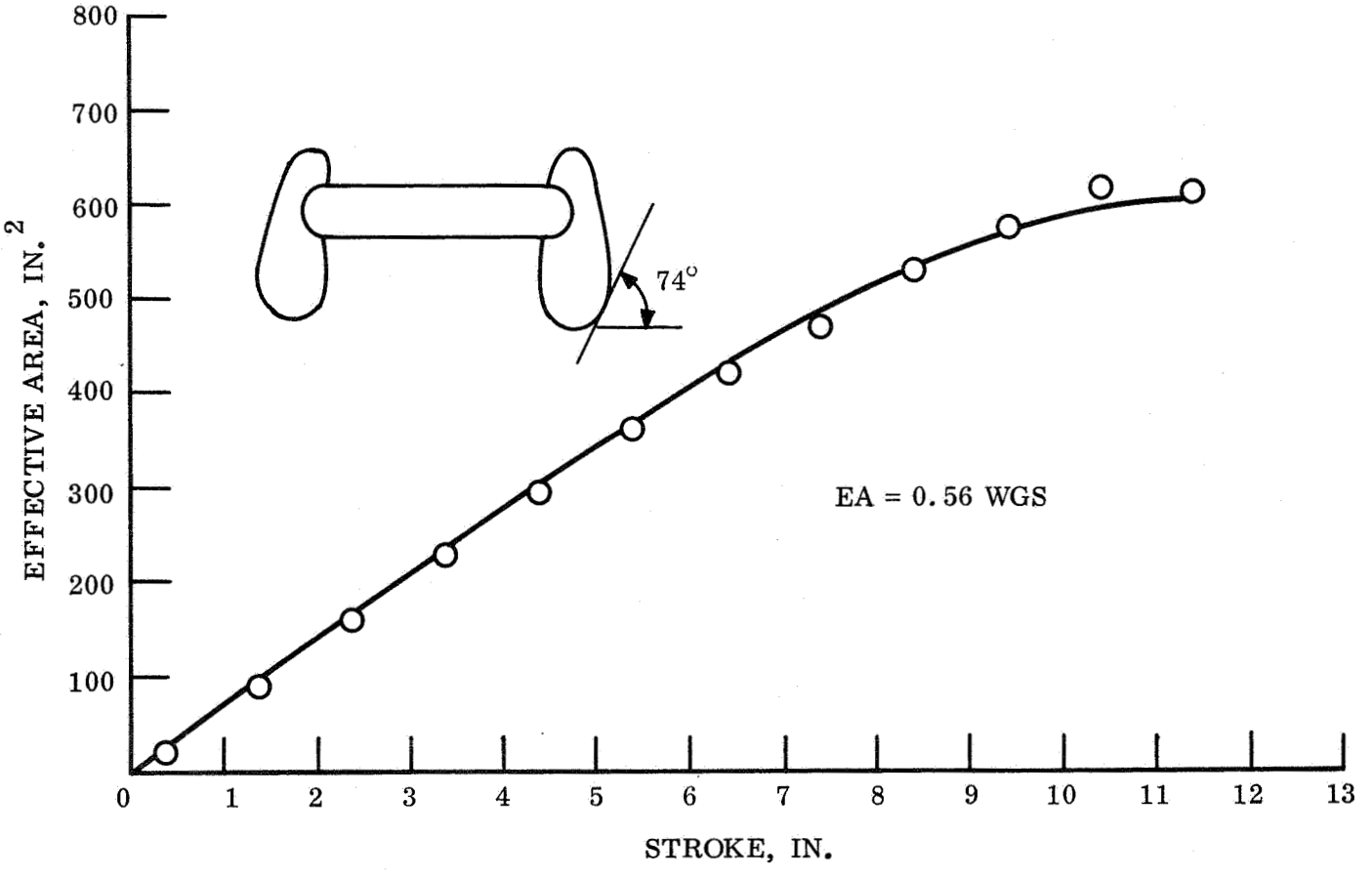

Figure 4.5.2-3. Effective Area vs Stroke for Multi-directional Shape $\theta = 0°$

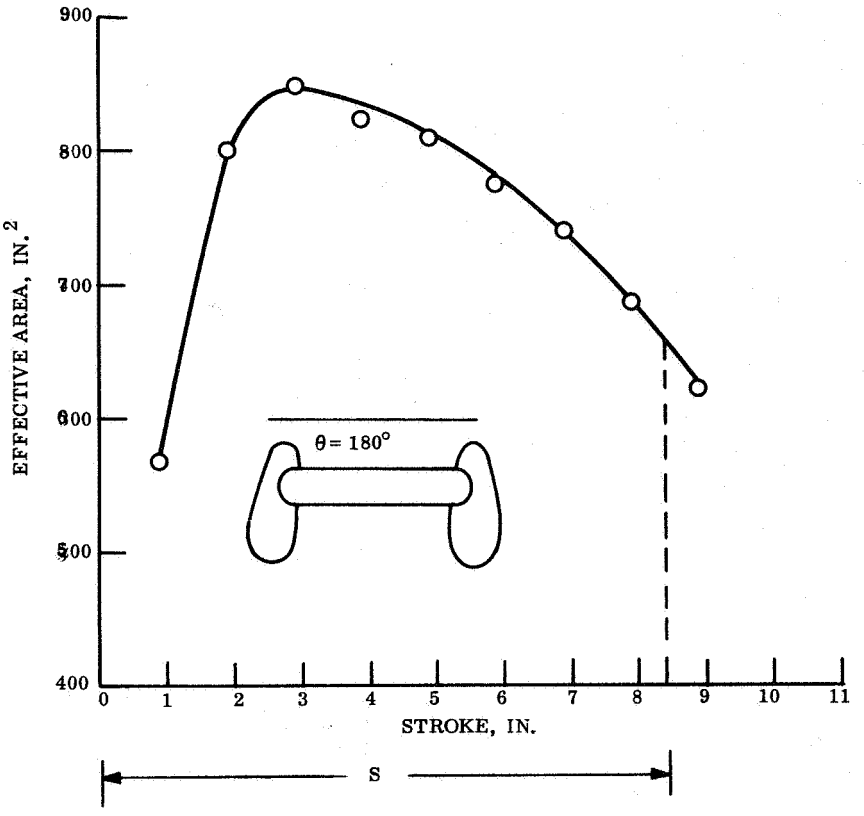

Figure 4.5.2-4. Effective Area vs Stroke for Typical Multi-directional Lander $\theta = 180^{\circ}$

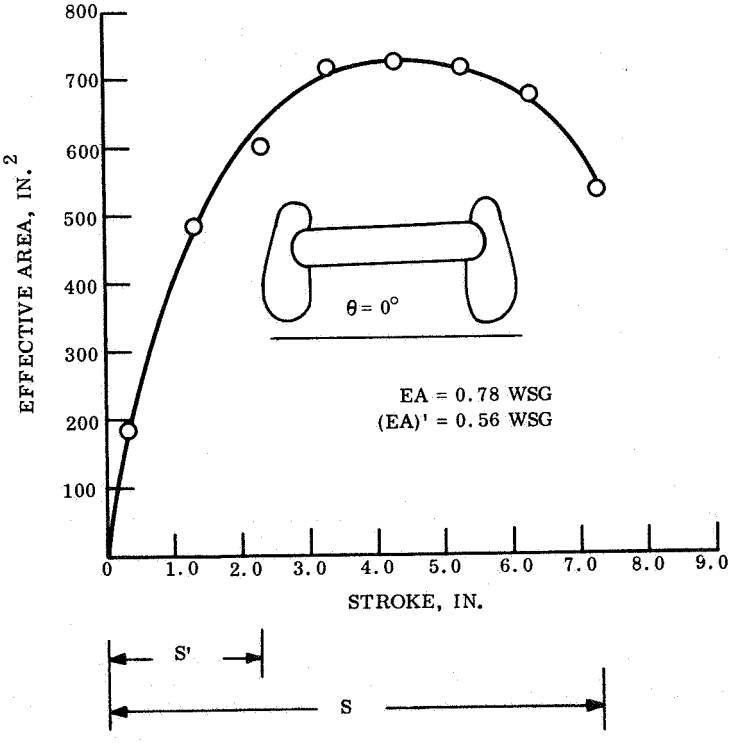

Figure 4.5.2-5. Effective Area vs Stroke for Typical Multi-directional Lander $\theta = 0^{\circ}$

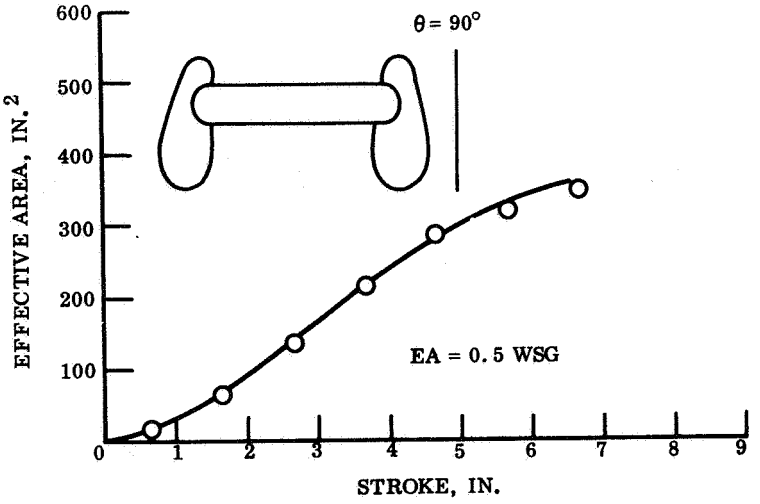

Figure 4.5.2-6. Effective Area vs Stroke forTypical Multi-directional Lander $\theta = 90^{\circ}$

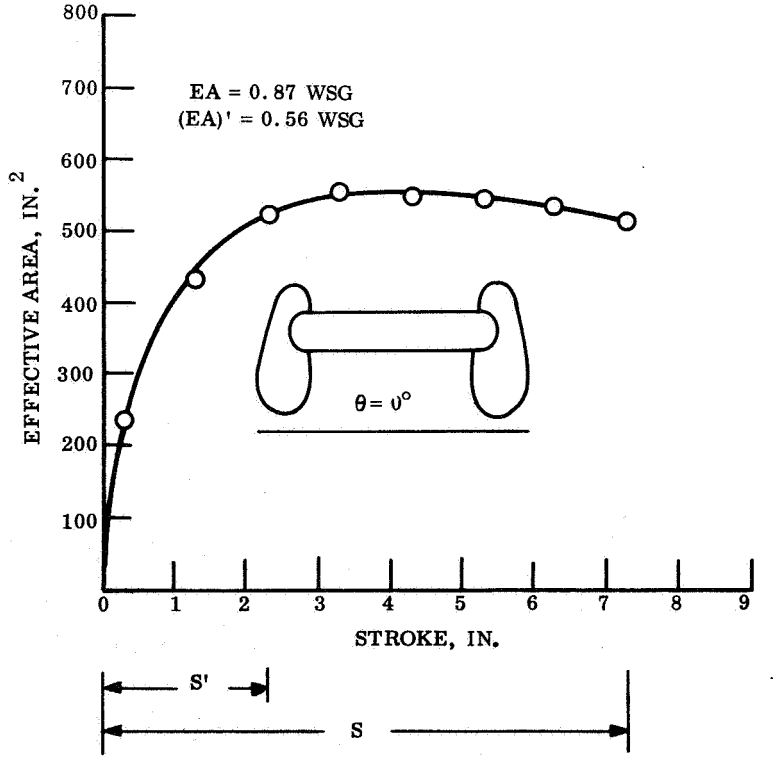

Figure 4.5.2-7. Effective Area vs Stroke for Typical Multi-directional Lander $\theta = 0^{\circ}$

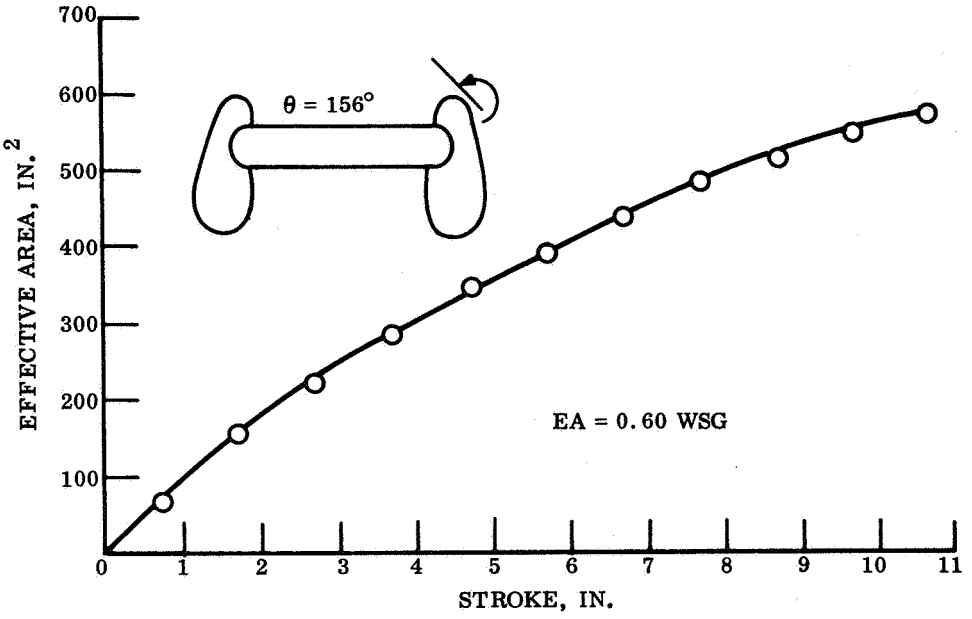

Figure 4.5.2-8. Effective Area vs Stroke for Typical Multi-directional Lander $\theta = 156^{\circ}$

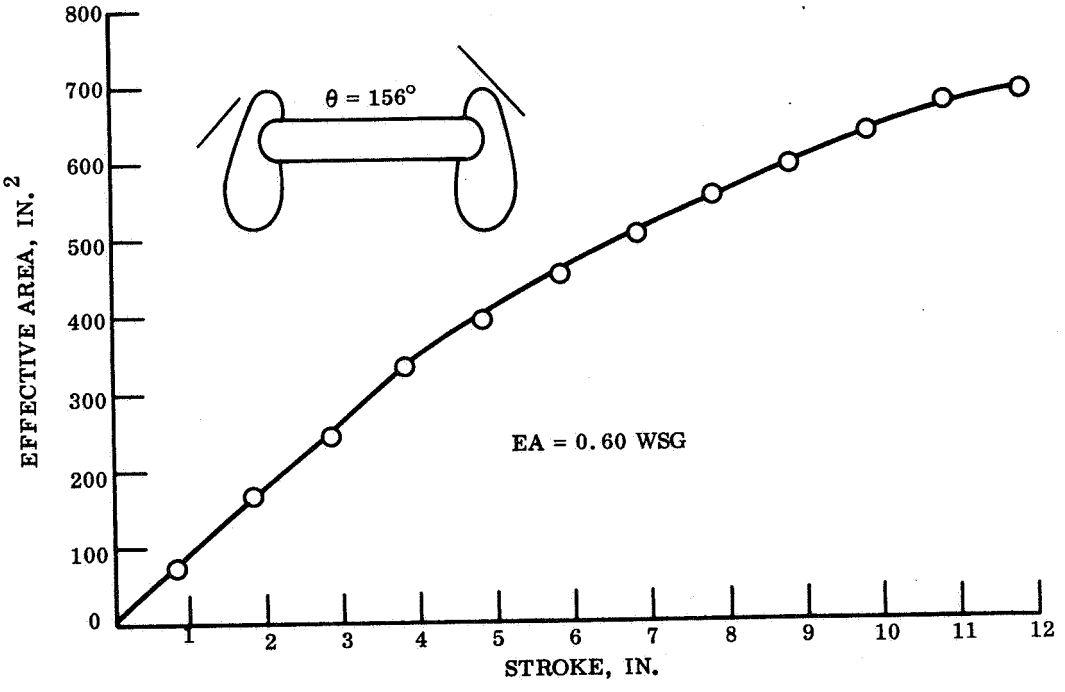

Figure 4.5.2-9. Effective Area vs Stroke for Typical Multi-directional Lander $\theta = 156^{\circ}$

4.5.2.2 Wind Effects

The specification of a wind has been interpreted as a steady state horizontal velocity component superimposed on the programmed descent velocity. Wind is treated as acting in the plane determined by the V_D descent velocity vector and the normal to the surface slope encountered. For parametric analysis wind magnitudes of 0, 110 and 220 fps were considered. The significance of the wind on the Lander design is elaborated upon in Section 4.5.3.

4.5.2.3 Secondary Impact

In designing the honeycomb crush-up contours of the Mars Hard Lander it is found that a considerable weight penalty is incurred if the Lander is made omnidirectional and sufficient crush-up material is included on top to accommodate an upsidedown impact at the full right-side-up impact velocity. This condition can exist with certain combinations of parachute sway angles, surface wind velocities, and surface slopes. However, the probability of obtaining such unfavorable combinations is quite low. The purpose of this analysis is to determine the probabilities of obtaining secondary impacts (on the top side of the Lander) at various velocities, and to ascertain what values of secondary impact velocity are appropriate for design purposes from a probabilistic point of view.

A complete dynamic analysis of the impact problem is quite difficult, tedious, and unwarranted at this time in view of the unknowns in the physical quantities required to perform the complete analysis. It would be necessary to make assumptions, for example, of the relative resistance of the Mars surface material in tangential deformation (friction) versus normal penetration. Fortunately, however, if the Lander is studied in a rigid-body mode, with impulsive normal and tangential inputs, it is found that some of these unknowns are not required in order to obtain solutions of the motion after the first impact. In order to obtain a representative value, secondary impact velocity, therefore, the impulsive momentum approach is employed in the following analysis.

4.5.2.3.1 Equations of Motion

In this analysis, it is necessary to assume that the first impact is impulsive, and that the Lander has not rotated appreciably during the impact. Examination of this assumption shows that it does introduce some error, since typical impact durations will result in rotations of the order of 20° to 40° while the impact is in process. In the equations that follow, this geometry change effect could be taken into account as a second iteration. However, for purposes of this first approximate analysis, it will be assumed that the Lander does not rotate during the first impact.

Another major assumption necessary to obtain simple solutions is that there is negligible rebound or bounce, such that the point of impact is brought to rest both tangentially and normally during the impact. In this way, the impact point becomes an instant center of rotation, and the c.g. of the Lander must move with velocity V_2 normal to the instant center-c.g. line after impact, as shown in the figure below:

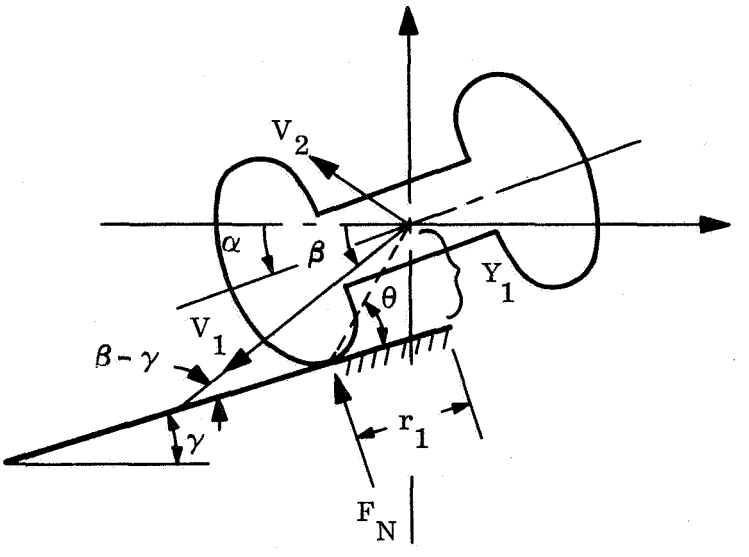

Observe that the Lander will flip over only if $\theta > \beta - \gamma$, as shown in the figure above. Angle θ is a function of the parachute swing angle, α, the surface angle γ, and the contours of the Lander:

$$\tan \theta = Y_1/r_1 \tag{3}$$

If motion stops at the point of contact:

$$V_2 = 2\sqrt{r_1^2 + Y_1^2}\ \ \frac{2r_1}{\cos \theta} \tag{4}$$

Writing an impulse-momentum equation for motion normal to the Mars surface:

$$\int F_n dt = M\left[V_1 \operatorname{Sin}(\beta - \gamma) + V_2 \cos \theta\right] \tag{5}$$

Tangent to the Mars surface:

$$\int F_r dt = M\left[V_1 \cos(\beta - \gamma) - V_2 \sin \theta\right] \tag{6}$$

Angular impulse momentum:

$$Y_1 \int F_r dt - r_1 \int F_n dt = I \dot{\alpha} \tag{7}$$

Combining eq. 2, 3, 4, and 5:

$$\frac{V_2}{V_1} = \frac{\frac{Y_1}{r_1} \cos(\beta - \gamma) - \sin(\beta - \gamma)}{\left(\frac{I}{r_1^2 M} + 1\right) \cos\theta + \frac{Y_1}{r_1} \sin\theta} \tag{8}$$

The maximum velocity of a point on the Lander after it flips over will be the sum of the c.g. velocity and the rotational velocity

$$\Sigma V = V_2 + r_2 \dot{\alpha}$$

$$\frac{\Sigma V}{V_2} = 1 + \frac{r_2}{r_1} \cos\theta \tag{9}$$

4.5.2.3.2 Calculation of Secondary Impact Velocity

In order to facilitate a rapid, hand calculation of ΣV, fig. 4.5.2-10(a) was prepared with scaled figures of the Lander; from which Y_1 and r_1 were obtained by direct scaling. Angle θ was calculated from eq. 3 and $I/r_1^2 M$ calculated using $I = 2,020$ lb -ft ^{2} and $M = 930$ lbs as typical values. With these quantities and with r_2 taken as 2 ft. as a reasonable estimate of the location of the point of secondary impact, eq. 8 and eq. 9 were employed to find ΣV. Fig. 4.5.2-10(b) contains the results of the computations for the two wind velocities in a matrix format.

4.5.2.3.3 Detailed Interpretation of the Specification as it Applies to the Secondary Impact Problem

After the design specifications have been synthesized, the impact attenuation system design is carried through as described in the next section. Prior to this discussion however, it is well to detail certain aspects of both the omni- and multi-directional designs which are subtly influenced by one or more of the specified criteria.

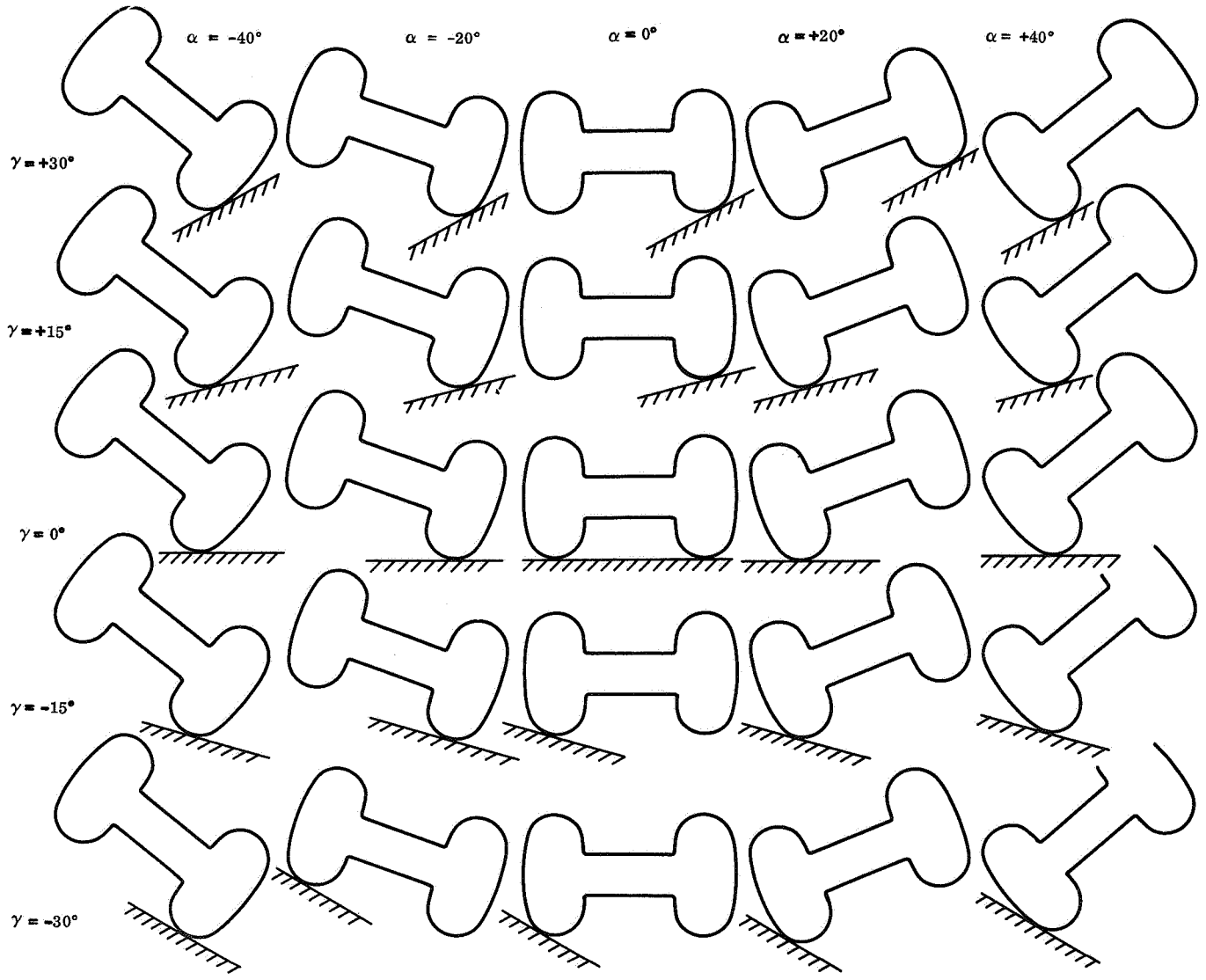

TOUCHDOWN CONDITIONS

COMPUTED SECONDARY VELOCITIES FOR TWO WIND CONDITIONS

	WIND (fps)									
	110	220	110	220	110	220	110	220	110	220
	α = -40°		α = -20°		α = 0°		α = +20°		α = +40°	
γ = +30°	V_1 = 148 V_2 = 138 ΣV = 226	V_1 = 241 V_2 = 232 ΣV = 378	V_1 = 148 V_2 = 109 ΣV = 179	V_1 = 241 V_2 = 196 ΣV = 320	V_1 = 148 ↓ NO FLIP	V_1 = 241 V_2 = 179 ΣV = 297	NO FLIP	NO FLIP	V_1 = 148 V_2 = 75.5 ΣV = 128	V_1 = 241 V_2 = 162 ΣV = 276
γ = +15°	V_1 = 148 V_2 = 100 ΣV = 159.5	V_1 = 241 V_2 = 193 ΣV = 308	V_1 = 148 V_2 = 75.5 ΣV = 125	V_1 = 241 V_2 = 163 ΣV = 270	V_1 = 148 ↓ NO FLIP	V_1 = 241 V_2 = 122 ΣV = 209	V_1 = 148 V_2 = 42 ΣV = 72	V_1 = 241 V_2 = 119 ΣV = 205	V_1 = 148 V_2 = 67.3 ΣV = 115	V_1 = 241 V_2 = 151 ΣV = 257
γ = 0°	V_1 = 148 V_2 = 59 ΣV = 151	V_1 = 241 V_2 = 146 ΣV = 375	V_1 = 148 V_2 = 28.7 ΣV = 48	V_1 = 241 V_2 = 103 ΣV = 171	V_1 = 148 V_2 = 10.9 ΣV = 19	V_1 = 241 V_2 = 75 ΣV = 129	V_1 = 148 V_2 = 32 ΣV = 53	V_1 = 241 V_2 = 108 ΣV = 177	V_1 = 148 V_2 = 59 ΣV = 97	V_1 = 241 V_2 = 144 ΣV = 236
γ = -15°	V_1 = 148 V_2 = 65.7 ΣV = 108	V_1 = 241 V_2 = 153 ΣV = 252	V_1 = 148 V_2 = 29 ΣV = 52	V_1 = 241 V_2 = 103 ΣV = 186	V_1 = 148 ↓ NO FLIP	V_1 = 241 V_2 = 136 ΣV = 230	V_1 = 148 V_2 = 78 ΣV = 127	V_1 = 241 V_2 = 168 ΣV = 273	V_1 = 148 V_2 = 96 ΣV = 156	V_1 = 241 V_2 = 185 ΣV = 302
γ = -30°	V_1 = 148 V_2 = 71 ΣV = 119	V_1 = 241 V_2 = 156 ΣV = 264	NO FLIP	NO FLIP	V_1 = 148 ↓ NO FLIP	V_1 = 241 V_2 = 186 ΣV = 308	V_1 = 148 V_2 = 111 ΣV = 180	V_1 = 241 V_2 = 197 ΣV = 322	V_1 = 148 V_2 = 114 ΣV = 189	V_1 = 241 V_2 = 199 ΣV = 331

ASSOCIATED COMPOUND PROBABILITIES OF SLOPE ANGLE AND SWAY ANGLE

PROBABILITIES WEIGHTING MATRIX

SWAY PROBABILITIES γ \ SLOPE PROBABILITIES α	.025	.395	.160	.395	.025	K sums
.0225	.00056	.00889	.00360	.00889	.00056	.02250
.1775	.00444	.07011	.02840	.07011	.00444	.17750
.6000	.01500	.23700	.09600	.23700	.01500	.60000
.1775	.00444	.07011	.02840	.07011	.00444	.17750
.0225	.00056	.00889	.00360	.00889	.00056	.02250
						1.00000

Figure 4.5.2-10. Touchdown Geometries for Secondary Impact Studies

In general, neither form of the Lander will dissipate its entire impact kinetic energy upon initial impact although it has the capability to do so. (For the multi-directional Lander this capability is restricted to the prime (head-on) direction only.) As a result,some provision might be made for repeated impacts on the same part of the Lander as was first contacted. Subsequent impacts on the identical surface are of such low probability that they may be neglected. Subsequent impacts on a portion of the Lander not crushed previously can be tolerated if such secondary hits are not more severe than the original velocity assumed in the vehicle design. The reasoning for this follows ipso facto from the basic nature of an omni-directional vehicle. For a multi-directional vehicle, secondary impact is not readily attenuated in all impacting directions because of the directionality built into the Lander shape. Because of the possibility of an aft end impact occurring as a second or subsequent impact crush-up, material was added to the "back" end of the multi-directional Lander.

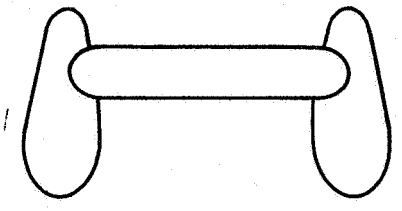

The thickness was developed from rock protection requirements and a triangular stroke history for a velocity of 100 fps. (Refer to eq. 10.)

The governing equation is

$$T_{\text{aft end}} = \frac{Va^2}{gG} \times 12 \text{ in.} + 5 \text{ in.} \qquad (10)$$

which for V_n in fps is valid for a triangular acceleration stroke history and a 5 in. rock requirement.

The significance belying the choice of 100 fps for the secondary velocity shall now be described.

Secondary impact is significantly affected by both parachute sway and the slope angle encountered. Parachute sway is analytically treated as follows. The simplest approximation is that of a pendulum. For a given maximum sway angle, φ, and neglecting wind effects the statistical distribution of φ is sinusoidal regardless of the Martian 'g'or the extent of the parachute chord. If the sophistication of an atmosphere is introduced into the analysis, the distribution of the angle φ is still sinusoidal. The atmosphere will produce an amplitude decay and produce a lower frequency, but it does not affect the basic distribution of φ . This cumulative distribution for the sway angle φ is given in fig. 4.5.2-11.

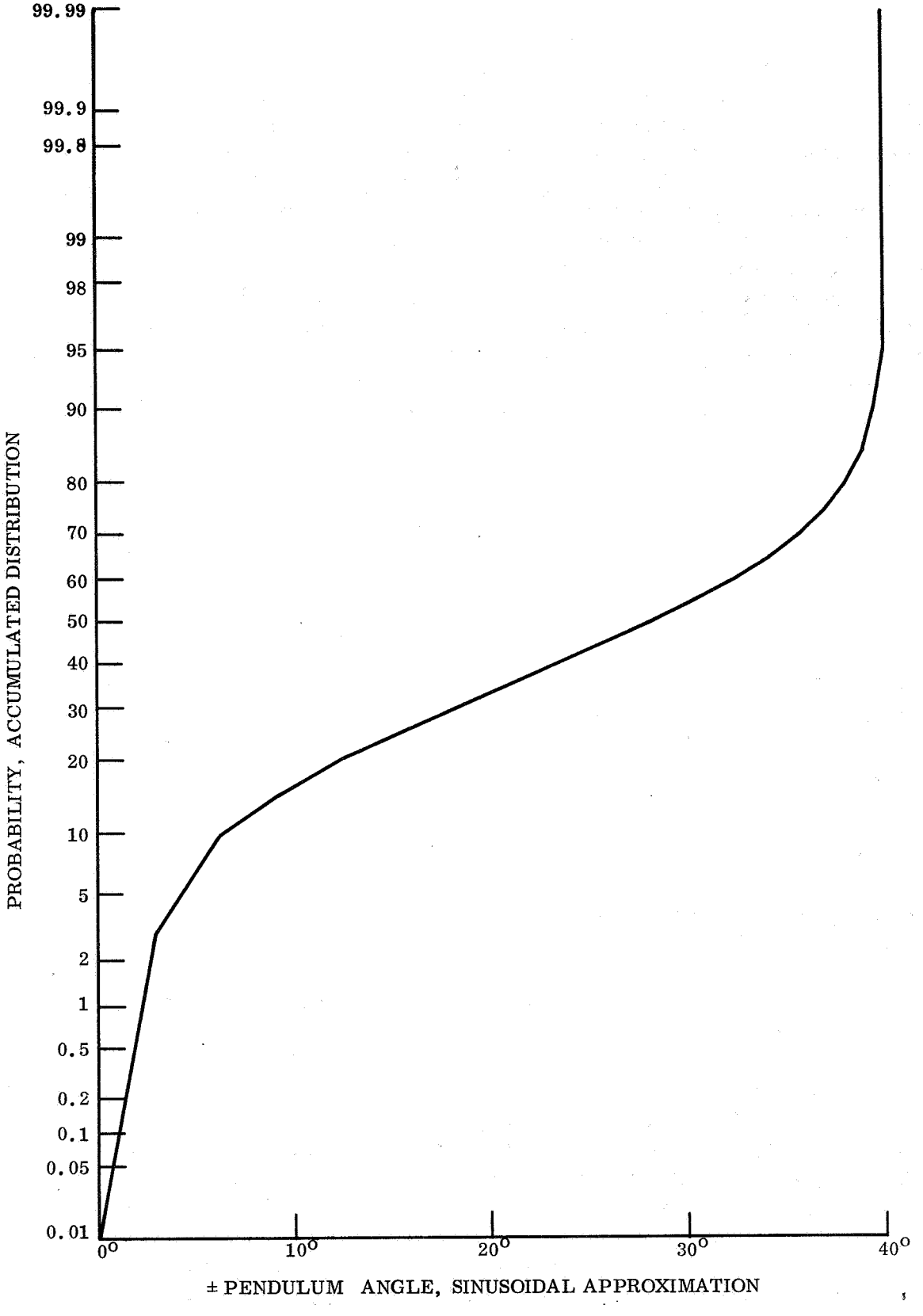

Figure 4.5.2-11. Cumulative Probability Distribution for± Pendulum Angle (Sinusoidal Approximation)

4.5.2.4 Large Amplitudes of Sway

Experience shows that the motion of a pendulum bob is periodic, and we have seen that it is approximately harmonic-sinusoidal as a first approximation. Martian gravity constant g and chord length r does not affect this time (probability) distribution of the pendulum angle.

The Newtonian constant k of the Martian atmosphere means that each amplitude is slightly less than the one before. We have studied small amplitudes of φ, where $\varphi \approx \sin \varphi$ is a good approximation. This is not true for $\varphi = 40°$ (0.69813 $\neq$ 0.64279). By conservation of energy (immersion in atmospheric fluid neglected), a result in terms of elliptic integrals is obtained.

Once again, a cumulative distribution function for φ may be plotted as in fig. 4.5.2-12. Overlaying the plotted cumulation distribution function derived from elliptic integrals upon the sinusoidal approximation, the difference is scarcely visible to the eye. However, the corresponding variations of frequency with amplitude (circular error) is significant in the sense of horology.

Slopes

Probabilistic considerations also surround surface slope definition as provided in the following table which is based on latest LRC specifications. (Use was made of fig. III-C-4 of Mars Engineering Model Parameters for Mission and Design Studies, Preliminary Draft, Langley Research Center, May 1968, the 40° abscissa was taken as 38° and the residual statistically interpolated from 40°to 90°. Normal probability paper was used, so that statistical interpolation, not linear, was used.) The result is plotted in fig. 4.5.2-13 and tabulated in table 4.5.2-1.

4.5.2.5 Wind Speed

Probabilistic analyses were also extended to include surface wind speed. From a reference developed by NASA/LRC, The Mars Engineering Model Parameters For Mission and Design Studies 1968, the median speed is 55 m/sec, the maximum is 67 and the minimum is 37 m/sec. There are no maximums or minimums in statistics, nor is there any physical reason for saying that winds speeds of 67.1 or 36.9 m/sec on Mars are impossible. Rather, one makes the usual assumption that these are the ± 3 equivalents, i.e., $P(S > 67) = P(S < 37) = 0.0013$. In this problem, this assumption is conservative, i.e., the statement "S can exceed 67 only 0.13 percent of the time" is more conservative the "S cannot exceed 67". Refer to fig. 4.5.2-14.

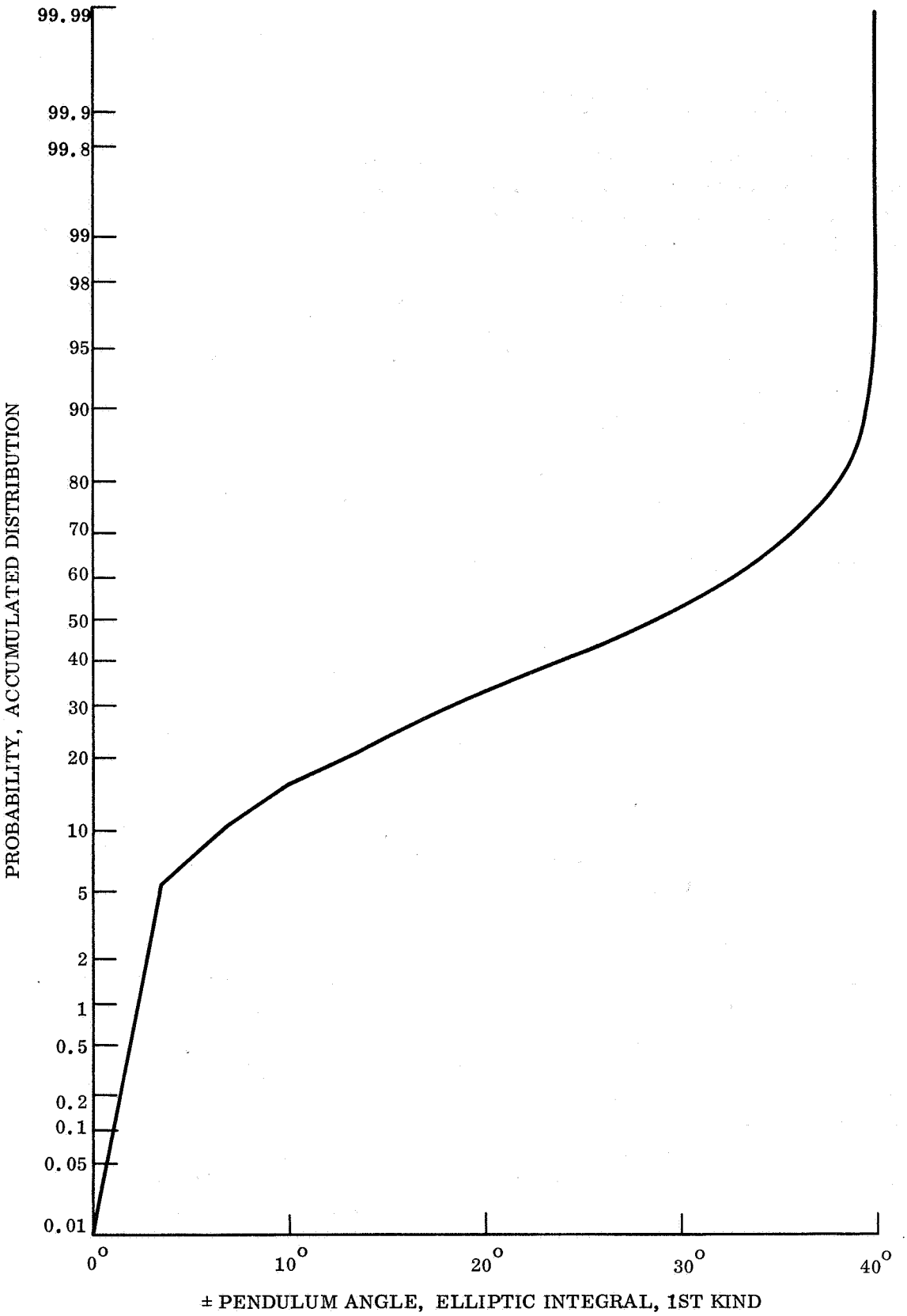

Figure 4.5.2-12. Cumulative Probability Distribution for ± Pendulum Angle (Elliptic Integral, First Kind)

TABLE 4.5.2-1. STATISTICAL DISTRIBUTION OF SLOPE ANGLE

Angle (deg)	Slope Angle Density Probability (%)	Cumulative Probability (%)
2	22	22
4	14	36
6	14	50
8	14	64
10	5	69
12	5	74
14	6	80
16	5	85
18	4	89
20	3	92
22	3	95
24	0.5	95.5
26	0.9	96.4
28	1.1	97.5
30	0.3	97.8
32	0.3	98.1
34	0.2	98.3
36	0.2	98.5
90	1.5	100

4.5.2.6 Compound Probabilities

Previously we have developed cumulation distribution groups for pendulum angle θ, wind speed v and surface slope λ. If f (θ, υ, α) is a monotonic function (change in one direction only as its variables each change in one direction) then the α percent level of f corresponding to the β percent levels of θ, υ, λ are:

α (simple) (%)	$\beta = \sqrt[3]{\alpha}$ (compound) (%)
0	0
5	36.8
10	46.4
20	58.5
30	66.9
40	73.7
50	79.4
60	84.3
70	88.8
80	92.8
90	96.6
95	98.3
100	100

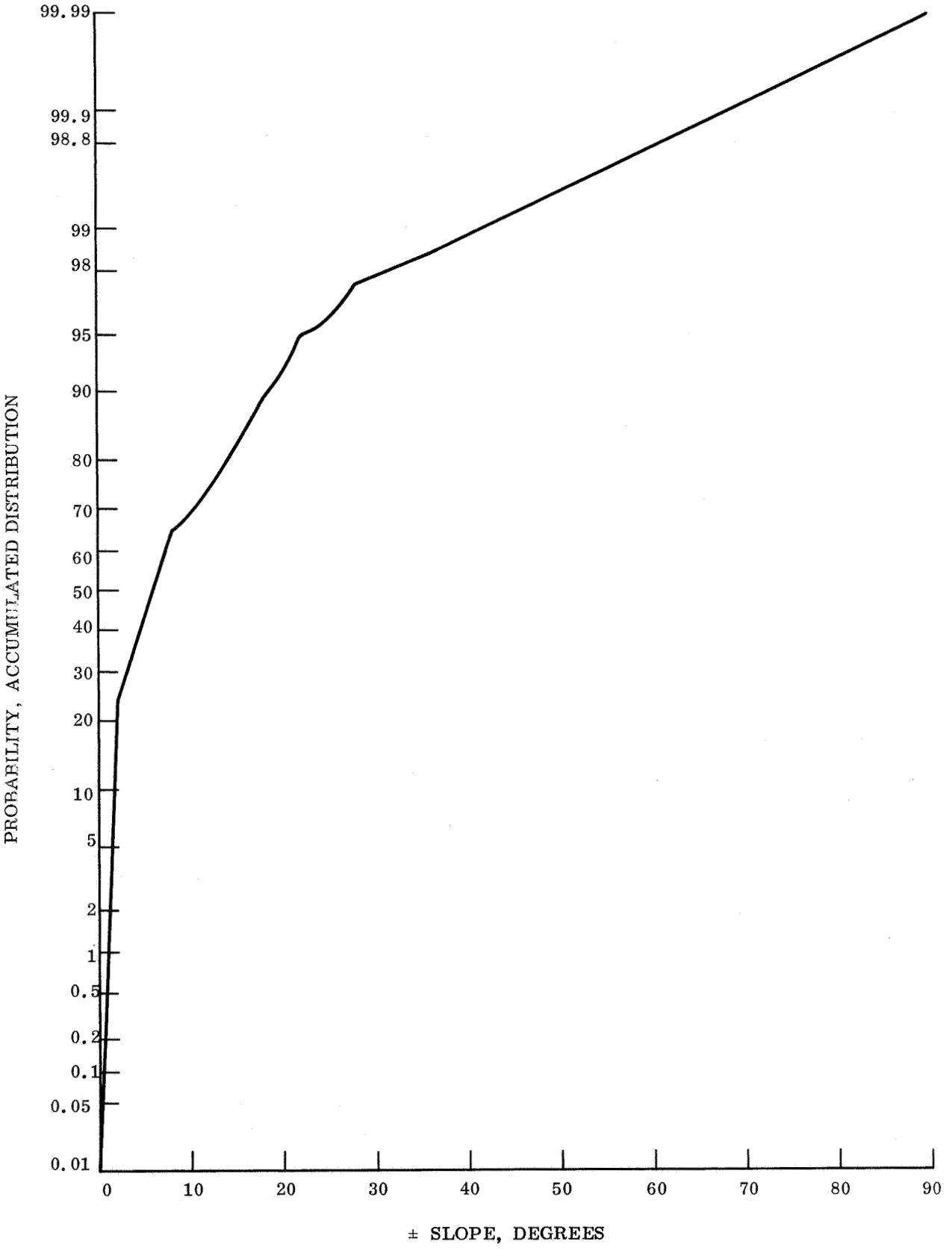

Figure 4.5.2-13. Cumulative Probability Distribution for ± Slope Angle

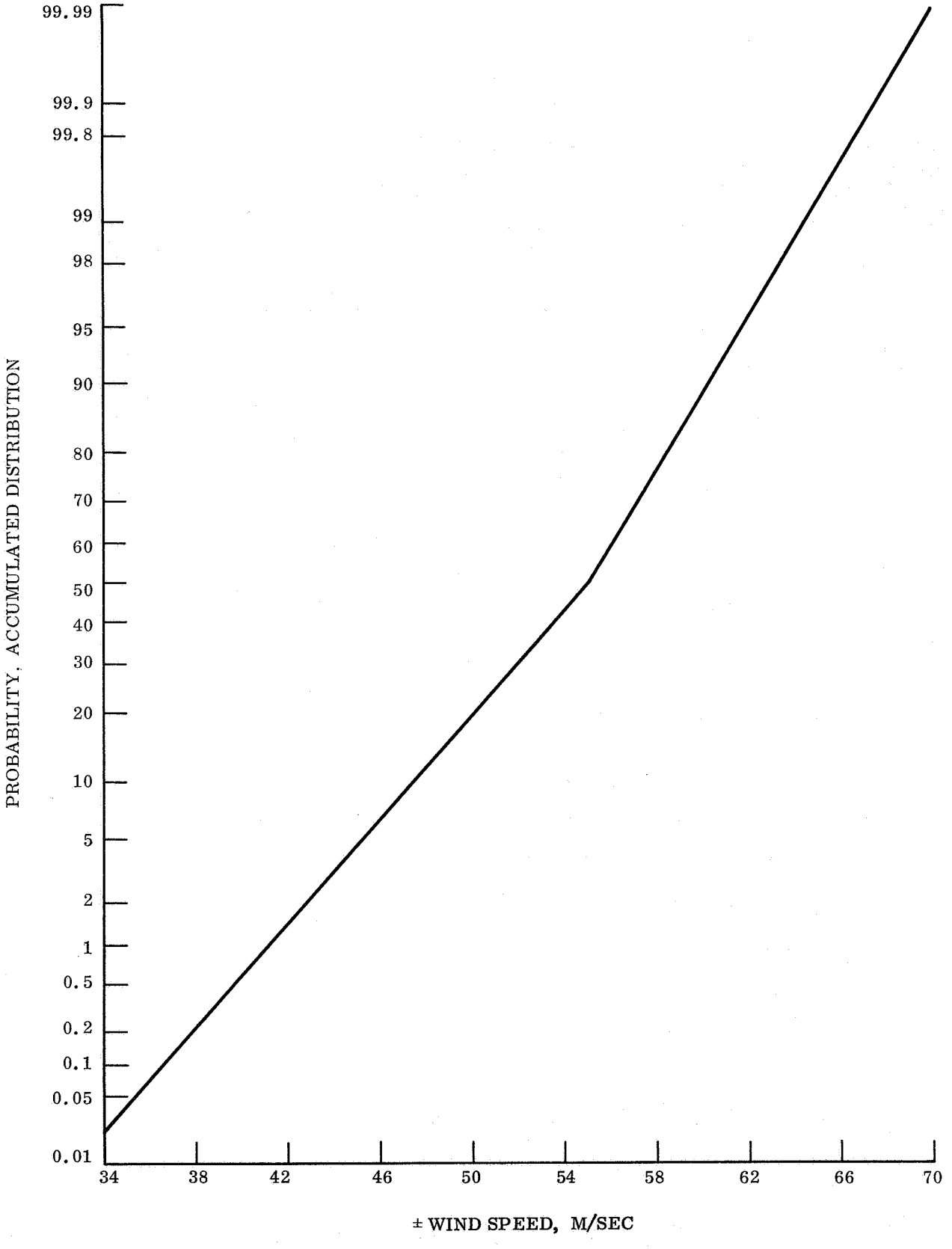

Figure 4.5.2-14. Cumulative Probability Distribution for Wind Speed

This enables one to report statistically on f by evaluating it 13 times. It is these compound probabilities which must be included in the rational analysis of the secondary impact problem. At the time of this report the full probabilistic nature of the wind has not been accounted for. Rather two isolated point estimates, corresponding to point design data furnished by NASA/LRC were investigated.

For convenience in computation, the matrix was calculated with uniformly spaced pendulum angles 0 = -40°, -20°, 0°, 20°, 40° and ground slopes = -30°, -15°, 0°, 15°, 30°

For computing averages and other statistical measures, each result for ΣV must be weighted by its likelihood or probability. The slope values are considered to represent the slope intervals with the associated probability as given below:

γ	Interval	Probability
-30°	-90°, -22.5°	0.0225
-15°	-22.5°, -7.5°	0.1775
0°	-7.5°, 7.5°	0.6000
15°	7.5°, 22.5°	0.1775
30°	22.5°, 90°	0.0225

The probabilities were obtained from the cumulative distribution graph for positive slope. Symmetry implies that the graph for negative shape is identical.

Similarly, the φ - angle values must represent the angular intervals with an associated probability as given below:

φ	Interval	Probability
-40°	-90°, -40°	0.025
-20°	-40°, -10°	0.395
0°	-10°, -10°	0.160
20°	10°, 30°	0.395
40°	40°, 90°	0.025

A probabilistic weighting matrix can therefore be constructed.

φ angle / γ-angle	$P(\gamma)$ \ $P(\varphi)$	-40° 0.025	-20° 0.395	0° 0.160	20° 0.395	40° 0.025	ck. sums
-30°	0.0225	0.00056	0.00889	0.00360	0.00889	0.00056	0.02250
-15°	0.1775	0.00444	0.07011	0.02840	0.07011	0.00444	0.17750
0°	0.6000	0.01500	0.23700	0.09600	0.23700	0.01500	0.60000
15°	0.1775	0.00444	0.07011	0.02840	0.07011	0.00444	0.17750
30°	0.0225	0.00056	0.00889	0.00360	0.00889	0.00056	0.02250
							1.00000

For a wind velocity of 110 ft/sec, results in the following table:

	Value, X_i	Probability, p_i	Cumulative Probability (%)
Cases of no flip of Lander	0	0.00360	
	0	0.00889	
	0	0.02840	
	0	0.02840	
	0	0.00889	
	0	0.00360	8.2
	19	0.09600	17.8
	48	0.23700	41.5
	52	0.07011	48.5
	53	0.23700	72.2
	72	0.07011	79.2
	97	0.01500	80.7
	108	0.00444	81.1
	115	0.00444	81.6
	119	0.00056	81.6
	125	0.07011	88.7
	127	0.07011	95.7
	128	0.00056	95.7
	151	0.01500	97.2
	156	0.00444	97.7
	159.5	0.00444	88.1
	179	0.00889	99.0
	180	0.00889	99.89
	189	0.00056	99.94
	226	0.00056	100

median value = 52.1

$\bar{x}$ = average value = $61.8 \Sigma p_i x_i$

standard deviation = 40.8

These results yield the cumulative plot of fig. 4.5.2-15 for secondary velocity when the wind is 110 fps.

Interpolating from the cumulative probability graph to obtain data for the bar graph for

V_{wind} = 110 ft/sec, results in:

Value in EPE	Cumulative Probability (%)	Probability Density (%)
0	8.2	
25	18.0	18
50	43.0	25
75	79.0	36
100	81.0	2
125	88.5	7.5
150	97.3	8.8
175	98.5	1.2
200	99.94	1.44
225	99.99	0.05
250	100.0	0.01

The associated histogram is plotted as fig. 4.5.2-16.

Arranging the values ΣV montonically for a wind velocity of 220 ft /sec yields.

Value	Distribution	Cumulative Distribution (%)	Value	Distribution	Cumulative Distribution (%)
0	0.00889		270	0.07011	87.9
0	0.00889	1.8	273	0.07011	94.9
129	0.09600	11.4	276	0.00056	95.0
171	0.23700	35.1	297	0.00360	95.4
177	0.23700	58.8	302	0.00444	95.8
186	0.07011	65.8	308	0.00444	96.25
205	0.07011	72.8	308	0.00360	96.6
209	0.02840	75.6	320	0.00889	97.5
230	0.02840	78.5	322	0.00889	98.4
236	0.01500	80.0	331	0.00056	98.4
252	0.00444	80.4	375	0.01500	99.9
257	0.00444	80.9	378	0.00056	100.0
264	0.00056	80.9			

median value = 176.3 average value = 195.5 standard deviation = 56.9

The associated histogram is plotted as fig. 4.5.2-17.

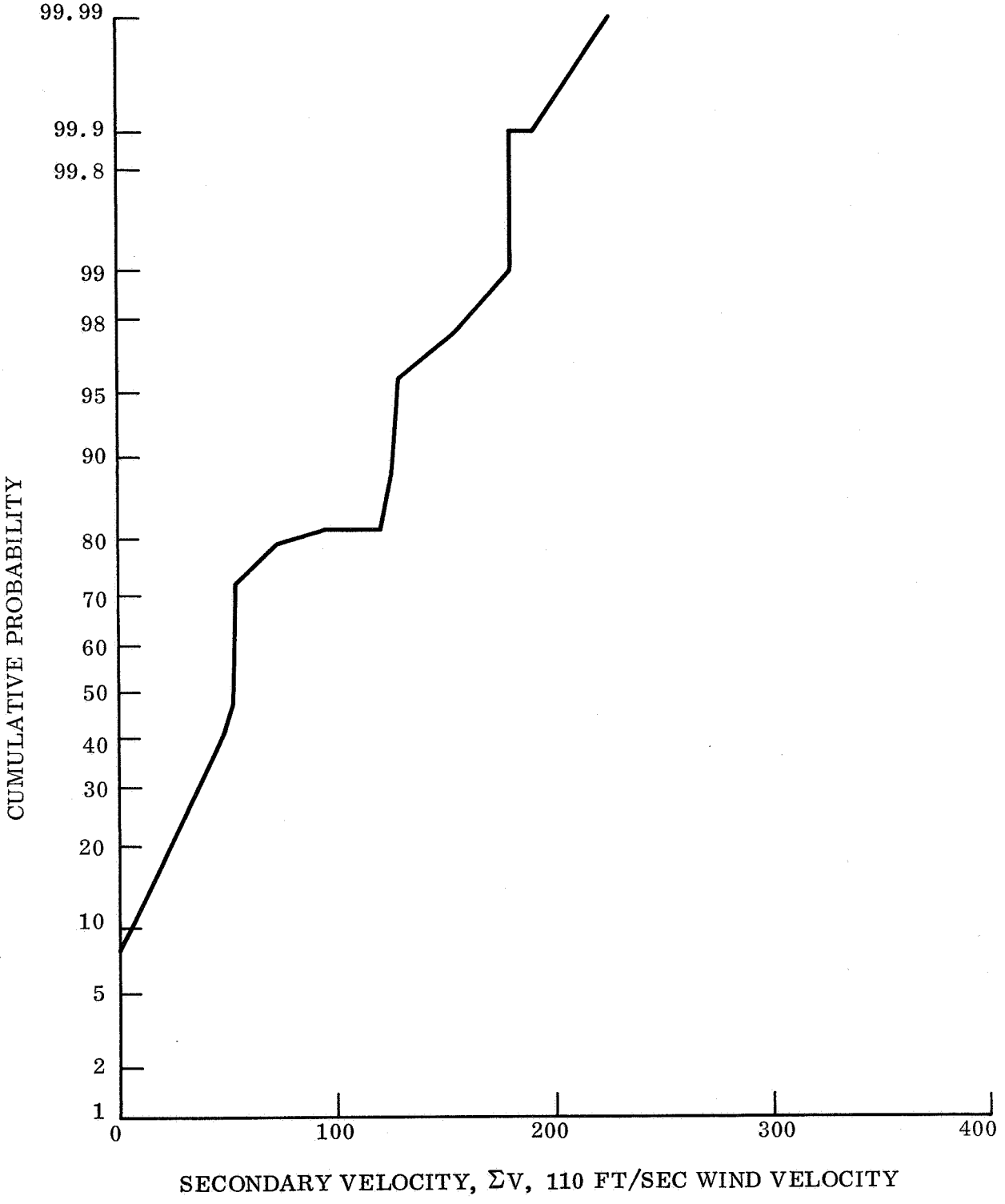

Figure 4.5.2-15. Cumulative Probability Distribution for ΣV Corresponding to Wind Speed at 110 ft/sec

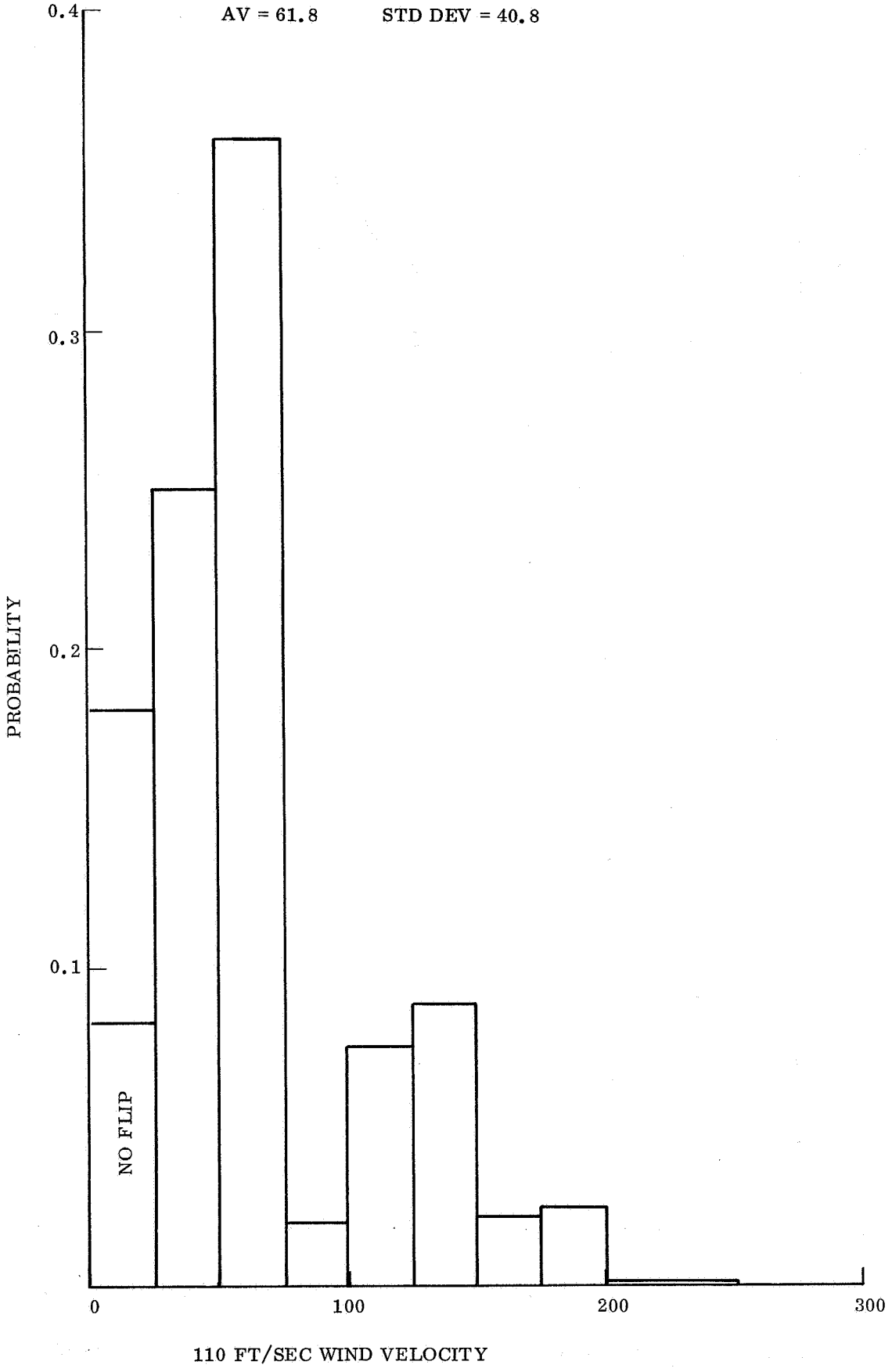

Figure 4.5.2-16. Histogram for ΣV Corresponding to Wind Speed of 110 ft/sec

Interpolating from the cumulative probability graph of fig. 4.5.2-17 for V_{wind} = 220 ft /sec produces:

Value	Cumulative Probability (%)	Probability (%)
0	1.8	
25	2.6	2.6
50	4.0	1.4
75	5.5	1.5
100	8.0	2.5
125	10.6	2.6
150	21.0	10.4
175	45.0	24.0
200	71.0	26.0
225	78.0	7.0
250	81.0	3.0
275	95.0	14.0
300	95.5	0.5
325	98.1	2.6
350	99.4	1.3
375	99.9	0.5
400	100.0	0.1

The associated histogram is presented as fig. 4.5.2-18.

The previous statistical analyses were performed for the purpose of determining the probability of equalling or exceeding a particular impact velocity. Based upon the limited first order approximation used, the following types of conclusions may be drawn. As an example, for a wind velocity of 110 fps the secondary velocity of impact will be 100 fps or less about 81 percent of the time given that the Lander does, in fact, flip over. In approximately 25 percent of the cases analyzed the Lander does not flip over. For the extreme wind velocity of 220 fps, of the cases analyzed the Lander flips 92 percent of the time and the secondary hit velocity is less than or equal to 100 fps only 8 percent of the time.

Further statements of this type can be made based on the information in figs. 4.5.2-16 and 4.5.2-17.

The first order analysis indicates the overwhelming importance of an accurate wind definition to be used in conjunction with a unidirectional Lander mission.

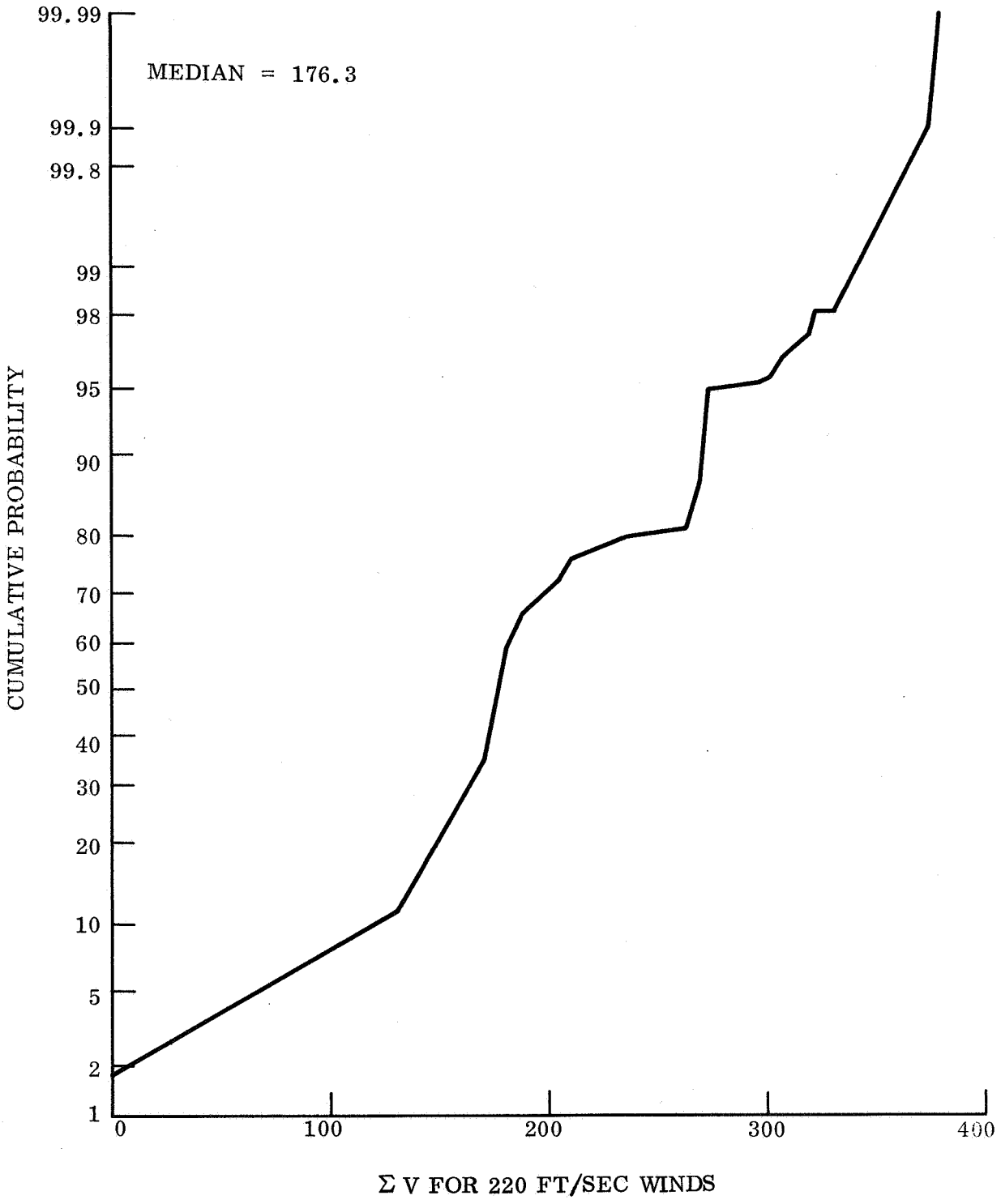

Figure 4.5.2-17. Cumulative Probability Distribution for ΣV Corresponding to Wind Speed of 220 ft/sec

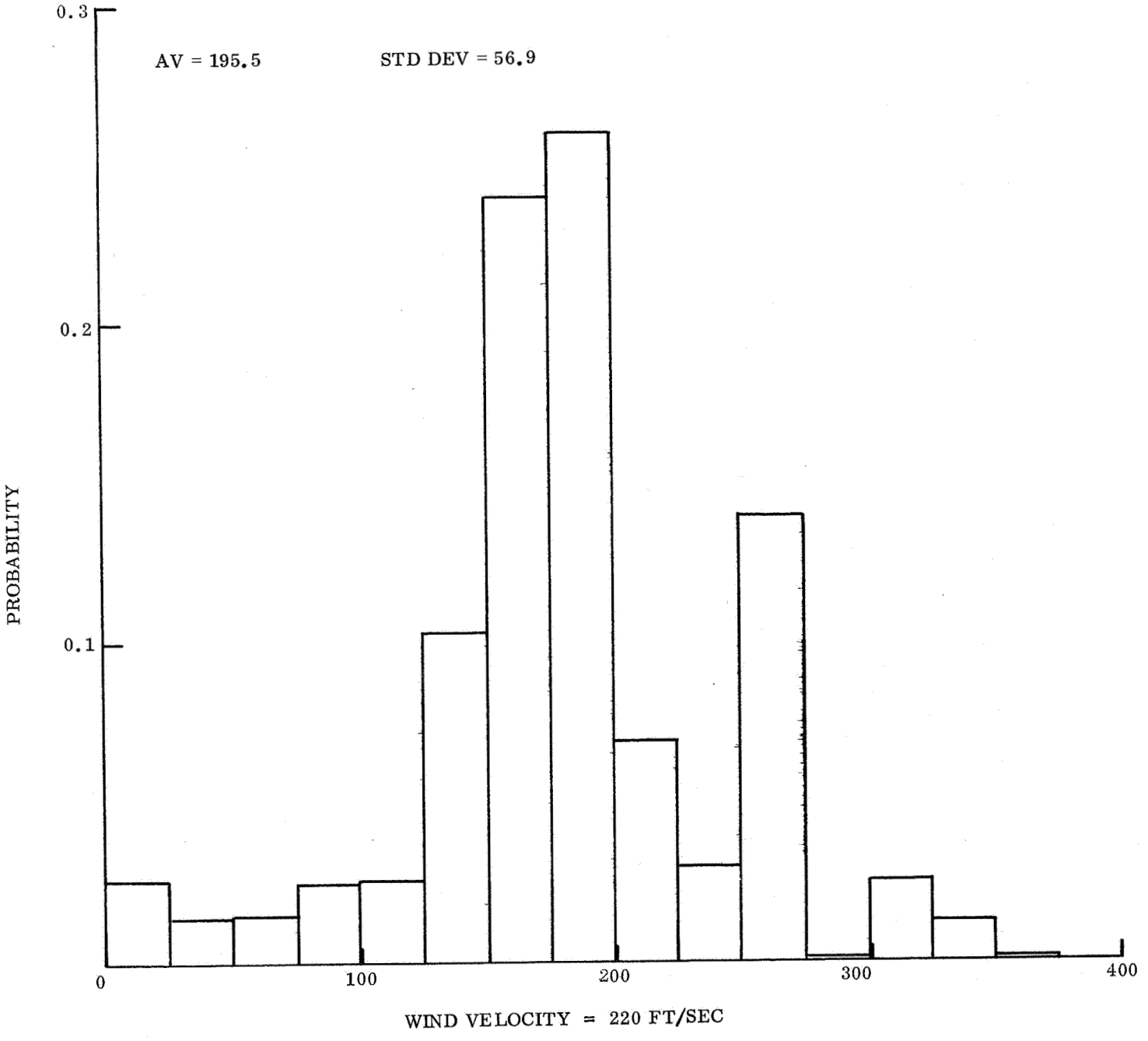

Figure 4.5.2-18. Histogram for ΣV Corresponding to Wind Speed of 220 ft/sec

4.5.3 PARAMETRIC DESIGN CRITERIA

4.5.3.1 Material Performance

Phenolic fiberglass honeycomb of 3/16 in. cell size was chosen for the design of this study. This represents a reliable, predictable, well-developed material whose performance has been experimentally proven. The development basis and physical properties of this honeycomb have been experimentally proven and are reported in ref. 4-29.

Two significant facets of this honeycomb material are best illustrated by figs. 4.5.3-1A and 4.5.3-1B, which are design curves. In fig. 4.5.3-1A the variation of material crushing stress with density is shown. From the curve it is seen that there is a definite maximum crushing stress attainable with this material configuration, and that an increase in density over and above the value associated with this peak stress is not warranted. This same argument applies to the specific energy versus density relationship directly (as shown in fig. 4.5.3-1B). Experimentation has also shown that honeycomb densities below about 4 pcf, while producible, result in unpredictable behavior. This fact thereby sets the lower limit on the density to be used in the hard Lander designs.

Fig. 4.5.3-2 shows the relation between phenolic fiberglass honeycomb effectively and the orientation of the applied load vector. This design curve is based on the experimental results shown in figs. 4.5.3-3 and 4.5.3-4. The experimentation underlying this effectivity relationship has been described in ref. 4-29. The effectivity is seen to decrease by about 2 percent per degree of difference between honeycomb longitudinal axis and the orientation of the applied load vector. This basic relationship has a decided influence on the design of the deep dish type of Lander because of the geometric characteristics inherent in the design. Since provision must be made for multi-directional or omni-directional impact capability, not all the material included in the impact attenuator will be active under any one time. This implies that the material is not used to its utmost efficiency under all conditions. Geometric limitations also limit material efficiency and add a weight penalty since once certain honeycomb cells are oriented in a given direction their usefulness in other directions is limited by the obliquity effects. This loss in material effectivity is compensated for in part by the increase in the gross area as the crush up stroke progresses. Nevertheless the obliquity effects are significant and markedly influence the pulse shape experienced for crush up at various orientations. Figs. 4.5.2-2 and 4.5.2-9 emphasize this point for some typical Lander designs.

Plotted in these figures is the crushed area vs stroke for various cutting plane orientations. For comparative purposes, a plot of gross crushed area against stroke for various orientations is also presented in fig. 4.5.3-5. In generating the

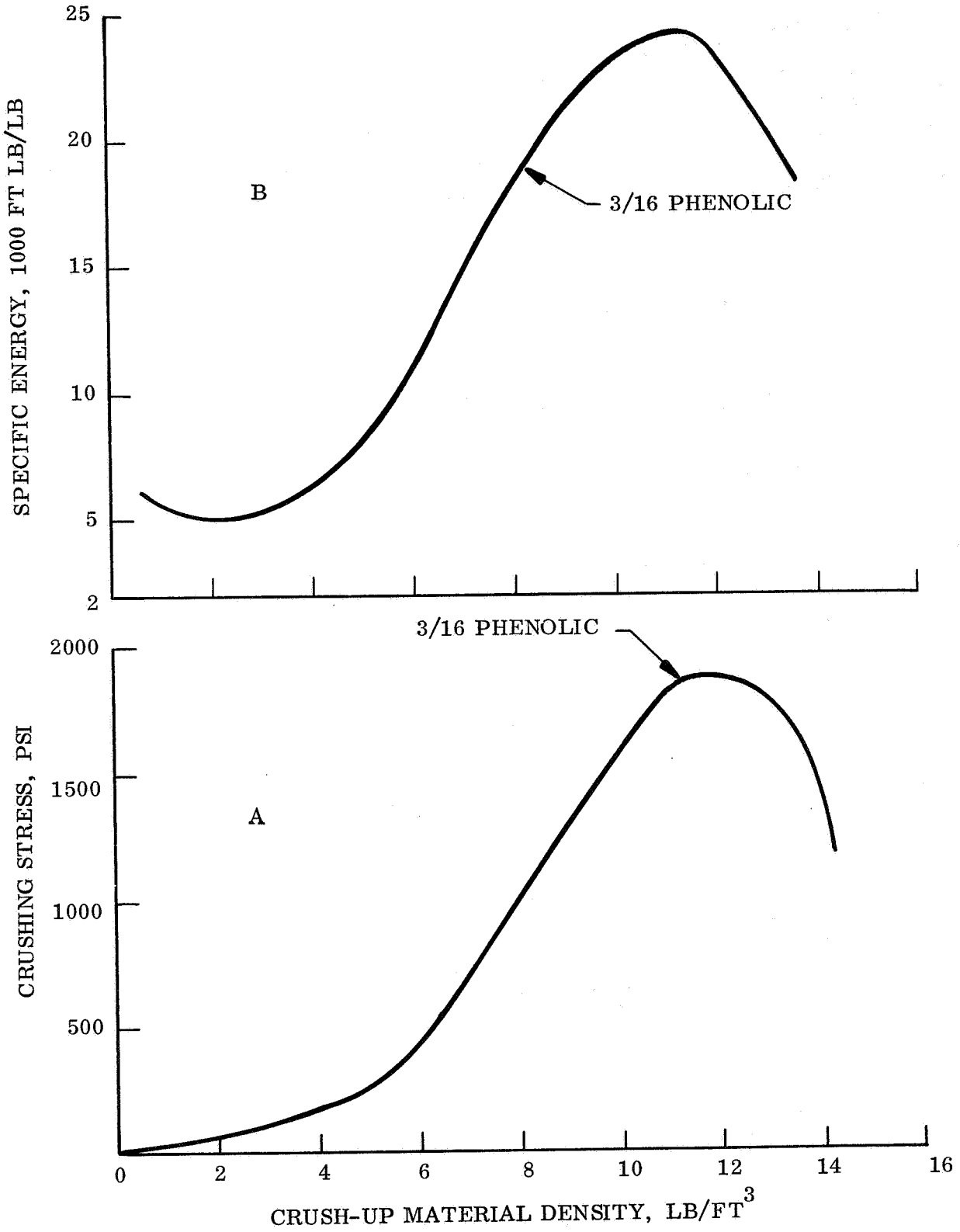

Figure 4.5.3-1. Crushable Honeycomb Properties

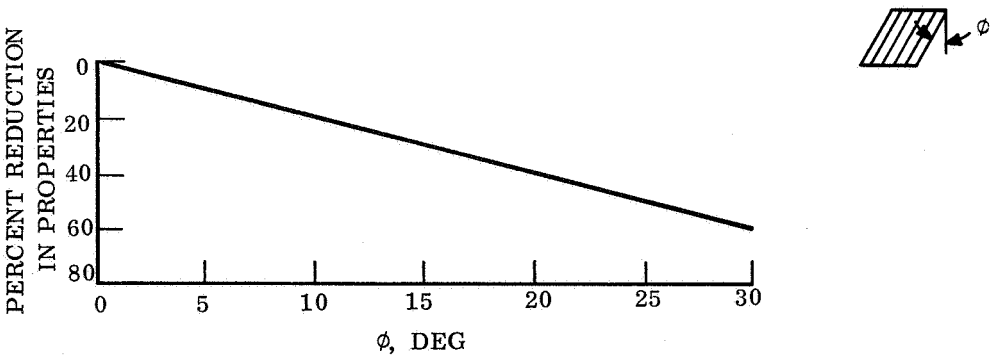

Figure 4.5.3-2. Design Curve for Material Effectiveness Computations

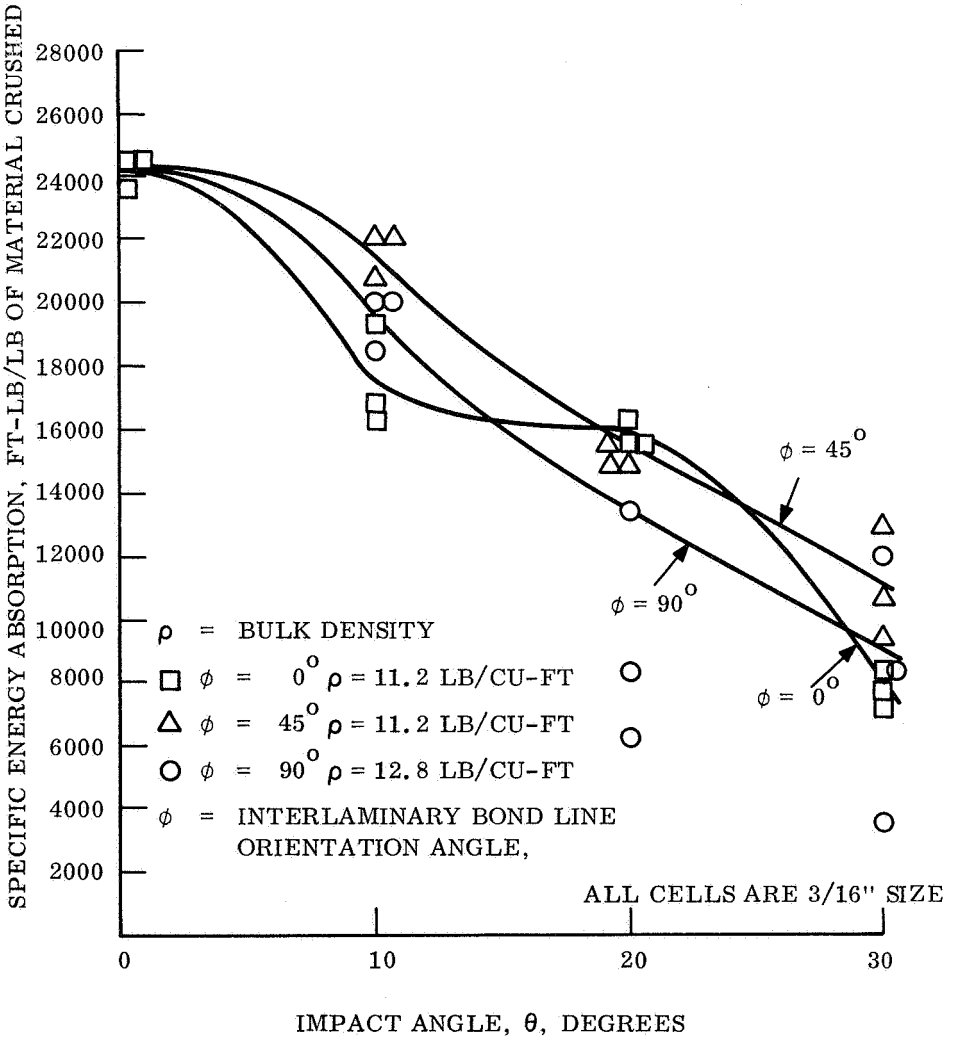

Figure 4.5.3-3. Specific Energy Absorption vs Angle of Impact vs Honeycomb Bond Line Orientation Angle

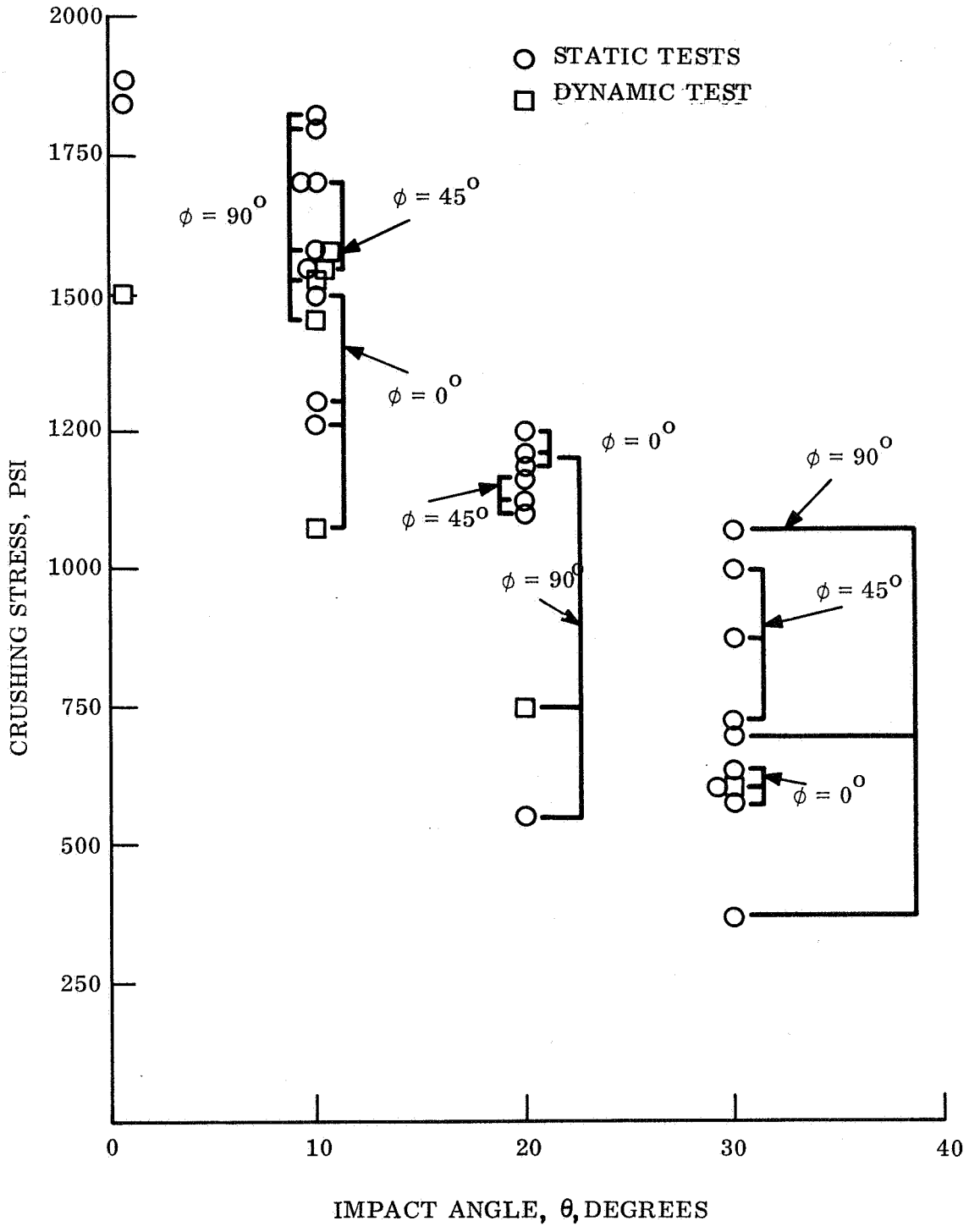

Figure 4.5.3-4. Comparison of Crushing Stress vs Angle at Impact for Static and Dynamic Loading

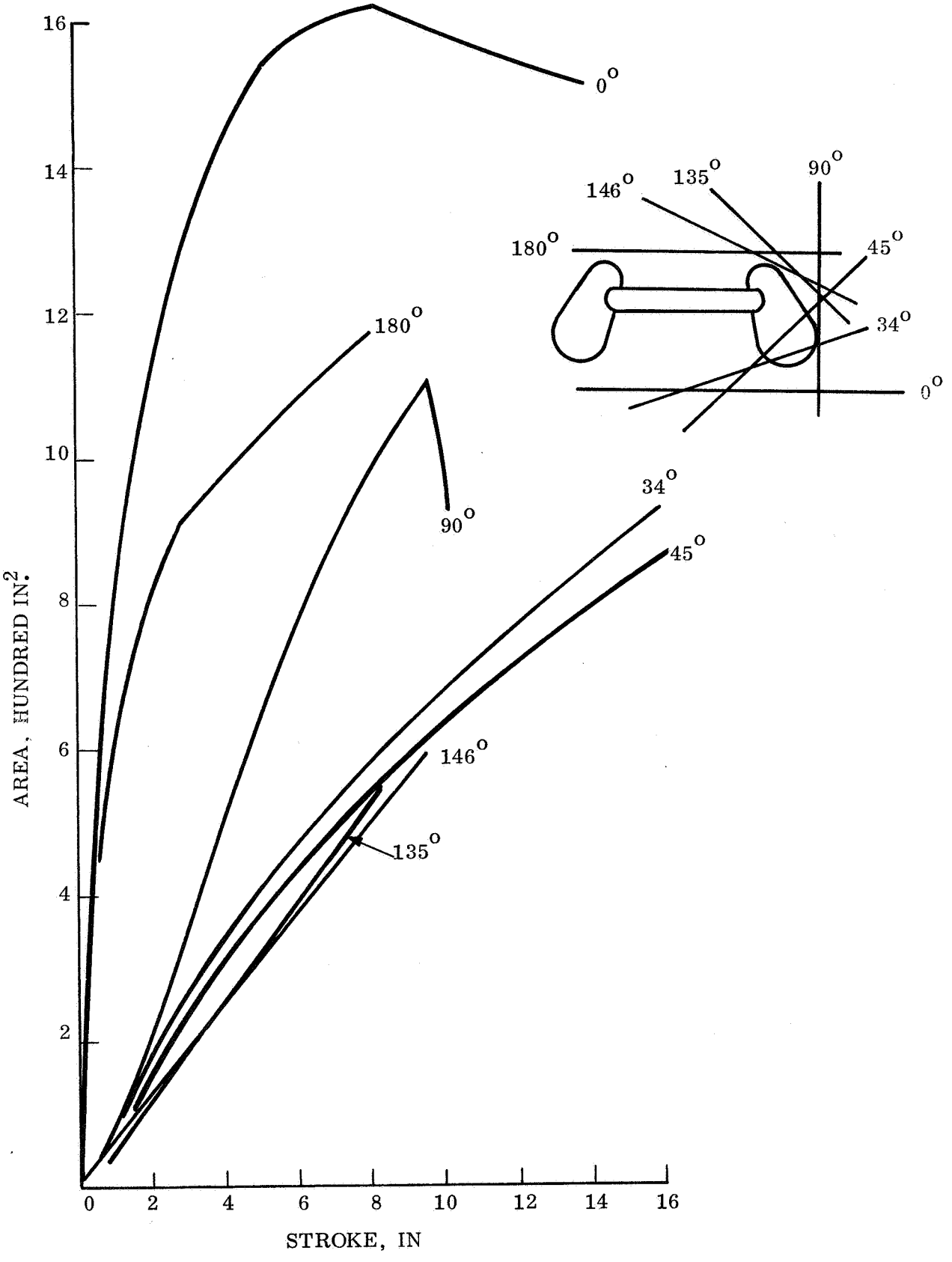

Figure 4.5.3-5. Gross Crushed Area vs Stroke for Typical Multi-directional Lander

above curves, an allowance for curvature in plan was also incorporated. This is believed to amount to no more than 20 percent due to the segmenting of the honeycomb attenuator into small elements. Further confirmation of this figure can be made with actual experimentation. The energy absorption mechanism is assumed to be purely crush-up. Failure of the bond of the individual cells or between honeycomb segments are eliminated by use of an adhesive which is stronger than the honeycomb material. This same adhesive is used to bond the honeycomb to the container structure and to the encapsulating structure.

Gross deformation effects are also investigated for two conditions. The first is excessive stroke requirements which produce a thickness sufficiently large to lead to impulsive buckling of the honeycomb cells without crushing behavior. If such strokes are indicated, the attenuator is segmented further to eliminate buckling and promote crushing of the attenuator.

Gross shear failures must also be considered. This possible mode involves the breaking off of an entire piece of material without crushing deformation. Where analysis indicates that gross shear is a possible, circumferential metallic strips welded to the payload container can be used to take out the shear in excess of what can be carried laterally by the honeycomb cells.

These elements, while resistant to shear are sufficiently slender to buckle when impacted along their length, and thereby crush-up with the phenolic honeycomb material.

4.5.3.2 Stroke Requirements

In Section 4.5.3 the influence of material effectivity was described. The crushing characteristics of the phenolic honeycomb intimately affect the stroke constants k_i appearing in the stroke equation

$$s_i = k_i \frac{V^2}{gG}$$

For a given Lander geometry, the various k_i values are determined as now described. The Lander geometry is inputted to the CRUSH Program, which returns the area crushed by various cutting planes. The effect of angular orientation is then incorporated into the computation by reducing the gross crush area by 2 percent for every degree of obliquity in elevation and then discounted further by a reduction factor of 0.8 for obliquity in plan. From the curve relating net effective area to stroke one can derive the expression for the energy absorbed in terms of stroke and peak g-level. This expression is then equated to the kinetic energy of impact normal to the cutting plan impacted. The resulting equation allows one to solve for

the stroke and implicity yields the stroke factor for the particular orientation measured with respect to the body. For design computations for multi-directional Lander, one of the stroke constants was derived as follows.

For the 0° case, the effective area versus stroke diagram takes the form shown in fig. 4.5.3-6. From this plot then,

$$\text{energy absorbed} = \frac{1}{2}\ WG\ S + \frac{1}{2}x\frac{3}{4}\ WG\ \frac{S}{2} + \frac{1}{4}\ x\ S\ x\frac{WG}{2}$$

$$\text{energy absorbed} = \frac{13}{16}\ WGS$$

$$\frac{1}{2}\ \frac{W}{g}\ V_N^{\ 2} = \frac{13}{16}\ WGS$$

$$S_0^{\circ} = \underbrace{0.62}\ \frac{V^2}{gG}$$

Bottom stroke distance — 0° slope factor

For crush-up at an angle of 45° and 90° with respect to the multi-directional Lander body (see fig. 4.5.3-6 and 4.5.3-7) the energy absorbed = 1/2 W/g $V_N^{\ 2}$ = WGS (1/3 + 1/2 x 2/3)

$$\frac{1}{2}\ \frac{W}{g}\ V_N^2 = \frac{2}{3}\ WGS$$

$$S_{45^\circ} = S_{90^\circ} = \frac{0.75\ V_N^{\ 2}}{g\ G}$$

Experience and judgement have indicated that certain critical crush-up conditions can be used to size the multi-directional Hard Lander. The aft end thickness of the multi-directional Lander is sized according to secondary impact considerations as detailed in the next subsection.

There is important physical significance attached to the stroke constants which can be derived for the multi-directional and omni-directional Lander concepts. If the deceleration pulse were ideal, that is, of the shape of fig. 4.5.3-8, then

$$S_{ideal} = 1/2\ \frac{V^2}{gG}$$

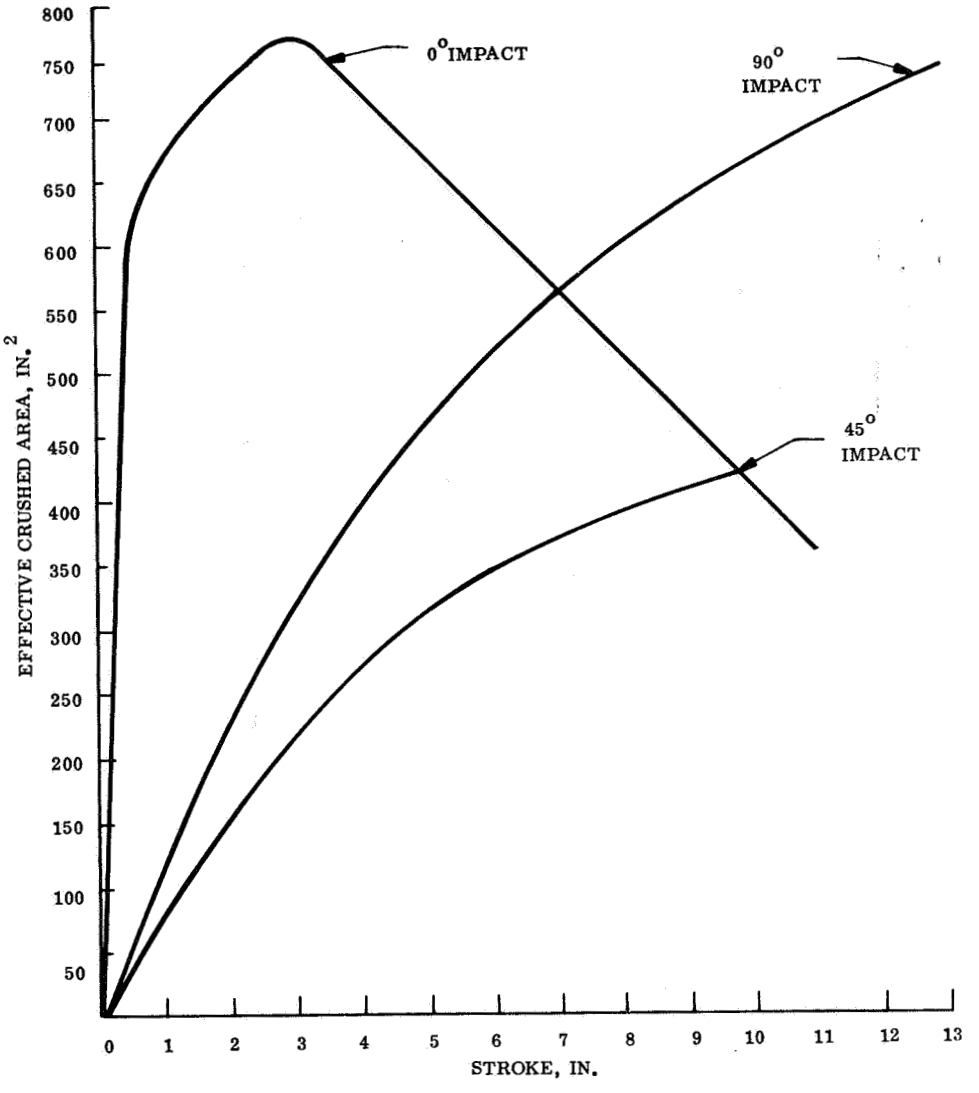

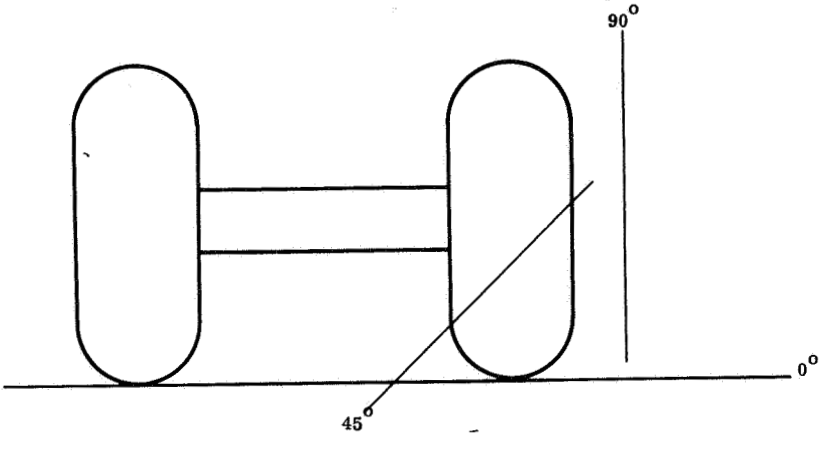

Figure 4.5.3-7. Cutting Plane Orientations for Stroke Computations

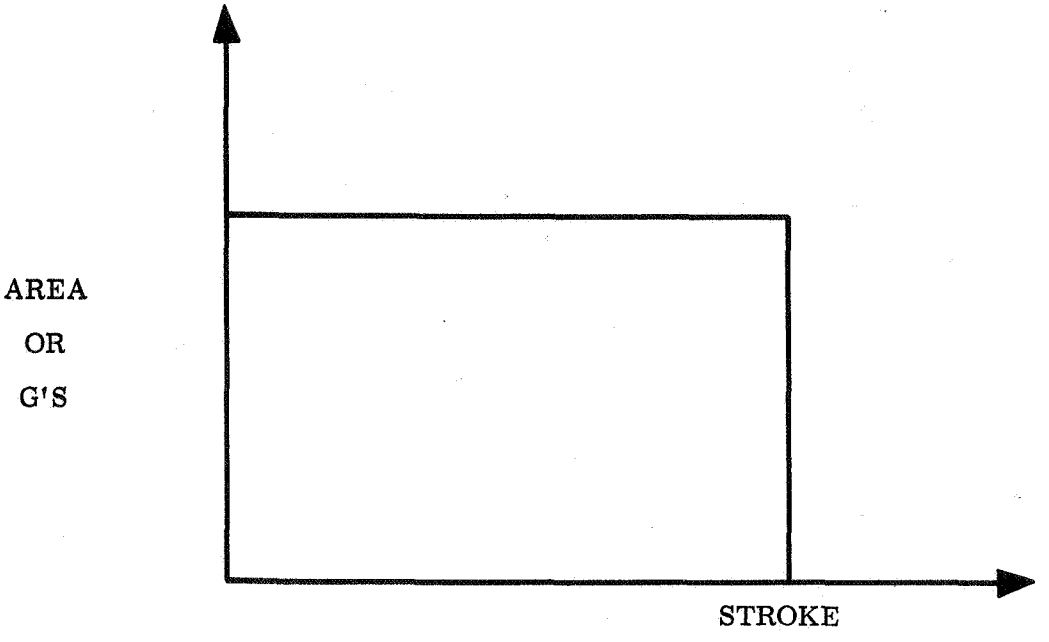

Figure 4.5.3-8. Ideal Deceleration Pulse

that is, S_{ideal} is a minimum with k = 1/2. An attenuator with these characteristics would occupy a minimum volume. If the pulse shape were triangular, then the stroke constant is unity and

$$S = \frac{V_N^2}{gG}$$

It is seen that the Deep Dish Lander geometry represents a concept which is tending toward the minimum stroke and hence a reduced volume.

Once the three principal strokes are known, one has the principal contributing factors to the attenuator thickness computation. Provision must still be made for stroke efficiency, a factor of safety, and rock protection dimensions. These are handled as follows. Ref. 4-29 contains data on honeycomb stroke efficiency. For the densities used, this efficiency is about 0.8. Stroke efficiency is defined as that fraction of total honeycomb thickness which will actually crush-up when impacted. This effect occurs because some of the total thickness provided is lost as accumulated crushed material builds up. See fig. 4.5.3-9.

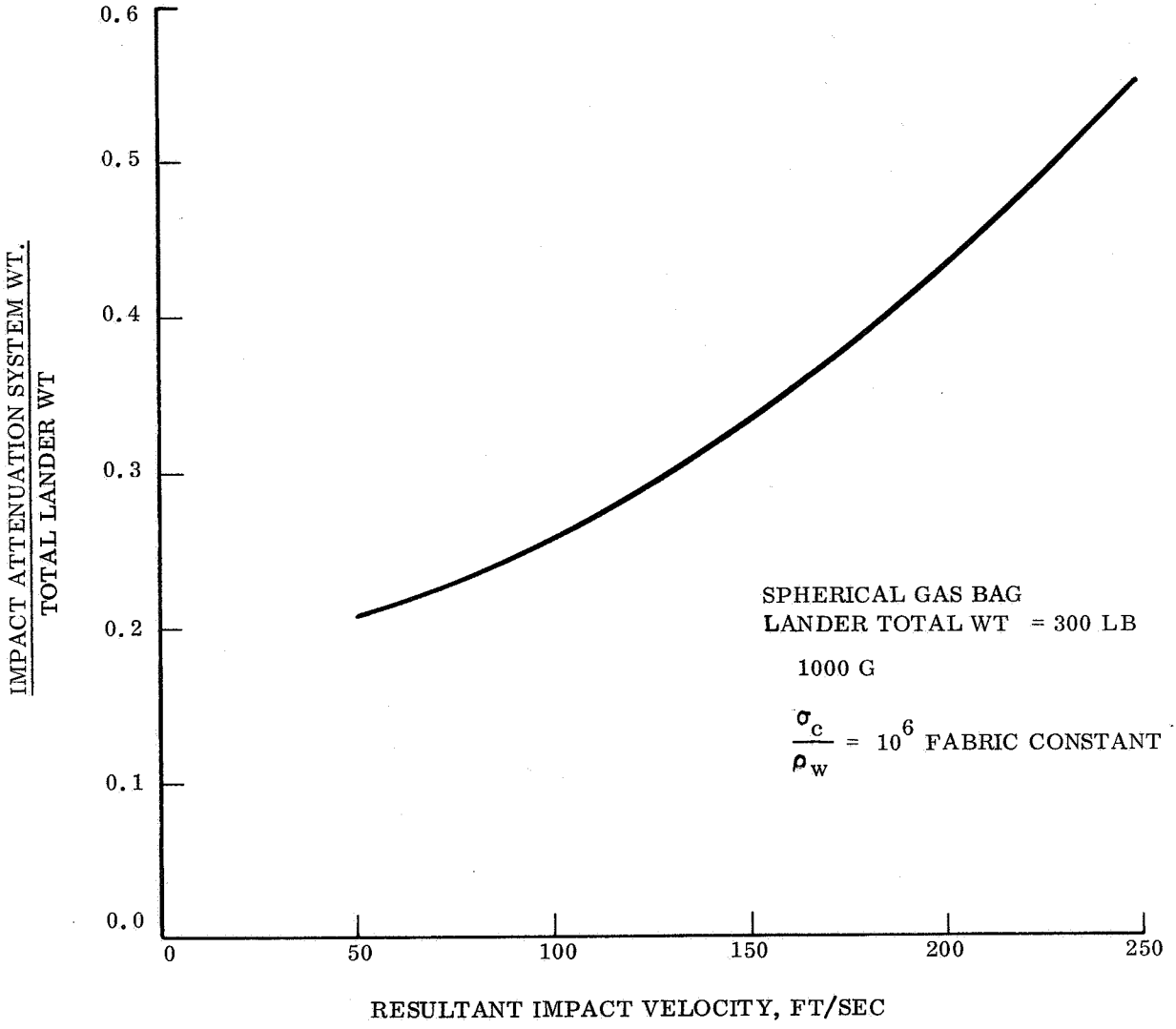

Figure 4.5.6-4. Attenuator Wt/Total Wt vs Impact Velocity for W_{total} = 300 lbs, g = 1000

The foregoing stroke computations were incorporated into computer codes used in the parametric analysis of impact attenuation system. The CRUSH and DISH codes allow one to input the basic touchdown condition, payload density, Lander aspect ratio, landed weight, and 'g' tolerance payload density, and receive the size, volume, weight, crushing stress and honeycomb density for various Lander configurations. The codes also indicate combinations of constraints which cannot be satisfied within the guidelines established for the study.

4.5.3.3 Sizing and Weight Estimation

For study purposes, the sizing and weight estimation were done with an automated procedure. As described in para. 4.5.3.2, the key stroke factors were determined in various directions. For the multi-directional Lander these directions were 0° (bottom end first), 45°, and 90° (side on). With these lay-off distances, the program logic fairs a curve approximated by chords through these points in order to define the surface periphery. The geometry is then subdivided, individual centroids computed and, by use of Gaudius rule, the volume of crush-up material is computed. The weight follows directly.

4.5.4 SECONDARY EFFECTS

There are two principal design details which were not included in the parametric analysis. At this stage it has not been established that such details are absolutely necessary; this point should be kept in mind throughout the following discussions.

The first of these is the honeycomb wrap around structure, or outer sheet casing. This casing is needed to produce the proper spreading of the impact loads, thereby mitigating localized damage to individual cells. The casing also functions to provide a surface for skidding while it prohibits the intrusion of sharp rocks or other outcroppings. Past experience with crushable Lander systems indicates that a very thin metallic skin can be bonded to encapsulate the honeycomb attenuator. The weight of this thin skin is a small fraction of the attenuator weight and is not sufficient to alter the trends and conclusions indicated by the parametric curves. Another design detail involves the shear strips used to take out gross shear forces which would otherwise tend to break off large chunks of attenuator material. These strips which can be welded to the landed subsystem container can be made of light gauge material and therefore will not add materially to the impact attenuation system weight.

The design lay-up sequence, although of secondary importance for parametric purposes, must also be evaluated for accurate estimation of attenuation weight. Empirical information is most suitable here. Past experience indicates that the double curvature introduced in this Lander concept can be wrapped effectively by segmenting the honeycomb into pieces which are then bonded together. See ref. 4-26 for details. In this way, the longitudinal axis of the honeycomb cells can be made near-radial with the payload contained structure. The wrapping proceeds around the

Lander circumference and then outward until the desired thicknesses are provided. The weight introduced by the adhesive is not included in the parametric curves. This effect can be accounted for by decreasing the (nominal) honeycomb density by a percentage to allow for adhesive bond weight.

4.5.5 PARAMETRIC ANALYSIS

4.5.5.1 Basic Parametric Data

Presented herein in graphical form is parametric data for the Mars Hard Lander Study. The data has been generated using both Lander geometries. For various landed weights and g-level combinations, the weight of attenuator material (as a fraction of landed weight) is plotted against descent velocity with variations shown for:

1. horizontal wind
2. peak deceleration
3. surface slopes
4. lander weights.

Refer to figs. 4.5.5-3 through 4.5.5-65. The combinations of weight and g-level shown were chosen because a representative number of meaningful points can be plotted to generate parametric curves. Note however, the inherent material and geometric constraints preclude the use of some g-level/weight combinations for a deep dish design. The reason for this is that the indicated crushing stress is either larger (high g's and weight) or lower (low g's and weight) than the stresses associated with the phenolic honeycomb densities presently available.

For these curves it is assumed that the most efficient 3/16 in. phenolic fiberglass honeycomb is used as attenuator material. To insure that the material has dependable properties a lower limit of 4 pcf is used; the density range is therefore 4 to 12 pcf. (Refer to fig. 4.5.3-1 for crushing stress versus density relations.)

It is also apparent that certain velocity limitations exist (for given g-level and landed weight constraints). This is reflected in those curves which do not cover the entire velocity spectrum. The exact cut-off points for the curves can be better approximated by successive iterations as required.

For reference purposes the presently used parameter matrix for the study is given in table 4.5.5-1 the analysis has been expedited by the use of DISH and KRUSH programs especially developed to treat the Deep Dish Landers. These codes account for varying Lander footprint areas with stroke and orientation as well as rock protrusions. Loss in material efficiency according to the empirical law of fig. 4.5.3-2 is also included; in addition an efficiency effect due to Lander curvature (in plan) is incorporated into the code.

TABLE 4.5.5-1. PARAMETER MATRIX

Parameter	Symbol	Dimensions	Range	Intermediate Values
Lander Weight	W_L	lb	200-1000	200, 400, 600, 800, 1000
Descent Velocity	V_v	ft/sec	50-210	50, 100, 150, 210
Horizontal Velocity	V_H	ft/sec	0-220	0, 110, 220
Peak Deceleration	a	'g' Earth	500-3000	500, 1000, 1500, 3000
Surface Slope	θ	deg	0-34	0, 34
Surface Protrusions	h	in.	0-5	0, 5
Attenuation Density	ρ	lb/ft^3	6-12	Continuous
Crushing Stress	σ	lb/in^2	400-2000	Continuous
Directionality	-		Omni and multi	Omni and multi

The DISH and KRUSH programs were constructed with this information and allow one to input the basic touchdown conditions and receive the size, volume, weight, crushing stress and material density for various deep dish configurations. The routine also indicates combinations of constraints which can not be satisfied within the deep dish -- crushable phenolic guidelines.

The geometry used in the programs is presented in fig. 4.5.5-1. The distances b and d are entered in the program along with landed weight, allowable 'g' and the rock clearance constant. The program sizes the attenuator system based on the geometric approximations shown. Fig. 4.5.5-2 shows typical program output information.

4.5.5.1.1 Discussion of Omni-directional Parametric Data

Figs. 4.5.5-3 through 4.5.5-37 present the parametric results for the various weight, g-level, velocity, slope, rock, and packaging density variations for an omni-directional Lander configuration. The individual characteristics of a particular curve are listed on the figure.

The figures show the fraction

$$\frac{\text{Crush-up Weight}}{\text{Lander Weight}} = K$$

against descent velocity for various parameter combinations. For a particular landed weight one can compute the associated Lander weight from the relation

$$\text{Lander Weight} = \frac{\text{Landed Weight}}{1 - K}$$

Comparison of the various curves shows the obvious trends that increasing weight penalties are paid due to increased in V_H, V_D or slope angle. It is also apparent that decreases in packaging density produce the same effect. As the operating g-level is decreased, an increasing weight penalty is paid for the necessary crush-up. For certain conditions, the effect of eliminating the rock criteria is also shown. Again, a weight penalty is paid for having to protect the container against rocks.

The curves are smooth functions for the ranges of parameters studied with one exception.

For certain combinations of velocities and g-levels the criteria which determines the thickness and thus the attenuator weight, changes from that of furnishing a rock protection thickness to be added to the stroke, to one of increasing the basic stroke to allow for a stroke efficiency factor.

Because of this transition between criteria some of the parametric curves have an abrupt change in slope.

Secondly, the parametric curves imply that for a given set of conditions a particular design is valid for angles up to and including the greatest slope angle. This means that for a nonzero slope, and no wind velocity the curve for $V_H = 0$ is actually determined for an impact on a zero slope with the full descent velocity. The reasoning for this is that the velocity component normal to the slope is used to size the stroke.

It is important to realize that this stroke-sizing criteria means that for an impact on a 0° slope the wind velocity is arbitrary. The families of parametric curves for 0° slope therefore reflect changes in packaging density. For an arbitrary V_H which is absorbed by sliding.

4.5.5.1.2 Discussion of Multi-directional Parametric Results

Figs. 4.5.5-38 through 4.5.5-65 present the parametric results for the various weight, g-level, velocity, slope, rock and packaging density variations for a multi-directional Lander configuration. The individual characteristics of a particular curve and other comments previously advanced for the omni-directional Lander curves also apply to these figures.

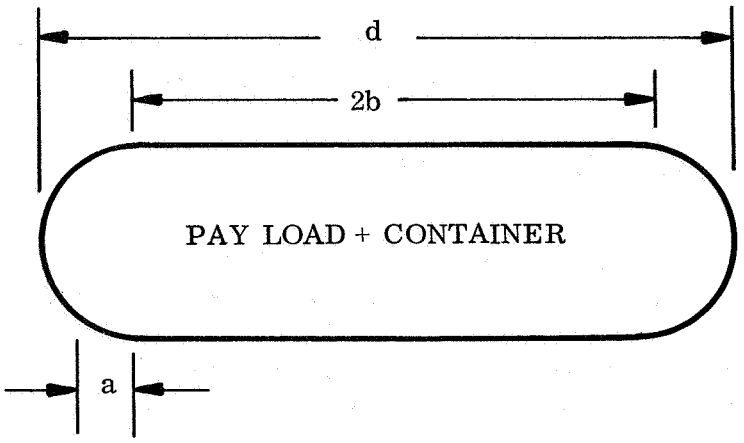

Figure 4.5.5-1. General Geometry for the Various Designs as Used for Computer Program Input

TYPE OUTSIDE DIAMETER (IN) = 44. "d"
TYPE INSIDE RADIUS (IN) = 17. "b"
TYPE NTH, NVV, NVH, NG, NWT = 1,1,1,1,3 (case information)
TYPE SLOPE ANGLE (DEGREES) = 34.
TYPE VERTICAL VELOCITY (FPS) = 100.
TYPE HORIZONTAL VELOCITY (FPS) = 220.
TYPE G LEVEL (EARTH G'S) = 1000.
TYPE TOTAL WEIGHT (LBS) = 1000., 1015., 1035.
TYPE STROKE CONSTANTS (THREE) = 0.6, 0.7, 0.7
TYPE ROCK DISTANCE (IN.) = 5.

SLOPE	DES. VEL	HOR. VEL	G LEVEL	WEIGHT
34.000	100.000	220.000	1000.000	1035.000

IMPACT ANGLE	NORMAL VELOCITY
58.4439	205.9261

S0	S45	S90
9,4820	11.0623	11.0623

T0	T45	T90
14.4820	16.0623	16.0623

STRESS = 1350.1876 DENSITY = 9.4533
AREA COEFFICIENT = 766.5601
TOTAL VOLUME OF CRUSH UP = 59.9513
TOTAL WEIGHT OF CRUSH UP = 566.7358
TOTAL WEIGHT AVAILABLE = 468.2642
CRUSH UP AS FRACTION OF TOTAL WT. = 0.5476

Figure 4.5.5-2. DISH Sample Input/Output

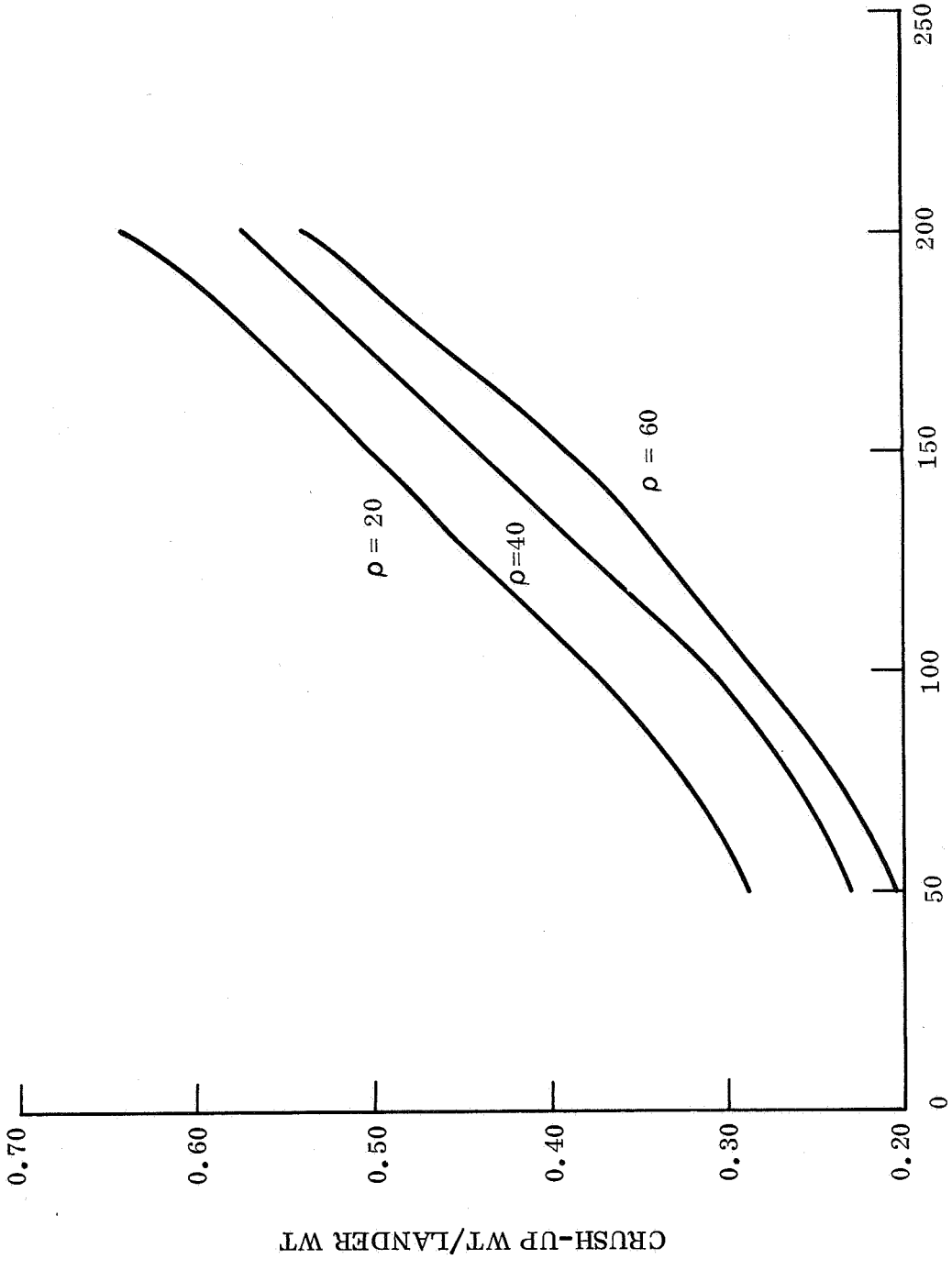

Figure 4.5.5-3. Crush-up Weight for Omni-directional Lander, Lander Wt = 300 lb, g-level = 1000, Slope = 34°, Packaging Density = 20, 40, and 60 pcf

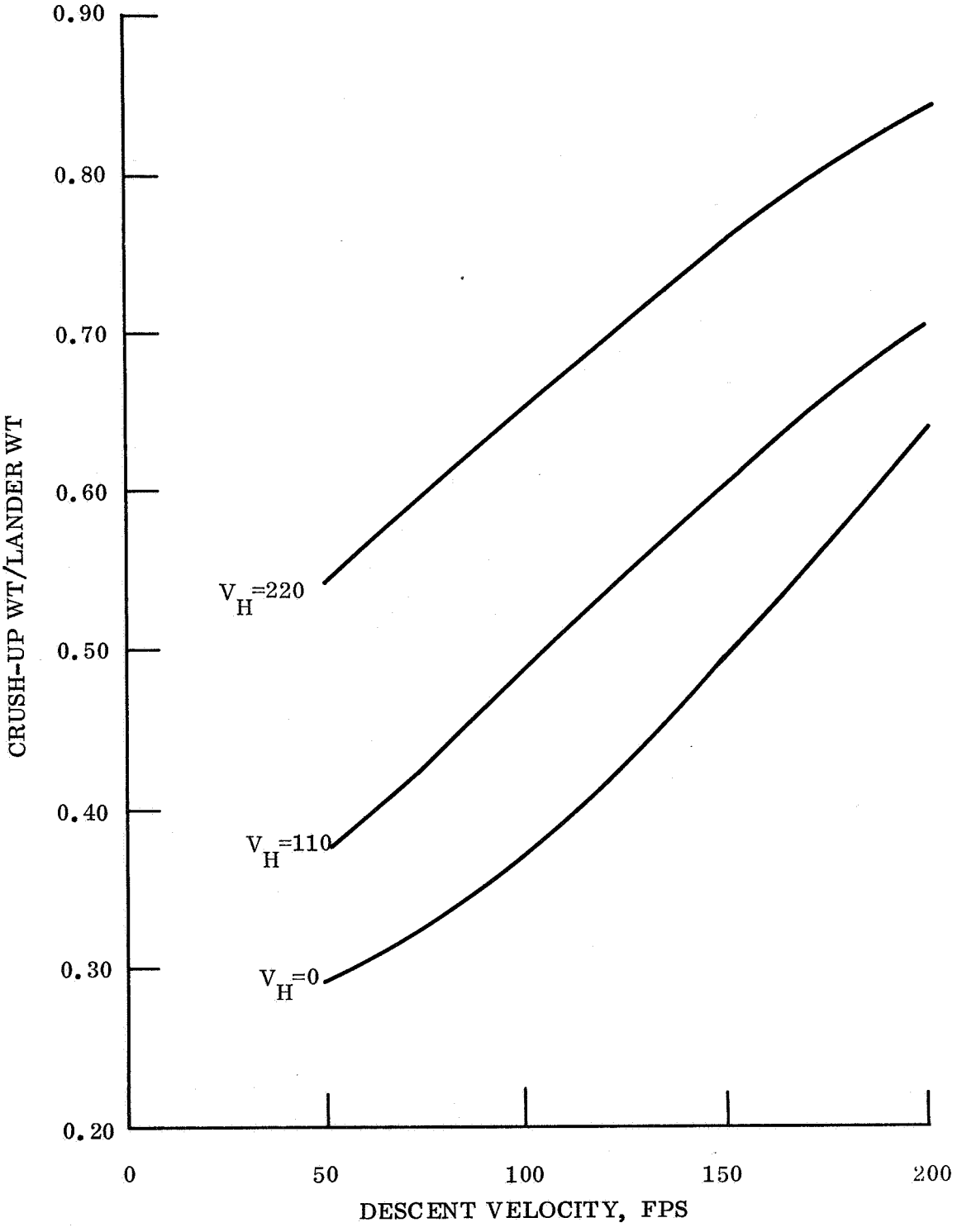

Figure 4.5.5-4. Crush-up Weight for Omni-directional Lander, Lander Wt = 300 lb, g-level = 1000, Slope = 34°, Packaging Density = 20 pcf

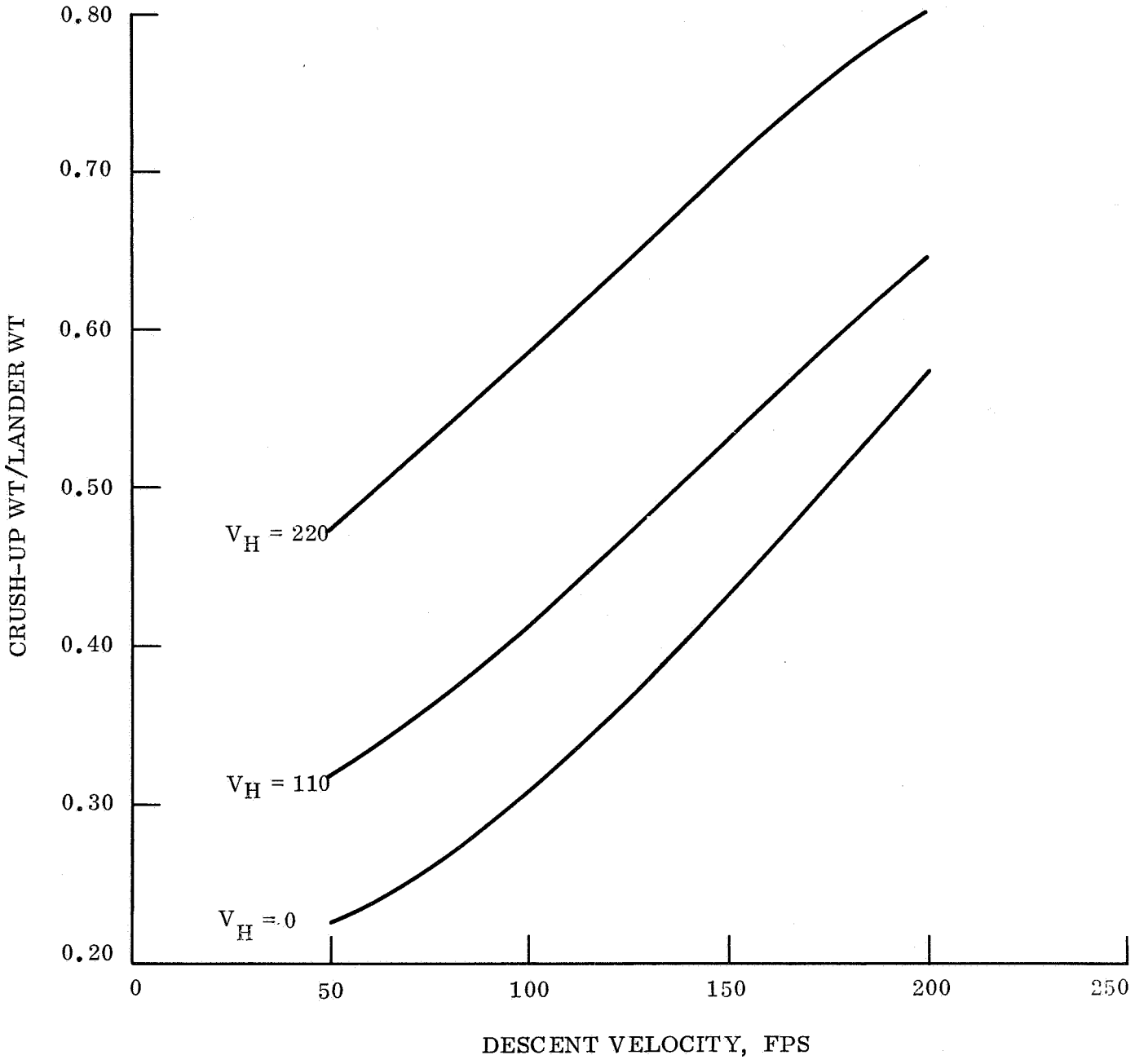

Figure 4.5.5-5. Crush-up Weight for Omni-directional Lander, Lander Wt = 300 lb, g-level = 1000, Slope = 34°, Packing Density = 40 pcf

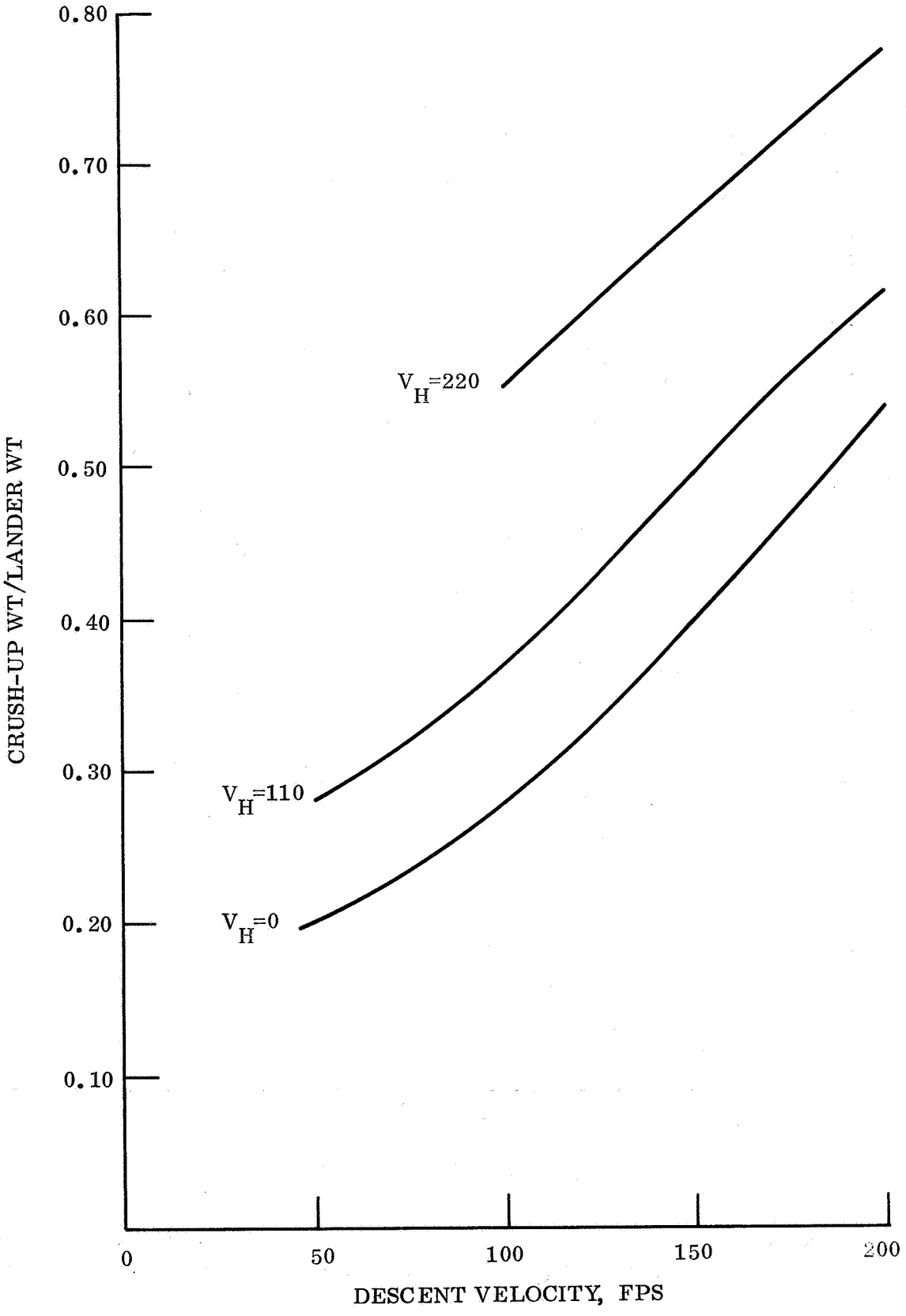

Figure 4.5.5-6. Crush-up Weight for Omni-directional Lander, Lander Wt = 300 lb, g-level = 1000, Slope = 34°, Packaging Density = 60 pcf

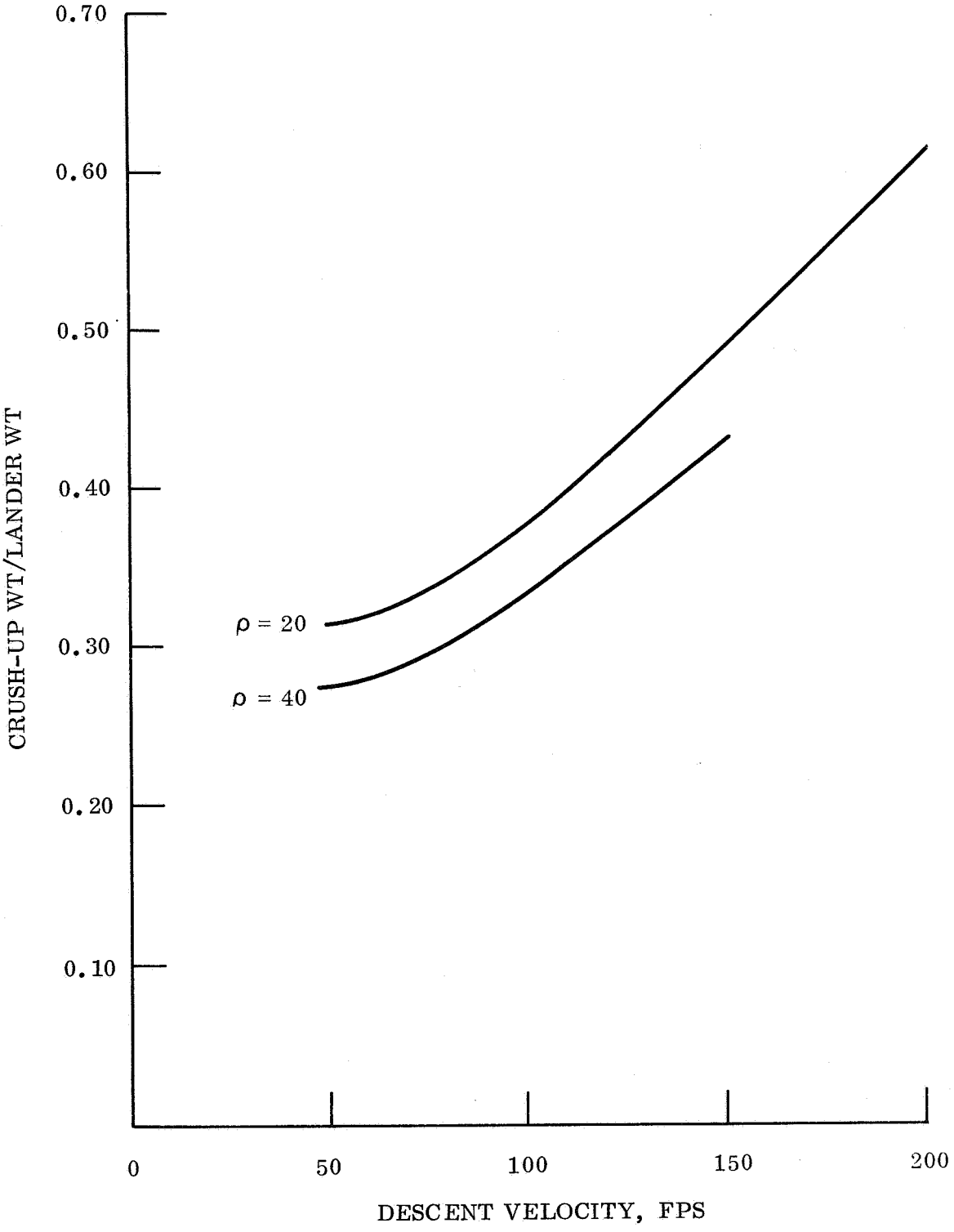

Figure 4.5.5-7. Crush-up Weight for Omni-directional Lander, Lander Wt = 300 lb, g-level = 1500, Slope = 0^{O}, Packaging Density = 20 and 40 pcf

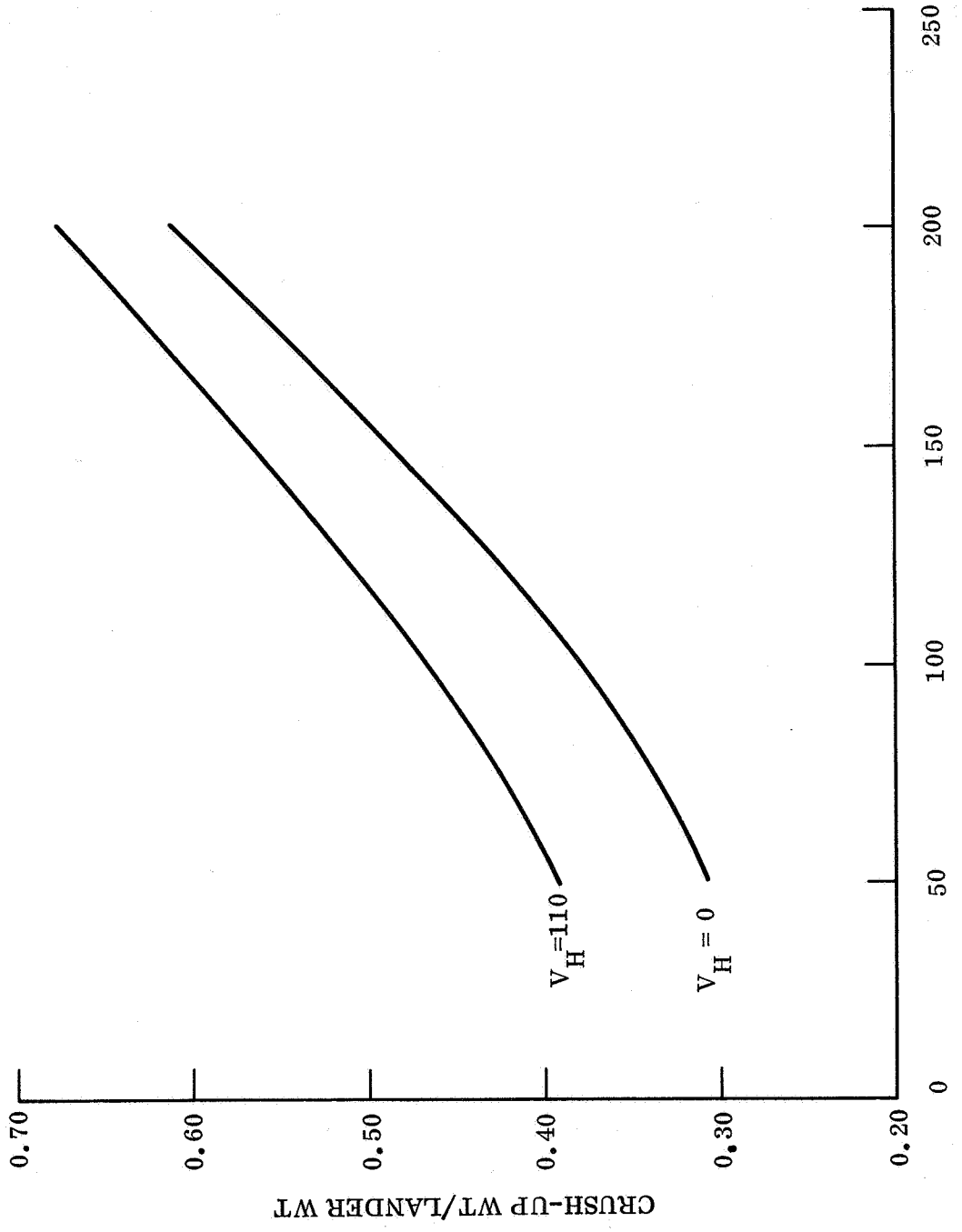

Figure 4.5.5-8. Crush-up Weight for Omni-directional Lander, Lander Wt = 300 lb, g-level = 1500, Slope = 34°, Packaging Density = 20 pcf

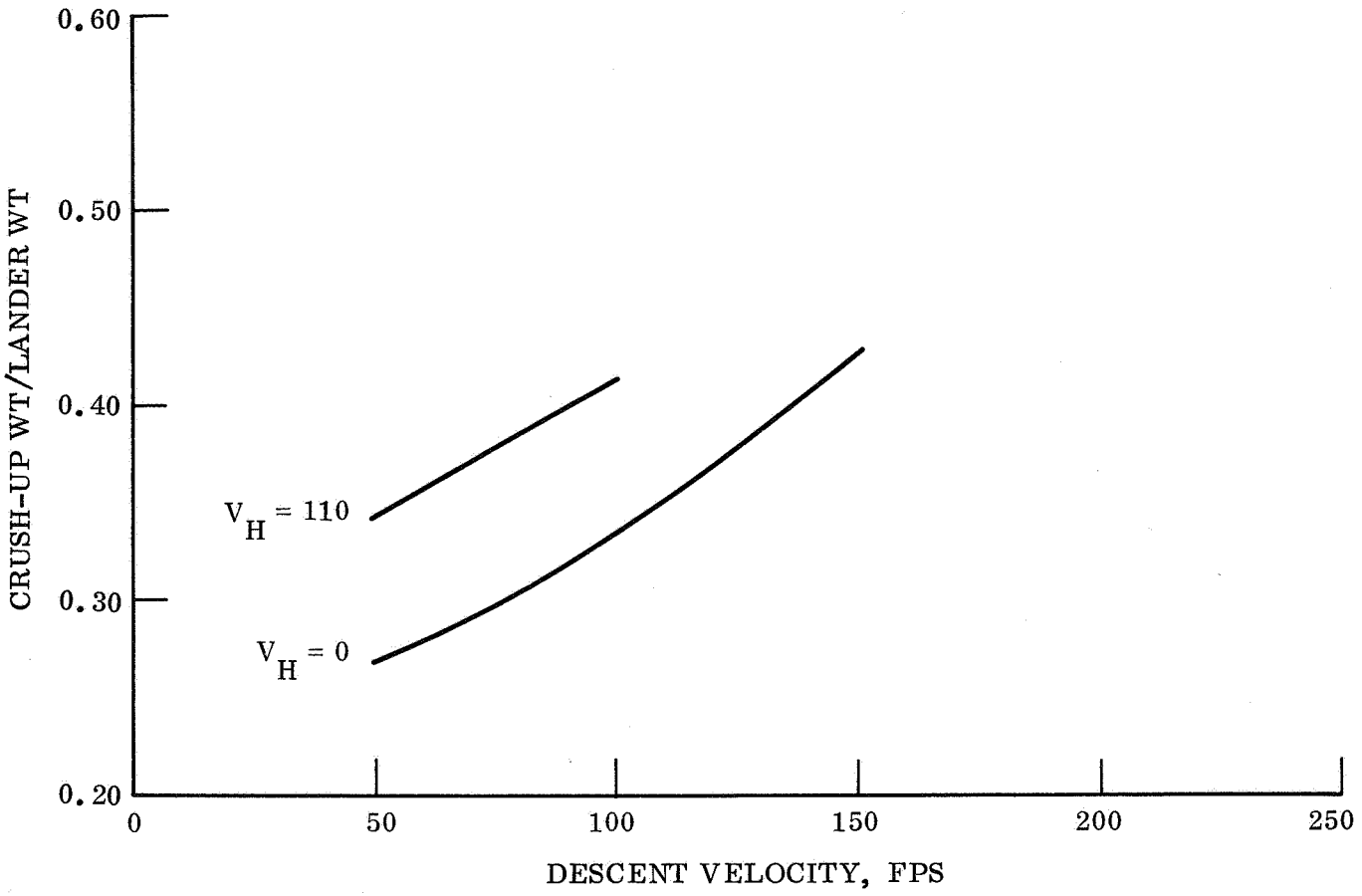

Figure 4.5.5-9. Crush-up Weight for Omni-directional Lander, Lander Wt = 300 lb, g-level = 1500, Slope = 34°, Packaging Density = 40 pcf

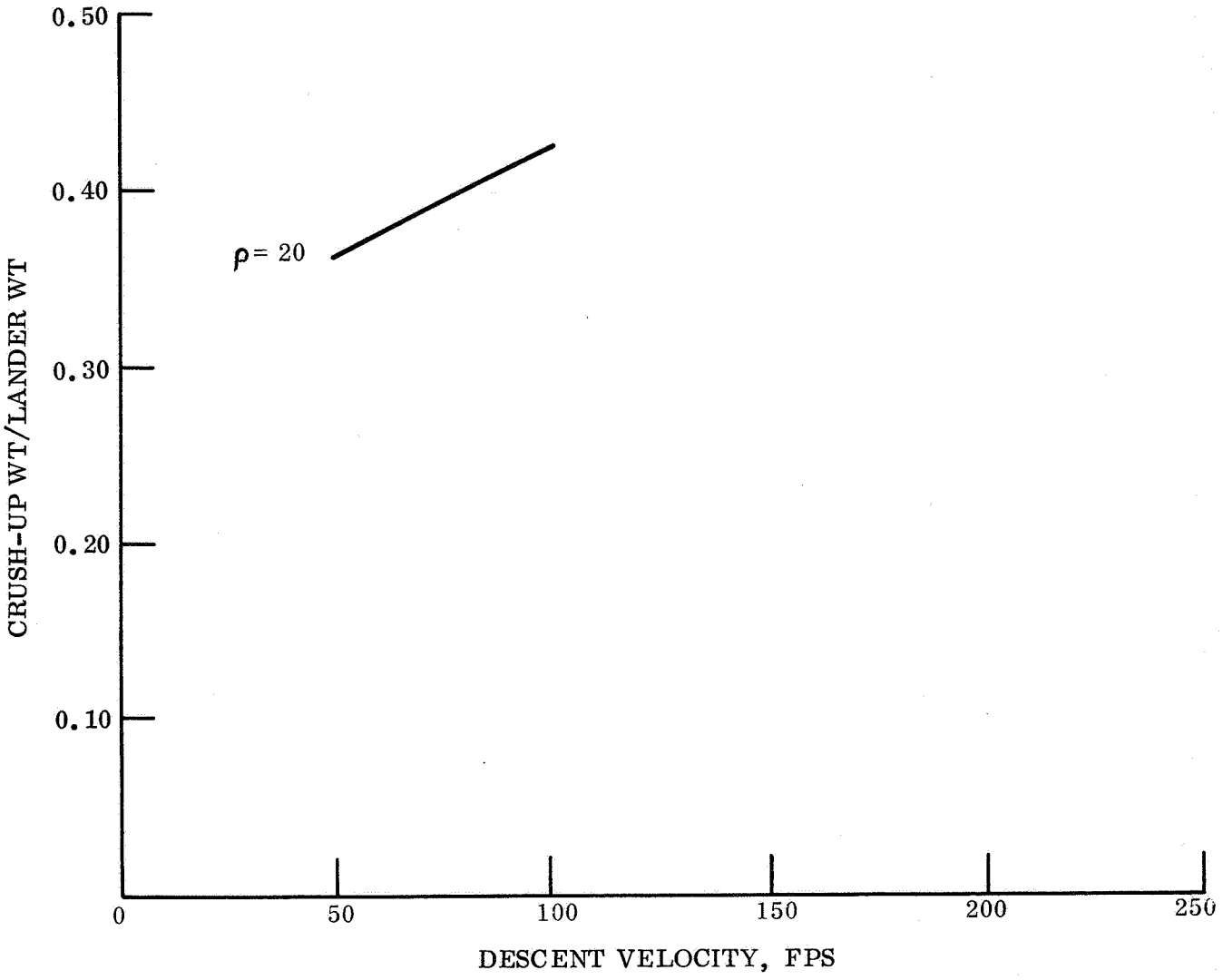

Figure 4.5.5-10. Crush-up Weight for Omni-directional Lander, Lander Wt = 300 lb, g-level = 2000, Slope = 0°, Packaging Density = 20 pcf

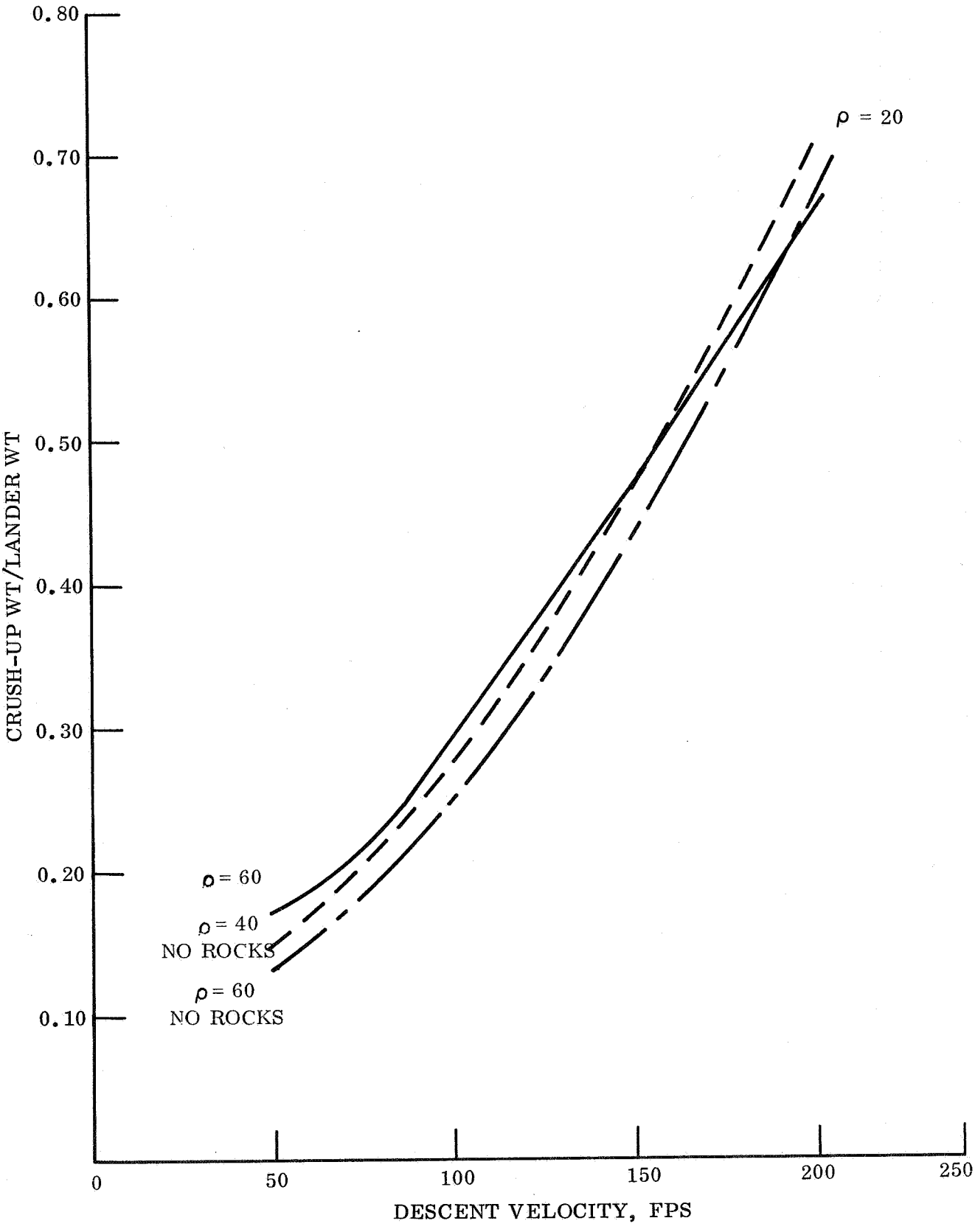

Figure 4.5.5-11. Crush-up Weight for Omni-directional Lander, Lander Wt = 400 lb, g-level = 500, Slope = 0°, Packaging Density = 40 and 60 pcf

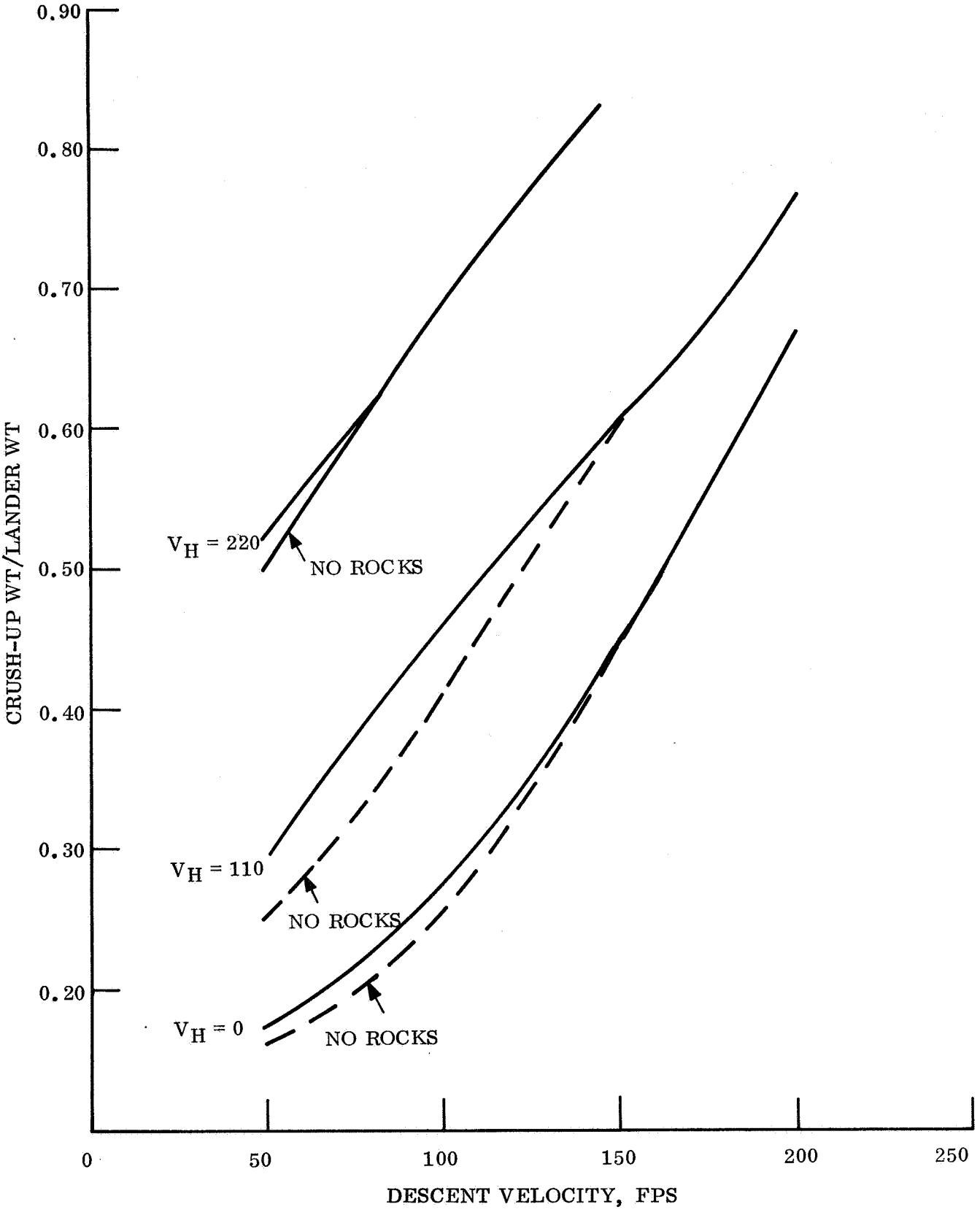

Figure 4.5.5-12. Crush-up Weight for Omni-Directional Lander, Lander Wt = 400, g-level = 500, Slope = 34°, Packaging Density = 60 pcf

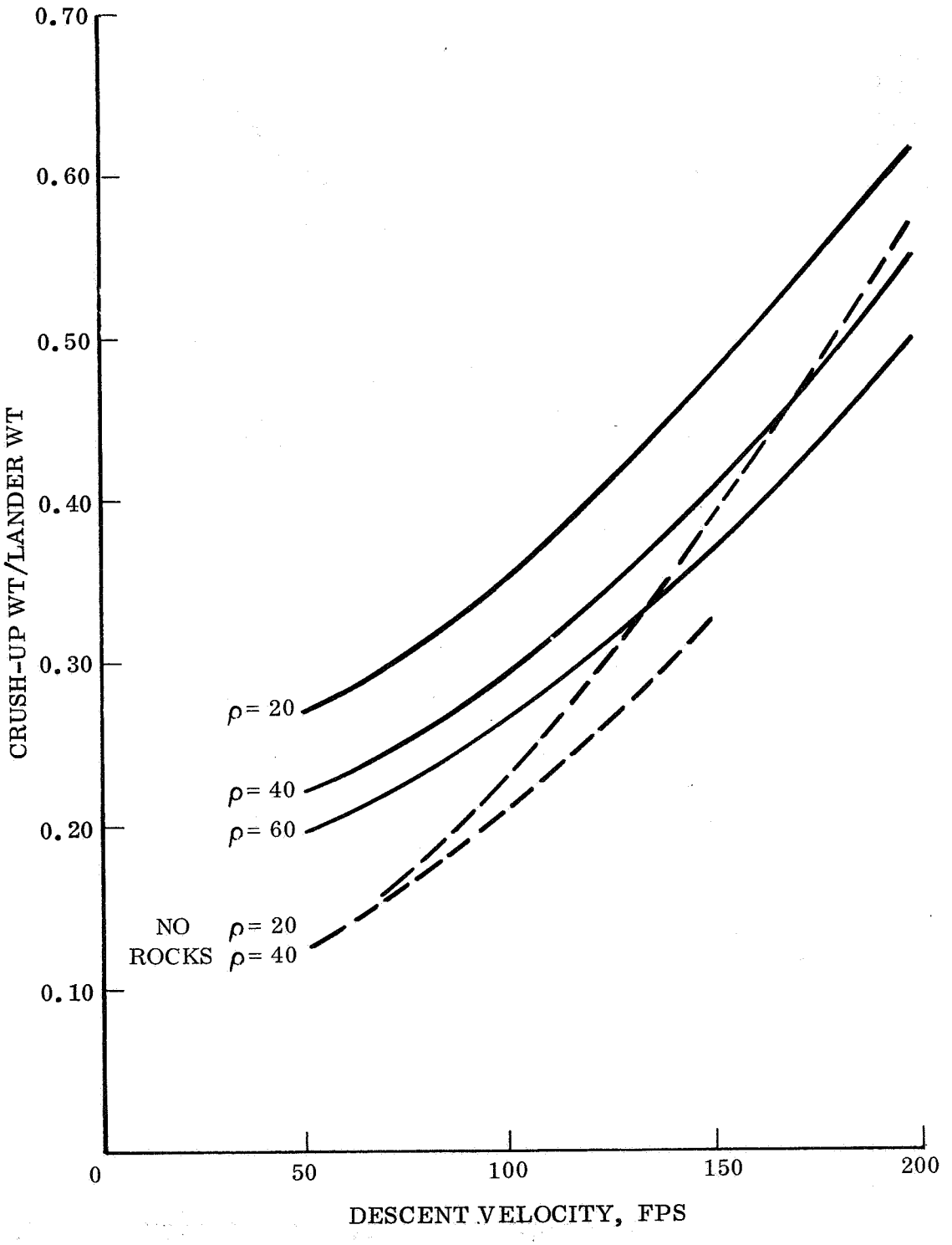

Figure 4.5.5-13. Crush-up Weight for Omni-directional Lander, Lander Wt = 400 lb, g-level = 1000, Slope = 0°, Packaging Density = 20, 40, and 60 pcf

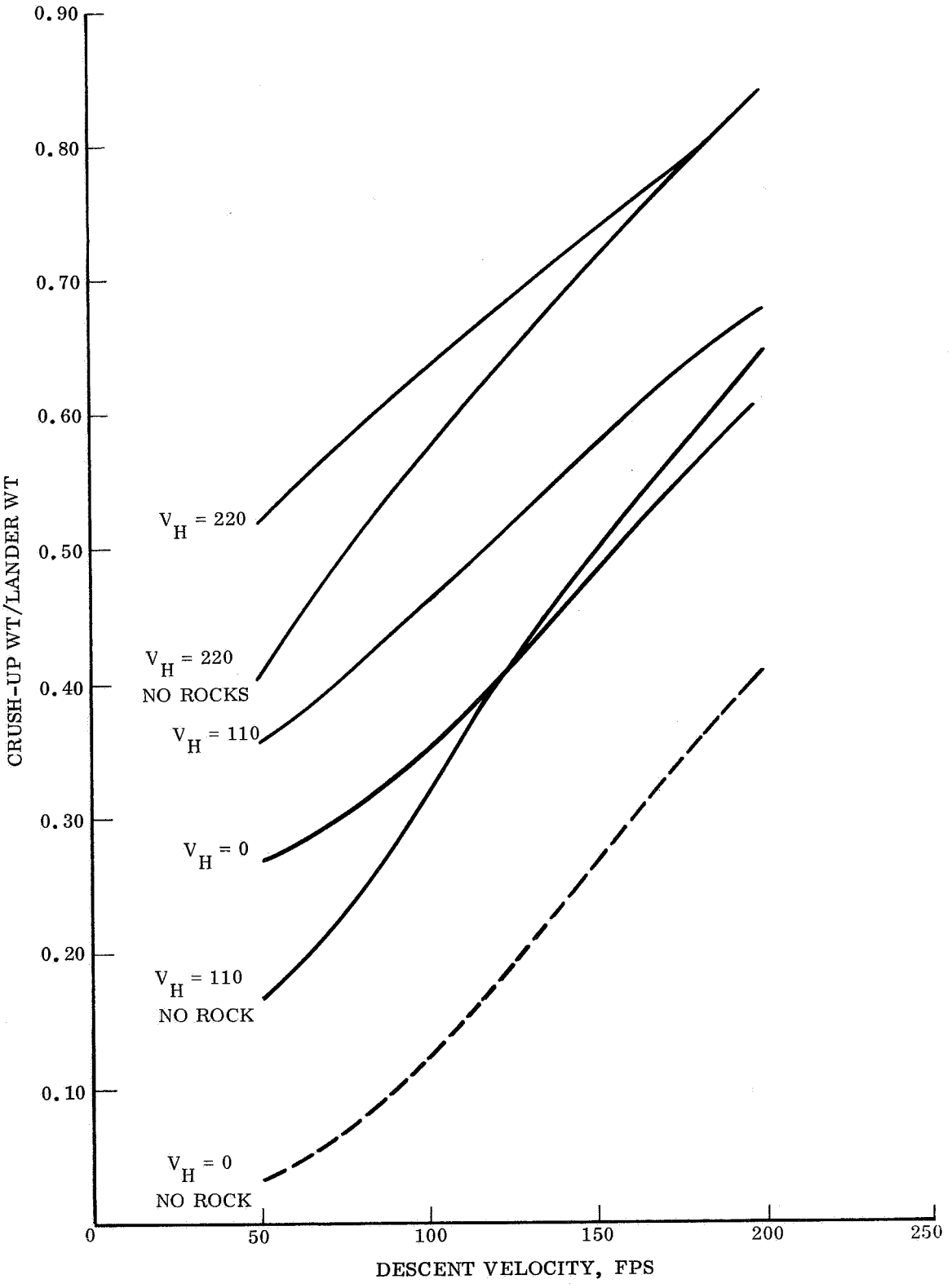

Figure 4. 5. 5-14. Crush-up Weight for Omni-directional Lander, Lander Wt = 400 lb, g-level = 1000, Slope = 34°, Packaging Density = 20 pcf

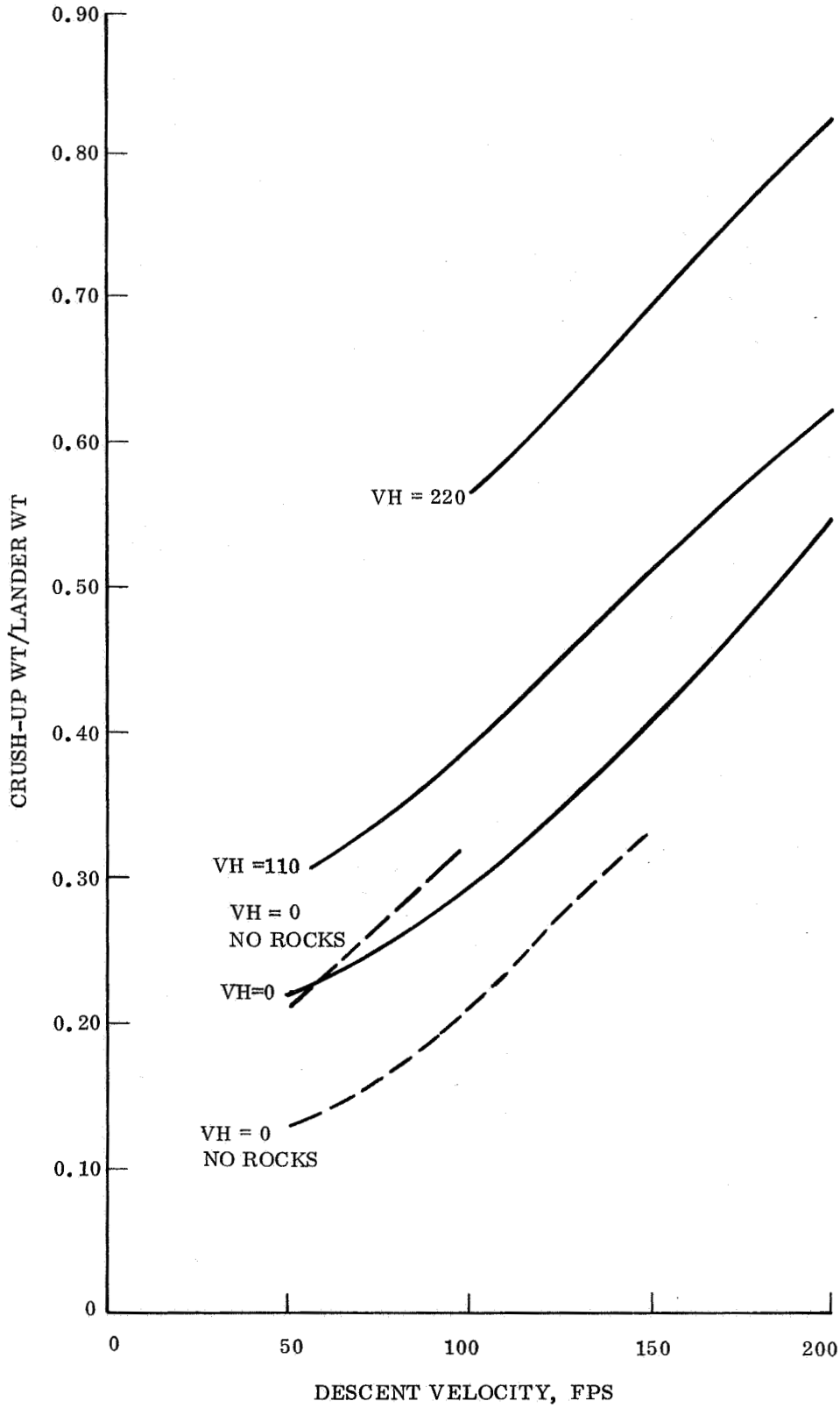

Figure 4.5.5-15. Crush-up Weight for Omni-directional Lander, Lander Wt = 400 lb, g-level = 1000, Slope = 34°, Packaging Density = 40 pcf

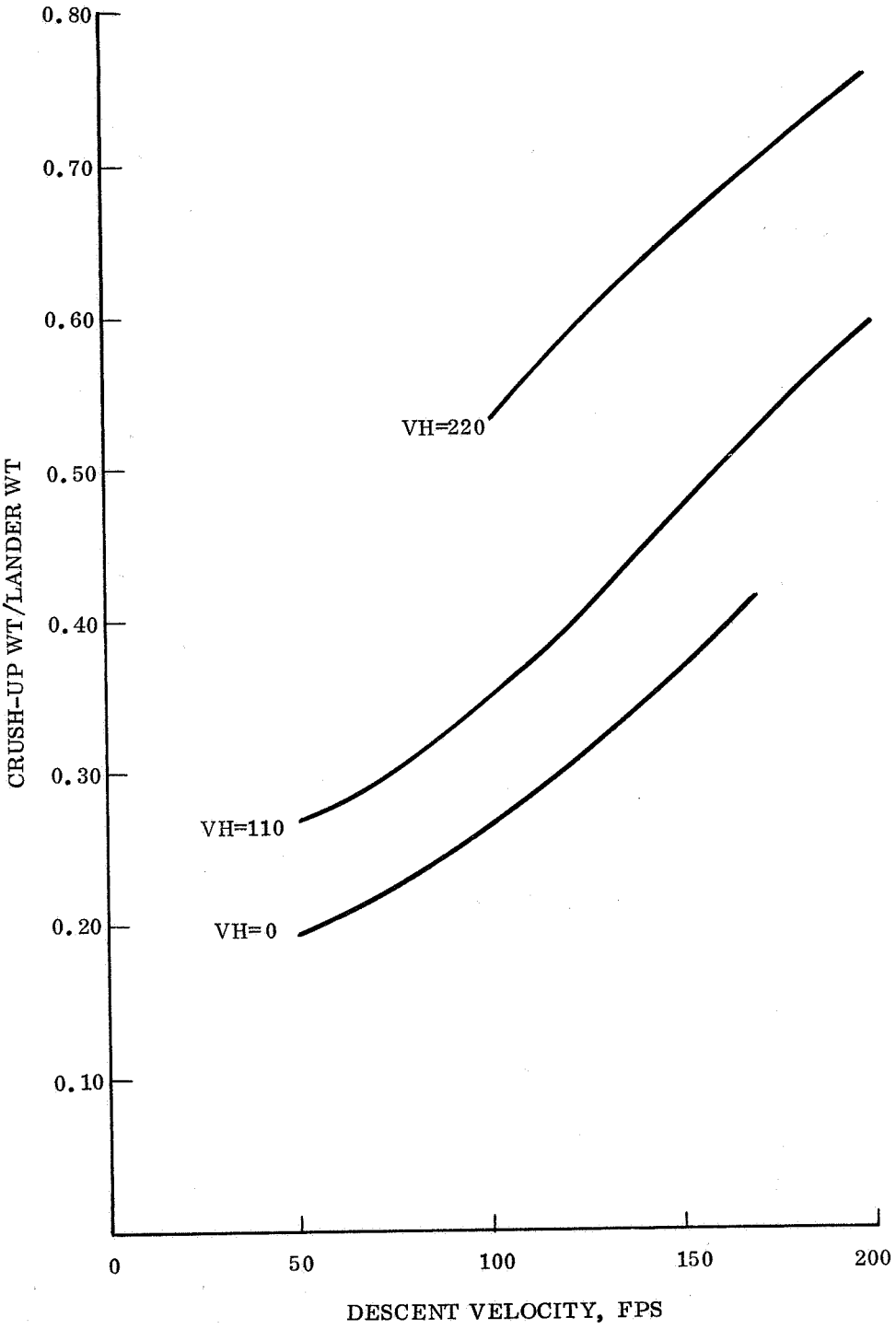

Figure 4.5.5-16. Crush-up Weight for Omni-directional Lander, Lander Wt = 400 lb, g-level = 1000, Slope = 34°, Packaging Density = 60 pcf

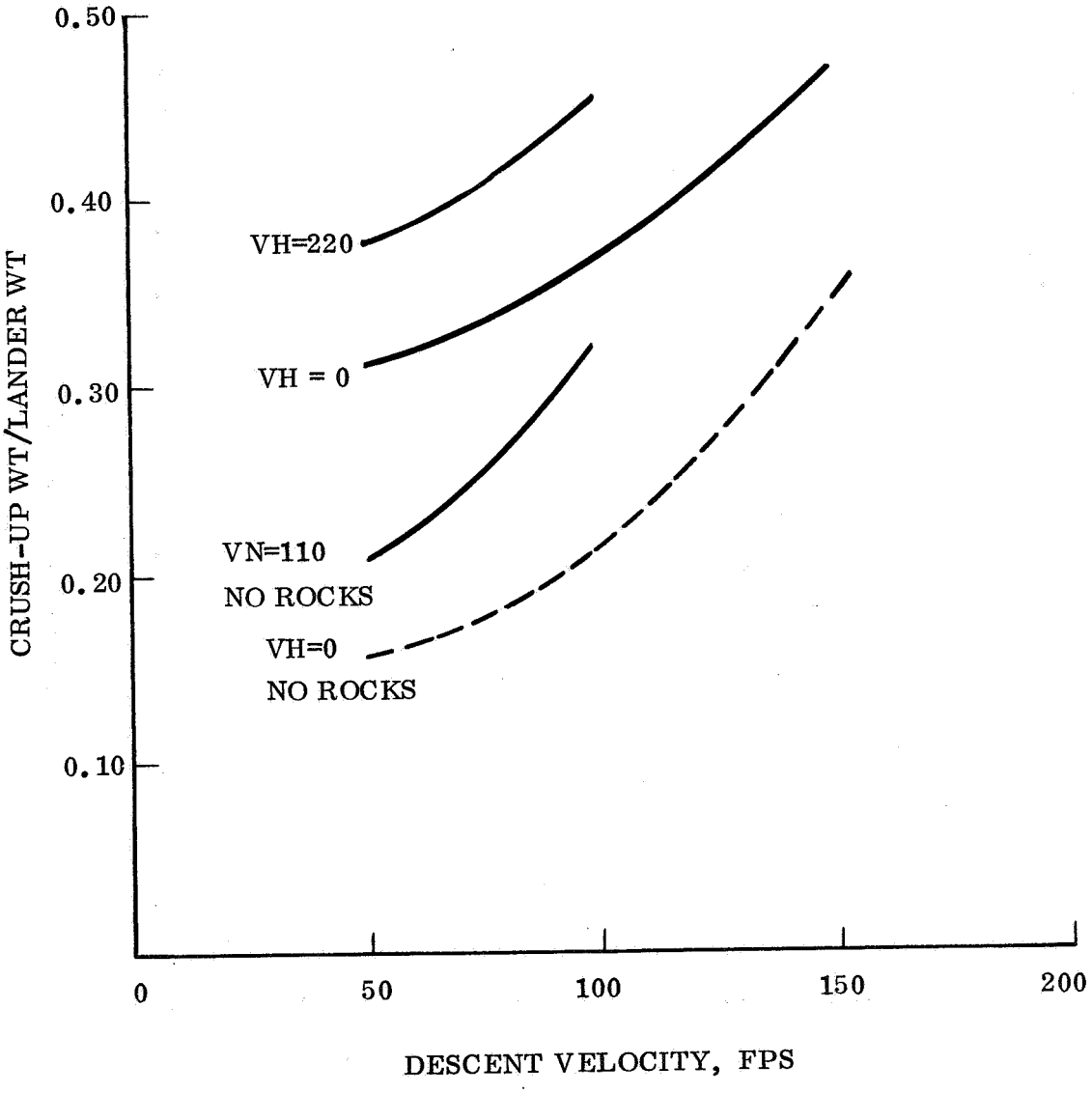

Figure 4.5.5-17. Crush-up Weight for Omni-directional Lander, Lander Wt = 400 lb, g-level = 1500, Slope = 34°, Packaging Density = 20 pcf

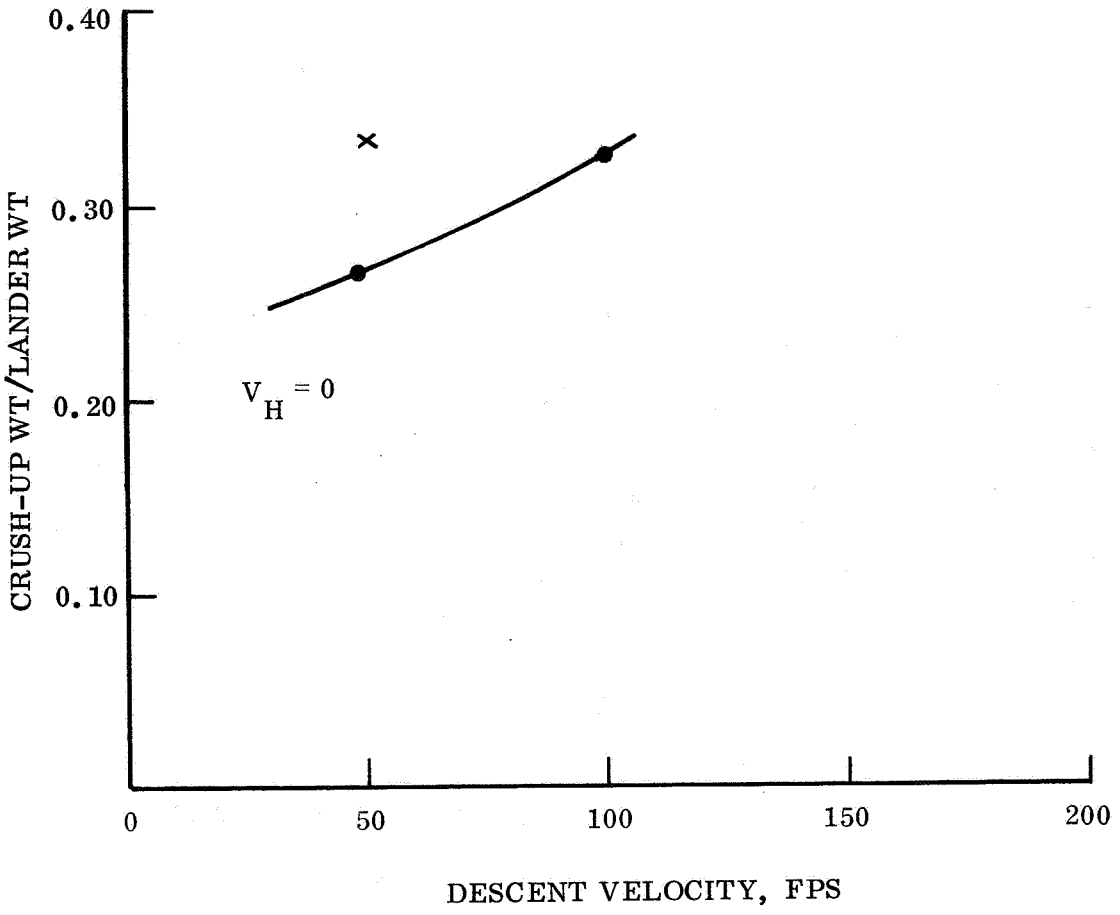

Figure 4.5.5-18. Crush-up Weight for Omni-directional Lander, Lander Wt = 400 lb, g-level = 1500, Slope = 34°, Packaging Density = 40 pcf

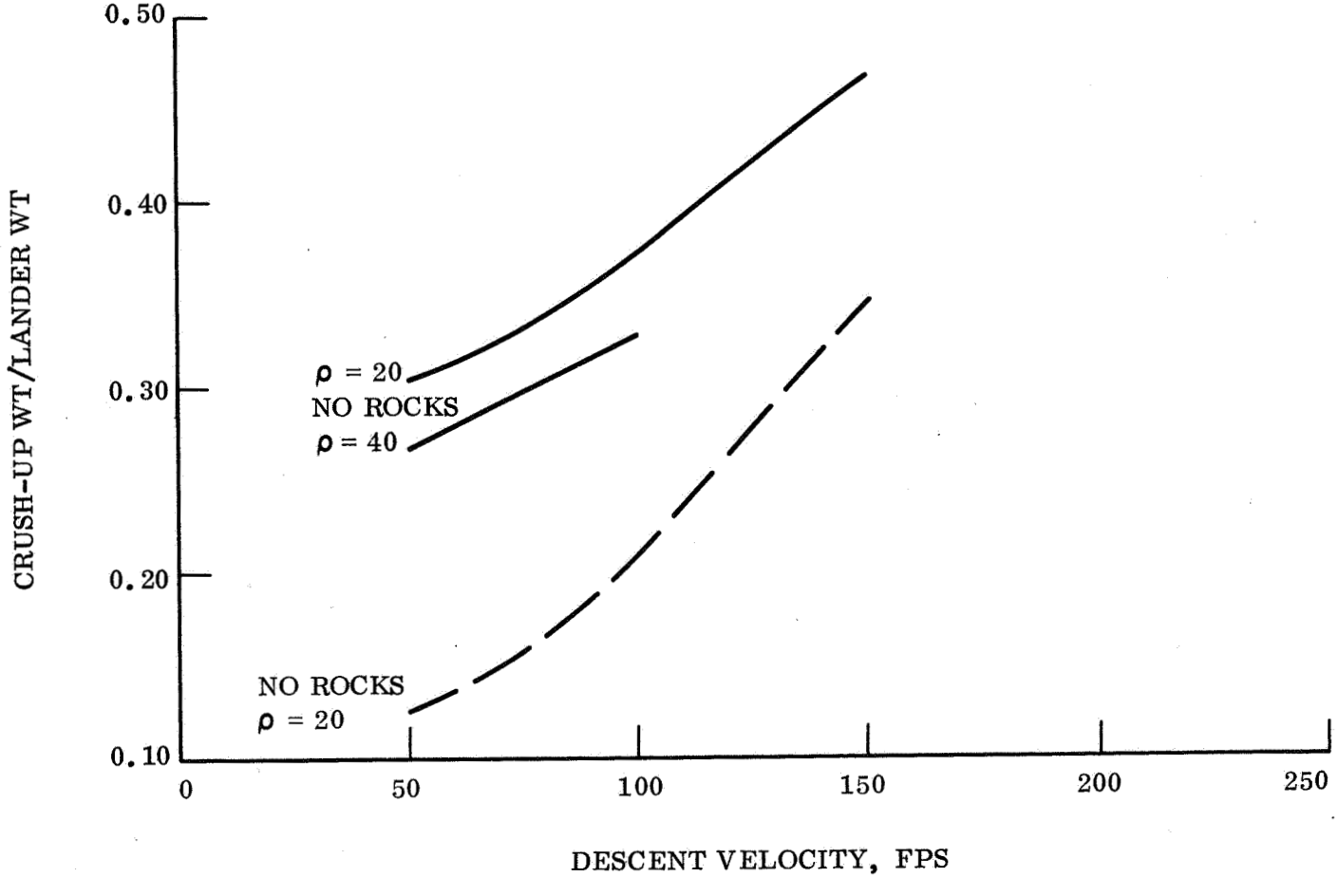

Figure 4.5.5-19. Crush-up Weight for Omni-directional Lander, Lander Wt = 400 lb, g-level = 1500, Slope = 0°, Packaging Density = 20, 40 pcf

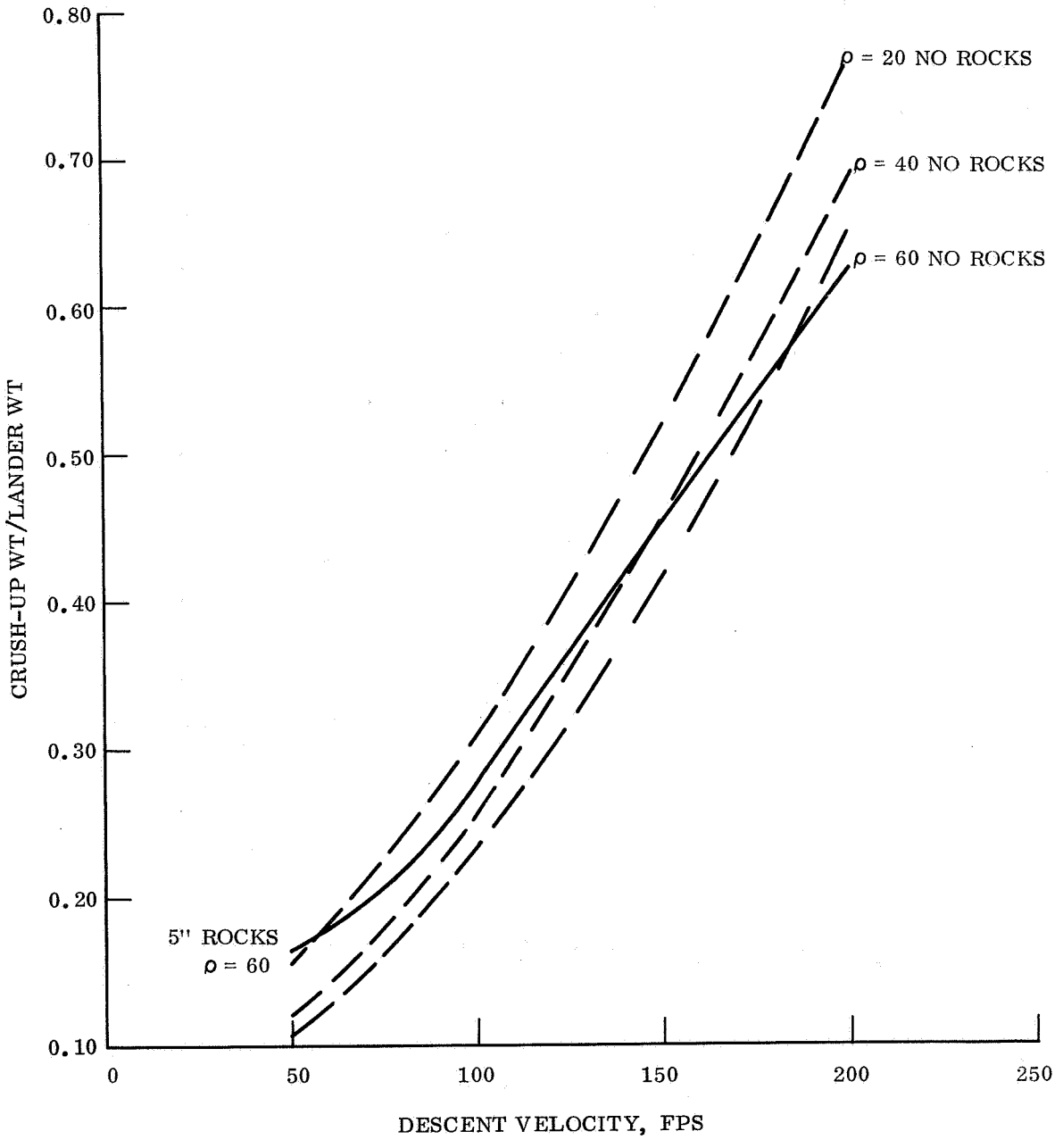

Figure 4. 5. 5-20. Crush-up Weight for Omni-directional Lander, Lander Wt = 500 lb, g-level = 500, Slope = 0°, Packaging Density = 20, 40, and 60 pcf

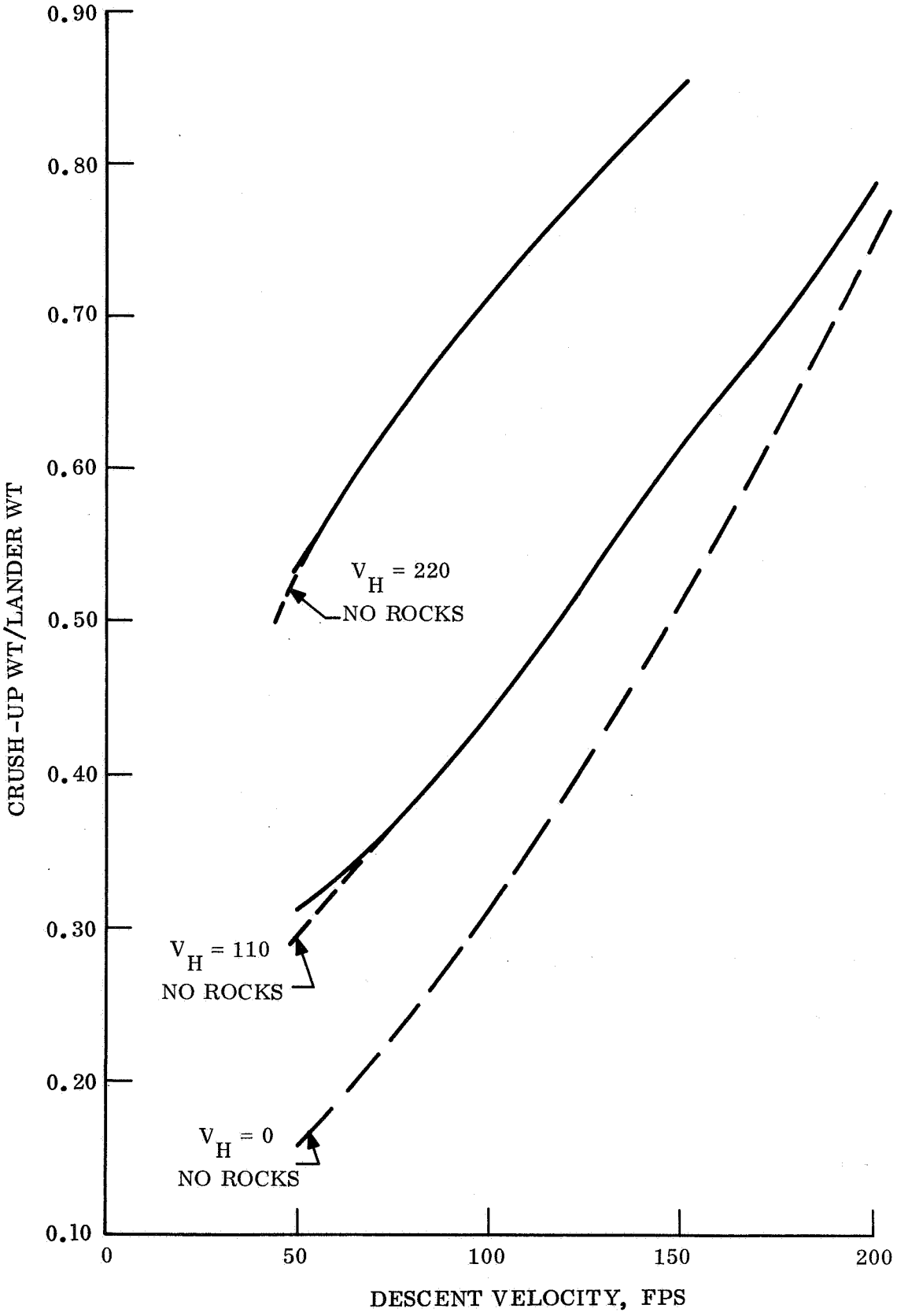

Figure 4.5.5-21. Crush-up Weight for Omni-directional Lander, Lander Wt = 500 lb, g-level = 500, Slope = 34°, Packaging Density = 40 pcf

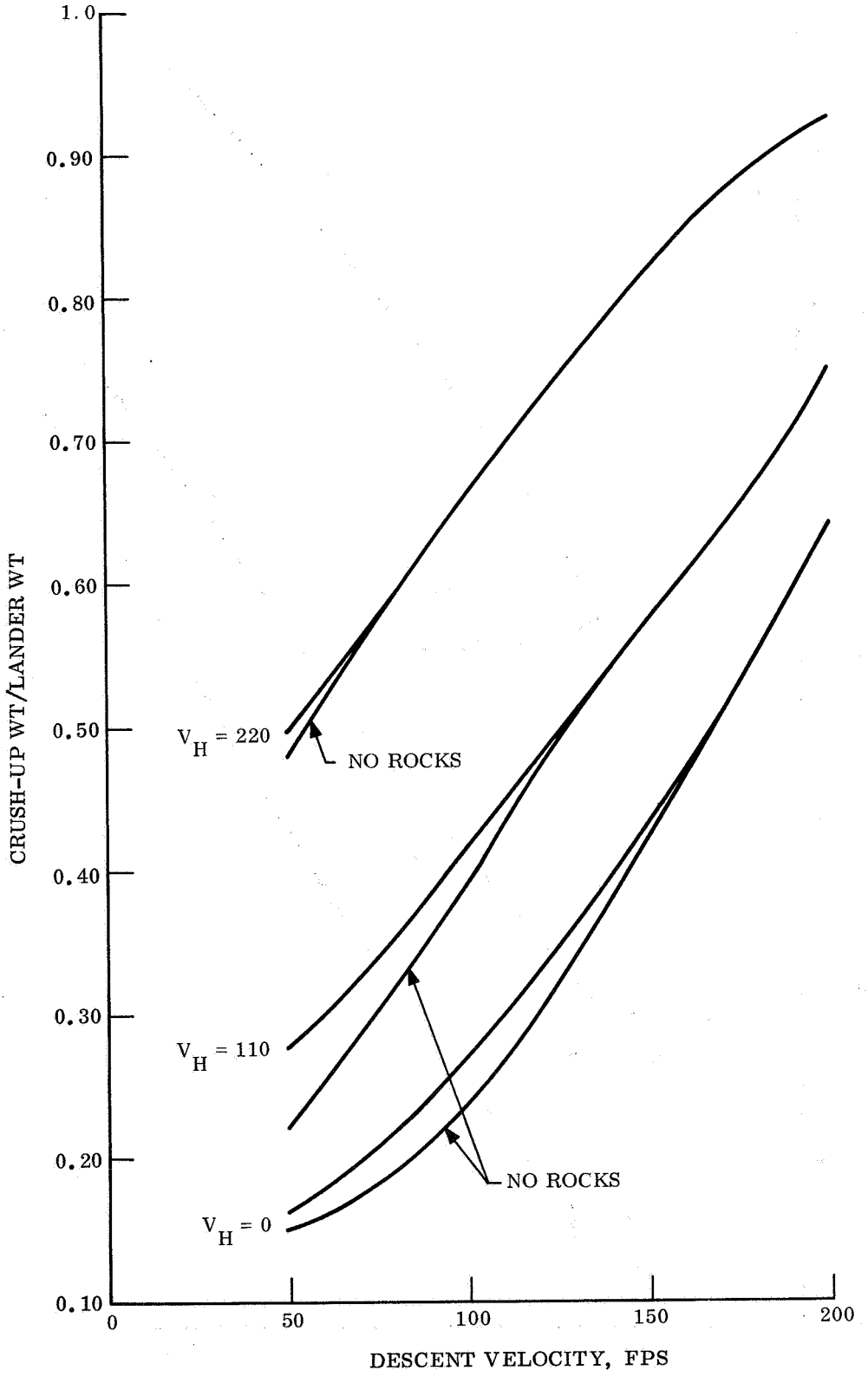

Figure 4.5.5-22. Crush-up Weight for Omni-directional Lander, Lander Wt = 500 lb, g-level = 500, Slope = 34°, Packaging Density = 60 pcf

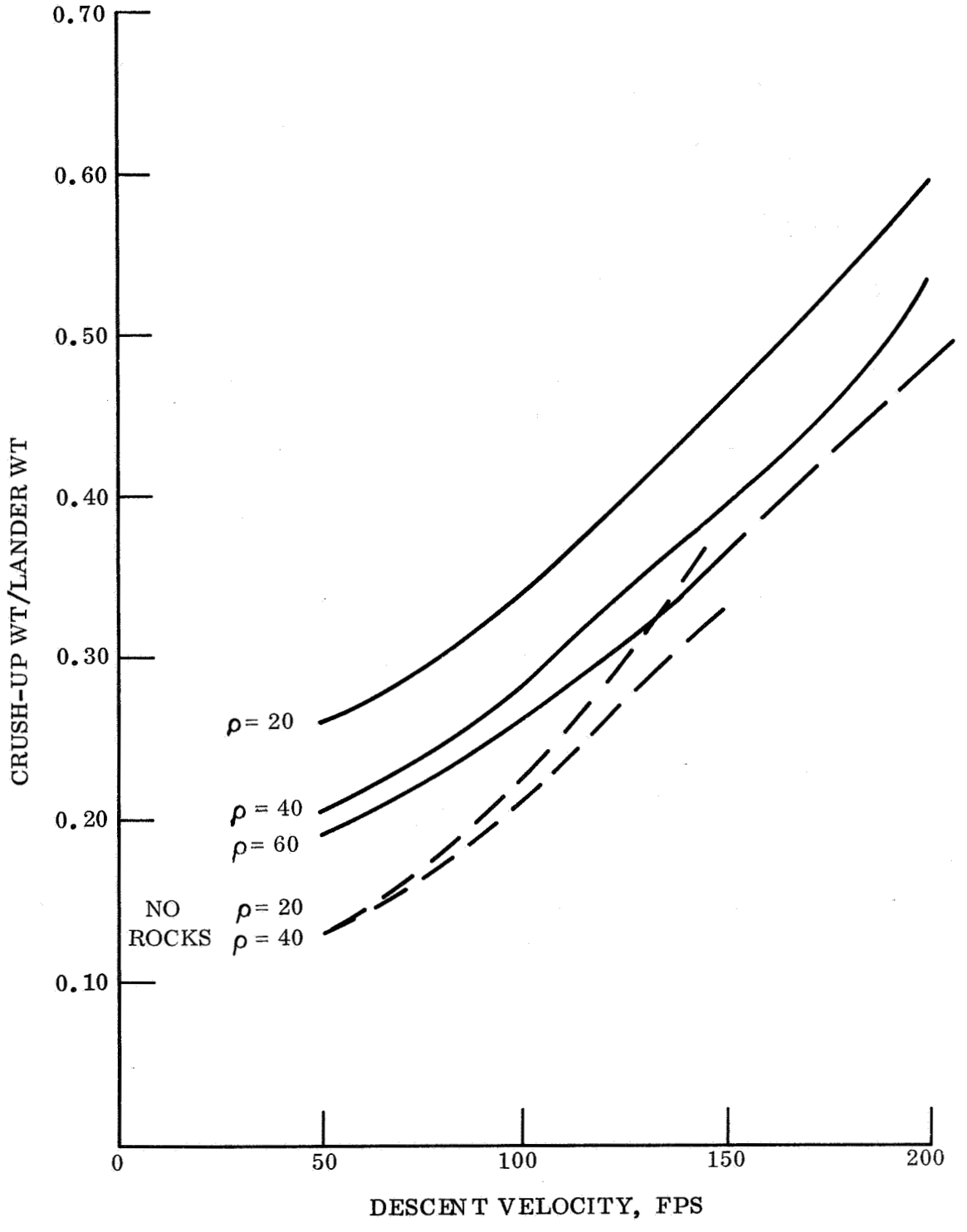

Figure 4.5.5-23. Crush-up Weight for Omni-directional Lander, Lander Wt = 500 lb, g-level = 1000, Slope = 0°, Packing Density = 20, 40, and 60 pcf

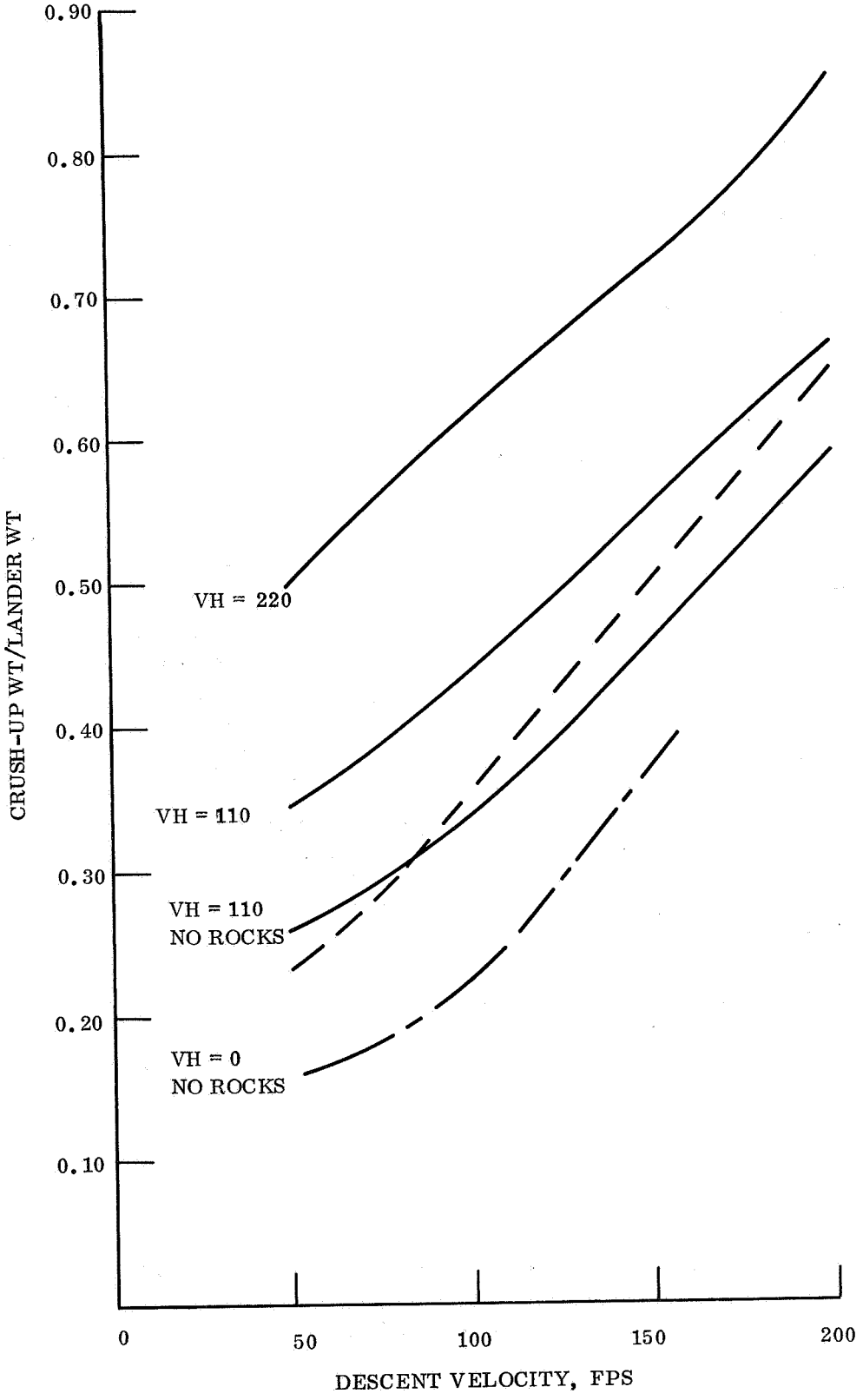

Figure 4.5.5-24. Crush-up Weight for Omni-directional Lander, Lander Wt = 500 lb, g-level = 1000, Slope = 34°, Packaging Density = 20 pcf

III

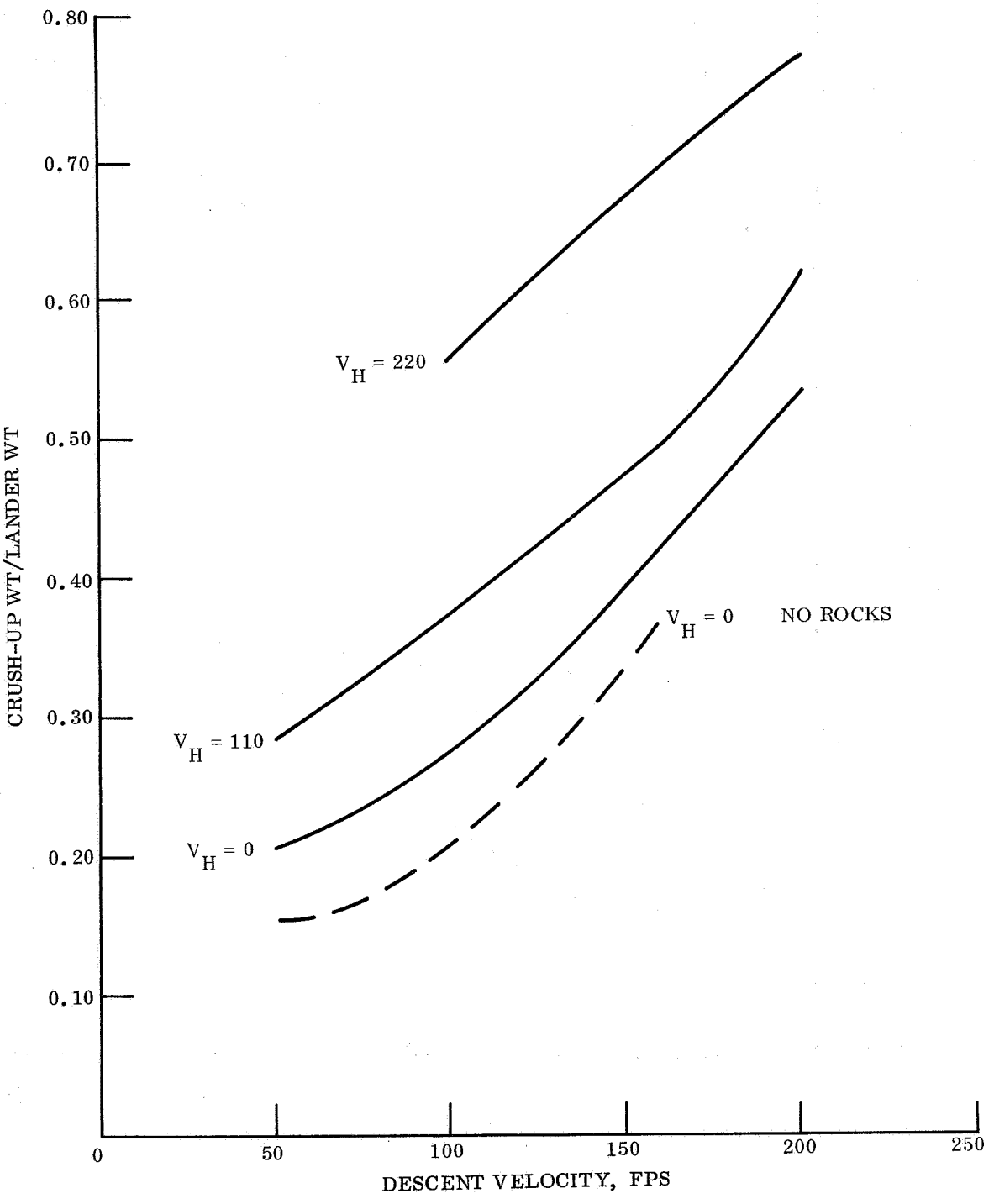

Figure 4.5.5-25. Crush-up Weight for Omni-directional Lander, Lander Wt = 500 lb, g-level = 1000, Slope = 34°, Packaging Density = 40 pcf

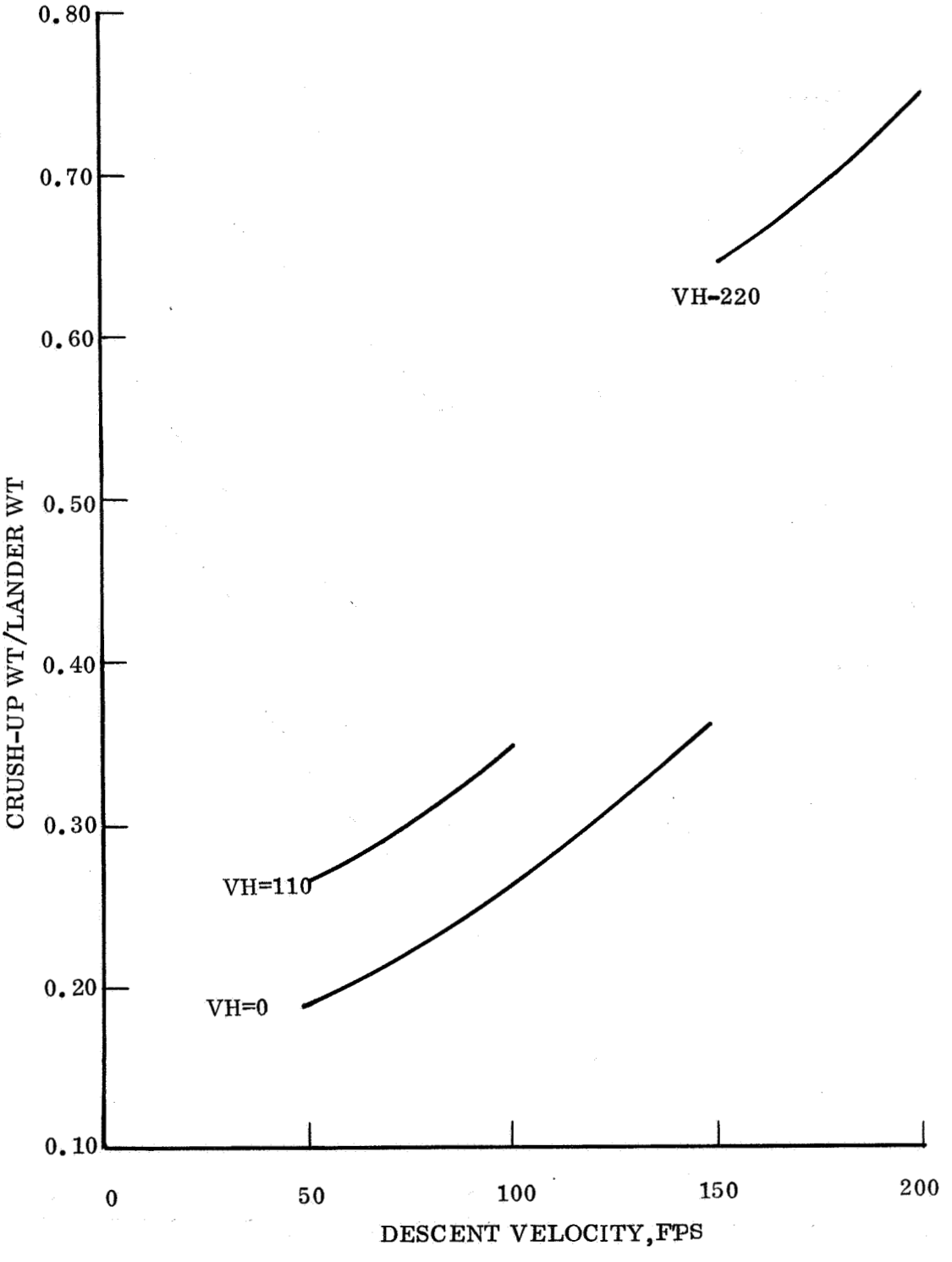

Figure 4.5.5-26. Crush-up Weight for Omni-directional Lander, Lander Wt = 500 lb, g-level = 1000, Slope = 34°, Packaging Density = 60 pcf

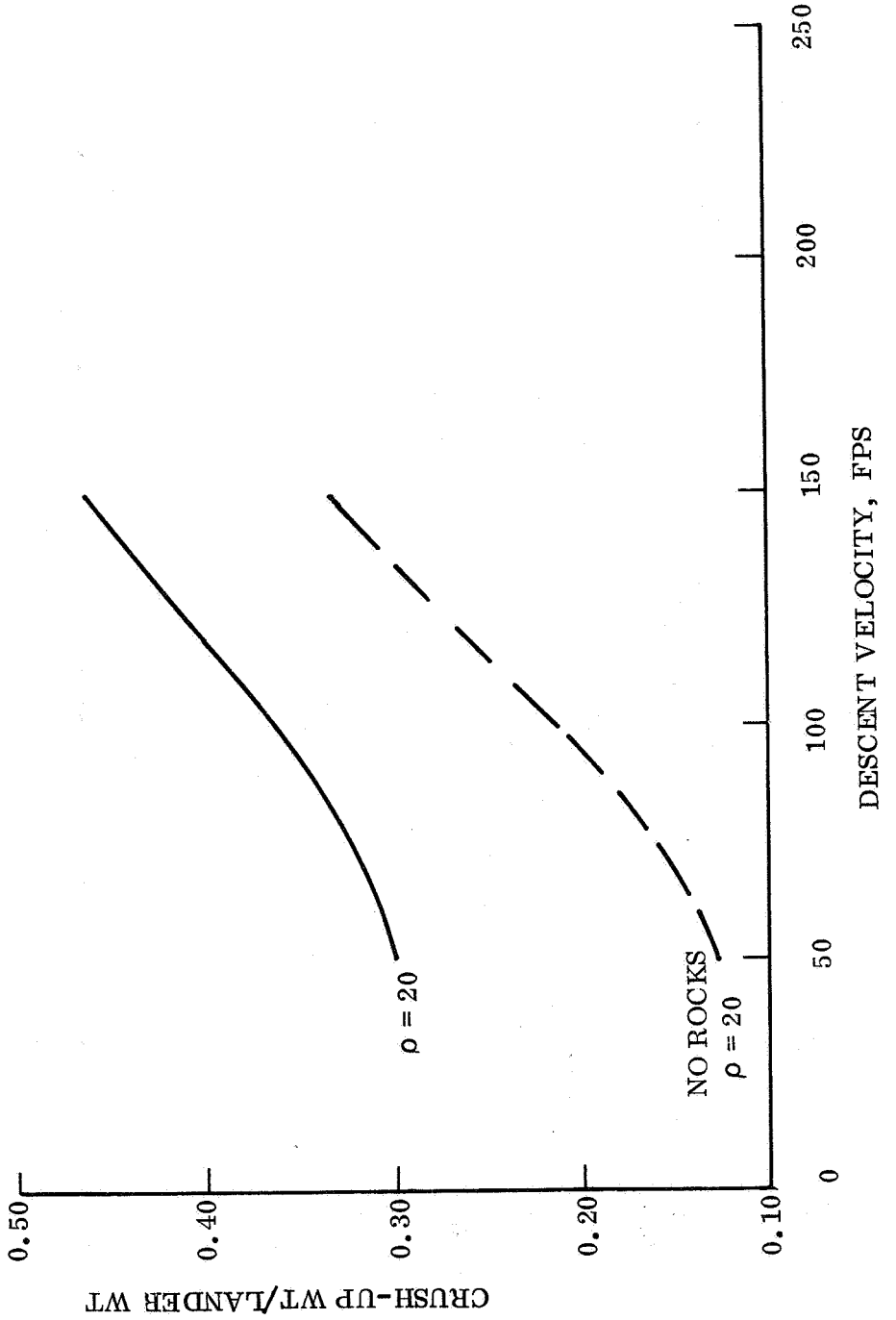

Figure 4.5.5-27. Crush-up Weight for Omni-directional Lander, Lander Wt = 500 lb, g-level = 1500, Slope = 0°, Packaging Density = 20 pcf

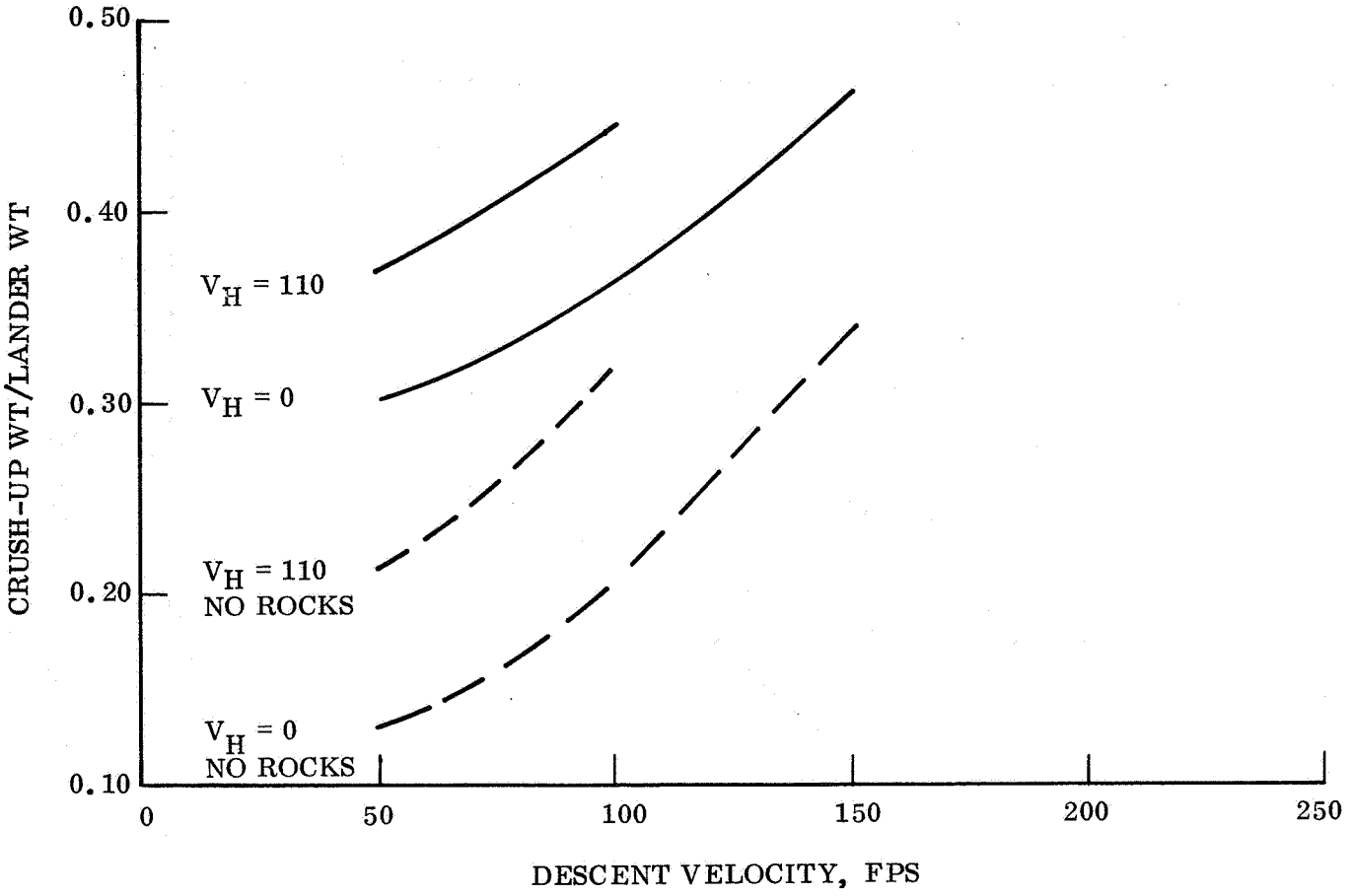

Figure 4.5.5-28. Crush-up Weight for Omni-directional Lander, Lander Wt = 500 lb, g-level = 1500, Slope = 34°, Packaging Density = 20 pcf

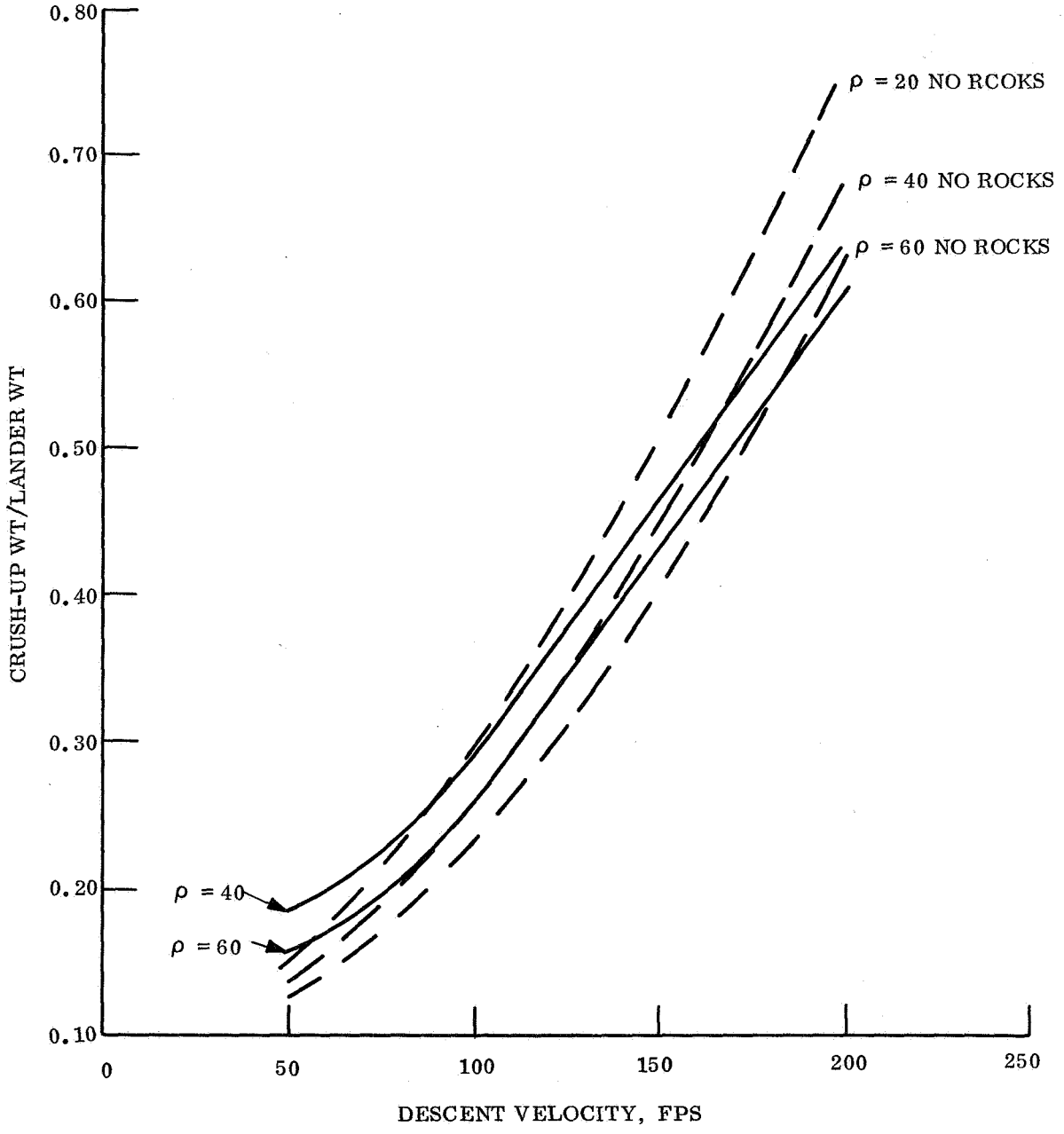

Figure 4.5.5-29. Crush-up Weight for Omni-directional Lander, Lander Wt = 600 lb, g-level = 500, Slope = 0°, Packaging Density, 20, 40 and 60 pcf

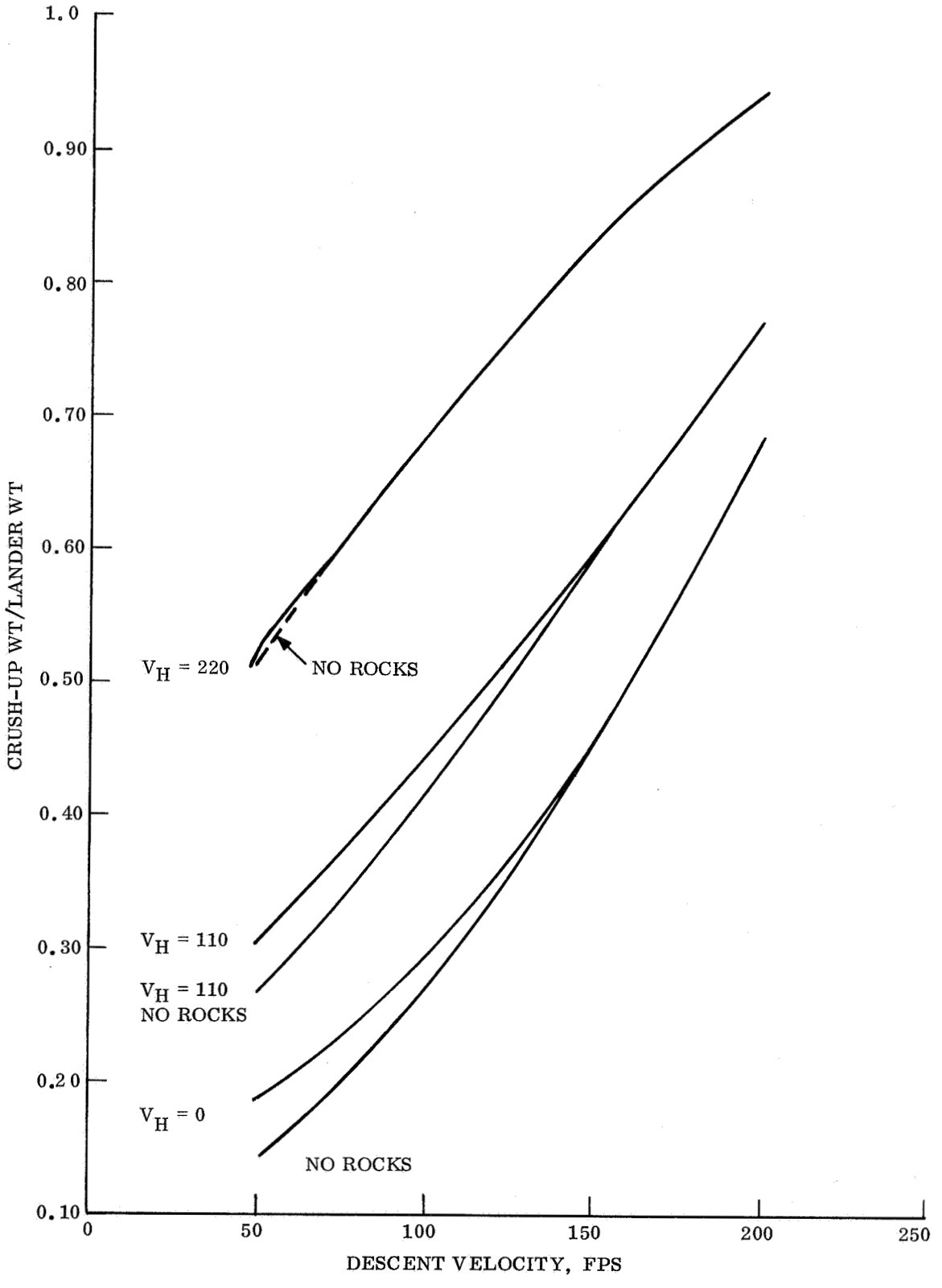

Figure 4.5.5-30. Crush-up Weight for Omni-directional Lander, Lander Wt = 600 lb, g-level = 500, Slope = 34°, Packaging Density = 40 pcf

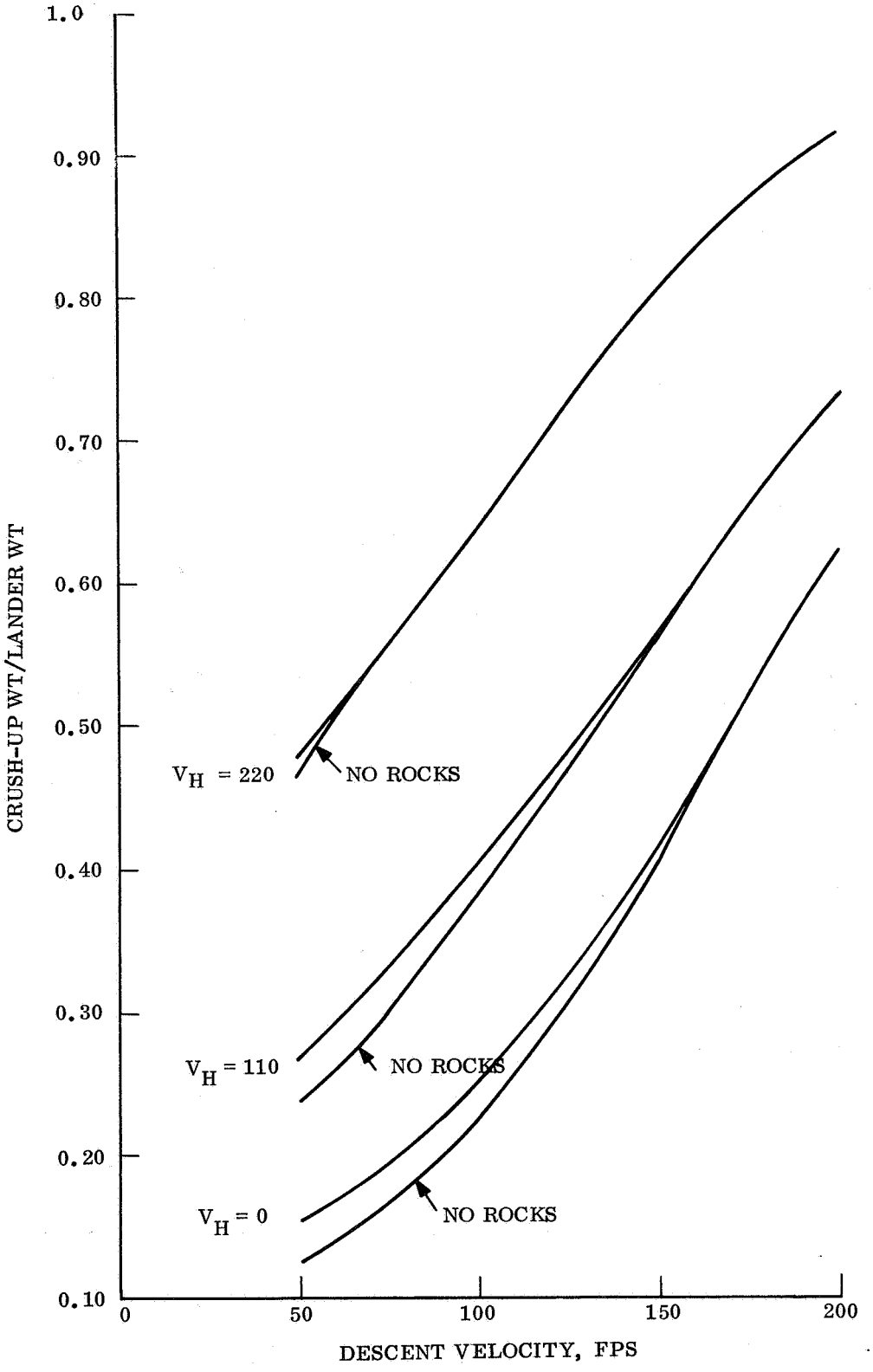

Figure 4.5.5-31. Crush-up Weight for Omni-directional Lander, Lander Wt = 600 lb, g-level = 500 lb, Slope = 34°, Packaging Density = 60 pcf

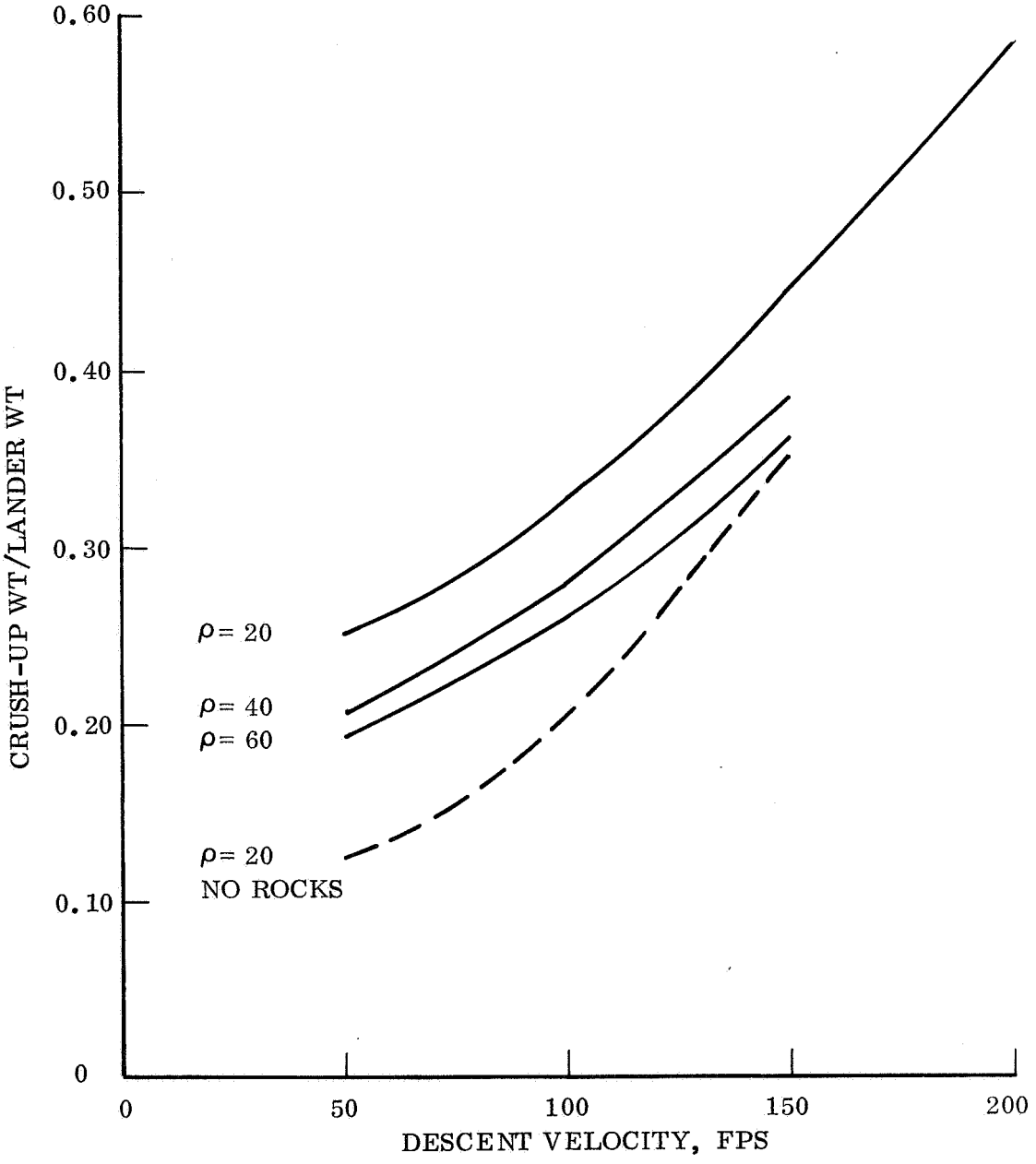

Figure 4.5.5-32. Crush-up Weight for Omni-directional Lander, Lander Wt = 600 lb, g-level = 1000, Slope = 0°, Packaging Density = 20, 40, and 60 pcf

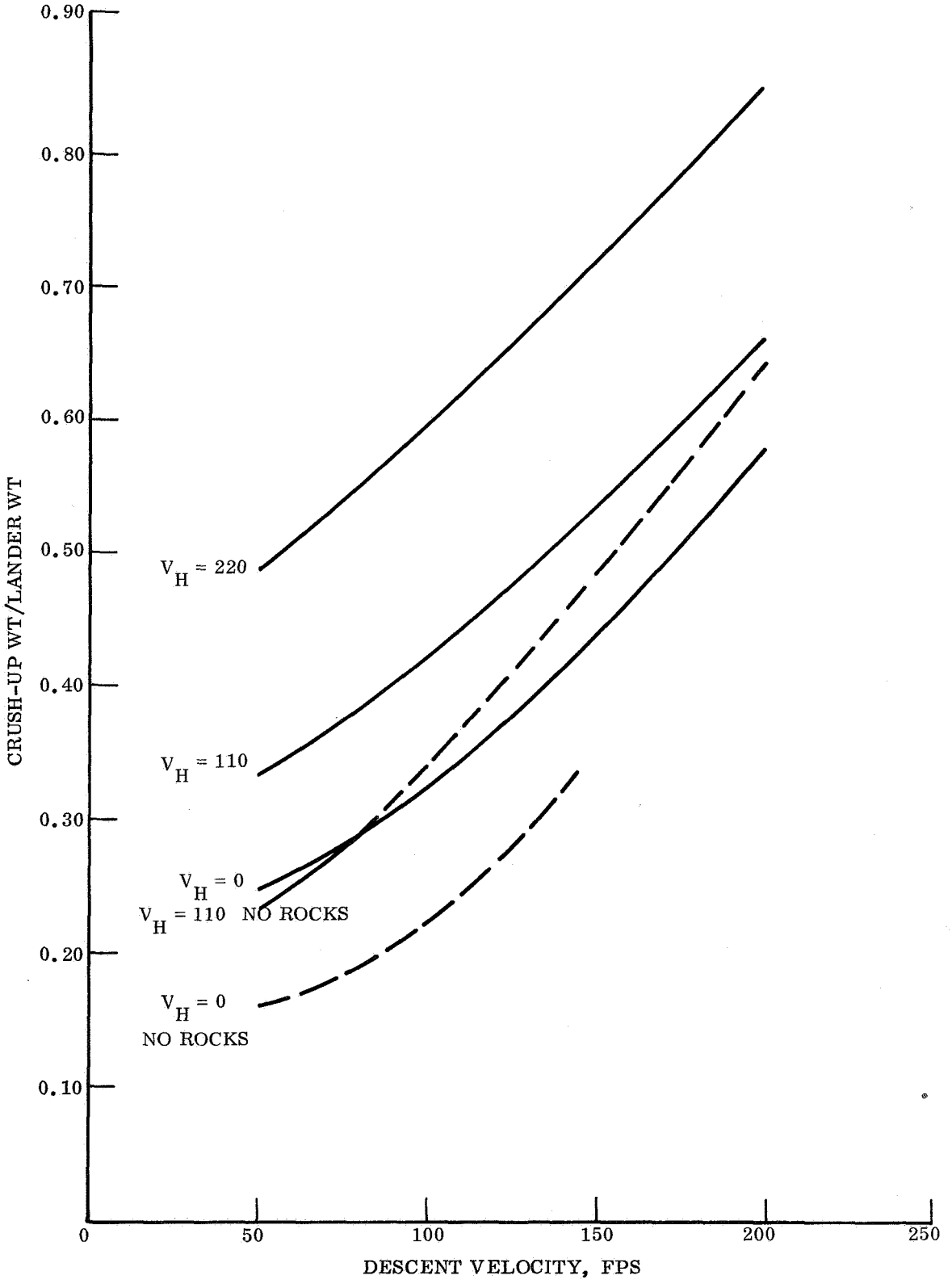

Figure 4. 5. 5-33. Crush-up Weight for Omni-directional Lander, Lander Wt = 600 lb, g-level = 1000, Slope = 34°, Packaging Density = 20 pcf

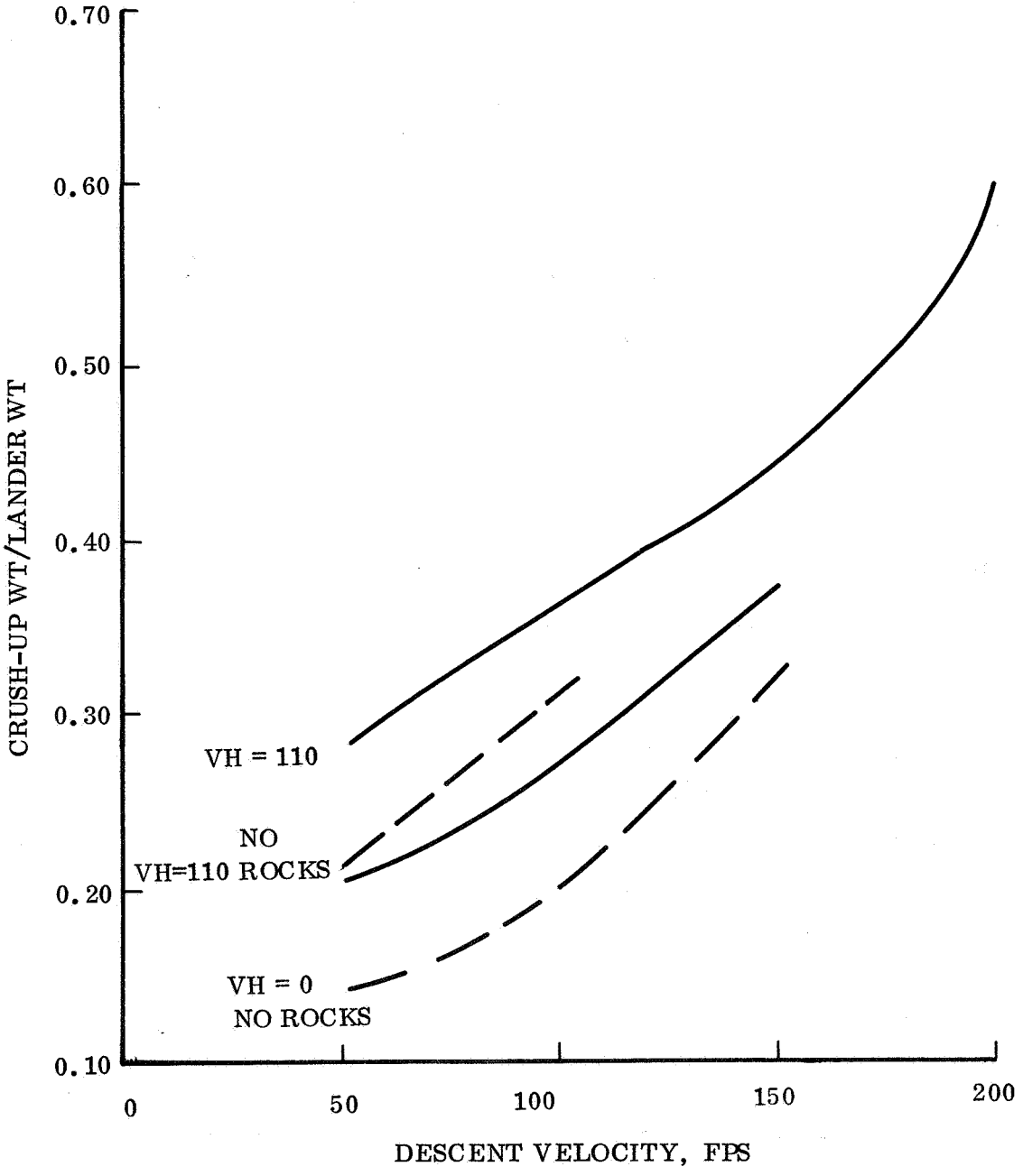

Figure 4.5.5-34. Crush-up Weight for Omni-directional Lander, Lander Wt = 600 lb, g-level = 1000, Slope = 34°, Packaging Density = 40 pcf

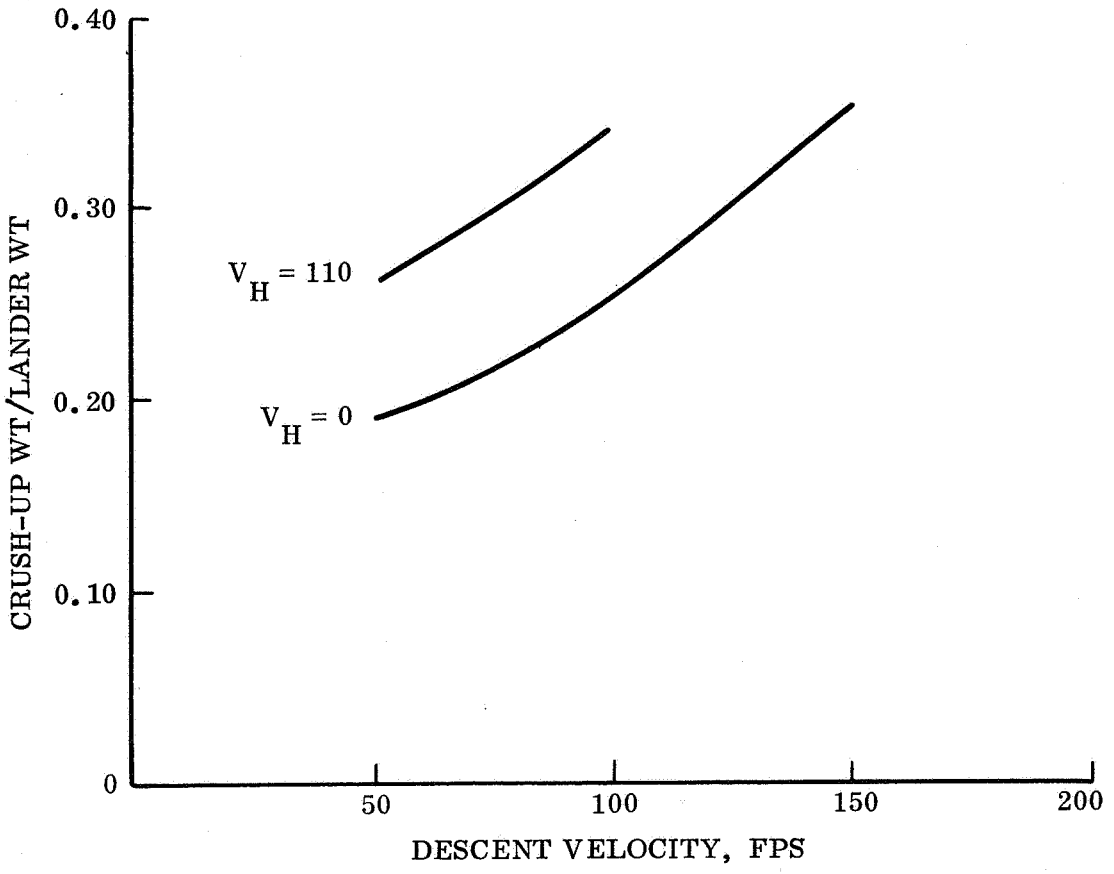

Figure 4.5.5-35. Crush-up Weight for Omni-directional Lander, Lander Wt = 600 lb, g-level = 1000, Slope = 34°, Packaging Density = 60 pcf

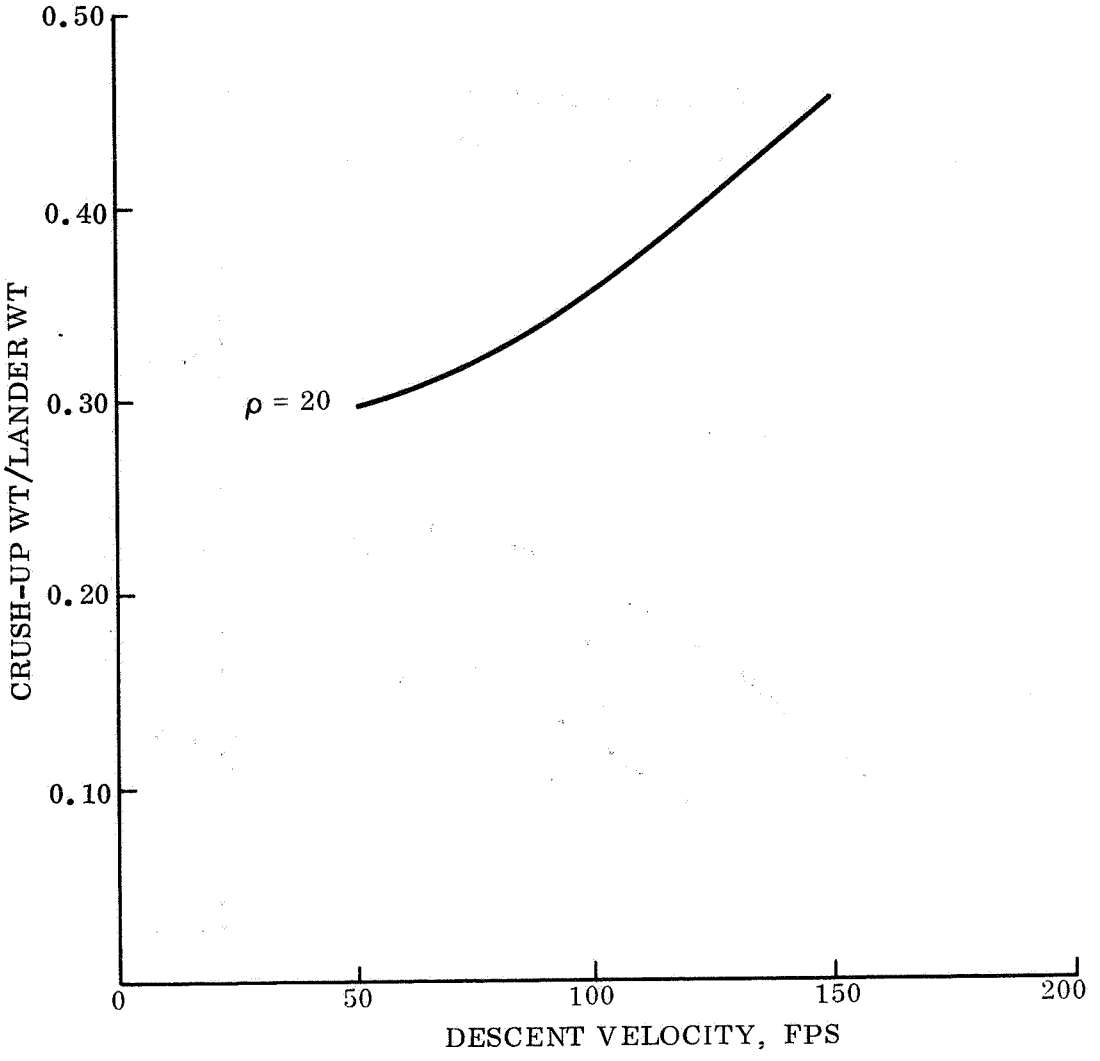

Figure 4.5.5-36. Crush-up Weight for Omni-directional Lander, Lander Wt = 600 lb, g-level = 1500, Slope = 0°, Packaging Density = 20 pcf

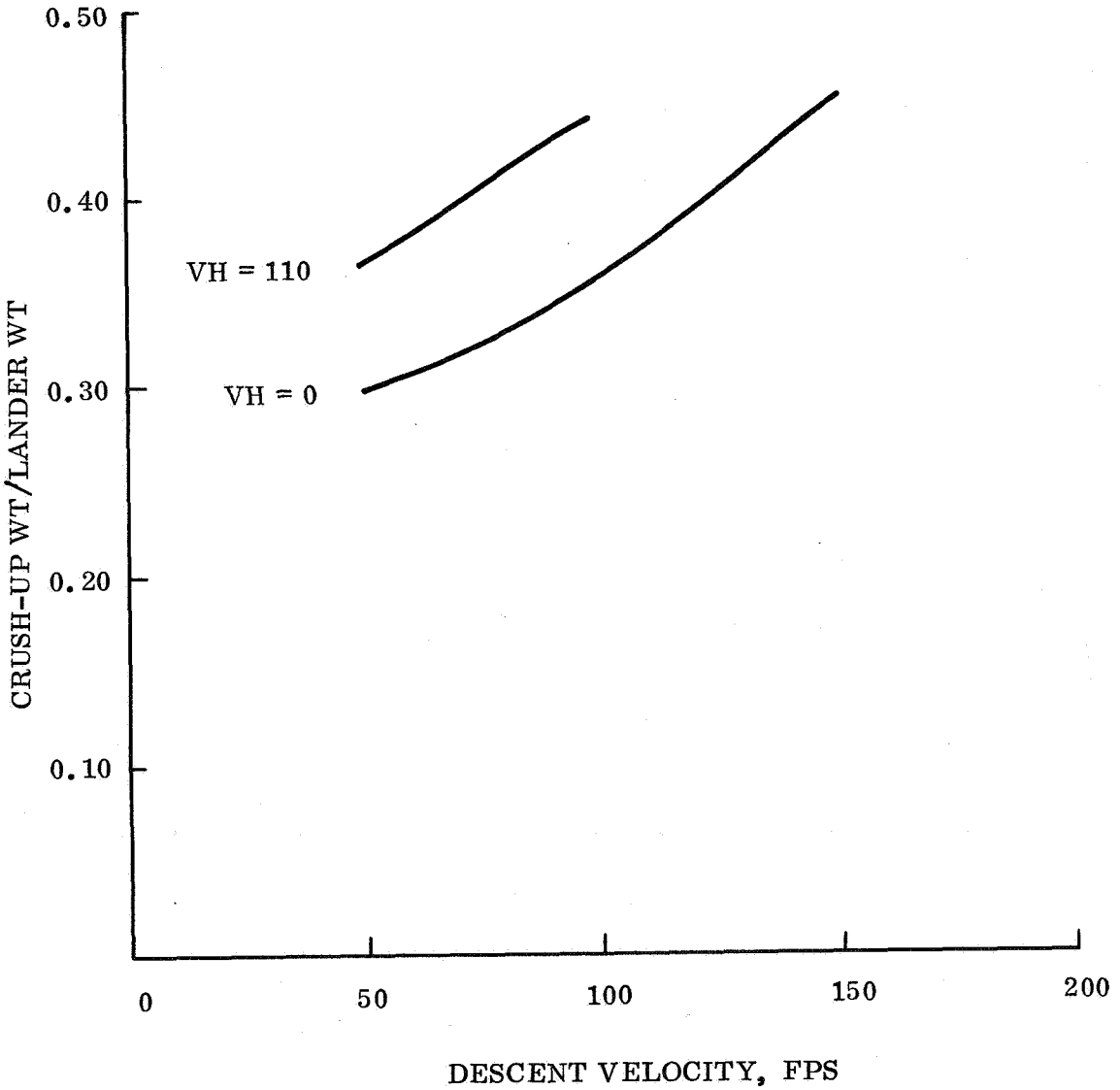

Figure 4.5.5-37. Crush-up Weight for Omni-directional Lander, Lander Wt = 600 lb, g-level = 1500, Slope = 34°, Packaging Density = 20 pcf

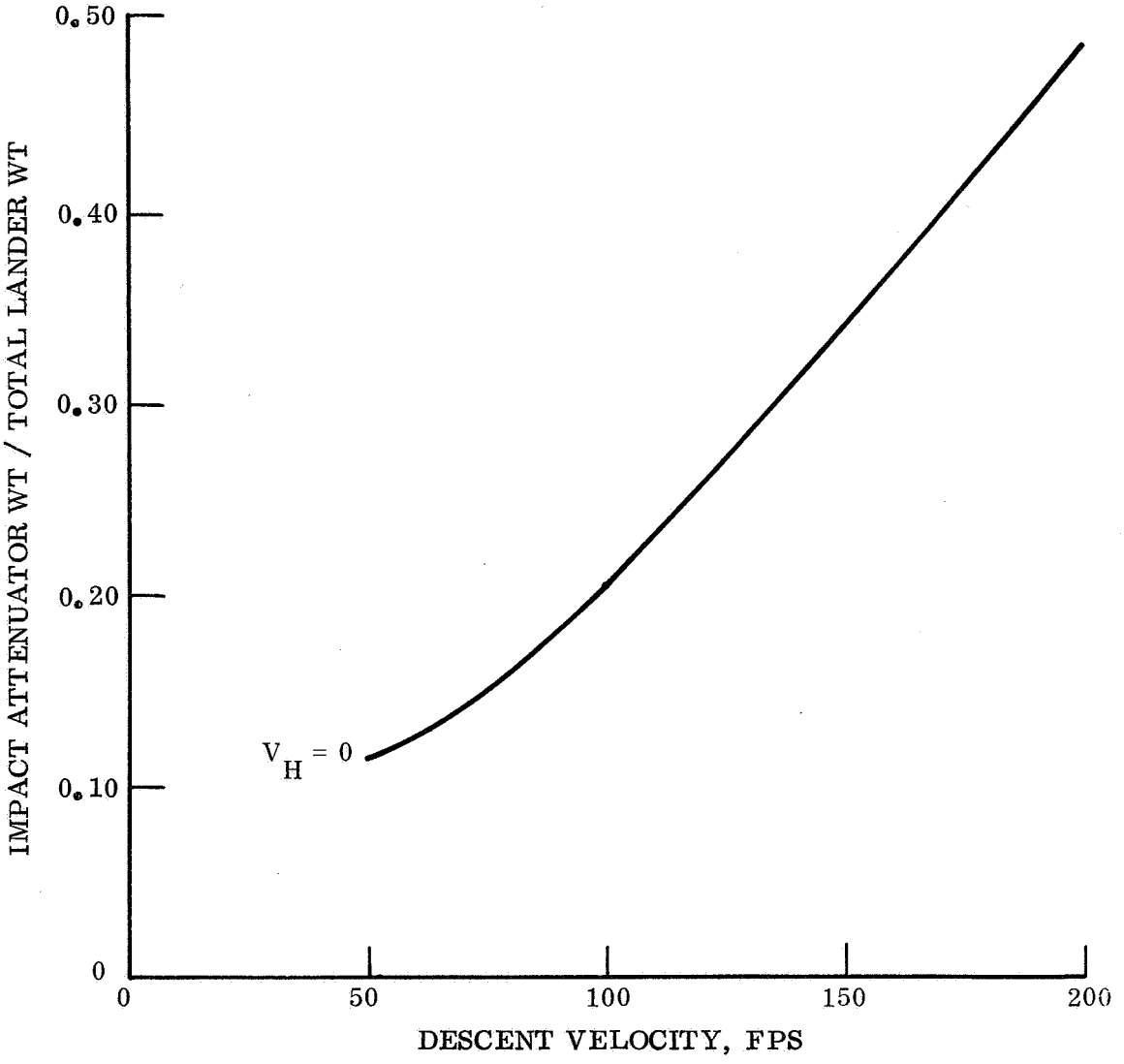

Figure 4.5.5-38. Crush-up Weight for Multi-directional Lander, Lander Wt = 300 lb, g-level = 1000, Slope = 0°, Packaging Density = 20 pcf

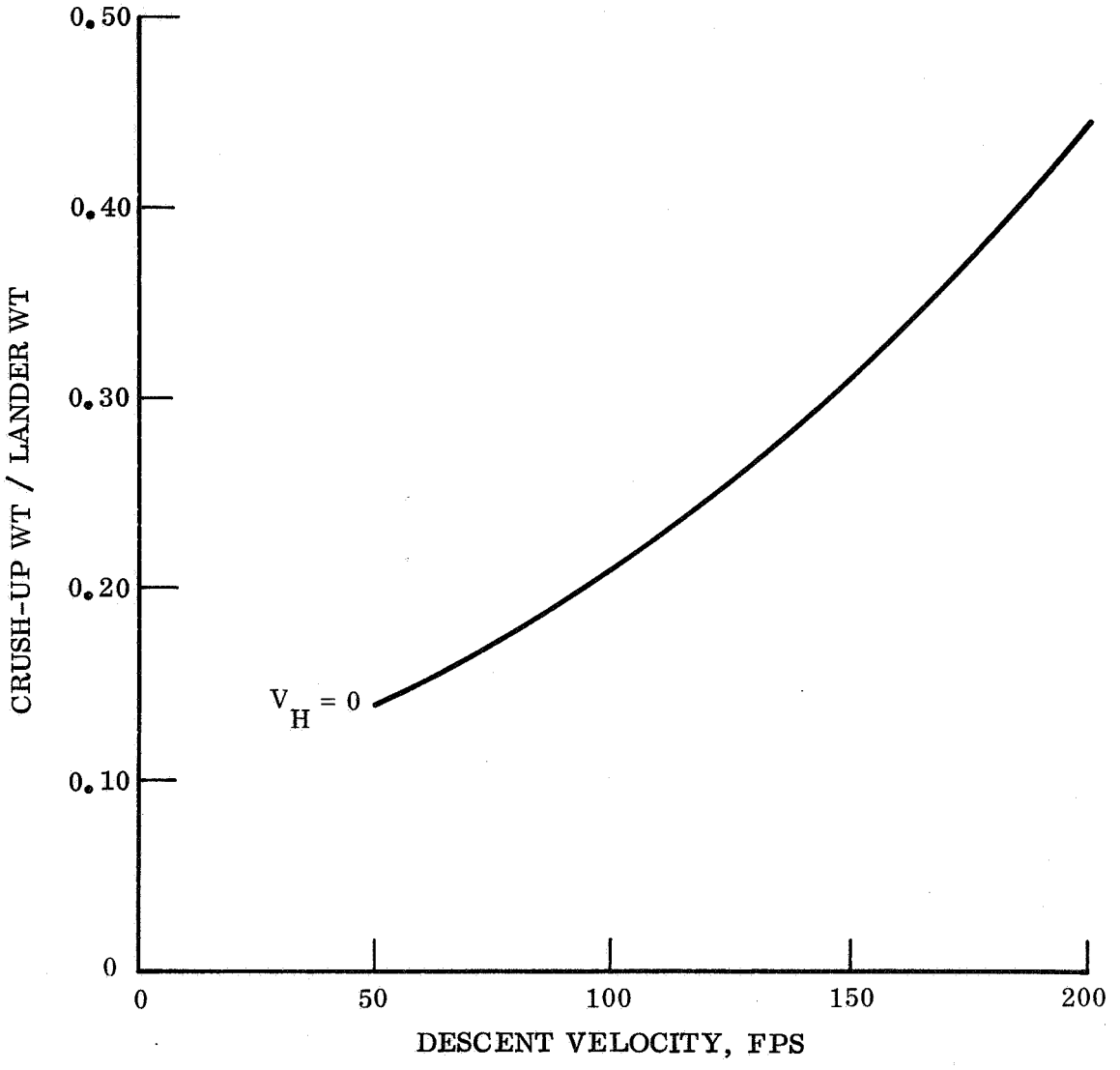

Figure 4.5.5-39. Crush-up Weight for Multi-directional Lander, Lander Wt = 300 lb, g-level = 1000, Slope = 0°, Packaging Density = 40 pcf

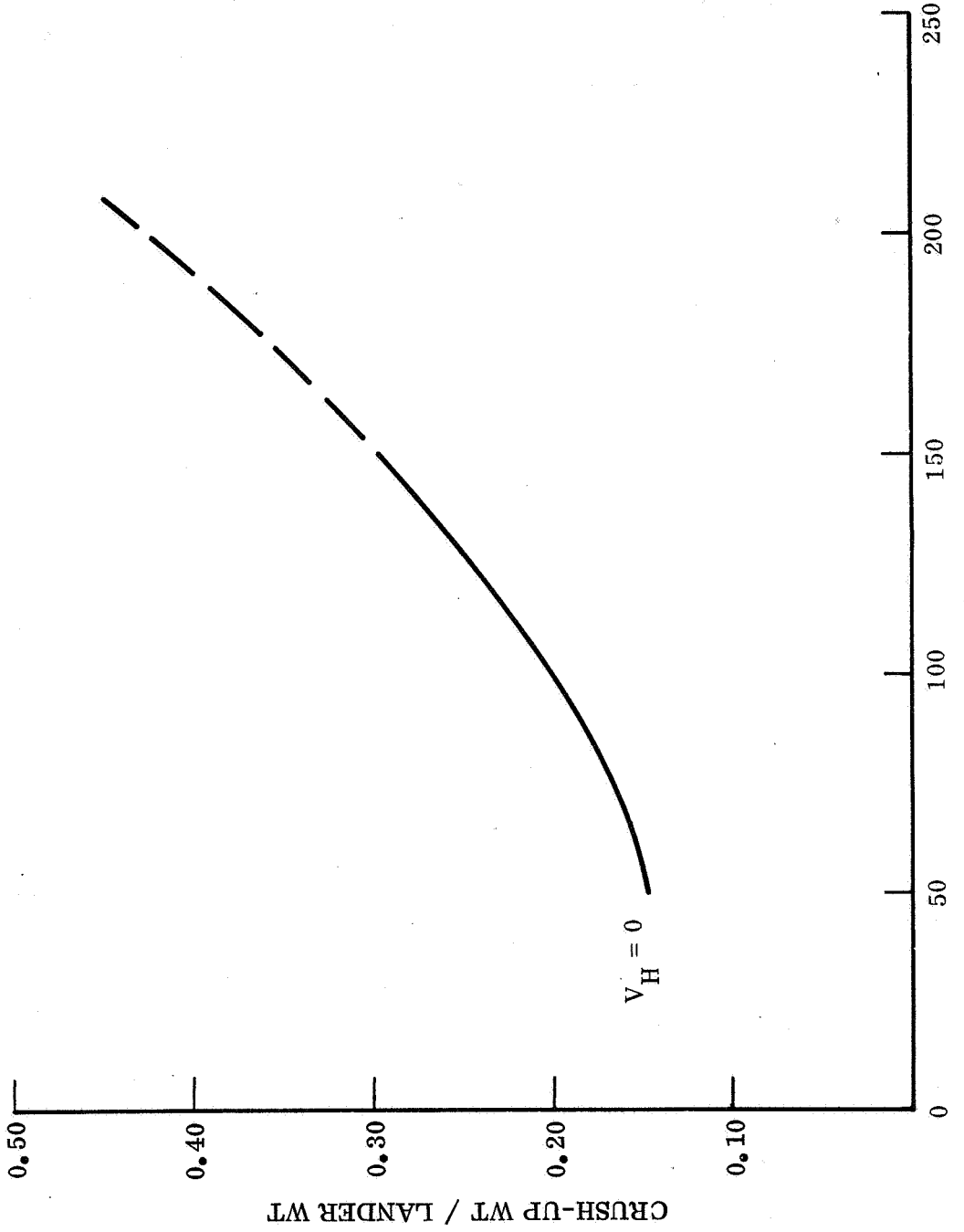

Figure 4.5.5-40. Crush-up Weight for Multi-directional Lander, Lander Wt = 300 lb, g-level = 1000, Slope = 0°, Packaging Density = 60 pcf

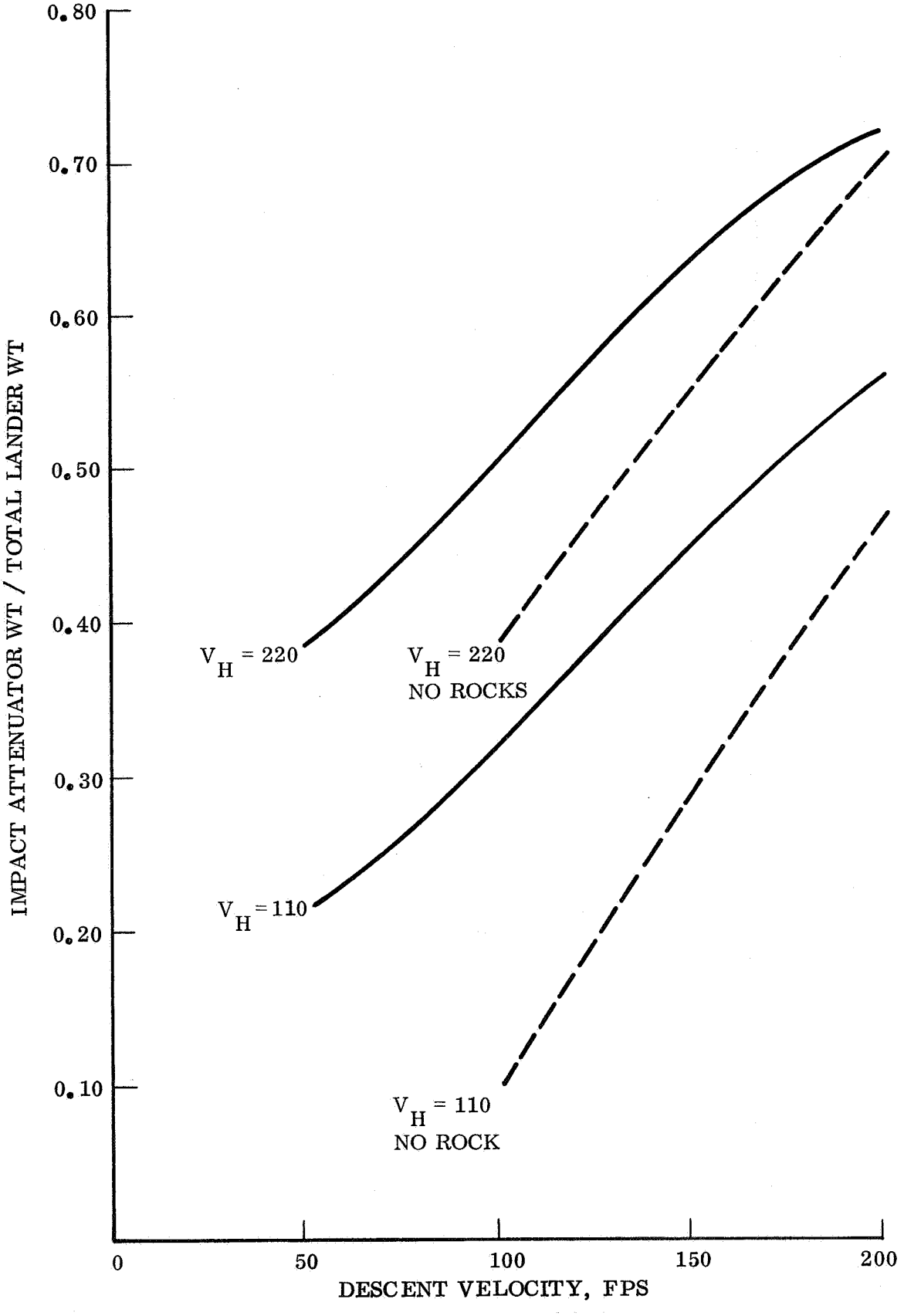

Figure 4.5.5-41. Crush-up Weight for Multi-directional Lander, Lander Wt = 300 lb, g-level = 1000, Slope = 34°, Packaging Density = 20 pcf

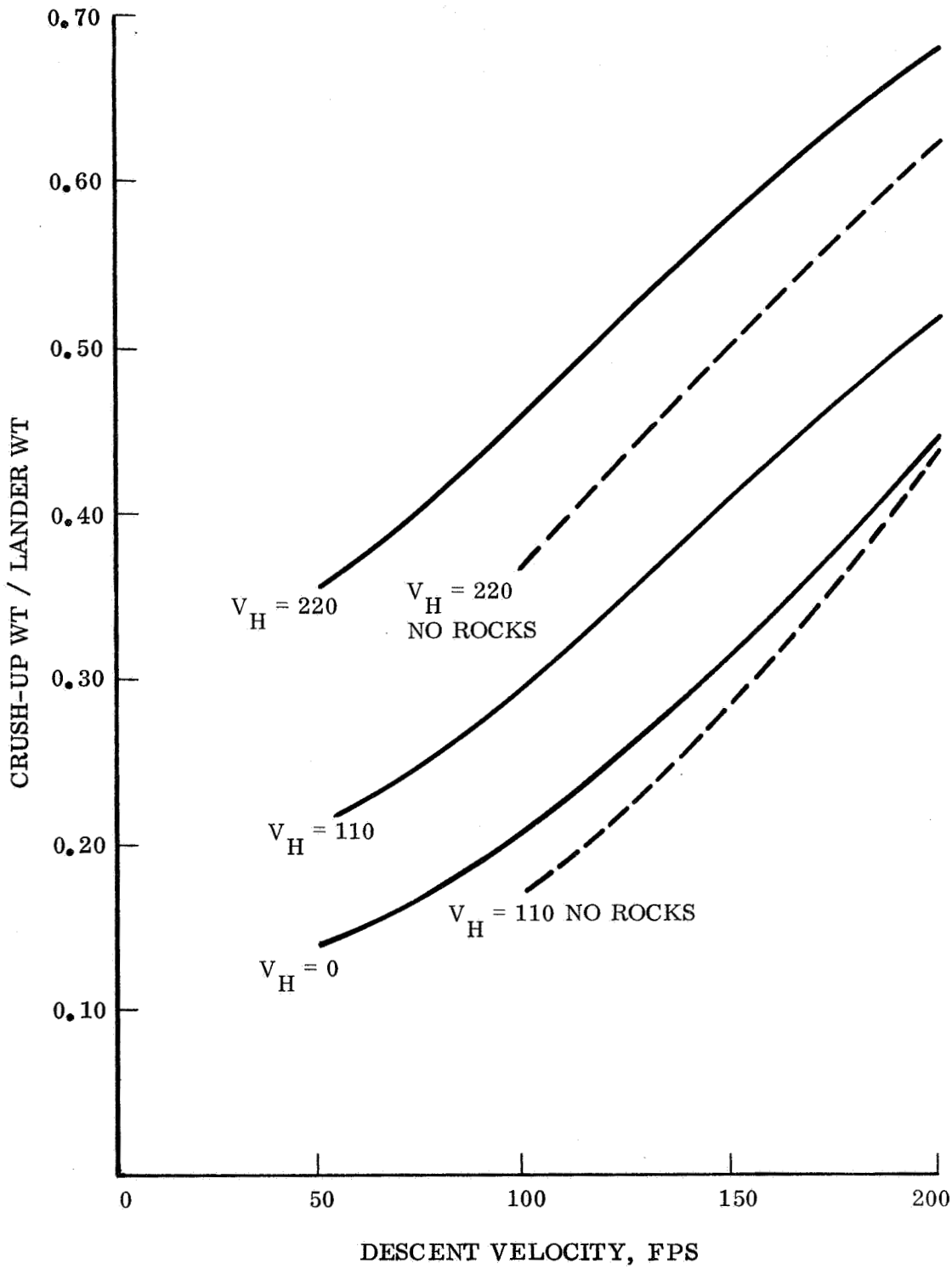

Figure 4.5.5-42. Crush-up Weight for Multi-directional Lander, Lander Wt = 300 lb, g-level = 1000, Slope = 34°, Packaging Density = 40 pcf

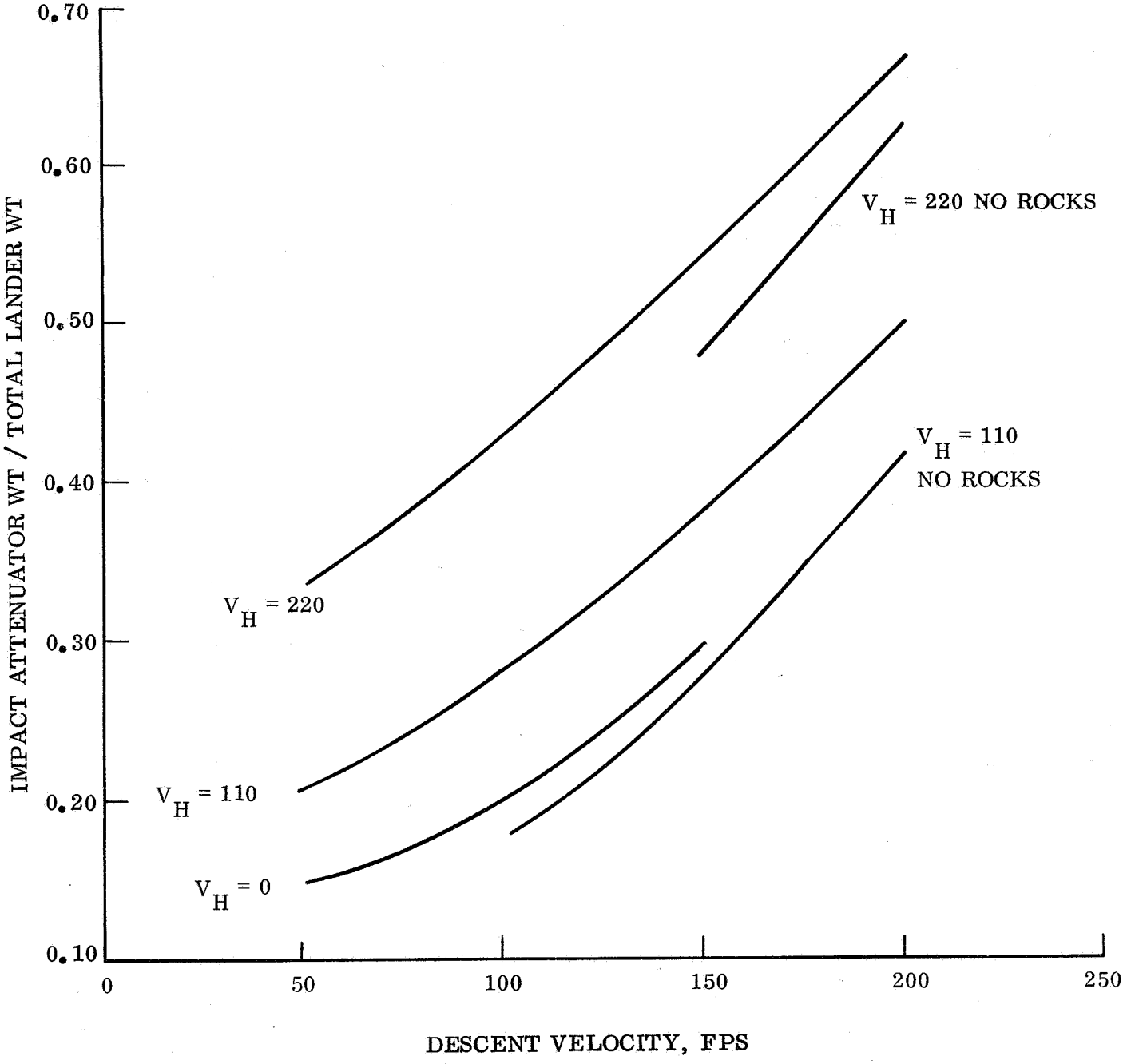

Figure 4.5.5-43. Crush-up Weight for Multi-directional Lander, Lander Wt = 300 lb, g-level = 1000, Slope = 34°, Packaging Density = 60 pcf

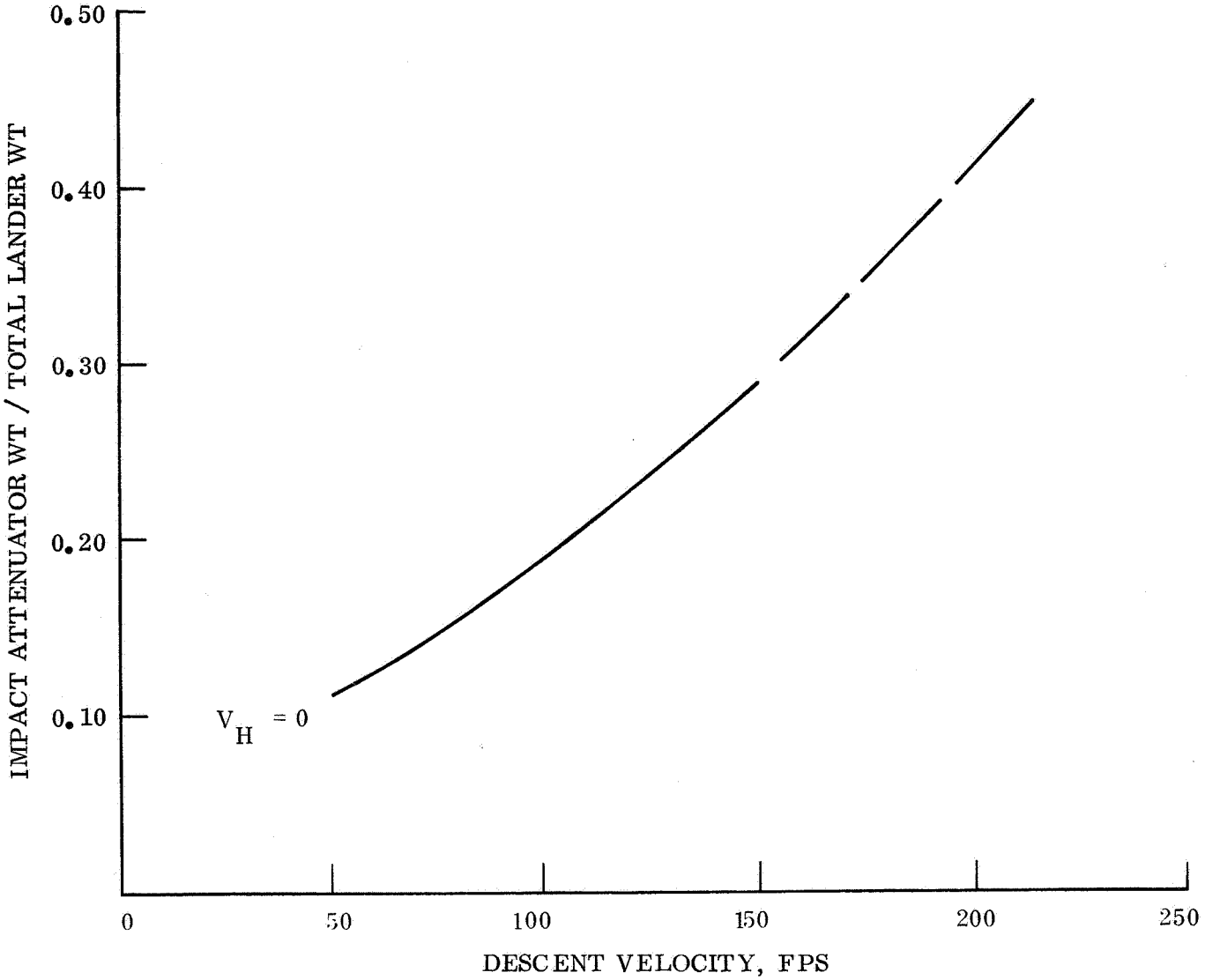

Figure 4.5.5-44. Crush-up Weight for Multi-directional Lander, Lander Wt = 300 lb, g-level = 1500, Slope = 0°, Packaging Density = 20 pcf

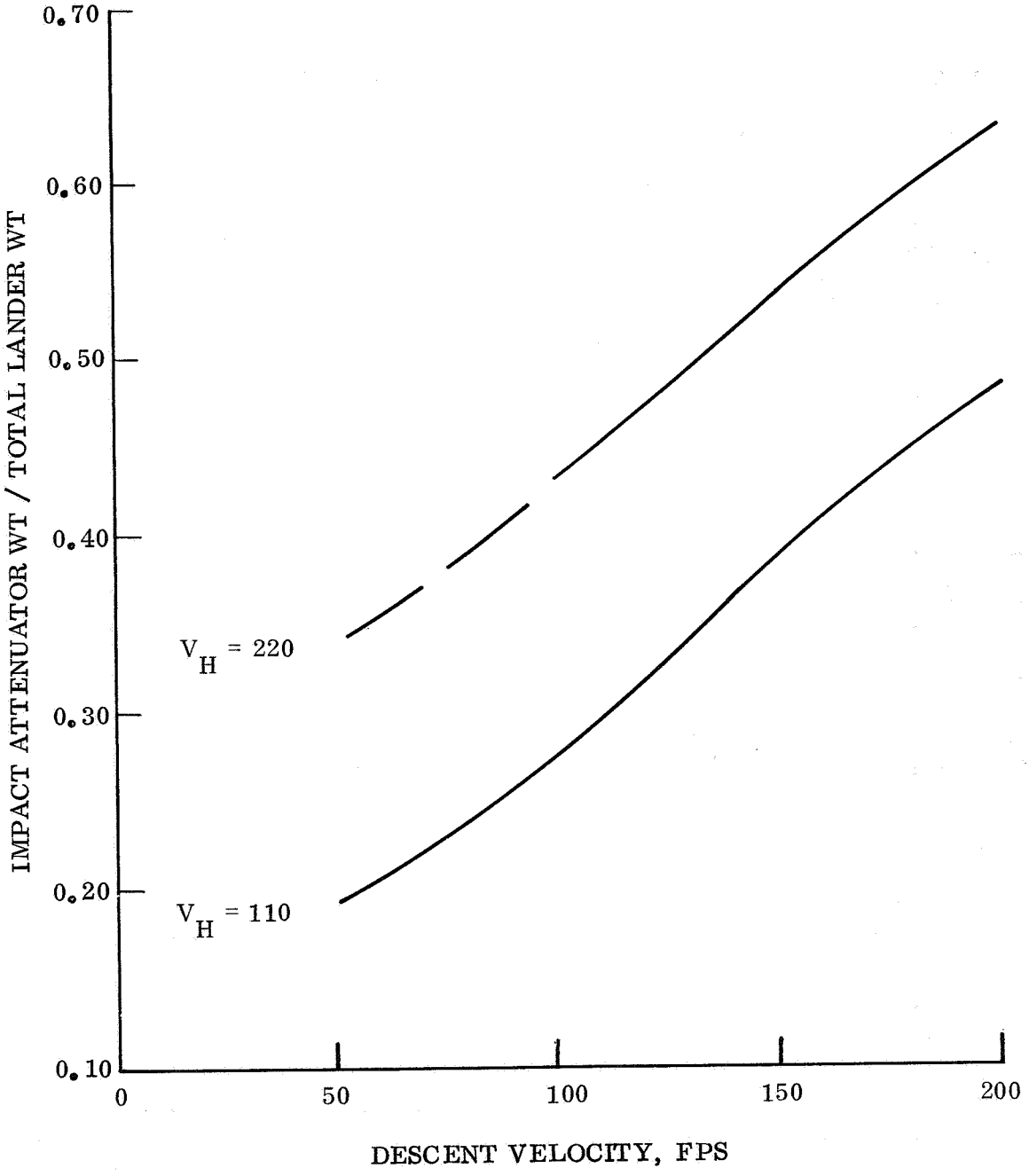

Figure 4.5.5-45. Crush-up Weight for Multi-directional Lander, Lander Wt = 300 lb, g-level = 1500, Slope = 34°, Packaging Density = 20 pcf

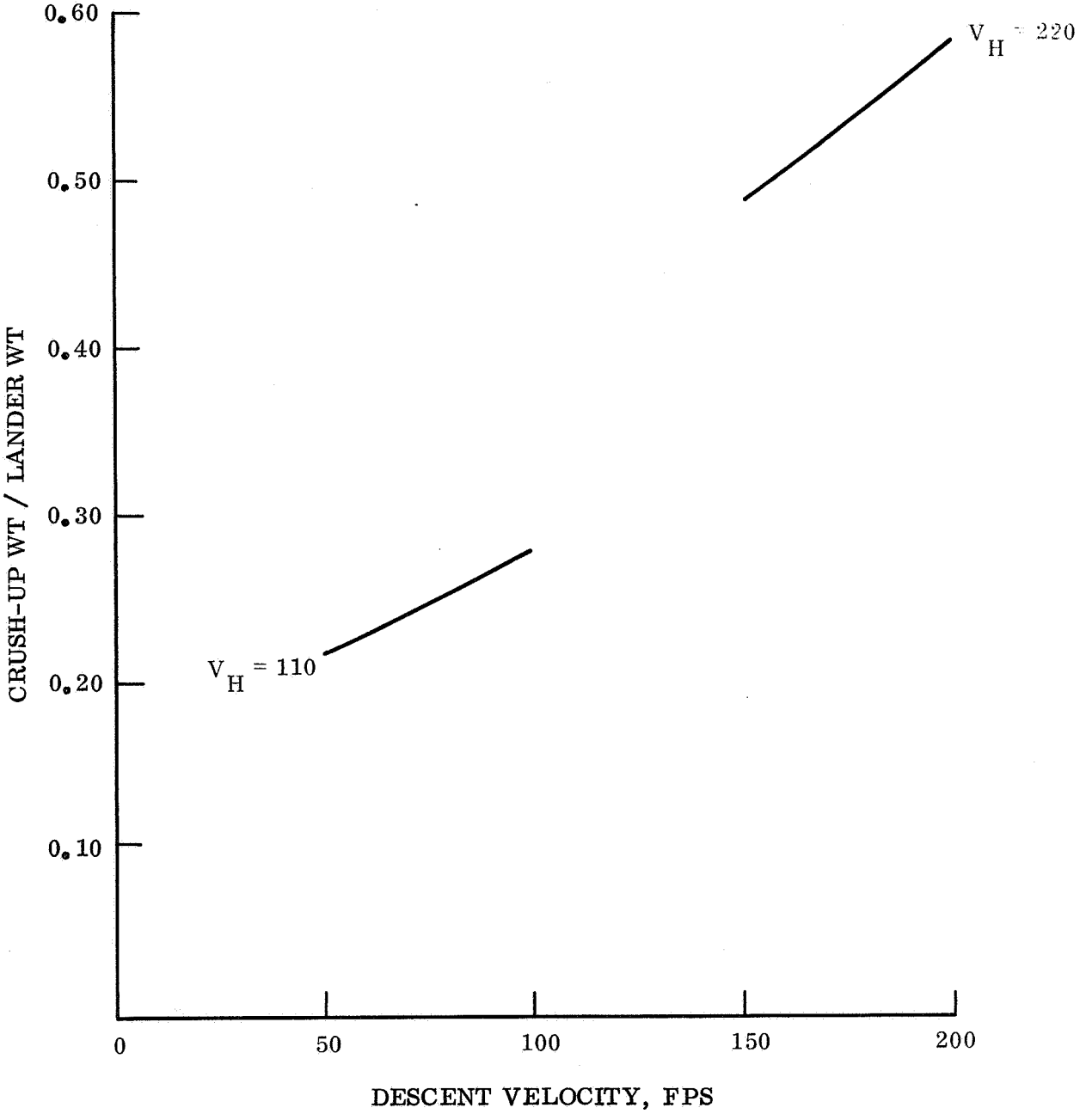

Figure 4.5.5-46. Crush-up Weight for Multi-directional Lander, Lander Wt = 300 lb, g-level = 1500, Slope = 34°, Packaging Density = 40 pcf

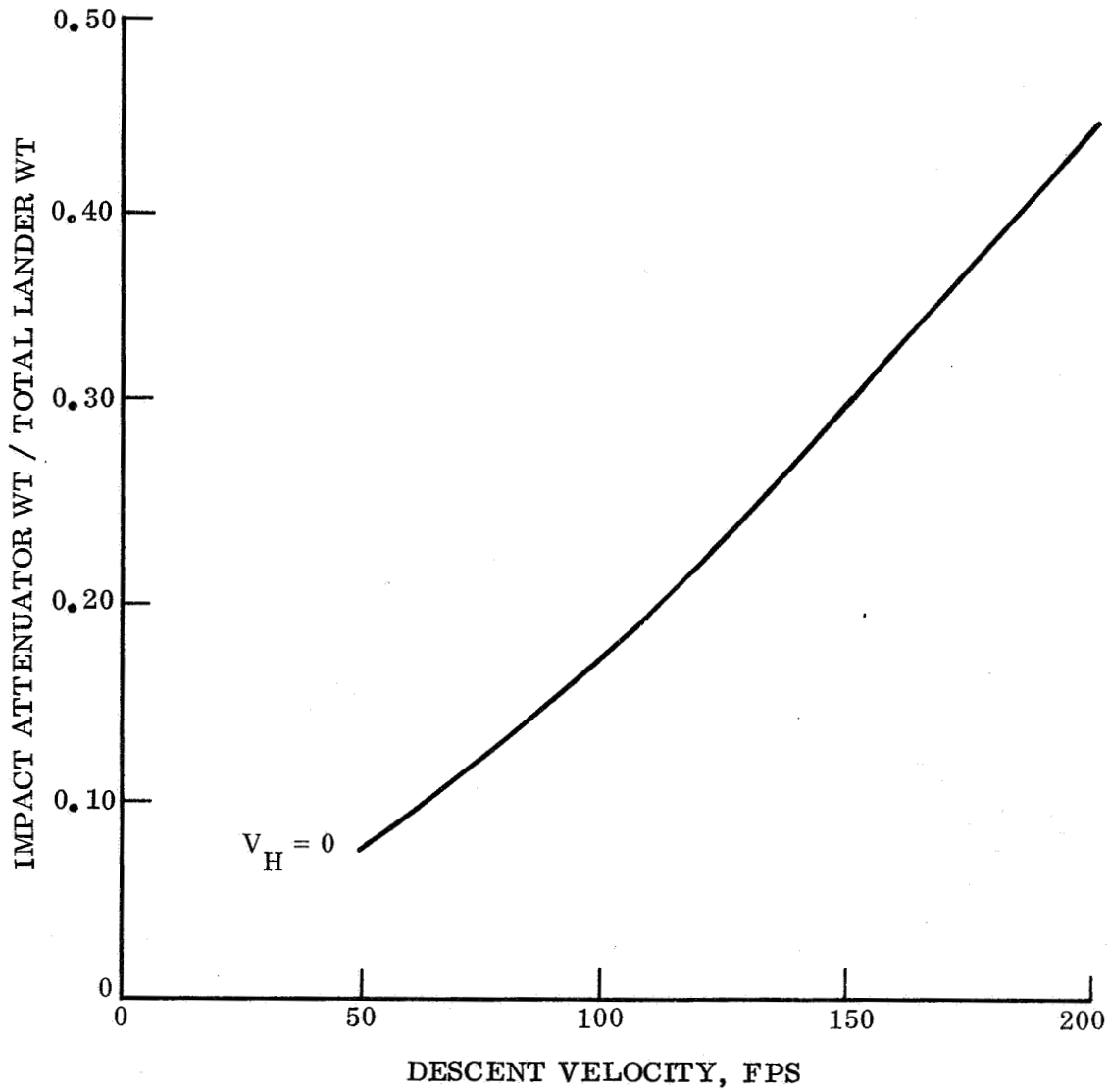

Figure 4.5.5-47. Crush-up Weight for Multi-directional Lander, Lander Wt = 300 lb, g-level = 1000, Slope = 0°, Packaging Density = 20 pcf

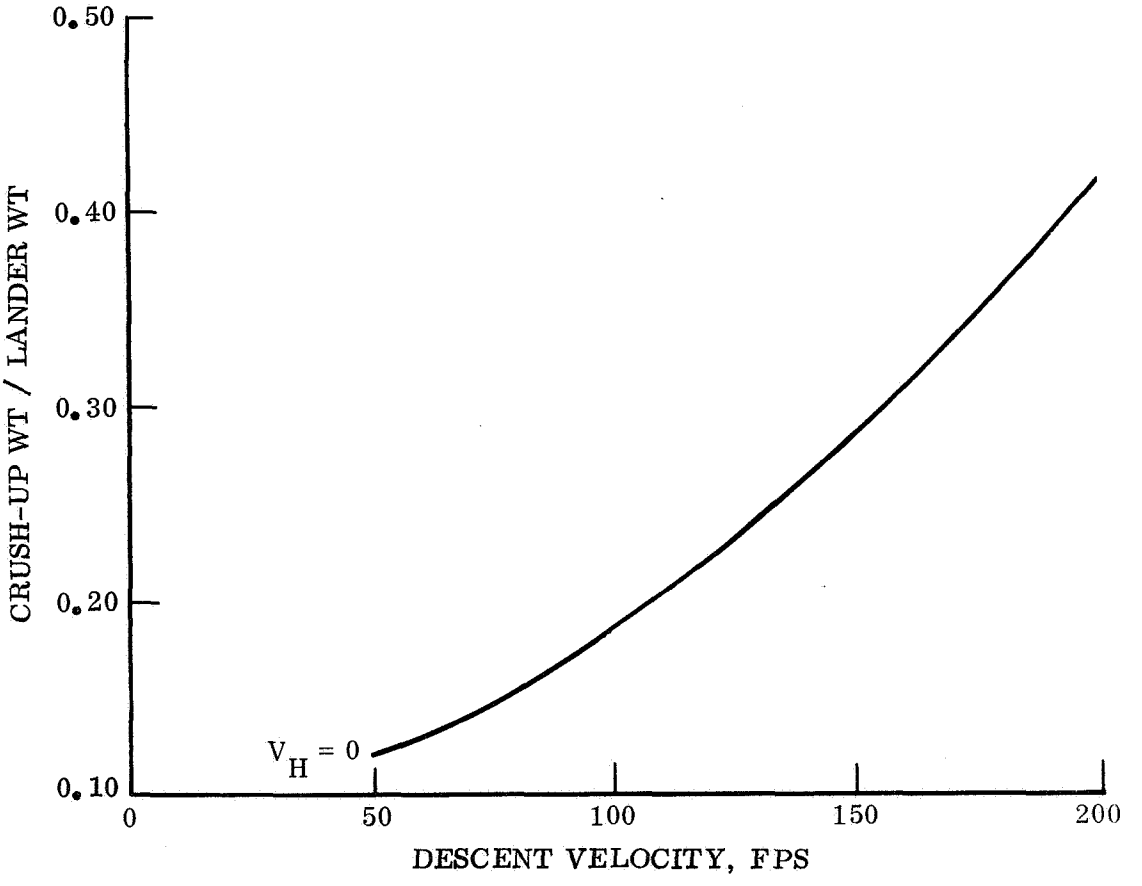

Figure 4.5.5-48. Crush-up Weight for Multi-directional Lander, Lander Wt = 400 lb, g-level = 1000, Slope = 0°, Packaging Density = 40 pcf

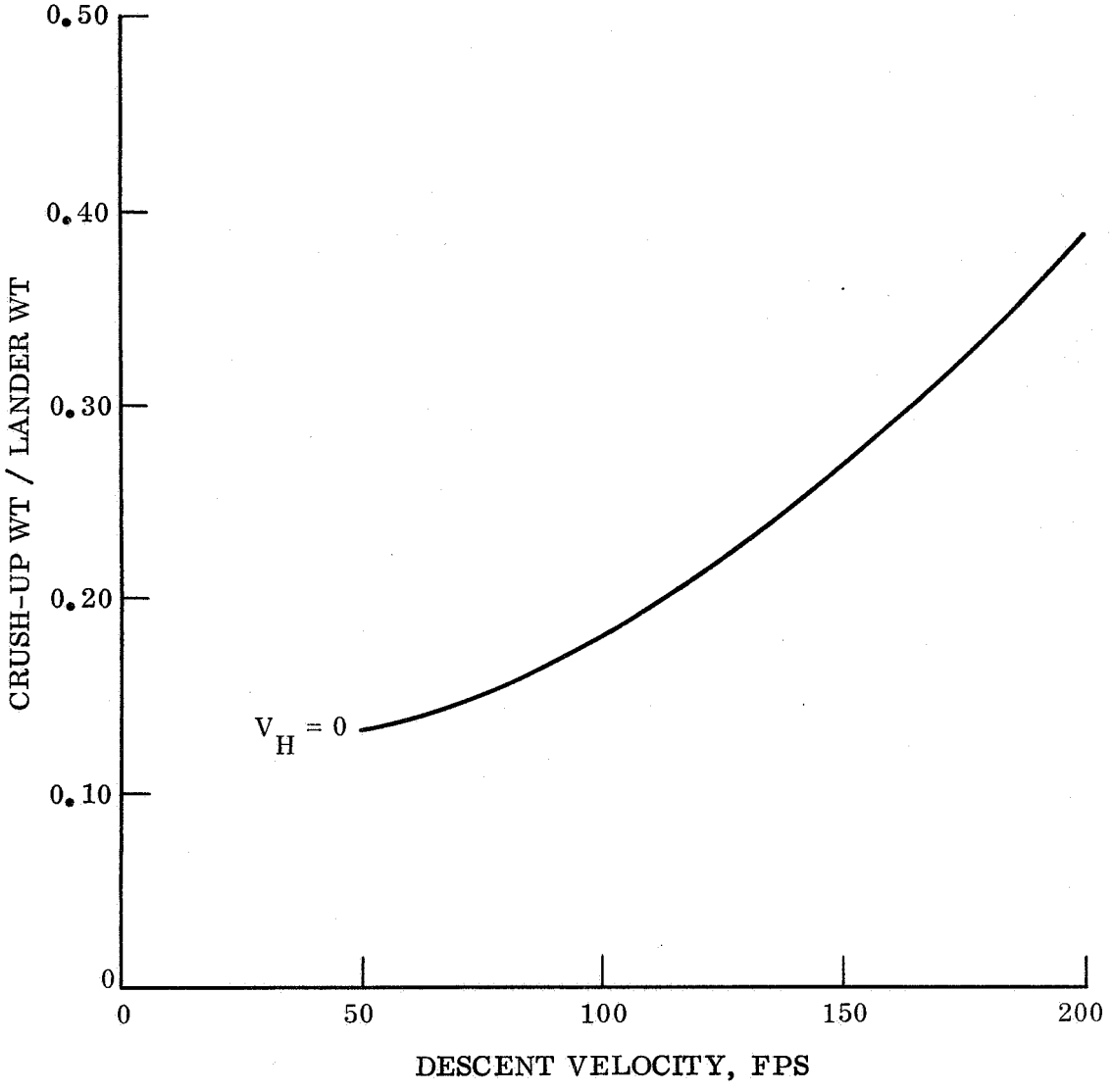

Figure 4.5.5-49. Crush-up Weight for Multi-directional Lander, Lander Wt = 400 lb, g-level = 1000, Slope = 0°, Packaging Density = 60 pcf

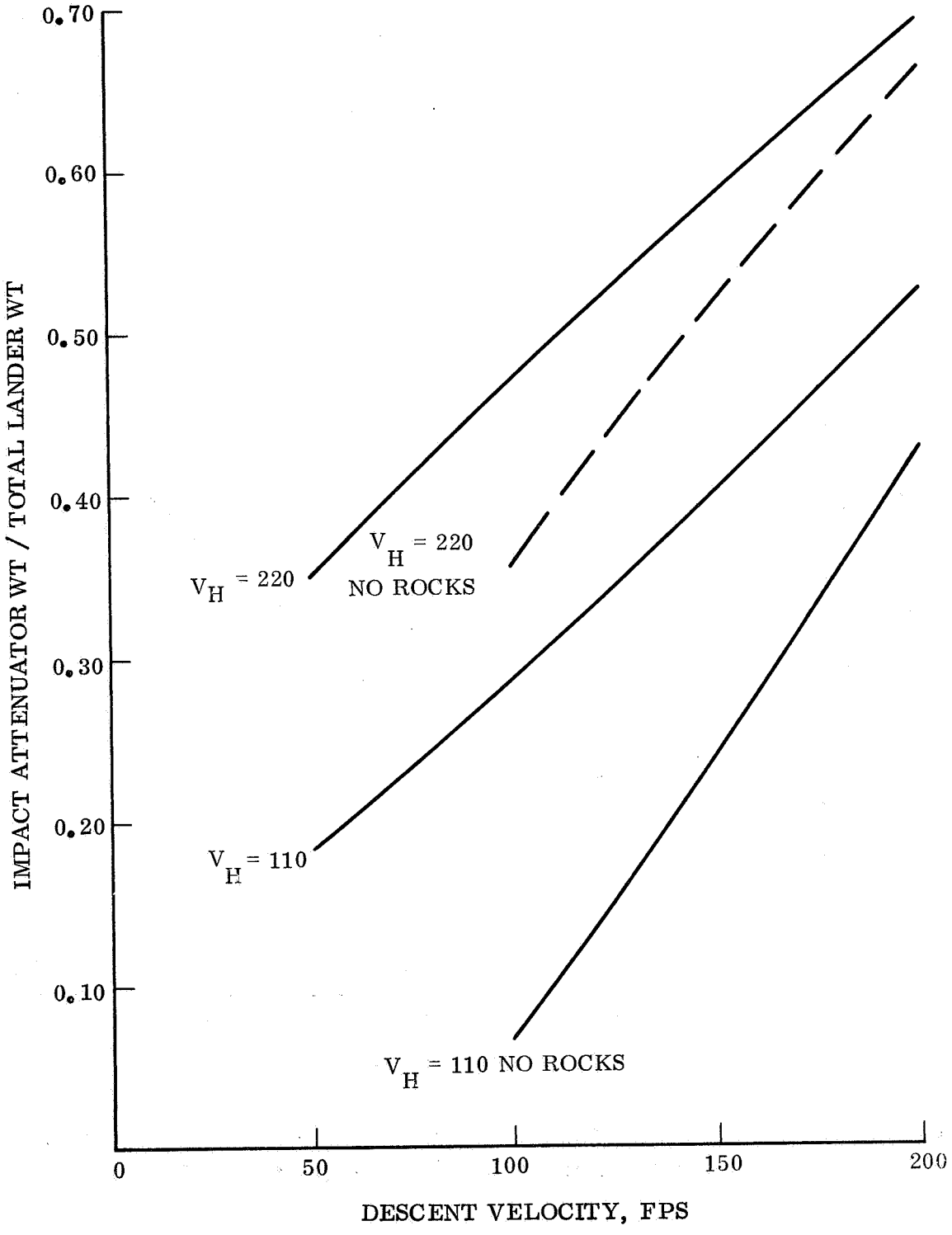

Figure 4.5.5-50. Crush-up Weight for Multi-directional Lander, Lander Wt = 400 lb, g-level = 1000, Slope = 34°, Packaging Density = 20 pcf

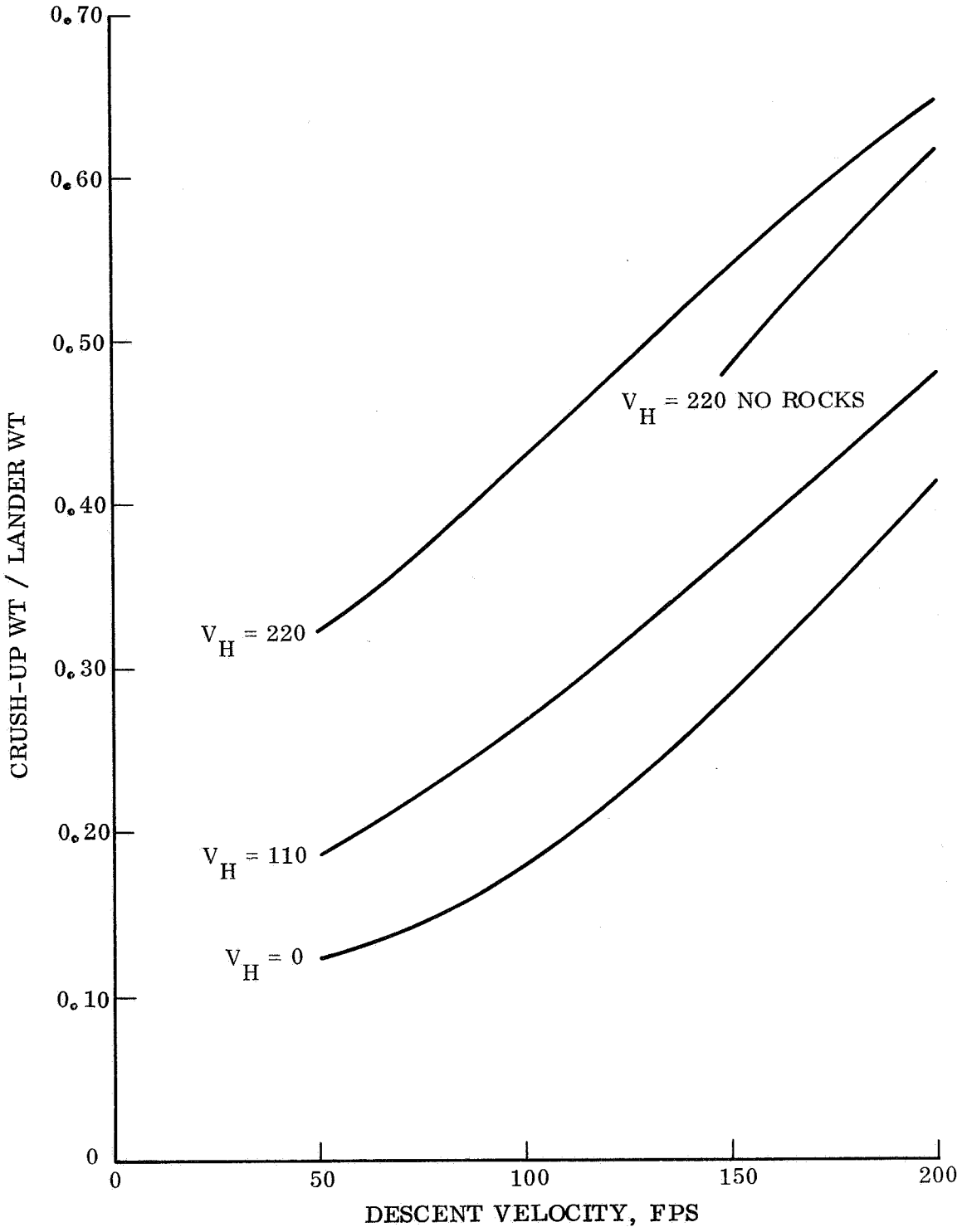

Figure 4.5.5-51. Crush-up Weight for Multi-directional Lander, Lander Wt = 400 lb, g-level = 1000, Slope = 34°, Packaging Density = 40 pcf

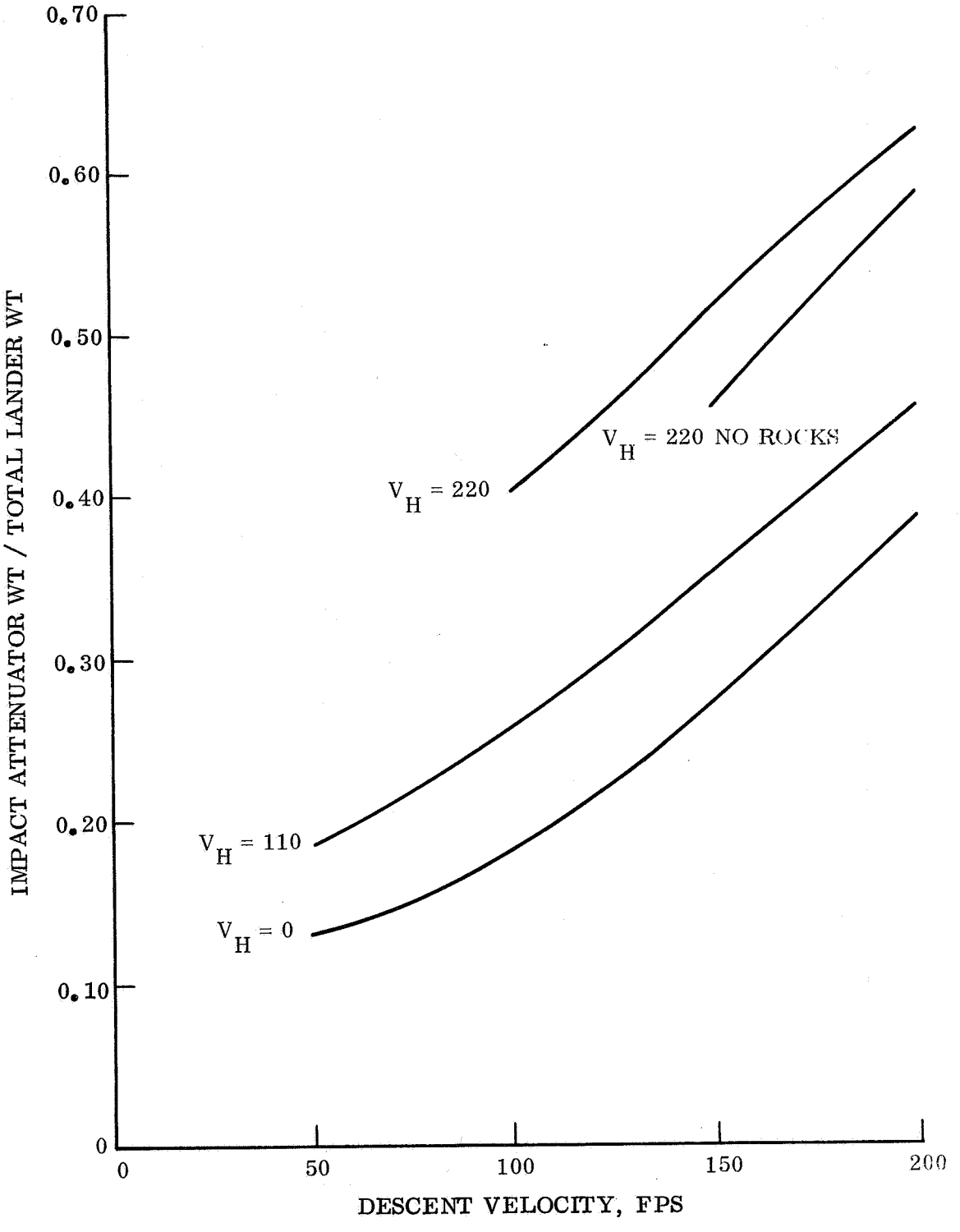

Figure 4.5.5-52. Crush-up Weight for Multi-directional Lander, Lander Wt = 400 lb, g-level = 1000, Slope = 34°, Packaging Density = 60 pcf

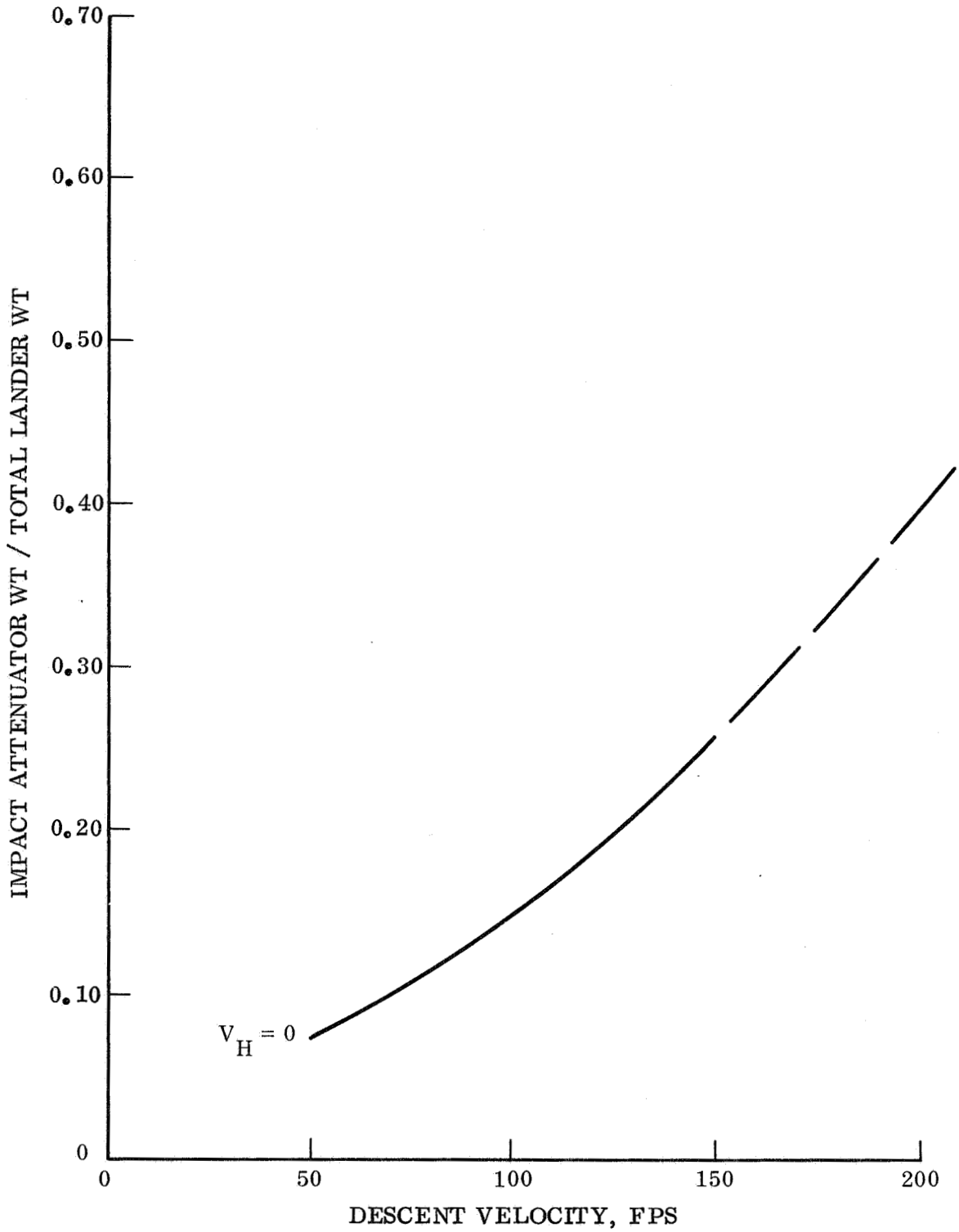

Figure 4.5.5-53. Crush-up Weight for Multi-directional Lander, Lander Wt = 400 lb, g-level = 1500, Slope = 0°, Packaging Density = 20 pcf

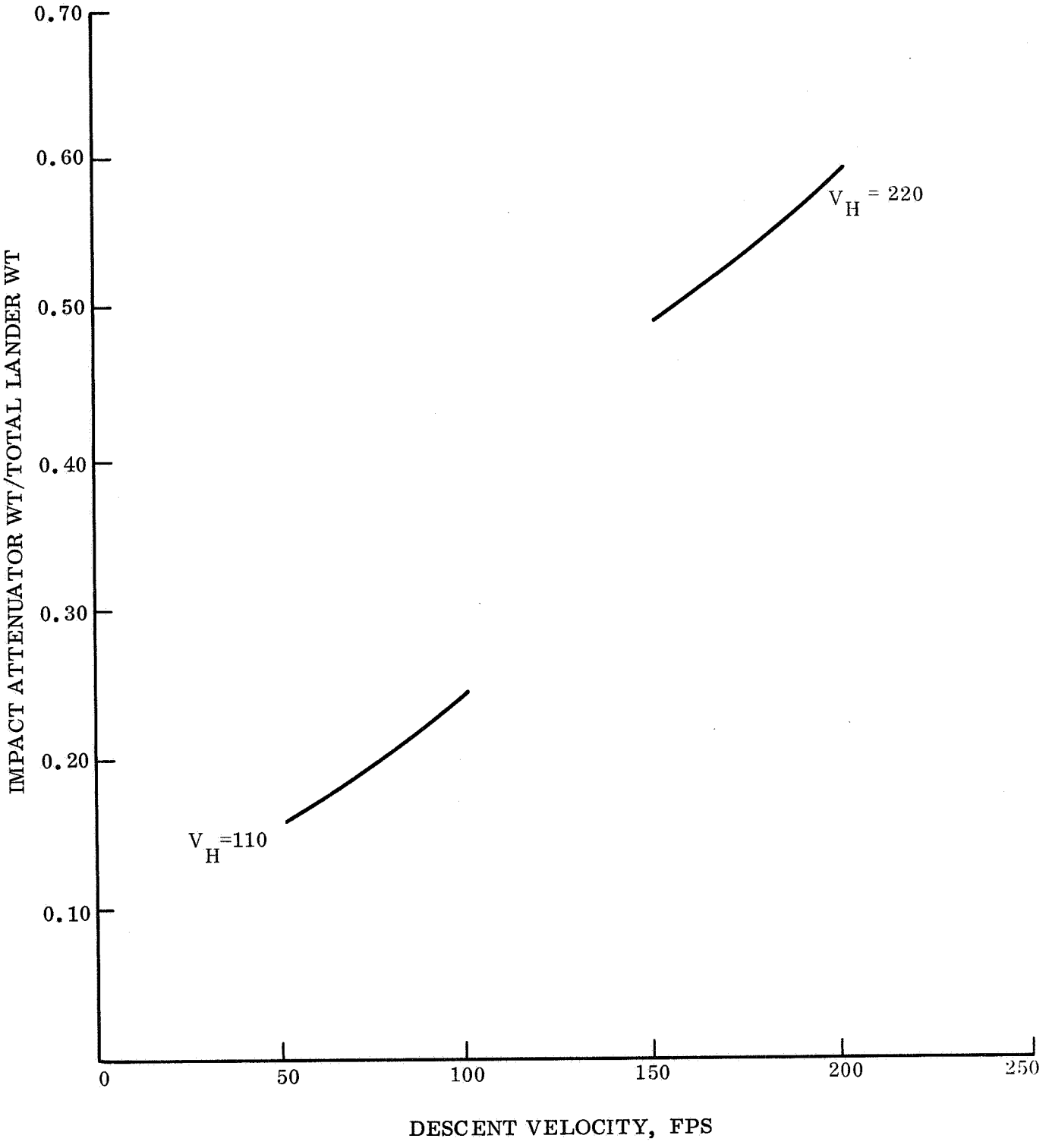

Figure 4.5.5-54. Crush-up Weight for Multi-directional Lander, Lander Wt = 400 lb, g-level = 1500, Slope = 34°, Packaging Density = 20 pcf

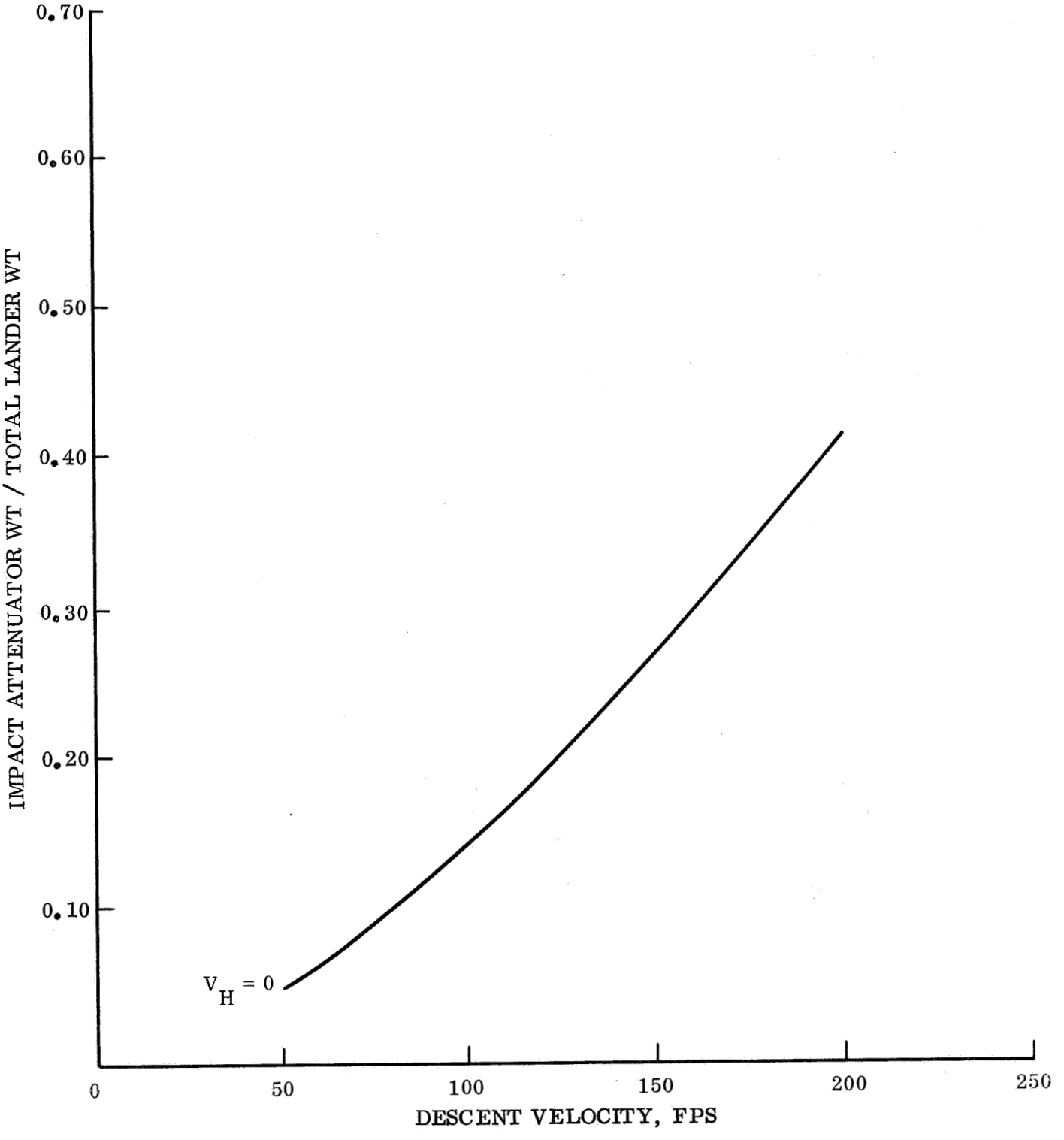

Figure 4.5.5-55. Crush-up Weight for Multi-directional Lander, Lander Wt = 500 lb, g-level = 1000, Slope = 0°, Packaging Density = 20 pcf

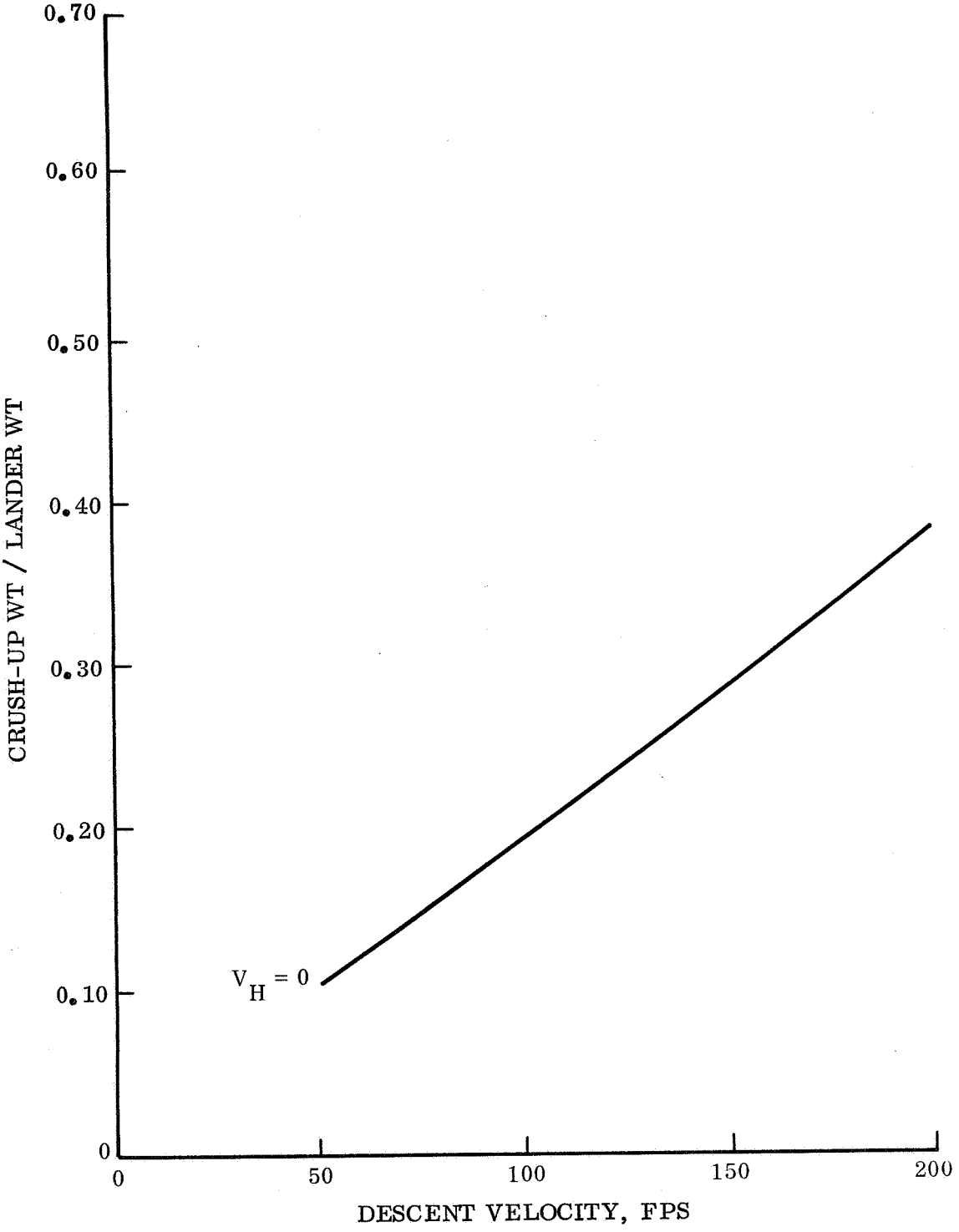

Figure 4.5.5-56. Crush-up Weight for Multi-directional Lander, Lander Wt = 500 lb, g-level = 1000, Slope = 0°, Packaging Density = 40 pcf

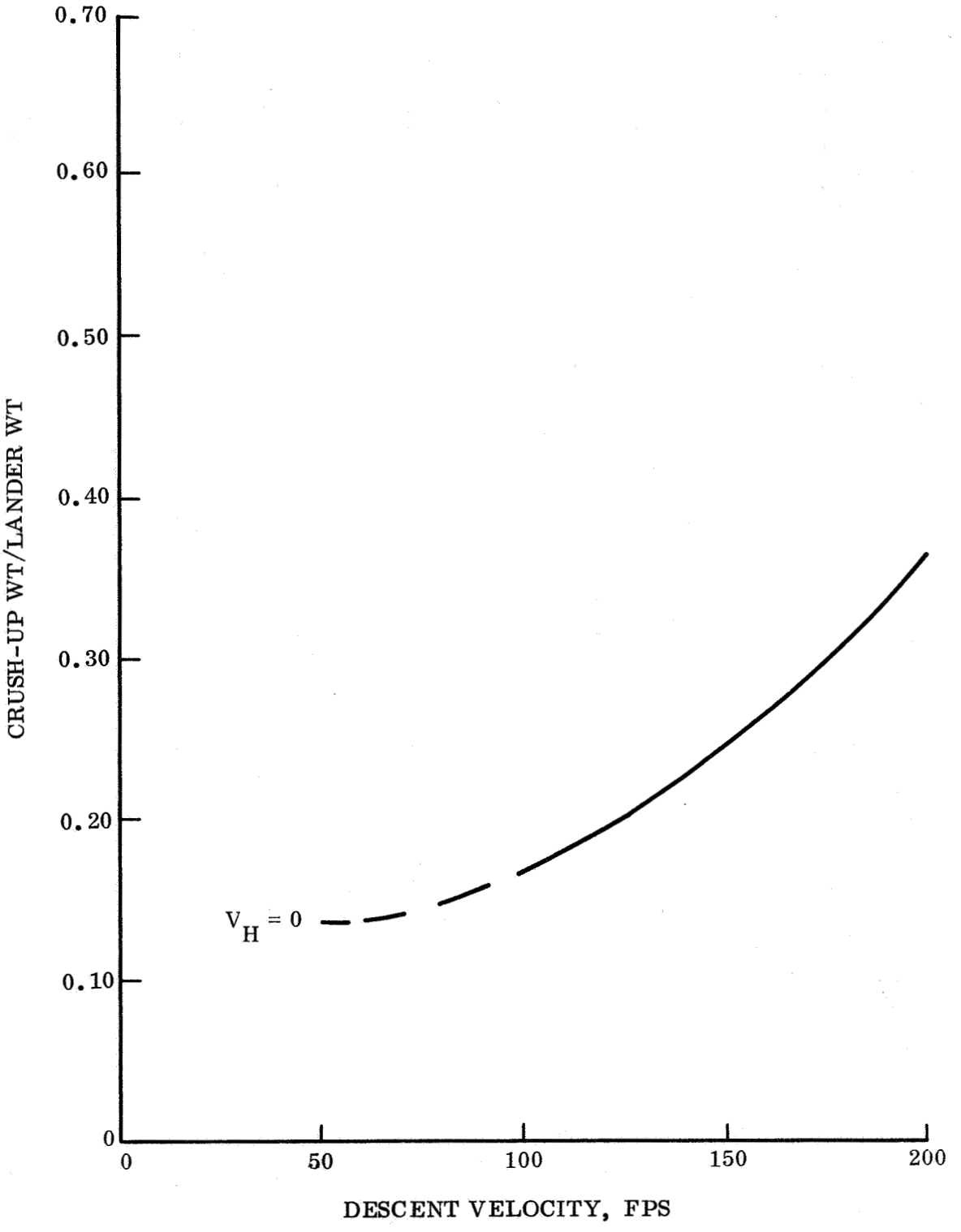

Figure 4.5.5-57. Crush-up Weight for Multi-directional Lander, Lander Wt = 500 lb, g-level = 1000, Slope = 0°, Packaging Density = 60 pcf

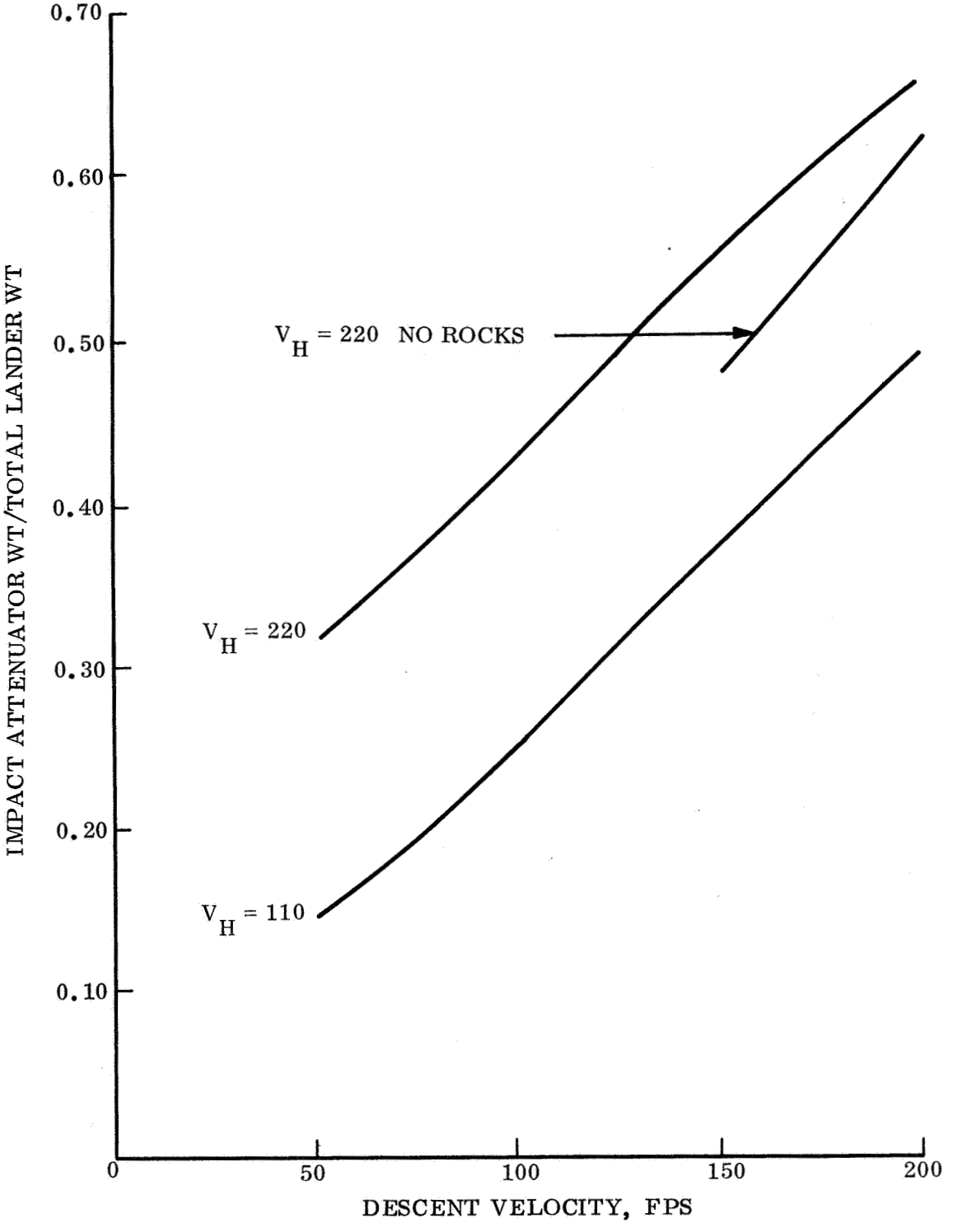

Figure 4.5.5-58. Crush-up Weight for Multi-directional Lander, Lander Wt = 500 lb, g-level = 1000, Slope = 34°, Packaging Density = 20 pcf

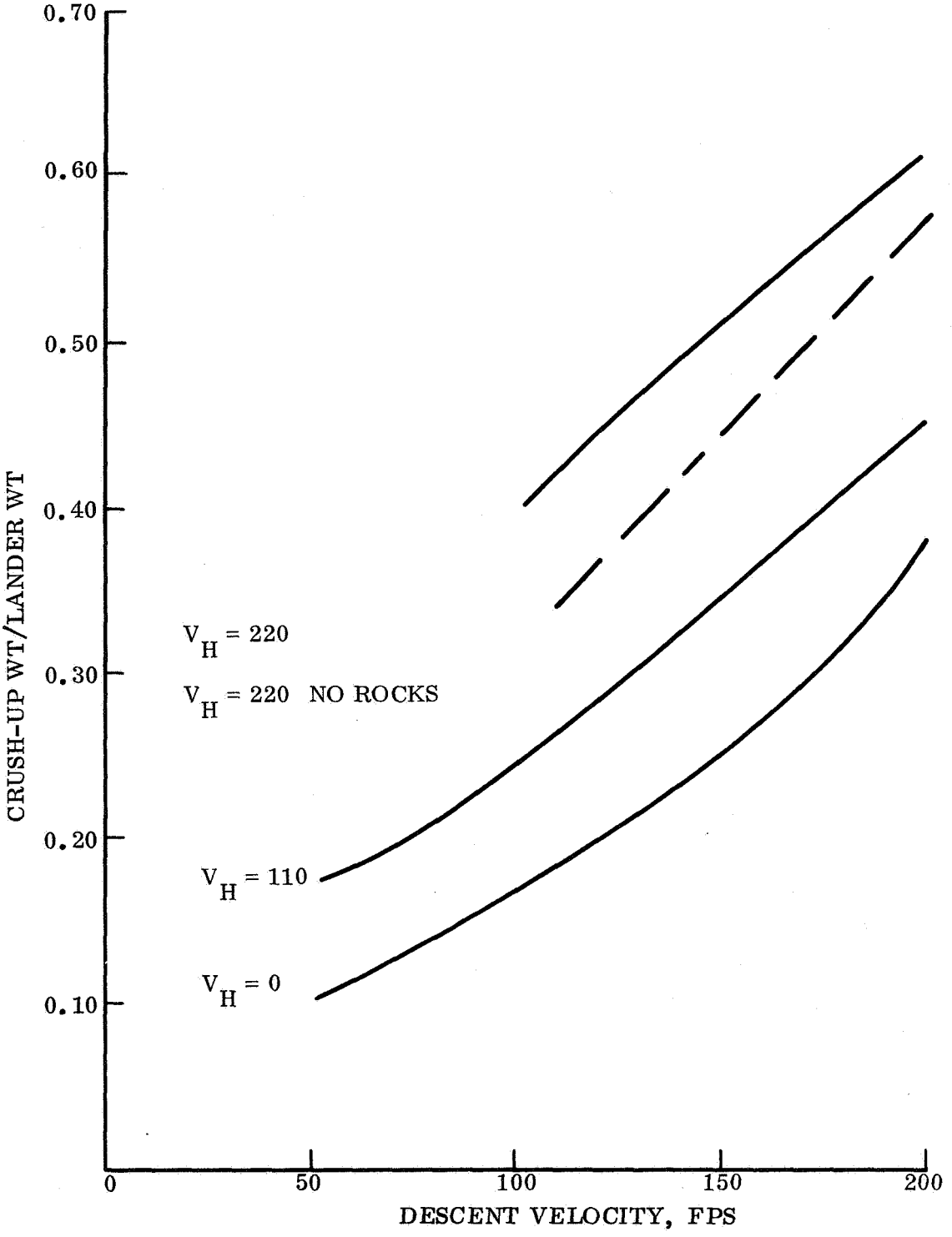

Figure 4.5.5-59. Crush-up Weight for Multi-directional Lander, Lander Wt = 500 lb, g-level = 1000, Slope = 34°, Packaging Density = 40 pcf

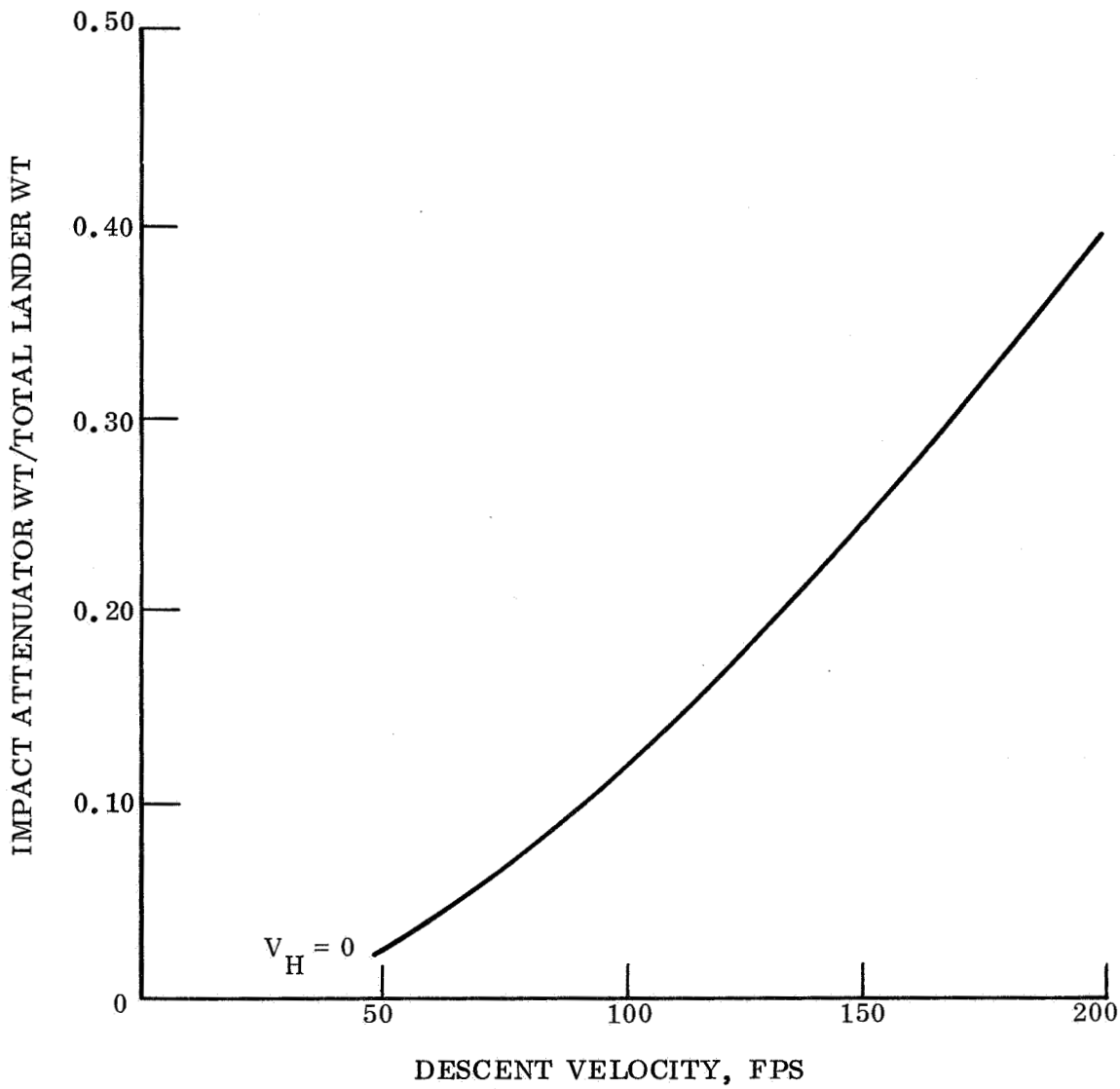

Figure 4.5.5-60. Crush-up Weight for Multi-directional Lander, Lander Wt = 500 lb, g-level = 1000, Slope = 34°, Packaging Density = 60 pcf

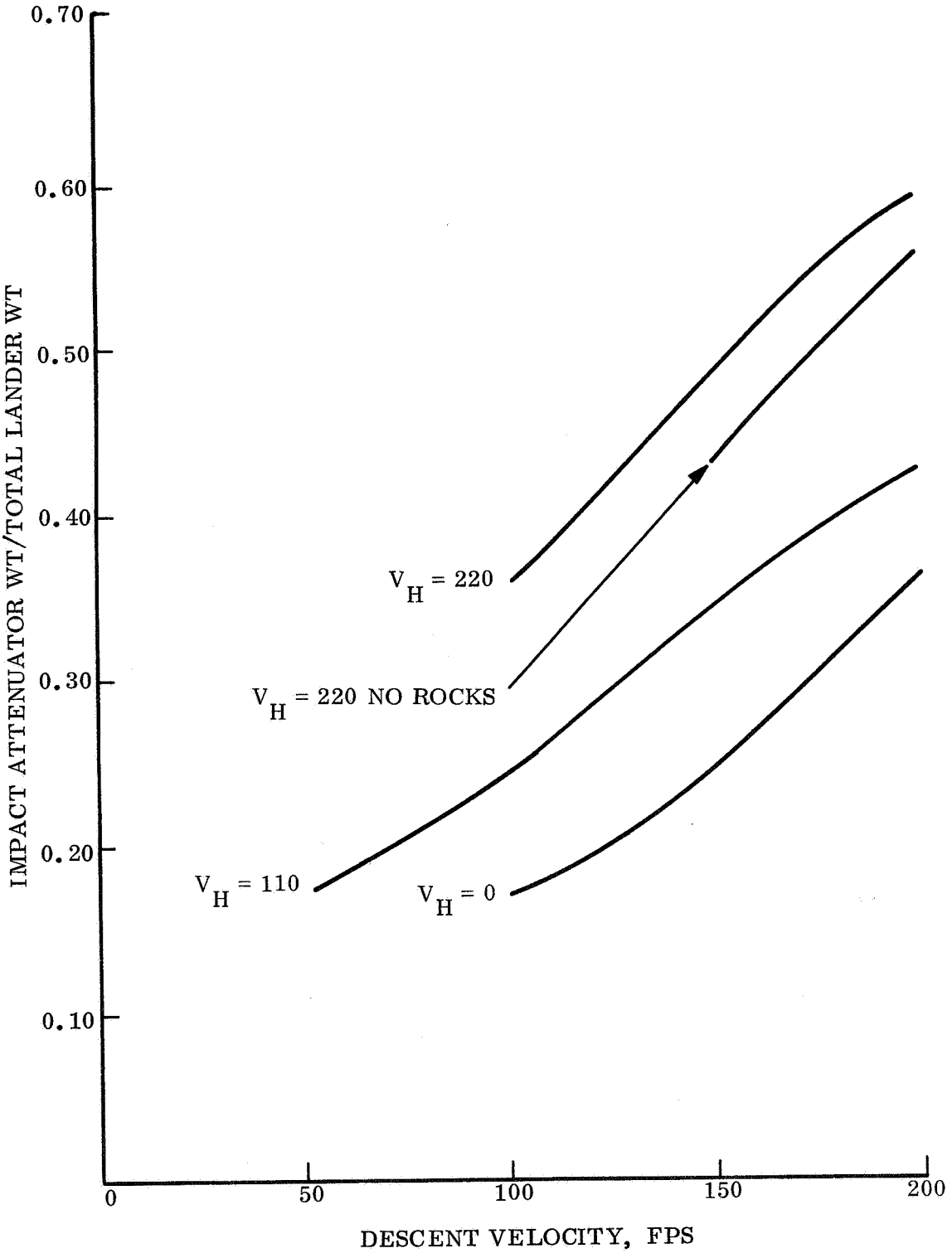

Figure 4.5.5-61. Crush-up Weight for Multi-directional Lander, Lander Wt = 600 lb, g-level = 1000, Slope = 0°, Packaging Density = 20 pcf

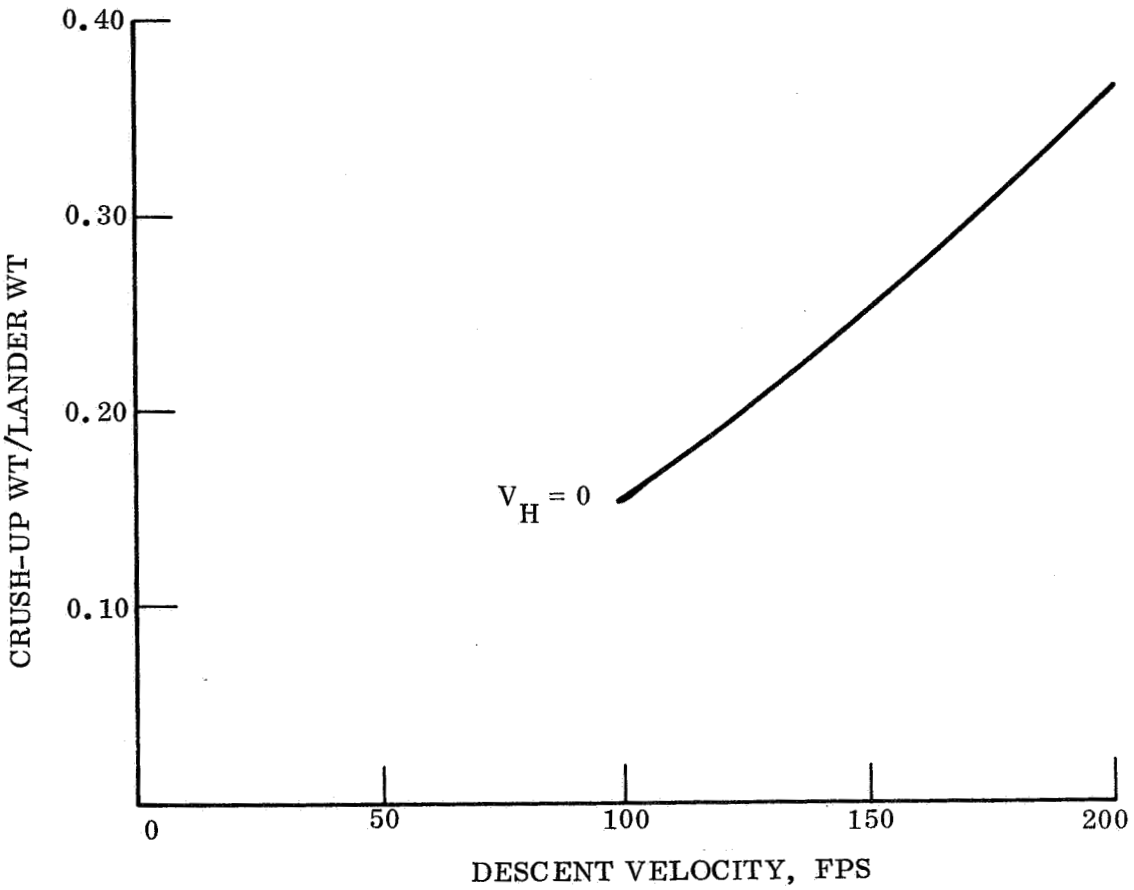

Figure 4.5.5-62. Crush-up Weight for Multi-directional Lander, Lander Wt = 600 lb, g-level = 1000, Slope = 0^o, Packaging Density = 40 pcf

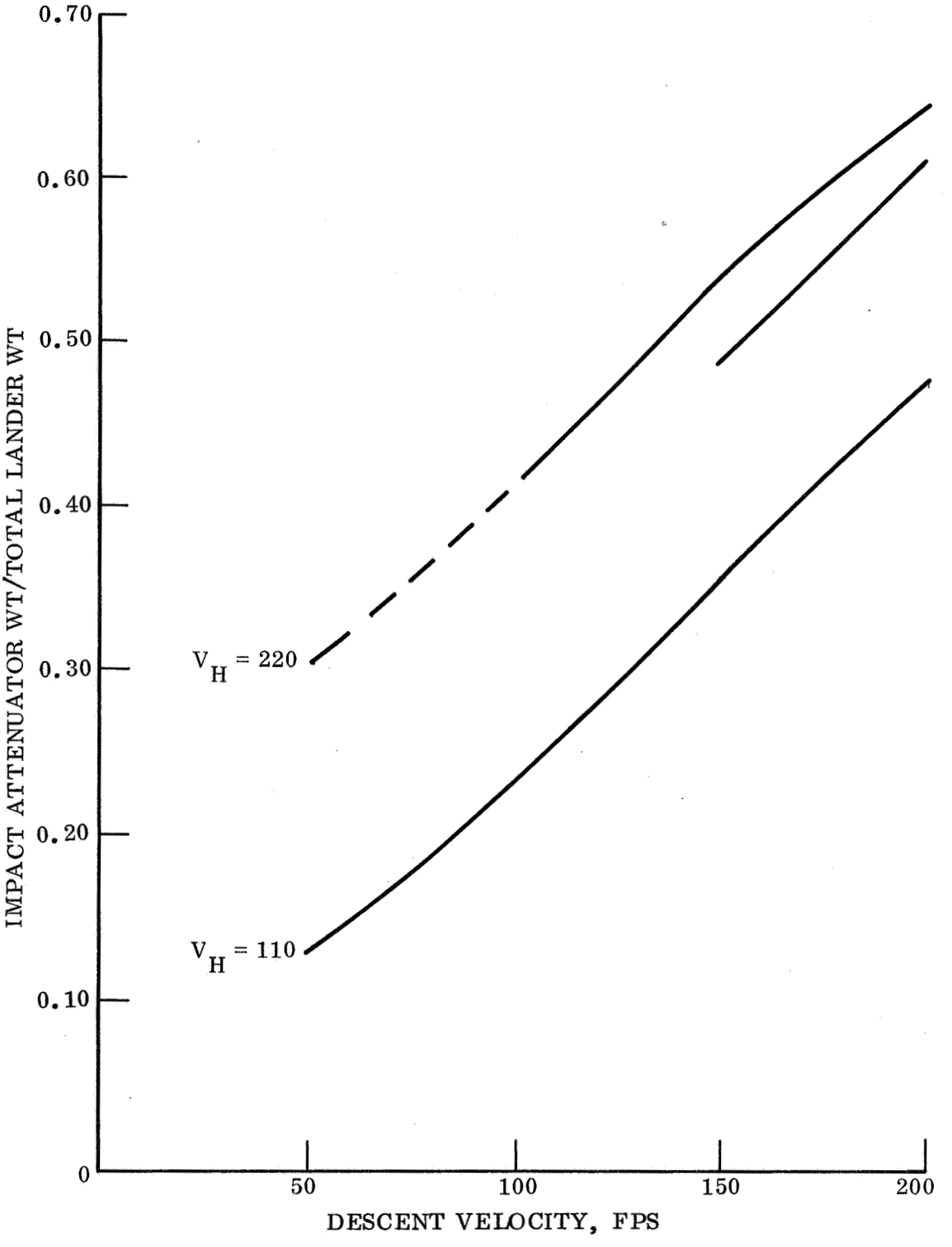

Figure 4.5.5-63. Crush-up Weight for Multi-directional Lander, Lander Wt = 600 lb, g-level = 1000, Slope = 34°, Packaging Density = 20 pcf

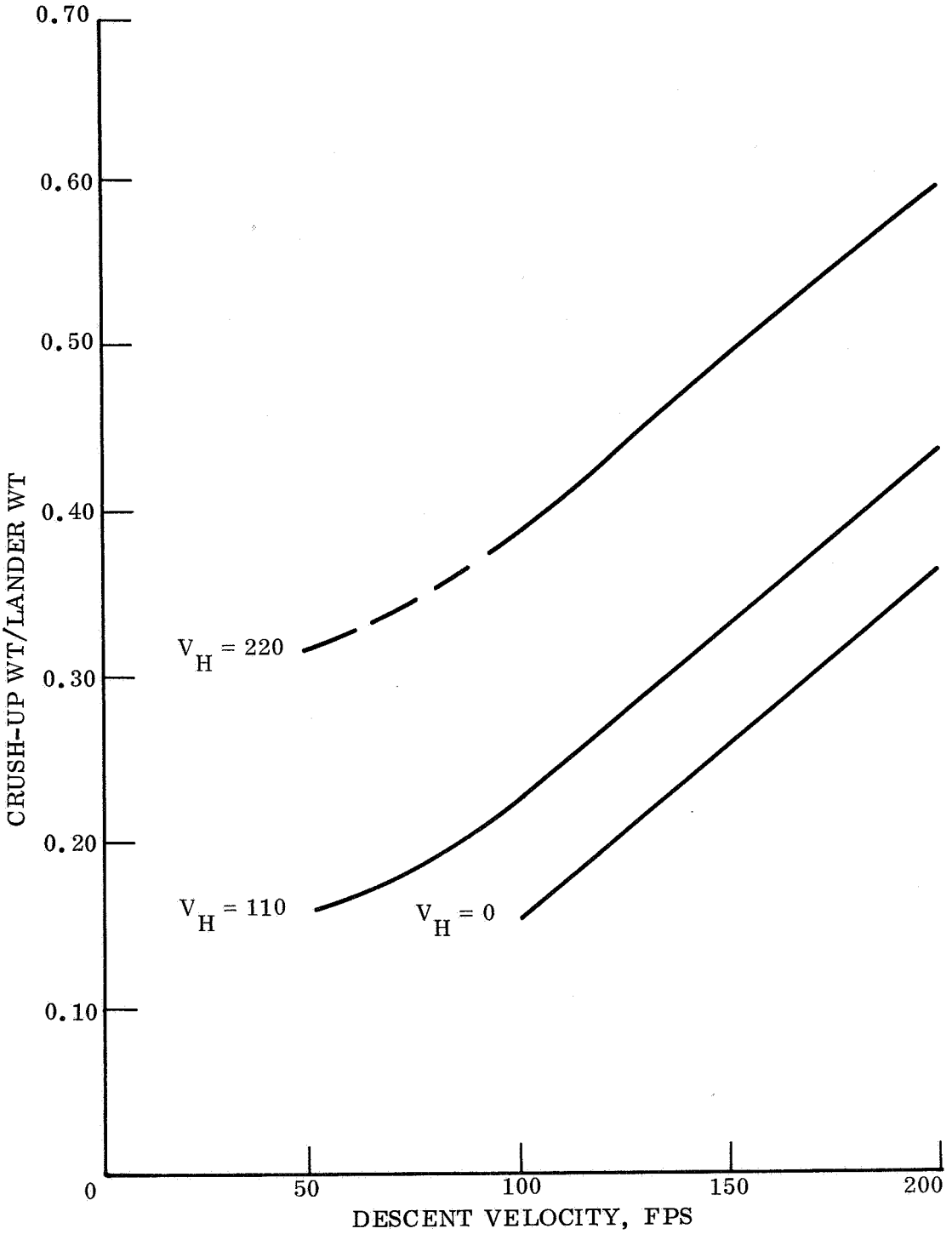

Figure 4.5.5-64. Crush-up Weight for Multi-directional Lander, Lander Wt = 600 lb, g-level = 1000, Slope = 34°, Packaging Density = 40 pcf

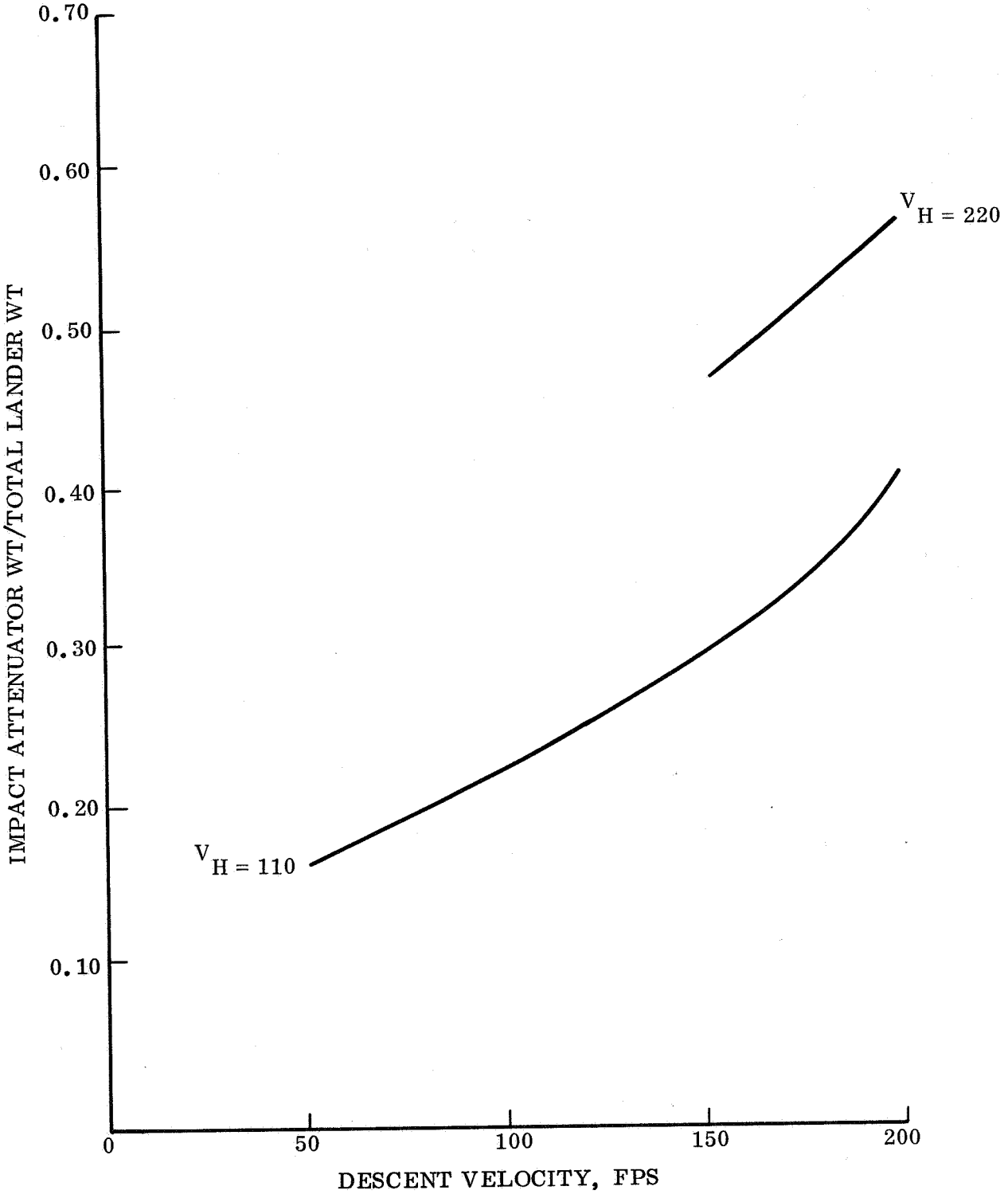

Figure 4.5.5-65. Crush-up Weight for Multi-directional Lander, Lander Wt = 600 lb, g-level = 1000, Slope = 34^{o}, Packaging Density = 60 pcf

4.5.5.2 Lander Map Parametric Synthesis

The second quadrant of the mission maps used in parametric synthesis introduces the requirements of the impact attenuation subsystem. Because this quadrant represents an important intermediate step between entry/retardation requirements and landed subsystem definition, the trends and associated mission significance merit elaboration. Presented in figs. 4.5.5-66 through 4.5.5-80 are Lander maps for the representative touchdown conditions indicated in the accompanying legends. The data given is summarized for reference in table 4.5.5-2.

The basic curves relate, for both the multi-directional and omni-directional Lander concepts, the decelerator load to the total weight of landed subsystems (including the container steel structure). By introducing the operating rigid body g-level as a parameter, a family of curves for each Lander results. Finally, Lander weight trends are incorporated as a family of lines parallel to the abscissa.

For any Lander map, two trends are evident. The first is that the curve families for the omni-directional Lander lie above those for the multi-directional Lander. The significance of this is that for a fixed decelerator load (and, consequently, fixed Lander weight) one can land more total subsystems on the planet with the uni-directional Lander than with the omni-directional Lander. The second trend is that increases in total landed subsystems produce greater increments in Lander weight (and decelerator load) for omni-directional than for multi-directional Landers.

TABLE 4.5.5-2. PRESENTATION OF LANDER MAPS

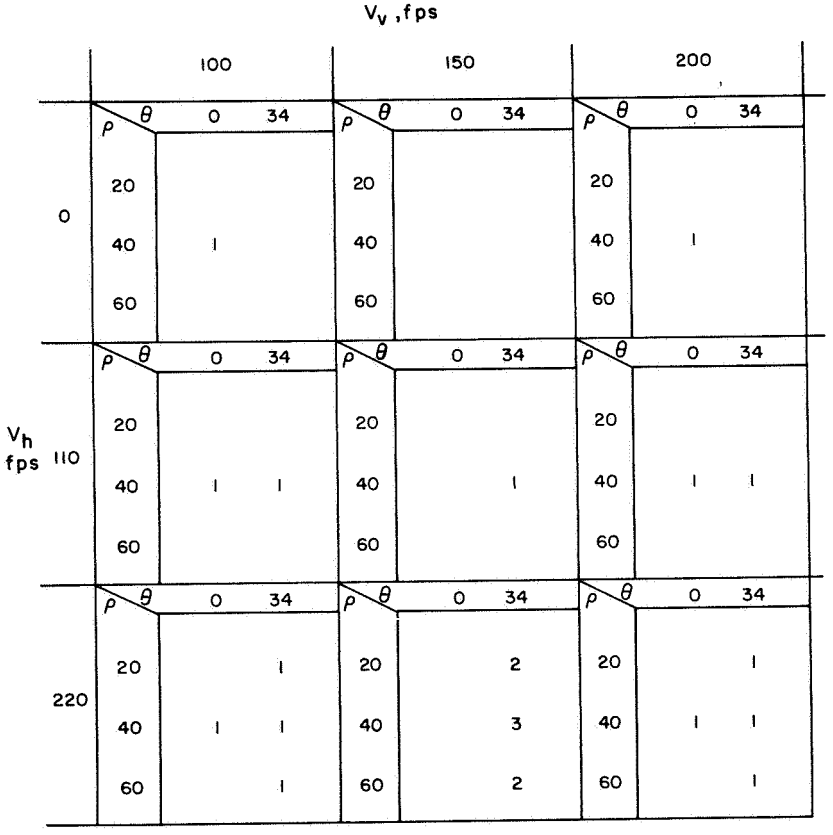

LEGEND: 1. 5" ROCKS
2. NO ROCKS
3. BOTH

Other conclusions may also be drawn from the Lander maps. If, for example, one chooses a decelerator load (hence a Lander weight), and fixes the g-level, he can compare omni-directional and multi-directional designs directly. For example, refer to fig. 4.5.5-66. For the touchdown conditions of the figure, assume a decelerator load of 820 lbs is specified (from a quadrant one mission map). Then the associated Lander weight is about 660 lbs. For a g-level of 1000 g's, a multi-directional vehicle can land 500 lbs of subsystems plus container; an omni-directional vehicle can land 450 lbs of subsystems including the container. The general superiority of the multi-directional shape is apparent, but the container geometry must be entered into the problem.

The weight of the container is included in the total landed subsystems. As one lands more science subsystems, a larger volume and hence, a larger, heavier container is required. As a result, the difference in landed science subsystems weight will not be as large as the difference in total landed weight. In general the difference in science landed weight for the two designs is about 60 percent of the difference in total landed weights.

Other significant trends can be identified with the aid of fig. 4.5.5-81. If fig. 4.5.5-66 is entered with the same decelerator load but with a lower g-level, the crushing stress and the container weight fraction will be reduced. The difference in the weight fractions for comparable omni-directional versus multi-directional landed weights is not as large, and therefore, the multi-directional Lander becomes more and more favorable. Alternately, if higher g-levels are compared the crushing stress increases and the container weight fraction increases. The difference in the weight fractions for comparable omni-directional and multi-directional landed weights becomes larger and the multi-directional Lander, while still preferable, is superior by a diminishing weight margin. Another way of phrasing this is to say that at the higher g-levels, one tends to be landing increasing heavy containers at the expense of landed science subsystems in order to protect these very subsystems.

Comparisons between Lander maps can also be drawn. See for example, figs. 4.5.5-66 through 4.5.5-68 which represent a wind velocity of 110 fps, 5 in. rocks, a 34° slope angle, 40 lbs/ft^3 landed science subsystem density, but differing vertical velocities of 100, 150 and 200 fps. It is noted that in general for both Lander types, the families of curves for the $V_D = 200$ fps case lie above those for $V_D = 150$ fps, which in turn lie above the $V_D = 100$ fps curves for corresponding g-levels. By the same reasoning discussed in comparing omni-directional to multi-directional Landers directly, one can say that for a given decelerator load (and Lander weight) one can land more subsystems as the descent velocity V_D is reduced. Also seen from figs. 4.5.5-66 through 4.5.5-68 is that changes in the operating g-level are more significant as the descent velocity increases. This is best seen by use of a particular numerical example. Assume a multi-directional Lander with a decelerator load of 800 lbs. If $V_D = 100$ fps an increase in operating g-level from 900 to 1000 g's increases the total landed weight from 478 to 485 lbs, or 7 lbs. At $V_D = 150$ fps, the difference is 460 to 475 lbs, or 15 lbs, and at $V_D = 200$ fps, the increase is from 365 to 395, or 30 lbs of total landed subsystem weight. Finally, some comparison may be drawn between maps in figs. 4.5.5-68 and 4.5.5-69. For these

maps, the conditions are similar except that the slope is 0° in fig. 4.5.5-69. A comparison of the curve families again shows the two sets of curves in fig. 4.5.5-69 to lie below those of fig. 4.5.5-68 indicating that, in general, a weight penalty is required for gaining increased slope capability. Comparison of figs. 4.5.5-66 and 4.5.5-67 with fig. 4.5.5-69 will reinforce and emphasize this comparison. Fig. 4.5.5-69 also emphasizes another point. Examination of the curves shows that the three g-levels are almost indistinguishable from one another. The reason for this is that the attenuator volume for these particular touchdown conditions is sized predominantly by the rock protection criterion and as a result, the g-level is of secondary significance. If the rock constraint were eased, the g-level effect would become more pronounced as in the other maps.

4.5.5.3 Substructure and Container

The conceptual design for packaging of landed science and systems components is based on a cylindrical flat disc type container structure. The container consists of the cylindrical wall with an "egg-crate" type structure composed of beams and webs to support the components in mutually orthogonal directions so as to provide for omni-directional impact conditions of the Lander.

The container is then installed within a toroidal substructure which sustains the impact loading, due to crushing of fiberglass honeycomb attenuation material. The cylindrical wall thus forms an interface between the attenuator impact loading and the component inertia.

4.5.5.3.1 Structural Loading and Parameters

Substructure - The substructure is subjected to crushing stresses due to impact attenuation. The crushing stress is a function of the impact velocity and deceleration level and is determined by selecting a suitable honeycomb density. For omni-directional impact, the loading conditions of the toroidal ring are shown in the illustrations below:

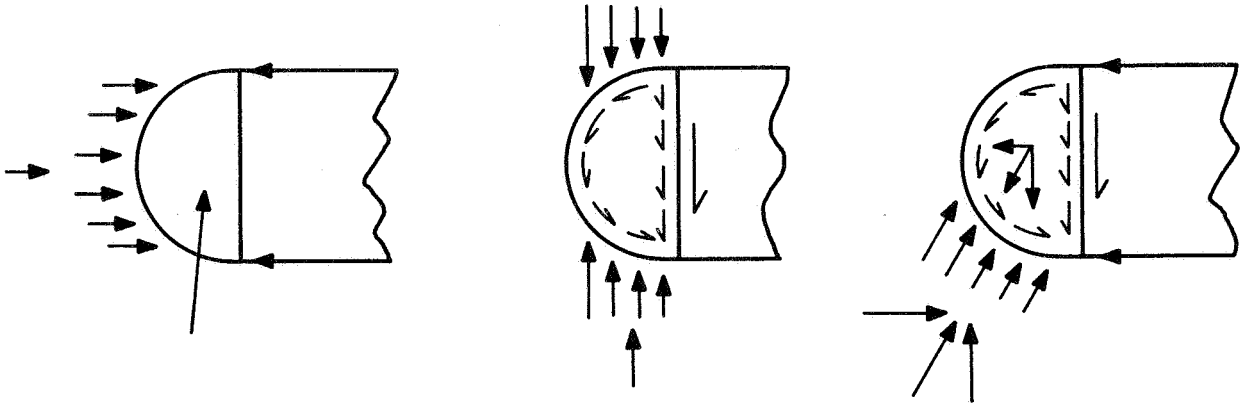

a. Edgewise Impact b. Flat-wise Impact c. Angular Impact

The critical loading thus occurs in the edgewise impact case. The angular impact case can be treated as a combination of the edgewise and flatwise cases. The toroid section is assumed to be semicircular and subjected to external crushing pressure. An ultimate factor of 1.25 was applied.

Honeycomb sandwich construction using aluminum alloy is considered as baseline since it provides an optimum structure to satisfy both strength and stiffness requirements.

Parametric Analysis - The primary loading parameter for the substructure is the attenuation of crushing stress. Secondary parameters are total landed weight (excluding attenuation weight) and maximum deceleration level. The geometric parameters are defined by the container diameter and height. The toroid section radius is taken as half the container height.

The parameters and their ranges are:

Crushing Stress:	600 to 1900 lb/in^2
Landed Weight:	200 to 1000 lb
Deceleration Level:	500 to 3000 Earth g's.

Analysis

For a circular torus section the strength and buckling critical structural thicknesses are given by:

for strength: $$t = \frac{P \times F \times r}{f_{allow}}$$

for buckling: $$p = \frac{E_e}{4\,(1 - \upsilon^2)} \left(\frac{t_e}{r}\right)^3$$

P = crushing stress, lb/in^2

F = ultimate factor

r = radius of torus

f_{allow}

e = effective

For honeycomb sandwich construction: with face sheet thickness t_f each and core thickness t_c,

$$t = 2\,t_f$$

$$t_e = \sqrt{3}\,(t_f + t_c)$$

$$E_e = \frac{2\,E_f\,t_f}{t_c}$$

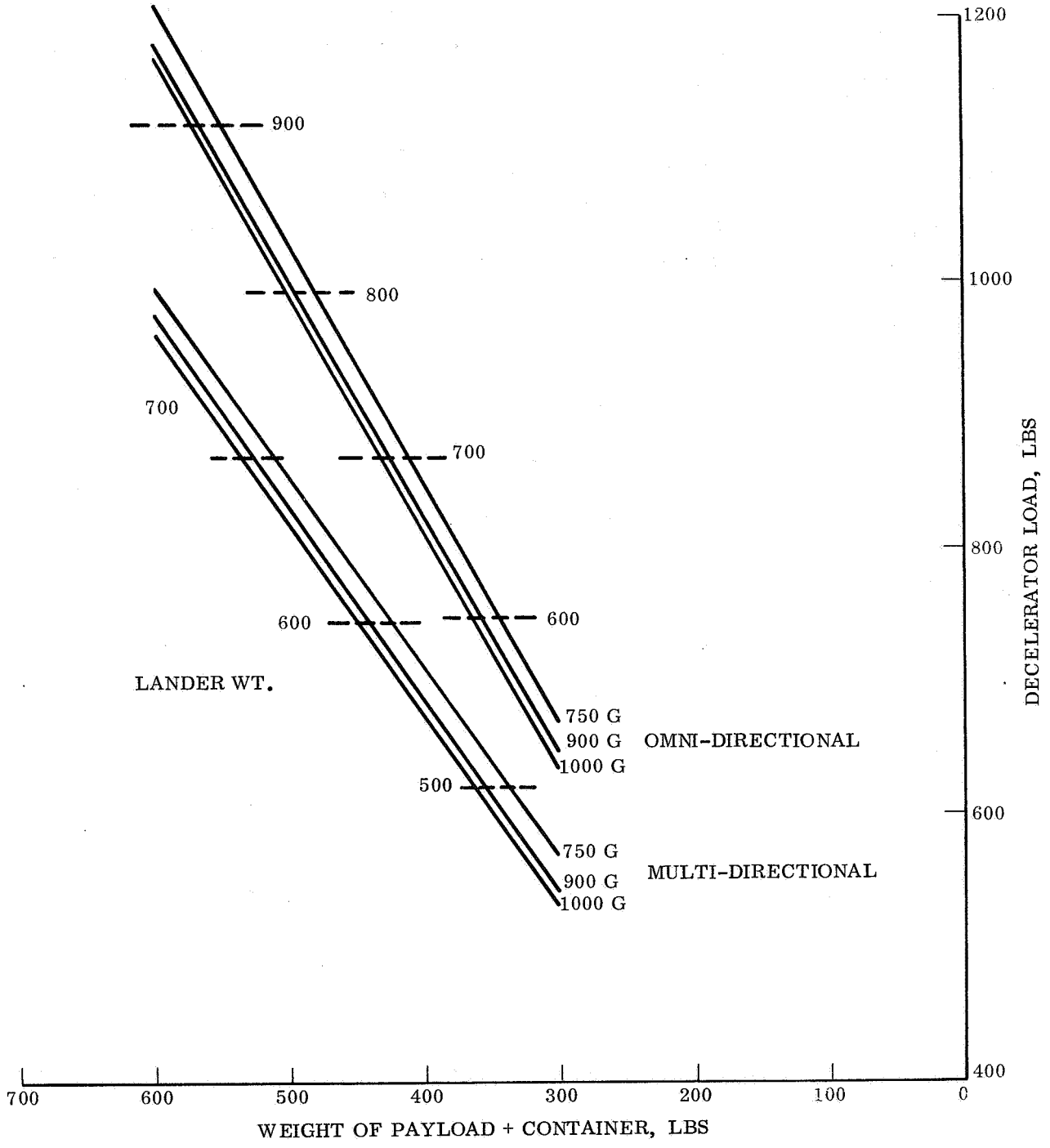

Figure 4. 5. 5-66. Impact Attenuation Lander Map for V_{wind} = 110 fps, $V_{descent}$ = 100 fps, Slope Angle = 34^{0}, Payload Density = 40 pcf, Rocks = 5 in.

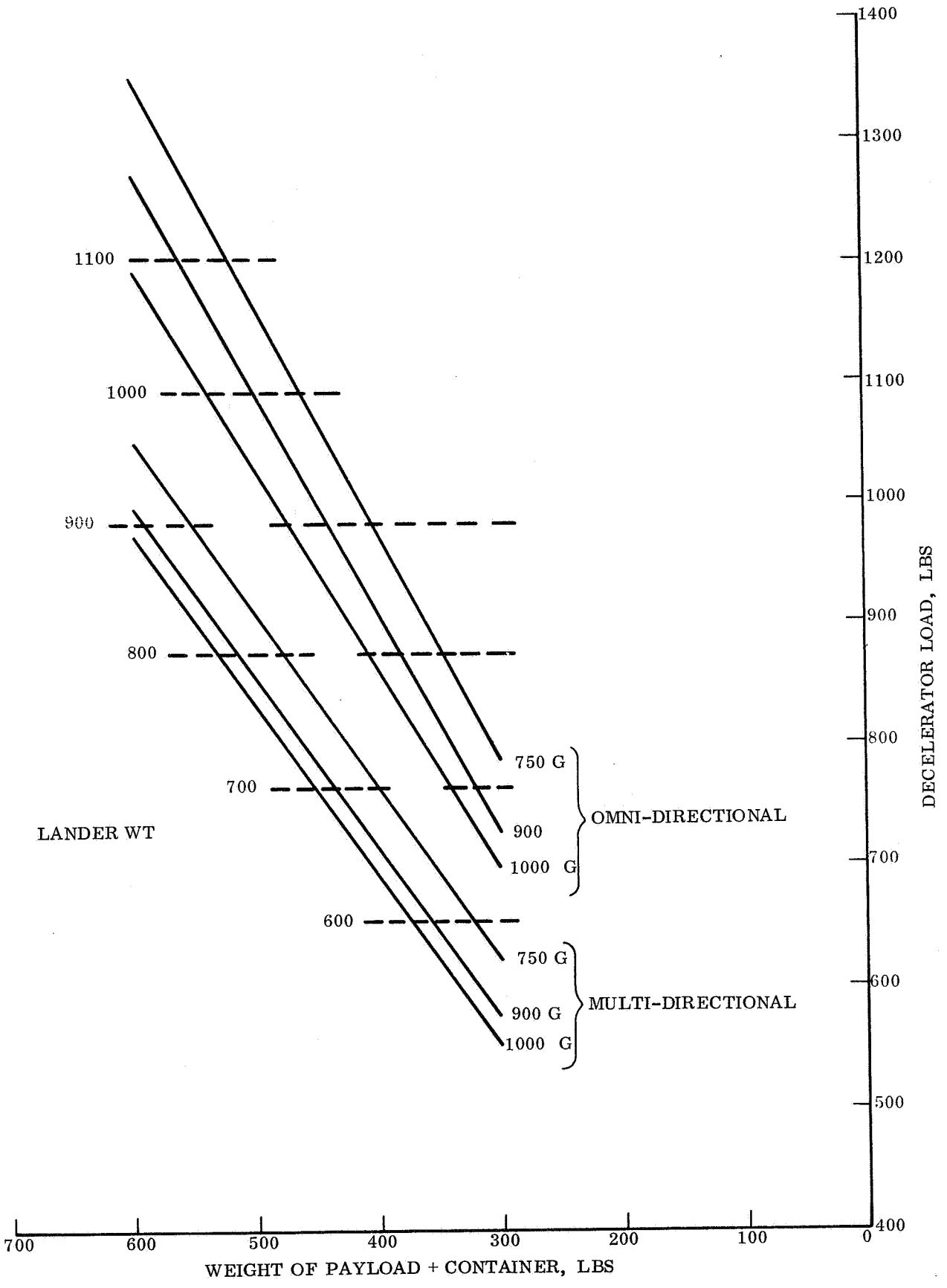

Figure 4. 5. 5-67. Impact Attenuation Lander Map for V_{wind} = 110 fps, $V_{descent}$ = 150 fps, Slope Angle = 34°, Payload Density = 40 pcf, Rocks = 5 in.

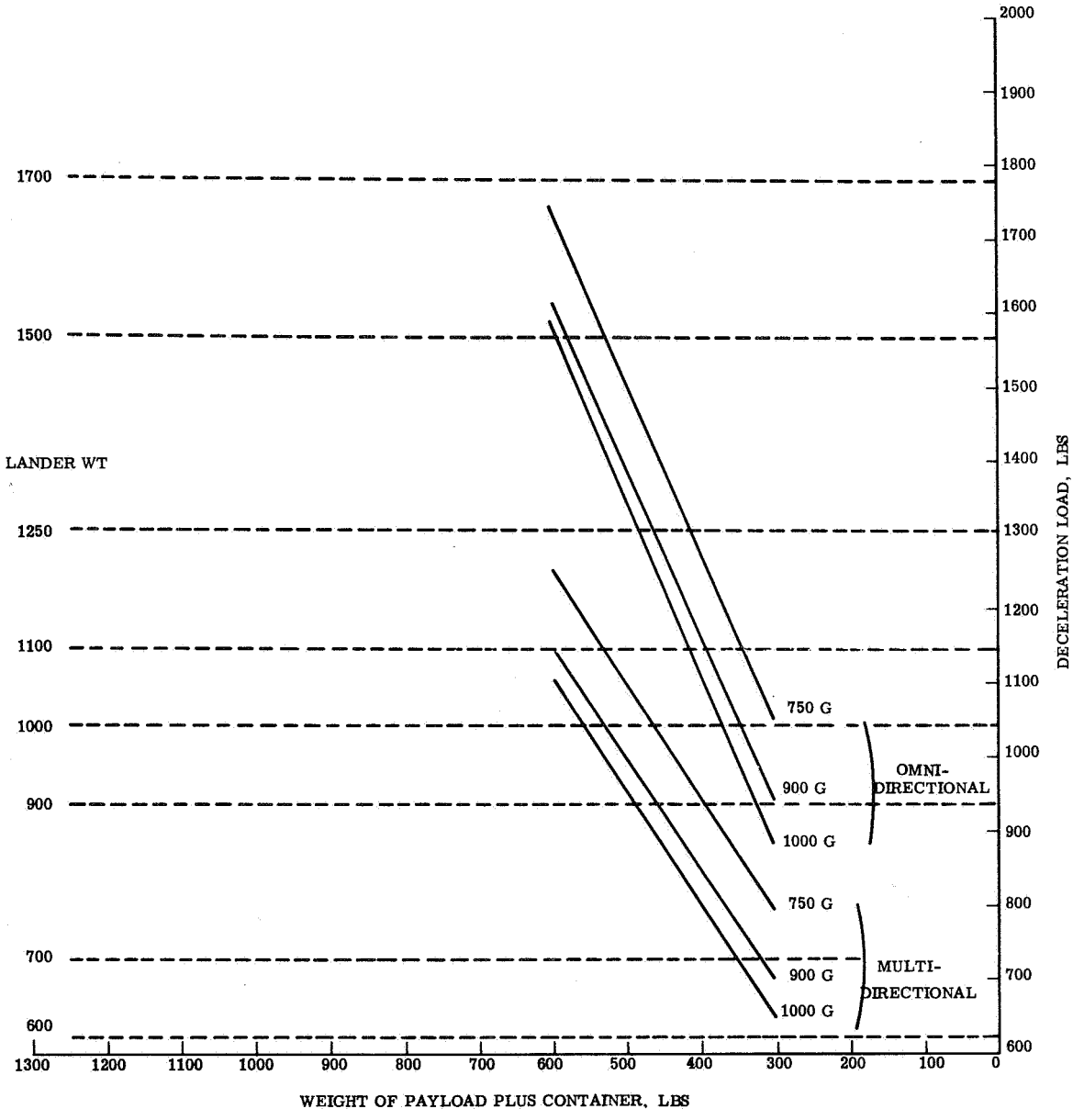

Figure 4.5.5-68. Impact Attenuation Lander Map for V_{wind} = 110 fps, $V_{descent}$ = 200 fps, Slope Angle = 34°, Payload Density = 40 pcf, Rock = 5 in

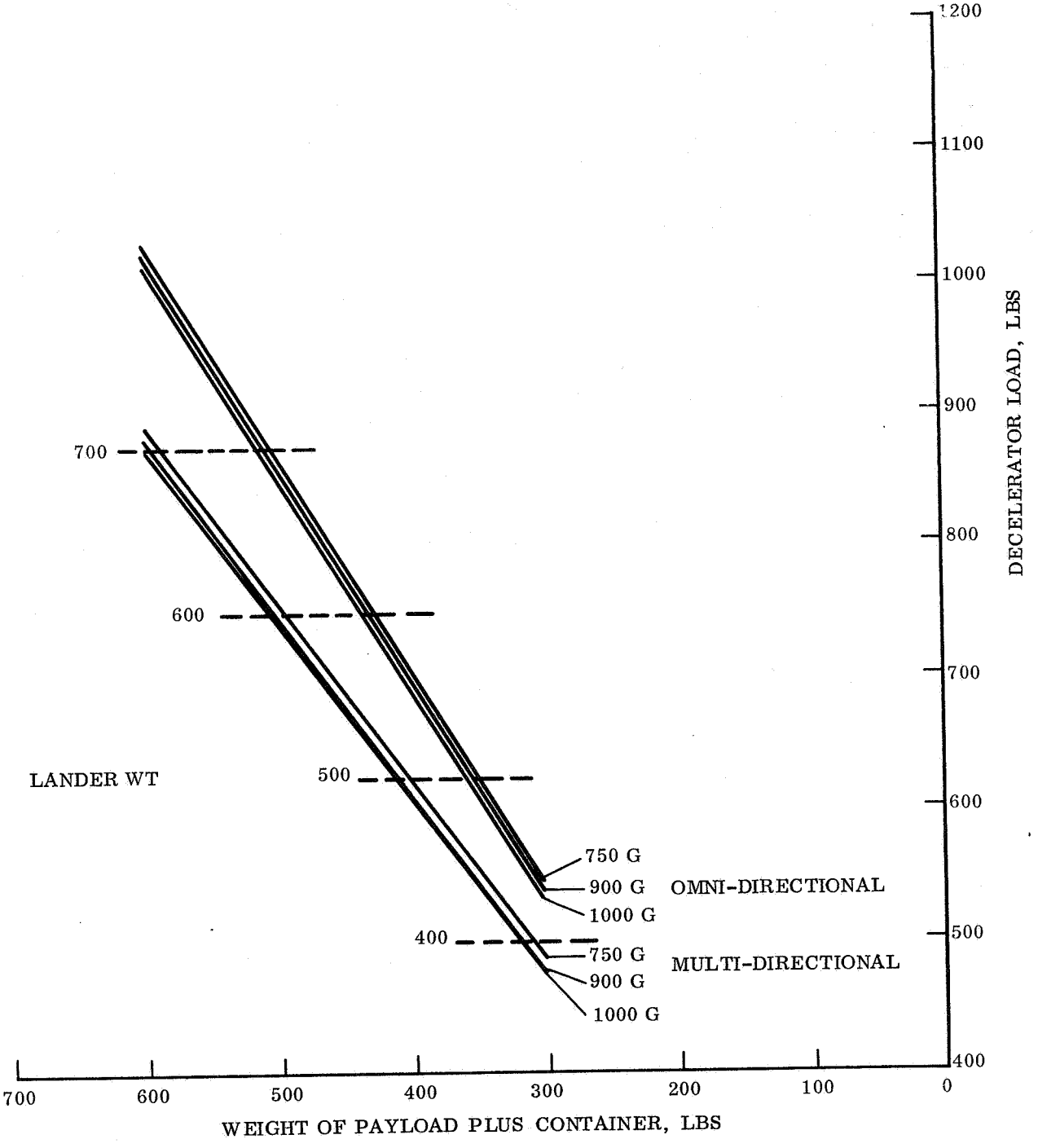

Figure 4.5.5-69. Impact Attenuation Lander Map for V_{wind} = Arbitrary, $V_{descent}$ = 100 fps, Slope Angle = 0°, Payload Density = 40 pcf, Rocks = 5 in.

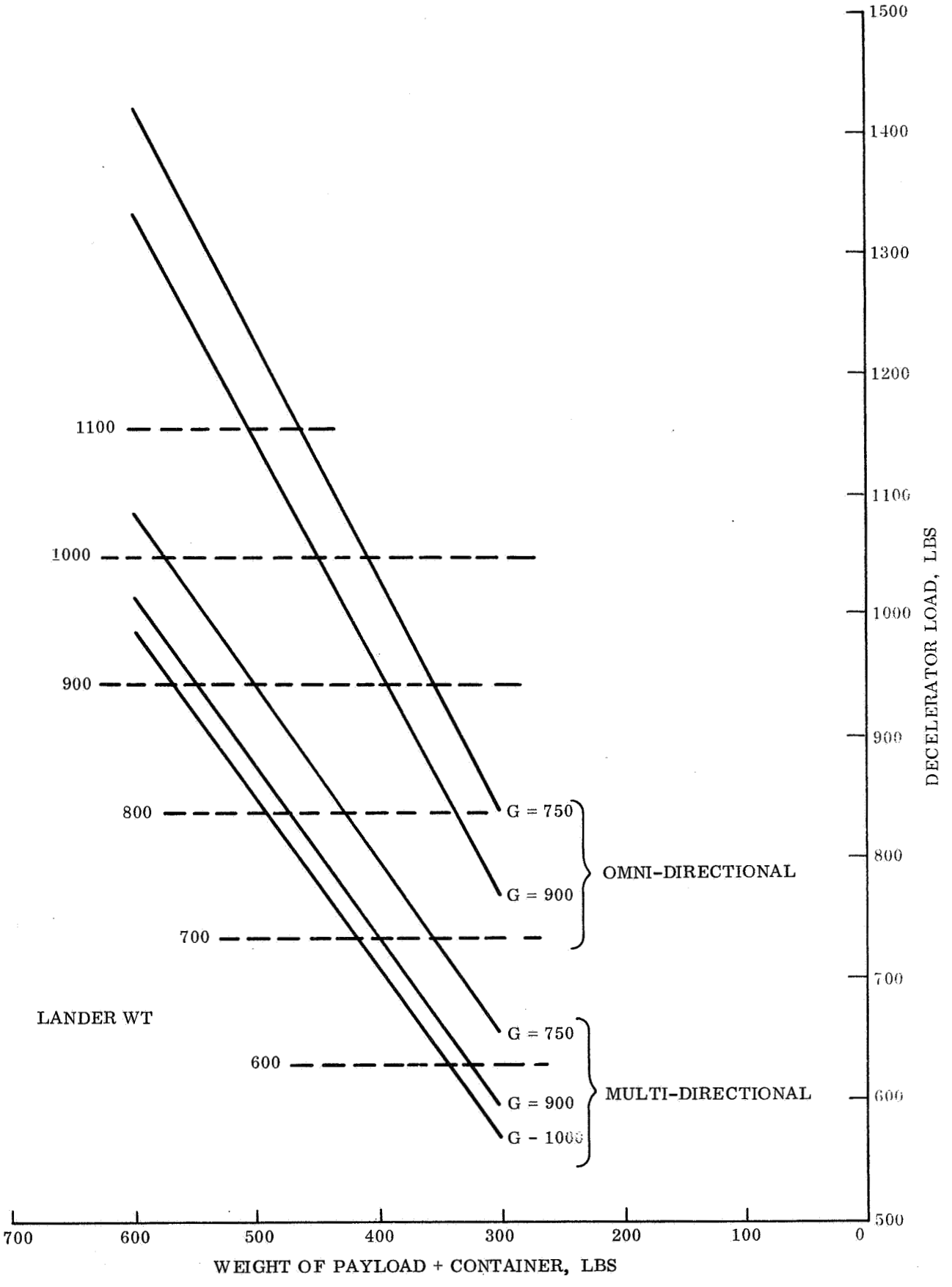

Figure 4. 5. 5-70. Impact Attenuation Lander Map for V_{wind} = Arbitrary, $V_{descent}$ = 200 fps, Slope Angle = 0^{o}, Payload Density = 40 pcf, Rocks = 5 in.

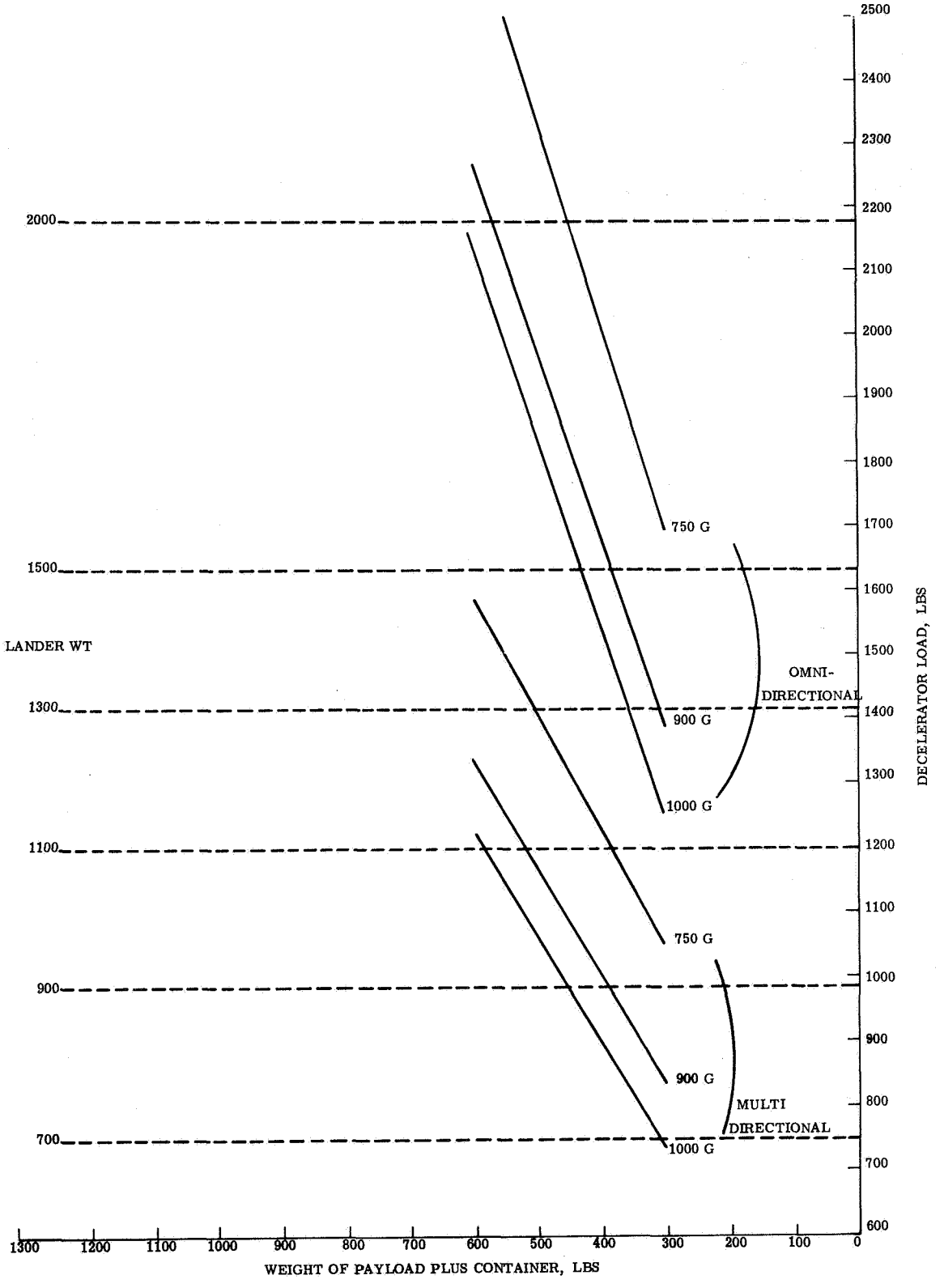

Figure 4.5.5-71. Impact Attenuation Lander Map for $V_{wind} = 220$ fps, $V_{descent} = 150$ fps, Slope Angle = 34°, Payload Density = 20 pcf, Rocks = 0 in.

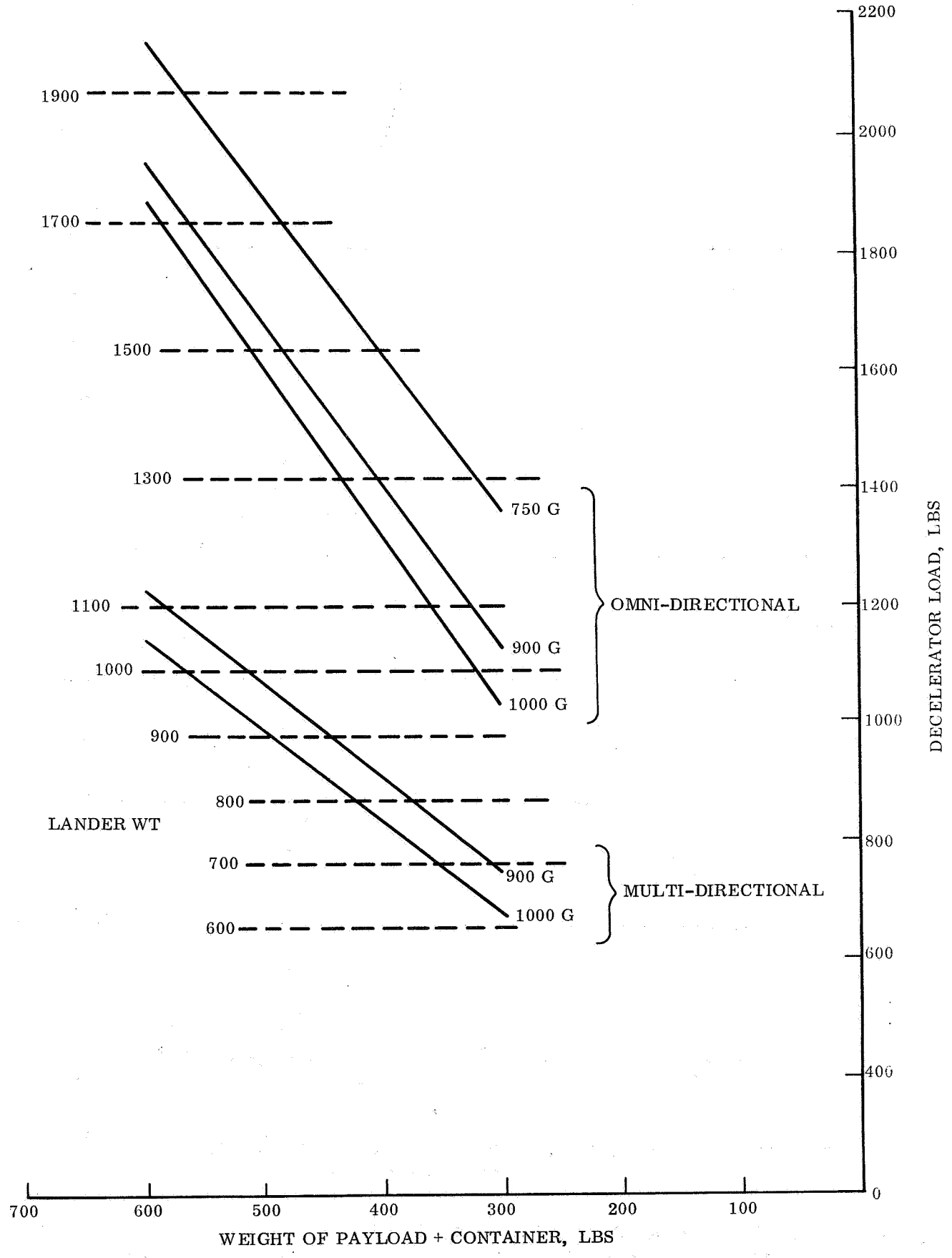

Figure 4.5.5-72. Impact Attenuation Lander Map for V_{wind} = 220 fps, $V_{descent}$ = 150 fps, Slope Angle = 34°, Payload Density = 40 pcf, Rocks = 0 in.

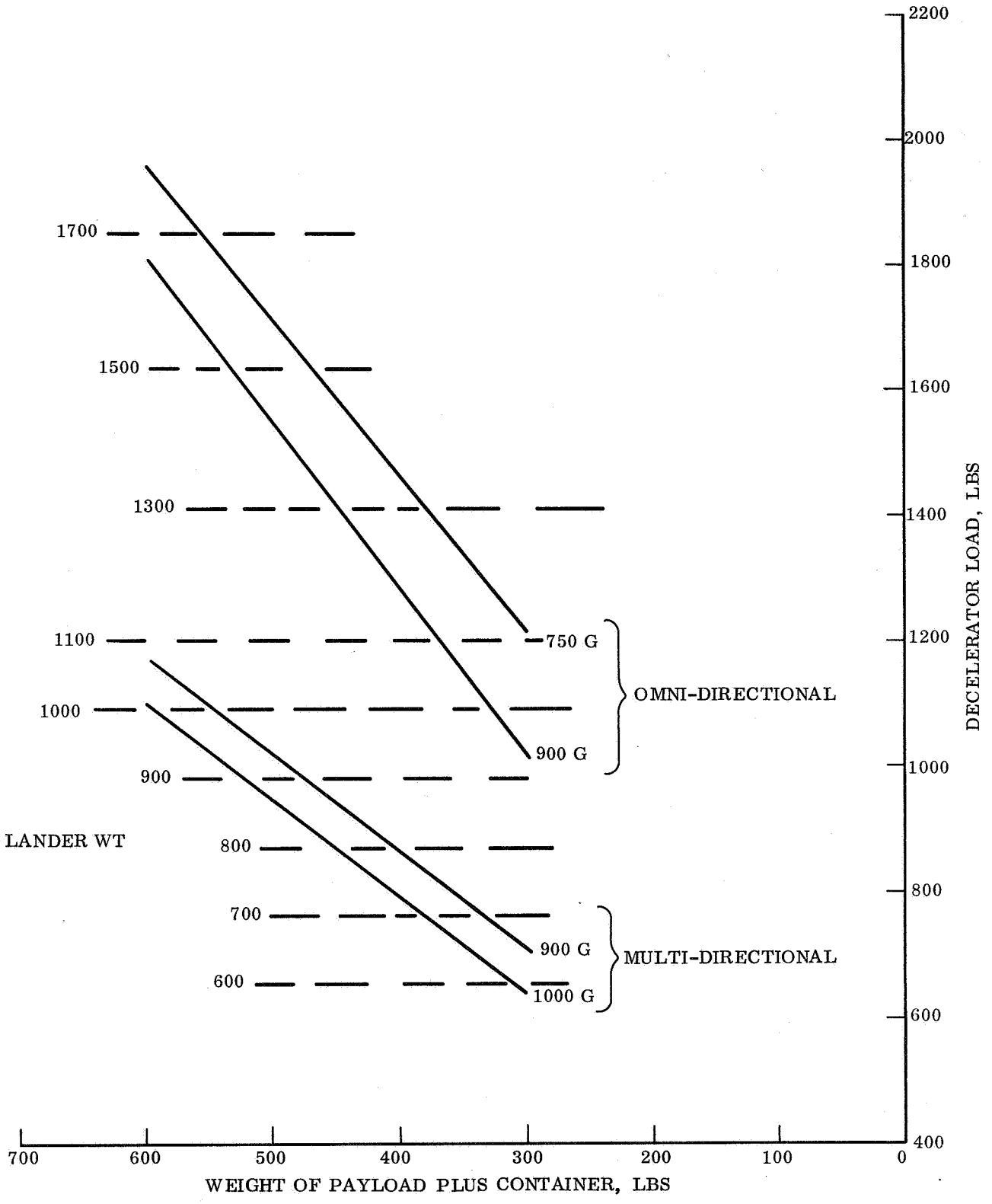

Figure 4.5.5-73. Impact Attenuation Lander Map for V_{wind} = 220 fps, $V_{descent}$ = 150 fps, Slope Angle = 34°, Payload Density = 60 pcf, Rocks 0 in.

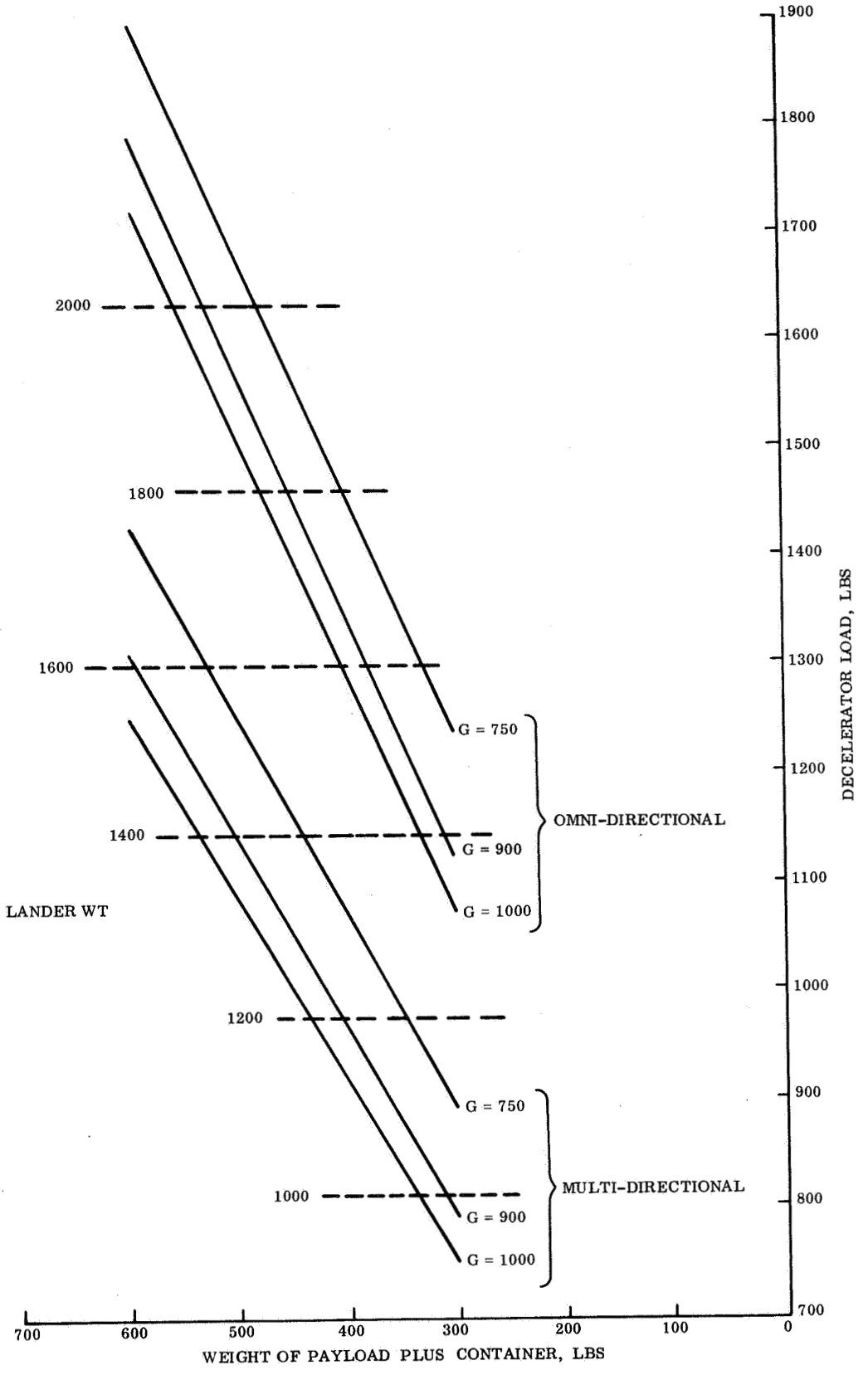

Figure 4.5.5-74. Impact Attenuation Lander Map for $V_{wind} = 220$ fps, $V_{descent} = 100$ fps, Slope Angle = 34°, Payload Density = 20 pcf, Rocks = 5 in.

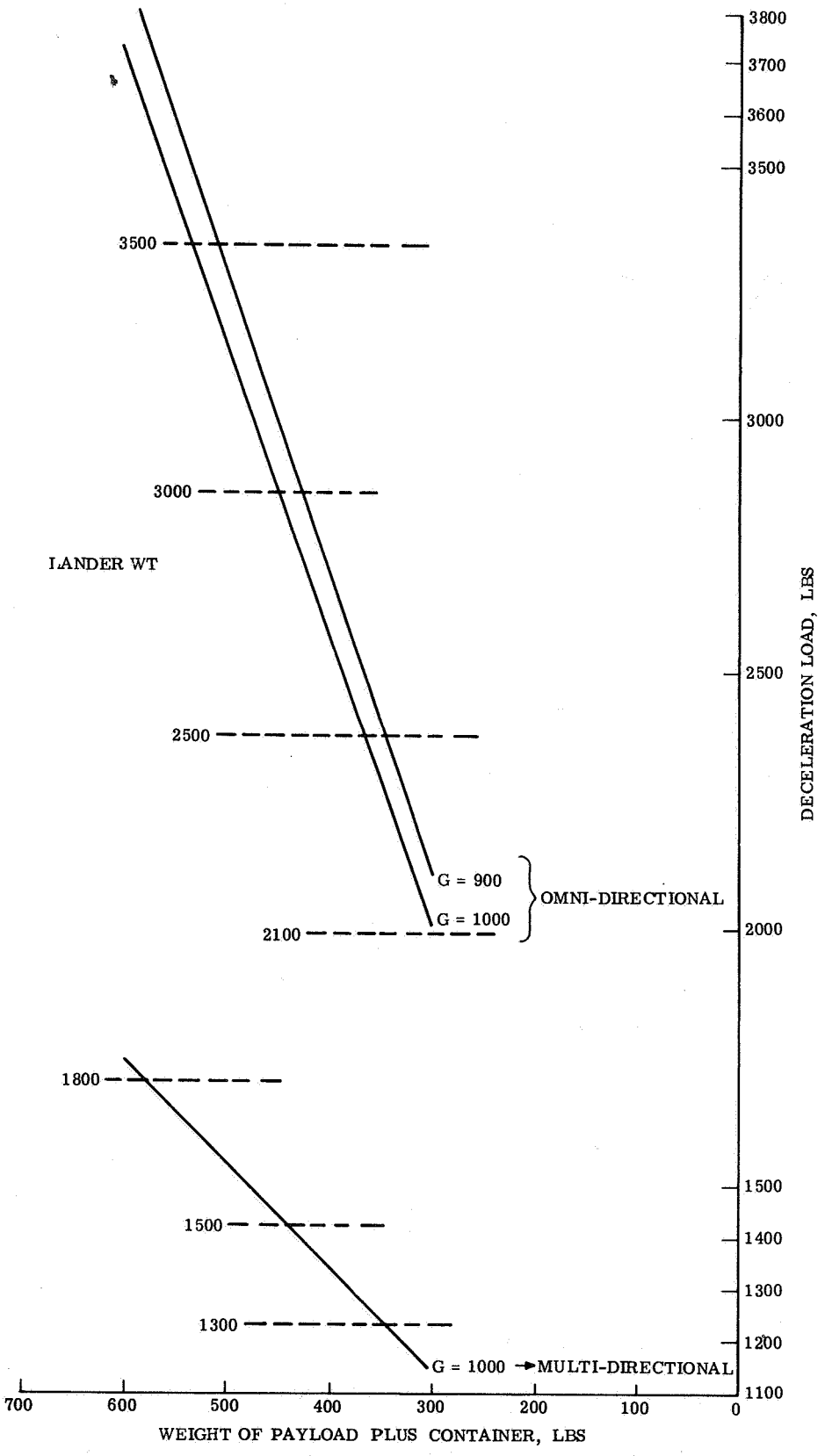

Figure 4.5.5-75. Impact Attenuation Lander Map for V_{wind} = 220 fps, $V_{descent}$ = 200 fps, Slope Angle = 34°, Payload Density = 20 pcf, Rocks = 5 in.

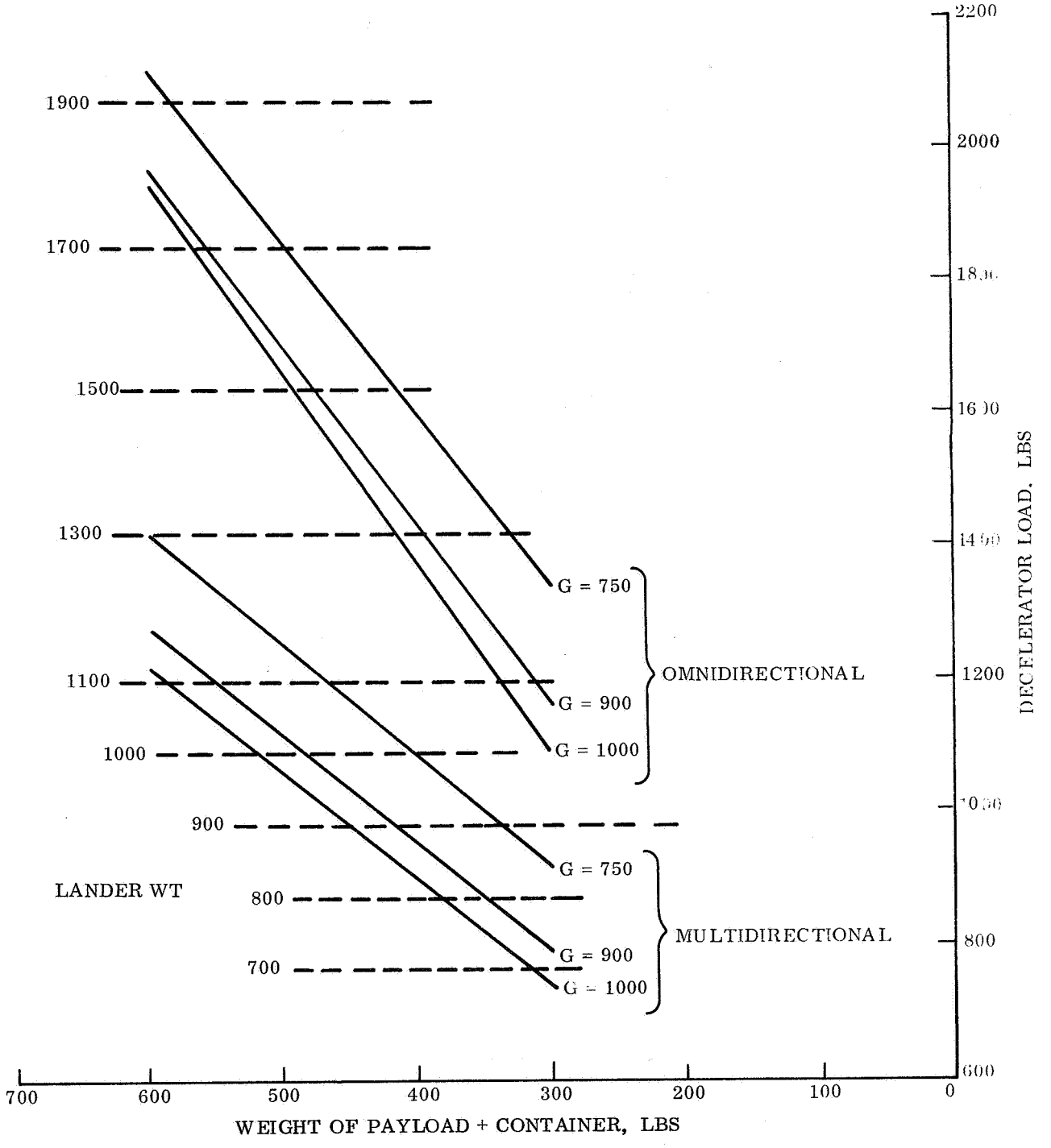

Figure 4. 5. 5-76. Impact Attenuation Lander Map for V_{wind} = 220 fps, Vdescent = 150 fps, Slope Angle = 34°, Payload Density = 40 pcf, Rocks = 5 in.

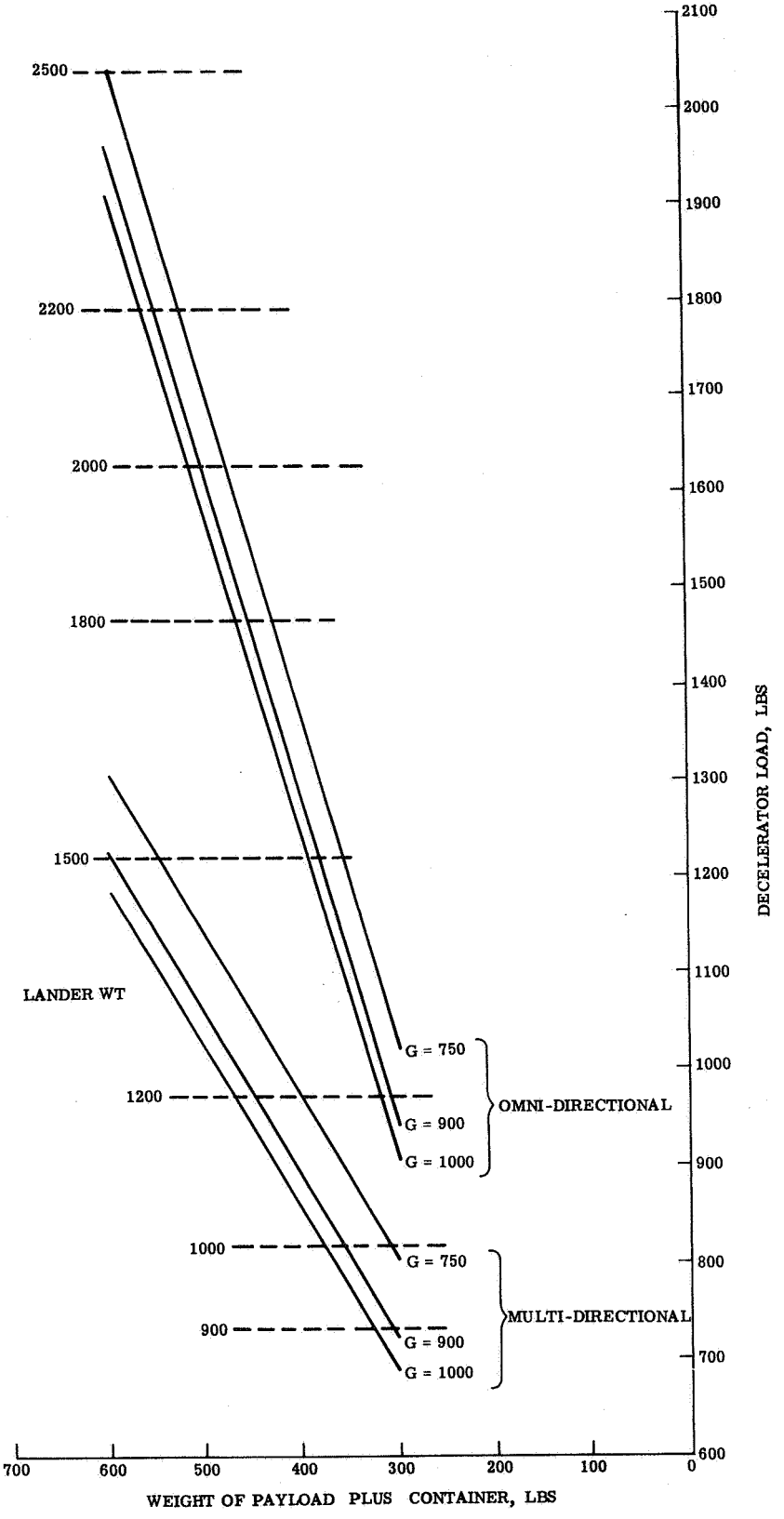

Figure 4.5.5-77. Impact Attenuation Lander Map for V_{wind} = 220 fps, $V_{descent}$ = 100 fps, Slope Angle = 34°, Payload Density = 40 pcf, Rocks = 5 in.

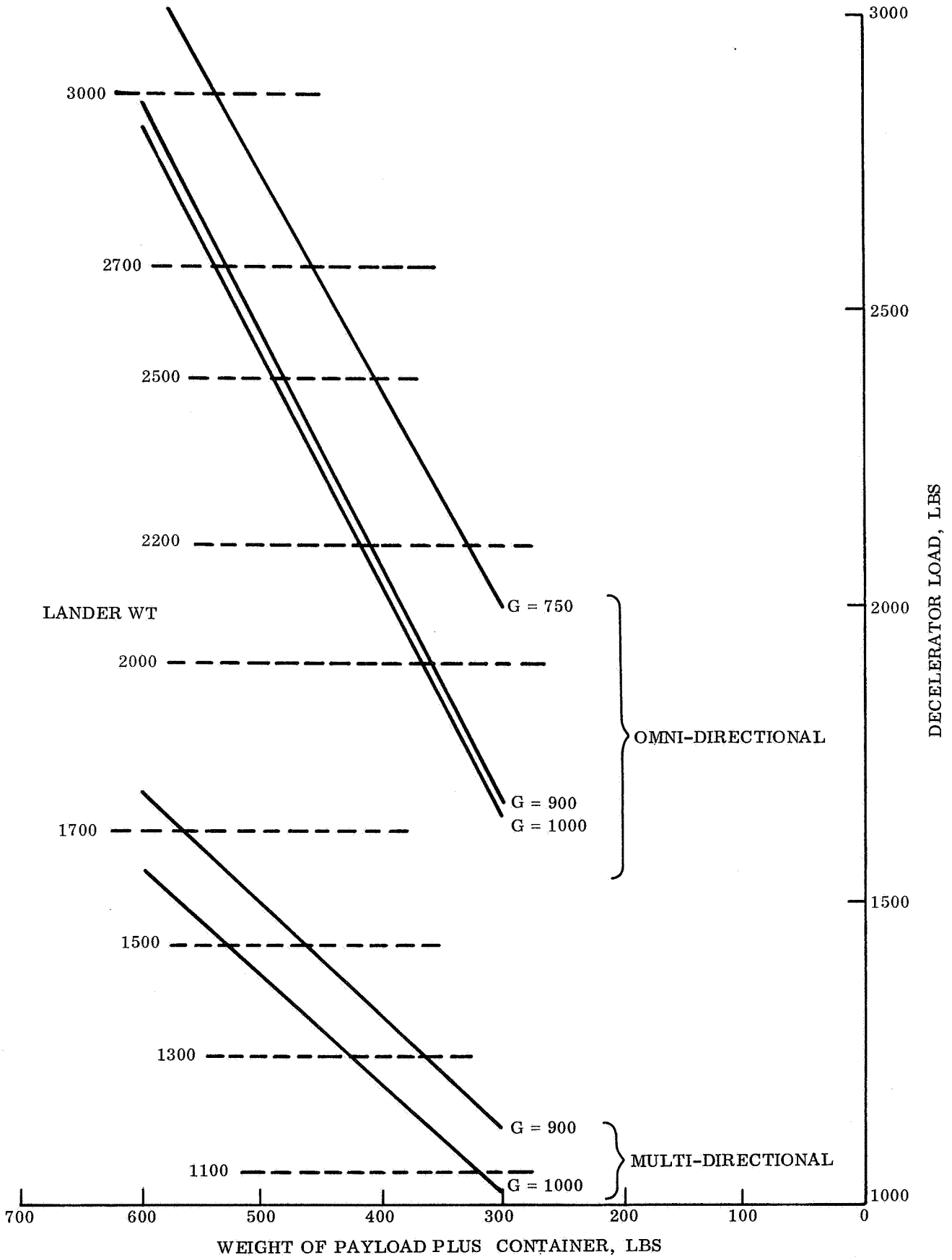

Figure 4. 5. 5-78. Impact Attenuation Lander Map for V_{wind} = 220 fps, $V_{descent}$ = 200 fps, Slope Angle = 34°, Payload Density = 40 pcf, Rocks = 5 in.

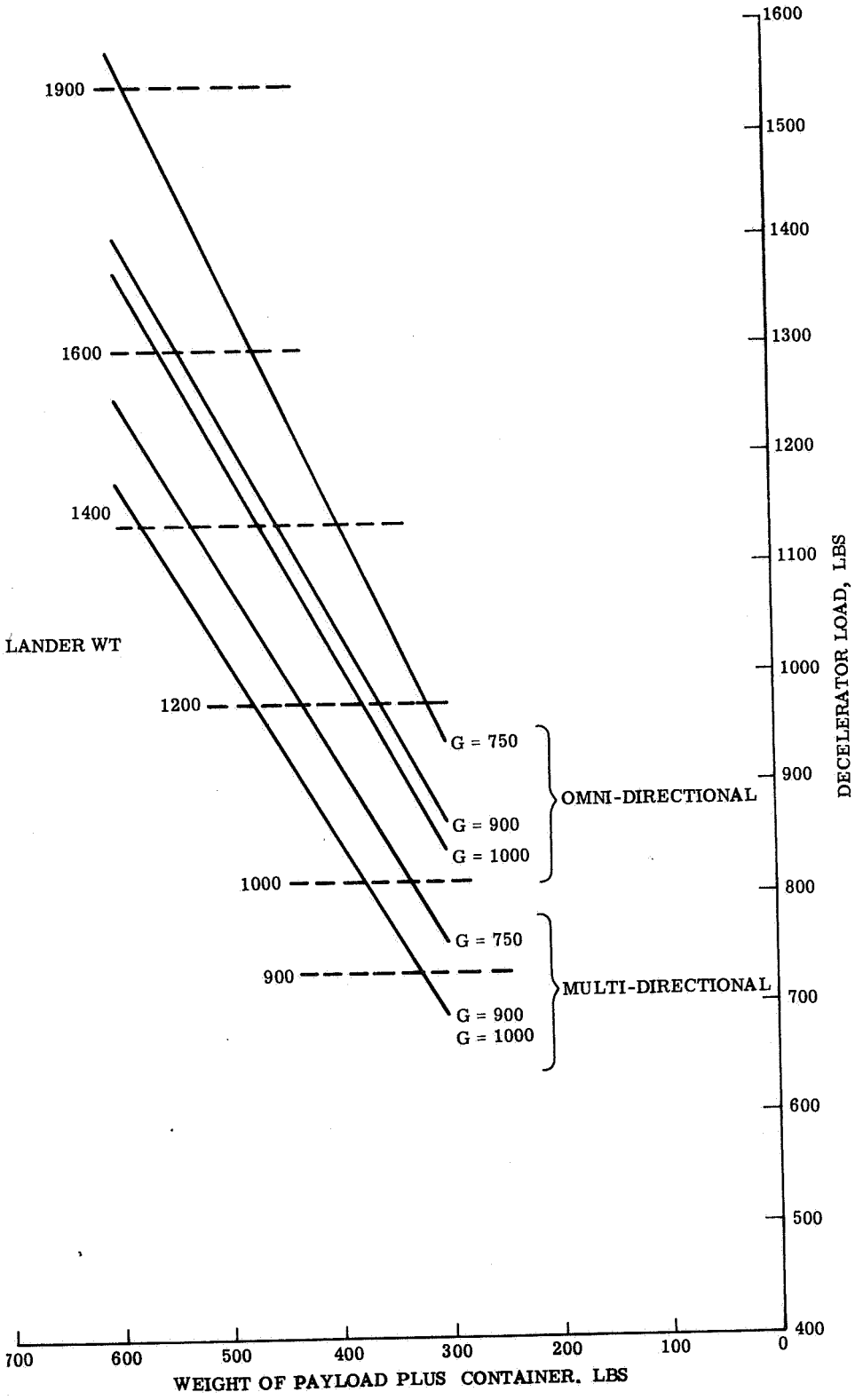

Figure 4.5.5-79. Impact Attenuation Lander Map for $V_{wind} = 220$ fps, $V_{descent} = 100$ fps, Slope Angle = 34°, Payload Density = 60 pcf, Rocks = 5 in.

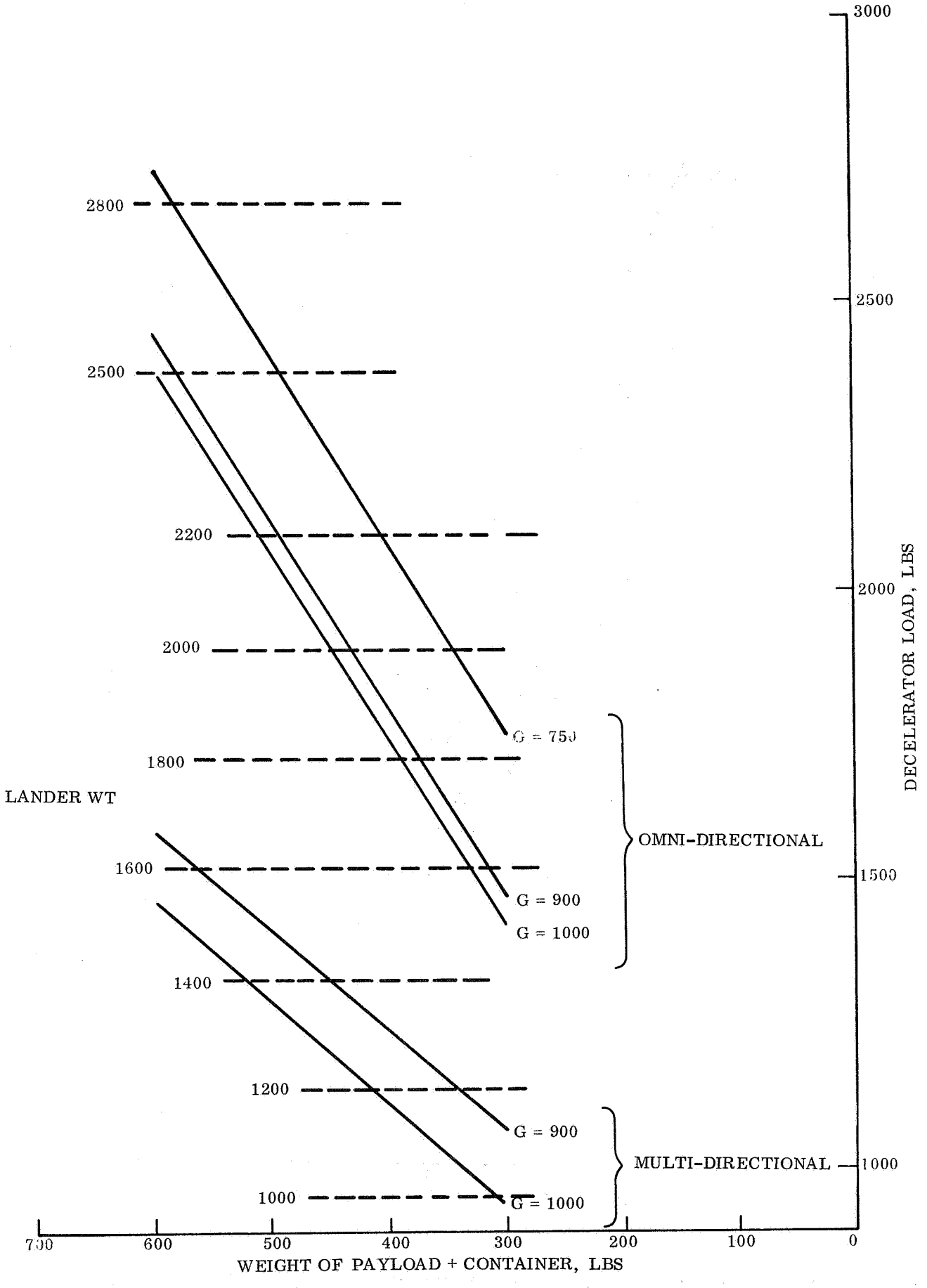

Figure 4. 5. 5-80. Impact Attenuation Lander Map for V_{wind} = 220 fps, $V_{descent}$ = 200 fps, Slope Angle = 34°, Payload Density = 60 pcf, Rocks = 5 in.

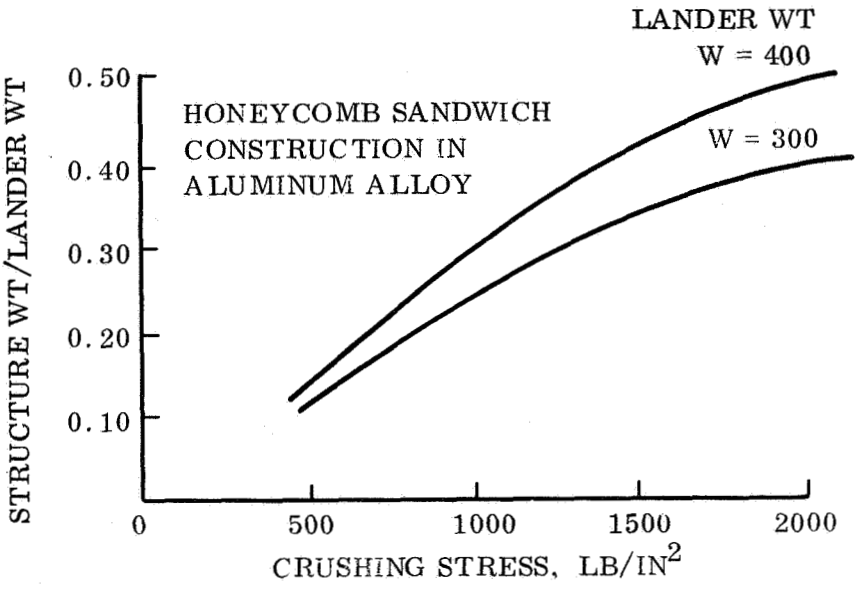

Figure 4.5.5-81. Landed Container Structure Trade-off

Structural weight densities for varying crushing stress and Lander container semi-height are shown in fig. 4.5.5-82.

4.5.5.4 Effect of Rock Size on Attenuator Weight

It was seen from the parametric studies that an increasing penalty is paid for rock protection. To see how pronounced this effect can be, figs. 4.5.5-83 and 4.5.5-84 were generated for rocks of 5, 10 and 15 in. along with the touchdown parameters indicated.

From figs. 4.5.5-83 and 4.5.5-84 it is apparent that a higher penalty in weight is associated with bigger rocks. This effect is most pronounced at the lower impact velocities were the attenuation thickness may be sized by rocks and not by the stroke found from velocity considerations.

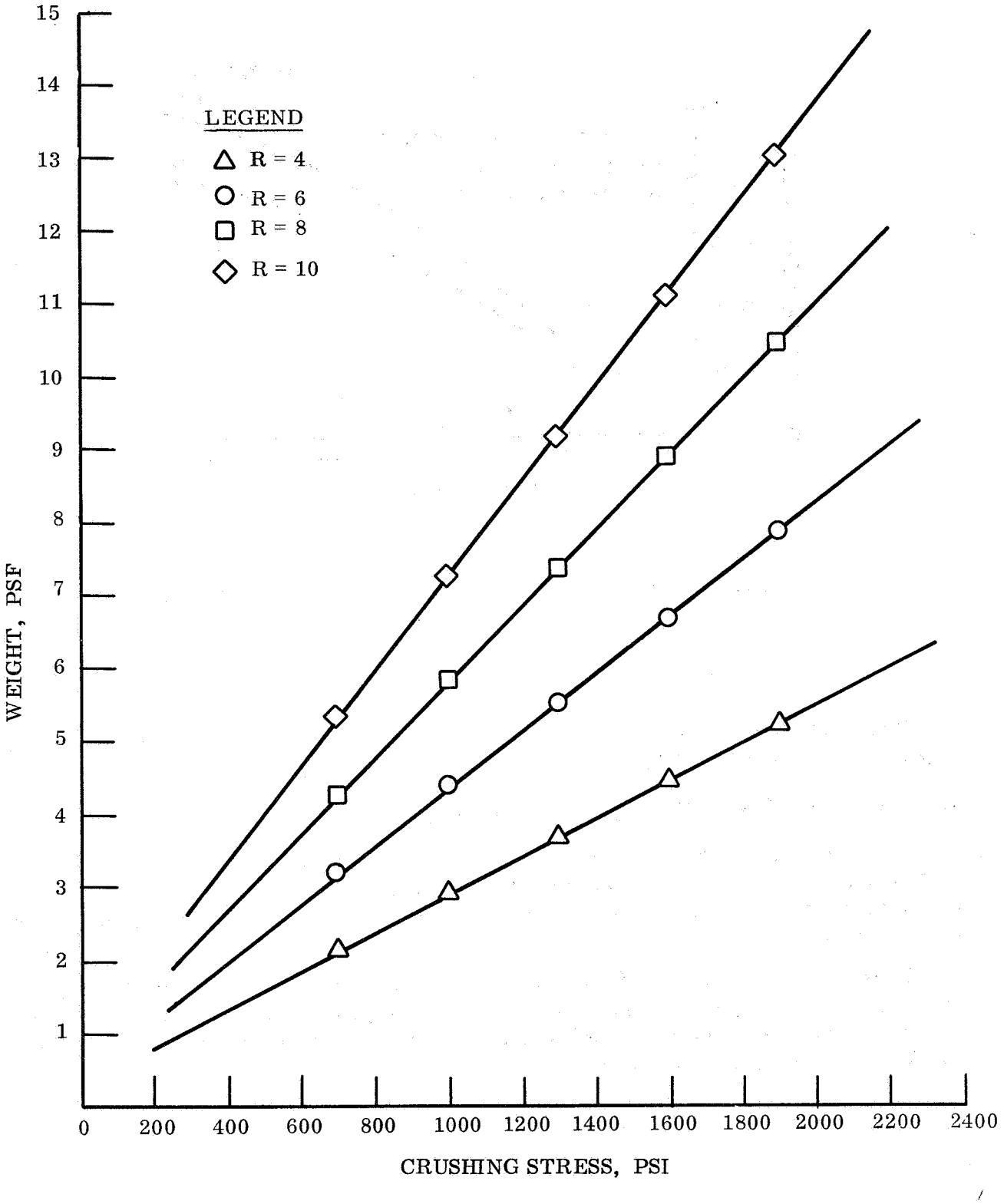

Figure 4.5.5-82. Torus Weight vs Crushing Stress for Various Lander Semi-Heights

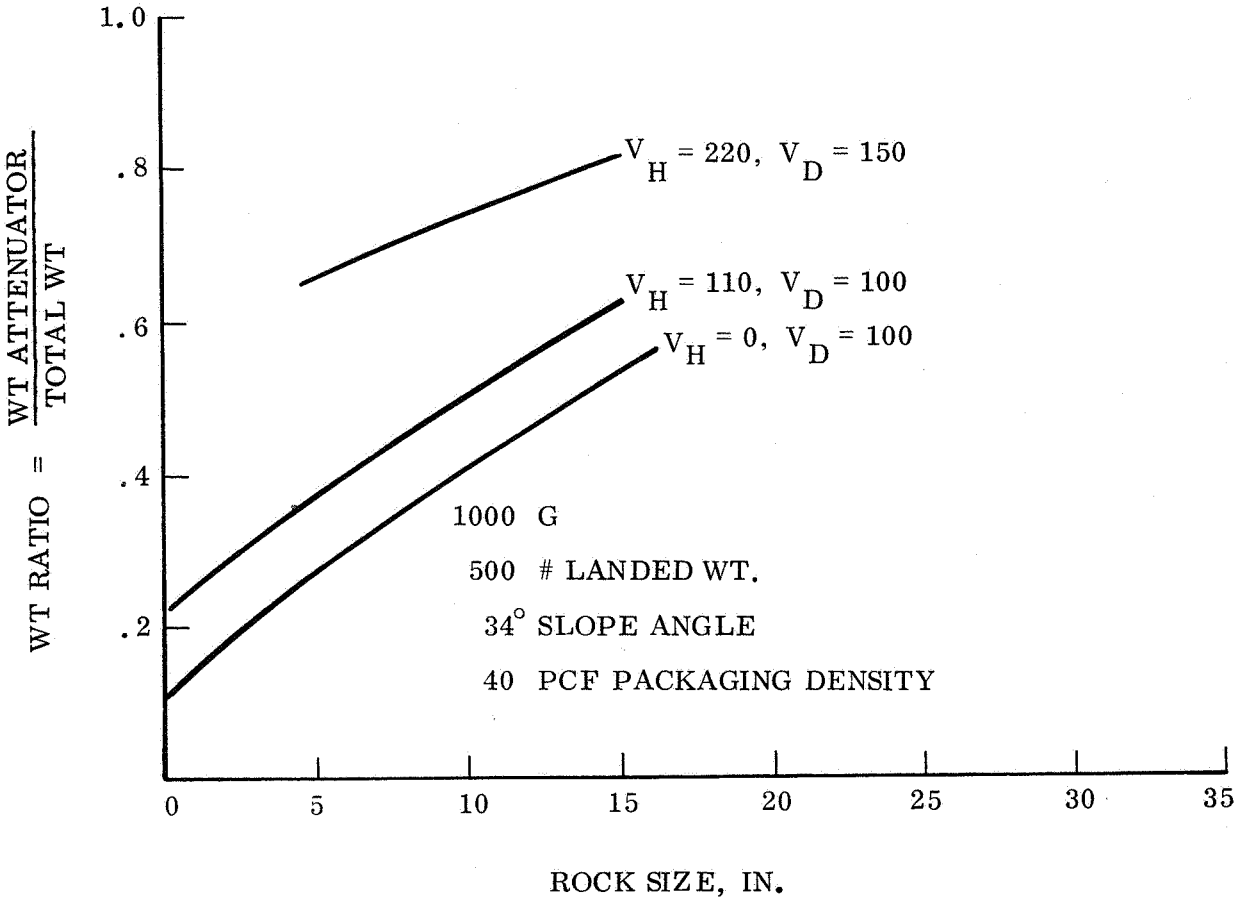

Figure 4.5.5-83. Crush-up Weight as a Function of a Lander Weight for Various Descent Velocities, Omni-directional Lander Configuration

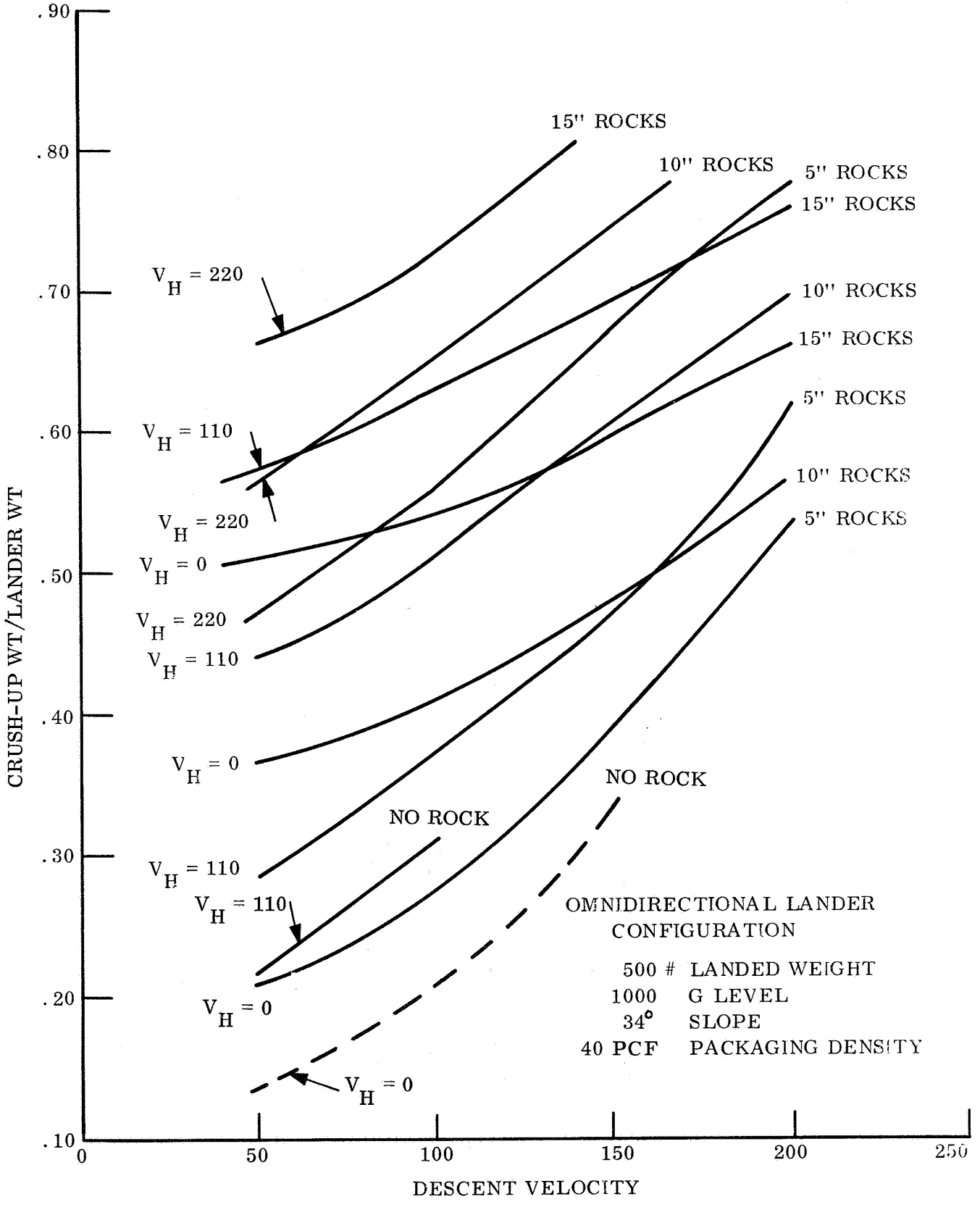

Figure 4.5.5-84. Crush-up Weight Fraction as a Function of Specified Rock Size for 1000g Loading

4.5.6 PNEUMATIC SYSTEMS (Alternate Method)

To provide comparative data on other Lander approaches, limited parametric trade-offs were performed on a spherical pneumatic bag system. The intent here is to furnish background information pertinent to the ranges of weight and g-loadings which appear attractive from a Hard Lander viewpoint.

4.5.6.1 Parametric Trade-offs for Spherical Pneumatic Bags - High Performance Pneumatic Bag Landing Systems

4.5.6.1.1 Introduction

Pneumatic bags have long been considered useful for landing spacecraft and have been successfully used in various programs. A great advantage of such devices is their storability during flight, a quality which sets them apart from rigid devices such as honeycombs which occupy valuable fixed volume in the spacecraft and their potential insensitivity to surface unknowns. Despite this and their potentially high performance, pneumatic bags have not enjoyed great popularity because of their non-passive character. Their operation depends on maintaining a rather predictable pressure-stroke variation and this requires achieving a particular gas discharge sequence during the deceleration stroke. If gas discharge occurs too rapidly, the stroke will be expended before all of the kinetic energy is removed from the vehicle, and the vehicle is then subject to undesirably high forces. If discharge occurs too slowly, the vehicle will rebound with resulting loss in landing control. Hence, maintenance of the proper gas discharge history is vital to the performance of gas bag Landers.

In order to achieve the maximum potential from gas bag systems, moreover, it is necessary that the gas discharge pressure be close to both the initial pressure prior to impact and the burst pressure of the bag, and that it be as constant as possible throughout the stroke. It is also desirable to maintain a constant bag cross section during the stroke, since, if the above conditions are met, the force-stroke variation is optimum (rectangular). Hence, a constant pressure bag in the form of a circular cylinder, whose central axis is aligned with the velocity vector throughout the impact is the most efficient configuration.

At the same time, the above configuration can only be considered an unattainable ideal. Practical considerations such as axial misalignment on impact, elasticity of the bag material, the necessity of maintaining safety margins, and gas discharge control limitations all act to separate the actual system from the ideal.

Realizing however, that the consideration of a near ideal system would preclude consideration of the gnawing realities of actual landing conditions, such as unpredictable landing attitude, a parametric study of spherical configurations containing a centrally mounted payload, was performed to indicate the potential of gas bag systems. This study is reported in the following section, Parametric Study of Spherical Systems.

4.5.6.1.2 General Description of System

The system studied consists of a spherical bag containing a centrally mounted spherically shaped payload at the center. The payload is attached to the bag by means of radial cell members which fan out in a uniform distribution around the payload. These cells, in addition to the above mentioned function, serve to compartmentalize the internal volume and provide shear strength.

The pressurizing gas is assumed to be stored in a spherical bottle prior to use. This container is itself stored within the payload volume.

4.5.6.1.3 Materials

The materials used for the spherical bag and cells are phrased in terms of the ratio, $\sigma\ c/\rho_w$, of a working stress to the material weight density. The value of σ_c/ρ_w used was 1.0×10^6 in. and is representative of high strength fabrics containing various safety factors. The following table lists two examples.

STRENGTH OF SUITABLE GAS BAG MATERIALS

Material	Tensile Strength (psi)	Density (pci)	σ_c/ρ_w in x 10^{-6}
Dacron	159,000	0.0498	3.191
Nylon	116,000	0.0411	2.818

The factor, k, includes a safety margin and takes into account the seams necessary to join sections of fabric and the weight of impregnating material required to render the fabric gas tight. This latter requirement applies only to the spherical portion of the bag.

The material of the spherical gas storage bottle was assumed to be a filament wound glass-plastic composite of high strength. A stress to density ratio of 2.0×10^6 in. is presently attainable.

Helium in its gaseous form was used as the pressurizing gas because of its low weight.

4.5.6.1.4 Assumptions

The following assumptions were made in the parametric study.

1. The entire weight of the landing vehicle including that of the gas bag system was considered to be concentrated in the centrally situated spherical payload having an average density of 25 lb/ft^3. This assumption results in an overestimation of the landing system weight since a portion of the energy of the landing system would be absorbed by direct contact with the ground surface.

2. The impact was considered to be normal to the ground surface, with no lateral component. The impact velocity was taken as the resultant of latest estimates of vertical and horizontal impact velocities.

3. The gas bag material was assumed to be inelastic, such that the bag remains spherical at its initial size everywhere except in the expended portion.

4. The gas pressure is maintained constant throughout the operation.

5. Full deceleration occurs when 80 percent of the available stroke has been expended.

6. A factor of safety of 3.0 was assumed for the gas storage bottle. In addition, 20 percent of the bottle weight was added to account for hardware and plumbing.

7. The effect of the Martian gravity was ignored.

4.5.6.1.5 Range of Parameters

Total vehicle weight, W_T = 300, 600, 1000 lb

Resultant impact velocity, V_R = 50, 100, 200, 500 ft/sec

Deceleration limit, A_g = 1000 g's.

4.5.6.1.6 Analysis

The relation describing the energy removed from the payload is

$$E_\varphi = p \pi R^3 \left[\frac{2}{3} - \cos \varphi_e + \frac{\cos^3 \varphi_e}{3} \right] = \frac{1}{2} \frac{W_T V_R^2}{g} \tag{1}$$

where φ_e is the central angle at which the body is fully stopped. Referring to fig. 4.5.6-1, φ_e is related to the outside radius, R, and the payload radius, R, by the expression,

$$\cos \varphi_e = \frac{1}{5} \left(1 + 4 \frac{R_p}{R} \right) \tag{2}$$

The pressure, p, is equal to the limiting decelerating force divided by the cross-sectional area of the bag corresponding to the angular position, φ_e, is

$$p = \frac{A_g W_T}{R^2 \sin^2 \varphi_e} \tag{3}$$

The above three equations, containing the three unknowns R, p, and φ_e were solved by first computing values of E_φ for several assumed values of R from the equation

$$E_\varphi = \frac{A_g W_T R}{\sin^2 \varphi_e} \left[\frac{2}{3} - \cos \varphi_e + \frac{\cos^3 \varphi}{3} \right] \tag{4}$$

obtained by substituting eq. 3 in eq. 1, using eq. 2 to obtain φ_e from R. Then from a plot of values of E_φ versus R the value of R corresponding to

$$E_\varphi = \frac{1}{2} \frac{W_T}{g} V_R^2 \tag{5}$$

was found. This value of R corresponds to full deceleration in 80 percent of the available stroke and a peak decelerating force equal to the product $A_g W_T$.

The weights of the system can be now calculated. Beginning with the spherical portion of the bag, the weight, W_s is

$$\begin{aligned} W_S &= 4 \pi R^2 h \rho_w = 4 \pi R^2 \left(\frac{pR}{2\sigma_c} \right) \rho_w \\ &= \frac{2 \pi R^3 p}{(\sigma_c / \rho_w)} \end{aligned} \tag{6}$$

The weight of radial cells is obtained from the fact that they must tensionally transmit decelerating force from the top portion of the bag to the central payload as shown in fig. 4.5.6-1. The stress sustained by any cell member on the upper half of the spherical part can be shown to be approximately

$$\sigma_\alpha = \sigma_o \cos \alpha \tag{7}$$

where σ is the tensile force per unit area of the spherical bag surface exerted along the line of deceleration and α is the central angle of the cell position. The total vertical force exerted by all cells on the bag surface is

$$\begin{aligned} F &= 2 \pi R^2 \sigma_o \int_o^{\frac{\pi}{2}} \sin \alpha \cos^2 \alpha \, d\alpha \\ &= \frac{2}{3} \pi R^2 \sigma_o \end{aligned} \tag{8}$$

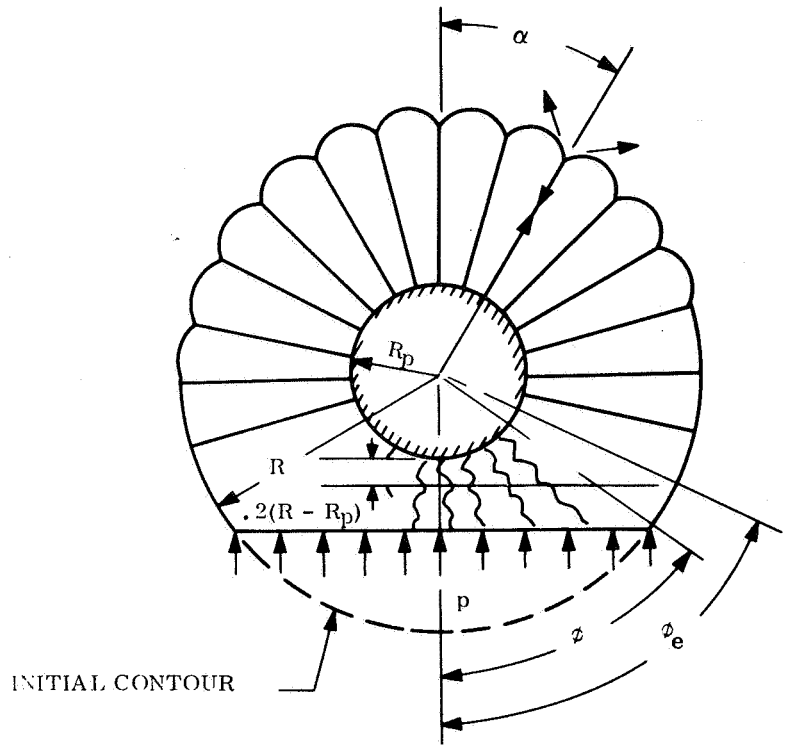

Figure 4.5.6-1. Pneumatic Bag Schematic

σ_o is exactly equal to p and, since it is due to the cell tension,

$$\sigma_c A_c = p\,(1) = \sigma_o \tag{9}$$

where σ_c is the longitudinal stress in the central cell wall and A_c the cell cross sectional area per unit of bag surface area. In all other cells the stress will be equal to

$$\sigma_{c\alpha} = \sigma_c \cos \alpha \tag{10}$$

It should be noted that the same unit force $\sigma_c A_c$ acting on the bag acts also on the payload, whose surface area is only R_p/R times the bag area. Hence the cross-sectional area of the cell must be maintained constant and equal to A_c at all radial positions. Substituting eq. 9 in 8 yields,

$$A_c = \frac{F}{\frac{2}{3}\pi R^2 \sigma_c} = \frac{W_T A_g}{\frac{2}{3}\pi R^2 \sigma_c} \quad . \tag{11}$$

Hence the total cell area is

$$A_{cT} = 4\pi R^2 A_c = \frac{6 W_T A_g}{\sigma_c} \tag{12}$$

which is constant for any radial position between the radii R and R_p. The total cell weight is therefore:

$$W_C = \frac{6W_T A_g (R - R_p)}{(\sigma c/\rho_w)} \tag{13}$$

The gas weight is given by the following:

$$W_G = 1.964 \times 10^{-6} p (R^3 - R_p^3) \tag{14}$$

based on a temperature of 460 °R.

The weight of the spherical gas storage bottle is expressible simply in terms of the gas weight, W_G

$$W_B = 4\pi R_B^2 h_B \rho_w f = \frac{18 W_G R_G T_G f}{(\sigma/\rho_w)} \tag{15}$$

where R_B = radius of bottle, h_B = wall thickness of bottle, (σ/ρ_w) = tensile stress/density of bottle material, f = design factor, R_G = gas constant, T_G = absolute temperature of the gas. Using a $\sigma/\rho_w = 2.0 \times 10^6$ in., representative of present filament wound pressure vessels, a safety factor, f = 3.0, an 18 percent allowance for hardware, and assuming Helium gas at a storage temperature of 460 ° R, eq. 15 becomes

$$W_B = 5.64 W_G \tag{16}$$

The total weight of the landing system is

$$W = 1.15 (W_S + W_C) + W_G + W_B \tag{17}$$

The payload weight is

$$W_P = W_T - W \tag{18}$$

An informative ratio is

$$\frac{W_P}{W} = \frac{W_T}{W_P} - 1 \tag{19}$$

The overall measure of performance is the specific energy, K_e,

$$K_e = \frac{1}{2} \frac{W_T}{g} \frac{V_R^2}{W} \tag{20}$$

Values of R, p, W_s, W_c, W_G, W_B, W, W_T/W_P, and K_e were computed for all 80 cases.

4.5.6.1.7 Parametric Study Results

The computed values for the system weight $\frac{W_{system}}{W_{total}}$, W, plotted against the resultant impact velocity, V_R, with parameters $\gamma = \sigma_c/\rho_w = 1.0$, x 10^6 in., are shown in figs. 4.5.6-2 through 4.5.6-4 inclusive.

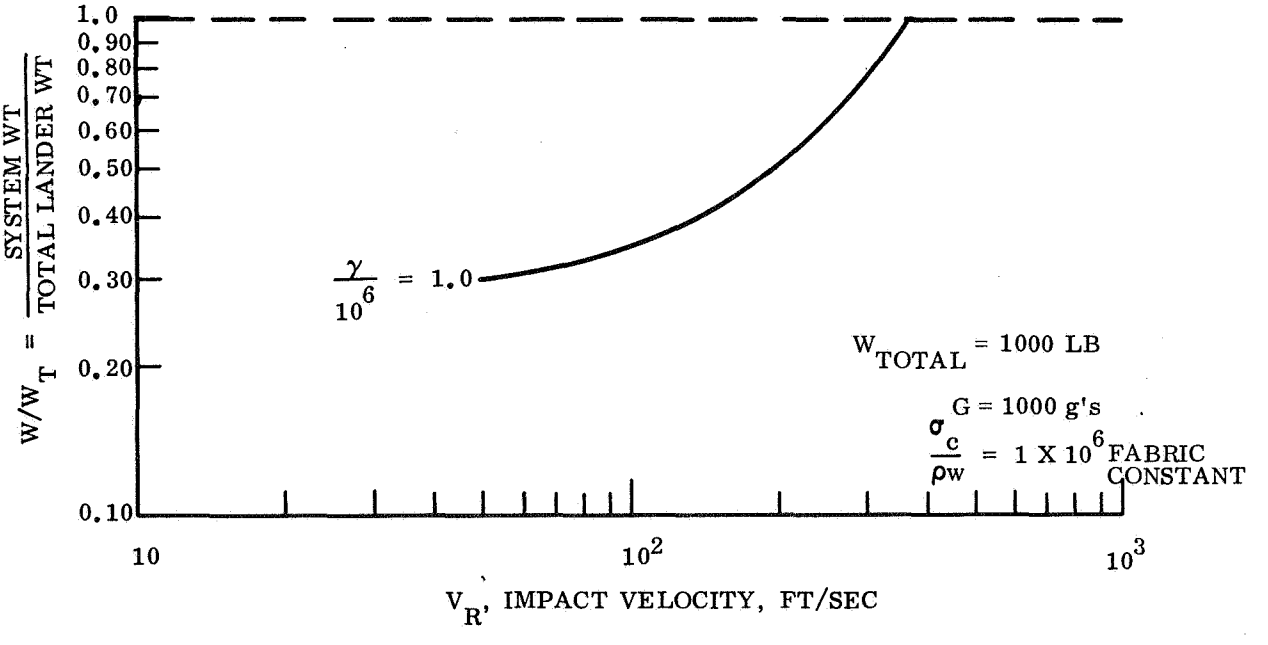

Figure 4.5.6-2. Attenuator Wt /Total Wt vs Impact Velocity for for W_{total} = 1000 lbs, g = 1000

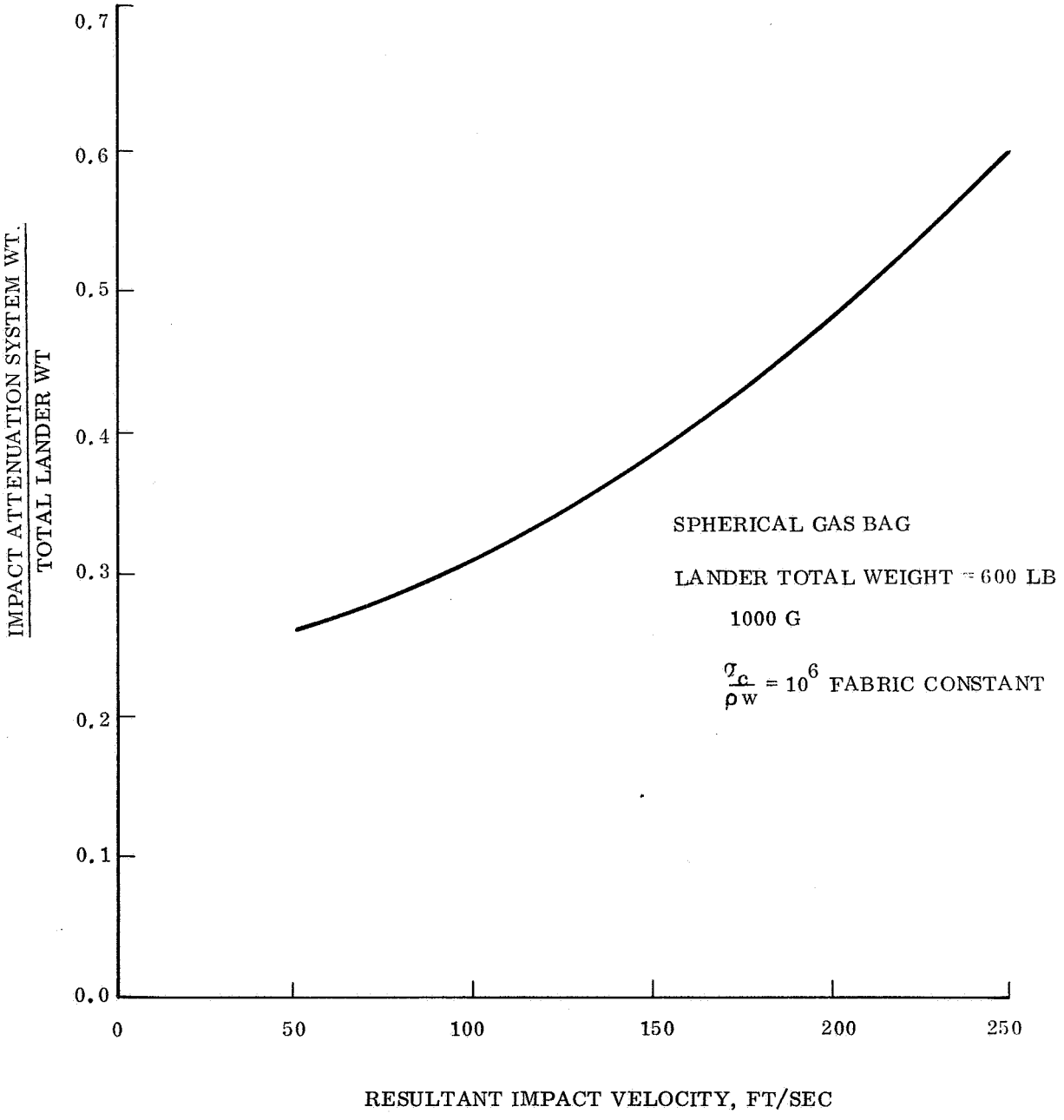

Figure 4.5.6-3. Attenuator Wt/Total Wt vs Impact Velocity for W_{total} = 600 lbs, g = 1000

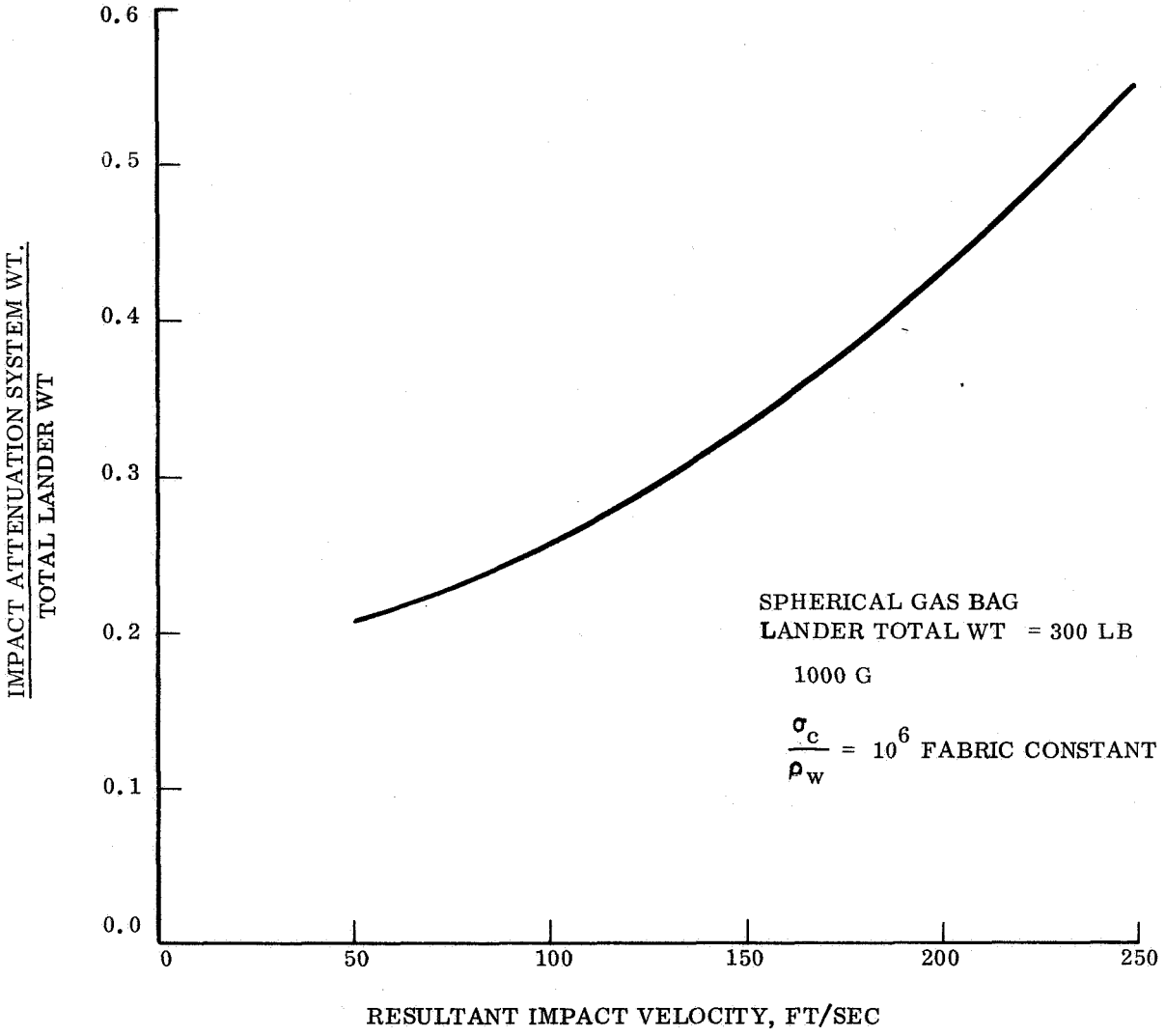

Figure 4.5.6-4. Attenuator Wt/Total Wt vs Impact Velocity for W_{total} = 300 lbs, g = 1000

The general trend is that, for a low deceleration level, the efficiency is almost constant with the total weight, W_T; for a high value of A_g, the efficiency drops significantly with increasing W_T. The trend at a given value of W_T with increasing values of A_g is much more pronounced than the former, with the deleterious effect being greater at the higher values of W_T.

4.5.6.2 Sphero-Toroid

This configuration is an original Company-evolved approach to an integrated solution to the problems of long stroke (low deceleration), pneumatic bag attachment to the payload, post-landing orientation and access, and stowability within the entry vehicle. It is felt that it offers a realistic balanced solution to these conflicting requirements, while retaining near-minimum weight and simplicity of construction. It is being developed independently of the Hard Lander Study as a company sponsored effort and is presented in this report because of its potential application. The two concepts described in this section are based on approximate analyses which must be refined to better define performance and weights. It is planned to pursue this development including testing of models and to report on this progress in the final issue of this report.

As noted above, the sphero-toroid offers an integrated design solution that meets all of the conflicting requirements of low deceleration, attachment to the payload, installation and access in the aeroshell, and post-landing orientation and access. This concept was evolved in consideration of all of the configurations developed in several years of system design. To reiterate, this concept offers the following structural and system advantages:

1. Simplicity of construction as compared to pneumatic systems employing internal cords, webs, and other attachments to the bag surface and the payload.

2. Greatly reduced deceleration loading as compared to crushable systems.

3. Simplicity of structural and electrical attachments (without penetrating the basic bag or attenuating structure) within the aeroshell and during descent.

4. Inherent simplicity of post-landing orientation by deflating the spherical bags leading to a torus configuration stable in one of two positions.

5. Ease of obtaining access to the planetary environment by opening one or both of the circular doors to erect and deploy sensors and experiments.

6. Light weight because of the natural load paths in the torus and sphere walls which minimize need for internal webs and other attachments, and distributed attachments to the payload which make use of the basic bag surface, as well as reduced structure weight in the payload container.

4.5.6.2.1 Conceptual Design for Point Design 2B

The sphero-toroid configuration, as the name indicates, is a simple combination of a torus and two spherical bags (see fig. 4.5.6-5) located over the hole of the "doughnut". This leads to an essentially spherical overall configuration which should have characteristics similar to that of a spherical bag of the same volume. For the purpose of this conceptual design, the torus and spheres are assumed interconnected to permit easy passage of gas. The size was based on a spherical bag analysis, in order to obtain rapid although preliminary results. The following assumptions were used.

1. Sphero-toroid with same volume and pressure as a sphere has same characteristics as the sphere.

2. A safety factor of 2.0 on the fabric (dacron).

3. Soil strength 6.0 psi to use 6.0 psi for maximum pressure.

4. Impact velocity 210 ft/sec (based on study conditions).

5. Maximum G = 1000 g

6. Use 695 lbs (Point Design 2B) landed weight.

A payload cylinder 30 inches in diameter and 18 in. long, as shown in fig. 4.5.6-5, was assumed in order to have a configuration compatible with the spherotoroid landing system. A kinetic energy analysis yields a 16.8 ft diameter spherical configuration which has the same volume as the sphero-toroid of fig. 4.5.6-1. The sphero-toroid landing system weighs 264 lbs plus 66 lbs for the storage tank as indicated in table 4.5.6-1 which also summarizes the weights of the Hard Lander Study Point Design 2B. The Lander container structure weight for the sphero-toroid is reduced because of the reduced g-level and more efficient structural load paths.

A potential payload and equipment increase of 37 lbs is indicated as well as a maximum deceleration level of approximately 250 g's (based on the spherical analogy).

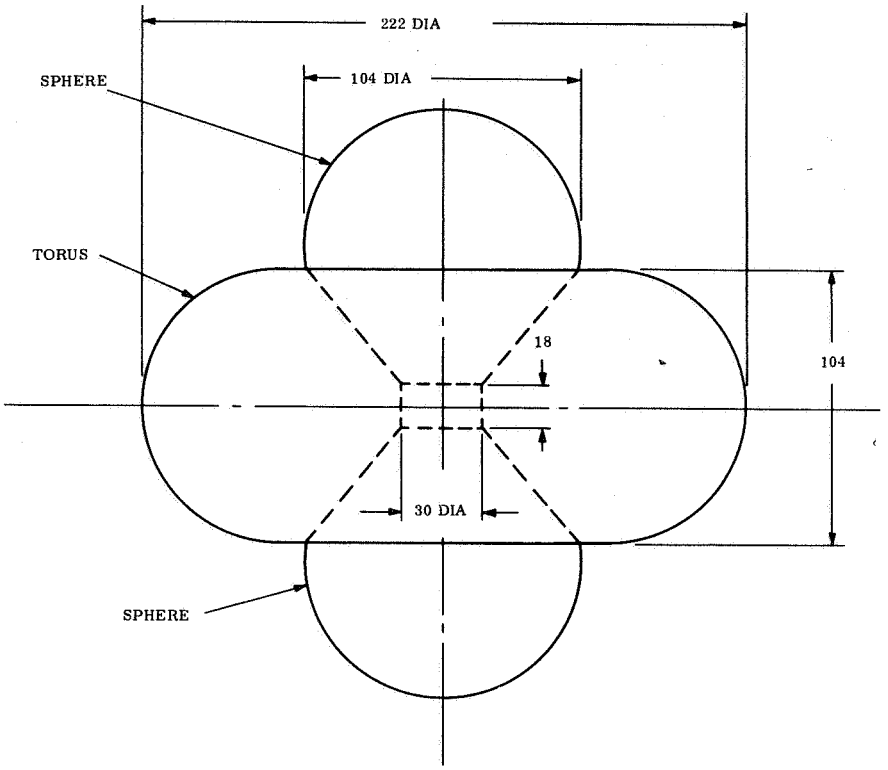

Figure 4.5.6-5. Sphero-toroid Pneumatic Landing System for Point Design 2B

TABLE 4.5.6-1. WEIGHT SUMMARY

Configuration	Point Design 2B (omni-directional) (lbs)	Sphero-toroid (omni-directional) (lbs)
Landed Science and Equipment Payload	228	265
Deployment Mechanisms	20	20
Lander Container Structure	160	80
Landing System	522	8 helium 256 bags 264
Landed Weight	930	629
Helium Tank	---	66
Decelerator Load	930	695

4.5.6.2.2 Conceptual Design for Point Design 7

A preliminary analysis was made for the Point Design 7 Lander using the following impact conditions:

Landed weight	600 lb
Vertical velocity	100 ft/sec
Horizontal wind	118 ft/sec
Maximum slope	20°

The above landing conditions result in a maximum normal impact velocity of 134 ft/sec on a 20° slope. A spherical pneumatic bag of 8 ft diameter was arbitrarily selected to yield a maximum impact loading of about 250 g's.

Using this sphere as an analogy for a sphero-toroid having the same volume and initial pressure, the configuration of fig. 4.5.6-6 results. This system was stressed using the following.

50 lb/in/oz/yd^2 for dacron fabric

Factor of 2 on fabric strength

Factor of 1.10 for seam allowance

Sealer weight = 150 percent of fabric weight

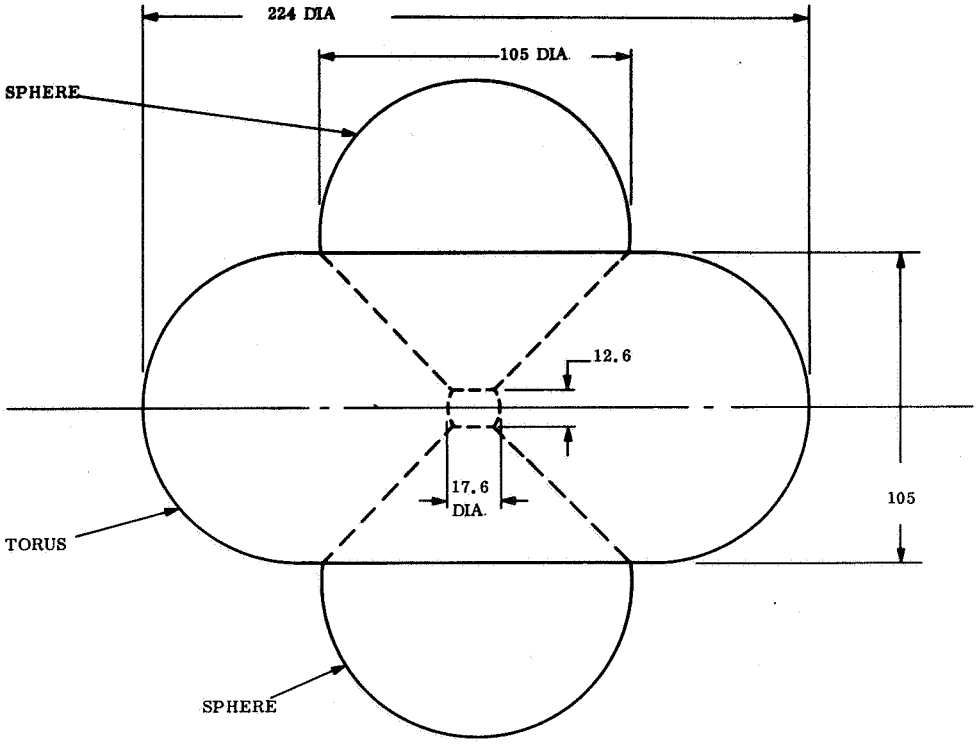

Figure 4.5.6-6. Sphere-toroid Pneumatic Landing System for Point Design 7

The analysis yielded a weight of 170 lbs for the torus and 12.5 lbs for each sphere. In addition, 3.0 lbs of helium and a 24.5 lbs tank are required. Comparing this design on a system basis with the Point Design 7 using a crushable attenuator, the following table of weights results.

Item	Crushable Attenuator (lbs)	Pneumatic (lbs)
Payload, etc.	302	302
Deployment	20	20
Structure	180	80
Landing System	233	170 torus 25 spheres 3 helium
		198
Landed Weight	735	600
Helium Tank	---	24.5
Decelerator Weight	735	624.5

The apparent net weight saving is due entirely to the structure which is estimated to be 100 lbs lighter because of the greatly reduced 'g' level (250/1000) and the design for distributed tension attachments to the bag rather than the "point" compression loading imposed on the structure of the crushable design.

This indicates that 198 lbs is the weight of a landing system to do the same job as the 233 lbs crushable approach. However, to this must be added the weight of a 24.5 lbs tank that must be carried through entry but can be jettisoned before landing.

4.5.6.2.3 Conclusions

On the basis of the limited analysis completed at this time, the following results are evident:

1. A pneumatic system is at least weight competitive with a crushable system in the regime of interest on the Hard Lander Study, and may save over a 100 lbs.

2. An increase in bag size results in a lower weights, although this effect is limited by practical limits of fabric construction.

3. Further optimization of fabric and sealer may also result in significant savings in weight.

4. The pneumatic system results in realistic designs, including fabric thickness, in the 'g' range of 200 - 500 g.

5. The Lander internal structure will be much lighter and cheaper to fabricate.

6. Development costs of the pneumatic bag may be less than for crushable attenuator since bags are essentially state-of-the-art.

7. The pneumatic bag is inherently conducive to efficient packaging and will result in a more forward c. g. location for the entry vehicle and other attendant advantages.

4.6 REFERENCES

1. "Venus-Mars Capsule Study", Vol. I, Section III-3.3, General Electric Company, Missile and Space Division, 30 July 1962. Final Report Contract 950250 for JPL.

2. "Voyager Design Study", Part I, Vol. III, Subsystem Design Section 1.5, Report 68SD801, 15 October 1963, Final Report Contract NAS W-696 for NASA.

3. "Study of Mars and Venus Orbiter Missions Launched by the 3-Stage Saturn C-1B. Vehicle", EPD-139, Vol. III, p. 4 - 224, Jet Propulsion Laboratory, 31 December 1963.

4. J. A. Martin, J. Chown, "Study of the Breakdown Characteristics of Antennas in the Atmospheres of Mars and Venus", Final Report JPL Contract 950380, Stanford Research Institute, February 1963.

5. W. K. Kinkead, "Antenna Breakdown in Planetary Atmosphere", Report No. 65SD316, GE Re-entry Systems Department, September 1965.

6. E. C. Gatz, R. B. Hartley, "Planned Capabilities of the DSN for Voyager 1973", Engineering Planning Document 283, Rev. 2, Jet Propulsion Laboratory, 1 January 1967.

7. "High Rate Telemetry Project", The Deep Space Network, Space Programs Summary 37-48, Vol. II, p. 83; Jet Propulsion Laboratory, November 30, 1967.

8. "Multiple Mission Telemetry System", The Deep Space Network, Space Programs Summary 37-46, Vol. III, p. 175 ff. July 31, 1967, Jet Propulsion Laboratory.

9. G. Huffman, "Final Report, Error Control Coding", General Electric Company, TIS 67SD4249, 3 March 1967.

10. J. A. Brady, "The Power Spectral Density of Manchester PCM-FM", General Electric Co., TIS No. 65SD373, 12/28/65.

11. T. C. Sayer, "Power Spectrum of Frequency-Shift-Keyed, Random, Split-Phase Signals", General Electric Co., PIR 1J41-62F-406, June 17, 1968.

12. T. C. Sayer, C. M. Hackett, Jr., and J. A. Lash, "Performance of Non-coherent FSK Employing Post-Detection Integration", General Electric Co., TIS No. 66SD200, March 1966.

13. D. W. Boyd, "Approximate Analysis of a Frequency-Shift Keyed System with Uncertainty in the Carrier Frequency", JPL SPS 37-41, Vol. IV, p. 233.

14. Frazier, J.P., and Page, J. - "Phase-Lock Loop Frequency Acquisition Study", Trans. IRE, SET-8, pp. 210-227, Sept. 1962.

15. Gardner, F.M., "Phaselock Techniques", John Wiley and Sons, Inc., 1966, p. 49.

16. K. Fong, "Statistical Theory on Propagation and Scattering of Electromagnetic Waves, near a Planet", General Electric Company, Memo Report No. MO-67-1532, October 1967.

17. P. Beckmann, "Scattering by Composite Rough Surfaces", Proc. IEEE, August 1965, p. 1012.

18. R.B. Dyce et al (1965), Astronomical Journal, 72, p.771.

19. A.B. Glenn "Fading from Irregular Surfaces for Line-of-Sight Communications, IEEE Trans. on Aerospace and Electronic Systems, March 1968.

20. Voyager Capsule Bus Study, McDonnell-Douglas, Report F694, Vol II, Part B, 31 August 1967 (p 5.5.-10).

21. Functional Specification DRF-1001-FNC, DSIF Tracking and Communications System, GSDS 1964 Model Receiver Subsystem, JPL, 1965.

22. Lindsey, W., "Phase-Shift-Keyed Signal Detection with Noisy Reference Signals", IEEE Trans. AES, July 1966.

23. Final Report, Voyager Spacecraft, Phase B, Task D, Vol. II, Book 2 of 5, Section 3.3, GE DIN 67SD4379, October 16, 1967.

24. J. Shatas, "Fifty Watt Solid State FM Transmitter for Deep Space Communications", General Electric Co., TIS 66SD2002, January 12, 1966.

25. Thermal Radiation Properties Survey by Gubareff, Janssen, and Torborg, Honeywell Research Center, Minneapolis Honeywell Regulator Co., 1960.

26. Kornhauser, M., "Structural Effects of Impact", Spartan Books, 1964.

27. Young, C.W., "The Development of Empirical Equations for Predicting Depth of an Earth-Penetrating Projectile", Sandia Laboratory SC-DR-67-60, May 1967.

28. NASA - Langley Research Center, Mars Engineering Model Parameters for Mission and Design Studies, May 1968. (Preliminary Draft)

29. General Electric Report #66SD4390, "Development of Energy Dissipating Plastic Honeycomb Quarterly Progress Report No. 7 and 8 - 1 February 1967 through 31 July 1967, dated 8/1/67.

5. PRE-ENTRY SUBSYSTEMS

5. PRE-ENTRY SUBSYSTEMS

5.1 DEORBIT PROPULSION

A parametric study for estimating the weight of propulsion subsystems to deorbit a Mars Hard Lander Vehicle has been conducted. This study includes solid propellant, liquid monopropellant, and liquid bipropellant propulsion subsystems, and provides the basis for satisfying the program requirements and synthesizing subsystem point designs.

5.1.1 REQUIREMENTS

The requirements for this study were to develop propulsion subsystem parametric design data for fixed impulse motors (with thrust termination capability) for a given range of velocity increments and vehicle masses. All propulsion subsystems considered are sterilizable and all curves were generated using programs written for use on GE's 605 Desk-Side Computer System.

The range of input variables for this study were:

1. Velocity increments:

   a. Solids: 50 to 1200 feet per second (15 to 366 meters per second)

   b. Liquids: 50 to 400 meters per second in 50 mps increments

2. Weight to be deorbited: 600 to 2000 pounds including propulsion subsystem weight.

5.1.2 SOLID PROPELLANT SYSTEMS

The solid propellant motor parametric data presented in fig. 5.1.2-1 of this report was obtained using empirical equations derived by the Aerospace Corporation and subsequently programmed on GE's 605 Desk-Side Computer System. These equations are based on solid propellant motor histories and the resulting curves presented herein are estimated to be within plus or minus 5 percent of actual design values.

The data is plotted in a series of five curves, all interrelated, and enabling the determination of propulsion system propellant weights and total weights knowing only the velocity increment required to deorbit a certain weight vehicle. The curves are plotted presenting a choice of propellants and ranges of expansion ratios, accelerations, thrusts, chamber pressures, and nozzle exit diameters.

The two propellants shown are UTC's UTREZ, a proven sterilizable propellant, and Aerojet's ANB 3289-2, an untried but very promising propellant, based on slab testing. UTREZ is a non-aluminized propellant (it can be aluminized if desired, but it

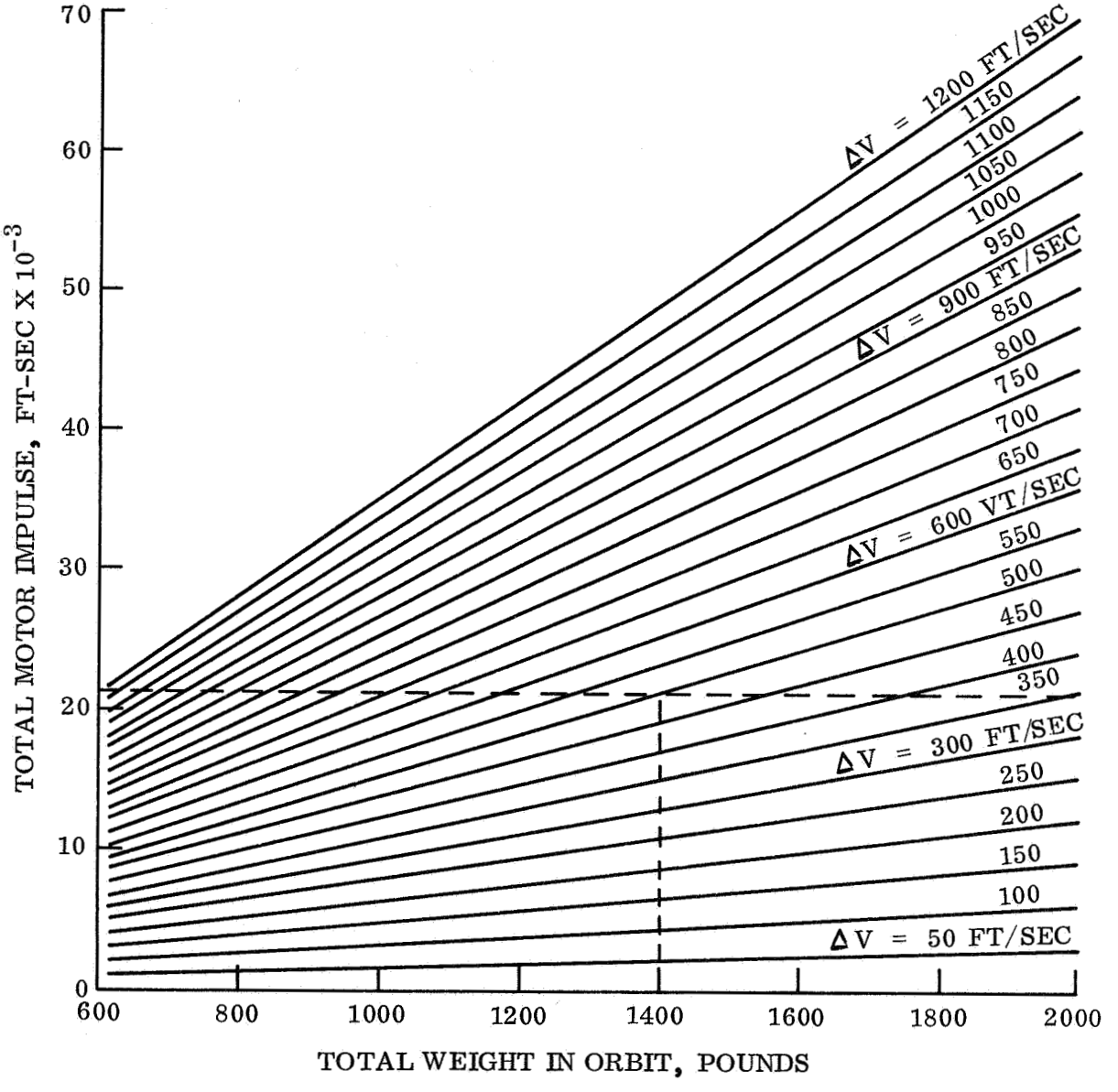

Figure 5.1.2-1. Total Motor Impulse vs Total Weight in Orbit

is unproven with aluminum) and ANB 3289-2 is aluminized, providing the basis of trade-offs for such criteria as performance versus possible contamination of vehicle sensors. Pertinent facts on both propellants, as well as assumptions used in generating the solid data are listed in table 5.1.2-1.

A solid propellant system design is synthesized by determining the propellant, expansion ratio, thrust or acceleration, and desired chamber pressures from the parametric curves. The point design is then conducted based on the steps and equations in Aerojet Report 2470-01F, "Space Vehicle Solid Rocket Analysis and Correlation Study", performed under contract NAS 7-519.

TABLE 5.1.2-1. SOLID PROPELLANT ASSUMPTIONS

Propellants	Aerojet's ANB 3289-2	UTC's UTREZ
Composition	15% Al, 85% Solid	0% Al, 75% Solid
Density	0.063 lb/in^3	0.056 lb/in^3
Isp (1000/14.7; optimum expansion)	243.0	207.0
Case Material	6 Al-4V Titanium	
Density	0.16 lb/in^3	
Case Configuration	Spherical	
Volume Loading Efficiency	90%	
Factor of Safety on Pc	1.5	
Nozzle	Fixed, contoured, ablative, partially submerged, no TVC	

5.1.3 LIQUID PROPELLANT SYSTEMS

The liquid propellant parametric data generated during this study is presented in figs. 5.1.3-1 and 5.1.3-2 for monopropellant systems and figs. 5.1.3-3 and 5.1.3-4 for bipropellant systems. The data was obtained from existing computer programs. An example of the monopropellant system analysis is shown in table 5.1.3-1

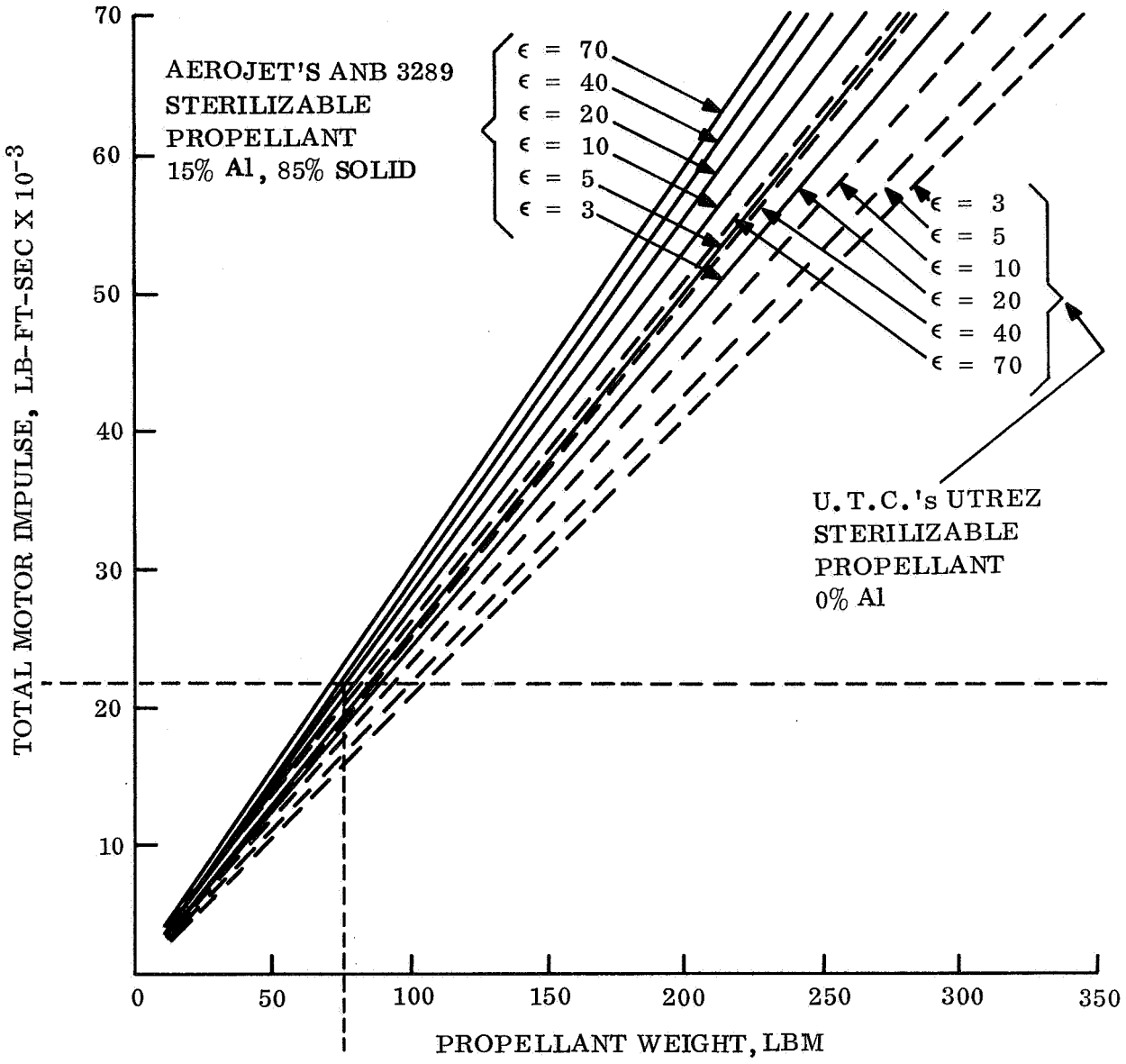

Figure 5.1.3-1. Total Motor Impulse vs. Total Weight

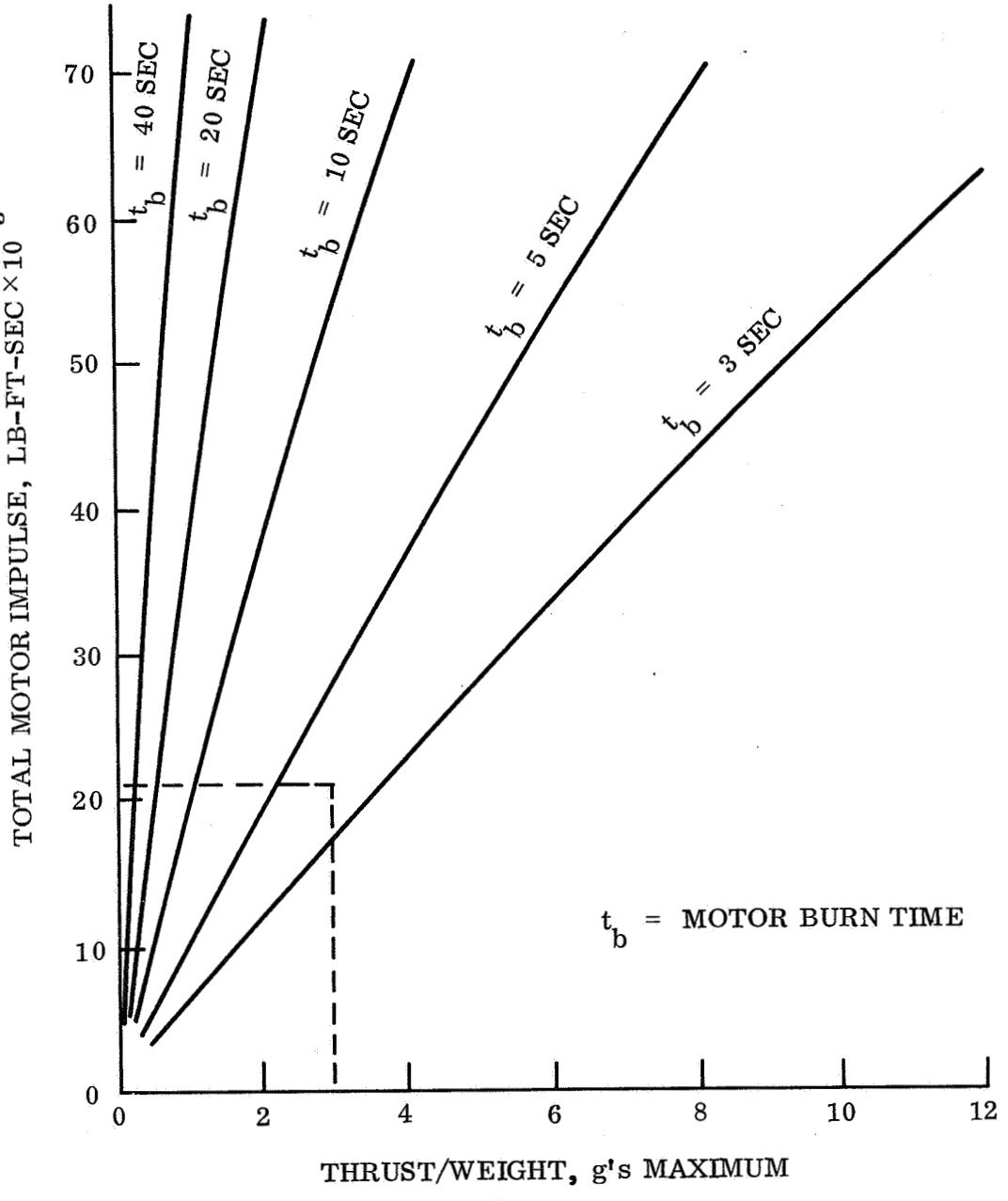

Figure 5.1.3-2. Total Motor Impulse vs. Thrust to Weight Ratio

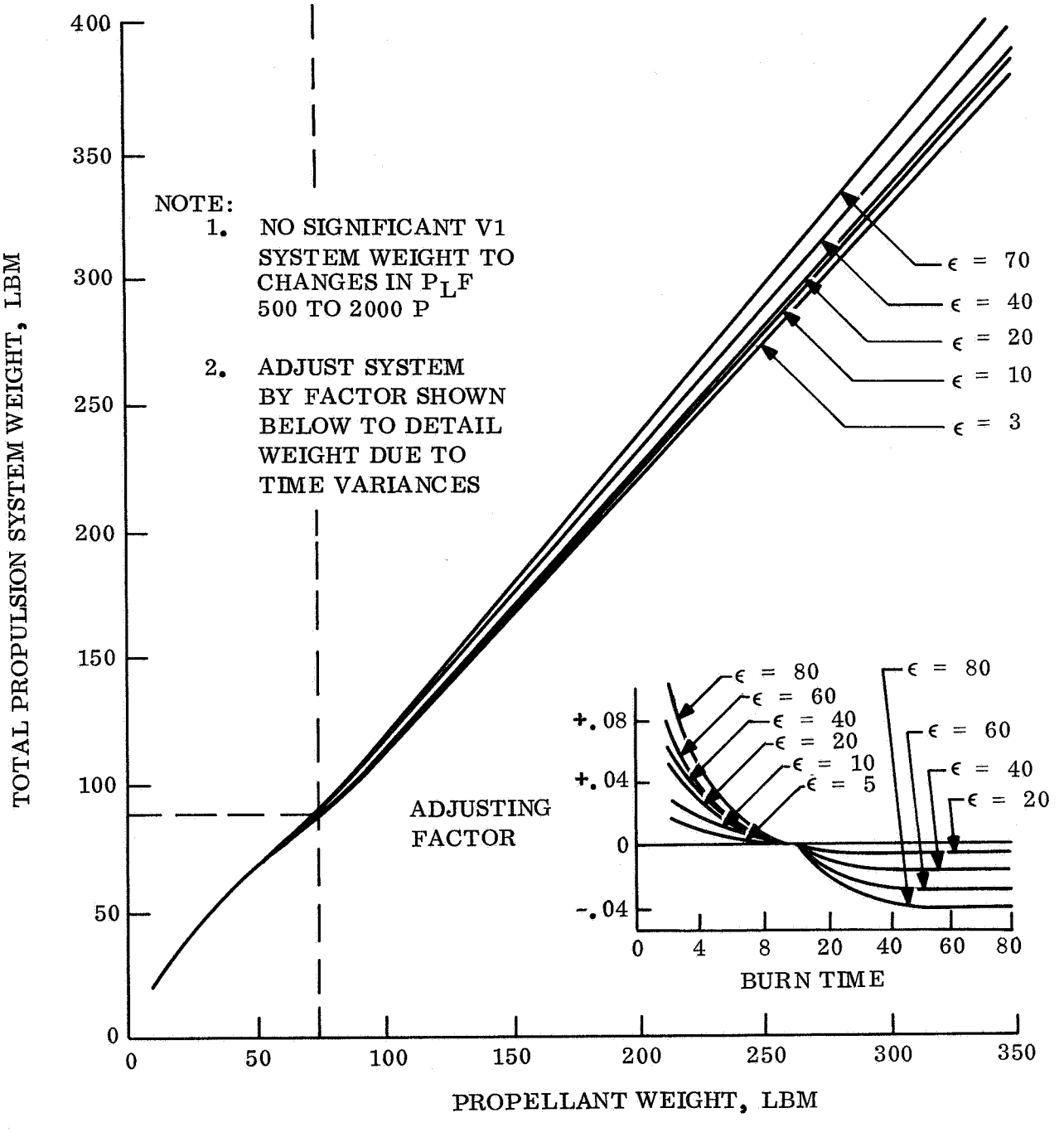

Figure 5.1.3-3. Total Mission System Weight vs. Propellant Weight

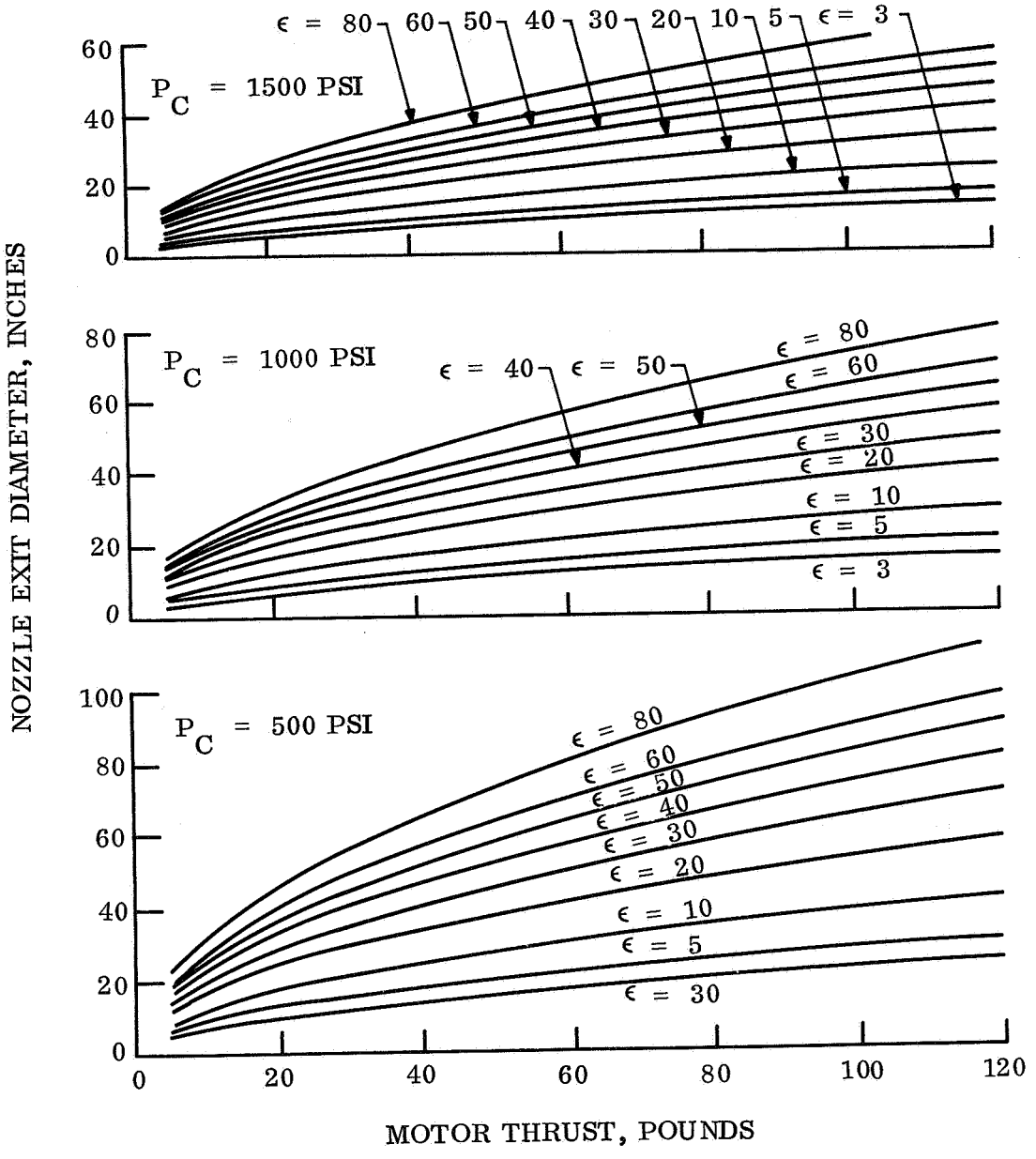

Figure 5.1.3-4. Nozzle Exit Diameter vs. Motor Thrust

TABLE 5.1.3-1. EXAMPLE MONO PROPELLANT SYSTEM CALCULATIONS

1. Given: Tot. Wt. to be deorbited = 1400 lb
   Required ΔV = 500 ft/sec
   Max. acceleration = 3.0 g's
   Max. nozzle exit dia. = 10.0 inches

2. From (1) find total impulse (I_T) = 21,250 lbf-sec

3. At I_T = 21,250 lb-sec & g max = 3 g. from (3)
   find t_b = 5 sec.
   $\therefore$ Thrust (F) = 21250/5 = 4250 lbf &
   g max = 2.2 g

4. Assume P_c = 1000 psi, $\therefore$ From (5) ϵ = 30 @ D_E = 10

5. Assume ANB-3289-2 propellant. From (2)
   wt prop ϵ = 30 & I_1 = 21,250 = 76 lbm

6. From (4) ϵ = 30 & wt prop = 76
   Total propul syst. wt. = 89 lbm

7. Adjust syst wt for L_b
   wt_{syst} = 89 + (89) (+.022) = 89 + 2 = 91 lbm

8. Mass fraction = 76/91 = .835

SUMMARY:

a)	Total weight in Mars orbit	= 1400 lbm
b)	Required ΔV	= 500 ft/sec
c)	Motor total impulse	= 21,250 lbf-sec
d)	Total propellant weight	= 76 lbm
e)	Total propulsion syst. weight	= 91 lbm
f)	Motor mass fraction	= .835
g)	Nozzle expansion ratio	= 30:1
h)	Nozzle exit diameter	= 10.0 inches
i)	Motor chamber pressure	= 1000 psi
j)	Motor thrust	= 4250 lbf
k)	Max. acceleration	= 2.2 g's
l)	Motor burn time	= 5 sec
m)	Total weight at burn out	= 1400-76 = 1324 lbm

The data shown for bipropellant systems is based on terminal heat sterilization, and, therefore, is considerably heavier than for a comparable system aseptically loaded. However, if an aseptically loaded bipropellant system is required, its data is essentially the same as that presented for the monopropellant systems.

The parametric studies were conducted based on an assumed subsystem configuration shown in fig. 5.1.3-5. The components are divided into fixed hardware (all hardware that is thrust and, therefore, essentially flow rate dependent) and variable hardware (all hardware that is total impulse dependent). Examples of fixed hardware are lines, brackets, regulators, valves, thrust chamber assemblies and filters. Examples of variable hardware include pressurant and propellant tanks and a portion of the intra-propulsion subsystem support structure. While not hardware per se, pressurant gas and residual propellants are propellant quantity (total impulse) dependent and constitute part of the subsystem burnout weight, thus they are included in the overall definition of variable "hardware."

With a schematic/configuration selected, weights are assigned to each of the fixed weight components. Where possible, weights of actual hardware are used. If these data are unavailable, a scaling factor, based on actual hardware and the anticipated thrust level (flow rate), is applied to arrive at the component weight. The weight of the items comprising variable hardware are calculated using existing computer routines and the input data shown in tables 5.1.3-2, 5.1.3-3, and 5.1.3-4.

5.1.4 CONCLUSIONS

Conclusions that can be drawn from these preliminary studies are:

1. Aerojet's ANB 3289-2 is a much higher performing propellant than UTC's UTREZ, and from preliminary data furnished by Aerojet, is much more capable of surviving the sterilization cycles than UTREZ. It has never been cast in a motor while UTREZ has and has been successfully fired. On the basis of performance potential, ANB 3289-2 is the recommended propellant.

2. For propulsion requirements up to and including a payload of 10,000 pounds, a velocity of 300 meters per second, and a propulsion system which must be loaded and then heat sterilized, monopropellant systems offer a weight advantage over bipropellant in addition to inherent reliability advantages.

3. Within current state-of-the-art, there is no monopropellant thrust chamber with a thrust greater than approximately 300 pounds.

4. There are several areas within the bipropellant system that require additional study for meeting heat sterilization requirements. These include required safety factors, maximum pressures, and different designs for fuel and oxidizer tanks. Refinement in these areas will lead to reductions in system weight and therefore extend the range of usefulness.

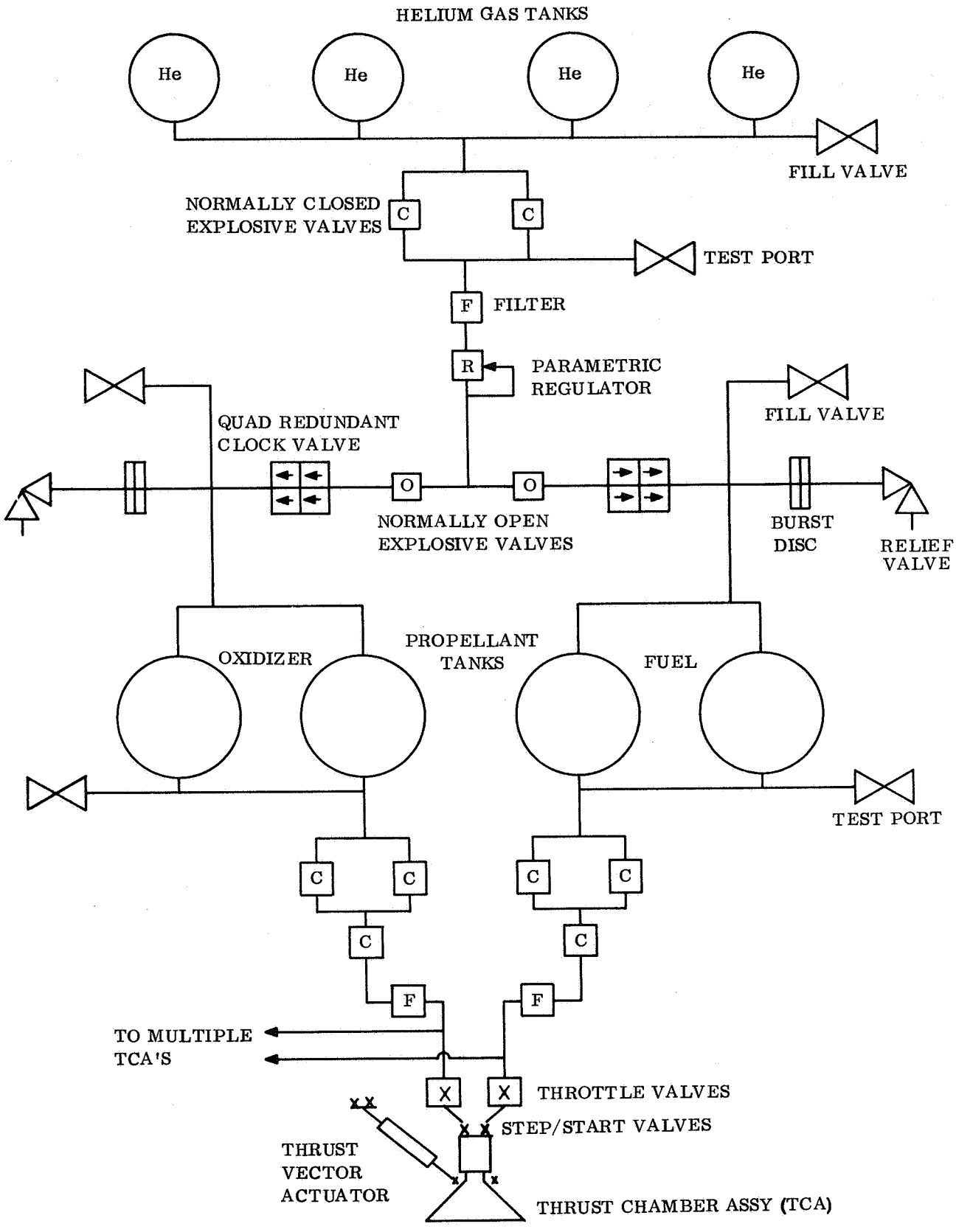

Figure 5.1.3-5. Liquid Propellant Schematic

TABLE 5.1.3-2. PROPELLANT DATA

	Monopropellant	Bipropellant
Fuel	Hydrazine	Aerozine 50 (50% hydrazine - 50% UDMH)
Oxidizer	---	Nitrogen Tetroxide
Mixture Ratio (O/F)	---	1.6:1
Density fuel (lb/ft^3)	56.16 @ 275°F	56.7 @ 100°F
Oxidizer (lb/ft^3)	---	88.2 @100°F
Ullage Volume	5% @275°F	35% @275°F

TABLE 5.1.3-3. VARIABLE HARDWARE DESIGN DATA

	Monopropellant	Bipropellant
Propellant Tank		
Material	6A1-4V Titanium Al.	6A1-4V Titanium Alloy
Ult. Strength, psi	136,000 @ 275° F	136,000 @ 275°F
Max. Tank Pressure, psi	300 @ 275°F	1200 @ 275°F
Number tanks	2	2
Min. Wall Thickness	0.02	0.02
Safety Factor on Ultimate	1.75-1.8 @ 275°F	2.0 @ 275°F
Weight Factor % (added to membrane for bosses, welds, etc.)	30	30
Pressurant & Pressurant Tank		
Material	6A1-4V Titanium Al.	6A1-4V Titanium Alloy
Ult. Strength, psi	136,000 @ 275° F	136,000 @ 275°F
Operating pressure, psi	3600	3600
Max. Pressure, psi	5300 @ 275° F	5300 @ 275°F
Safety Factor	1.75 = 1.8 @ 275° F	1.75 = 1.8 @ 275°F
Minimum Pressure, psi	400	400
Polytropic Process constant	1.25	1.25
Allowable Leakage	15%	15%
Compressibility Factor	9.028%	9.028%

TABLE 5.1.3-4. MISCELLANEOUS DESIGN DATA

Residual Propellants	3.06% of usable (based on TRW Task C data)
Propulsion Structure*	15% of Propulsion system burnout weight
Thrust Chamber Assembly** & Fluid controls weight	Thrust / Weight (Fixed Hardware) 100 / 28.2 300 / 53.9 2200 / 222.2 3500 / 352.6 8000 / 437.4

*Propulsion module only - not entire load carrying members.
**These are "actual" for bipropellant systems. For purpose of this study, there was assumed to be a 1:1 correspondence for monopropellant systems. Subsequent studies will refine these assumptions.

In comparing liquid and solid heat sterilizable propulsion systems, the following general conclusion can be reached; solids offer a weight advantage over either monopropellant or bipropellant systems. However, the conclusions noted earlier apply and the considerations of mission operation suggested by such things as flexibility, restartability, thrust termination, and reliability must also be evaluated.

5.2 ATTITUDE CONTROL

5.2.1 SCOPE OF PARAMETRIC DESIGN

There are three broad requirements for the Capsule Attitude Control Subsystem (ACS). First, control of Capsule attitude is required during firing of the propulsion system to accomplish deflection from the approach trajectory or deorbit from the planetary orbit. Second, control of Capsule attitude is required at the beginning of entry into the atmosphere to satisfy entry angle of attack requirements. Finally, attitude control of entry roll rates are required to reduce lateral accelerations and to insure stability.

To meet these requirements, both an active, three-axis attitude control and a spin/de-spin control system have been examined. The three-axis control can readily accomplish all these requirements for Capsule control. Parametric data is described in the following section for systems using either cold gas nitrogen or hot gas hydrazine monopropellant control thrusters. The spin control can meet the first and second requirements. However, it can not perform the third function since entry roll torques, generated by built-in and ablation-induced asymmetries, may cause excessive spin rates. The system studied, therefore, combines a spin control, used during propulsion firing and pre-entry phases, and an active roll axis control used during entry.

The following three sections present parametric design data for these two attitude control concepts.

5.2.2 PARAMETRIC DATA FOR THREE-AXIS CONTROL

The three-axis ACS performs these functions in the sequence listed.

1. Separation. Removes initial angular rates and establishes an attitude reference at Capsule separation from the Spacecraft.

2. Maneuver. Maneuvers the Capsule to the orientation desired for propulsion firing.

3. Autopilot. Controls the attitude during propulsion firing.

4. Limit Cycle. Maneuvers to the entry (or other) orientation and maintains this attitude by a limit cycle mode of operation until entry.

5. Entry. Controls the roll rate during entry.

The weight of the three-axis ACS is dependent on the Capsule mass and inertia characteristics as well as on the performance requirements. This weight is shown in the following parametric plots as the variation in the thruster fuel (hydrazine or nitrogen) and associated tankage weight with the most important parameters for each of the five listed functions. All tank weights include allowances for bosses and mounting lugs and brackets.

The remainder of the ACS weight (sensors, electronics and the rest of the thruster hardware) does not vary appreciably over a large range of Capsule sizes. This fixed weight is discussed in Section 5.2.4, where the overall subsystem configuration is presented.

5.2.2.1 Separation

The weight of fuel and tankage of a three-axis ACS required to stabilize a Capsule following separation from the Spacecraft with residual body angular rates is plotted in fig. 5.2.2-1. The weights are computed for a nitrogen reaction control system. The weight is smaller by a factor of 5.7 for hydrazine. In either case, the separation phase requires relatively little control fuel weight.

5.2.2.2 Maneuver

Even less control weight is required to accomplish large reorientations of the Capsule in reasonable times. For example, if a maneuver rate of 0.2 degree per second is assumed, reorientation to any direction can be accomplished in less than 30 minutes. The fuel and tankage weight required to do this, and to return the Capsule to its original direction, is typically less than 0.1 pound.

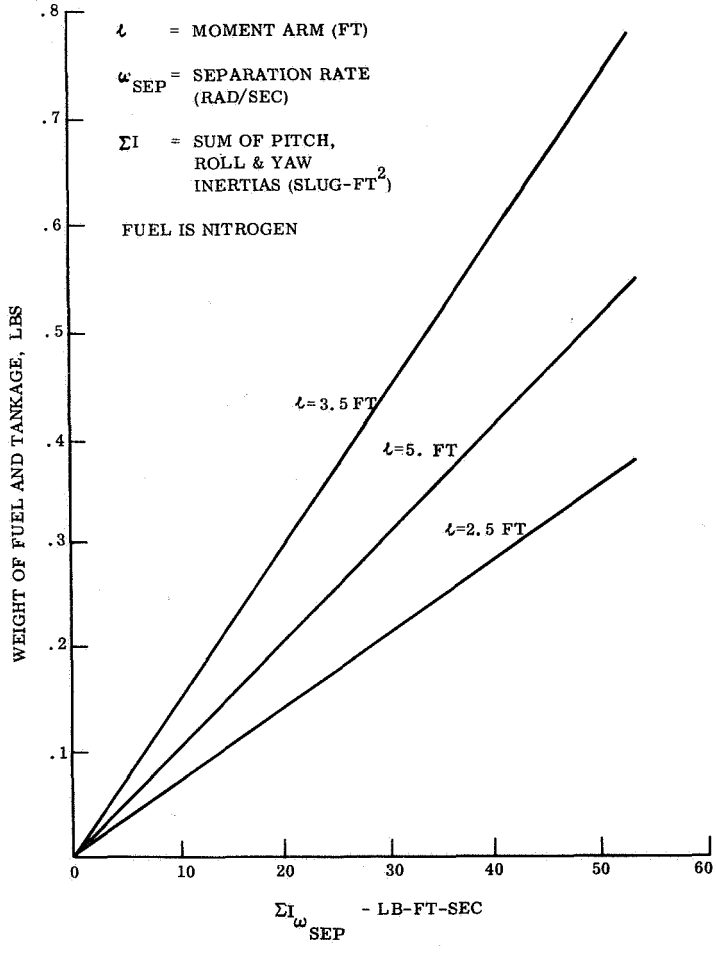

Figure 5.2.2-1. Separation Requirements; Fuel and Tank Weight of a Three-Axis Control System

5.2.2.3 Autopilot

A major requirement for three-axis control system weight is autopilot control during propulsive deflection from the approach trajectory for direct entry or deorbit from planetary orbit for the out-of-orbit entry. Fig. 5.2.2-2 presents the weight of fuel and tankage required to oppose the disturbing torque set-up because the propulsion thrust axis is offset from the Capsule center of mass. Since, as the curve shows, the weight is a direct function of the velocity increment (ΔV), the fuel and tank weight for direct entry is typically much lower than that for out-of-orbit entry. The significant weight advantage of hydrazine over nitrogen is due to its higher specific impulse and lower tank weight.

5.2.2.4 Limit Cycle

After propulsion firing, the ACS will maintain a fixed attitude until entry. If disturbing torques are low, the ACS will be in a limit cycle mode during this period and significant fuel weight will be required for high control torques and long duration of operation. The fuel and tankage weight is plotted in fig. 5.2.2-3 for direct entry. Since the duration of this phase for out-of-orbit entry is much shorter, the corresponding weight for the out-of-orbit mission is more than an order of magnitude less than those shown in fig. 5.2.2-3.

However, another difference between out-of-orbit and direct entry is that a larger control torque is required for out-of-orbit if a higher thrust level is used by the propulsion system in producing the larger velocity increment required. As shown in fig. 5.2.2-3, this sharply increases the fuel and tank weight required and, therefore, may offset the effect of the shorter time duration.

The weight advantage of hydrazine over nitrogen is not due to its higher specific impulse since, in the pulse mode required for limit cycle operation, the high specific of hydrazine is reduced to a value of roughly 100 seconds. However, the torque level is also reduced in the pulse mode, and this is the major factor in reducing both the limit cycle rate and the rate of fuel usage. The reduction in torque is assumed to be a factor of 3 for the data plotted in fig. 5.2.2-3.

5.2.2.5 Entry

The Capsule will tend to spin up during entry under the action of aerodynamic torques about the roll axis. This torque is a function of the Capsule base diameter as shown in figs. 5.2.2-4 and 5.2.2-5 for the out-of-orbit and the direct entry cases. The maximum spin-up rate must be constrained to prevent a possible divergence of the Capsule angle of attack at low dynamic pressures. The roll rate limit to assure Capsule stability during entry is shown in fig. 5.2.2-6.

It is necessary to provide sufficient roll control torque and impulse to prevent Capsule roll rate from approaching this limit. Note, however, that it is not necessary to provide roll control torque greater than the peak disturbance torque since there is no

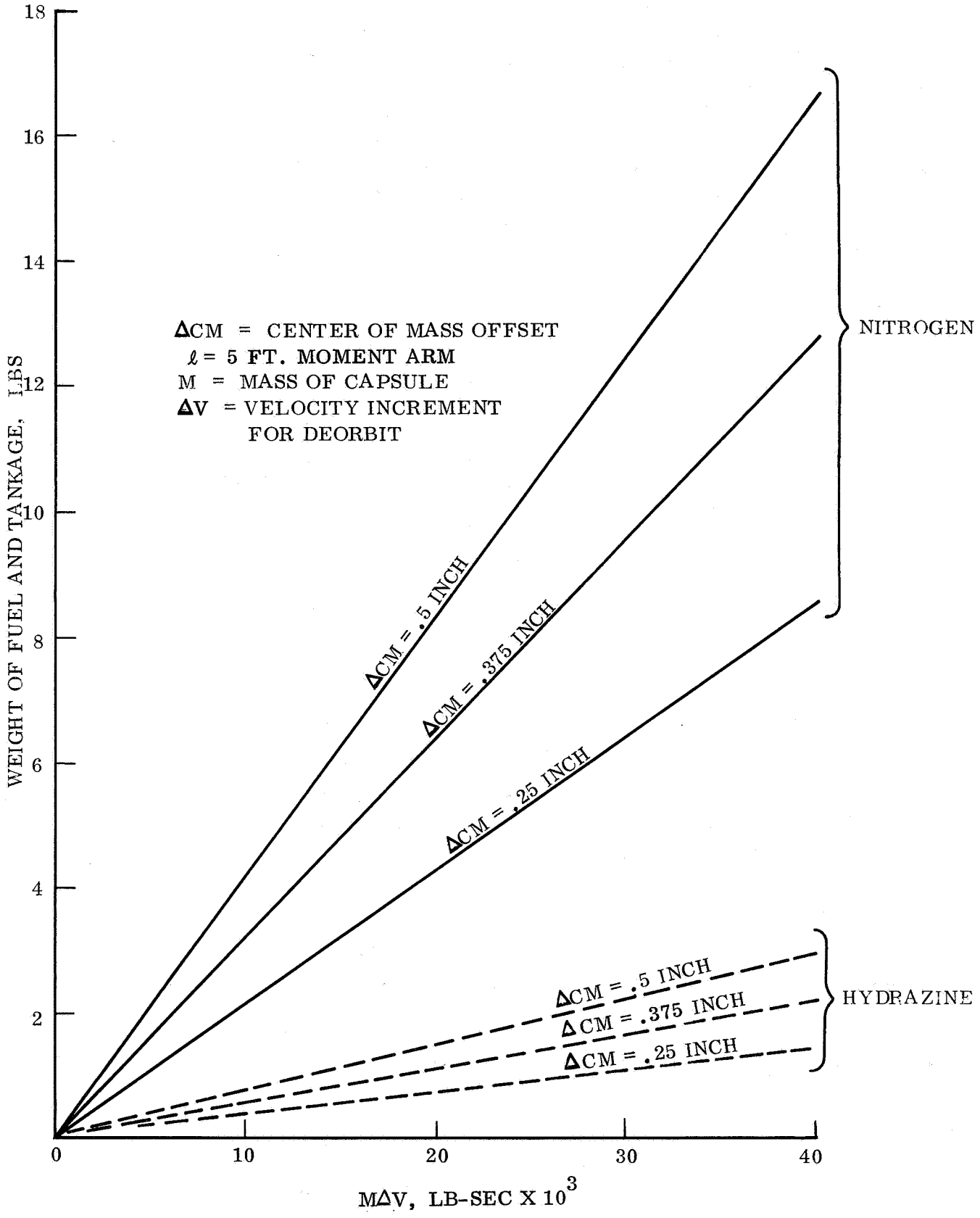

Figure 5.2.2-2. Autopilot Requirements; Fuel and Tank Weight of a Three-Axis Control System

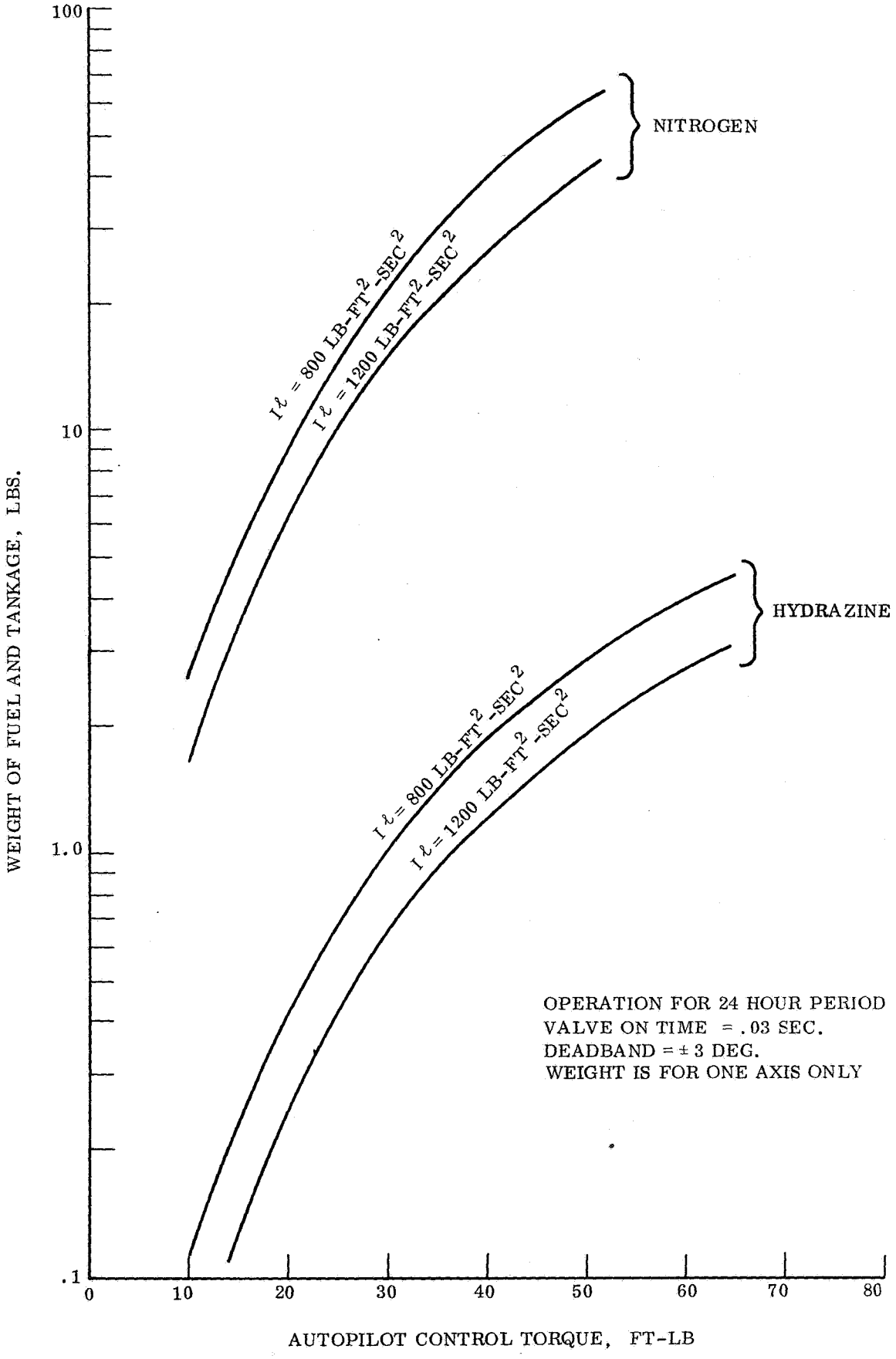

Figure 5.2.2-3. Limit Cycle Requirements, Direct Entry; Fuel and Tank Weight of a Three-Axis Control System

III

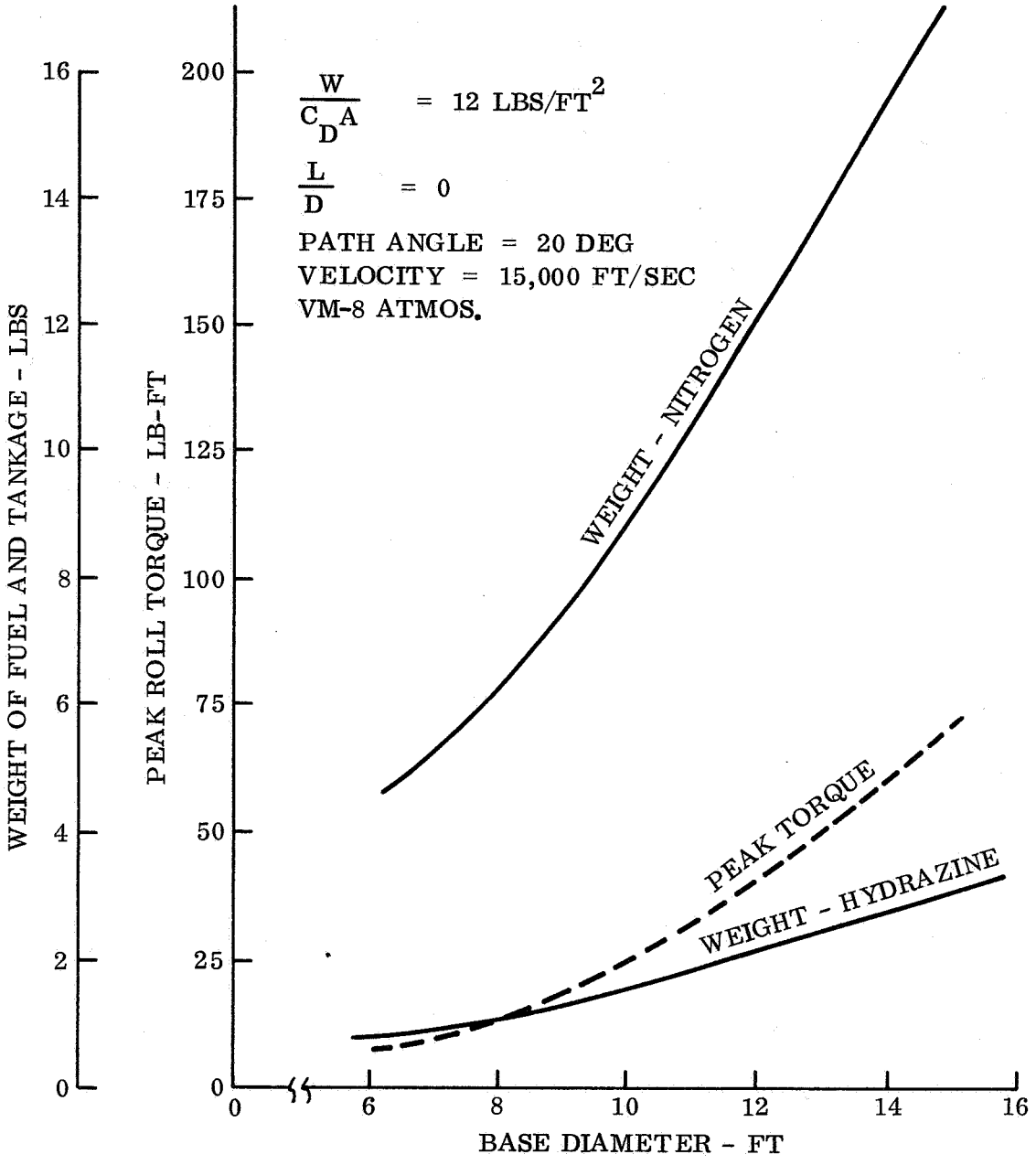

Figure 5.2.2-4. Out-of-Orbit Entry Requirements; Fuel and Tank Weight of a Roll Control System

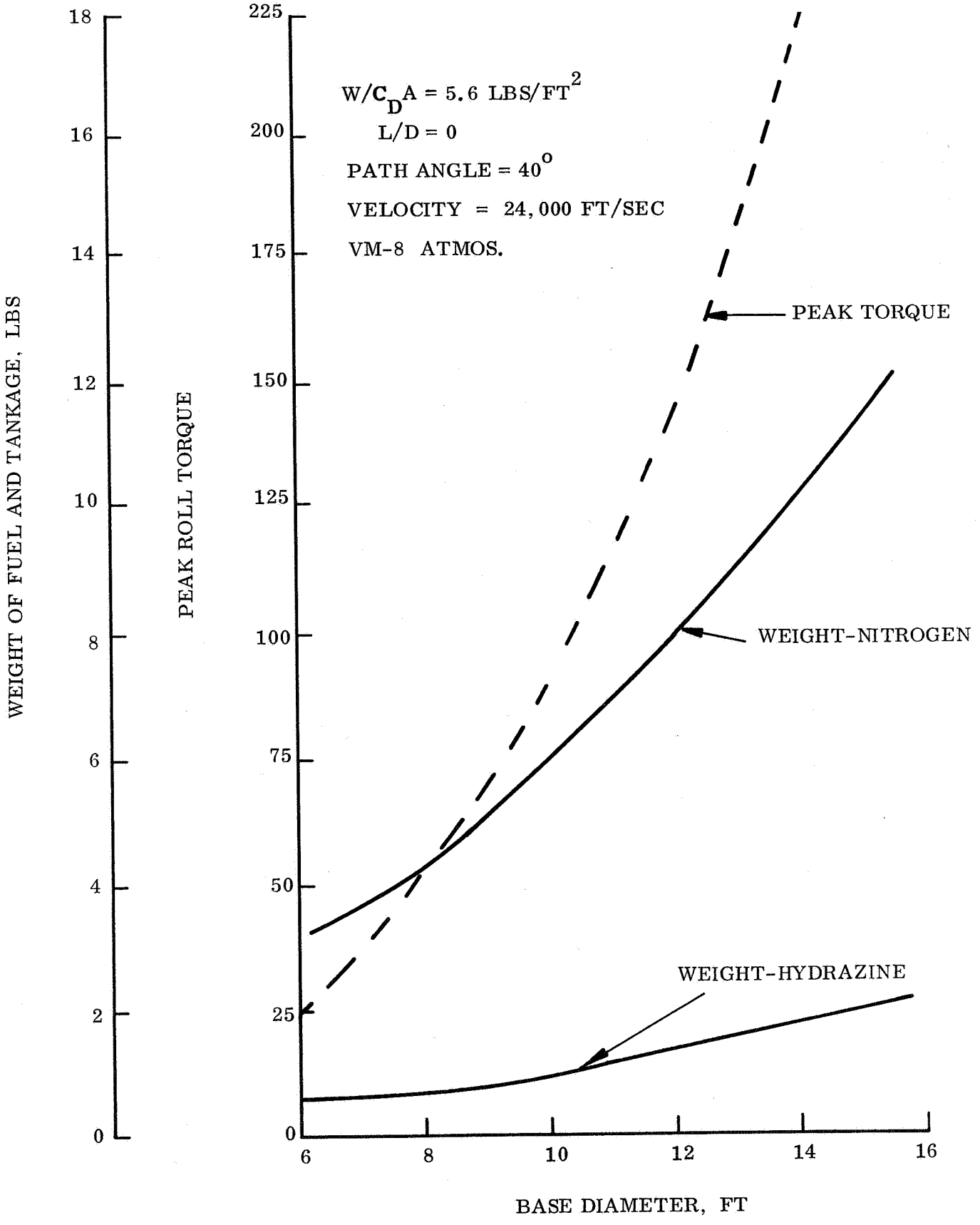

Figure 5.2.2-5. Direct Entry Requirements; Fuel and Tank Weight of a Roll Control System

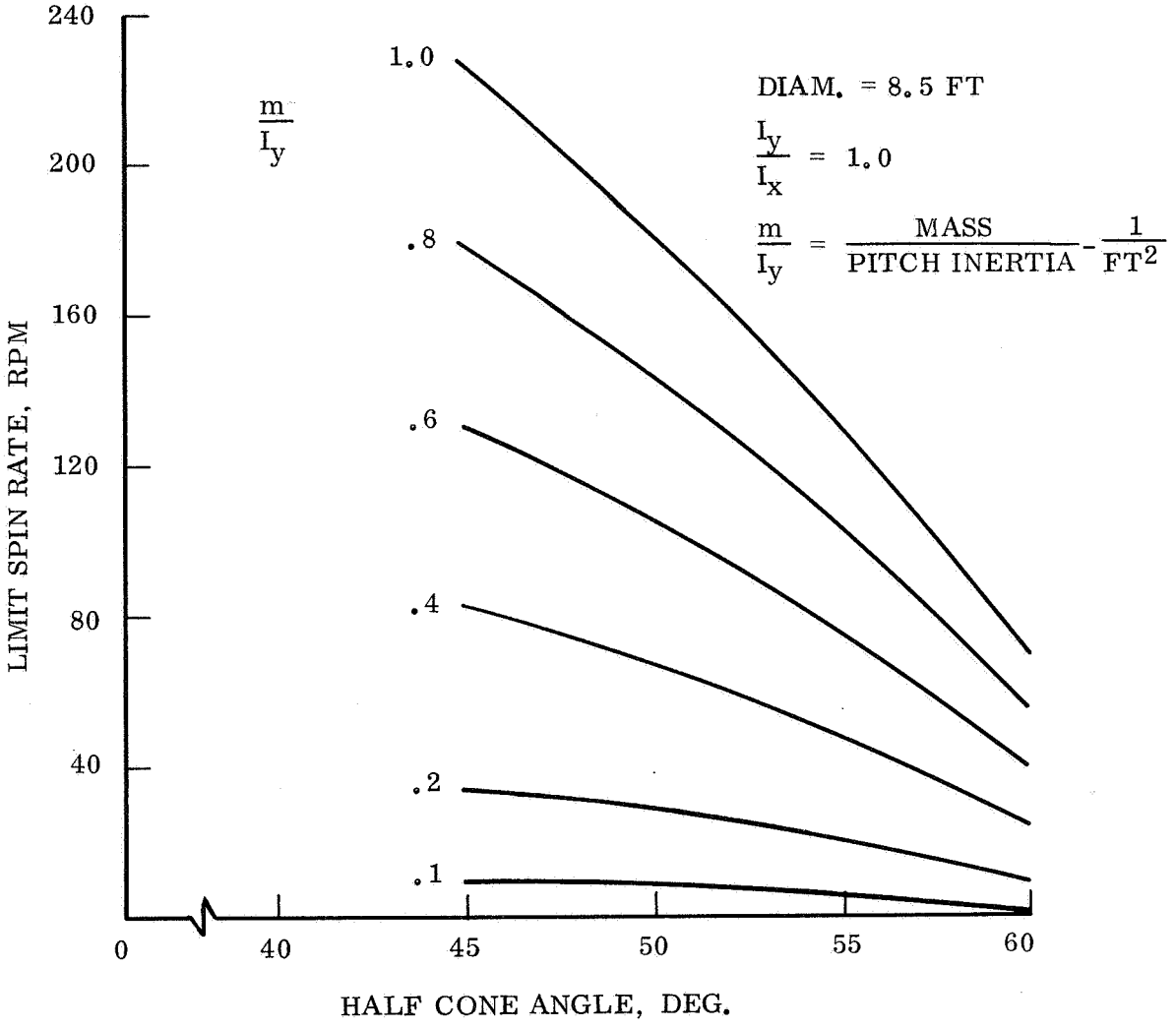

Figure 5.2.2-6. Limit Spin Rate for Blunt Body Sphere Cones in Terminal Descent on Mars

requirement for roll attitude control in a non-lifting vehicle and the peak torque occurs for a very short period.

The weight of control fuel and tankage is also shown on figs. 5.2.2-4 and 5.2.2-5 for both nitrogen and hydrazine systems.

5.2.3 PARAMETRIC DATA FOR SPIN CONTROL

The spin control performs these two functions:

1. Spin. The Capsule is spun up to a high angular rate immediately after separation from the Spacecraft. This spin rate provides gyroscopic stability during firing of the propulsion engine for deorbit. The Capsule is de-spun to a low rate after propulsion firing. This low rate maintains the inertial attitude until the beginning of entry.

2. Entry. The roll rate is held below a maximum limit during entry. This function is identical to that for the three-axis ACS and is discussed in the previous section.

5.2.3.1 Spin

The magnitude of spin rate required is a function of the propulsion thrust level, Capsule mass characteristics and ΔV orientation accuracy required. A parametric set of data has been computed using a six-degree-of-freedom computer program to simulate the capsule motion histories. The primary source of ΔV orientation error is the torque resulting from the thrust not passing through the vehicle center of mass. Secondary sources such as products of inertia, unequal pitch and yaw moments of inertia are considered only in detail analysis and in fact these studies are used in reverse to determine manufacturing tolerances based on orientation error requirements.

Figure 5.2.3-1 is a nomograph of the results of the computer simulations for ΔV orientation errors. The curves are valid provided that the thrust acts long enough to allow averaging over several cycles of motion. For short burn times the errors can be either larger or smaller depending on the phase of the motion at thrust termination. An approximation for the minimum burn time is:

$$t_{burn} > 100 \left(\frac{T\,C_2}{Iy}\right)\left(\frac{Iy}{Ix}\right)\frac{I}{P}$$

and is of the order 5 or 10 seconds.

5.2.4 SUBSYSTEM CONFIGURATIONS

The two reaction control systems investigated during this study are the cold gas regulated nitrogen system and the hydrazine monopropellant non-regulated (blow-down) system shown in fig. 5.2.4-1. There is a minor difference in the fixed hardware weight of these systems. The major difference is the weight of the fuel and tankage as discussed

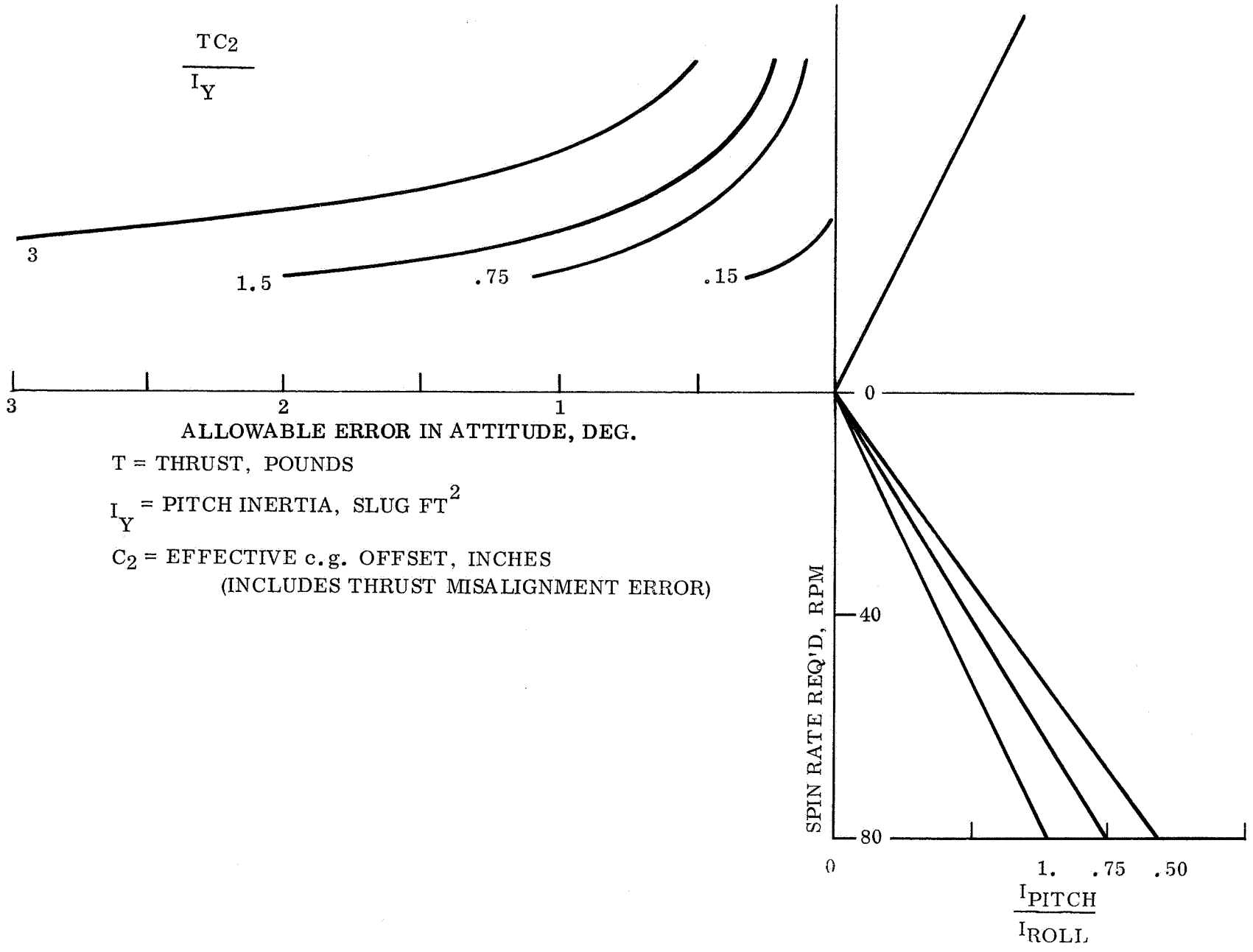

Figure 5.2.3-1. ΔV Orientation Error

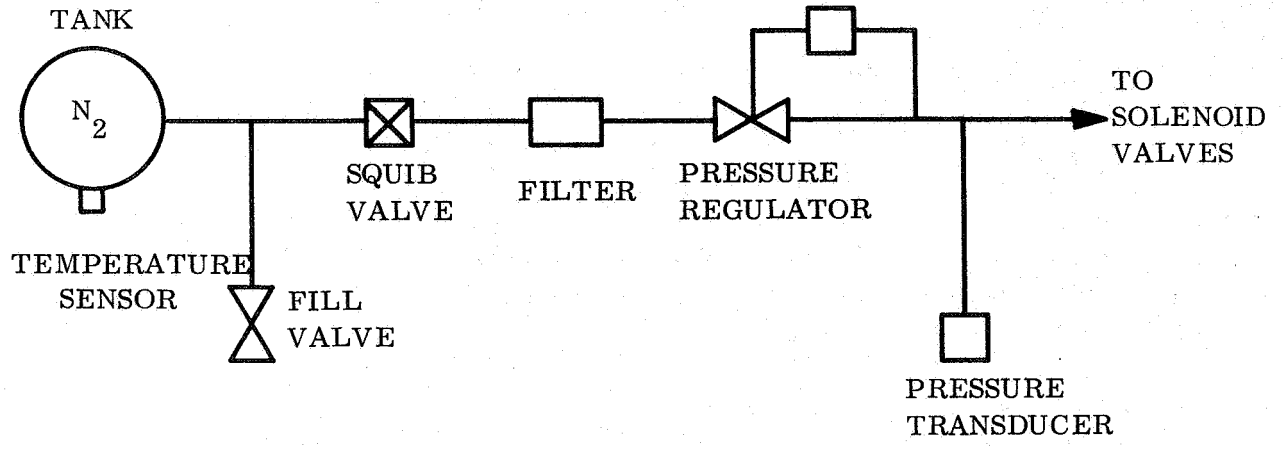

NITROGEN SYSTEM

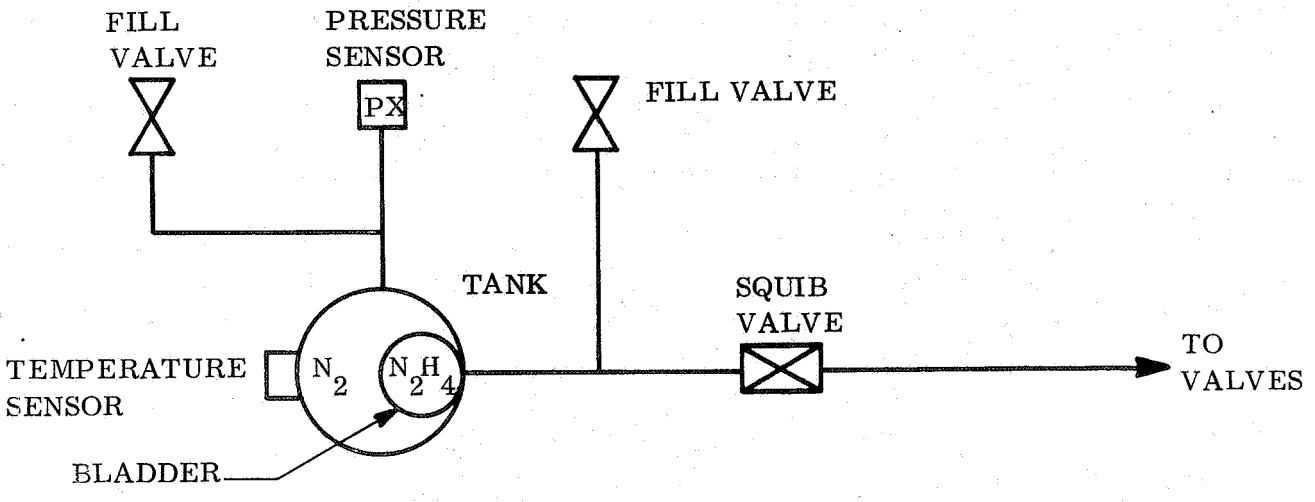

HYDRAZINE SYSTEM

Figure 5.2.4-1. Reaction Control Systems

earlier. Both systems seal off the fuel until Capsule separation from the Spacecraft. The squib valve is then fired, which enables the control system.

A block diagram of the three-axis ACS is shown in fig. 5.2.4-2. It can be used, of course, with either reaction control method. The pitch and yaw torques are generated by single thrusters rather than as couples since forward pointing thrusters are not possible. The possible velocity problem with this arrangement is discussed in a later section.

System operation of the three-axis control is as follows. The gyros are caged before separation from the Spacecraft. Immediately prior to separation, the gyros are switched to their position mode. This establishes an inertial reference identical to the S/C reference. Sufficient control torque is provided so that the reference is not lost during separation because of limited gyro gimbal freedom. The Capsule maintains its attitude within a ± 0.25 degree deadband about each axis. Maneuvers are performed by torquing the gyros at a preset rate of 0.2 deg/sec. This is done one axis at a time. Following ΔV thrusting the Capsule is maneuvered to the proper attitude for entry. A ± 3-degree deadband is assumed for the remainder of the mission to reduce fuel consumption and the number of required thruster valve operations. During entry the ACS is placed in its rate damping mode. The ACS maintains this mode throughout entry.

A block diagram of the spin control subsystem is shown in fig. 5.2.4-3. This system provides control about only one axis of the Capsule and is, therefore, simpler than the three-axis ACS. However, it is not as simple as a basic spin de-spin system because it also provides roll control during entry to prevent aerodynamic torques about the roll axis from spinning the Capsule at an excessive rate.

Providing roll control is more than a matter of providing additional impulse in the reaction system. It results in a different system configuration. Without roll control the ACS would consist of two separate blow-down systems, one for spin, one for de-spin. With roll control it is necessary to provide roll rate control. This requires a roll rate gyro, simple electronics, a pressure regulator, and additional valves. Once this function is provided, it is best to use it for all functions of the mission: spin, de-spin, and roll control during entry. For these reasons the attitude control system has been designed to also provide roll control during entry. The weight penalty for providing the capability of roll rate control is 4 to 7 pounds, excluding additional gas and tanks, over a basic spin/de-spin system.

5.2.5 SELECTION OF ATTITUDE CONTROL SUBSYSTEM

In selecting an attitude control subsystem for the point designs, three-axis stabilization was compared to spin stabilization, using in both cases, nitrogen or hydrazine reaction control thrusters. Criteria of weight, reliability, performance capability, and ability to do other functions were used in this comparison. These criteria are listed in table 5.2.5-1. The most important of which are reliability and the ability to perform an adequate mission.

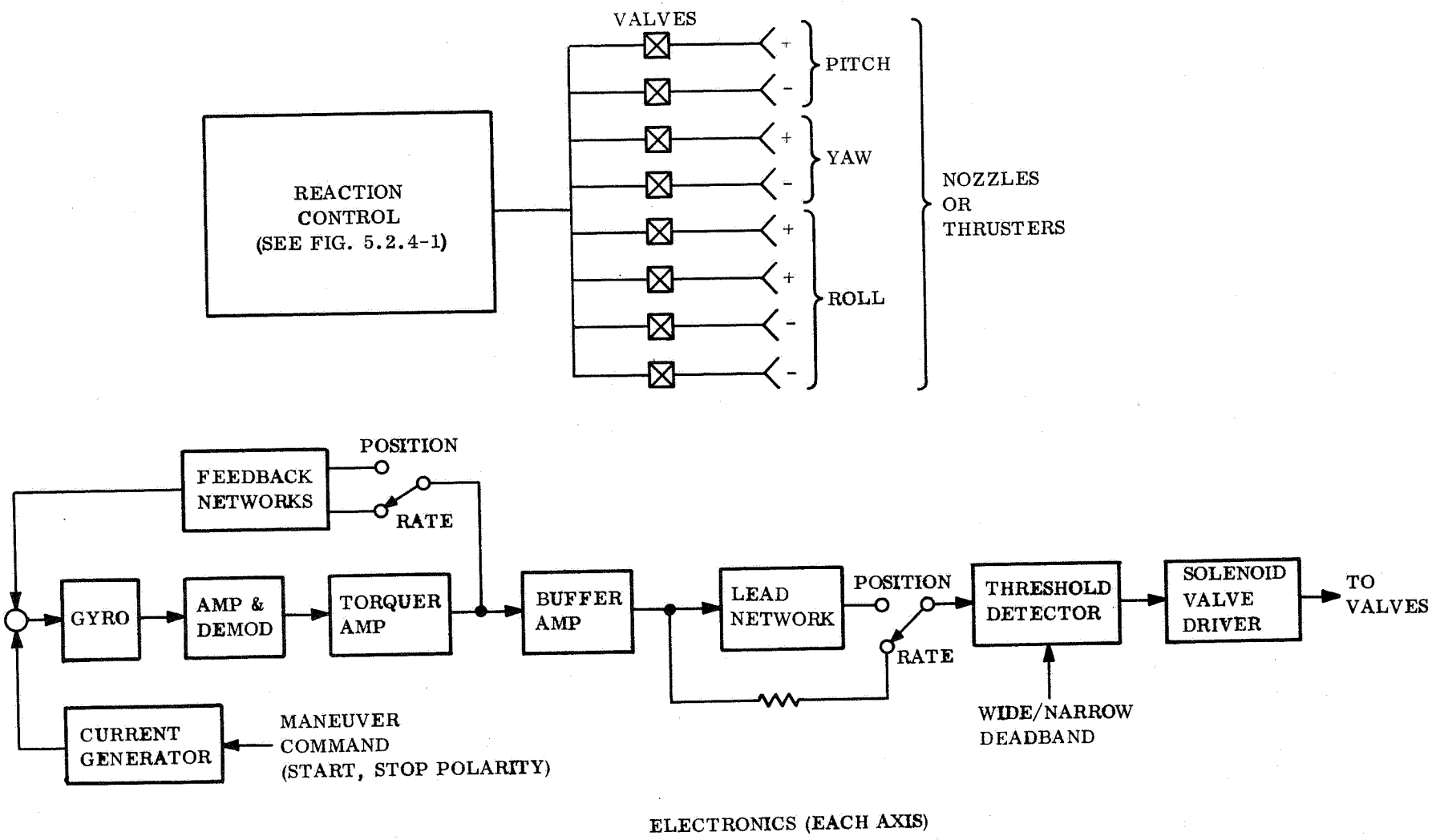

Figure 5.2.4-2. Three-Axis Attitude Control Subsystem, Block Diagram

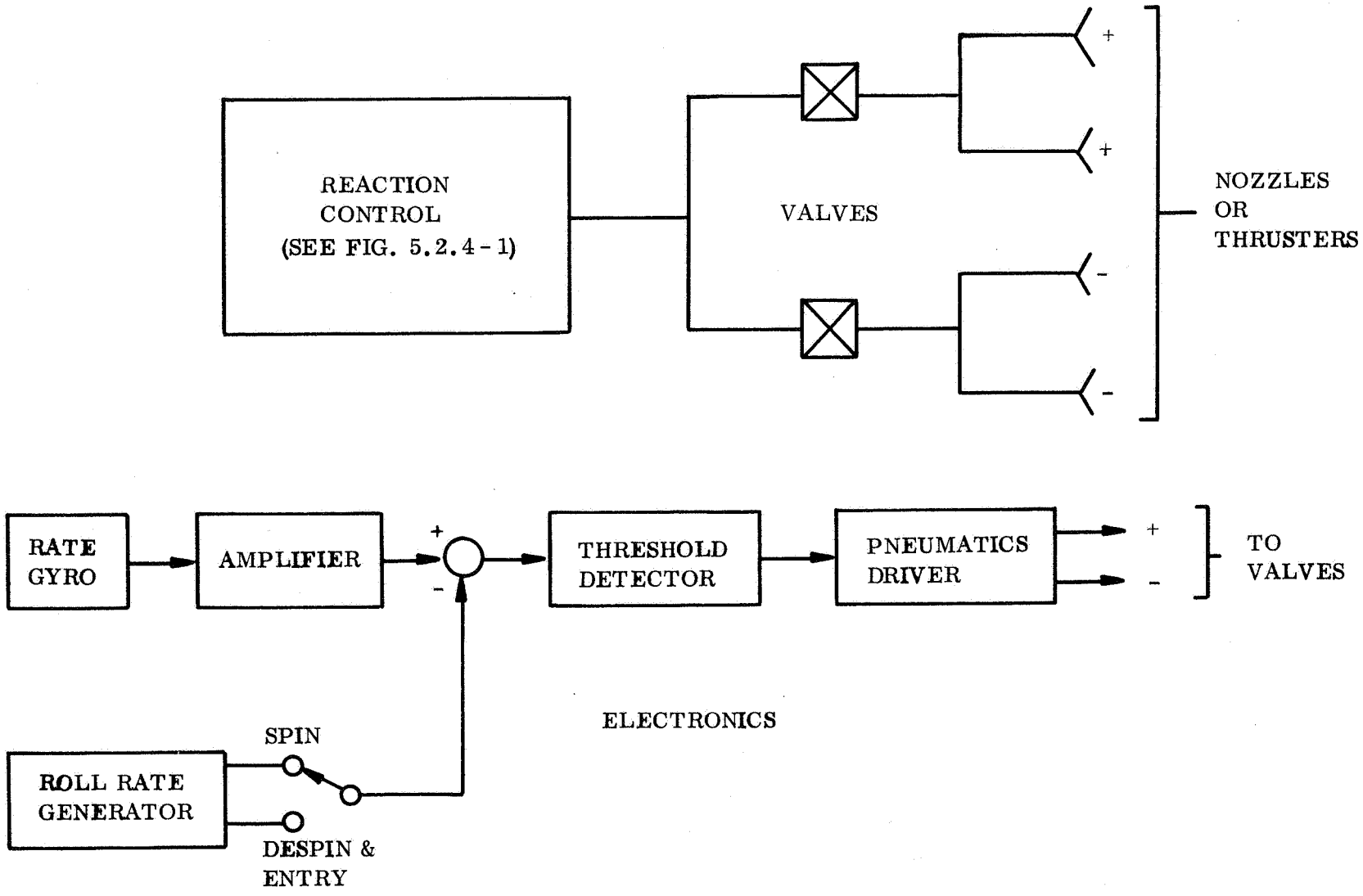

Figure 5.2.4-3. Spin Attitude Control System, Block Diagram

A spin control subsystem employing hydrazine thrusters has been selected for all the point designs. This subsystem has higher reliability and lower weight than the three-axis subsystem because it controls about only one axis and uses fewer, less complex components. It also holds the pointing direction during deflection or deorbit to an accuracy (0.7 degree, one-sigma) sufficient to hold the entry dispersion to reasonable limits. The three-axis subsystem can achieve a better accuracy (0.5 degree, one-sigma); however, this improvement is not felt sufficient, in terms of the mission requirements, to justify the additional weight and complexity.

The following sections describe, in more detail, the comparison between these two types of control subsystems. The four criteria listed in table 5.2.5-1 are used as an outline.

5.2.5.1 Weight Comparison

Several of the point designs were used as a basis for a weight comparison. The subsystem weight of each type of control, using the two types of reaction thrusters, were computed for each point design. The results, as shown in fig. 5.2.5-1, demonstrate that a spin subsystem is lighter by at least 15 pounds than an active three-axis subsystem, and that hydrazine control is lighter by at least 20 pounds than nitrogen control.

The four vertical lines plotted in fig. 5.2.5-1 represent the fixed hardware weight. An itemized list is shown in table 5.2.5-2. Comparison of the vertical lines with the plotted subsystem weights shows that the weight difference between the two hydrazine subsystems is due chiefly to the difference in fixed hardware weight, and that the weight difference between the two nitrogen subsystems is due to the variable weight of nitrogen and tankage.

TABLE 5.2.5-1. CRITERIA FOR CONTROL SUBSYSTEM SELECTION

1. Weight
2. Reliability
3. Performance
   - Pointing Accuracy
   - Initial Entry Angle of Attack
   - ΔV Accuracy
4. Other Functions
   - Stability Augmentation
   - Integration With Propulsion System

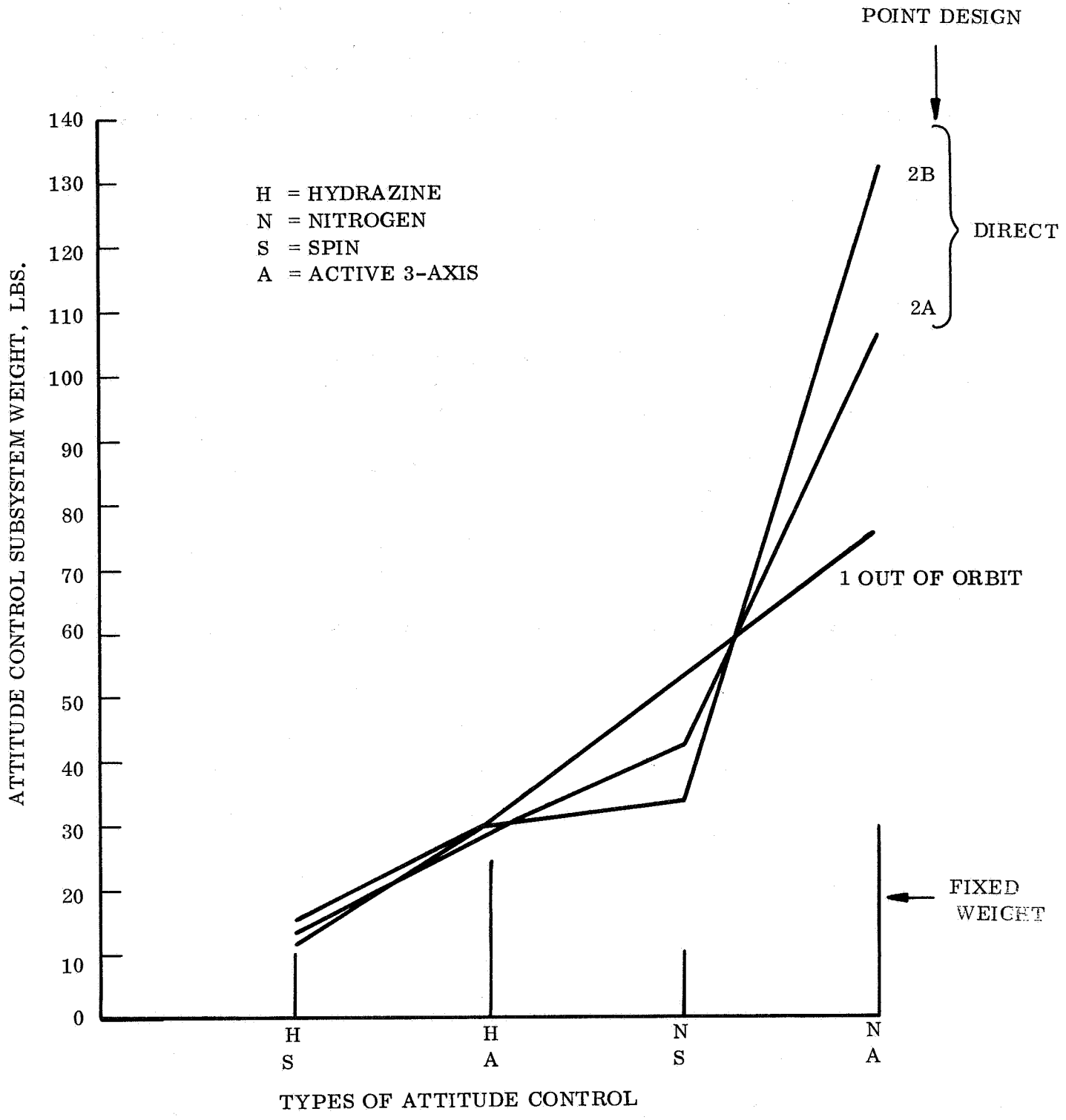

Figure 5.2.5-1. Attitude Control Weight Comparison

TABLE 5.2.5-2. FIXED HARDWARE WEIGHT

Component	Unit Wt.	Spin		3-Axis	
		GN_2	N_2H_4	GN_2	N_2H_4
Fill Valve	.25	.25	.5 (2)	.25	.5 (2)
Squib Valve	.5	.5	.5	.5	.5
Filter	.25	.25	---	.25	---
Press. Regulator	2.0	2.0	---	2.0	---
Press. Sensor	.5	.5	.5	.5	.5
Temp. Sensor	.25	.25	.25	.25	.25
Solenoid Valves	.5	1.0 (2)	---	4.0 (8)	---
Nozzles	.4	1.6 (4)	---	3.2 (8)	---
Thrusters	.25	---	1.0 (4)	---	2.0 (8)
Valves	.3	---	.6 (2)	---	2.4 (8)
Tubing, Fittings		1.05	1.05	.205	2.05
Rate Gyro	1.0	1.0	1.0	---	---
Gyro Assembly	11.1	---	---	11.1	11.1
Spin Electronics	2.4	2.4	2.4	---	---
Electronic Assem.	6.1	---	---	6.1	6.1
Total	lbs	10.8	7.8	30.2	25.4

5.2.5.2 Reliability Comparison

An indication of relative reliability is given by the component list of table 5.2.5.2 and the block diagrams of figs. 5.2.4-1, 5.2.4-2, and 5.2.4-3. Due chiefly to the reduced number of valves, both spin subsystems have 10 fewer components than the three-axis subsystems. Of more importance, however, is the use of a single rate gyro and simple spin electronics instead of the assembly of three integrating gyros and gyro electronics, and the three channels of control electronics required for the three-axis design.

It cannot be argued, of course, that as of today the reliability of a hydrazine control is equivalent to that of a nitrogen control. However, it is felt that the present industry effort will result in reliable flight proven hydrazine thrusters and control subsystems prior to the design phase of this program.

A final reliability question is the effect on the spacecraft of possible momentary jet impingement of the hydrazine thrusters. The products of hydrazine decomposition are ammonia, nitrogen and hydrogen. No ill effects are known of these products for the possible impingement the spacecraft may endure during the initial attitude control or spinup of the Capsule. Similar products of combustion, plus water, were present on the Gemini flights (with bipropellant thrusters) with no known effects on the Spacecraft subsystems. For these reasons, it is felt that the use of hydrazine is not a reliability hazard, although further data should be obtained as more flights are made with this fuel.

5.2.5.3 Performance Comparison

The primary performance requirement is to maintain pointing errors during deflection or deorbit propulsion firing so that the entry path angle and down range dispersion are within mission requirements. As discussed in Section 3.3 of Volume II, a pointing error (ΔV orientation) of 0.6 degree, one sigma with an 0.6 percent velocity error will result in approximately 600 KM down range dispersion for the out-of-orbit entry mission. Although the dispersion is inherently greater for the direct entry mission, control of the pointing error is required to hold path angle errors to reasonable limits.

An error analysis of the two control subsystems was performed to compare their pointing accuracies. The results, summarized in table 5.2.5-3, show that the three-axis subsystem is slightly more accurate than the spin subsystem. However, the performance of the spin subsystem (nearly 0.7 degree, one sigma pointing accuracy) is judged adequate to achieve good control of the entry path angle and reasonable low down range dispersions.

TABLE 5.2.5-3. ERROR ANALYSIS

No.	Error Source	3σ or Max. Value	
		Three-Axis (deg)	Spin (deg)
	Spacecraft		
1.	Control Deadband	.458	.458
2.	Sensor Align./Repeatability	.150	.150
3.	Electronic Drift Error	.050	.050
4.	Maneuver Error		.200
5.	Gyro Drift		.154
	Capsule		
6.	Capsule Align. Error	.300	.300
7.	Maneuver Error	.200	
8.	Gyro Drift	.154	
9.	Nozzle Align. Error	.250	
10.	Tip-off Error		.750
11.	Spin-up Coning Error		.200
12.	ΔV Coning Error		.750
13.	Control Deadband	.250	
TOTAL ERROR (1 σ)		.51°	.67°

(Gaussian errors are assumed except for No. 1 - uniform distribution - and No. 13 - a known fixed value.)

Another performance criteria, as listed on table 5.2.5-1, is the ability to maneuver to and hold an inertial attitude prior to entry so that the initial angle of attack will be nominally zero. The three-axis subsystem can do this; the spin system cannot. The aerodynamic design, however, can tolerate an initial angle-of-attack of 40 degrees. Since the spin attitude for propulsion firing is within 40 degrees of the inertial direction of the entry angle, both the spin and the three-axis design can meet this requirement for these missions.

A final performance criteria is the possible linear velocity generated by the attitude control subsystem after propulsion firing. This velocity must be considered in determining the overall velocity accuracy of the Capsule deflection or deorbit. The spin subsystem, since its thrusters form a couple about the roll axis, will not generate a linear velocity change. However, the three-axis subsystem, since it is constrained to use single thrusters in both the pitch and yaw axis, will produce a net velocity change during the limit cycle operation following propulsion firing and prior to entry.

The magnitude of the velocity error can be significant for the direct entry case even with the hydrazine thrusters selected. For example, up to a two percent error in the velocity increment can be caused in point design one if a three-axis control were used. There are several solutions to this potential problem. One solution is to reduce

the thrust level of the control thrusters. This requires an increase in burn time and lower thrust of the propulsion system, both of which appear to be feasible.

The performance comparison of the spin and the three-axis control subsystems, then, indicates that both can perform an adequate lander mission. Even though the three-axis is slightly better in achievable pointing accuracy, the resulting improvement in mission performance does not appear to warrant the increased complexity and weight of this type of control.

5.2.5.4 Other Functions

The three-axis subsystem can be modified to perform two additional functions that have been briefly considered in this study. The first of these functions is to provide entry stability augmentation, or rate damping about the pitch and yaw axis in addition to that about the roll axis. This would require additional fuel only. However, the present analysis indicates that this is not now needed, nor likely to be.

The second additional function is that of supplying the deflection or deorbit propulsion. This would require the integration of the present propulsion subsystem with the attitude control subsystem. Such a design is being utilized in the "Direct versus Out-of-Orbit Entry" study. A single source of hydrazine is used in that study to generate the velocity increment, provide three-axis control, and to produce the vernier thrust required for the soft landing. Such a design offers the advantages of simplicity with only a small weight penalty. However, since the Hard Lander does not need the vernier thrust, a brief consideration of this integrated design indicates it would be a significant weight penalty.

5.2.6. ATTITUDE CONTROL REQUIREMENTS

The attitude control requirements for successful completion of the mission are an item to be considered in trade-off analyses. The principle requirements to be considered are the ΔV orientation error and the terminal stability performance. The former affects the mission study trade-off, the latter the configuration trade-offs.

Considering first the problem of attitude stability in the lower speed portion of the flight (Mach 8), the low speed stability is a function of roll rate and thus keeping the roll rate from exceeding some particular level will result in a stable vehicle for vehicle cone angles up to and at least slightly exceeding 60 degrees. (See Section 3.1.2, Vol III Aerodynamic Stability Criteria) For cone angles of 70 degrees and greater, a pitch/yaw damping system may be required for stability in the flight regime of decreasing dynamic pressure.

The allowable ΔV orientation errors are dependent on mission design and other errors associated with the trajectory. The problems are discussed in Vol II Section 3.2, Path Angle and Downrange Dispersions. The intent in this section is to demonstrate how the orientation requirements vary with the trajectory design and constraints.

The out-of-orbit mission design control requirements are based on holding the 3σ in plane dispersion to $\approx$ 600 Km based on a postulated desire to land in Syrtis Major (diameter 700 Km). Figure 5.2.6-1 shows the approximate 3σ dispersion versus the 1σ error in ΔV orientation assuming a 1σ error in ΔV magnitude of 0.5 percent. This figure indicates the trade-off available between system complexity/ reliability and mission constraints. As can be seen, there is not an absolute requirement for the 0.6 degree orientation error considered in the preceding section, rather it is an example based on the reference out-of-orbit mission discussed in Volume II.

Direct entry requirements are based on minimum path angle considerations, since the dispersions are on the order of 2000 Km and cannot reasonably be held to the 700 Km value. Figure 5.2.6.2 shows the trade-off of ΔV attitude requirement versus nominal entry path angle as a function of a 1σ error in the impact parameter. The direct entry reference mission has been chosen with an entry path angle of 25 degrees and a reasonably conservative estimate of impact parameter uncertainty taken as 100 Km (1σ). This leads to a ΔV attitude requirement of 0.5 degree, 1σ. As can be seen in figure 5.2.6-2 a smaller value of impact parameter uncertainty relaxes the attitude requirement as does increasing the nominal path angle. For example, increasing the nominal path angle to 26 degrees allows a relaxation in ΔV attitude requirement from 0.5 degree, 1σ to 1.0 degree, 1σ at a cost of $\approx$5 percent maximum allowable ballistic coefficient (see Section III-3.1.2).

Tables 5.2.6-1 and -2 are a summary of the attitude control requirements, spin system and three-axis performance in each of the three mission phases for the out-of-orbit and direct entry reference missions. The three-axis system meets all requirements, but the spin system is slightly over on the ΔV orientation error. As was seen in the preceding curves it involves a very small compromise to allow the errors associated with the spin system to be used.

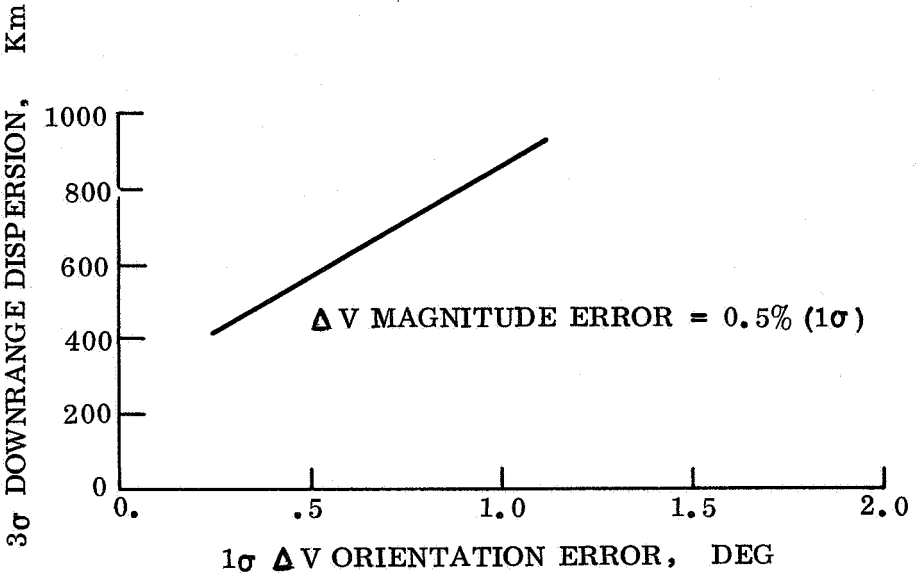

Figure 5.2.6-1. Out of Orbit Downrange Dispersion

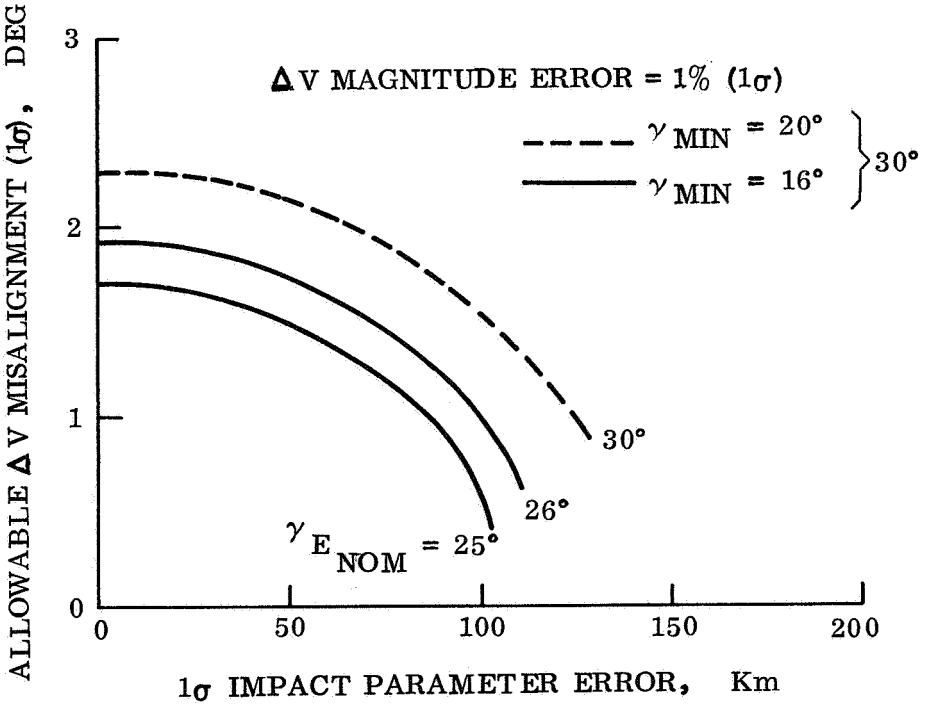

Figure 5.2.6-2. Direct Entry ΔV Orientation Requirements

III

TABLE 5.2.6-1. DIRECT ENTRY MISSION

Mission Phase	Requirement Determined By	Requirement	Spin System Performance	Three Axis Performance
Deorbit	Skip limit (Based on 25° γE, ΔB = 100 Km) 100 Km)	$\Delta\varphi < .5°$ (1σ)	$\Delta\varphi = .67°$ (1σ)	$\Delta\varphi = .51°$ (1σ)
Entry	Loads & Heating	αE < 30°	Det. by ΔV direction Nominal 10° Uncertainty ± 10°	± 5°
Terminal Phase of Atmospheric Flight	Stable Base for data sampling	Small (α<10°)	Vehicle stable	Vehicle stable

TABLE 5.2.6-2. OUT-OF-ORBIT MISSION

Mission Phase	Requirement Determined By	Requirement	Spin System Performance	Three Axis Performance
Deorbit	Desire to hold 3σ inplane dispersion to ~700 Km (diameter of Syrtis Major)	$\Delta\varphi < .6°$ (1σ)	$\Delta\varphi = .67°$ (1σ)	$\Delta\varphi = .51°$ (1σ)
Entry	Entry Loads and Heating (Aft Corner Beefed-up)	$\alpha E < 30°$ $(\alpha E < 50°)$	Determined by ΔV direction Nominal 15° uncertainty ±10°	± 5°
Terminal Phase of Atmospheric Flight (M < 8)	Stable base required for data sampling	Small $(\alpha \leq 10°)$	Vehicle stable for low spin rate. (Roll rate control req'mt based on configuration)	Vehicle stable

5.3 CANISTER/ADAPTER

The biological sterilization canister and the internal adapter form the major structural components of the pre-entry systems. Conceptually, the design alternatives are: either separate structural units or a single integrated unit, in which the portion of the canister shell remaining with Spacecraft, (subsequent to separation of the entry vehicle) acts as the adopter to support the entry vehicle prior to deorbit sequence. Previous studies on the MM'73 mission have shown that a separate adapter offers a minimum weight system and provides simplicity in design for considerations such as thermal control and separation. This concept of separate units is, therefore, adapted for the parametric studies. Parametric data for the canister and adapter were generated for use in structure, environmental control, pressure and venting system and separation systems parametric analyses.

Figure 5.3-1 represents a schematic of the canister, adapter and aeroshell with lettered dimensional parameters. Figure 5.3-2 presents, as a function of canister diameter, plots of all of the lettered dimensions of fig. 5.3-1. Knowing the specific canister diameter, all other relevant dimensions for the canister, adapter and aeroshell relating to the specific canister diameter, can be determined from these plots.

Figure 5.3-3 represents the canister internal vented volume as a function of the canister diameter in feet. This is the gross internal volume available less the volume taken up by aeroshell, Lander parachute and deorbit propulsion (or entry propulsion systems).

Figure 5.3-4 represents the surface areas in square feet, of the hemispherically shaped forward canister, conical aft canister and the canister aft closure as a function of the canister diameter in inches. These areas were derived using the parametric dimensions shown in fig. 5.3-2.

Figure 5.3-5 gives the hemispherical forward canister weight for several area weight densities as a function of the canister diameter in inches. These weights were calculated using the curves of fig. 5.3-4.

The weight of the canister and adapter structure, as a function of canister diameter, can be determined from fig. 5.3.1-1 for the structure alone and from fig. 5.3.1-2 for the field joint rings.

With the heater power (in watts) known and the total surface area to be insulated (from fig. 5.3-4) the insulation thickness can be determined from fig. 5.3.2-5.

The separation system weight as a function of the canister can be determined from fig. 5.3.3-1 and the pressure and vent system weight from fig. 5.3.2-1.

For a fixed diameter canister the total weight of the canister can be obtained by adding the individual weights from the figures.

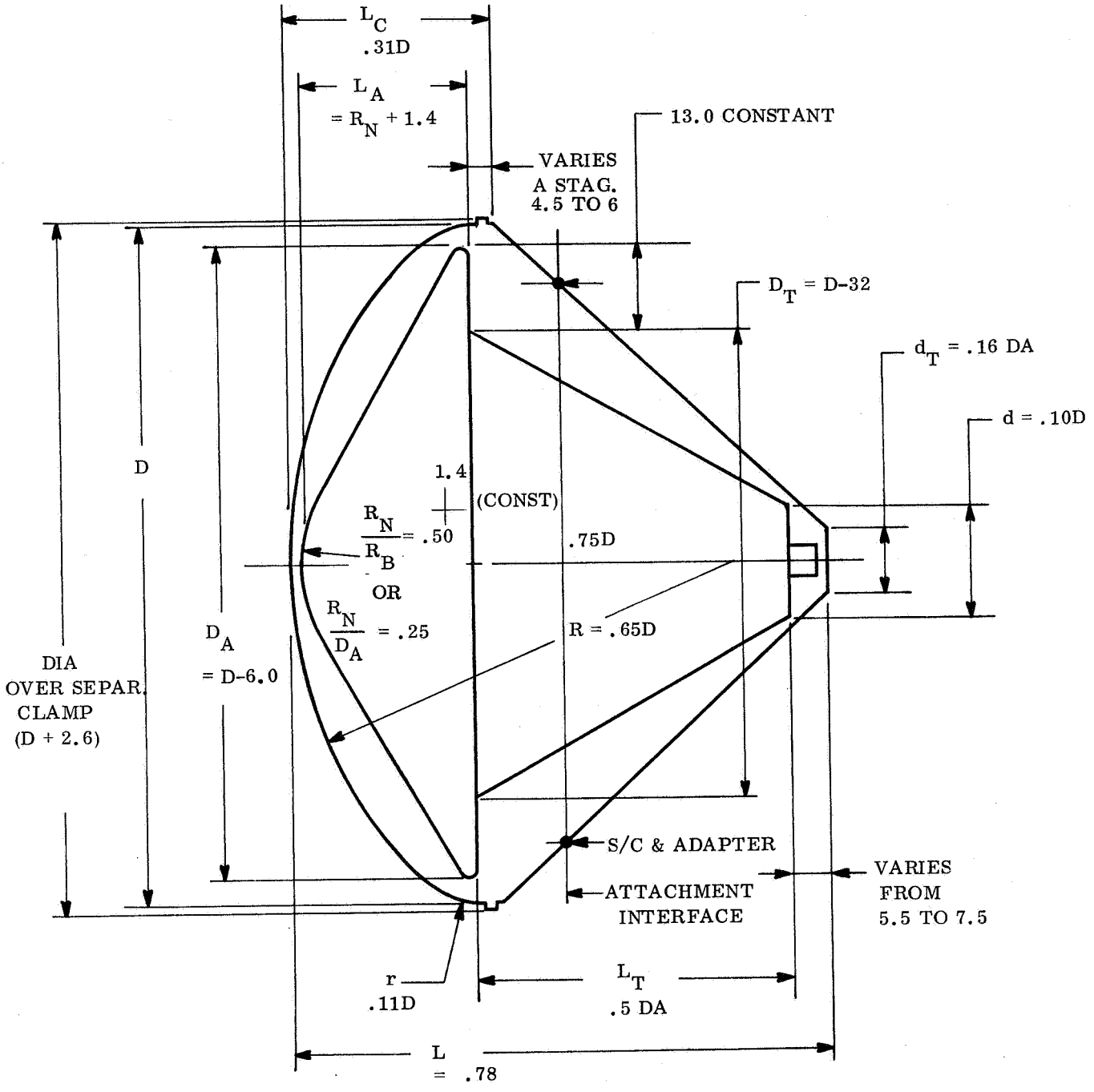

Figure 5.3-1. Canister/Aeroshell Schematic Arrangement

5.3.1 STERILIZATION CANISTER

Analyses conducted for the MM '73 Phase B study show that, if no account is taken of meteoroid protection requirements for the canister design, the critical loading due to launch inertias can be satisfied with minimum manufacturing gage materials and that the critical loading for design is governed by internal shell pressure. The design is also critical for stiffness requirements both under static handling and dynamic loading for which the structural configuration must be optimized.

5.3.1.1 Structural Criteria, Assumptions and Baseline

5.3.1.1.1 Criteria

1. Loading and Load Factors:

   a. Flight inertia and dynamic loading based on Titan III-C environments are:

Axial inertia	-3g to +6g	Including dynamic limit
Lateral inertia	±2g	loading factor based on
Ultimate factor	1.25	quasisteady environment.

   b. Ground Conditions: Inertia 2g with ultimate factor 1.5

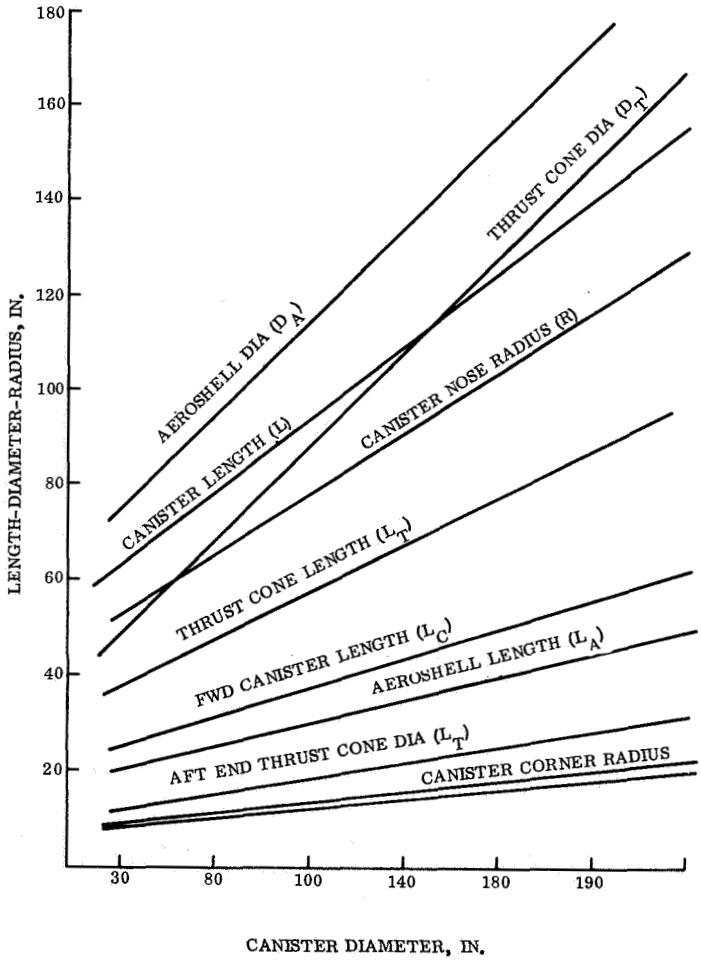

Figure 5.3-2. Canister/Aeroshell Dimensions as a Function of Canister Diameter

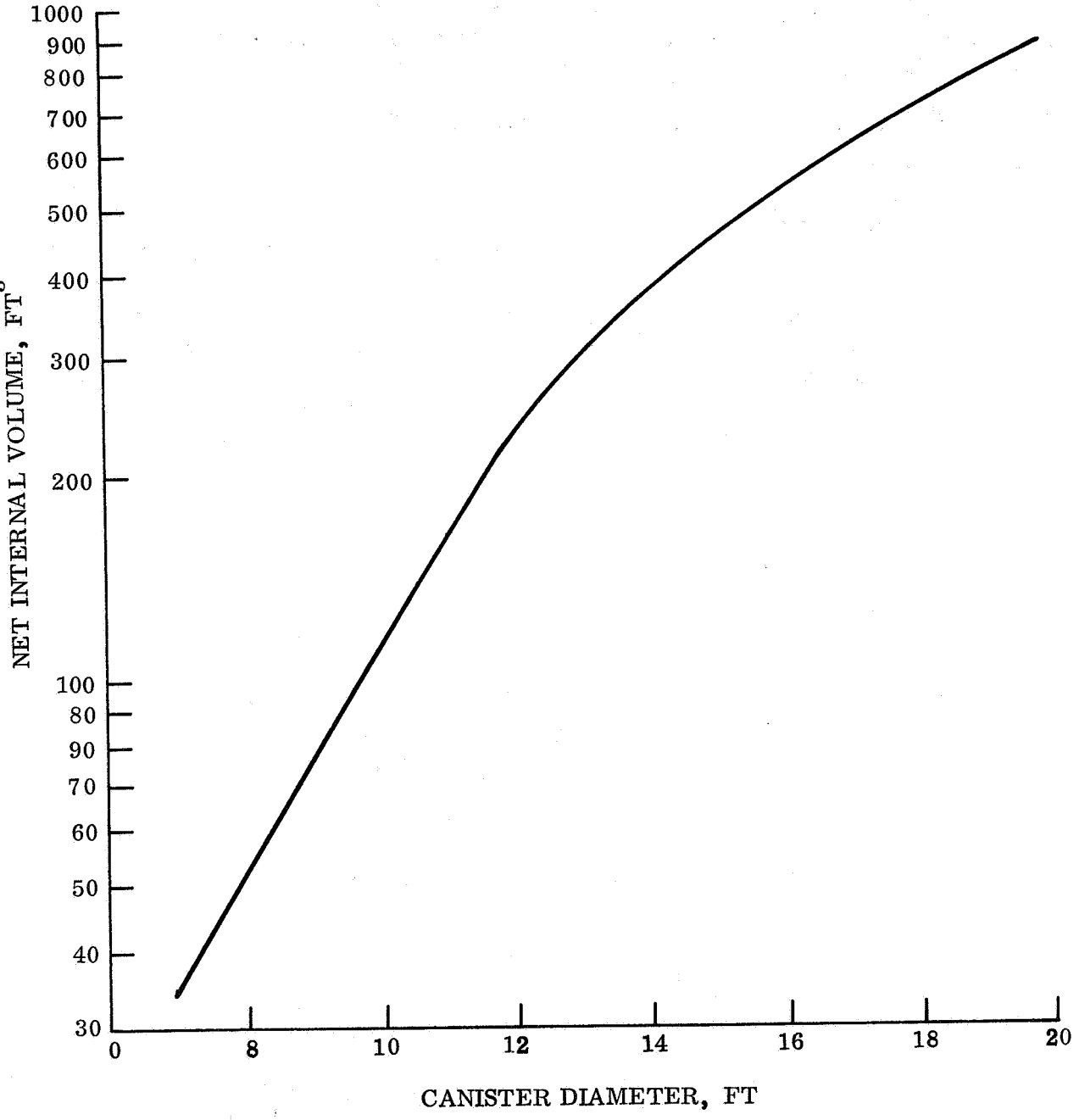

Figure 5.3-3. Canister Internal Vent Volume

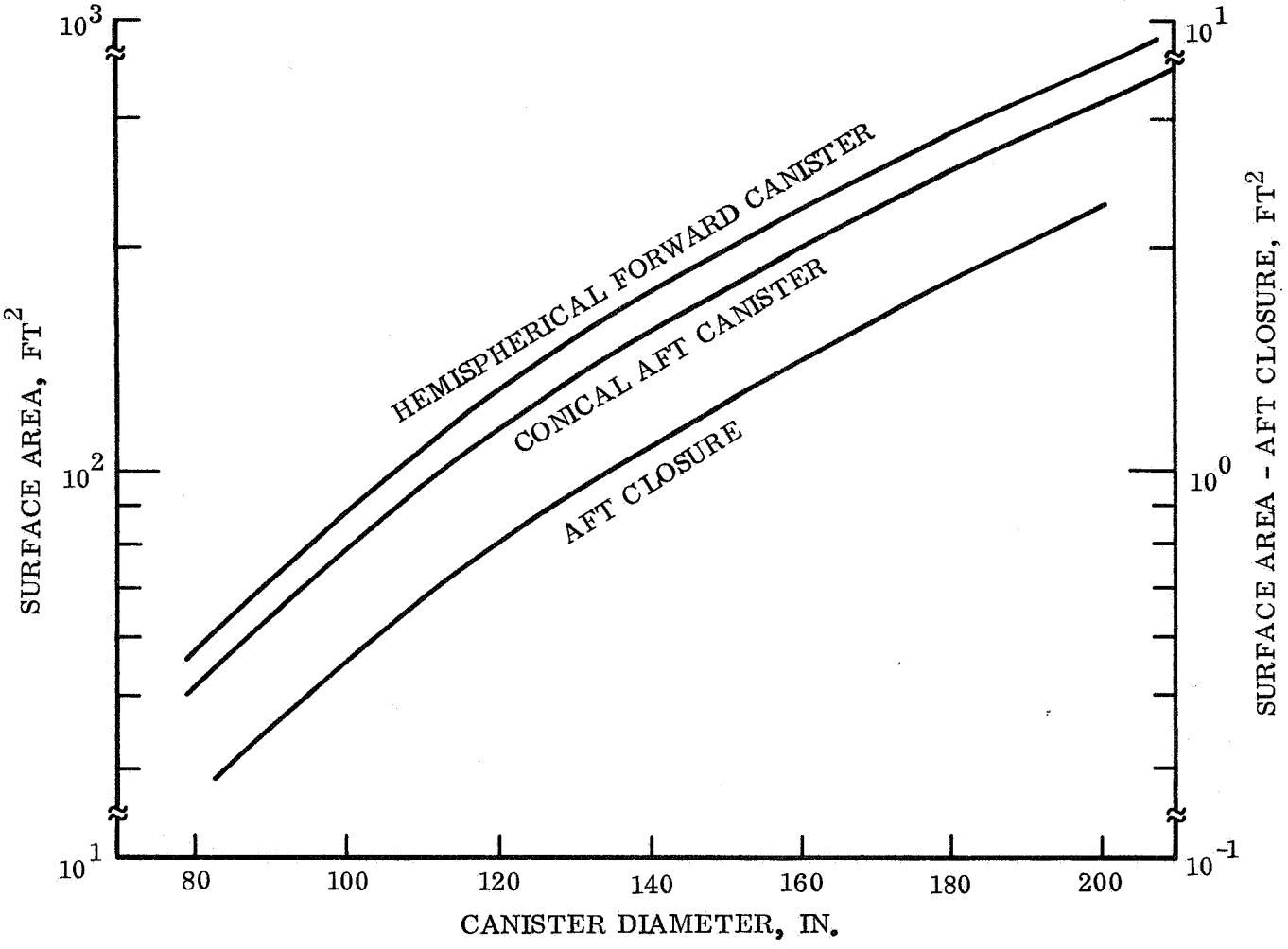

Figure 5.3-4. Canister Surface Areas

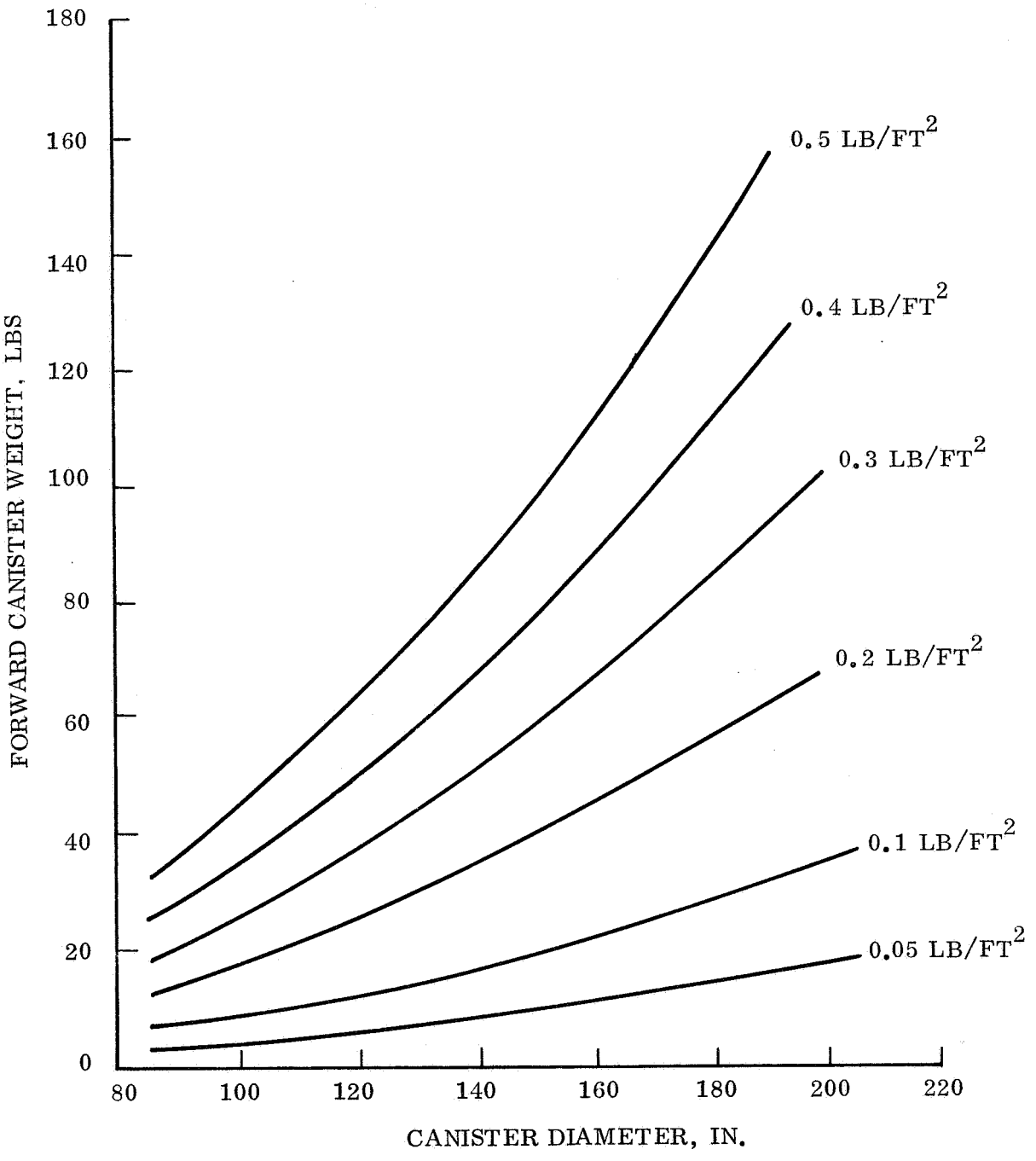

Figure 5.3-5. Hemispherical Forward Canister Weight for Various Weight Densities

c. Internal Pressurization: (minimum differential 0.5 lb/in.^{2})

Yield pressure = 1.33 x design limit pressure
Ultimate pressure = 1.67 x design limit pressure

d. Temperature: Sterilization temperature 275^{o}F constant for six cycles of 24.5 hr each at 0.5 lb/in.^{2} differential. Interplanetary temperatures of -300^{o}F to 150^{o}F.

e. Vibration: Launch frequencies of 10-15 cps with 140 dB acoustic.

2. Assumptions and Baseline:

a. Forward canister to be spherical in shape, with toroidal shape at the joint ring.

b. Aft canister to be conical in shape, also with toroidal shape at the joint ring.

c. Canister is independent of a separate adapter.

d. Geometry related to nominal diameter as shown in figs. 5.3-1 and -2.

e. Minimum gauges are shown in table 3.1.2-7(a) with corresponding weight densities for the shells shown in table 3.1.2-7(b).

f. No consideration is given to protection against meteoroid impact.

5.3.1.2 Parametric Data Requirements: Parameters and Ranges

The objective of parametric analysis is to obtain data to enable extrapolation of structural sizes, weight densities and total weights for the canister (forward and aft sections) structure for ranges of various design parameters.

Parameters and Ranges:

Canister geometry: Nominal diameter: 7 to 16 feet (Other geometry related to this diameter as shown in fig. 5.3-2)

Canister internal pressure differential	0 to 6 lb/in.^{2}
Type of structural construction	Monocoque Semi-monocoque Honeycomb sandwich

Other constructions are inherently heavier and hence not considered. Typical constructions are shown diagrammatically in fig. 3.1.2-102.

Structural Materials:

Aluminum
Titanium
Steel
Beryllium
Magnesium
Fiberglass

Material properties are summarized in table 3.1.2-6. Of these materials, Beryllium is unsuitable for cost and fabricability, Magnesium for corrosion and storage and fiberglass for porosity and stiffness considerations.

5.3.1.3 Analysis

5.3.1.3.1 Pressure Loading

Consider the limiting case of a 16-foot canister with 6 lb/in.^{2} differential pressure (which occurs during launch condition at about 160^{o}F).

Forward Canister $\quad t = \frac{6 \times 1.67 \times 16 \times 12}{4 \times 6 \text{ allow.}} = \frac{450 \text{ in.}}{6 \text{ allow.}}$

Material	Al	Ti	Steel
σ allow lb/in.^{2}	60,000	120,000	200,000
t in.	0.0075	0.0038	0.0023
t min. in.	0.012	0.008	0.008

Aft Canister $\quad t = \frac{6 \times 1.67 \times 16 \times 12 \times \sec}{4 \times \sigma \text{ allow.}} = \frac{623 \text{ in.}}{\sigma \text{ allow.}}$

Material	Al	Ti	Steel
σ allow lb/in.^{2}	60,000	120,000	200,000
t in.	0.0104	0.0052	0.0031
t min. in.	0.012	0.008	0.008

Hence for both sections the design is based on minimum gauge for all ranges of diameter and internal pressure.

5.3.1.3.2 Buckling Considerations

During sterilization and launch phases, there is a requirement for minimum internal pressure of 0.5 lb/in.^{2}. Under launch conditions, assuming a structural weight density of 0.5 lb/ft^2,

The equivalent pressure loading $= \frac{0.5 \times 1.25 \times 6}{144} = 0.026$ lb/in.^{2}

Which is overridden by the internal pressure and is not a critical loading condition. The same is also true for the lateral inertia case.

5.3.1.3.3 Stiffness Requirements

Minimum material gauges referred to above are necessary for fabricability and manufacturing considerations. For handling requirements, a monocoque shell will necessitate stabilization. Hence, either semi-monocoque (ring and stringer stiffened), corrugation stiffened or honeycomb sandwich constructions in minimum gauges would be more appropriate. Voyager Phase B canister studies have shown that both the latter constructions provide adequate stiffness for launch vibration environment frequency response considerations.

5.3.1.4 Structural Weights

The weight densities (ρ) in lb/ft^2 for the canister shells in minimum gauge design for various materials and constructions are shown in table 3.1.2-7(b) and fig. 3.1.2.102.

The total canister weights can be derived as follows:

Weight of forward canister $= 1.266\ D^2\rho$

Weight of aft canister $= 1.125\ D^2\rho$

Weight of aft closure $= 0.008\ D^2\rho$

where D is nominal diameter, feet and ρ is weight density, lb/ft^2.

Canister Junction Ring

Ring loading due to juncture:

$$Q\ (\text{Factored}) = \frac{.967 \times 12 \times 1.67 \times PD}{4}\ \text{lb/in.}$$

For the critical case of 6 lb/in.^{2} pressure, with a factor of 1.25 to allow for inertia and dynamic loading,

$$\text{Maximum load in ring} = \frac{Q\max \times D}{2} = \frac{574 \times 16 \times 12}{2} = 55,100$$

$$\text{Area required} = \frac{55,100}{60,000} = 0.919\ \text{in.}$$

$$\text{Ring weight} = \pi D \times 12 \times 0.919 \times 0.1 = 55.4\ \text{lb.}$$

Variation of the canister shell weight and the junction ring weight with canister diameter are shown in figs. 5.3.1-1 and -2.

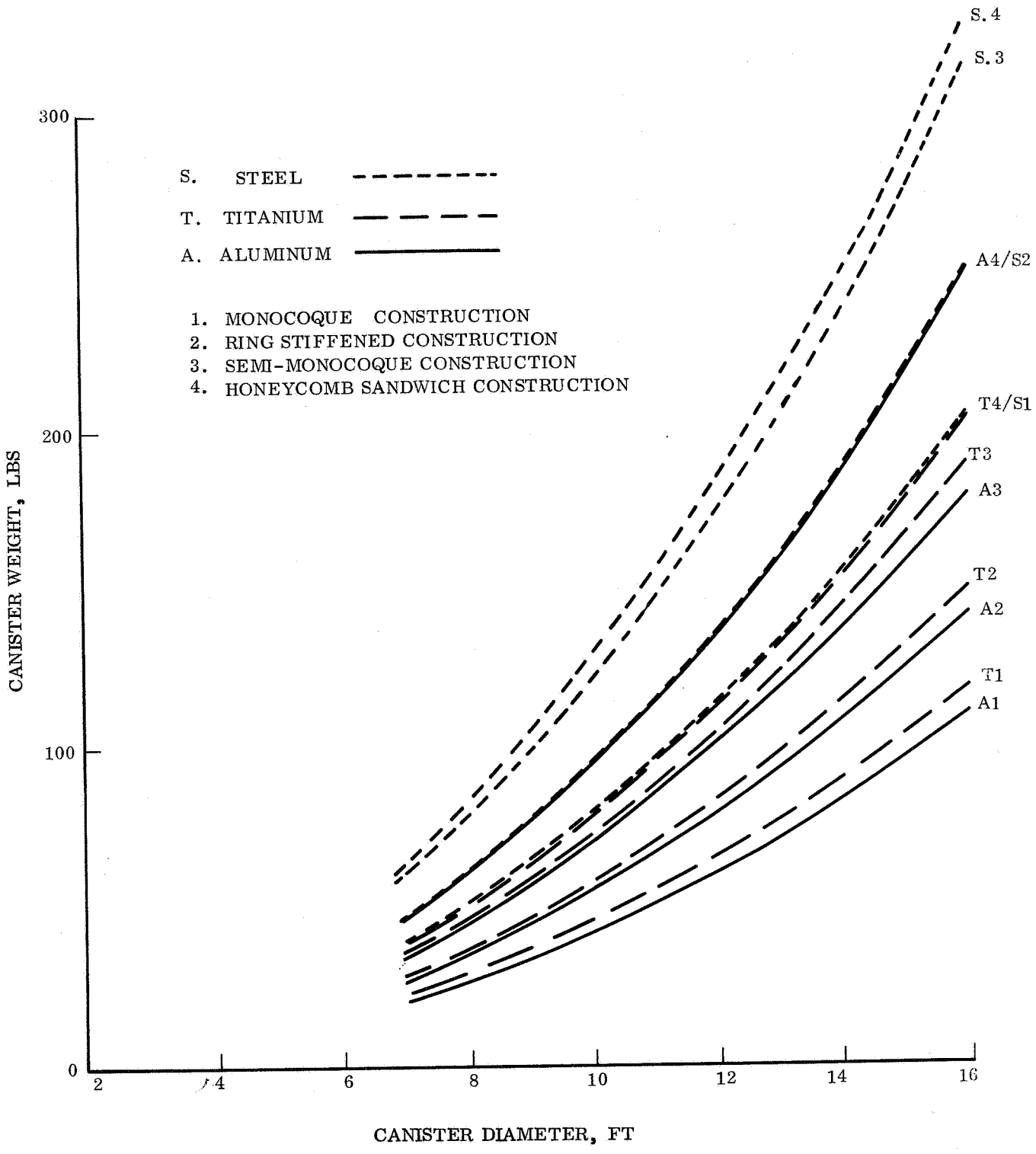

Figure 5.3.1-1. Canister Weights Parametric Variation

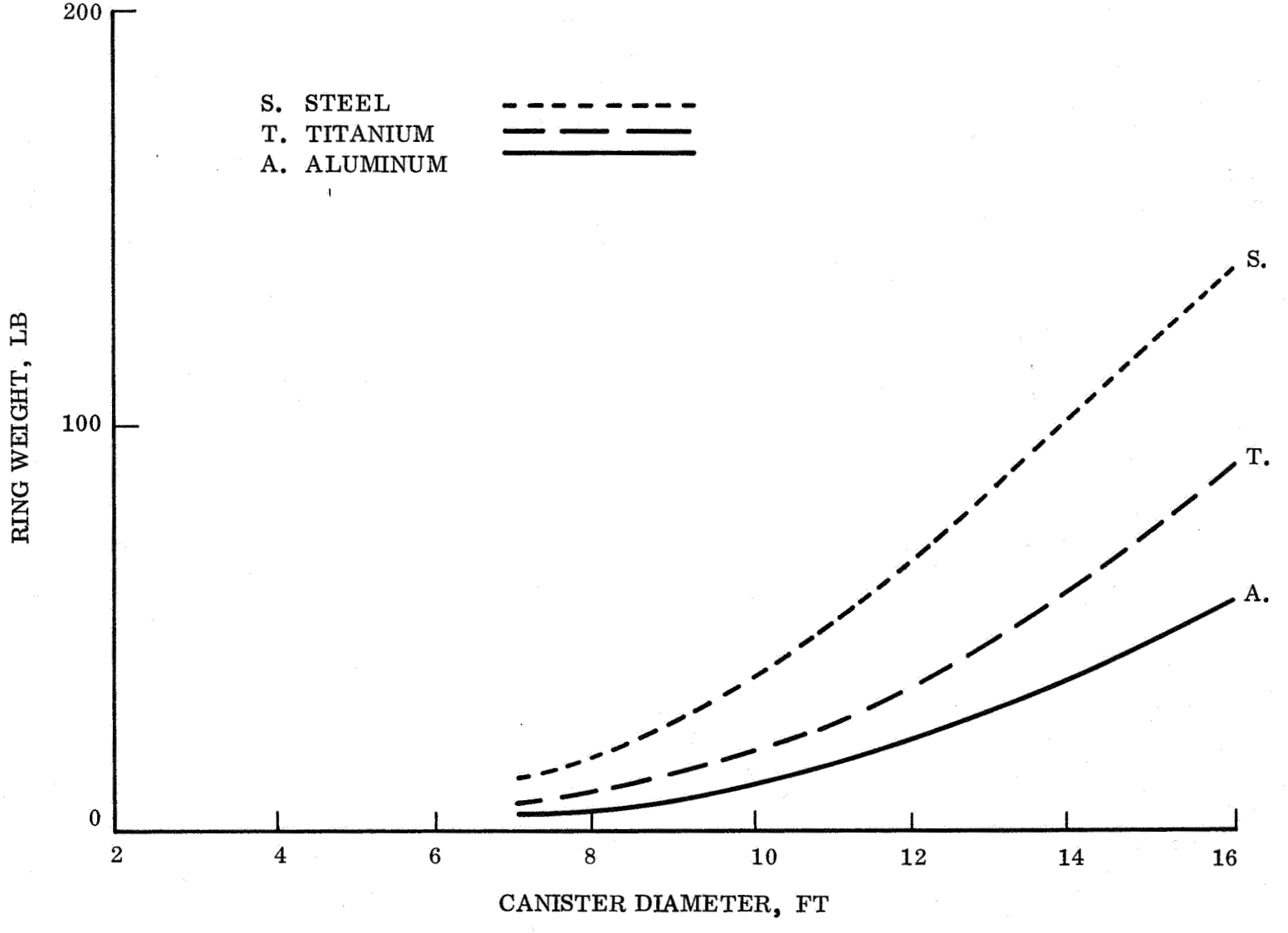

Figure 5.3.1-2. Joint Ring Weights Variation

5.3.1.5 Capsule Adapter

The adapter forms the structural interface between the interplanetary/orbital Spacecraft/bus and the planetary entry vehicle. It must be designed to sustain and transfer the loading due to the entry vehicle to the Spacecraft during mission phases prior to the separation of the entry vehicle in planetary orbit (out-of-orbit entry mode) or from interplanetary transit orbit (direct entry mode). (ref. Vol. II, para 2.2.3.3). The adapter must also be designed to show stiffness and frequency characteristics, when subjected to the vibration shock, and acoustic environments during these mission phases, such that no excessive excursions, interferences and couplings ensue.

The critical loading conditions occur during launch and powered flight phases with high axial and lateral inertias, as defined for the canister in para 5.3.1.1. The vibration environments are also critical during these phases. The extremes of temperature environments are also as defined for the canister and occur during sterilization and interplanetary transit. The impulsive loading during separation is small and no deleterious effects on the Spacecraft may be anticipated for an adapter stiffness designed for launch vibration environment.

The adapter may be designed integral with another structural member such as the aft canister or deorbit thrust motor supports or as a separate component. The structural concept may be either a stiffened shell, cylindrical or conical, depending on the geometry of the interface or of truss type. The concept is determined by the method of attachments of the interfaces of the entry vehicle and the Spacecraft. For discrete point attachments at both faces, a truss design is optimum, however, for continuous attachment at one or both faces, the shell type concept is more suitable with appropriate stiffening circumferentially and axially, to distribute the loading. For the designs of the current study the latter is selected as the candidate with continuous attachment at the Spacecraft interface and for point attachment at the entry vehicle/Lander interface.

Parametric study involves the size and weight of the entry vehicle. Data is based on a cylindrical axially stiffened adapter of diameter and length varied to accommodate different Lander Capsule configurations. The entry vehicle weight is varied from 400 to 1600 pounds. However, even for maximum entry vehicle weight, due to tensile loading being critical, minimum gauge design, with stiffeners at loading points and stiff rings at interfaces, satisfy the strength requirements.

Aluminum alloy 7075-T6 is chosen as the structural material, because of its familiarity and ease of fabrication. It also has a modulus-to-density ratio almost the same as steel or titanium alloys; only beryllium alloys offer a large improvement on this basis, but present fabrication problems. (ref. table 3.1.2-7(a)). Structural weight densities are the same as those given in table 3.1.2-7(b).

For vibrational stiffness considerations, previous studies on MM '73 mission show that the shell type adapter with minimum gauge faces provides adequate structural stiffness for vibration environments.

5.3.2 ENVIRONMENTAL CONTROL

5.3.2.1 Requirements and Discussions

Thermal control of the Lander components during the transient mode from Earth to Mars will be accomplished by insulating the Lander from the space environment and using heater power from the Spacecraft to control the Lander temperatures. The parametric data was computed based on the assumption that the transit configuration has no prolonged periods of significant biobarrier solar illumination. It was further assumed that the insulation is a multi-radiation barrier type composed of a number of layers of either aluminized mular or aluminum foils separated by an insulating material. An effective thermal conductivity of 1×10^{-4} BTU/Hr-ft-^{o}R was selected for this type of insulation.

Several variables were considered in order to establish an optimized definition of the insulation details and heater power requirements; surface emissivity properties E = 0.1 to 0.8, compartment allowable temperatures 310^{o}R to 540^{o}R and canister surface areas to 300 ft^{2}.

During deorbit the Lander is no longer insulated from the space environment and the heat shield temperature will be controlled by the vehicle orientation with respect to the sun. The trajectory assures that the Lander will not be occulted by the planet. Two solar orientations are included in the study; solar vector parallel to vehicle axis, and solar vector normal to the vehicle axis. Equilibrium heat shield temperatures were computed for α_S/E_{IR} ratios between 1.0 and 8.0.

5.3.3 PARAMETRIC DATA/TRADE-OFFS

Thermal control requirements for the Lander during interplanetary travel are presented parametrically in fig. 5.3.3-1 through 5.3.3-5. For a specified payload temperature requirement, a trade-off results in insulation thickness and heater power requirements. Figures 5.3.3-1 through 5.3.3-3 show the results of the heat balance for some representative payload temperatures. Although it may not be possible to store the Lander at low temperatures due to battery limitations, fig. 5.3.3-4 (Lander temp = 310^{o}R) is included in the event that radiosotope heat sources are available to help maintain acceptable battery environments. Data in these curves are plotted for unit surface areas of the biobarrier. The total heater power requirements can be computed from fig. 5.3.3-5. This data is shown for the practical range of insulation thicknesses and temperature specifications.

Equilibrium temperatures of the heat shield as a function of α_S/E_{IR} is shown in figs. 5.3.3-6 and 5.3.3-7. In fig. 5.3.3-6 the solar vector is parallel to the vehicle axis and incident on the concave side of the heat shield. An average heat shield thickness of 0.37 inch of ESM results in a 20^{o}R temperature drop across the shield. Figure 5.3.3-7 shows the solar vector normal to the vehicle axis. The resulting temperature gradient is 2^{o}R.

Circumferential temperature profiles of the heat shield are shown in figs. 5.3.3-8 and 5.3.3-9 as a function of altitude. The shield is heated by direct solar

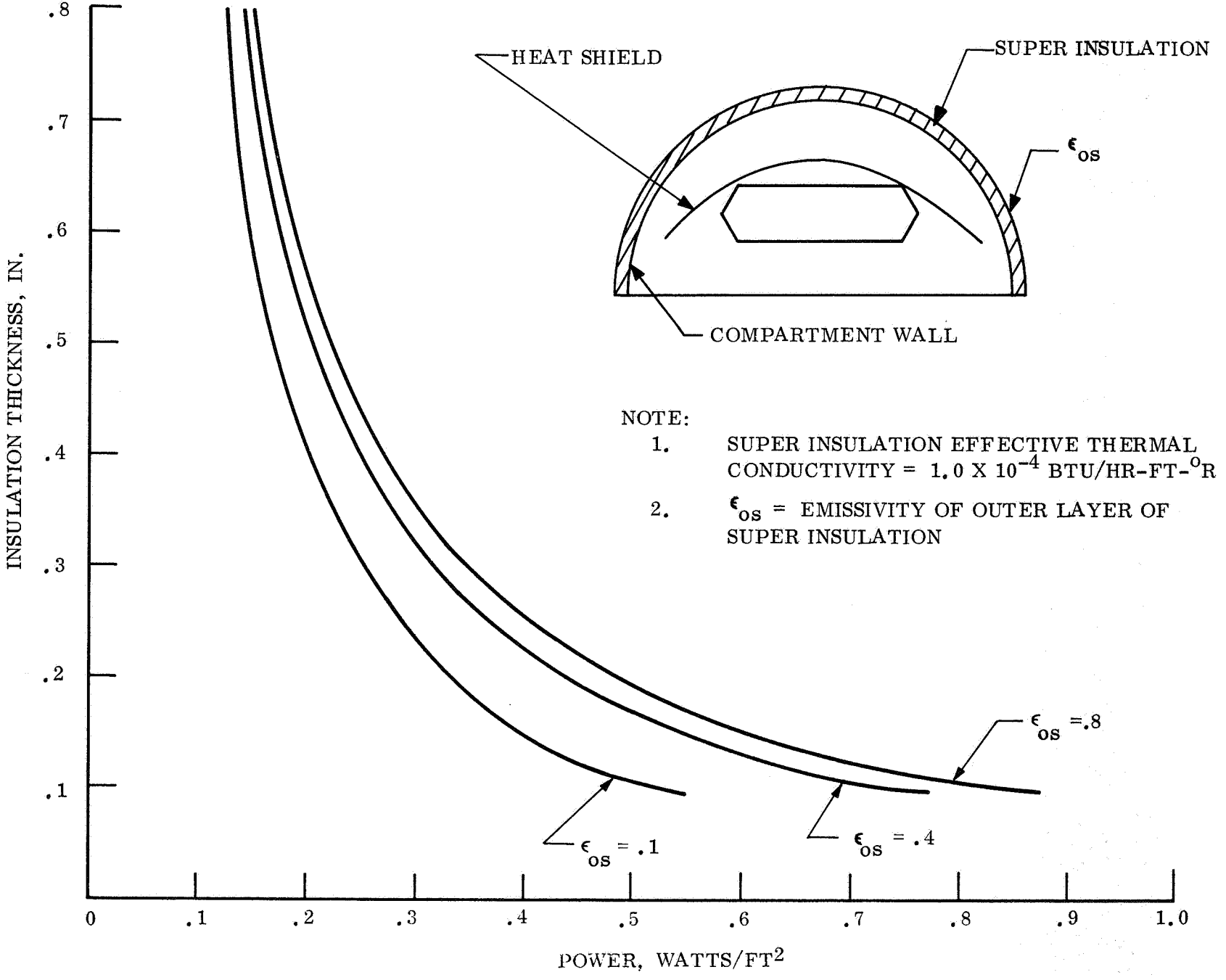

Figure 5.3.3-1. Super Insulation and Power Requirements to Maintain 460° on Compartment Wall and Heat Shield

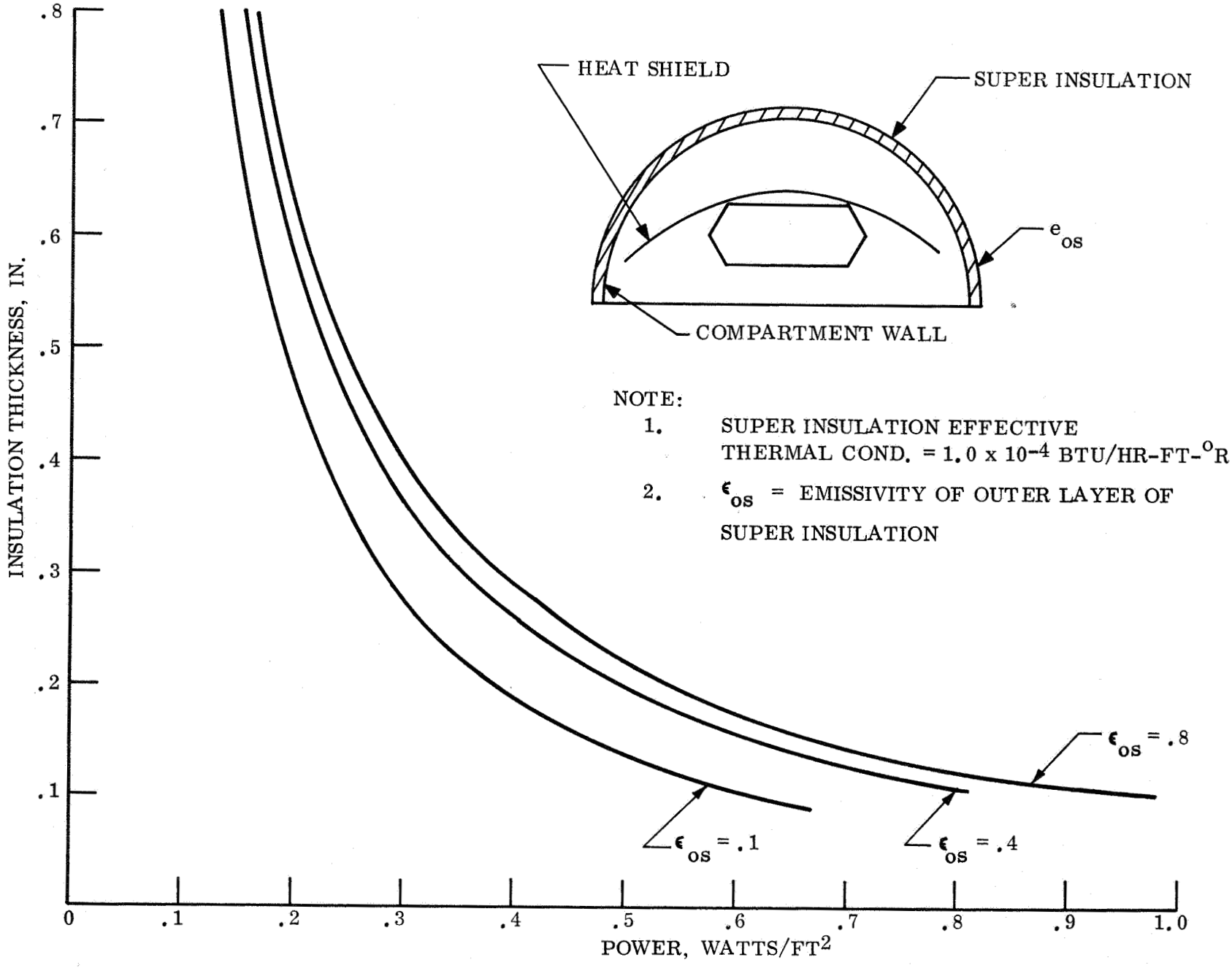

Figure 5.3.3-2. Super Insulation and Power Requirements to Maintain 500° R on Compartment Wall and Heat Shield

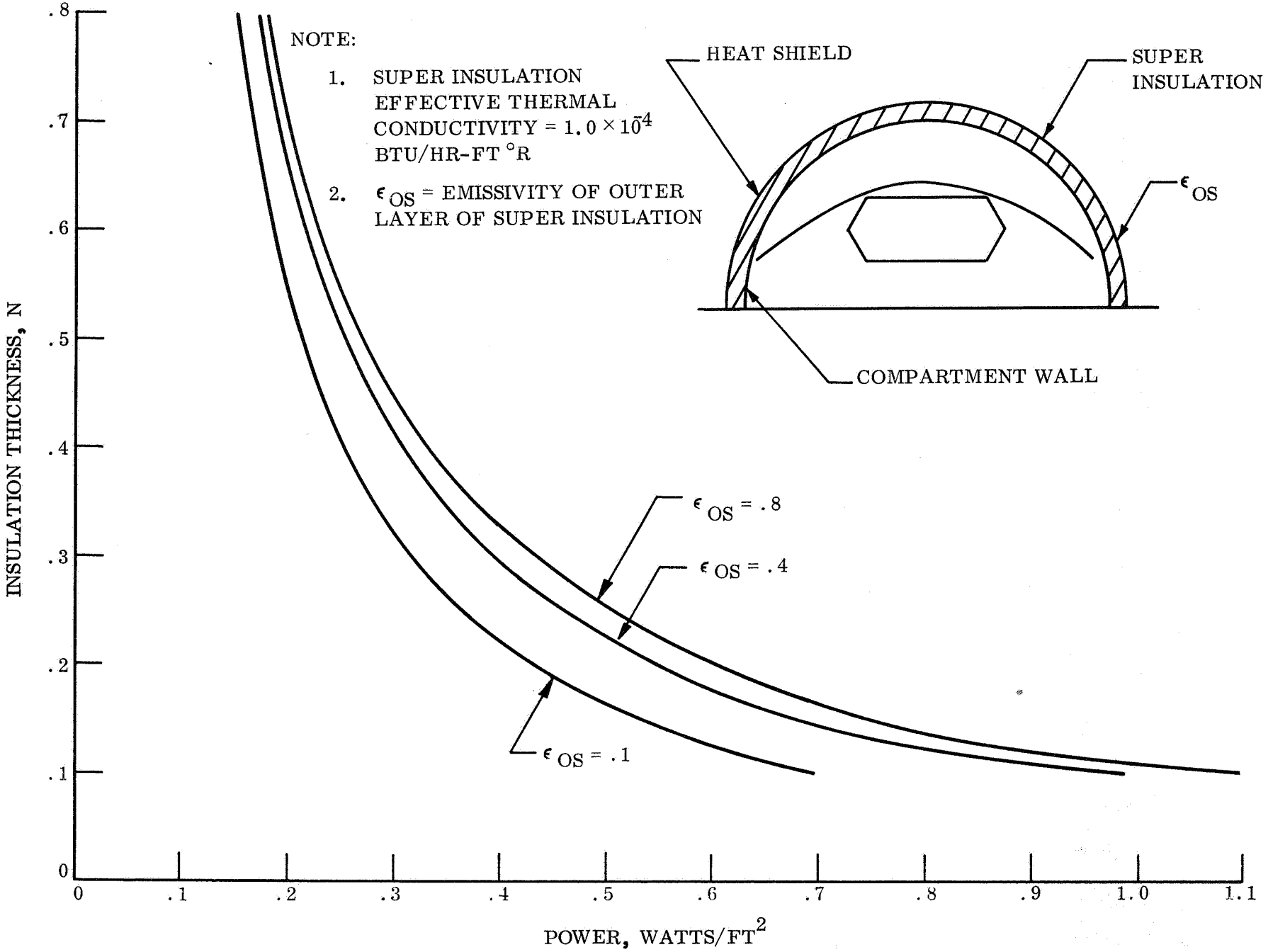

Figure 5.3.3-3. Super Insulation and Power Requirements to Maintain 540° R on Compartment Wall and Heat Shield

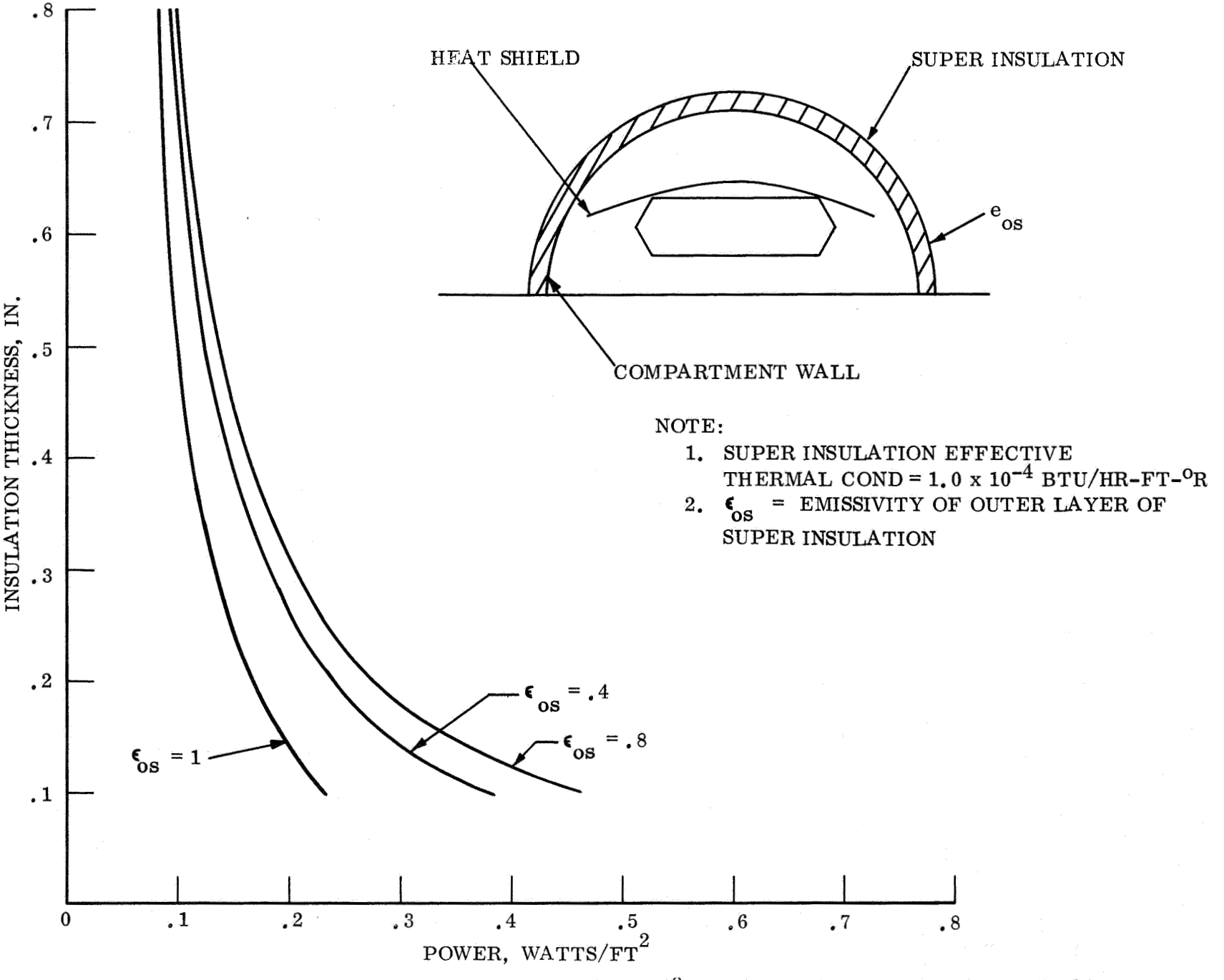

Figure 5.3.3-4. Super Insulation Requirements to Maintain 310^{o} R on Compartment Wall and Heat Shield

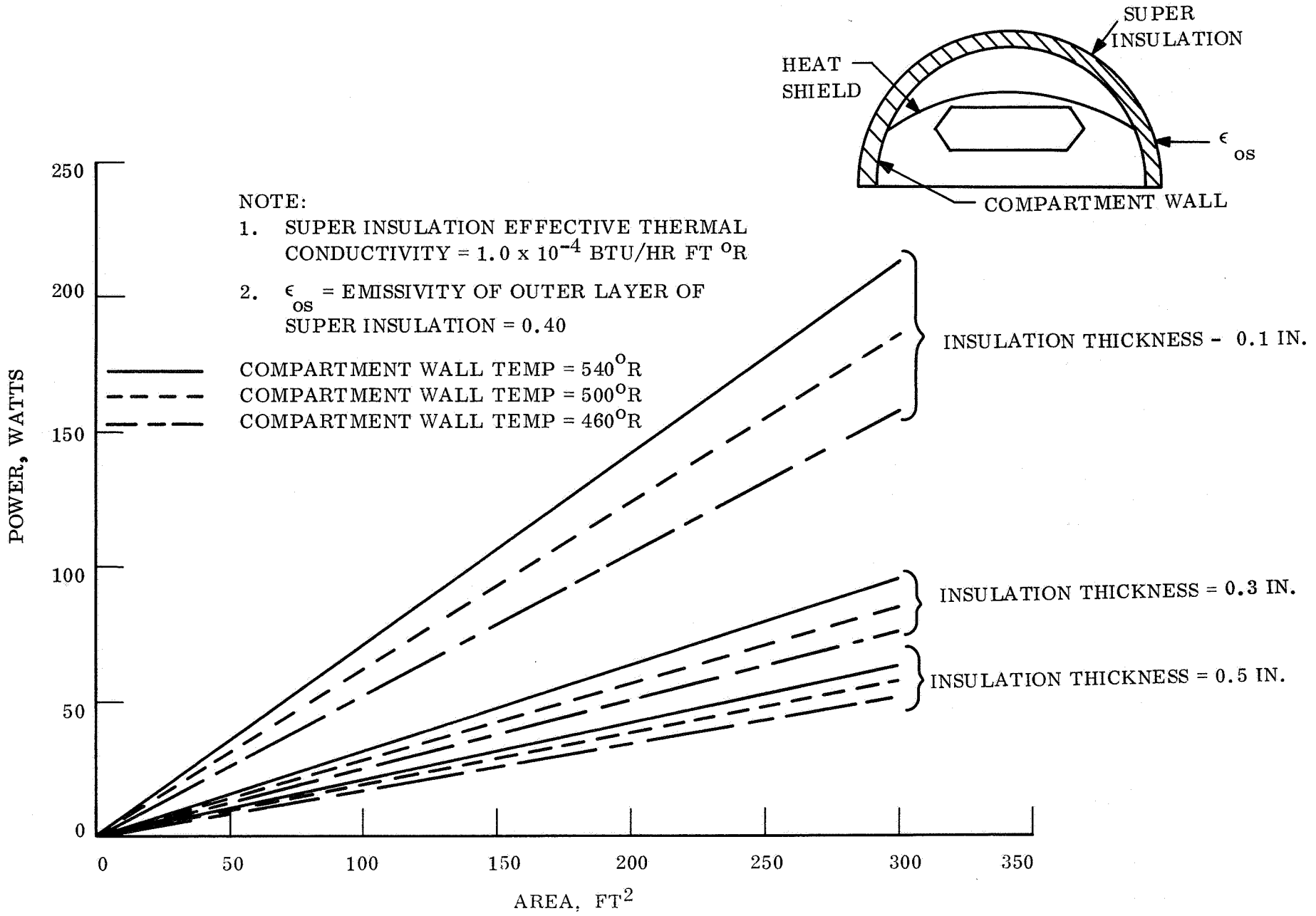

Figure 5.3.3-5. Transit Mode-Power and Insulation Requirements for Various Canister Areas

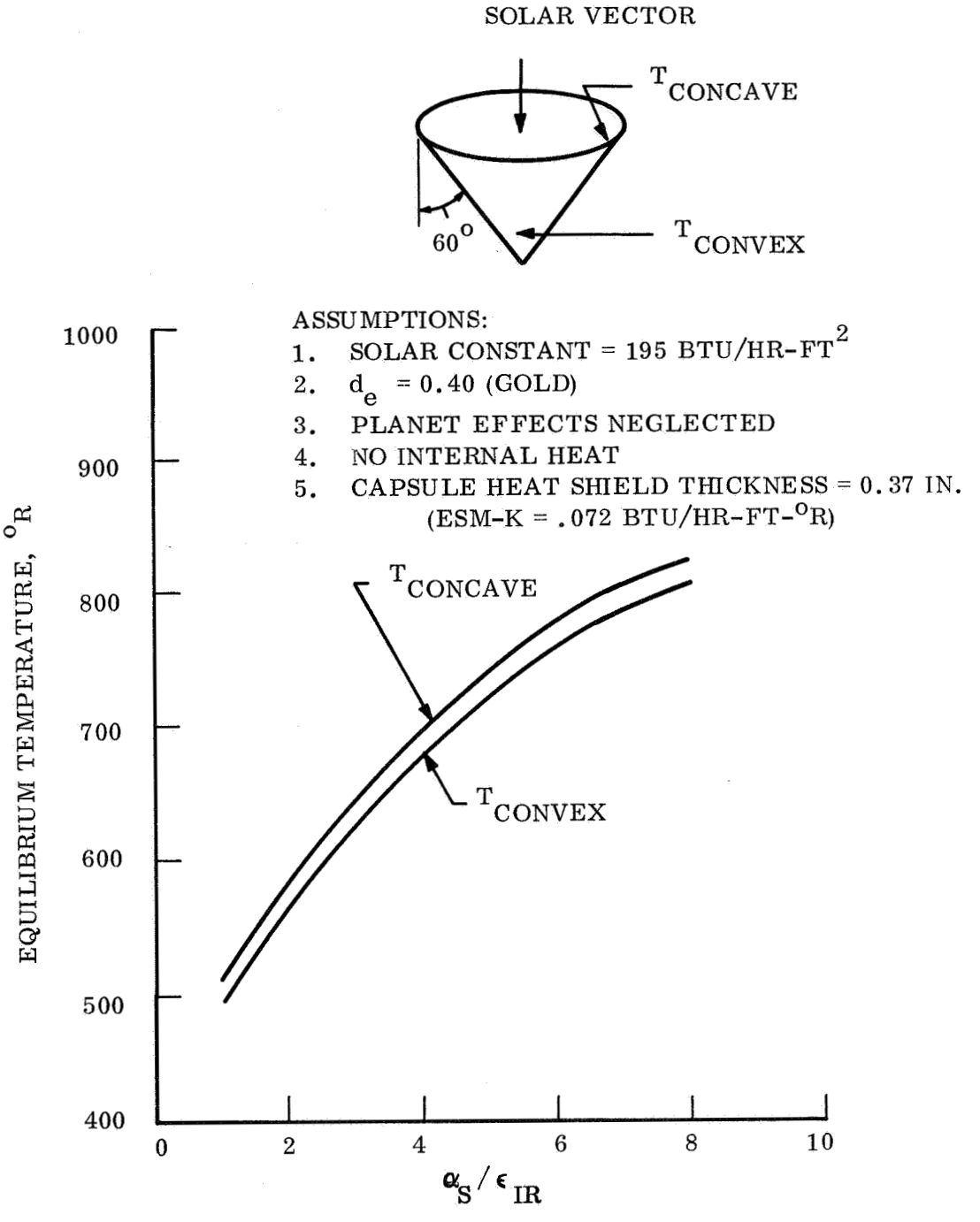

Figure 5.3.3-6. Equilibrium Temperature of the Lander Capsule Heated Only by Solar Radiation

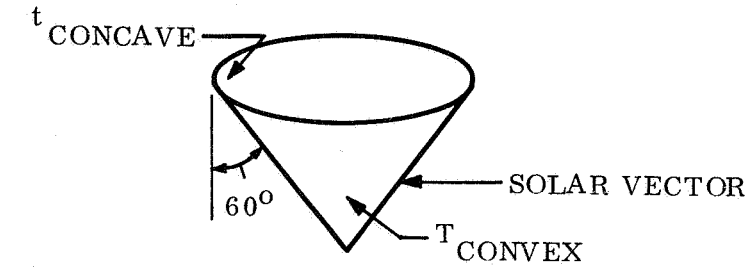

ASSUMPTIONS:

1. SOLAR CONSTANT = 195 BTU/HR-FT^2
2. α_S = 0.40 (COLD)
3. PLANET EFFECTS NEGLECTED
4. NO INTERNAL HEAT
5. CAPSULE HEAT SHIELD THICKNESS = 0.37 IN
6. VEHICLE SPINNING
   (ESM-K = .072 BTU/HR-FT-°R)

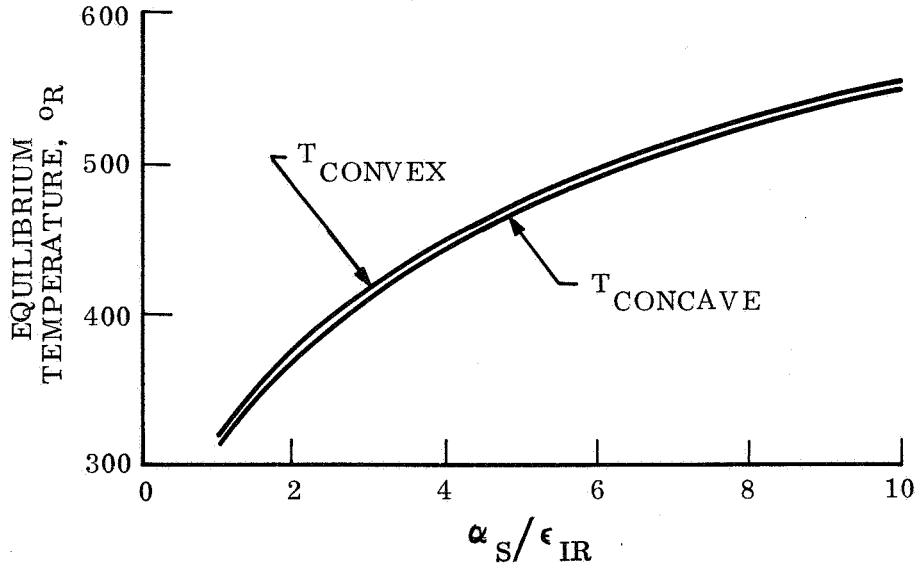

Figure 5.3.3-7. Equilibrium Temperature of the Lander Capsule Heated Only by Solar Radiation

ASSUMPTIONS:

1. SOLAR CONSTANT = 195 BTU/HR-FT^2
2. α_S = 0.40 (GOLD)
3. MARS ALBEDO = 0.15
4. MARS THERMAL RADIATION = 40.48 BTU/HR-FT^2
5. NO INTERNAL HEAT

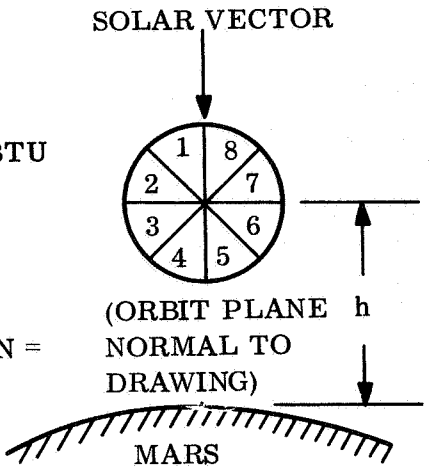

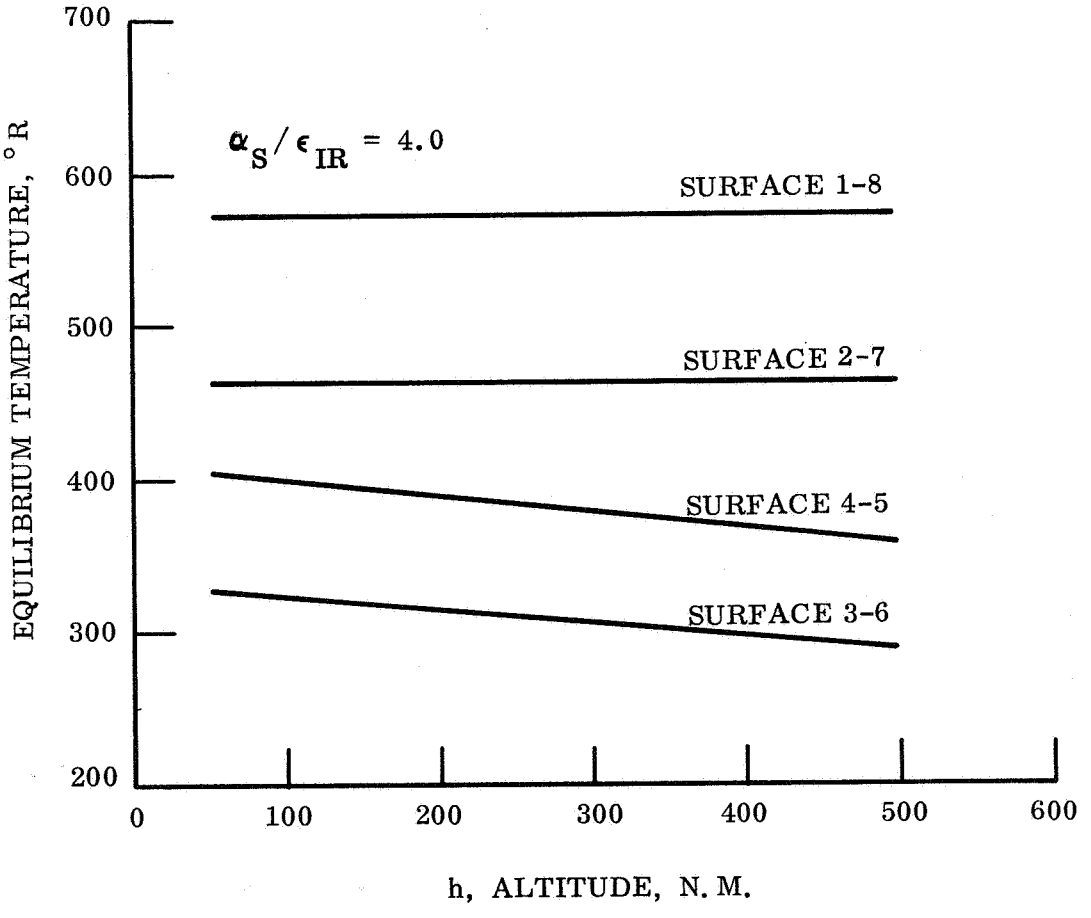

Figure 5.3.3-8. Circumferential Temperature Profile

ASSUMPTIONS:

1. SOLAR CONSTANT = 195 BTU/HR-FT^2
2. α_s = 0.04 (COLD)
3. MARS ALBEDO = 0.15
4. MARS THERMAL RADIATION = 40.48 BTU/HR-FT^2
5. NO INTERNAL HEAT

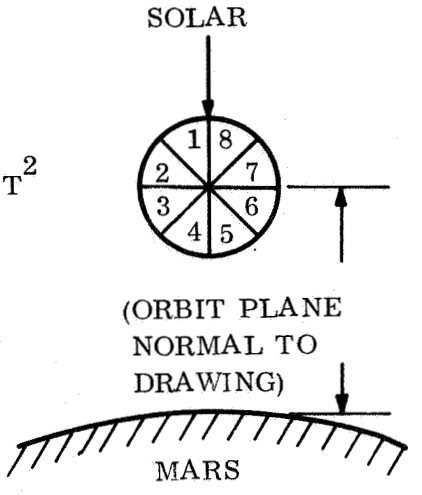

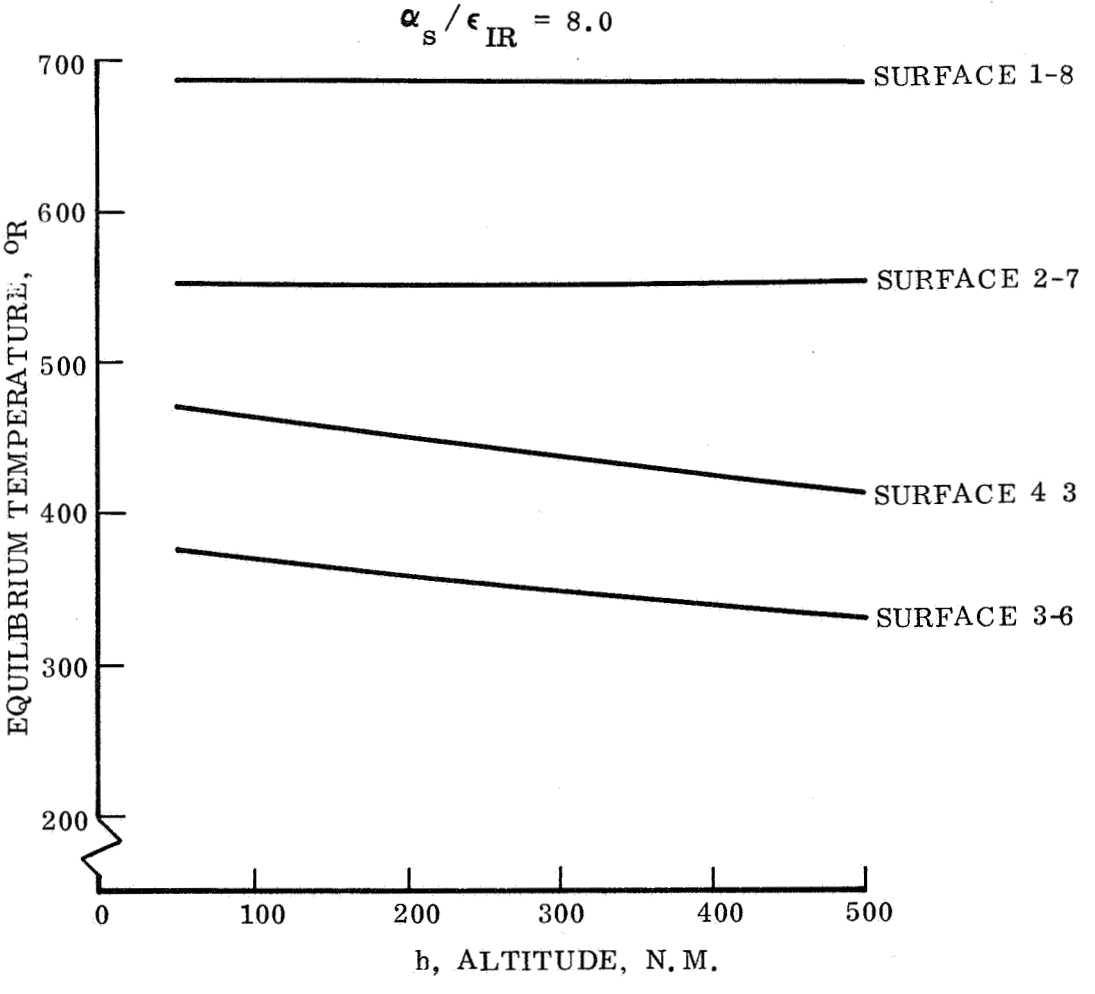

Figure 5.3.3-9. Circumferential Temperature Profile

radiation on surfaces 1, 2, 7 and 8, and Mars reflected solar and Mars thermal radiation on surfaces 3, 4, 5 and 6. Additional assumptions include no internal heating by the experiment package and cross radiation on the concave side of the vehicle is insignificant. Figure 5.3.3-8 depicts the circumferential temperature using α_s/E_{IR} of 4.0 and fig. 5.3.3-9 shows the responses for $\alpha_s/E_{IR} = 8.0$.

5.3.3.1 Subsystem Capability

Maintaining the payload compartment at a specified temperature through the use of multiradiation barrier insulation, local electrical heaters operated by Spacecraft power and surface coatings is feasible for a battery powered Lander. Achieving the ideal combination of these parameters will be highly dependent on the available power from the Spacecraft. Minimum insulation weight can be obtained by utilizing the maximum available Spacecraft power and the lowest surface emissivity attainable.

A design which incorporates an RTG power supply complicates the method of thermal control. Either an active coolant circulation loop or a heat pipe design utilizing a space radiator must be introduced as a means of rejecting the waste thermal energy from the RTG. A heat pipe loop is particularly attractive from a weight standpoint but requires extensive development to achieve a high confidence level.

5.3.4 PARAMETRIC STUDY OF SEPARATION SUBSYSTEM

5.3.4.1 Introduction

This section discusses the parametric design of the separation subsystem. The subsystem is used to provide structural attachment and upon remote command, mechanical separation of various components of the entry system.

The study was conducted by investigating the weight variation in each component of the subsystem as a function of the critical parameter. In the case of attachment hardware, the critical parameter is the total load seen by the component. (Weight X acceleration, etc.). In the case of ejection hardware, the parameters are separation velocity and equivalent system mass. However, in the case of the canister attachment, the weight varies as the pressure load (ΔP and diameter). Because this latter condition has the largest influence on the subsystem, it was used as the independent variable for the purpose of summarizing the subsystem weight.

This section is broken down into a listing of functions and requirements, general design descriptions and a description of typical components and associated weights. Appendix B presents a tip-off analysis and V-band loading considerations.

5.3.4.2 Summary

This study shows that the weight of the separation subsystem is very dependent on the size of the sterilization canister, and the maximum ΔP tolerated in the canister.

The use of a V-band canister attachment pretty much limits the allowable ΔP to 1 psid, with attendant constraints on the pressure and venting system (see Section 5.3.5). Fig. 5.3.4-1 shows that the subsystem weight varies from 11 pounds for an 8 foot diameter canister to 30 pounds for a 16 foot diameter canister, using a one psid system. The subsystem weight arrived at in the six point design studies are identified to show the correlation between predicted and actual results. The V-band contributes approximately 1/2 of the total weight in the 8 foot canister and 2/3 of the total subsystem weight in the 16 foot canister. Fig. 5.3.4-2 shows the V-band assembly weight for various ΔP's.

Capsule separation is important in achieving proper orientation and landing footprint dispersion. Major contributions are the separation velocity increment (ΔVc) and the tip-off rates (Wc) imparted to the Capsule by the separation subsystem. Figs. 5.3.4-3 and -4 show the effect of varying Orbiter and Capsule mass properties on ΔVc and Wc. The worst case ΔVc, is 1.1 ft/sec, which is less than the 2.5 ft/sec imparted the forward canister. Tip-off rate correction is shown in fig. B-2 of Appendix B. Tip-off is also inversely proportional as Capsule's pitch/yaw inertia.

Canister separation system design is of paramount importance in maintaining the sterilized status of the Capsule. The separation joint potentially presents the largest opening to bacteria entry. The proposed system of a V-band with redundant seals utilizes proven concepts in meeting a critical function, at the expense of added weight.

5.3.4.3 Design Constraints, Functions and Requirements

5.3.4.3.1 Separation Subsystem Functions

1. Separation of the forward canister
2. Separation of the Capsule assembly
3. Separation of the thrust cone assembly
4. Separation of the aeroshell.

5.3.4.3.2 Separation Subsystem Requirements

1. Provide field and separation joints for the canister
2. Eject a canister at 2.5 ± 0.3 fps, canister weight between 30 and 120 pounds
3. Maintain a pressure-tight joint from sterilization through exit from the Earth's atmosphere for a maximum internal pressure of 5.0 psid. Pressure-tight is defined as leakage which results in less than 0.002 psi drop/hr at 70^{o}F.
4. Maintain maximum attainable pressure sealing during space cruise where outside temperature may be as low as -300^{o}F

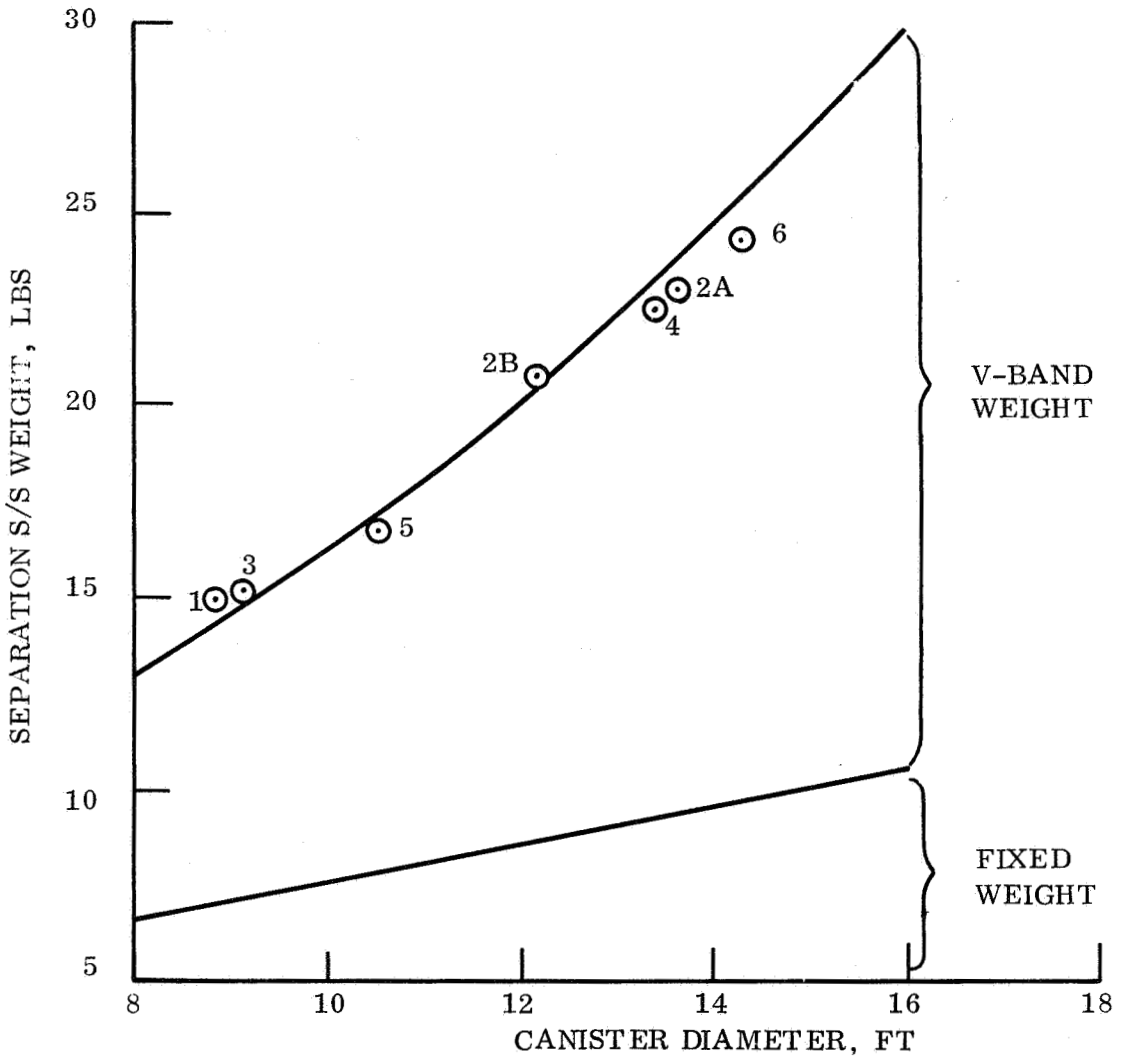

Figure 5.3.4-1. Separation S/S Weight vs Canister Diameter (1 PSID)

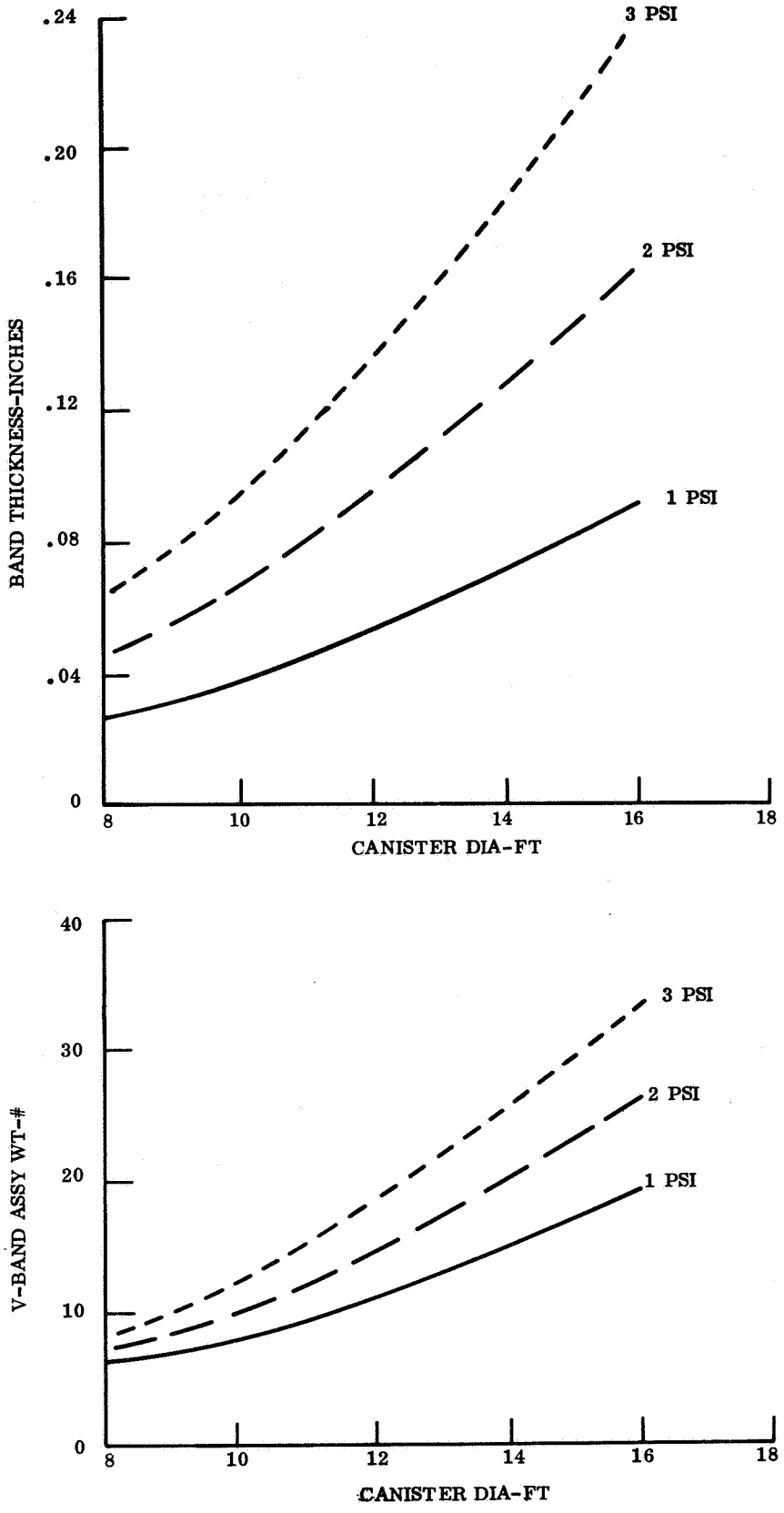

Figure 5.3.4-2. V-band Assembly Weight vs Canister Diameter

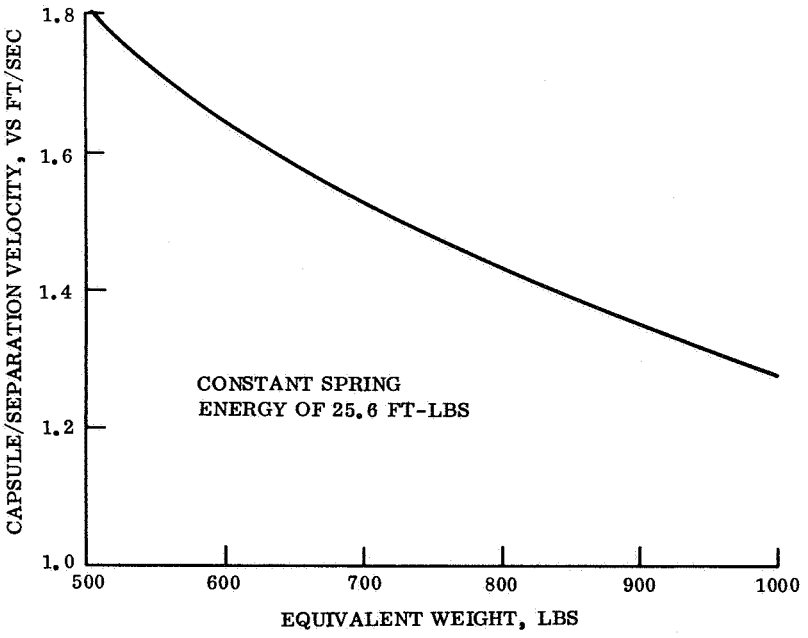

Figure 5.3.4-3. Capsule Separation Velocity vs Equivalent Weight

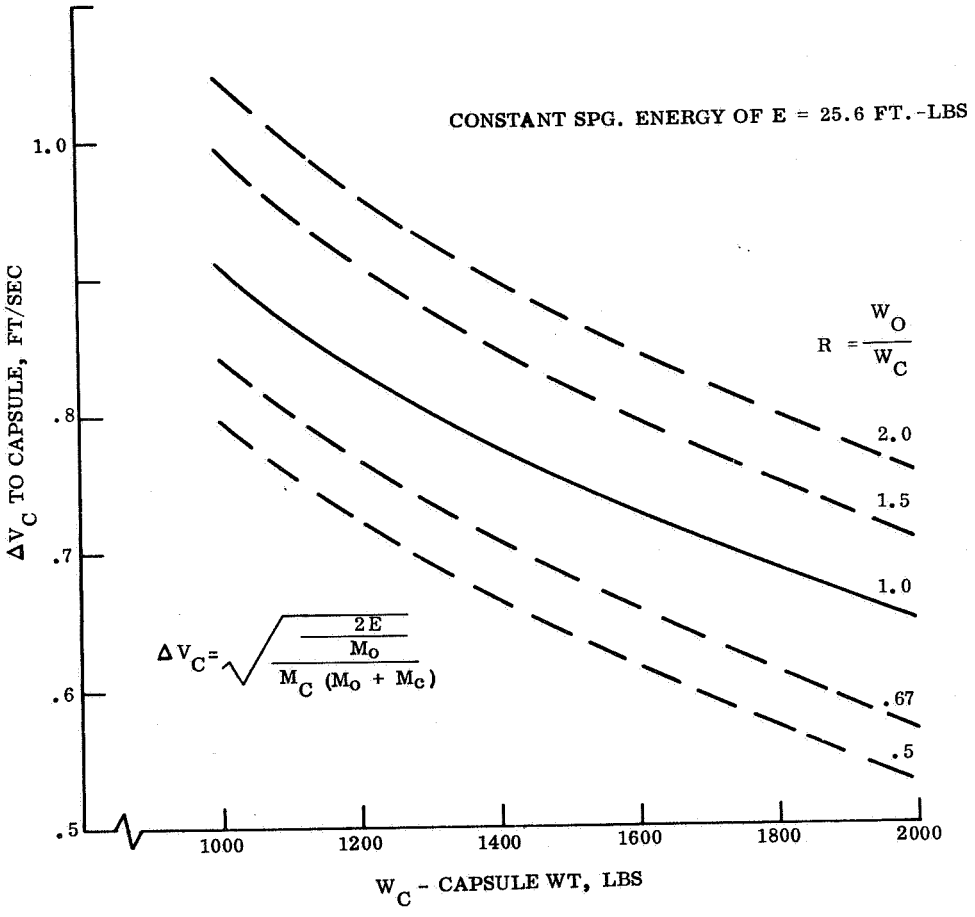

Figure 5.3.4-4. Capsule Separation Velocity Increment, ΔV_C for Various Orbiter to Capsule Weight Ratios

5. Maintain sterility of Capsule

6. Separation shall not produce debris or loose objects

7. Attach a Capsule at four points. Capsule weight: 1000-2600 pounds, IP = 50-200 slug-ft^2

8. Eject Capsule at 1.5 ± 0.25 fps separation velocity from Orbiter with tip-off rates of 0.5°/sec to the Capsule. Orbiter weight 1000-2000 pounds, IP = 50-200 slug-ft^2

9. Separation shall not cause collision with any of the remaining payload

10. Attach and separate a thrust cone at 1.0 fps minimum. Empty thrust cone weight is 30 to 100 pounds

11. Attach and release the aeroshell

12. Provide electrical separation as required

13. Optimum reliability and subsystem performance is paramount to mission success. Use proven concepts.

Other system constraints-electrical power, distribution, timing and signal lockout shall be provided by the EP&D subsystem.

5.3.4.3.3 Information Required to Perform a Detail Design of the Separation S/S

A. General Requirements Applicable to All Separations

1. Weight, c.g., location and moments of inertia of ejected and remaining vehicle.

2. Loads and accelerations

3. Number of electrical connections, location, separation time

4. Ejected ΔV or separation velocity and tip-off constraints if any

5. Time of separation

6. Clearance between ejected body and adjacent structure for collision study

7. Motion rates, accelerations, position of parent vehicle for a two second period prior to/and after separation.

B. Detail Requirements

1. Canister internal diameter

2. Capsule attachment bolt circle and number of attachments

3. Thrust cone attachment bolt circle and number of attachments.

5.3.4.4 Discussion of Peculiar Separation Problems

5.3.4.4.1 Canister Separation

The selection of the separation method for the canister is governed by the requirement for a sterile, pressure tight joint for a large, flexible structure. This basic requirement limits the separation joint design to one that can apply a continuous distributed force, such as flexible shaped charge, various types of MDC or primer cord, V-bands, closely spaced bolted joint, "pyro fuze" joint system or a thermal heat pad joint system. A shaped charge or regular primer cord joint must be discarded because they forcibly cut material, generating unwanted debris and high shock. The "pyro fuze" joint and the thermal heat pad joint were investigated by GE-RS in 1967, and require substantial development work. Some testing was done on small, 2 to 6 inch sample pieces. The mild detonating fuze (MDF) type of joint, encapsulated either in plastic tubing or stainless bellows, appears to give a lighter weight system. However, there are many disadvantages:

1. They have not been used at the temperature extremes contemplated, and there is question as to the behavior of the explosive.

2. They necessitate the use of a separate field joint, which adds weight and more sealing problems.

3. They contain a large amount of pyrotechnic material and therefore must be handled as Class 1 or 2 explosives.

4. They require the use of additional safing components such as S&A devices or baroswitches.

5. They generate high shocks at separation, which could affect electronic equipment or dislodge unsterile particles external to the canister, which may later contaminate the Capsule.

6. They rely on rupturing a large number of bolts (2 inch spacing between bolts) which can be at different temperatures ($150^{o}F$ variation), thus having different rupture strengths and therefore causing potentially large tip-off rates.

The V-band system was selected because of its simplicity, reliability, low separation shock, lack of debris, tolerance to temperature environment, elimination of field joint, and it presents a tortuous path for microbial access to the separation interface.

However, for systems with large ΔP and/or diameter the V-band becomes too thick and is not feasible.

5.3.4.4.2 Capsule Separation

The main consideration for Capsule separation and ejection was the stringent tip-off rate requirement. To meet this requirement, it is necessary that the impulse generated by the separation device be either very low or nearly the same at all points. Likewise the ejection system must have controlled force and energy, with low variances; and lastly, c.g. offsets, and ejection system force axes must be controlled.

Separation devices that meet the above needs are ball locks, collet releases, and explosive nuts. The latter was chosen because of their compactness and ease of use and installation. All of the above utilize pressure cartridges for operation, and for high reliability dual cartridges will be used. This introduces the problem of wide impulse variance as a function of gas pressure (a function of cartridge design, simultaneity and number of cartridge firing). Centrally located pressure cartridges feeding through a common manifold are not practical on the large diameters involved here. A central, high pressure, a pneumatic collet system heavier system than dual squibs. A non-pyrotechnic device, similar to the hot wire tension bolt discussed previously will be very seriously considered, because of its obvious advantages. Its main draw back is that it is new and needs to be developed.

The ejection systems are pneumatic pistons, pyrotechnic thrusters, reaction systems and springs. Springs were selected for their obvious simplicity, and low weight. For heavier payloads or high ΔV, pneumatic collet system becomes lighter in weight than springs. It will also perform the separation function (ref. 5-1). To minimize tip-off rates, the energy and force of the ejection system must be controlled. A guide/roller system may also be required if rates are too high. The proposed solution uses preset springs in an energy package, with selective assembly, and gives a maximum tip-off rate of 0.3^{o}/sec when the maximum and minimum spring forces are combined with the worst case c.g. offset.

5.3.4.5 Typical Design Solution

The preceding sections lead to a typical design solution which is generally common to the various size and weight Landers being considered for this study. The solution involves the use of a V-band with hot wires and springs for canister separation, explosive nuts and springs for Capsule separation, hot wires and springs for thrust cone separation and strap with hot wires for aeroshell separation. The components used in the system are listed below. The sections that follow present the analyses required to design each component to meet the various payload combinations. The analyses will enable a compilation of total separation system weight as a function of canister diameter (see fig. 5.3.4-1).

The separation subsystem requires the design of the following items:

1. V-band

2. Hot wire bolt

3. Explosive nut

4. Separation spring-canister

5. Separation spring-Capsule

6. Separation spring-thrust cone

7. Attachment strap-aeroshell.

Of these, the V-band contributes the greatest weight and is affected the most by changes in canister diameter.

5.3.4.5.1 V-Band Assembly

The V-band assembly consists of a flat metal strap and slippers attached to it by clips. Both the band and the slippers are made of aluminum alloy to match the thermal coefficient of the aluminum separation rings in the canister. The slippers weigh 0.19 pounds each, and are 5.75 inches long (66E49508P1), using the Mark 12 referenced part. The V-band assembly weight, excluding the strap, is 0.41 pound/liner foot for a 10,000 pound load. The weight was arbitrarily reduced to 0.20 pound/linear foot for a 1000 pound load.

The strap weight is a function of the pressure and diameter as discussed in Appendix B and using proof pressure as a limiting condition, the following strap size size and weight data can be derived using A1-A1 2024T86 (69,500 psi UTS post + 300°F) for a slipper contact angle of 20°.

The strap load consists of a variable element (dependent on pressure and diameter) and a fixed element which accounts for "O" ring load and separation ring out of flatness. The tensile load on the strap analyzed as a hoop tension load is then: (See fig. 5.3.4-5).

$$F_t = \frac{(12\ D\ F_N)}{2} \text{ Tan } \theta\ K_3, \text{ maximum preload}$$

$$F_{Nu} = (K_1 \times 3 \times \Delta P \times D + (15\ K_3) \text{ ultimate normal force}$$

ΔP = canister maximum differential pressure = 1 psi

D = canister diameter - feet

F_N = normal force pounds/linear inch

θ = slipper contact angle = 20°

K_1 = safety factor for burst press = 1.67

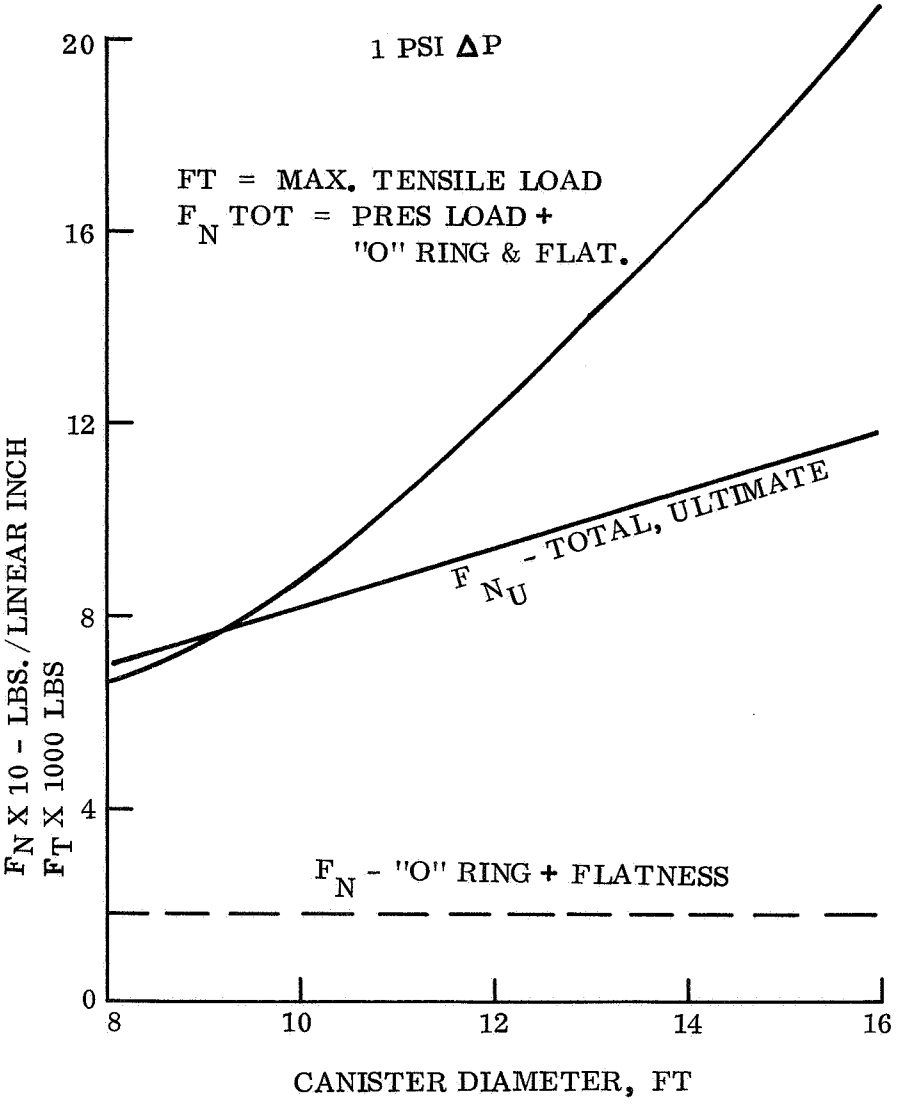

Figure 5.3.4-5. V-band Loads vs Canister Diameter

K_2 = design safety factor = 1/25

K_3 = allowance for preload variation and uncertainty = 1.32

It is quite evident that the allowable ΔP is the governing criteria in designing the separation system for the canister. The above analysis assumed that the strap and the rings were of the same material, thus the coefficient of thermal expansion were nearly equal. Using a stainless steel strap causes very high strap stresses during sterilization and band loosening during the space voyage. These problems could be solved by tensioning the band after sterilization and using thermal insulation. However, at this juncture it is better to limit the canister design pressure to 1 psi in order to keep the strap thickness and weight relatively small. A reduction in the contact angle achieves the same result, however, it is not recommended because it compromises band release after a long voyage thru space.

5.3.4.5.2 Hot Wire Assembly

The loads acting on the hot wire bolt are primarily the maximum tensile load (preload) on the V-band. The bolt is sized on that basis using the standard UNF thread series.

The size and weight of the hot wire bolt assembly are tabulated on table 5.3.4-1. This size includes a casing and the weight is an estimate based on dimensions A and B only.

TABLE 5.3.4-1. HOT WIRE TENSION BOLT DATA

Max. Loads (lbs)	Physical Data			A. F. * Current	Weight (lbs)
	A	B	T		
8000	0.90	1.00	3/8	6.0	0.20
12000	1.15	1.32	7/16	9.0	0.44
19000	1.40	1.62	1/2	12.0	0.81

*The all fire current given above may need to be increased by a factor of 1.5-3 to meet simultaneity requirements.

5.3.4.5.3 Explosive Nut

The size of the explosive nut is a function of the load to be carried by the attaching bolts. Using the following data, the capsule weight which can be carried by four bolts is calculated.

Ax = 2 g's, Ay = 6 g's, bolt circle = 94 inches, c.g. location

is 10 inches aft of bolt down plane

Root diameter of 1/4 inch bolt = 0.19 inch

Root diameter of 3/8 inch bolt = 0.32 inch

P_t = 3650 lb for 1/4 inch bolt

P_t = 10350 lb for 3/8 inch bolt

From the Capsule geometry, the worst load occurs when one bolt carries the moment load, thus.

$$P_t = \frac{W\,Ay}{4} + WA_x \frac{10}{94}$$

$$W = \frac{P}{1.71} = 2130 \text{ lb for 1/4 inch bolts}$$

$$= 6050 \text{ lb for 3/8 inch bolts}$$

TABLE 5.3.4-2. EXPLOSIVE NUT DATA

Size (in.)	P_T #	Allow Capsule Wt = (lb)	*Wt/Nut (Incl. 2 Squibs)	*Size (in.)
1/4	3650	2130	4 oz.	1.15 Dia x 2.35 Long
3.8	10350	6050	5.5 oz.	1.38 Dia x 2.50 Long
*Size and Weight data based on Hi-Shear Corp. Part No. SN 7321 - Separation - Nut - Captive, Interal Base, Bolt Torquing				

The pressure cartridge to be used with the explosive nut will be designed to meet range safety criteria, sterilization requirements and long life in space as special design requirements. The cartridge design will follow the concept of a common pyrotechnic design for the program to minimize reliability testing and demonstration of multiple designs.

The stringent Capsule tip-off requirements dictate simultaneous release of the explosive nuts, with the implied simultaneous actuation of the cartridges.

The selection of the pyrotechnic materials, and construction must be such as to minimize the potential effect and degradation due to sterilization and outgassing

in space. The applied firing current will most likely be increased two or three times the normal all fire current to enhance simultaneity. The simultaneity requirement for nut separation will likely be < 0.005 seconds, making the requirements for peak pressure in the cartridge and < 0.002 seconds.

5.3.4.5.4 Separation Springs

The design of the separation springs is based on using an allowable stress of 90,000 psi for 302 stainless wire, using helical coil springs with free length to mean coil diameter ratio of less than five. Ground and square end turns will be specified; and the number of springs is optional. The following requirements apply:

	Canister	Capsule	Thrust Cone
Ejected Weight - lbs	*30 - 120	1000 - 2600	60 (empty)
Remaining Weight - lbs	Large (> 10x)	1000 - 2000	> 10x
Separation Velocity - fps	2 - 3	1 - 2	Optional
Tip-off	No Reqmt.	< 0.5°/sec	No reqmt.
Number of Springs	Optional	2 or 4	2 or 4
*Based on 0.5 lb/sq ft canister surface area - as shown in fig. 5.3-5			

Where the remaining mass is large (> 10); the energy required is given simply by $E = 1/2\ MV^2$. In the case of the capsule, the equivalent mass is first calculated $Me = \frac{M_1 M_2}{M_1+M_2}$. The choices for detail spring design are many, however, the lightest springs with acceptable stability - obviate the need for guides - are those with a spring index, C = D/d of 8-10.

The theoretical spring weight can be calculated on the basis of energy required and is given in parametric curves in fig. 5.3.4-6.

The weight of the spring adjusting mechanism is estimated at 0.4 pounds each for the smallest spring and to vary in the same proportion as the spring weight, or 0.8 pounds each for the heaviest capsule.

The effect of varying the Orbiter and Capsule weight is to change the necessary separation energy required to obtain the same separation velocity (Vs) and ΔV to the Capsule. The curve on fig. 5.3.4-3 shows that using the same energy (same springs) the required separation velocity for the expected range of vehicle weights can be attained The ΔV imparted to the capsule will be between 0.5 to 1.0 fps (see fig. 5.3.4-4).

The curves can be used to obtain the expected velocities as a function of Capsule weight and Orbiter/Capsule weight ratio.

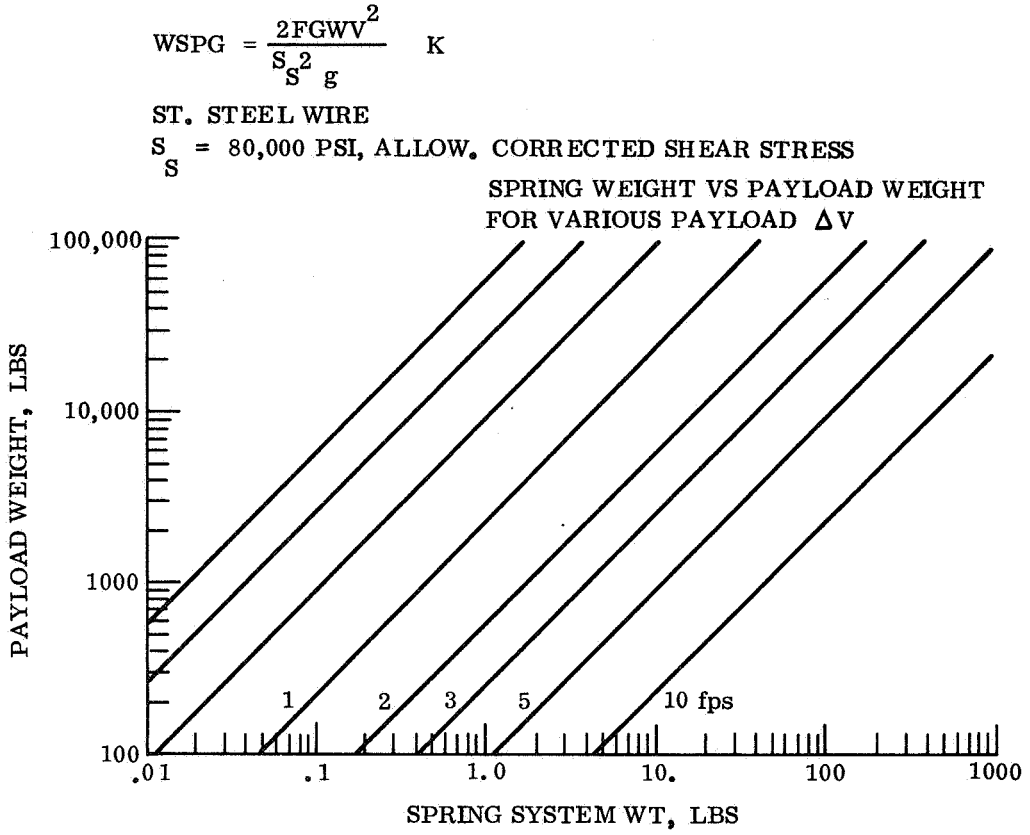

Figure 5.3.4-6. Spring Weight vs Payload Weight for Various Payload ΔV

The stringent tip-off requirement on the capsule separation dictates the use of special design considerations. Spring guides, controlled spring energy and capsule/adapter guides maybe necessary. Appendix B discusses the tip-off analysis. An allocation of 0.1^{o}/sec is made to the explosive nuts and the remaining 0.4^{o}/sec is allocated to the spring system. The tip-off requirement can be met by using an adjustable spring assembly which controls initial spring load and total energy, or using springs with high spring constant and selectively installing the springs.

The sample calculation shows a tip-off rate of 0.3^{o}/sec for a Capsule and Orbiter having a weight of 1500 pounds and a pitch/yaw inertia of I = 110 slug-ft^2. For the heaviest anticipated Orbiter (2000 pounds) a seven percent increase in rate can be expected (see fig. B.1 in Appendix B).

The pitch inertias of the capsules being considered are greater than the assumed value of 110 slug-ft^2 and therefore the tip-off rates would be proportionally lower.

5.3.4.5.5 Thrust Cone Separation

The thrust cone will be attached to the Lander using 3/8 inch hot wire tension bolts identical to those discussed in the V-band attachment. The loads are considerably lower, thus there is ample margin. The T/C ejection must not interfere with the Lander. This is accomplished by means of two springs identical with those for canister ejection. Since the ΔV is not critical, this concept gives common hardware.

5.3.4.6 Aeroshell Attachment

A retractable strap assembly joined by three hot wire bolts were assumed for this function. The strap was assumed to be 1 inch wide x 0.06 inch thick aluminum 120 inches long.

W = 0.1 x 1 x 0.06 x 120 = 0.72 pound

Weight of hot wire bolt = 0.66 pound

1.38 pounds

5.3.4.7 Summary of Parametric Subsystem Weights

From the preceding sections, a tabulation can be made of fixed and variable weights. This data is plotted as fig. 5.3.4-1, and shows the fixed weight arbitrarily plotted as a sloping line connecting the limit weights given in part 1 below.

1. Fixed Weight

		Total Item Wt. Capsule Wt/Canister Dia	
		<2000#/10'	>2000#/10'
4 Explosive Nuts	Capsule Attachment	1.0	1.4
4 Hot Wires	T/C Attachment	0.8	0.8
4 Hot Wire Assemblies	Canister Separation	0.8	0.8
Strap + H.W.	A/S Attachment	1.0	2.0
2 Springs	T/C Separation	0.1	0.3
2 Springs	Canister Separation	0.1	0.3
2 Adjustable Spring Mechanisms	Canister Separation	0.7	0.7
4 Adjustable Spring Mechanisms	Canister Separation	1.6	3.2
4 Springs	Capsule Separation	0.5	1.1
		6.6 lb	10.6 lb

2. Variable Weight

This is associated only with the V-band, a function of canister size, and varies from 6.4 to 19.2 pounds (See fig. 5.3.4-2).

5.3.5 PRESSURE AND VENTING SYSTEM PARAMETRIC STUDY

5.3.5.1 Introduction

This section discusses the parametric study of the Pressure and Venting (P&V) system. The primary system function is to vent the internal air within the canister as the booster ascends to prevent the internal pressure from exceeding design limits. These limits are predicated by structural considerations of the canister and the canister separation joint. The parametric study of the separation subsystem (Section 5.3.4) shows that the allowable ΔP should be as low as possible, especially for the large diameter canisters, (>12 ft). The P&V system design is a function of canister size only and maximum allowable ΔP.

5.3.5.1.1 Function and Requirements

The P&V system performs the following functions:

1. Inlet and outlet ports into the canister for sterilization
2. Circulation of air during sterilization
3. Pressure relief due to temperature variations
4. Maintain a positive ΔP between 0.5 and 2.0 psid between the canister and ambient atmosphere
5. Vent up to 500 ft^3 of internal air during ascent to maintain specified ΔP
6. Evacuate all entrapped gases to ambient space vacuum just prior to canister separation
7. Prevent bacteria access into canister by mechanical filtering of particles larger than 0.3 microns.

5.3.5.1.2 Constraints on Other Systems

1. EP&D will provide power to operate valves
2. OGE/TSE must provide sterilized and prefiltered make-up gas supply to be used from sterilization through pad operations, for system operating at less than 5 psid ΔP
3. Air conditioning on pad is required after removal of make-up gas supply to control canister gas temperature on systems operating at less than 5 psid ΔP
4. It is assumed that air introduced during sterilization is dry and prefiltered to prevent degradation and clogging of the flight
5. It is assumed that the booster shroud provides adequate venting.

5.3.5.2 Summary

The pressure and venting parametric study led to a relatively simple and reliable design solution using a single valve to perform all of the basic subsystem functions. This valve is a pilot operated relief valve with a latching solenoid-operated override. It is used for pressure relief, canister venting during ascent, and evacuation of final entrapped air and outgassing products to space vacuum prior to canister separation. During flight venting the valve will automatically open within the first two seconds of flight and close as the ΔP reaches 0.5 psid. It is expected that the valve will cycle a few times until about 30 seconds after launch, thence remain open until about 85 seconds; at which time, it will remain closed until just prior to canister separation. It is recommended that a positive pressure be maintained within the canister for as long as possible after exiting from the Earth's atmosphere to prevent biological contamination.

The P&V system was designed on the basis of a 1 psid canister, ΔP. The use of a higher ΔP system, reduces the vent valve and filter sizes, which for a 5 psid ΔP system means reducing the system weight by approximately one-half. The subsystem weight is tabulated on table 5.3.5-1 and plotted in fig. 5.3.5-1. Weight varies from 5.8 to 17.8 pounds and is approximately linear with canister volume. The subsystem weights estimated for the six point designs are plotted also for reference.

It is recommended that in further studies, the cyclic operation of the vent valve be included in the vent down computer program to verify component sizing, and filter rating test method be reviewed to assure compatibility with the sterilization requirements. System reliability can be enhanced by making use of the valve position indicating switch and the telemetry ΔP sensor to command electrical operation of the valve during canister venting.

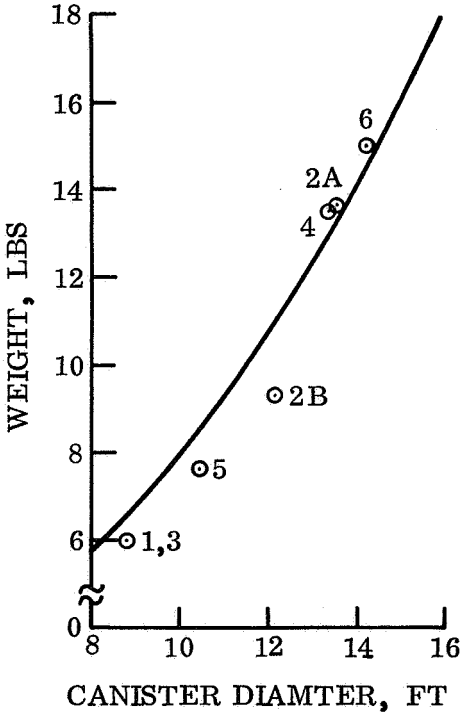

Figure 5.3.5-1. Pressure and Venting Subsystem Weight vs Canister Diameter

5.3.5.3 System Analysis

5.3.5.3.1 Venting Analysis

The venting analysis is performed with the aid of a computer program that solves the basic thermodynamic gas flow equations. Isothermal flow is assumed, to obtain a more severe case, whereas the actual flow will be between isothermal and adiabatic. The computer program assumes a quasi-steady state equilibrium over a 0.001 second interval and computes the flow across the nozzle. It then calculates the new stagnation pressure and repeats the process. The external atmospheric pressure as a function of time is programmed from a best fit polynomial of a series of pressure-time points obtained from a rough plot of a Titan III-C (see figs. 5.3.5-2 and -3) trajectory with a 2000 pound payload. The computer program, using nozzle area and initial volume as input, computes ΔP, Mach No., mass flow rate and total mass flow.

The results of the computer analysis are plotted on figs. 5.3.5-4 and -5. It is noteworthy that the ΔP vs time is insensitive to the initial pressure after the first 20 seconds. ΔP is a maximum, except for the initial condition, in the 40 to 80 second interval, and is fairly constant in this region. Higher initial pressures make the peak flow rate, which occurs immediately upon valve opening, higher.

Sizing of the subsystem components can be accomplished from the above data. The valve is sized as a function of nozzle area modified by appropriate discharge coefficients. Nozzle area is proportional to canister interval gas volume, for constant ΔP. The flow rate is used to size the biological filter. Filter element area is proportional to flow rate for constant ΔP and pressure drop. A pressure drop of 0.1 psi was initially assigned to the filter. Flow rates and nozzle areas are plotted on fig. 5.3.5-4 as a function of canister diameter and ΔP.

TABLE 5.3.5-1. PRESSURE AND VENTING WEIGHT SUMMARY

	8 Ft Canister 50 Ft^3	16 Ft Canister 500 Ft^3
1 Vent Valve	4.0	7.0
1 Biological Filter	1.0	7.0
1 Fill Valve	0.3	1.8
2 Fans	0.5	2.0
TOTAL	5.8	17.8

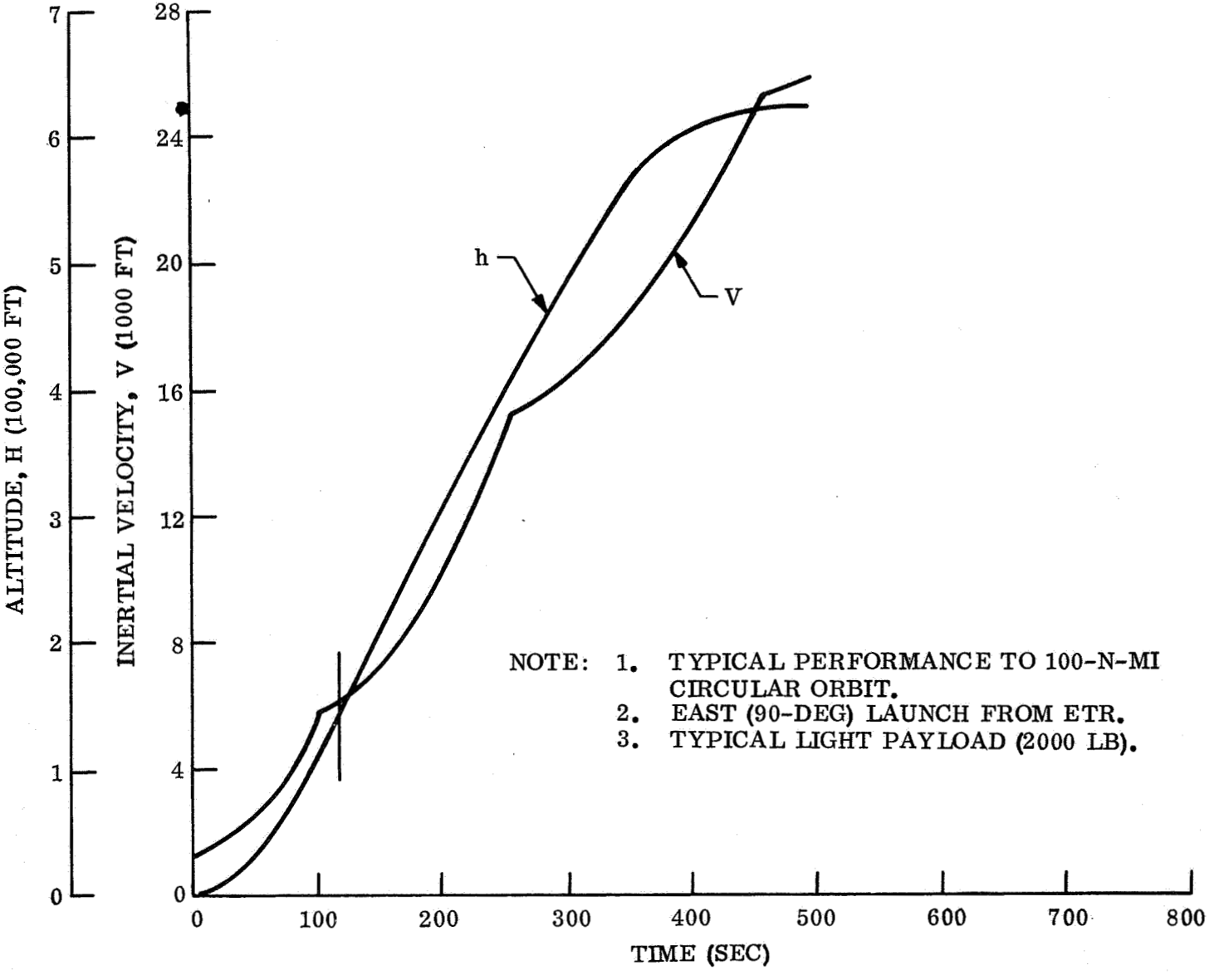

Figure 5.3.5-2. Altitude and Velocity Time History, Titan III-C

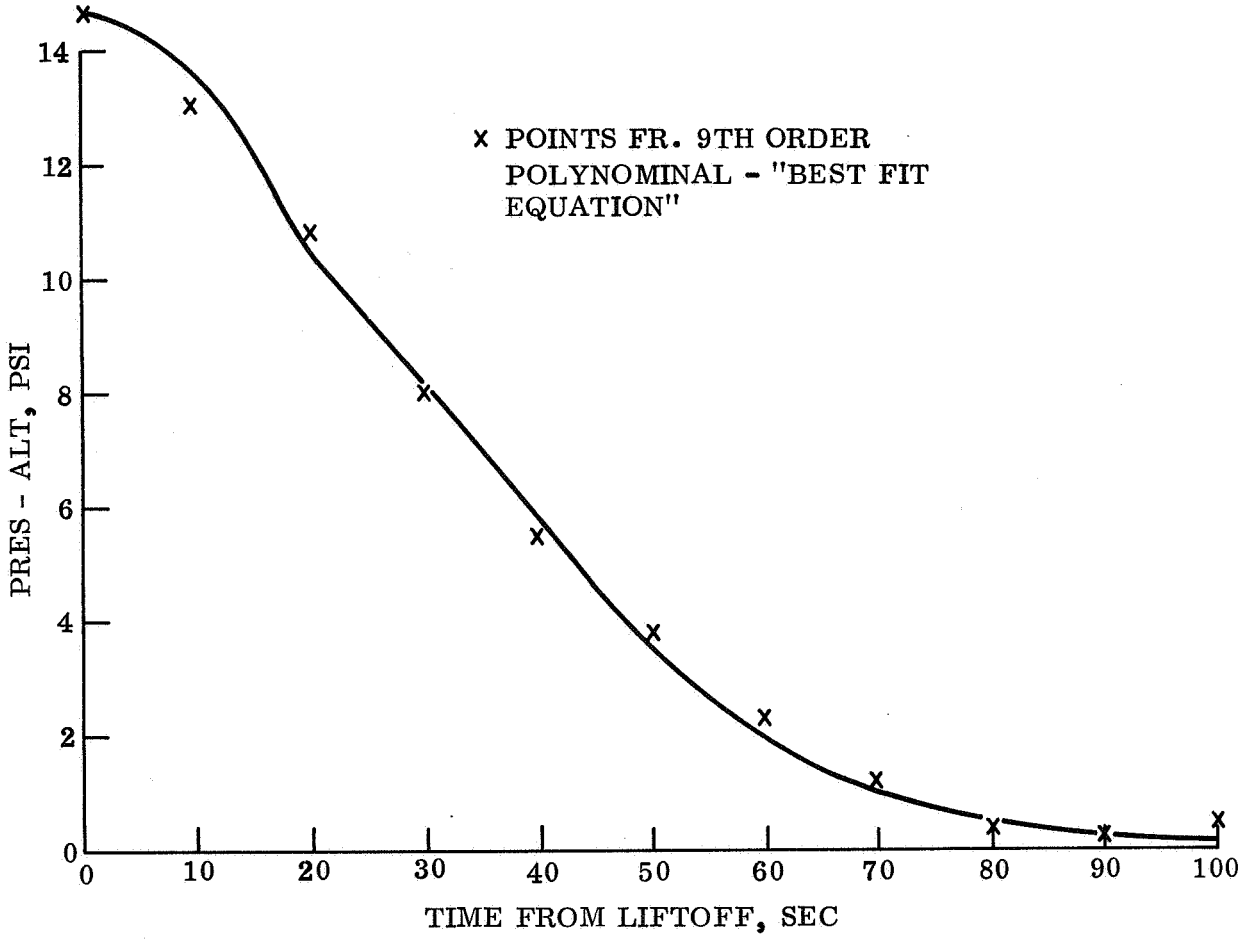

Figure 5.3.5-3. Ascent Pressure - Time Curve, Titan III-C and 2000 Payload

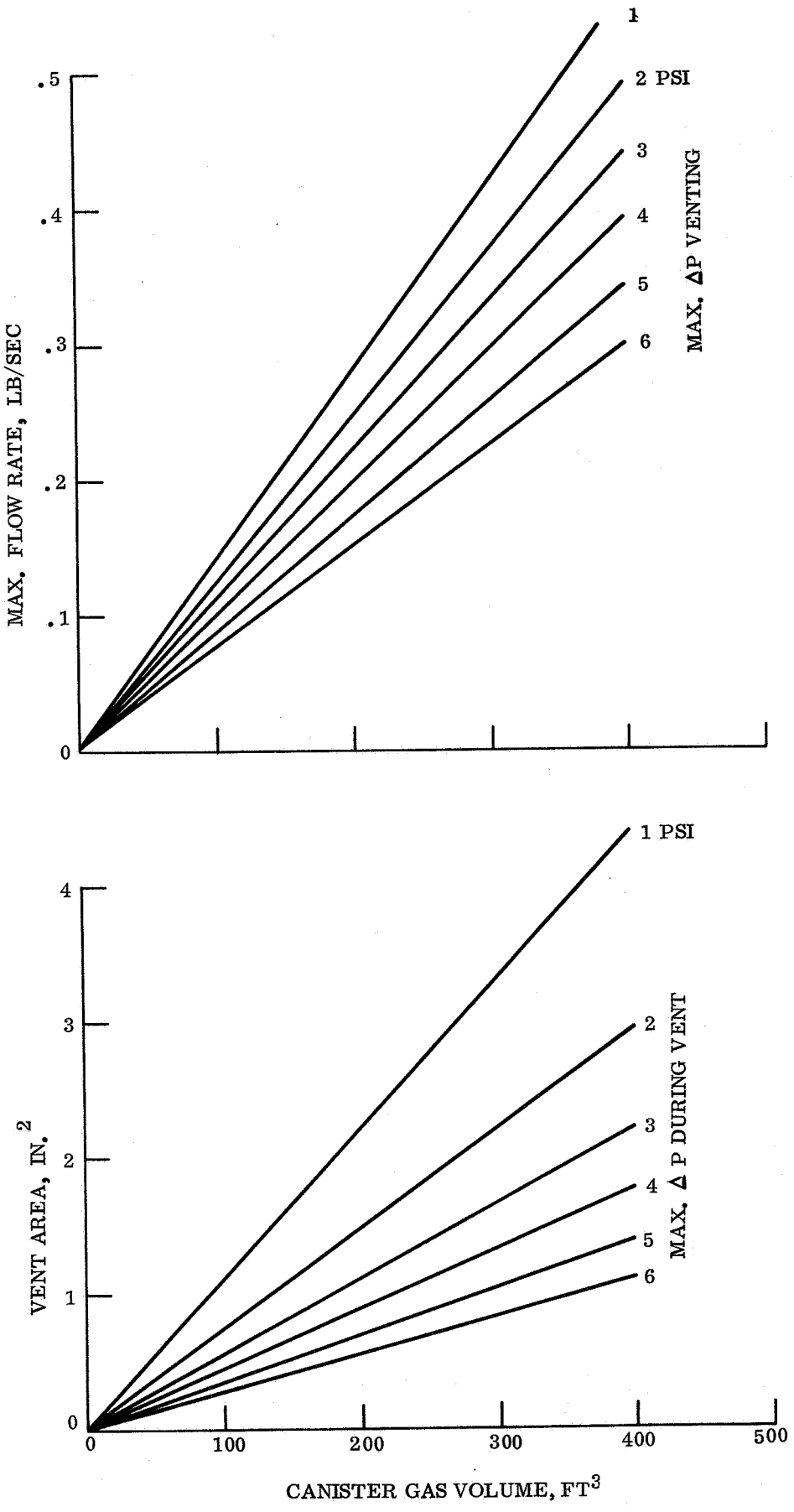

Figure 5. 3. 5-4. Canister Gas Volume

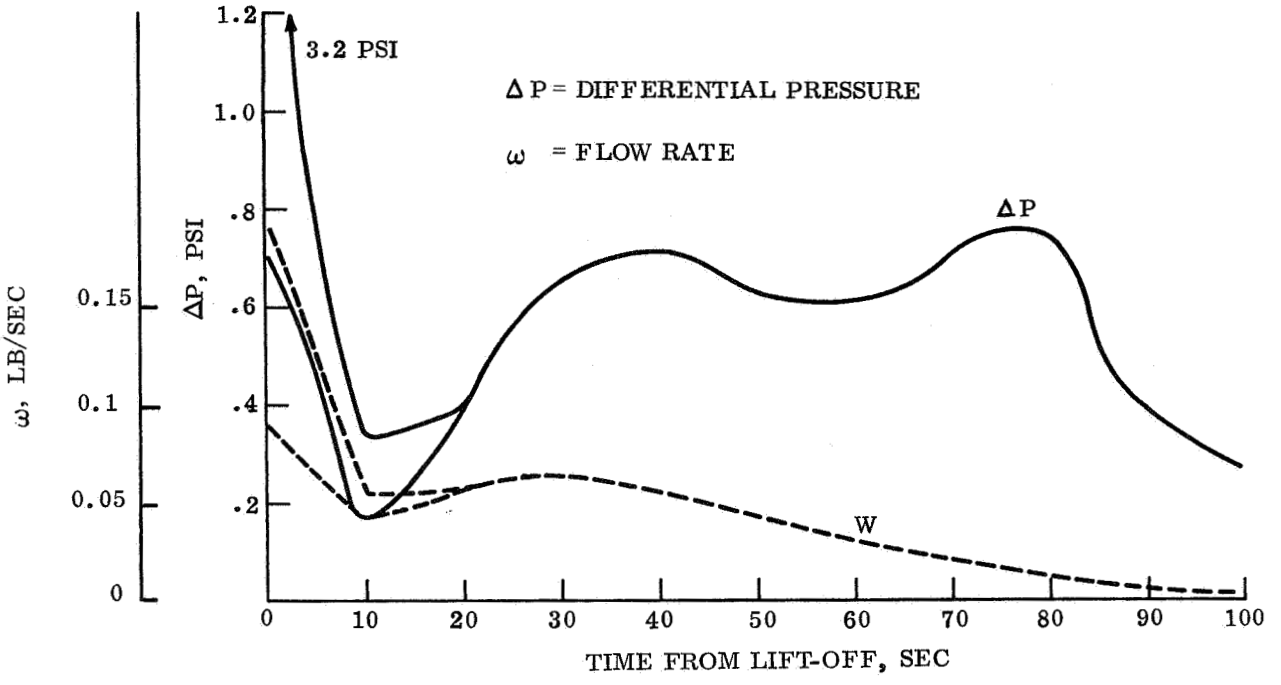

Figure 5. 3. 5-5. ΔP and Flow Rate vs Time Titan III-C Pressure Profile for Normal Canister

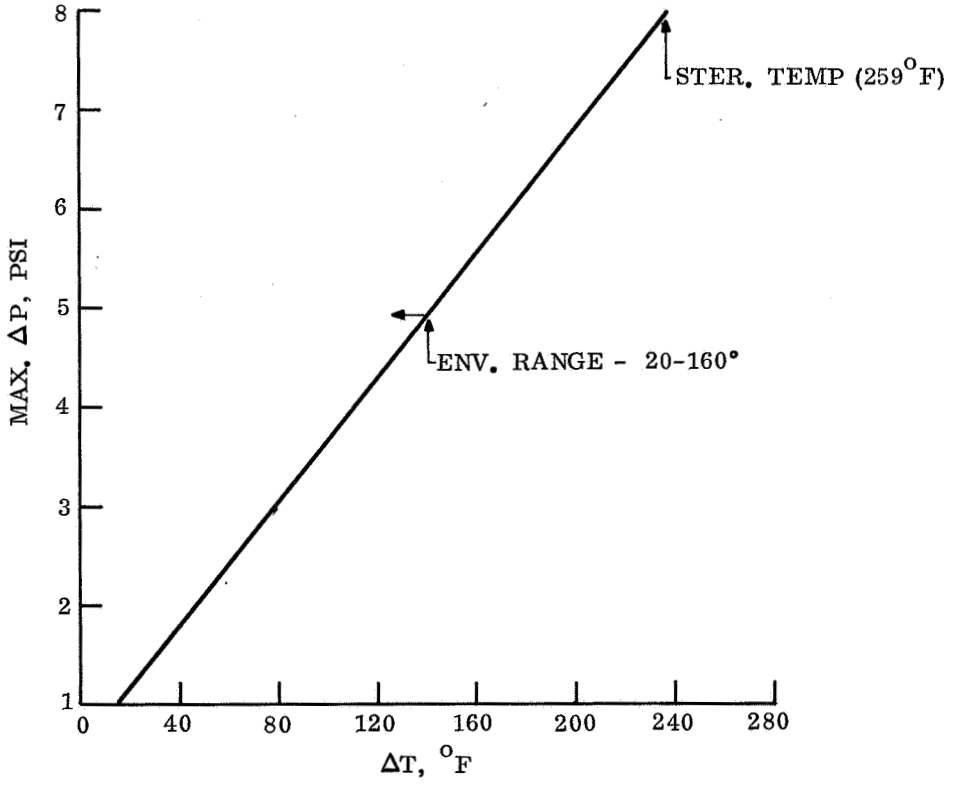

Figure 5. 3. 5-6. Maximum Canister ΔP vs Operating Temperature Range Based on 480°R (20°F) Initial Temperature

5.3.5.3.3 Effect of Temperature Variations

The allowable temperature variation within the canister depends on the initial pressure. This relation for a constant volume system is plotted in fig. 5.3.5-6. It shows that a 5 psid system can tolerate the +20°F to 160°F temperature range without any make up gas, whereas a 1 psid system can tolerate a maximum total temperature excursion of 18°F.

5.3.5.3.4 Allowable Leak Rates

Leakage can be tolerated, provided a positive pressure is maintained within the canister to "guarantee" sterile conditions. The minimum allowable ΔP (0.5 psi) will decay to 0.0 in approximately 10 days at an average drop of 0.002 psi/hr.

This rate can be monitored with the telemetry pressure transducer. The flow rate of any leaks will be more critical in the small canister, because of the lesser gas available.

5.3.5.4 Basic Design Solution

The philosophy followed in selecting a P&V system was to utilize the least number of valves required to perform reliably. Biological filters are required at every outlet in the canister, however, redundant valves performing the same function can be connected to a single filter. The functions to be performed which require valves are given in table 5.3.5-2 with the type of valve which can perform that function.

Requirements for the various functions are not really critical except for the venting functions, where large flows, 50 to 500 cfm, and fast response - 1/4 second are required. Relief and evacuation flow rates are less than 10 cfm and sterilization air inlet is governed by inlet pressure and number of air changes desired.

Considerations of reliability must include the pressure sensor, where this element is a series function to command the valve.

5.3.5.4.1 Venting Function

Since the venting function is most critical, several approaches were investigated and presented below.

1. Minimum component system - consists of one electrically actuated vent valve, one filter, one pressure sensor

2. Redundant system - consists of two electrical vent valves, one filter, two pressure sensors

3. Redundant system - different failure mode - consists of a relief valve, with a solenoid operated override, one filter, one pressure sensor

4. Combination of 2. and 3. above, one mechanical relief valve, one electrical vent valve, one filter, one pressure sensor.

Concept (3.) was selected as the basic approach, since it gives a minimum weight system with excellent reliability. The solenoid function could be time programmed or pressure programmed through a sensor during its redundant function. This same solenoid is operated toward the end of the space travel to completely evacuate the canister prior to separation.

A vent valve of this type was successfully used by LMSC to vent a Spacecraft. Important features of the valve are - pilot operated pneumatic relief, latching solenoid, position indicating switch. This one valve will perform all required valve functions listed in table 5.3.5-2 except sterilization and make-up gas inlet.

TABLE 5.3.5-2. PRESSURE AND VENTING SYSTEM VALVE FUNCTIONS

Function	Type Valve	Mode of Operation	Internal Filter Req'd	Sensing Req'd
a) Pres. Relief	Relief	Mechanical	Yes	No
	Solenoid or Motor	Electrical	Yes	Yes
b) Sterilization - inlet & outlet	Check Valve	Mechanical	Yes	No
	Fill Valve	Manual	No	No
	Solenoid or Motor	Electrical	Yes	No
c) Make-up gas inlet	Same as (b)			
d) Canister Vent	Solenoid*	Electrical	Yes	Yes
	Relief	Mechanical	Yes	No
e) Canister Evacuation	Solenoid or Motor	Electrical	Yes	No-Timed

*Motor operated valves are too slow for this function (2-3 seconds opening time)

Valve weight has a fixed portion associated with the solenoid and a variable part which is a function of operating pressure and flow. For the proposed valve, a weight estimate of 4 to 6 pounds was made based on a 3 pound actual valve with an opening of 0.4 inch diameter.

5.3.5.4.2 Biological Filters

Maintenance of the sterile status of the Capsule is of primary importance, and to this end biological filters are required to prevent bacteria entry. Contact was made with the Pall Corporation, and they have various types of their "Ultipor" filter media capable of meeting the filtering requirement of 0.3 microns. The trade off consists of attaining a balance between desired pressure drop across the filter and filter size- the larger the filter, the lower the pressure drop. In the low ΔP system being considered, pressure drop is more significant, and therefore 0.1 psi was assigned as the pressure drop for this study. Filter sizes obtained were based on this requirement for a one and five psid ΔP system, using "Ultipor" media.

"Ultipor" filter medium consists of multiple layers of extremely fine inorganic fibrous materials bonded by epoxy impregnant. Various filtration ratings are available; "Ultipor" .9 has a catalog rating of 100 percent removal of 0.08 micron particles; where as "Ultipor" .15 has a rating of 0.015. The finer filter increases the pressure drop, and since that level of filtration does not appear necessary at this time, it was not selected.

Filter weights are plotted in fig. 5.3.5-7 and assume a 0.06 aluminum housing in arriving at total weight. Filter sizes tabulated in table 5.3.5-3 are typical, in that total filter element area determines the element basic shape. Housing size is governed also by required flow rates in the inlet/outlet ports.

TABLE 5.3.5-3. BIOLOGICAL FILTERS

P = 1 PSI								
		Element			Housing			
Flow Rate cfm	Can. Vol. Ft^3	L In.	D In	Wt Lbs.	L In.	D In.	Wt Lbs.	Total Wt lbs
20	20	1.5	2.5	.70	2.25	3.0	.35	.47
100	100	6.6	2.5	.24	7.60	3.2	.71	1.00
250	400	9.0	6.2	1.70	10.25	7.5	2.82	4.52
P = 5 PSI								
20	32	1.8	2.5	.14	2.55	3.0	.36	.50
100	165	8.3	2.5	.50	9.30	3.2	.81	1.31
250	415	6.9	6.2	1.34	8.20	7.2	2.37	4.76
400	660	11.3	6.2	2.10	12.6	7.5	3.15	5.25

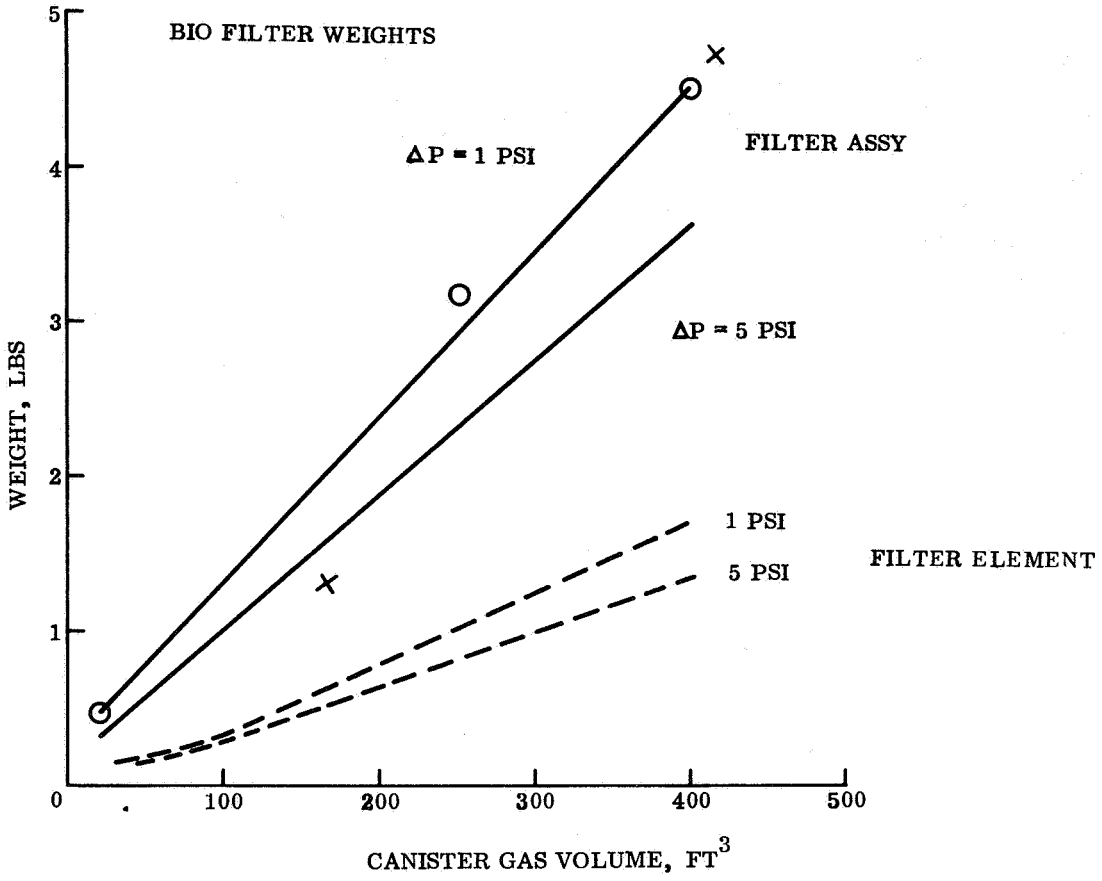

Figure 5.3.5-7. Biofilter Weights vs Canister Gas Volume

5.3.5.4.3 Other P&V Components

The fill valve to be used during sterilization and for OGE make-up gas hook up can be a manually operated valve with an external plug cap; thus obviating the need for a biological filter. The valve size is a function of ΔP and flow rate. A ΔP of 1 psid was assumed during sterilization and provisions for four air changes in one hour. For a 70 ft^3 system a valve with an area of 0.25 $in.^2$ gives 4.5 air changes/hour. This size can be scaled directly for other canister volumes.

The fans to be used during sterilization assist in reaching an equilibrium temperature within one hour. It was assumed that air delivery equivalent to two air changes per minute would suffice. Light weight, high rpm, vaneaxial type fans are recommended. The fans are used only during sterilization, but they could also be used during equipment checkout to prevent hot spots. Power to the fans is from external OGE.

The make up gas supply is envisioned as OGE equipment. It must have capabilities for monitoring internal pressure or to accept inputs from the telemetry ΔP sensor. The OGE must also sense ambient atmospheric pressure and supply make up gas during high barometric pressure times as well as during decreasing ambient temperatures.

APPENDIX A
MAJOR COMPUTER PROGRAMS

APPENDIX A MAJOR COMPUTER PROGRAMS

This appendix presents descriptions of some of the major computer programs employed in the Mars Hard Lander study by this contractor. The programs described are those employed in the thermodynamics, configuration selection, and recovery system selection analyses.

The program descriptions are not complete, the more commonly available programs, such as those for flight path analysis, are omitted for brevity.

A.1. DESCRIPTION OF REACTION KINETICS ABLATION PROGRAM

To describe the thermal behavior of a material in a re-entry environment, table A-1 and ref. A-1, it is necessary to solve the transient heat conduction equation for each element of material through the char (if a char exists), the reaction zone, and the virgin material continuously and simultaneously throughout the re-entry heating period. In order to solve these second-order differential equations simultaneously, it is necessary to prescribe several boundary conditions: (1) at the surface the net heat transfer rate to a non-permeable surface is reduced by both surface re-radiation, and the mass transfer effect of the injection of the decomposition gases into the boundary layer (blocking action), and (2) at the backface of the virgin plastic or supporting substructure the heat conducted out is zero.

In general, the heat conducted into a material element is equal to the sum of the heat stored in the element and the heat absorbed in the decomposition of the material element by the decomposition gases passing through the material element, and by cracking or recombination of the decomposition gases. The general heat conduction equation, valid in both the porous char and virgin material is written in cartesian co-ordinates as

$$\frac{\partial}{\partial x}\left[\frac{k\ \partial T}{\partial x}\right] = \rho C_p\ \frac{\partial T}{\partial t} + H_{GF}\frac{\partial \rho}{\partial t} - \left(Cp_G + \frac{\partial H_k}{\partial T}\right)\frac{\partial T}{\partial x}\int_{x = X'}^{x = \text{BACKFACE}} \frac{\partial \rho}{\partial t}\, dx \quad \text{(A1)}$$

$$\frac{\partial \rho}{\partial t} = \rho_v \left[\frac{\rho - \rho_c}{\rho_v}\right]^{\eta} \sum_{i=1}^{n} A_i\, e^{-\Delta E_i/RT} \quad \text{(A2)}$$

At the material surface - boundary layer interface, boundary condition eq. A1 is the thermal energy balance written as:

$$\dot{q}_{net} = \dot{q}_c - \dot{q}_{RR} - \dot{q}_{Block} - \dot{q}_{Vaporization} \quad \text{(A3)}$$

where:

$\dot{q}_c$ = hot wall convective heat flux = $H\ (h_r - h_w)$

$\dot{q}_{RR}$ = re-radiated heat flux = $\sigma\ Fe\ Fa\ T_w^4$

$\dot{q}_{Block}$ = transpiration cooling due to injected gases

For laminar flow

$$\dot{q}_{Block} = \dot{q}_c \left[\left(\frac{\overline{M}_{BL}}{\overline{M}_{GAS}} \right)^{1/3} (.69) \frac{\Phi_o}{Pr^{1/3}} \right] \quad \text{(A4)}$$

For turbulent flow

$$\dot{q}_{Block} = \dot{q}_c \left[1 - e^{-.38 \left(\frac{Cp_{GAS}}{Cp_{BL}} \right) \phi_o} \right] \quad \text{(A5)}$$

$$\Phi o = \int_{\text{Frontface}}^{\text{Backface}} \frac{\partial \rho}{\partial t} \, dx \left[\frac{h_r - h_w}{\dot{q}_c} \right] \quad \text{(A6)}$$

$\dot{q}_{VAP}$ = phase change energy associated with surface recession = $\rho_c \dot{L}s$

Surface recession rate is assumed to be a reaction rate controlled process that can be best described by an expression of the form

$$\dot{S} = \beta_1 T_w \beta 2_e - \beta 3/T_w$$

At the backface of the virgin plastic or supporting substructure, the second boundary condition on eq. A4 is

$$k \left(\frac{\partial T}{\partial x} \right)_{BF} = 0$$

By solving the above equations simultaneously and continuously through the heating period, the surface and subsurface temperatures and material degradation time histories are obtained. The Reaction Kinetics Ablation Program (REKAP) is the mechanized numerical solution to the above model.

The validity of this approach for the prediction of the thermal response of a material undergoing thermal degradation has been proven by comparing calculated results with those obtained during ground and flight tests.

TABLE A-1. AEROTHERMODYNAMIC AND THERMAL PROTECTION SYSTEM CALCULATION PROCEDURE SUMMARY

Aerothermodynamic Boundary Condition	Method or Procedure	Substantiation or Reference Documents
1. Stagnation Point Convective Heat Trans. 2. Local Laminar and Turbulent Heat Transfer Distribution. Local flow properties and boundary layer parameters required for boundary layer transition and mass transfer effects, $\rho_e, \mu_e, T_e, h_e, M_e, R_{e_s}, R_e$, H (film coefficient). Planetary Aerodynamic Heating Program includes provision for subsonic cooling/heating for low speed phase analysis. Provision for calculation of above information at a max. of 50 body locations. Other: For detailed design - Low density regimes defined by Knudsen number criteria - as applied to air atmosphere and earth entry. Low density heat transfer in slip, transitional and merged flow included as correction to results calculated for continuum flow.	Planetary Aerodynamic Heat Transfer Program. Primary Subroutines. 1. Normal shock relations Rankine-Hugoniot relations for pressure rise across normal shock, P_2/P_1 and stagnation pressure. Atmosphere ambient. 2. High Temperature N_2 - CO_2 Composition Equil. Gas Properties ($800^oR \leq T \leq 18000^oR$) S, ρ, T, and P 3. Pressure Distribution - options of modified Newtonian, modified Newtonian and Prandtl Meyer expansion, table look up of P_2/P_s or CP/CP_{max} as f(s/R_N, M_∞) to location of flow separation. 4. Local Boundary Layer Flow Quantities ρ_e, T_e, μ_e, h_e (1) obtained by isentropic expansion to local pressure using (2) option for vorticity effects available.	1. Normal shock relations developed by Scala, for N_2 - CO_2 atmospheres. 2. Development by Browne, for N_2 - CO_2 atmospheres as part of JPL contract 950226. Routine utilized to generate equilibrium composition for several foreign planet atmospheres. 3. Comparison of stagnation theories of Scala. Hosizaki, etc. with exp. data of Gruszczynski and Collins show close agreement for Argon free N_2 - CO_2 atmospheres and small difference from air at u_e = 27,000 ft/sec. Full-scale blunted MK2 ICBM heat sink vehicle and recent RMV heat sink vehicle and recent RMV heat sink vehicle ($0 < Me < 12$), ($6 < M_\infty < 22$) confirms laminar turbulent level and distribution techniques.

TABLE A-1. AEROTHERMODYNAMIC AND THERMAL PROTECTION SYSTEM CALCULATION PROCEDURE SUMMARY (Cont'd)

Aerothermodynamic Boundary Condition	Method or Procedure	Substantiation or Reference Documents
Aerodynamic heating in presence of non-equil. flow field are independently evaluated with edge of boundary layer flow conditions from flow field predictions. Free molecular heating estimated with $\alpha_T = 0.7$.	5. Aerodynamic heating (equil. attached flow) Stagnation point - Scala $\dot{q}_s = \frac{K_1}{P_r^{2/3}} \frac{0.707}{(\rho^* \mu^* u'_o)^{0.5}} (hr - hw)$ where $K_1 = 1.1$ $\Delta h = h_s - h_w$ Local laminar heat transfer Locally Similar Solutions $\dot{q}_L = \frac{K_1 .354 \rho^* \mu^* u_e y (hr - hw)}{P_r^{2/3} \left[\int_o^s \rho^* \mu^* u_e y^2 ds\right]^{1/2}}$ Turbulent Heat Transfer $\dot{q}_T = \frac{.0296 (\rho_e \mu^*)^{.2} \rho^{*.8} \mu_e^{.05} u_e y^{.25} (hr - hw)}{P_r^{2/3} \left[\int_o^s \rho_e u_e \mu_e^{.25} y^{1.25} ds\right]^{.2}}$ 6. Shock layer thermal radiation (approximate) One-dimensional, isothermal shock layer $\dot{q}_r = 48.1 LK_r \alpha_w I,\ I = f(\rho/\rho_o, T)$ in table form	

TABLE A-1. AEROTHERMODYNAMIC AND THERMAL PROTECTION SYSTEM CALCULATION PROCEDURE SUMMARY (Cont'd)

Aerothermodynamic Boundary Condition	Method or Procedure	Substantiation or Reference Documents
	7. Base flow separation and dividing streamlines determined from hypersonic shadowgraphs. Heat transfer in separated regime determined from multiple flat based, recessed and domed aft cover flight data correlations of form. $\dot{q}_L = 0.0192\, Re_\Delta^{.5} (\mu_e/\Delta)(h_s - h_w)$ $\dot{q}_T = 0.014\, Re_\Delta^{.75} (\mu_e/\Delta)(h_s - h_w)$ where $Re_\Delta = (\rho_e \mu_e \Delta/\mu_e)$	
3. Shock Layer Thermal and Spectral Radiation	Hot Gas Radiation Program (HGR) Shock layer radiation digital computer program incident absorbed radiation. $\dot{q} = \sum_\nu \sum_\phi \sum_\theta \alpha_\nu B_\nu \Delta\nu \frac{\sin^2\theta}{2}$	• Developed for NASA-Langley FIRE Flow Field Contract (NASI-3418) radiation predictions made in 0.05 to 0.16, 0.66 to 3 microns spectrum. For FIRE flight - extended to non-air gases. $\theta + \Delta\theta \quad \Delta\phi \prod_i \tau_{\nu_i}$ θ

TABLE A-1. AEROTHERMODYNAMIC AND THERMAL PROTECTION SYSTEM CALCULATION PROCEDURE SUMMARY (Cont'd)

Aerothermodynamic Boundary Condition	Method or Procedure	Substantiation or Reference Documents
	Input Routine: Flow Field (1) Tape input of arbitrary body flow field, ρ, T, P and species concentration for radiance from nonequal flow fields. (2) Gas emissivity/absorptivity - Table input in form of $K_\nu = f(\rho/\rho_o, T)$ $\epsilon_\nu = 1 - e^{-K_\nu \Delta r}$ $B_\nu = \frac{2hc^2}{\lambda^5}\left[e^{\frac{hc}{KT\lambda}} - 1\right]^{-1}$ $\tau_{\nu_i} = e^{-K\nu_i \Delta r}$	
4. • Temperature Response of Material • Material Degradation • Mass Injection into Boundary Layer	Reaction Kinetics Ablation Program (REKAP) Solution of one-dimensional transient heat conduction problem by combined implicit/explicit math techniques with the following options (6-layer composite) $\frac{\partial}{\partial x}\left[k\frac{\partial T}{\partial x}\right] = \rho Cp\frac{\partial T}{\partial t} + H_{gf}\frac{\partial \rho}{\partial t}$ $-\left(C_{p_g} + \frac{\partial H_k}{\partial T}\right)\frac{\partial T}{\partial x}\int_{x=X'}^{X=\text{Backface}}\left(\frac{\partial \rho}{\partial t}\right)dx$ where $\frac{\partial \rho}{\partial t} = \rho v\left(\frac{\rho - \rho_o}{\rho v}\right)^{\eta}\sum_{i=1}^{n} A_i\, -\Delta E_i/RT$	Utilized as primary GE-RSD thermal shield design technique for ballistic and satellite re-entry for nylon phenolic, refrasil phenolic, carbon graphite phenolic, and graphite materials, and elastomeric materials.

TABLE A-1. AEROTHERMODYNAMIC AND THERMAL PROTECTION SYSTEM CALCULATION PROCEDURE SUMMARY (Cont'd)

Aerothermodynamic Boundary Condition	Method or Procedure	Substantiation or Reference Documents
	(1) Variable external boundary condition ($\dot{q}$ vs time) (applicable to heat sink analysis) (2) Option (1) plus decomposition in depth in accordance with thermogravometric analysis data converted to multiple temp. region Arhenius relations. (3) Option (1) and or (2) with the transfer of radiation in depth by absorption and emission including multiple reflections used for semi-transparent materials. Boundary conditions $\dot{q}_o$, qRAD, $\dot{q}$ combustion, $\sigma \epsilon T_w^4$ Mass transfer effects defined as $\frac{\dot{q}}{\dot{q}_o} = \left[1 - .69\left(\frac{\overline{M}_{BL}}{\overline{M}_g}\right)^{1/3} \varphi \frac{1}{Pr^{1/3}}\right]$ laminar $\dot{q}/\dot{q}_o = e^{-.38 \frac{C_{pg}}{Cp_{BL}}} \varphi_o$ turbulent $\varphi = \frac{\partial \rho}{\partial t}\left(\frac{h_r - h_w}{\dot{q}_c}\right)$	

A.2. CONSEP PROGRAM DESCRIPTION

A.2.1 DEVELOPMENTAL BACKGROUND

Entry vehicle proposal response efforts, design studies and the associated initial phases of design development require rapid definition of basic design trends and trade-off capabilities and, quite frequently, early establishment of optimum design configurations. The ever diminishing response time requirements obviate the traditional, detailed design lay-out procedures for such initial program efforts.

GE-MSD has, for a period of over eight years, been engaged in the development of a series of digital programs which permit such broad-scale, comprehensive design analysis and specification within an extremely short period of time.

This CONSEP series (CONSEP from CONfiguration SElection Programs) currently consists of CONSEP II and III programs principally concerned with vehicles designed for entry into Earth's atmosphere, and a third program, CONSEP IV.

This latter program has been recently developed for the specific purpose of investigating axisymmetric vehicle design characteristics for entry into Mars and Venus atmospheres. Its development has drawn heavily from prior experience gained during the CONSEP II and III program growth and utilization.

This CONSEP IV program consists of a basic composite of simplified empirical design techniques which, when combined with packaging calculations, permits rapid determination of a wide variety of vehicle parameters. This program is capable of designing approximately 100-200 vehicles per minute. The program logic and design techniques are briefly described in the following paragraphs.

A.2.2 CONSEP PROGRAM LOGIC

The basic program logic is based upon outside-in design techniques. The envelope of a given vehicle is first described which, when combined with an initial assumption of vehicle weight and specified entry conditions, permits establishment of heat shield and structural thickness distributions. These values then permit calculation of internal cavity geometry. The mathematically described payload components can then be inserted into this cavity. This procedure is followed by total vehicle weight and balance, and moment of inertia calculations. The resultant vehicle weight is then compared to the assumed initial value to determine the degree of convergence. If adequate, the design procedure is completed. If not, the design cycle is iterated until the proper degree of convergence is obtained. This logic and step-by-step procedure is schematically described in fig. A-1.

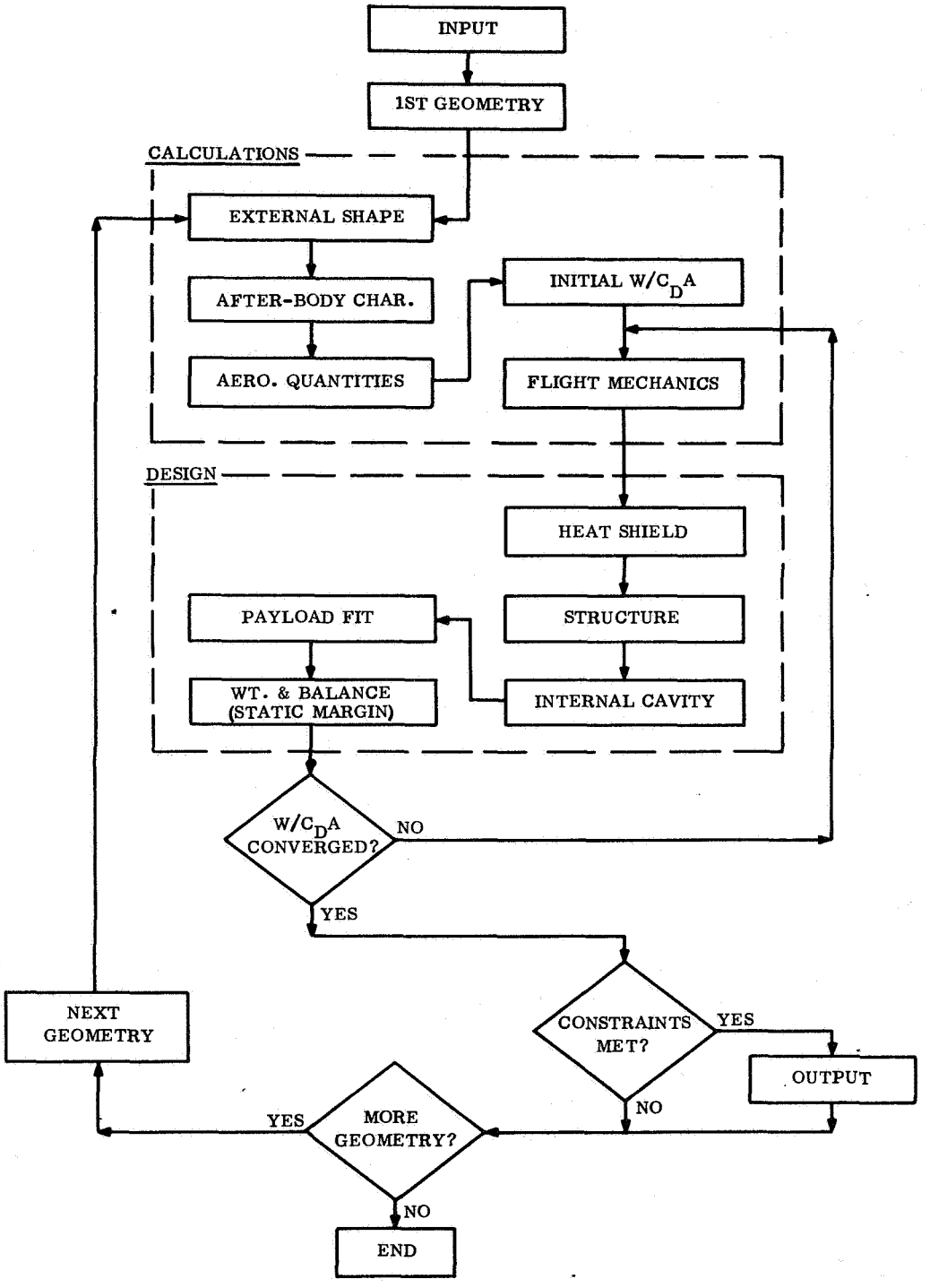

Figure A-1. CONSEP Schematic

The program input consists of description of internal payload component geometry and inertial characteristics, structural materials properties, heat shield thickness variations with vehicle W/C_DA and integrated heat load (or maximum heating rate), shield density, design options and constraints, entry conditions, and an array of vehicle geometric parameters to be investigated.

Up to ten values for each of the geometric parameters can be treated during a single run. Sphere-cone concepts, for example, are described by specification of semi-apex angle, bluntness ratio, and base radius. Each production run can then evaluate anywhere from one to one thousand sphere-cone designs.

The program checks each vehicle design for payload component overlap or insufficient internal cavity dimensions for payload insertion, which then results in automatic design rejection. Additional elimination criteria, or constraints, can be imposed upon each study. These constraints are supplied by the user in the form of maximum and/or minimum allowable values for length, weight, W/C_DA, and stability margin. Each vehicle design is checked against these values before final design acceptance is made, as indicated in fig. A.2.2-1.

A.2.3 CAPABILITY AND PROCEDURE

The following material presents a brief word description of the salient procedures contained within CONSEP. Further detailed information is contained in ref. A-2.

A.2.3.1 Geometric Descriptions

Specification of vehicle external geometry within CONSEP is divided into two major sections; forebody and afterbody. Each area has separate modes of treatment and scope.

The forebody description has been constructed to permit treatment of sphere-cone, sphere-power law, and sphere-ogive bodies of revolution. The generatrix of such configurations is expressed by:

$$R = A + B\,(X - X_R)^E + C\sqrt{R_O^2 - (X_O - X)^2}$$

where A, B, C, E and R_O are constants of the equation, and X_R and X_O permit translation of the section origin from the coordinate origin. Complex forebody configurations can be represented by combining up to 7 sections of the above form. All configurations are considered to be spherically blunted, the sphere being assumed tangent to the following body section. The power-law exponent, E, is currently restricted to discrete values of 2/3, 3/4 and unity.

Afterbody configurational types are fixed, consisting of: 1) circular flat plate hemispheres, 2) non- tangent spherical segment domes, 3) ogives, 4) ogive domes, 5) conica frustums, and 6) tangent spherical domes. The proportions associated with each of these

concepts is controllable by the user. Special cut-out flat plate aft-cover capability was included for the subject Mars Hard Lander study.

Payload geometries are treated in the same manner as the external geometry, utilizing the following relation.

$$R = A + BX + C \sqrt{R_O^2 - (X - X_O)^2}$$

The origin of the payload coordinate system, for input purposes, is taken to be at the nose of the payload. Up to ten such geometric segments may be utilized to describe all payload components. These payload components may be arranged in three separate packages, which are located in the vehicle in an independent manner. The forward and middle components are located as far forward as internal tangency will permit. The aft package is located at a fixed distance from the vehicle base. This value is supplied by the user.

A.2.3.2 Aerodynamics

The key aerodynamic parameters utilized by CONSEP are vehicle drag coefficient, center-of-pressure, and local surface pressure coefficients. The program has been basically constructed to provide Newtonian values for these parameters for any described vehicle at both 0° and 180° angle-of-attack. Provision has been made, however, for table look-up of drag and center-of-pressure as a function of two geometric parameters. These arguments are currently fixed as being bluntness ratio and length-to-diameter ratio; however, these reference parameters can be readily changed.

An option also exists which permits calculation of viscous effect drag increments for addition to the above discussed inviscid drag values.

A.2.3.3 Flight Mechanics

Information regarding flight environment is normally supplied to CONSEP in the form of entry velocity and flight path angle at the edge of the effective atmosphere, the atmospheric molecular weight, and a reference density and inverse scale height parameter.

These quantities are then incorporated into Allen and Eggers relationships for calculation of stagnation point integrated heat load (and/or maximum heating rate) and maximum dynamic pressure. These quantities are then made available for use during heat shield and structural design.

A second mode of treatment is available, for use during heat shield and structural design, which provides a triple table look-up of the trajectory dependent parameters as functions of W/C_DA, entry angle, and velocity.

A.2.3.4 Thermodynamics

The integrated heating distribution over sphere-cones includes, for Mars entry, contributions due to convective heating and also to equilibrium and/or non-equilibrium boundary layer radiation effects. The procedures involved in the calculation of radiative heating are discussed in Section 3.1.2 and will not be repeated here.

The convective heating is calculated assuming cold wall conditions in laminar flow. The stagnation point heating, normalized by the square root of nose radius, is calculated in the Flight Mechanics subroutine using these assumptions and Allen and Eggers-developed relationships.

This stagnation point heating is then applied to a distribution function for calculation of conical skirt heat load distribution.

This distribution function is expressed in terms of wetted length and local pressure. The pressure distribution is calculated for spherically blunted conical segments, using a combination of Newtonian and Prandtl-Meyer expansion theories. This pressure distribution is expressed by curve fitted relationships, using cone angle as the independent parameter.

Vehicle geometries, other than sphere-cones, use the same relations wherein local flow angle is substituted for cone angle.

The calculated integrated heat load is then used in conjunction with the subject vehicle W/C_DA to enter a two-way table look-up analysis for final specification of heat shield thickness. This table is input by the user, based upon thermodynamic analytical data for the particular heat shield material, flight path, and design backface temperature under consideration.

Afterbody heat protection, if any, must be also input into the program.

A.2.3.5 Structural Design

The forebody structure can either be input into, or calculated by the program. Design capability for either honeycomb or ring-stiffened shell structure is available. Materials characteristics (density, Young's modulus, compressive yield stress, minimum gage thicknesses) are input into the program. This permits treatment of a wide range of materials at any effective structure temperature representative of a given design condition.

Each geometric segment of a vehicle is sub-divided into sections; each of which is treated as an equivalent cylinder. This cylindrical segment is designed to resist yield and buckling due to aerodynamic pressure loading. No axial inertia effects are treated, and no structural support from the heat shield is assumed.

Experience with CONSEP II and III has indicated that these two simplifications tend to counteract each other, resulting in structural thickness distributions and weights comparable to those obtainable through more complex and detailed analyses.

The local pressure loading is obtained from the previously calculated peak dynamic pressure (see Section A.3.2) and modified Newtonian estimates of local pressure coefficient.

The afterbody structure is either input to the program, or calculated utilizing an input value of internal differential pressure value.

A.2.3.6 CONSEP Data Output

Provision has been made within CONSEP output logic for the generation of both paper and magnetic tape output. This permits visual data inspection and manual treatment, as well as automatic plotting and/or subsequent digital program manipulation of the CONSEP-generated data.

Three choices of the degree of CONSEP information to be printed are available. The most complete set of data includes (for each valid vehicle) items such as:

1. External Geometry: Bluntness ratio, nose and base radii, cone angle, length, and center of gravity.

2. Aerodynamic Quantities: Drag coefficient, W/C_DA, m/C_DA, center of pressure, and stability margin.

3. Weight Breakdown: Heat shield, skin, rings, payload, and total vehicle.

4. Weight Distribution: Heat shield weight per body section (includes section surface area, average pressure, and integrated heat load).

5. Thickness Distributions: Heat shield and structural thicknesses at selected axial locations.

The logic and simplified design techniques, outlined here, have resulted in a program which is easily used, highly flexible, and characterized by a complete design capability rate which is believed to be unmatched throughout the corporate aerospace community.

A.3 STRUCTURAL ANALYSIS SUB-ROUTINE IN CONSEP IV PROGRAM

The function of the structural mechanics subroutine in the CONSEP program is to provide a realistic estimate of the structural mass and inertia properties for each entry vehicle being considered.

Two types of structural shell configurations are considered: a honeycomb sandwich shell and a ring stiffened shell. For the honeycomb sandwich shell each geometric section is of constant thicknesses. In the ring stiffened shell, a ring is placed at the end of each geometric section and at each subdivision (the split index controls subdivisions). Each subdivided section of the ring stiffened shell is then of constant thickness and as such, the thickness of each geometric section is not necessarily uniform. Interactions between the heat shield and structure are neglected in the design.

A.3.1 STRUCTURE LOAD CONDITIONS

The forebody structural design load conditions are taken to occur at the peak dynamic pressure condition. For simplicity only pressure loads are considered.

A.3.1.1 Forebody

The pressure at any point on the forebody surface is given by

$$p - p_\infty = \overline{C}_p \, q_\infty \sin^2\theta \tag{A7}$$

The design load conditions are evaluated from eq. A7 with the dynamic pressure being the peak dynamic pressure found in the Flight Mechanics Subroutine.

A.3.1.1.1 Spherical Segment

For a spherical segment, the average pressure acting over the section is given by

$$\overline{p} \equiv p_{avg} - p_\infty = \frac{1}{S}\int_s (p - p_\infty)\, ds \tag{A8}$$

where ds is the elemental surface area:

$$ds = 2\pi \, rR_N d\theta = 2\pi \, R_N^2 \cos\theta \, d\theta \tag{A9}$$

Therefore,

$$S = 2\pi \, R_N^2 \int_{\theta_t}^{\pi/2} \cos\theta \, d\theta = 2\pi \, R_N^2 (1 - \sin\theta_t) \tag{A10}$$

where θ_t is the body angle at the tangency point.

Then the peak average pressure is

$$\overline{p'} = \frac{\overline{C}_p\, q'_\infty}{1 - \sin\theta_t} \int_{\theta_t}^{\pi/2} \sin^2\theta \cos\theta\, d\theta = \frac{\overline{C}_p\, q'_\infty}{(1 - \sin\theta_t)} \frac{\sin^3\theta}{3}\Bigg|_{\theta_t}^{\pi/2} \tag{A11}$$

$$\overline{p'} = \frac{1}{3}\overline{C}_p\, q'_\infty\, (1 + \sin\theta_t + \sin^2\theta_t)$$

Hence, for a hemisphere the peak average pressure is, from eq. A11

$$\overline{p'} = \frac{1}{3}\overline{C}_p\, q'_\infty .$$

An alternate method of defining the average pressure is to consider the loading to be two dimensional. In this sense the resulting average is greater than that given by the above method, where the loading is considered to be three dimensional, and is therefore conservative in design. As any calculation based on an average pressure is at best only approximate, it was decided that a conservative approach would be taken where all average pressures are taken to be two dimensional in the above sense. Then for this case, the peak average pressure is given by

$$\overline{p'} = \frac{1}{\frac{\pi}{2} - \theta_t} \int_{\theta_t}^{\pi/2} \overline{C}_p\, q'_\infty \sin^2\theta\, d\theta$$

$$\overline{p}_s{}' = \frac{1}{2}\overline{C}_p\, q'_\infty \left[1 + \frac{\sin 2\theta_t}{2\left(\frac{\pi}{2} - \theta_t\right)}\right] \tag{A12}$$

which for a hemisphere is equal to $\frac{1}{2}\overline{C}_p\, q'_\infty$.

A.3.1.1.2 Conical Frustrum

For a conical segment the pressure is constant, thus the peak average pressure is

$$\overline{p'_c} = \overline{C}_p\, q'_\infty \sin^2\theta_c \tag{A13}$$

A.3.1.1.3 Other Geometries

For skirt geometries other than conical frustrums each segmented section of the skirt is taken to be a conical frustum with an angle equal to the average of the extremity angles.

A.3.1.2 Afterbody

If the structural thickness is to be calculated for an aft cover, the design pressure difference, Δp (psf), across the cover must be specified as input (Δp must be positive). It has been assumed in stability considerations that the internal pressure is greater than the external pressure.

A.3.2 STRUCTURAL REQUIREMENTS

The structural requirements for a given geometry, loading condition and material are a function of the structural shell configuration (type of construction). Two types of configurations are considered: (1) honeycomb sandwich shell and (2) ring stiffened shell. Any interactions between the heat shield material and the structure are neglected, namely the strength contribution of the heat shield and associated thermal stresses.

A.3.2.1 Honeycomb Sandwich Shell

The honeycomb sandwich structure consists of two high density faces separated by a low density core material. The face thickness is determined by allowing the material to work at its yield stress, unless fabrication limitations (e.g. minimum gages) dictate other requirements. The associated core depth is then generally determined from stability considerations.

The minimum gage face thickness used for all materials is 0.01 inches. The core density is assumed to be 0.035 times the face density.

A.3.2.1.1 Forebody

A. Spherical Segment

For a spherical shell segment of thickness t under uniform pressure load $\overline{p'_s}$, the stress is

$$\sigma = \frac{\overline{p'_s}\ R_N}{2t} \qquad \text{(A14)}$$

Then if the face material is allowed to work at its yield stress, the design thickness of one face is given by, ($t_f = t/2$):

$$t_{f,1} = \frac{\overline{p'_s}\ R_N}{4\sigma_y}\ \Phi_{s,1};\ (t_f \geq .833 \times 10^{-3}\ \text{ft}) \tag{A15}$$

where $\Phi_{s,i}$ is a structural design factor for the i th section (the spherical segment is the first section).

In buckling, the honeycomb shell is analyzed as an equivalent monocoque shell of thickness t_e and modulus E_e for which the critical load is

$$p_{cr} = \frac{.312\ E_e\ t_e^{\,2}}{R_N^{\,2}} \tag{A16}$$

with

$$E_e = 2E_f t_f / t_e \tag{A17}$$

$$t_e = \sqrt{3}\ (t_f + t_e) \tag{A18}$$

So that the design equivalent thickness is

$$t_e = \frac{\overline{p'}\ R_N^{\,2}}{.312\ (2\ E_f t_f)} \tag{A19}$$

and finally

$$t_c = 0.925\ \frac{\overline{p'_s}\ R_N^{\,2}}{E_f t_f} - t_f \tag{A20}$$

Neglecting the last term in eq. A20 the design core thickness for the sphere is given by

$$t_{c,1} = .925\ \frac{\overline{p'_s}\ R_N^{\,2}}{E_f t_{f,1}}\ \Phi_{s,1};\ (t_c \geq .0476\ \text{ft}) \tag{A21}$$

The requirement that $t_c \geq 0.0476$ ft. is determined by assuming that the minimum allowable core weight is equal to the minimum gage weight of the faces, viz.

$$t_c \geq \frac{2\rho_f t_f(\min)}{\rho_c} = \frac{2 \times .833 \times 10^{-3}}{.035} = 0.0476 \text{ ft.}$$

The overall thickness of the first section is simply

$$t_1 = 2\, t_{f,1} + t_{c,1} \tag{A22}$$

In the calculation of the forebody shell mass and inertia characteristics, it is assumed that the shell is homogeneous. The reference density is calculated for the forebody based on the mass characteristics of the first section (sphere).

The mean reference density for the forebody is taken to be

$$\bar{\rho} = 1.25\, \rho_f \left(\frac{2\, t_{f,1} + .035\, t_{c,1}}{t_1} \right) \tag{A23}$$

where the fabrication factor is taken to be 1.25. This mean reference density is now used throughout the forebody in calculations of mass and inertia.

B. Conical Frustum

A conical frustrum is treated as a circular cylinder of effective radius

$$\bar{R}_i = \frac{r_i + r_{i+1}}{2 \cos \theta_c} \tag{A24}$$

and effective length

$$L_i = \frac{X_{i+1} - X_i}{\cos \theta_c} \tag{A25}$$

For a cylindrical shell segment of thickness t, the hoop stress is

$$\sigma = \frac{\bar{p}_c' \bar{R}}{t} \tag{A26}$$

If the face material is now allowed to work at its yield stress, the design thickness of one face is given by (with $t_f = t/2$)

$$t_{f,i} = \frac{\bar{p}'_c \bar{R}_i}{2\sigma_y} \Phi_{s,i}; (t_f \geq .833 \times 10^{-3} \text{ ft}) \tag{A27}$$

In buckling the honeycomb shell is again analyzed as an equivalent monocoque shell of thickness t_e and modulus E_e, for which the critical load is

$$p_{cr} = \frac{.74 E_e}{\left(\frac{t}{\bar{R}}\right)\left(\frac{\bar{R}}{t_e}\right)^{5/2}} \tag{A28}$$

So that

$$E_e t_e^{5/2} = 2 E_f t_f t_e^{3/2} = \frac{\bar{R}^{3/2} \bar{L} \bar{p}_c'}{.74}$$

$$t_e = \sqrt{3}\,(t_e + t_f) = \bar{R}\left(\frac{\bar{p}'_c \bar{L}}{1.48 E_f t_f}\right)^{2/3}$$

Finally the design core thickness is given by

$$t_{c,i} \cong t_{c,i} + t_{f,i} = \frac{\bar{R}_i}{\sqrt{3}}\left(\frac{\bar{p}'_c \bar{L}_i}{1.48 E_f t_{f,i}}\right)^{2/3} \Phi_{s,i}; (t_c \geq .0476) \tag{A29}$$

The overall thickness is

$$t_i = 2 t_{f,i} + t_{c,i} \tag{A30}$$

with an overall density

$$w_i = 1.25 \rho_f \frac{2 t_{f,i} + .035 t_{c,i}}{t_i} \tag{A31}$$

Using a mean reference density for the forebody of $\bar{\rho}$, eq. A23, a corresponding thickness of

$$\tau_i = \frac{w_i \, t_i}{\bar{\rho}} \tag{A32}$$

is used in subsequent mass and inertia calculations.

C. Other Forebody Geometries

For forebody geometries other than a spherical segment or a conical frustrum, the section is treated structurally as a conical frustrum with an angle equal to the average of the extremity angles.

A.3.2.1.2 Afterbody

On the afterbody, as on the forebody for a honeycomb sandwich shell, the shell is treated as being homogeneous in mass and inertia calculations. Furthermore, the afterbody is treated separately from the forebody. The mean reference density used on the afterbody may vary depending on whether the afterbody thicknesses are specified as input or whether the thicknesses are to be computed.

If the thicknesses on the afterbody are specified as input, then

$$t = 2 \, t_f + t_c$$

$$\bar{\rho} = 1.25 \, \rho_f \, \frac{2 \, t_f + .035 \, t_c}{t}$$

where the t_f and t_c are input values for the aft cover.

If the thickness are to be calculated, minimum gage thicknesses are used in the above relations to determine a mean reference density for the afterbody.

A. Flat Plate

For a flat plate, the bending moment is assumed to be

$$M = \frac{(\Delta\rho) \, r_i^2}{5} \tag{A33}$$

If the bending moment is assumed to act only in the faces, we have

$$M = (\sigma_y \, t_{f,i}) \, t_{c,i} \tag{A34}$$

Furthermore, if the face weight is assumed to be equal to the core weight, that is

$$t_{f,i} = .0175 tc,i \tag{A35}$$

we have from eq. A33 through eq. A35

$$tc,i = \sqrt{\frac{(\Delta p)\, r_i^2}{.0875\, \sigma_y}} \tag{A36}$$

In view of the above simplifying assumptions an additional 20% design margin has been applied such that the design core thickness is given by

$$t_{c,i} = \sqrt{\frac{r_i^2 \Delta p}{.06\sigma}}\ \Phi_{s,i,}\ (t_c \geq .0476 \text{ ft}) \tag{A37}$$

The associated face thickness is then given by eq. A35

The overall thickness is then

$$t_i = 2\, t_{f,i} + t_{c,i} \tag{A38}$$

with an overall density of

$$w_i = 1.25\, \rho_f\ \frac{2\, t_{f,i} + .035\, t_{c,i}}{t_i} \tag{A39}$$

In mass and inertia calculation the reference thickness is

$$\tau_i = \frac{w_i\, t_i}{\bar{\rho}} \tag{A40}$$

B. Dome

For the afterbody dome thicknesses, the equations derived previously for the forebody spherical segment, para A.3.2.1.1.1, are used with a pressure load of Δ p:

$$t_{f,i} = \frac{(\Delta p)\, R_D}{4\sigma_y}\ \Phi_{s,i,};(t_f \geq .833) \tag{A41}$$

$$t_{c,\,i} = \frac{.925\,\Delta p\,R_D^{\,2}}{E_f\,t_{f,\,i}} \quad \Phi_{s,\,i}\,;(t_c \geq .0476) \tag{A42}$$

The overall thickness and the mean reference thickness are then given by eq. A38 through A40.

A ring is needed if the dome is not preceded by an annular plate. The ring is designed to withstand the radial component of loading in the dome. The load in the faces per inch is $\Delta p\,R_D/2$ and the outward component is

$$\frac{\Delta p\,R_D}{2}\sqrt{1-\left(\frac{r_i}{R_D}\right)^2}$$

The ring load is then

$$L_R = \frac{r_i\,\Delta p R_D}{2}\sqrt{1-\left(\frac{r_i}{R_D}\right)^2} \tag{A43}$$

Assuming that the ring acts at its yield stress, the ring weight is given by

$$W_R = p_f\,\left(\frac{L_R}{\sigma_y}\right)\,(2\pi r_i)$$

$$W_R = \pi\rho_f\,r_i^{\,2}\,\frac{\Delta\rho\,R_D}{\sigma_y}\sqrt{1-\left(\frac{r_i}{R_D}\right)^2}\,(1.25) \tag{A44}$$

where the structural design factor is assumed to be 1.25.

C. Conical Frustum

For the afterbody cone thicknesses, the equations derived previously for the face body, para A.3.2.1.1.2, are used with a pressure load of Δp:

$$t_{f,\,i} = \frac{\Delta p\,\bar{R}_i}{2\,\sigma_y} \quad \Phi_{s,\,i}\,;(t_f \geq .833\,X\,10^{-3}) \tag{A45}$$

$$t_{c,\,i} = \frac{\bar{R}_i}{\sqrt{3}}\left(\frac{\Delta\rho\,\bar{L}_i}{1.48E_f\,t_{f,\,i}}\right)^{2/3} \quad \Phi_{s,\,i}\,;(t_c \geq .0476) \tag{A46}$$

where

$$\bar{R}_i = \frac{r_i + r_{i+1}}{2 \cos \theta} \tag{A47}$$

and

$$\bar{L}_i = \frac{X_{i+1} - X_i}{\cos \theta} \tag{A48}$$

The overall thickness and the mean reference thickness are then given by eq. A38 through eq. A40.

D. Other Afterbody Geometries

For other afterbody geometries, the section is treated in structural calculations as a conical frustum with a half angle equal to

$$\theta = \tan^{-1}\left(\frac{r_{i+1} - r_i}{X_{i+1} - X_i}\right).$$

A.3.2.2 Ring Stiffened Shell

The ring stiffened shell is esentially a monocoque shell supported at various lengthwise locations. The minimum gage skin thickness is assumed to be .02 inches for all materials. The skin and rings may be of different materials.

A.3.2.2.1 Forebody

A. Spherical Segment

In the spherical segment, it is assumed that there are no internal supports. The required skin thickness for a spherical shell allowed to work at its yield stress under load $\bar{p}_s$, is given by

$$t_{s,1}^{(1)} = \frac{\bar{p}s\ {}^{1}R_N}{2\sigma_{ys}} \tag{A49}$$

In buckling, the critical load is

$$p_{cr} = \frac{.312\ Et^2}{R_N{}^2} \tag{A50}$$

Hence, the skin thickness required to resist buckling is

$$t_{s,1}^{(2)} = R_N\sqrt{\frac{3.21\bar{p}_s{}^{1}}{E_s}} \tag{A51}$$

Taking the greater of the two thicknesses given in eq. A49 and A51, the design skin thickness is given by

$$t_{s,1} = \text{Max}\left[t_{s,1}^{(1)} ; t_{s,1}^{(2)}\right] \Phi_{s,1}, (t_s \geq 1.6667 \times 10^{-3}) \tag{A52}$$

B. Conical Frustum

Each subsection of a cone frustrum section is treated as a circular cylinder of effective radius

$$\bar{R}_j = \frac{r_j + r_{j+1}}{2 \cos \theta_j} \tag{A53}$$

and effective length

$$\bar{L}_j = \frac{X_{j+1} - X_j}{\cos \theta_j} \tag{A54}$$

where j refers to the jth subsection of the cone frustrum.

For a cylindrical shell segment of thickness t, the hoop stress is

$$\sigma = \frac{p_j' \bar{R}_j}{t_j} \tag{A55}$$

If the skin is allowed to work at its yield stress the required skin thickness is given by

$$t_{s,j}^{(1)} = \frac{\bar{p}_j' \bar{R}_j}{\sigma_{ys}} \tag{A56}$$

We note, however, that yielding is a local function, and as such we must insure that the skin does not yield at any point in the jth subsection. Using the maximum value of the local effective radius, viz. $\bar{R}_j$ as given by eq. A53 as r_j approaches r_{j+1}, the required yield skin thickness is

$$t_{s,j}^{(1)} = \frac{\bar{p}_j' r_{j+1}}{\sigma_{ys}} \tag{A57}$$

In buckling the critical load is

$$p_{cr} = \frac{.74E}{\frac{\bar{L}}{R}\ \frac{\bar{R}}{t}}^{5/2} \tag{A58}$$

Thus, the required buckling skin thickness is given by

$$t_{s,j}^{(2)} = \left[\frac{p_j'\ \bar{L}_j\ \bar{R}_j}{.74\ E_S}^{3/2}\right]^{2/5} \tag{A59}$$

The design thickness is then taken to be the greater % of the two thicknesses given in eq. A57 and A59:

$$t_{s,j} = \text{Max}\left[t_{s,j}^{(1)},\ t_{s,j}^{(2)}\right] \Phi_{s,i}; (t_s \geq 1.6667 \text{X} 10^{-3}) \tag{A60}$$

The rings are designed to support the pressure load over the jth subsection. The load is $\bar{p}_j'\ \bar{L}_j\ r_j$. The ring weight is then given by

$$W_{R,j} = \rho_R\ (2\ \pi r_j)\ \frac{\bar{p}_j'\ \bar{L}_j\ r_j}{\bar{\sigma}_{yr}}\ \Phi_R \tag{A61}$$

C. Other Forebody Geometries

For forebody geometries other than a spherical segment or a conical frustrum, each subsection is treated structurally as a conical frustrum with an angle equal to the average of the extremity angles of the subsection.

A.3.2.2.2 Afterbody

For a ring stiffened shell afterbody, the thickness of the aftcover must be specified as input.

A.3.3 KNOWN STRUCTURAL REQUIREMENTS

In some cases the structural requirements may be known. In these instances the structural thicknesses for each geometric section of the forebody and/or for the aft cover may be specified as input to the program. For the honeycomb sandwich shell, both the face and core thicknesses can be specified.

A.4 RECOVERY SYSTEM SELECTION PROGRAM

A.4.1 INTRODUCTION

The Recovery System Selection Program (RESSEP) utilized within the General Electric Company to perform parachute selection on earth and planetary entry missions is herein described. A general description of the basic program and associated subroutines is provided with a detailed analysis of the design subroutine, where retardation system weights are generated. The primary application of the RESSEP computer technique is for preliminary design and parametric analysis purposes.

A.4.2 GENERAL PROGRAM

RESSEP is programed in FORTRAN IV for the GE 635 computer.

The program operation is conducted by the exective (EXEC.) subroutine. Input requirements, options, trajectory, vehicle characteristics, etc., are items discussed in the input (INPUT) subroutine. The atmospheric data required, as well as that available within the program are detailed under the atmospheric subroutine (ATMOS). With this direction and information, the RESSEP program procedes through parachute sizing and selection (SIZSEC) subroutine. Then it procedes through the staging (STAGE) subroutine where the final unperturbed trajectory match point to impact loadings, time delays, etc. are determined. The final retarded trajectory is determined in the trajectory subroutine (TRAJ). Then the weight, riser line lengths, etc. are selected in the last subroutine (DESIGN).

The various subroutines are described below.

A.4.2.1 Subroutine Exec

This subroutine merely directs the order of sequence of the program, and reflects good programming practice.

A.4.2.2 Subroutine Input

The inputs required to perform a deceleration system design and recovery trajectory are prepared. These inputs include: the terminal altitude and velocity; the reefing maximum force allowable calculation, the parachute type selection, the atmospheric, and the air snatch options; the drag, stability, porosity, loading, cost, and weight weighing factors; the values of vehicle diameter, payload mass, heat shield mass, and descent time; the unperturbed trajectory table of altitude, velocity, and path angle; and finally, if an atmosphere other than those carried within the program is required, a table of altitude, speed of sound, density and the gravitation constant for the desired atmosphere is submitted.

A.4.2.3 Subroutine Atmos

This subroutine contains the tables of altitude, speed of sound, density, and the gravitation constants for the most common atmospheres used for planetary entry. These include the 1962 Earth Standard Atmosphere, all current model atmospheres for Venus and Mars planetary entry, and of recent inclusion, the NASA Langley Minimum, Mean, and Maximum atmospheres for Martian entry.

A.4.2.4 Subroutine Sizsel

This subroutine has the capability of sizing and selecting the parachute and/or drogue chute types for the input mission. Selection of chute type utilizes input weighing factors and is also dependent upon deployment, Mach number and dynamic pressure. Selection can be made from the following parachute types: solid textile, flat circular, extended skirt, ribless guide surface, and personal guide surface, ribbon type: ring slot, ringsail, Fist Ribbon, Modified Ringsail, and Disc-Gap Band, and for supersonic use, the Hyperflo type.

Following selection, sizing is performed. Provisions are made for a maximum diameter, when fully deployed, of 100 ft; however, if necessary clustering can be accomplished, whereby the decreased effectiveness of clustered parachutes is also considered.

A.4.2.5 Subroutine Stage

This subroutine is by far the most complex currently within the RESSEP program.

The basic philosophy of this subroutine is to start with the terminal conditions desired and to back up the unperturbed vehicle trajectory until a "match point" is obtained. If this cannot be done with one chute, provisions for reefing, and/or 2 additional drag stages i.e., pilot, drogue, reefed main and main parachutes consists of four drag stages. Obviously, this is an interative procedure, and several initial approximations are assumed from which iterations can be made. Some of the considerations within this subroutine are maximum load calculations, filling time with and without reefing calculations, and opening shock calculations for each of the drag stages considered.

A.4.2.6 Subroutine Trajectory

This subroutine combines the results of the STAGE subroutine, the unperturbed trajectory, and the equations of motion similar to those of a point mass trajectory to determine the vehicle trajectory with retardation. Provisions are made for final fill time and opening shock calculations. In addition, a "linearized" atmosphere loop is available when decelerations become small at lower altitudes. This loop significantly reduces computer time and print out in the cases where it is applicable (acc. $\leq$ 0.01 g's).

A.4.2.7 Subroutine Design

A.4.2.7.1 Initiation

The subroutine starts with the maximum drag stage number, which has been determined by subroutine STAGE earlier in RESSEP. Provision for reefing must also be made, i.e., the reefed main is the same chute as the main, however, the drag stage number is different.

A.4.2.7.2 Number of Suspension Lines

The number of suspension lines is set equal to the parachute full open diameter in feet plus one.

A.4.2.7.3 Force on Suspension Line

Suspension line force is then equal to the maximum force imported to the vehicle divided by the number of suspension lines. Safety factors are then applied to this value. For the main chute, a safety factory of 1.75 is used, and for all other chutes required, a safety factory of 2.30 is used. Because of the possibility of small line force values under low loading conditions, a minimum strength value of 375 lbs. is employed, i.e., if, after safety factors have been applied, the suspension line force is below 375 pounds this line strength is selected.

A.4.2.7.4 Force on Riser Line

This quantity is determined by dividing the maximum force imparted to the vehicle (including safety factors of 1.5 for main chute and 2.0 for others) by 0.6859. The 0.6859 results from a multiplication of strength reducing factors such as strength loss at connection loops (20% i.e., 0.8), strength loss in material due to water vapor (5% i.e., 0.95), strength loss due to abrasion (5% i.e., 0.95), and strength loss due to fatigue (5% i.e., 0.95).

A.4.2.7.5 Length of Riser Line

An initial estimate of the riser line length is taken as 71.5 percent of the full open chute diameter. A check is then made to see if this is equal to or greater than 6 vehicle diameters. If it is, the riser length is taken as 0.2 of the full open chute diameter, and if it is not, the riser length is taken as 6 vehicle diameters less 71.5 percent of the full open chute diameter. This assures that a small parachute (drogue) is positioned a sufficient distance down stream to see near free-stream dynamic pressure.

A.4.2.7.6 Riser Line Weight

This calculation is dependent upon two quantities, the riser line length and the force it must withstand. Both are known at this point. A table of standard riser line ultimate strengths (lbs.) and accompanying weights (lb./ft.) are used where strengths

vary from 500 to 10,000 lbs. Thus, a comparison is made on the riser line force, with safety factor included, against this table of available riser line strengths until the internal tabular value exceeds the riser force requirement. The weight in lb./ft. of this strength line is then multiplied by the riser length to obtain the weight of the riser. If the 10,000 pound maximum ultimate strength available is exceeded, a provision has been made to re-cycle within the table and use a combination of lines to meet the force requirement.

A.4.2.7.7 Parachute Weight

Parachute weights for light, medium and heavy construction, based upon data and plots from ref. A-3 are used as a basis for Ringsail canopy plus suspension line weights in the program (fig. A-2).

Because the variations are linear on a log-log plot, they may be defined by an equation of the form:

$$\text{Chute Weight} = (\text{Chute Diameter}/a)^{1/m}$$

where "a" is a constant to define location (varies with material weight) and "m" is the slope. Thus, an internal table of "a" and "m" values for each type of chute and for each material weight would be required. However, it has been found that the "a" value also varies linearly on a log-log plot with the suspension line force, i.e.,

$$a = (\text{Suspension Line force}/A)^{1/M}$$

By incorporating tables of m, A, and M for each chute type and solving these equations, the parachute weight is obtained.

The DESIGN subroutine first calculates the "a" value utilizing the chute type, the suspension line force calculated earlier, and the tabular inputs of "A" and "M" from the internal table. It then calculates the parachute weight utilizing the chute type, the full open diameter, the tabulation input of "m" from the internal table, and the "a" value just determined.

A.4.2.7.8 Air Snatch Option

If air snatch is desired, the main chute weight is increased by 11 percent to cover the increased weight and associated hardware required for the air snatch. This percentage was determined from a careful analysis of the weight breakdown of several working retardation systems, which include the H 30A system, the GE 810 system, and the Apollo C/M system.

A.4.2.7.9 Final System Weight

The final parachute system weight consists of adding the canopy plus suspension line weight to the riser line weight. A 25 percent increase in system weight is also incorporated to allow for associated hardware commensurate with the satisfactory deployment and operation of a retardation system. This value resulted from an evaluation of the weight breakdown of numerous working recovery systems.

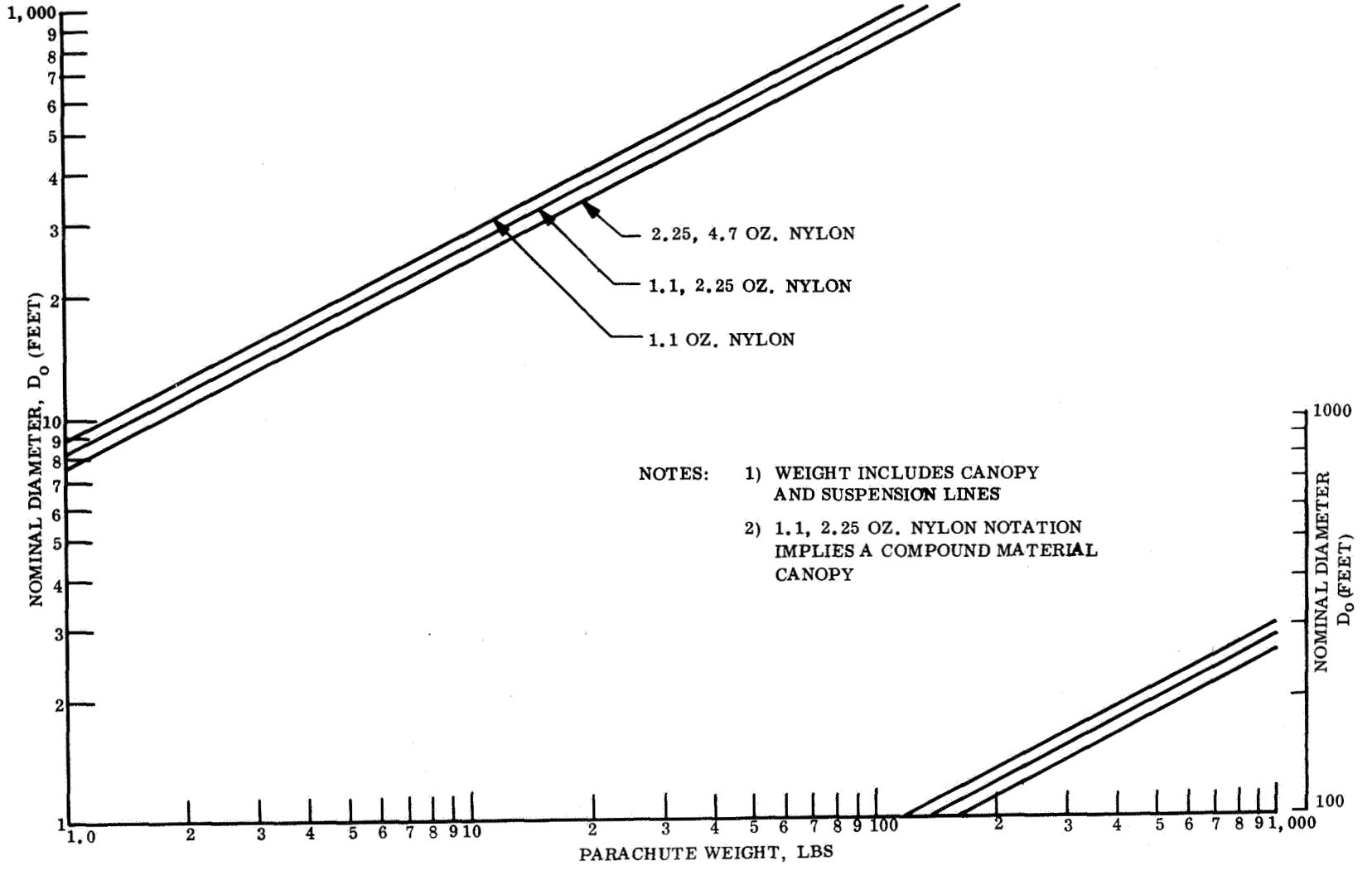

Figure A-2. Parachute Weight Variation with Diameter, Ring-Sail Canopy

A.5 COVER EJECTION PROGRAM

The calculation of the cover ejection characteristics is performed by a computer program following a method originally suggested by Wilcox, Reference A-4. The approach is basically to determine the relative acceleration between the cover and the vehicle.

$$\ddot{X}_{relative} = \ddot{X}_{cover} + \ddot{X}_{vehicle}$$

where

$$\ddot{X}_{cover} = \ddot{X}_{wake\ flow} + \ddot{X}_{attached\ body} + \ddot{X}_{external\ force}$$

The $\ddot{X}$ due to wake flow is that acceleration resulting from the drag force (positive or negative) of the aerodynamic wake. The $\ddot{X}$ due to an attached body can account for the force produced by another drag body located at another location in the wake and attached to the cover by a line (for example a drogue parachute located downstream of the cover and aiding in its deployment). The $\ddot{X}$ due to an external force (thrust, for example) allows a constant force to be applied to the cover which would aid in its deployment. In the present case, $\ddot{X}_{attached\ body} = \ddot{X}_{external\ force} = 0$. This leaves the acceleration due to the wake flow. A reverse flow portion exists which tends to counter the ejection of a body until the body has passed through the wake stagnation point. This reverse flow sets up a drag force on the body which decreases its initial ejection velocity. If the drag force is sufficiently strong, it can cause the ejected body to return to the vehicle. Further, due to the deceleration of the vehicle itself, caused by its own drag and the lack of a similar freestream drag on the body in the wake until sufficiently aft of the vehicle, there is a tendency for the body to return to the vehicle. That this phenomenon of the body returning to the parent vehicle occurs has been demonstrated in wind tunnel, ballistic range and drop tests.

Since little was known of the magnitudes of the drag forces produced by the wake flow, GE conducted wind tunnel tests on the RVX1 and RVX2 (1958) and Discoverer (1960) programs to determine the forces produced on relatively flat covers placed in the wake of a re-entry configuration. On the basis of these tests, measures of the magnitudes and directions of forces in the wake were made, and employed in the program.

Since the velocity of the cover opposes the velocity of the reverse flow region and parallels that of the far wake, it was necessary to break the force measured in the wake down to an effective dynamic pressure (q_W). From this q_W, the wake velocity can be calculated and the cover velocity added or subtracted to arrive at the relative velocity. The force on the cover is then determined using this relative velocity. In order to perform the correlation of available data, the measured force on the cover in the wake and thus the effective q_W was assumed to follow a sine wave

variation from the vehicle base to the point in the wake where the force was zero (F = 0).

$$\frac{q_W}{q_\infty} = \frac{(q_W)_{max}}{q_\infty} \sin \frac{(\pi X)}{X_{F=0}}$$

From the point for F = 0 on downstream and exponential variation was assumed.

$$\frac{q_W}{q_\infty} = 1.0 - e^K$$

where

$$K = \frac{2.52\ X_{F=0}}{7.0 - X_{F=0}} - \frac{2.52X}{7.0 - X_{F=0}}$$

From these equations, the two parameters to be correlated are (q_W/q_∞) max and $X_{F=0}$. These two correlations of static force data provide the necessary inputs to the computer program along with cover ejection velocity, mass freestream conditions, etc.

Using the wake model, the cover motion is calculated for incremental positions in the wake (increments of X/D = 0.05 are usually used). Outputs from the computer program are time, acceleration, and velocity of the cover as functions of location in the wake.

A.6 REFERENCES

A-1 Segletes, J. "Thermal Degradation of a Thermo Setting Plastic", GE-RS #62SD202, November 1962.

A-2 Kyriss, C., "CONSEP IV Program Operating Procedures and Description", a forthcoming General Electric Company document.

A-3 E. G. Ewing, "Ringsail Parachute Characteristics", Radioplane Report No. PTM-323-A, January 1961, Rev. A, July 1961.

A-4 Wilcox, B., "A Method for Computing the Relative Motion Between a Ballistic Vehicle and a Capsule Ejected from the Base of the Vehicle", GE MSVD ADM No. 4:63, February, 1961.

APPENDIX B
SEPARATION TIP-OFF ANALYSIS AND V-BAND LOADING CONSIDERATIONS

APPENDIX B
SEPARATION TIP-OFF ANALYSIS AND V-BAND LOADING CONSIDERATIONS

This Appendix presents the analyses of the loads acting on the canister separation joint and the tip-off imparted to the capsule as a result of separation from the Orbiter.

B.1 SEPARATION TIP-OFF ANALYSIS

This analysis considers the tip-off imparted to the capsule (aeroshell, lander, retro rocket) as a result of separation, using simplified body dynamics.

B.1.1 ASSUMPTIONS

1. There are no rates associated with orbiter at separation.

2. Orbiter has the same pitch/yaw inertia and weight as the capsule.

3. The attachment rings between capsule and adapter have flat contact pads and are not distorted; therefore their energy is equally released during separation and all spring energy is used for separation.

4. The tip off occurring during the spring action is so small that the cosine vector is negligible for this simplified analysis.

B.1.2 CONCLUSIONS AND RECOMMENDATIONS

The out-of-orbit mission without attitude control capability (Point Design 1) requires tip-off rates of less than 0.3°/sec. instead of 2.0°/sec. as the contribution from separation. The recommended design is a modification of case "c" to allow for the added considerations discussed below. Pertinent data on the recommended spring and others discussed here is presented in table B-1.

To guarantee spring performance, it should be operated in the linear portion of its total available stroke; thus the available stroke is increased 20 percent over the required stroke from the separation energy requirements. In addition, to the above, trimming of the spring is required, and it is desirable to have the spring in a sub-assembly, completely bench tested and adjusted. For the proposed adjustable sub-assembly, it is necessary that the solid height (Ls) of the spring be longer than the stroke. The recommended spring material was changed from 302 to NS355* to reduce weight and eliminate load relaxation at the sterilization temperature. The spring assembly consists of telescoping sleeves with adjustable stops at both ends. The inner sleeve will be coated with Teflon on both inner and outer surfaces to minimize friction.

---

*National Standard Company.

TABLE B-1. SEPARATION SPRING DATA

	F #	wire d in.	do in.	f in/coil	x 153/F	N x/f	$\frac{d(N+2)}{I_S}$ in.	LS L_F in.	WT/SPG #	k F/*	k/ko k/17	Wc o/sec	Uncorr. Ss PSI
Orig. Pt.#1	51.0	.135	1.485	.275	3.0	10.9	1.74	4.74	*.216	17.0	1.0	.99	90,000
Case A	53.1	.121	1.250	.252	2.88	11.4	1.62	4.50	.153	18.5	1.1	.94	101,000
B	89.60	.135	1.000	.122	1.71	14.1	2.18	3.89	.175	52.5	3.1	.56	99,000
C	102.0	.148	1.150	.147	1.50	10.2	1.81	3.31	.085	68.2	4.0	.56	97,200
D	152.4	.177	1.250	.134	1.01	7.54	1.69	2.70	.221	151.0	8.9	.33	93,800
E	208.6	.207	1.400	.134	.74	5.5	1.55	2.29	.244	282.0	16.6	.24	90,000
New Pt.#1	120.0	.148	1.034	.126	1.60	12.7	2.19	3.79	**.198	75.0	4.4	.29	110,000

*The point design #1 spring is heavier because of the lower allowable stress to compensate for creep, life and temperature.

**Spring design based NS355 stainless steel with higher allowable stress.

B.1.3 SUBSYSTEM DESIGN FOR 2^{o}/SECOND

I_P	110 slug ft^2	110 slug ft^2
W_T	1500 lbs	1500 lbs
E	0.0	0.7

Standard Manufacturing errors of spring are:

spring rate, k, - ±4.5%

initial load, P, - ±7.4%

free length, L, - ±3.6%

The 1st cut separation springs for the capsule have an initial load of P of 51.0 lbs and a rate of 17.0 lbs/in.

The torque producing forces are oriented such that the two springs with the higher force are contiguous and act with the largest moment arm. Using the notation from the sketch, then, the torque is:

$$T = 2 F_H R_H - 2 F_L R_L$$

where

$$F_H = F\left(1 + \frac{\Delta F}{F}\right); F_L = F\left(1 - \frac{\Delta F}{F}\right)$$

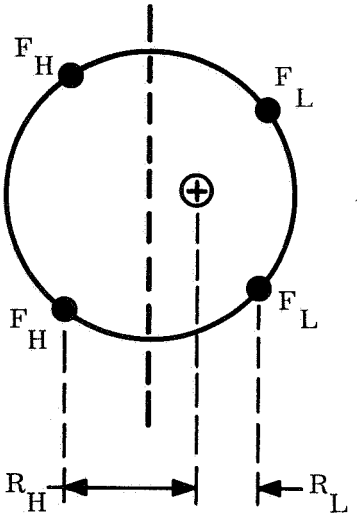

$$T = 2F \left[\left(1 + \frac{\Delta F}{F}\right) R_H - \left(1 - \frac{\Delta F}{F}\right) R_L \right]$$

$$R_H = \frac{(DIA)}{2} \text{ SIN } 45 + E; \; R_L = \frac{(DIA)}{2} \text{ SIN } 45 - E$$

$$T = \frac{2 \times 51.0}{12} \left[(1.074)\ (28-98) - (.926)\ (27.58)\right]$$

$$T = 47.5 \text{ lb-ft}$$

Since the spring force decays as f (cos (t)), it is assumed that the average torque is 0.707T.

The tip-off rate, W, is calculated from

$$Tt = I \quad W$$

t = is the time of action of the springs, where

$$t = \frac{II}{2} \sqrt{K/M}, \text{ for one quarter cycle}$$

$$= \frac{\pi}{2\sqrt{K/M}}$$

$$t = \frac{II}{2\left(\frac{17x12x4x32.2}{750}\right)} .5 \quad \text{, where equiv. mass/spring } = \frac{750}{4}$$

$$t = \underline{0.266 \text{ sec}}$$

The equivalent inertia of the two bodies, I_e

$$I_e = \frac{(Ic)\ (Io)}{Ic + Io} = \frac{110 \times 110}{2 \times 110} = \underline{55.0 \text{ Slug-ft}^2}$$

$$W = \frac{Tt}{I_e} = \frac{(47.5 \times 0.707 \times 0.266)}{55.0} \; 57.3$$

= 9.3°/sec, total relative tip-off rate between the orbiter and the capsule.

The rate for the capsule alone is

Wc = 4.65°/sec, for equal inertia case.

This rate is greater than the requirement for 2°/sec and by selective spring installation and reducing c.g. off set it can be reduced to 1.5°/sec as follows:

1. Select springs so that the load difference between diametrically opposite spring is less than 2 lbs.

2. Reduce allowable c.g. off set to 0.1 inch.

With the springs mounted as shown below (worst case) the tip-off rate becomes:

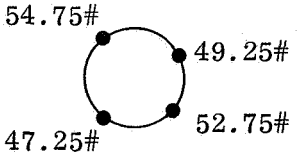

$$F \pm 7.4\% = 51 \pm 3.75 \text{ lbs}$$

$$T = \frac{(54.75 + 49.25)\ 28.38 - (47.25 + 52.75)\ 28.18}{12}$$

$$= \frac{(2945 - 2818)}{12} = \underline{\underline{10.6 \text{ lbs/ft}}}$$

$$Wc = \frac{10.6}{47.5} \times 4.65 = 1.04°/\text{sec}$$

B.1.4 SUBSYSTEM DESIGN FOR 0.5°/SECONDS

Tip-off rates can be further reduced effectively without substantial spring trimming and selection by increasing the spring constant. Increasing "K" by a factor "n", reduces "t" by $\sqrt{n}$ and consequently "w" is reduced by $\sqrt{n}$. Although, theoretically there is no change in weight by varying the spring constant, the effect of increasing k is to reduce the number of active turns and thus the spring weight actually incrases because of the larger proportion to weight contributed by the "dead" end coils. A higher "k" also requires an increase in wire diameter with attendant lower allowable stress. Fig. B-1 reflects springs selected from a table, with the pertinent data summarized below.

New spring design recommended for Point Design 1 (see table B-1 for spring detail data) spring material - National Standard NS355 stainless steel.

Ult. Tensile Str. = 330,000 PSI for up to 0.159 inch wire

Torsional Shear - 45% x UTS = 148,000 PSI

Initial load - 108 lbs at 0.16" from solid

Final load - 12 lbs at 1.44" from solid

Max. load - 120 lbs. at solid height

Max. stroke, Xm = 1.60"

Operating stroke - 1.60" - 20% (1.60) = 1.28"

Energy Req'd - 25.5 Ft/lbs

Energy Avail. - $\frac{(108 + 12)}{2} \frac{(1.28)}{12}$ (4 springs) = 25.6 Ft/lbs

Control Spring Rate to 75 ± 3% lbs/in

Adjust Spring to 108 ± 2 lbs Initial Load

Install Springs, so that diametrically opposite springs have an initial load within .5 lb.

B.1.5 TIP-OFF CALCULATION

Worst case assembly condition, c.g. offset and spring alignment is depicted below.

c.g. offset, E = .1

error in SPG ℄action ± .025"

E tot = ±.11"

$$T = \frac{(216.5 \times 28.39 - 215.5 \times 28.17)}{12}$$

T = 6.32 Ft/lbs

The new tip off rate predicted on a worst case basis is

$$Wc = 1.04 \times \frac{6.17}{10.6} \times \sqrt{\frac{17}{75}} = .29°/sec$$

The effect of the initial assumptions in orbiter mass properties on the tip-off rate is as follows:

$$Wc = Wt \frac{I_o}{I_o + I_c}$$

$$Wt \sim \frac{1}{Ie}, \quad Ie = \frac{Io \times Ic}{Io + Ic}$$

$\therefore Wc \sim \frac{1}{Ic}$, thus the capsule tip-off rate is independent of the orbiter's moment of inertia.

The mass of the spacecraft affects the time constant.

$$Wc \sim Wt \sim t \sim \sqrt{Me}$$

Me = Mo x Mc/(Mo + Mc), therefore an increase in orbiter weight increases the tip off rate. This relationship is plotted in fig. B-2 for orbiter mass to capsule mass ratios of 0.4 to 1.6. Similarly, the effect of changing the mass of capsule affects Wc as follows:

$$Wc \sim Wt \sim t \sim \sqrt{Mc1/Mc2}$$

Tip-off rates imparted to capsules of different mass properties can be converted by using the following relationship

$$W_{(new)} = W_{(orig)} \left(\frac{110}{Ic}\right) \sqrt{\frac{Mc}{1500}} \quad K$$

where K is correction for orbiter mass from fig. B-1, and Mc is the capsule weight in lbs.

$$W_n = 0.85 \frac{\sqrt{Mc}}{Ic} K, \text{ deg/sec}$$

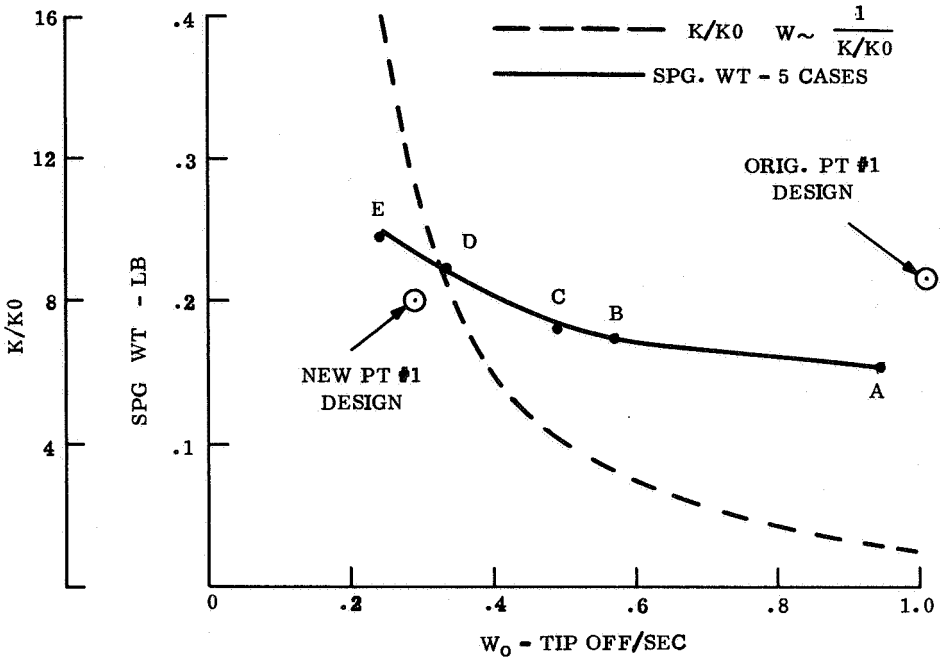

Figure B-1. Capsule Separation SPG Wt Versus Tip-off Rate and SPG Cor Ratio Versus Rate Change

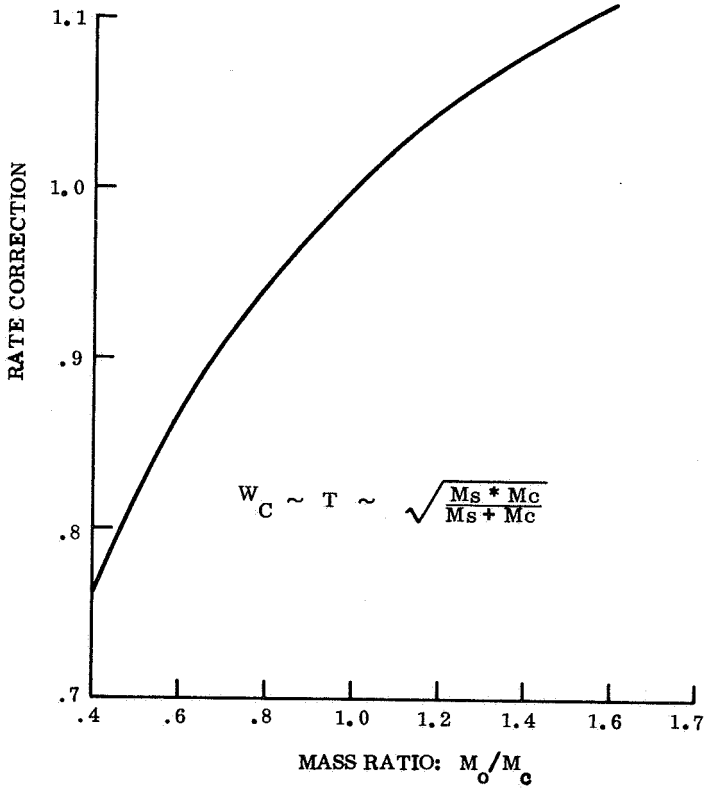

Figure B-2. Correction to Capsule Tip-off Rate as a Function of Orbiter to Capsule Mass Ratio

B-2. V-BAND LOADING CONSIDERATIONS

This appendix presents the analysis of the loads acting on the separation joint and the analysis of the V-Band to resist these loads.

The factors directly affecting the normal load to be resisted by the band preload are:

1. Internal pressure
2. Canister diameter
3. Load required to seal the joint - flattening load + "O" ring compression load
4. Dynamic loads during launch and ascent
5. Separation spring force

The contribution of each of the above factors in terms of normal load/running inch of circumference which the band must provide to maintain a sealed joint is discussed below.

1. Pressure Load:

$$F_N = \frac{\Delta PA}{C} = \frac{\Delta P \pi D^2}{4 \pi D} = 3 \Delta PD, \text{ lb/in}$$

where ΔP = Max Diff Pressure in, lb/in^2 D = can. dia-ft

ΔP lb/in^2	Diam Ft.	Normal Force F_N #/In
1	8	24
	16	48
3	8	72
	16	144
5	8	120
	16	240

2. Dynamic Load on Forward Canister:

$$F_N = \frac{A_x W_c}{\pi D} + \frac{2A_y W_c h}{D^2}$$

where A_x, A_y are booster accelerations, h = vertical height from c. g. of forward canister, W_c = weight of forward canister. It is assumed that the moment load is carried over an arc = to 1/2 diameter in length.

For A_x = 5g's, A_y = 2. 0g's, h = 12 in., W_c = 40 lb., D = 8 ft.

$$F_N = \frac{5x40}{\pi x8x12} + \frac{2x2x40x12}{(8 \times 12)^2}$$

= 0. 66 + 0. 28 = 0. 94 lb/in

For W_c = 100 lb., D = 16 ft. (Canister weight increases 2-1/2 times when diameter doubles)

F_N = . 83 + . 18 = 1. 01 lb/in.

This will be considered a constant force of 1. 0 lb/in.

3. The total force required to create a pressure tight seal has two contributors - one, the force to compress the "O" ring, which for 30 percent compression of 50 durometer silicone rubber is 12 lb/in. and; second, the force required to bring the canister rings into contact. This later force is a function of out of flatness or waviness of the rings, and their inertia. For a uniformly loaded simple beam the uniform load w, lb/in. is given by:

$$w = \frac{384\ E\ I\ d}{5\ 1^4\ I}$$

Three limiting cases were considered, based on manufacturing capability, where the unrestrained out flatness of the forward ring was:

a) 0. 005 in. max over a 12 in. length

b) 0. 50 in. max over a minimum arc length of 1/4 diameter

c) 0. 010 in. max over a 24 in. length

It is assumed that the inertia of the aft ring + canister structure is 5 times greater than inertia of the forward ring and its light weight structure; whereby the clamping force brings the fwd. canister into contact with the aft canister. The ring cross section given in Figure 3.3.3-6, Vol. IV, Book 1 was used, where I = 0.062 IN^4 and the ring material is aluminum. The load for the 3 cases was:

d = 0.005 in.; w = 12.3 lb/in.

d = 0.50 in.; w = .81 lb/in.

d = 0.010 in.; w - 2.0 lb/in.

Condition (a) above cannot be tolerated because of high loading.

4. Separation Spring Force:

The force required to impart 2 FT/Sec Δ v to a 40 lb. canister using a two inch spring stroke is:

$$P = \frac{MV^2}{X} = \frac{40 \times 2^2}{32.2 \times 2} = 29 \text{ lb.}$$

$$F_N = \frac{\Delta P}{\pi D} = \frac{29}{\pi \times 8 \times 12} = 0.1 \text{ lb/in.}$$

This force is negligible.

From the above analyses it can be concluded that the normal force is largely influenced by the choice of Δ P and the canister diameter.

Table B-2 below recaps the range of normal force expected:

TABLE B-2. NORMAL FORCE - lb/in.

Load Condition	Capsule 8 Ft	Diameter 16 Ft
ΔP	24-120	48-240
Dynamic	1 ± 1/4	1 ± 1/4
"O" Ring Seal	3-12	3-12
Flatness	1-2	1-2
Spring	.1 ± .02	.12 ± .02

The nominal normal force, F_{Nn} can be expressed as:

$$F_{Nn} = 3 (\Delta P) (D) + 15,$$

The limit normal force, based on proof pressure is:

$$F_{N1} = 1.25 \left[3 (\Delta P) (D)\right] + 15,$$

The ultimate normal force, based on burst pressure is:

$$F_{N\mu} = 1.67 \left[3 (\Delta P) (D)\right] + (15)\ 1.25$$

Fig. B-2 plots the above equations with the yield and ultimate factors incl.

The relationship between the normal clamping force required and the tension that must be applied to the band is obtained from the hoop tension equation and the slipper/ring geometry.

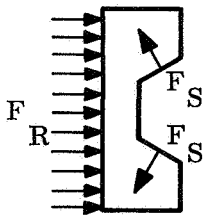

The tension force on the strap, F_t, produces a unit radial force F_R, lb/in.

$$F_R = \frac{2 F_t}{D}, \text{ where D - dia.}$$

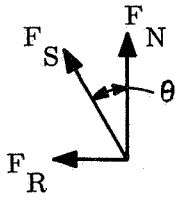

The rings act on the slipper with a force F_s, such that

$$F_R = F_N \tan\theta \text{ ; thus}$$

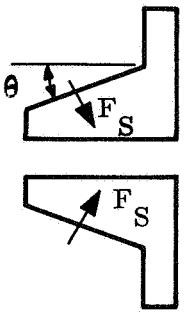

$$F_t = \frac{F_N D \tan\theta}{2}$$

The above equation gives the theoretical band load. It must be increased to guarantee the minimum clamping force needed for a tight seal by the following factors: 10 percent variance in preload throughout the circumference and ± 10 percent variation in actual load as obtained from the tensioning procedure. Therefore the nominal preload = 1.21 ft and the maximum preload = 1.32 ft. The band must withstand this maximum preload based on the limit normal load without yielding and because of the long duration space voyage, the allowable design stress will be 60 percent of creep allowable stress. The band must also withstand rupture under ultimate load conditions. Fig. B-4 shows the maximum band preload for various internal canister pressures. The effect of decreasing the slipper contact angle, θ, is shown for 5 psid systems.

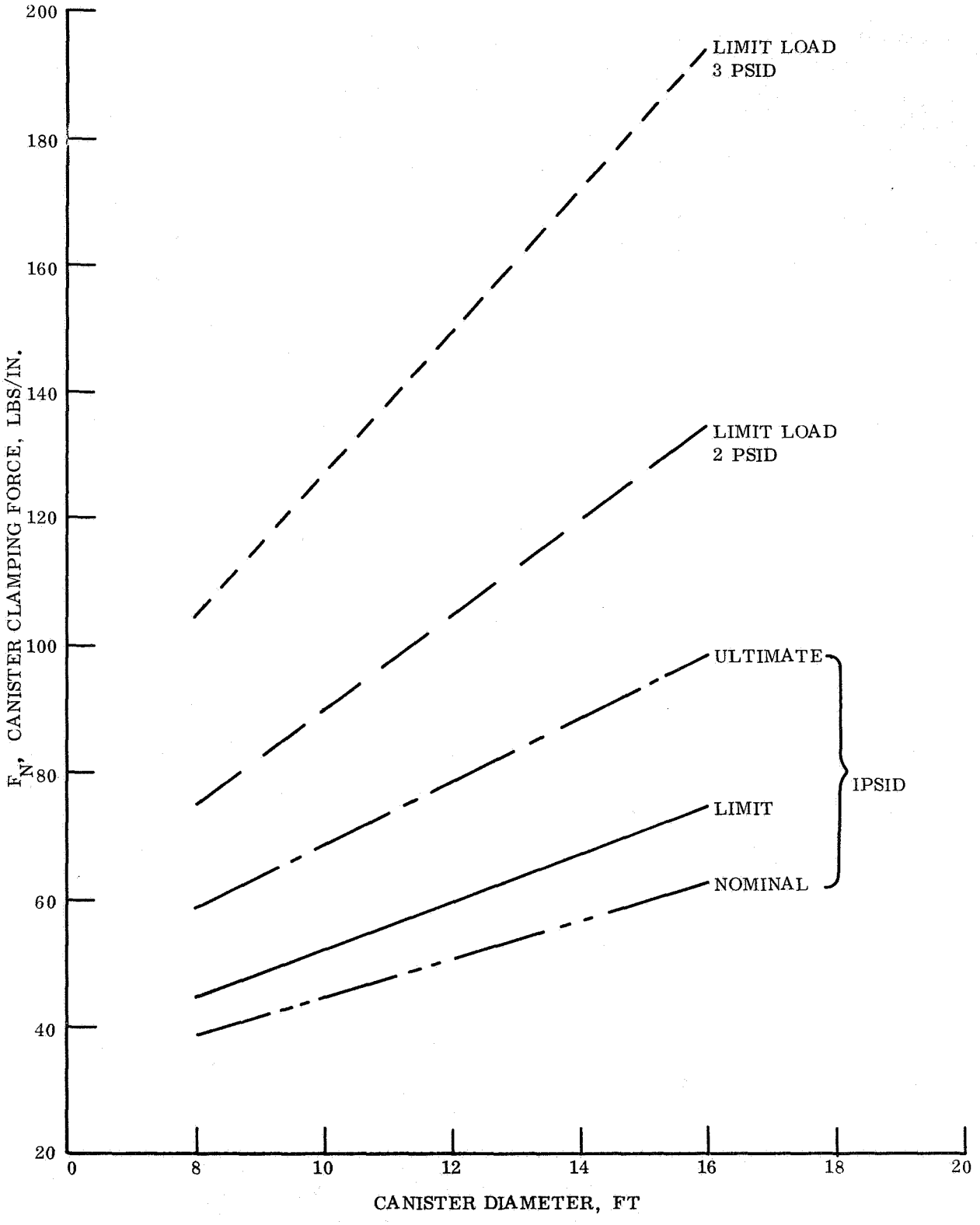

Figure B-3. Band Tension Load vs Canister Diameter and ΔP

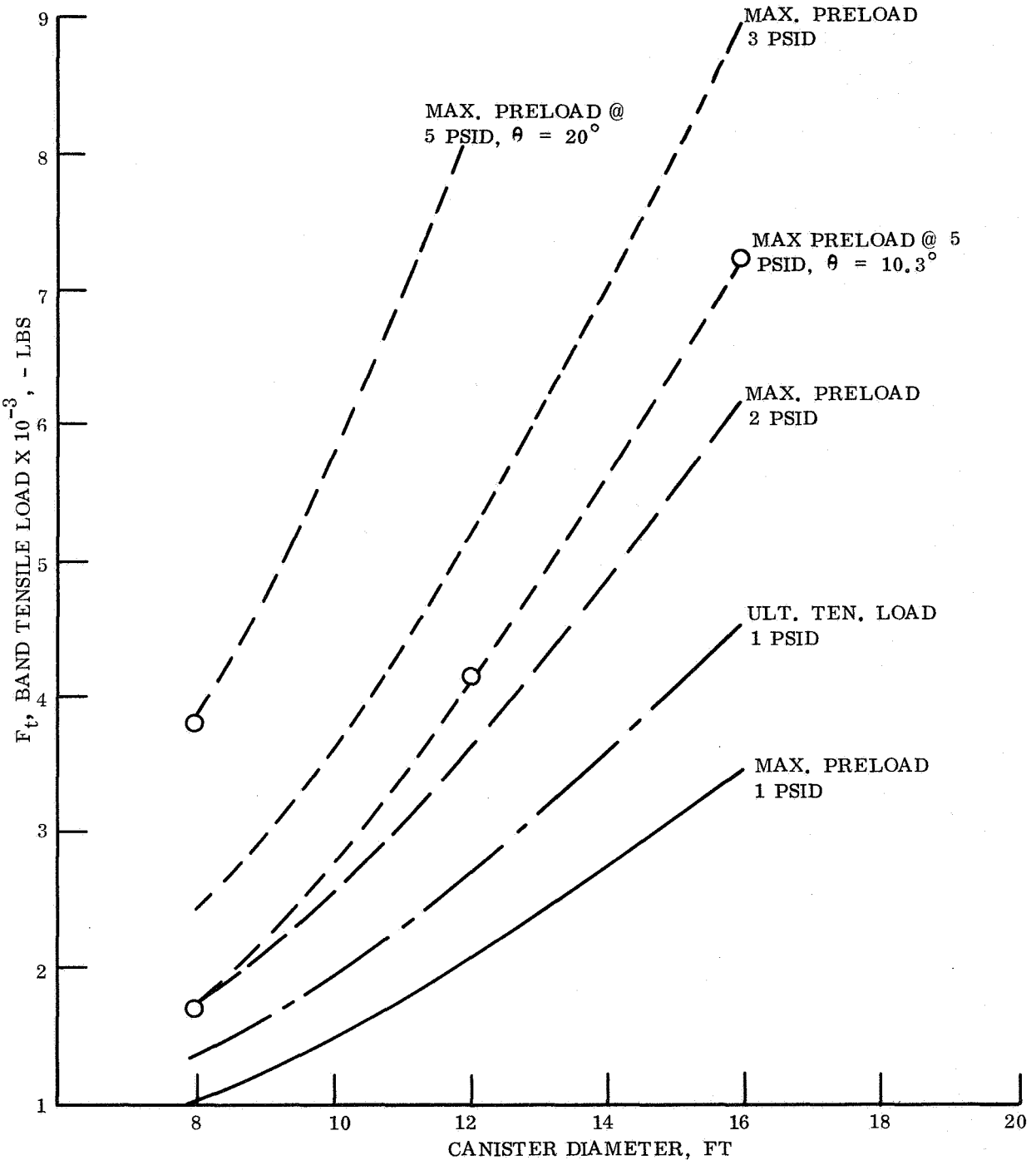

Figure B-4. Clamping Force Required at Canister Separation Joint vs Canister Diameter and ΔP

This approach would require additional separation testing, since most of the experience has been with a 20° angle.

A band material of aluminum alloy 2024-T86 was selected as having optimum high temperature, creep, temperature recovery, toughness, and notch sensitivity properties combined with high basic yield and ultimate stress. For the expected conditions, the allowable stresses are: (Per MIL-HBK-5)

Stu - room temperature stress = 0.97 x 72000 = 69,800 psi

Sty - after exposure to $+300^{\circ}$ F = 0.97 x 67000 = 65,000 psi

Sty - at $+ 300^{\circ}$ F = 0.82 x 67,000 = 55,000 psi

Sty - creep allowable = 0.80 x 72000 x 1.1 = 63,400 psi

(The creep allowable is increased 10 percent, because of operation at low temperature.)

Inspection of the load conditions and allowable stresses show that the limit load condition is the governing design case, therefore the parametric study of band size is based on yield stress.